

# The Gaseous Exchange of Ozone at Terrestrial Surfaces: Non-stomatal Deposition to Grassland

*Mhairi Coyle*





# **The Gaseous Exchange of Ozone at Terrestrial Surfaces: Non-stomatal Deposition to Grassland**

Mhairi Coyle

University of Edinburgh



## Declaration

I declare that the thesis has been composed by myself and the work is my own or the result of collaboration with colleagues at CEH-Edinburgh (as indicated). It has not been submitted for any other degree or professional qualification except as specified here.

Mhairi Coyle, April 2005



# Contents

Declaration .....	5
Contents .....	i
List of symbols, abbreviations and acronyms .....	v
Abstract .....	xi
Acknowledgments.....	xiii
1 Ozone in the Atmosphere .....	1-1
1.1 Tropospheric vs. Stratospheric.....	1-2
1.2 Chemistry of O <sub>3</sub> Production in the Troposphere .....	1-3
1.3 The Global, Regional and Local Ozone Budget .....	1-5
1.3.1 Seasonal Cycle.....	1-6
1.3.2 Local Scale and the Diurnal Cycle .....	1-8
1.4 Effects of ozone on human health, vegetation and materials .....	1-11
1.4.1 Effects on Vegetation: thresholds and critical levels.....	1-11
1.4.2 Effects on Human Health: thresholds and critical levels.....	1-14
1.4.3 Effects on Materials: thresholds and critical levels .....	1-15
1.5 Global and UK Ozone Trends .....	1-16
1.5.1 Precursor Emissions.....	1-16
1.5.2 Historical Trends .....	1-17
1.5.3 Current and Future Trends.....	1-18
1.6 Hypothesis, Objectives and Thesis Plan .....	1-21
2 Measuring the Ozone Flux: Micrometeorological Theory and Methods.....	2-25
2.1 Introduction.....	2-25
2.2 Structure of the PBL.....	2-25
2.3 Gradients and Stability in the Surface Layer .....	2-27
2.3.1 Neutral Conditions (Fully-Forced Convection) .....	2-27
2.3.2 Unstable (Mixed or Free Convection).....	2-27
2.3.3 Stable (Damped or No Convection) .....	2-28
2.4 Describing the Surface Layer and Measuring Fluxes .....	2-28
2.4.1 The Eddy-Correlation Method.....	2-30
2.4.2 The Aerodynamic Gradient Method .....	2-31
2.4.3 The Bowen Ratio .....	2-34
2.4.4 Practical Consideration and Limitations of Micrometeorological Methods.....	2-35
2.5 Ozone Deposition and the Resistance Analogy.....	2-40
2.5.1 Measuring the Components of Total Canopy Resistance .....	2-45
3 Modelling the Dry Deposition of Ozone .....	3-57
3.1 Current Ozone Models .....	3-57
3.1.1 Global Ozone Models.....	3-57
3.1.2 Regional Ozone Models .....	3-59
3.1.3 Local Scale Models .....	3-60
3.2 Methods of Treating of Dry Deposition and Proposed Models for the Grassland Site.....	3-62
3.2.1 Parameterising Aerodynamic Resistance, $R_a$ .....	3-62
3.2.2 Parameterising Boundary-Layer Resistance, $R_b$ .....	3-63
3.2.3 Modeling Stomatal Resistance, $R_{c1}$ .....	3-63
3.2.4 Models for Non-Stomatal Resistance, $R_{ns}$ .....	3-70
4 Measurements of Ozone Flux to Grassland: Experimental Setup and Characterisation of the Field-site.....	4-71
4.1 Introduction.....	4-71
4.2 Site Location and Topography.....	4-71
4.3 Site Management: Harvests, Grazing, Experiments .....	4-72
4.4 Vegetation Measurements.....	4-74

4.4.1	Vegetation Survey .....	4-74
4.4.2	Canopy Height ( $h$ ) .....	4-75
4.4.3	LAI – Leaf Area Index.....	4-78
4.4.4	Photosynthesis – Stomatal Resistance.....	4-78
4.5	Instrumentation: Setup and Operation .....	4-79
4.5.1	Standard Meteorological Measurements and Energy Balance (BR system).....	4-79
4.5.2	Ozone, Wind-speed and Temperature Gradient .....	4-89
4.5.3	Eddy-Correlation: Turbulence, CO <sub>2</sub> , Water-vapour, Ozone.....	4-95
4.5.4	Other Measurements: Soil Water Content, Present Weather .....	4-101
4.6	Data Treatment (QA/QC) and Preliminary Analysis .....	4-102
4.7	Site Meteorology .....	4-111
4.7.1	Wind Direction.....	4-111
4.7.2	Wind-speed.....	4-113
4.7.3	Ambient Air Temperature .....	4-114
4.7.4	Total Solar Radiation ( $St$ ) and $PAR$ .....	4-115
4.7.5	Rainfall, Surface Wetness and Soil Water Content.....	4-120
4.8	Summary.....	4-123
5	Measurements of Ozone Flux to Grassland: .....	5-125
5.1	Introduction .....	5-125
5.2	Data Treatment and Quality .....	5-125
5.2.1	Gradient Data .....	5-125
5.2.2	Eddy-correlation Data.....	5-127
5.2.3	Wind Direction and Fetch .....	5-137
5.2.4	Displacement Height, $d$ .....	5-140
5.2.5	Storage Correction .....	5-141
5.2.6	O <sub>3</sub> /NO <sub>x</sub> or VOC Chemistry .....	5-141
5.2.7	Gradient vs. Eddy-correlation Results for $u^*$ and $H$ .....	5-142
5.2.8	Closing the Energy Balance .....	5-143
5.3	Aerodynamic Resistance, $R_a$ and Boundary Layer Resistance, $R_b$ .....	5-147
5.4	Ozone Concentration and Flux.....	5-148
5.4.1	Ozone Concentrations.....	5-148
5.4.2	Total Ozone Fluxes.....	5-154
5.4.3	Total Canopy Resistance and Deposition Velocity .....	5-160
5.5	CO <sub>2</sub> and Water-vapour Fluxes, Stomatal Conductance and $R_{c1}$ .....	5-163
5.6	Silage Harvests.....	5-168
5.7	Day-time vs. Night-time Deposition .....	5-172
5.8	Summary.....	5-181
6	What Controls Ozone Deposition to the Canopy? .....	6-183
6.1	Modelling Fluxes at Easter Bush.....	6-183
6.1.1	Introduction.....	6-183
6.1.2	Parameters for <i>Lolium Perenne</i> .....	6-183
6.1.3	Parameterising the Jarvis Type Models (Jmod and JmodG).....	6-184
6.2	Comparison of Measured and Modelled Stomatal Conductance .....	6-190
6.2.1	Leaf-level measurements in the field .....	6-190
6.2.2	Results for the canopy-scale.....	6-192
6.3	Stomatal vs Non-stomatal Flux.....	6-195
6.4	What Controls Non-Stomatal Resistance .....	6-196
6.4.1	Measured $R_{ns}$ in Dry-Daylight Conditions .....	6-196
6.4.2	The $R_{ns}$ Temperature Response .....	6-198
6.4.3	Other Factors Influencing $R_{ns}$ .....	6-203
6.5	A Model of Total Canopy Canopy Resistance .....	6-211
6.5.1	Parameterisation of $R_{ns}$ in JModG.....	6-212
6.5.2	Measured and Modelled Total Canopy Resistance.....	6-213
Addendum	.....	6-215

7	Errors and Uncertainties.....	7-219
7.1	Systematic Errors .....	7-219
7.2	Random Errors .....	7-220
7.3	Errors in the Easter Bush Results .....	7-221
7.3.1	Measurements .....	7-221
7.3.2	Derived Values.....	7-225
7.3.3	Models.....	7-230
7.3.4	Overall Uncertainty in $R_{ns}$ .....	7-231
8	Synthesis and Conclusions.....	235
8.1.1	Ozone Deposition and Water-vapour/CO <sub>2</sub> Fluxes over Grassland .	236
8.1.2	Measured and Modelled Stomatal Resistance - $R_{cl}$ .....	237
8.1.3	Processes Controlling $R_{ns}$ and a New Model Parameterisation .....	239
8.1.4	Conclusions .....	242
8.1.5	Future Work .....	243
	<i>Appendix A</i> Suppliers and Manufactures of Instrumentation .....	245
	<i>Appendix B</i> Tables of Summary Data .....	247
	<i>Appendix C</i> Relevant Publications.....	265
	<i>Appendix D</i> Simple Aqueous O <sub>3</sub> /SO <sub>2</sub> /NH <sub>3</sub> Chemistry Model.....	269
	List of figures and tables.....	271
	References .....	281



## List of symbols, abbreviations and acronyms

Symbols	Unit/Value	Description
<b>Roman Alphabet</b>		
$A_n$	$\mu\text{g-CO}_2 \text{ m}^{-2} \text{ s}^{-1}$	net CO <sub>2</sub> flux of the whole canopy or an individual leaf
$A_g$	$\mu\text{g-CO}_2 \text{ m}^{-2} \text{ s}^{-1}$	soil respiration (CO <sub>2</sub> emission)
$a_s$	-	scaling factor used in calculation of a trace-gas flux to ensure the result has the desired units
$a$	m	area of leaf enclosed by a porometer chamber
$b$	$14 \text{ s m}^{-1}$	empirical constant in the calculation of $R_{\text{inc}}$ (81)
$c_p$	$1.01 \text{ J g}^{-1} \text{ K}^{-1}$	specific heat at constant pressure for moist air
$D_s$	$\text{m}^2 \text{ s}^{-1}$	molecular diffusivity of entity $s$
$d$	m	zero plane displacement height; the height at which canopy effectively becomes closed and all momentum is dissipated (m; typically 60 to 80% of the canopy height)
$e$	kPa	vapour pressure
$e_s(T)$	kPa	the saturation vapour pressure at air temperature $T$
$f_{\text{nb}}$	$\text{m}^3 \text{ s}^{-1}$	dry air inflow rate of a null balance porometer
$f$	Hz	frequency
$f_{a..b}$	dimensionless	scaling functions (value 0 to 1) used to estimate stomatal conductance in multiplicative models, the subscripts denote the variable the function scales for.
$E$	$\text{g m}^{-2} \text{ s}^{-1}$	water-vapour flux
$F_s$	$\text{g m}^{-2} \text{ s}^{-1}$	flux of entity $s$
$G$	$\text{W m}^{-2}$	soil heat flux
$g$	$9.81 \text{ ms}^{-2}$	gravitational acceleration
$g_{s..s}$	$\text{ms}^{-1}$ or $\text{mol m}^{-2} \text{ s}^{-1}$	stomatal conductance for entity $s$ , $w$ denotes water vapour
$g_{\text{max}}$	$\text{ms}^{-1}$ or $\text{mol m}^{-2} \text{ s}^{-1}$	maximum stomatal conductance to water-vapour
$h$	m or Js	crop height or Plank's constant when in conjunction with wavelength ( $\lambda$ )
$H$	$\text{W m}^{-2}$	sensible heat flux
$I_{\text{dir}}$	$\text{W m}^{-2}$ or	Direct (dir) and diffuse (diff) components of incident
$I_{\text{diff}}$	$\text{mol m}^{-2} \text{ s}^{-1}$	solar radiation or PAR
$K$	$\text{m}^2 \text{ s}^{-1}$	eddy diffusivity or coefficient of turbulent diffusion, subscripted $H$ for heat and $m$ for momentum
$k$	0.41	von Karman's constant, which is independent of the surface type
$L$	m	Monin Obukhov length, the height above which convectively driven turbulence dominates over mechanically driven turbulence. $L$ becomes smaller as the vertical heat flux becomes larger during the day. Hence $L$ is indirectly a measure of the convective instability generated by the vertical heat flux through the surface layer.

<i>LAI</i>	$\text{m}^2\text{m}^{-2}$	leaf area index, total leaf area relative to a reference area (ground or porometer chamber) eg $LAI = \text{total leaf area/ground area}$
<i>m</i>	$\text{g m}^{-1} \text{s}^{-1}$	momentum
<i>p</i>	kPa	barometric air pressure
<i>PAR</i>	$\text{W m}^{-2}$ or $\text{mol m}^{-2} \text{s}^{-1}$	Photosynthetically active radiation ( $\lambda \approx 400$ to $700$ nm)
<i>Pr</i>	0.71	Prandtl number for air
<i>Pr<sub>0</sub></i>	0.95	Prandtl number in neutral conditions used in MODELS-3
<i>q<sub>s</sub></i>	$\text{kg m}^{-3}$	water vapour density at balance point in a null-balance porometer
<i>q<sub>i</sub></i>	$\text{kg m}^{-3}$	water vapour density at the saturation vapour pressure corresponding to the leaf temperature
<i>R</i>	$8.314 \text{ J K}^{-1} \text{ mol}^{-1}$	molar gas constant
<i>R<sub>a</sub></i>	$\text{s m}^{-1}$	atmospheric aerodynamic resistance to turbulent transfer momentum, heat or a trace-gas (height dependant)
<i>R<sub>b_s</sub></i>	$\text{s m}^{-1}$	canopy boundary layer resistance to transfer of entity <i>s</i>
<i>r<sub>b_s</sub></i>	$\text{s m}^{-1}$	boundary layer resistance to transfer of entity <i>s</i> over a plane or leaf
<i>R<sub>c_s</sub></i>	$\text{s m}^{-1}$	total canopy resistance for entity <i>s</i>
<i>R<sub>c1_s</sub></i>	$\text{s m}^{-1}$	bulk canopy stomatal resistance for entity <i>s</i>
<i>r<sub>c1w</sub></i>	$\text{s m}^{-1}$	stomatal resistance to water-vapour transfer of a leaf
<i>R<sub>c2_s</sub></i>	$\text{s m}^{-1}$	bulk cuticular and other plant surface resistance for entity <i>s</i>
<i>R<sub>c3_s</sub></i>	$\text{s m}^{-1}$	soil resistance for entity <i>s</i>
<i>R<sub>d</sub></i>	$\mu\text{g-CO}_2 \text{ m}^{-2} \text{ s}^{-1}$	daytime respiration of an individual leaf or canopy
<i>Re</i>	dimensionless	Reynolds number – ratio of inertial to viscous forces, $u(z-d)\delta/\nu$
<i>RH</i>	dimensionless	relative humidity – the ratio of the actual vapour pressure to the saturation vapour pressure at the ambient air temperature ( $e/e_s(T)$ ), given as either a percentage or fractional value.
<i>R<sub>inc</sub></i>	$\text{s m}^{-1}$	in-canopy aerodynamic resistance
<i>r<sub>l</sub></i>	$\text{s m}^{-1}$	resistance to water vapour flow of a leaf = $r_{c1w} + r_b$
<i>R<sub>n</sub></i>	$\text{W m}^{-2}$	net radiation
<i>R<sub>ns</sub></i>	$\text{s m}^{-1}$	the non-stomatal resistance to trace-gas transfer presented by a surface, for ozone unless indicated otherwise
<i>SAI</i>	$\text{m}^2 \text{ m}^{-2}$	surface area index
<i>Sc<sub>s</sub></i>	dimensionless	Schmidt number ( $\nu/D_s$ )
<i>Sh<sub>s</sub></i>	dimensionless	Sherwood number = $0.66Re^{0.5}Sc_s^{0.33}$
<i>St</i>	$\text{W m}^{-2}$	total solar radiation
<i>SWC</i>	%	soil water content by mass or volume
<i>SWP</i>	kPa or MPa	soil water potential usually
<i>T</i>	°C or K	temperature
<i>T<sub>d</sub></i>	°C or K	dew point temperature
<i>T(z<sub>0</sub>)</i>	°C or K	temperature of the bulk canopy surface

$u_*$	$\text{m s}^{-1}$	friction velocity, the mean velocity at which turbulent eddies are rotating (independent of height)
$u$	$\text{m s}^{-1}$	the horizontal wind velocity with the mean flow, $u'$ indicates the instantaneous deviation from the mean value (the turbulent component) and $\bar{u}$ the mean value (height dependant)
$v$	$\text{m s}^{-1}$	the horizontal wind velocity perpendicular to the mean flow, $v'$ and $\bar{v}$ as for $u$
$v_{d,s}$	$\text{m s}^{-1}$	deposition velocity of $s$ , indicates the rate of deposition (height dependant)
$vpd$	kPa	saturation vapour pressure deficit – the difference between the saturation vapour pressure at the ambient air temperature and the actual vapour pressure ( $e_s(T) - e$ )
$w$	$\text{m s}^{-1}$	the vertical wind velocity, $w'$ and $\bar{w}$ as for $u$
$Wd$	$^\circ\text{N}$	wind direction
$z$	m	height above ground
$z_0$	m	aerodynamic roughness length, the height at which $u = 0$ , typically about $0.1 h$ .

### Greek Alphabet

$\alpha$	-	exponential parameter used in the equations of molecular diffusivity (72) and the light response of stomata (85)
$\beta$	dimensionless	Bowen Ratio, $H/\lambda E$
$\beta_H$	8.21	stable profile coefficient for heat used in MODELS-3
$\delta$	m	mean leaf-length in direction of the wind
$\beta$	radians	compliment of the solar zenith angle
$\delta$	radians	solar zenith angle
$\zeta$	radians	mean angle of leaf orientation to the sun
$\Delta$	$\text{kPa K}^{-1}$	rate of change in saturation vapour pressure with temperature ( $\partial e_s(T)/\partial T$ )
$\theta$	$^\circ\text{C}$ or K	Potential temperature $\theta$ is the temperature which would result if air were brought adiabatically to a standard pressure of 1000 hPa, $\theta = T - \Gamma_z$ . Virtual potential temperature $\theta_v$ is the potential temperature of dry air at the same pressure and density as the moist air parcel.
$\varepsilon$	0.622	the ratio of the molecular weight of water to that of dry air (18/29)
$\Gamma$	$\approx 0.01 \text{ K m}^{-1}$	dry adiabatic lapse rate
$\Gamma_{\text{CO}_2}$	$\mu\text{mol m}^{-3}$	carbon dioxide compensation point concentration
$\lambda$	m	wavelength of radiation
$\lambda$	$2470 \text{ J g}^{-1} \text{ K}^{-1}$	latent heat of vaporisation of water
$\gamma$	$66 \text{ Pa K}^{-1}$	psychrometer constant (value given at $0^\circ\text{C}$ , 101.3 kPa, (Monteith and Unsworth, 1990)
$\gamma_H$	11.6	unstable profile coefficient for heat used in MODELS-3
$\tau$	$\text{N m}^{-2}$ ( $\text{kg s}^{-1} \text{ m}^{-2}$ )	momentum flux (or shearing stress)
$\rho$	$\text{kg}$ or $\text{g m}^{-3}$	air density

$\chi_s$	$\mu\text{g m}^{-3}$ or ppbV	concentration of $s$
$\psi(\zeta)$	dimensionless	height integrated similarity function which results in the stability correction, subscripted $H$ for heat and $m$ for momentum
$\Phi(\zeta)$	dimensionless	empirical stability correction, subscripted $H$ for heat and $m$ for momentum
$\zeta$	dimensionless	non-dimensional height, $(z-d)/L$
$\lambda E$	$\text{W m}^{-2}$	latent heat flux
$\nu$	$14.2 \times 10^{-6} \text{ m}^2 \text{ s}^{-1}$	kinematic velocity of air (value at $10^\circ\text{C}$ )

## Abbreviations and Acronyms

### ABA

Abscisic acid

### AOT40

Accumulated ozone concentration over a threshold of 40 ppb, when the hourly average ozone concentration exceeds 40 ppb the difference between it and 40 ppb is added to the AOT40

### CAM

Crassulacean acid metabolism

### SUM06

All hourly average ozone concentrations that exceed 60 ppb are summed.

### AFst

Accumulated stomatal flux, may be calculated over a threshold in a similar manner to AOT40 or simply the sum of all values.

### COMEAP

The UK Committee on the Medical Effects of Air Pollution – an advisory body for the Department of Health  
(<http://www.advisorybodies.doh.gov.uk/comeap/>)

### Dobson unit (DU)

a unit used in geophysics to measure the ozone in the atmosphere. One Dobson unit represents the amount of atmospheric ozone that would form a uniform layer 0.01 millimeter (10 micrometers) thick at standard temperature ( $0^\circ\text{C}$ ) and pressure (1 atmosphere or 1013.25 millibars). 1 ppb of tropospheric  $\text{O}_3 \approx 0.65$  DU. The unit is named for the British physicist G.M.B. Dobson; in 1920 he invented a spectrometer to measure ozone concentrations from the ground.

### EMEP

Co-operative Programme for Monitoring and Evaluation of the Long-range Transmission of Air pollutants in Europe – part of the UNECE Convention on Long-range Transboundary Air Pollution (<http://www.emep.int/>)

### EPAQS

Expert Panel on Air Quality Standards – an advisory body for the Department of Food, Environment and Rural Affairs  
(<http://www.defra.gov.uk/environment/airquality/aqs/>)

### IPCC

The Intergovernmental Panel on Climate Change (IPCC) has been established by WMO and UNEP to assess scientific, technical and socio-economic information relevant for the understanding of climate change, its potential impacts and options for adaptation and mitigation. It is open to all Members of the UN and of WMO.

<http://www.ipcc.ch/>

STE

Stratosphere/Troposphere exchange of ozone.

UNECE

United Nations Economic Commission for Europe (<http://www.unece.org/>)

TDR

Time domain reflectometry, technique used to measure water content, of soil for example

TDL

Tunable diode laser, instrument for measuring trace gas concentrations

METAR

Meteorological data representation - Colloquial name for weather reporting codes FM 15 - IX Ext. for more information see the WMO website

PBL

Planetary Boundary Layer: *that part of the troposphere that is directly influenced by the presence of the earth's surface, and responds to surface forcings with a timescale of about an hour or less* (Stull, 1989).

PCB

Printed circuit board

NH

Northern Hemisphere

SH

Southern Hemisphere

SYNOP

Colloquial name for standard synoptic weather reporting codes FM 12 - IX for more information see the WMO website

WHO

World Health Organisation (<http://www.who.int/en/>)

WMO

World Meteorological Organisation (<http://www.wmo.ch/>)



## Abstract

Tropospheric ozone has detrimental effects on the health of vegetation and humans. It is also a direct greenhouse gas and plays a role in the chemistry of many other gases. Current measurements and model results show concentrations have increased and this is likely to continue. Thus it is important to understand how ozone is generated and processed in the atmosphere. New critical levels that use accumulated stomatal uptake rather than atmospheric concentration have recently been set by the UNECE to quantify the effect of ozone on vegetation. There are models available that can estimate the stomatal flux but the non-stomatal component is not well described.

The total flux of ozone was measured over grassland in central Scotland during 2001 to 2004 using micrometeorological methods and the uptake by stomata estimated by similarity with the water-vapour flux. The non-stomatal component is estimated using  $R_{ns} = (R_c^{-1} - R_s^{-1})^{-1}$  where  $R_{ns}$  = non-stomatal surface resistance to ozone deposition,  $R_c$  = total canopy resistance,  $R_s$  = stomatal resistance. The dataset is used to examine the processes controlling deposition at this site and a new parameterisation for the non-stomatal component is described.

There are two forms of model commonly used to estimate stomatal resistance: Jarvis type multiplicative models, and Ball-Berry photosynthesis based approaches. Both methods are employed to estimate bulk-canopy stomatal conductance and so gap-fill the measured time series. The resulting estimates of  $R_{ns}$  were found to decrease with increasing surface temperature, solar radiation, humidity and friction velocity. The response of  $R_{ns}$  to these variables was also dependant on surface wetness with deposition being enhanced over wet surfaces compared to dry, upto temperatures of  $\sim 20^\circ\text{C}$ .

New parameterisations based on these results are developed and implemented in a total-deposition model. The results are compared to the measured data and estimates from both a standard type of model and one utilising an existing parameterisation for  $R_{ns}$  based on humidity. The parameterisation was found to improve estimates of total canopy resistance for wet surfaces compared to both the other models, although for dry surfaces it did not perform as well as the humidity based model.



## Acknowledgments

There are multitudes of thank-yous I need to give here, so firstly I'd like to thank my supervisors, Keith Weston and David Fowler - doing this PhD part-time has had its advantages and disadvantages but it would not have been possible without their support and assistance. Secondly, and it's a big one, being to my best-friend/partner Nick who has always encouraged me to do my best and supported me over the years, despite some difficult times. This may sound a bit odd, but I'd also like to thank my now sadly departed dog, Barney, and my new one, Millie, for getting me out of the office and bringing a smile to my face when it all seemed hopeless.



I'm also very grateful to all my colleagues at CEH who have helped with the instruments, field measurements, data analysis and given bucket loads of moral support: Margaret Anderson, Neil Cape, Jennifer Carfrae, Daniela Famulari, Ken Hargreaves, Celia Milford, Jennifer Muller, Eiko Nemitz, and Robert Storeton-West to name but a few!



# 1 Ozone in the Atmosphere

Ozone is a photochemical oxidant that is present throughout the Earth's atmosphere. In the troposphere it has been found to have detrimental effects on the health of vegetation and humans as well as damaging materials. It is also a direct greenhouse gas and plays a role in the chemistry of many other gases. The past increase in tropospheric O<sub>3</sub> is estimated to provide the third largest increase in direct radiative forcing since the pre-industrial era (Houghton, *et al.*, 2001). In addition, through its chemical impact on OH, it modifies the lifetimes of other greenhouse gases, such as CH<sub>4</sub>. Thus it is important to understand how it is generated and processed in the atmosphere.

In unpolluted areas there is a rapid chemical turn-over of ozone in which it is produced and destroyed often without a net change in concentration, whereas in polluted areas either net production or destruction may occur depending on concentrations of the ozone precursor species and weather conditions. Other processes influence ozone concentration in the troposphere, such as stratosphere/troposphere exchange (STE) and removal at the surface. The dry deposition of ozone to the Earth's surface is the major removal process for ozone in the planetary boundary layer (PBL). As ozone is highly reactive, it rapidly deposits to most surfaces and it is also removed by plants taking it in through their stomata as they respire (stomatal uptake). It is accepted that the stomatal uptake of ozone causes most damage to vegetation (Fuhrer, *et al.*, 1997). The downward flux of ozone can be easily measured in the field using micrometeorological methods. However, distinguishing between different deposition pathways, eg stomata and leaf cuticle, are more difficult but necessary if the processes controlling deposition are to be fully understood and the threat to vegetation assessed.

Field measurements of ozone deposition were made over grassland in central Scotland during the summers of 2001 to 2004. In conjunction with ozone, CO<sub>2</sub> and water vapour were measured, which allows the stomatal uptake of ozone to be estimated. These measurements have rarely been made for whole growing seasons and so the data set is an important contribution to the understanding of ozone dry deposition. This thesis describes the field site, measurements, summarises the main results and proposes a model for non-stomatal ozone deposition.

## 1.1 Tropospheric vs. Stratospheric

Ozone is a natural component of the atmosphere in both the stratosphere (~15 – 50 km) and troposphere (0 – ~15 km). In the stratosphere incoming solar UV radiation (wavelength,  $\lambda = 40 - 240$  nm) causes the photolysis of molecular oxygen which recombines with free oxygen to produce ozone. In the troposphere photochemical reactions of nitrogen oxides (NO<sub>x</sub>) and volatile-organic compounds (VOCs) produce ozone and it plays an important role in the chemical processing of natural and man-made trace gases. However, concentrations of stratospheric ozone have declined in polar regions, particularly during the Antarctic spring (Newman, *et al.*, 2004) while concentrations of tropospheric ozone have increased, especially in the mid-latitude Northern Hemisphere (NH) (Vingarzan, 2004; Staehelin and Schmid, 1991). There are therefore two very different and largely unrelated problems of atmospheric ozone.

The largest concentrations of ozone occur in the stratosphere (Figure 1.1) but the subject is only relevant here for the small contribution it makes to the tropospheric ozone budget through stratosphere-troposphere exchange (STE).

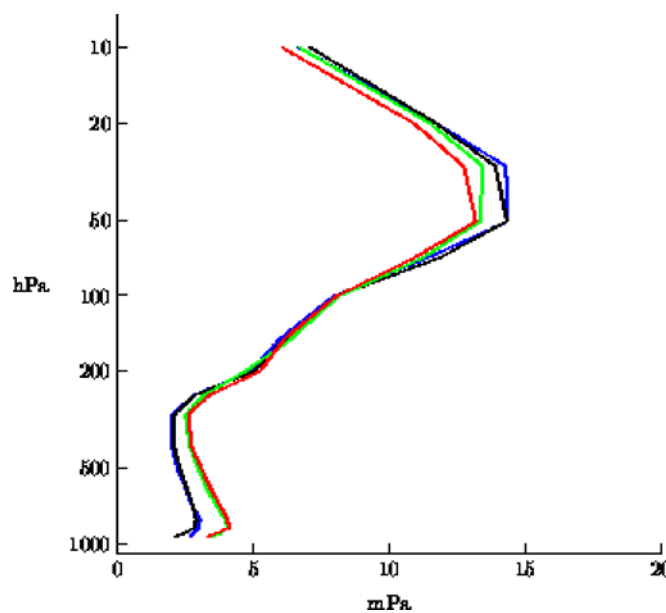


Figure 1.1 Ozone soundings by balloon sonde at Payerne, Switzerland (46.80 N, 6.95 E, 490 a.s.l.). Blue = 1976, Black = 1977, Green = 1987, Red = 1996. The annual mean tropopause height at Payerne is ~10 km, ranging from ~8 km in the winter to 12 km in the summer. Staehelin and Schmid, 1991

Although STE is difficult to directly measure, the presence of air from the stratosphere can be detected using a tracer such as humidity or <sup>7</sup>Be. Studies of the process using measurements and modelling have estimated the global

contribution of STE to tropospheric ozone to be only 5 to 20% (~5 to 10 ppb) (Allen, *et al.*, 2003; Beck and Grennfelt, 1994; Beekmann, *et al.*, 1997; Collins, *et al.*, 2003; Derwent, *et al.*, 2004; Lelieveld and Dentener, 2000). However, seasonal variations in STE are thought to contribute to the seasonal cycle of tropospheric ozone concentrations in some parts of the world.

## 1.2 Chemistry of O<sub>3</sub> Production in the Troposphere

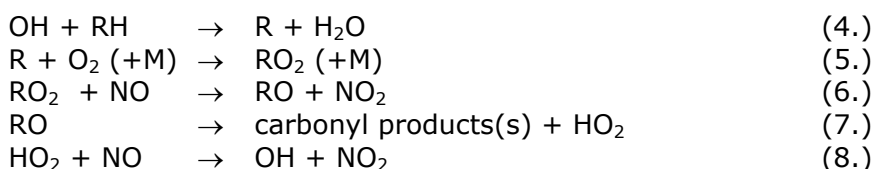
As noted above, ozone in the troposphere is produced through photochemical reactions of NO<sub>x</sub> and VOCs. Both groups of compounds are emitted by natural processes, such as bacterial activity in soil, forest fires and VOC release from vegetation. However, the large emission of these gases through combustion, especially by motor vehicles and industrial processes, has led to an increase in tropospheric ozone around the globe. Trends in tropospheric ozone are discussed in detail below.

The cyclical reactions of NO, O<sub>3</sub> and NO<sub>2</sub> (equations 1 to 3), govern the concentration of O<sub>3</sub> in an unpolluted atmosphere and can generate a few ppb of ozone depending on the initial concentrations of each gas. Under typical daytime conditions with a well-mixed atmosphere the 3 reactions reach an equilibrium where no net chemistry occurs, termed the photostationary state.



where:  $h\lambda$  = sunlight with wavelength 280-430 nm  
M = any molecule eg N<sub>2</sub> or O<sub>2</sub>

Where other daytime chemical reactions supplement the available NO<sub>2</sub> for reaction (2) without consuming ozone, net ozone production can occur. The processes that produce additional O<sub>3</sub> are very complex involving several hundred VOCs, radicals and NO<sub>x</sub>, however the reactions can be summarised as follows (PORG, 1998):



where: OH = hydroxy radical  
RH = saturated hydrocarbon (eg alkane)  
R = alkyl radical  
RO<sub>2</sub> = alkyl peroxy radical  
HO<sub>2</sub> = hydroperoxy radical  
RO = alkoxy radical

As OH is regenerated in reaction (8) the process forms a catalytic cycle and several molecules of ozone can be produced from the oxidation of a single hydrocarbon compound (Figure 1.2). The oxidation of carbon monoxide (CO) also involves hydroperoxy and alkyl peroxy radicals and so these processes may also perturb the photostationary state and generate ozone (PORG, 1998).

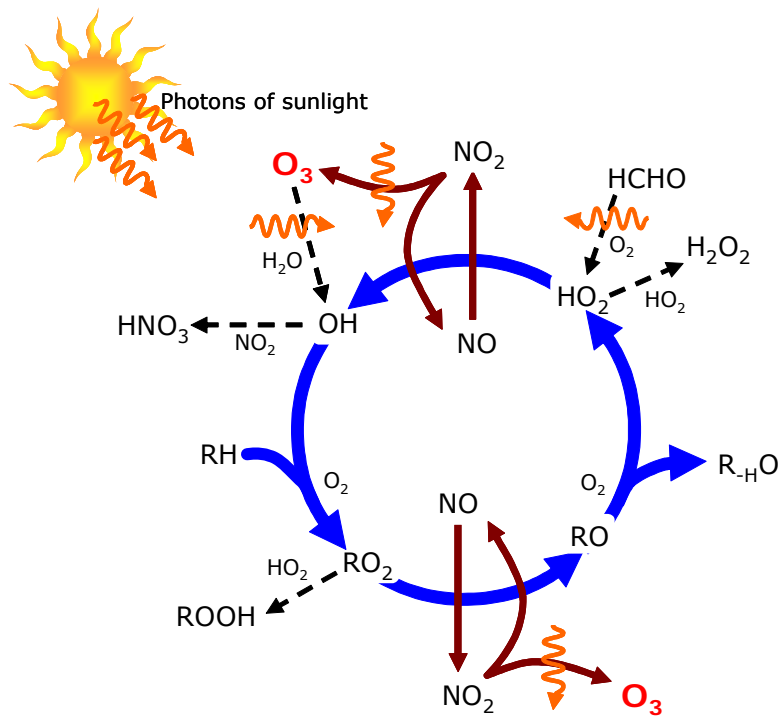


Figure 1.2. Schematic representation of ozone chemistry showing the free-radical (OH) catalysed oxidation of a generic saturated hydrocarbon, RH (after PORG, 1998, Figure 2.4).

Prior to the industrial revolution natural sources of NO<sub>x</sub> and VOCs would have generated ozone in the troposphere, adding to that transported from the stratosphere. However the NO<sub>x</sub> and VOCs released by human activity have led to a large increase in the NH background concentration. Anthropogenic emissions of the ozone precursors can also cause large transient increases in ozone concentration, termed episodes or smogs. These occur when high levels of precursors coincide with weather conditions favourable to ozone production. It was the occurrence of eye irritation, breathing problems and visible plant damage during smogs in southern California in the 1950s that led to increased research into ozone photochemistry and effects (Figure 1.3).

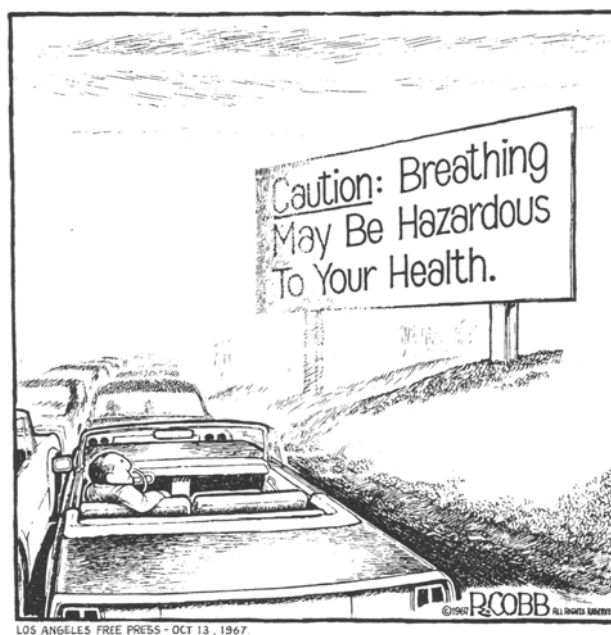


Figure 1.3 Cartoon by Ron Cobb highlighting the issue of air pollution in California during the 1960s.

### ***1.3 The Global, Regional and Local Ozone Budget***

As described above, ozone is a secondary pollutant generated and destroyed via many complicated chemical reactions. Thus its total budget throughout the troposphere is difficult to measure and can vary considerably across temporal and spatial scales. Figure 1.4 shows an image of the global distribution of tropospheric ozone in Dobson Units (1 ppb  $\approx$  0.65 Du) derived from satellite measurements of total and stratospheric concentration (Fishman *et al.*, 2003). This map illustrates several processes that control the distribution such as: photochemistry, surface deposition, atmospheric mixing, intercontinental transport, regional emission plumes (natural and man-made), and human-population density. For example:

- Concentrations are smaller over the tropical Pacific as this area is relatively unpolluted ( $\text{NO}_x < 20$  ppt) and the atmosphere is quite humid so that ozone is very effectively scavenged. Figure 1.4a-d
- Throughout the year, industrial emissions, mainly from N America, Europe and E Asia, generate plumes of enhanced ozone “down-wind” of these regions. Measurement campaigns, using aircraft, surface stations and shipping often detect the transport of ozone across large distances, e.g. Trickl *et al.*, (2003) tracked a parcel of ozone travelling across the Atlantic from N America to Europe. Figure 1.4b

- During the NH spring/summer, concentrations are enhanced over areas of dense human population and industry. Figure 1.4b-c
- In the S Hemisphere areas of high population are generally more sparsely distributed, but regions of enhanced ozone due to industrial emissions can be seen in Eastern Australia, West Africa (Liberia, Ivory Coast, Ghana, Togo, Benin and Nigeria). Figure 1.4c
- During the Austral spring, concentrations are enhanced in the South Atlantic due to biomass burning (mainly in South America). Figure 1.4d

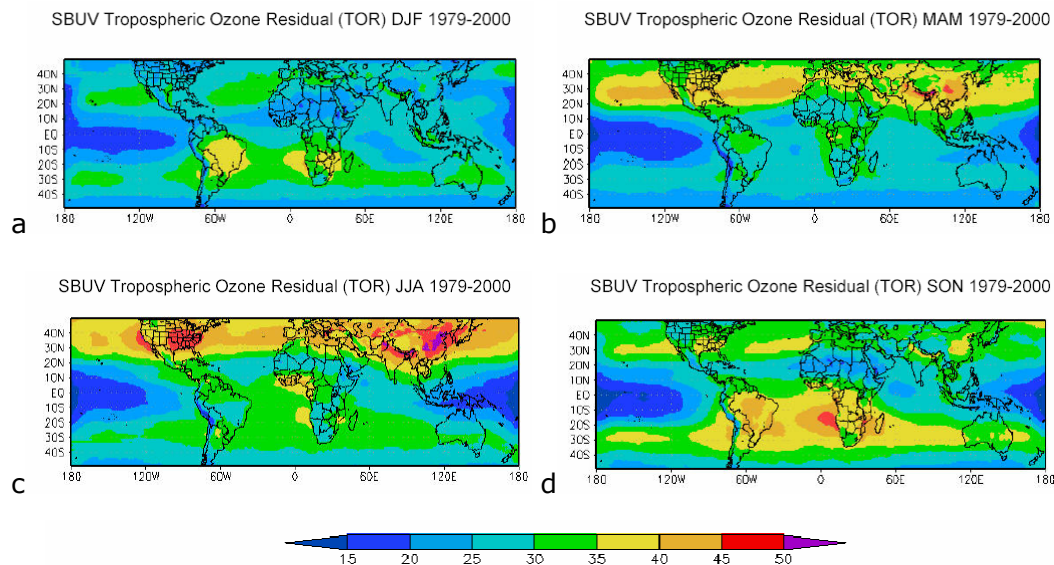


Figure 1.4 Global distribution of total tropospheric ozone from satellite measurements of total atmospheric and stratospheric ozone (Fishman, *et al.*, 2003).

There have been many studies of the processes outlined here, which describe them in more detail for example: Derwent *et al.*, (2004); Fiore *et al.*, (2002); Li *et al.*, (2002); Naja *et al.*, (2003); Pochanart *et al.*, (2003); Pochanart *et al.* (2002); Pochanart *et al.*, (2004); Swap *et al.*, (2003); Wild *et al.*, (2004). However, the scope of this thesis is the surface deposition of ozone in the UK and so the following sections focus on ozone in the lower troposphere (planetary boundary layer, PBL) of Western Europe and the UK.

### 1.3.1 Seasonal Cycle

As illustrated above ozone concentrations vary with time of year with peak levels occurring in the northern and southern hemisphere spring/summer periods. In Western Europe the shape of the seasonal cycle changes with latitude; at less polluted northern sites the seasonal cycle tends to show a peak in the spring whereas at more polluted southerly sites the peak is spread from April to

September, as illustrated by the plots in Figure 1.5. There are several processes involved in producing this cycle: the summer peak is due to warm, sunny weather and the accumulation of precursor species in anti-cyclonic conditions increasing the photochemical production of ozone as well as enhanced long-range transport of ozone precursors from Asia and N. America (Derwent *et al.*, 2004); the spring peak is less well understood but may be partly due to tropospheric production from precursors accumulated over the polar region during the winter and partly due to an increase in STE during the spring (Monks 2000; Stohl *et al.*, 2003).

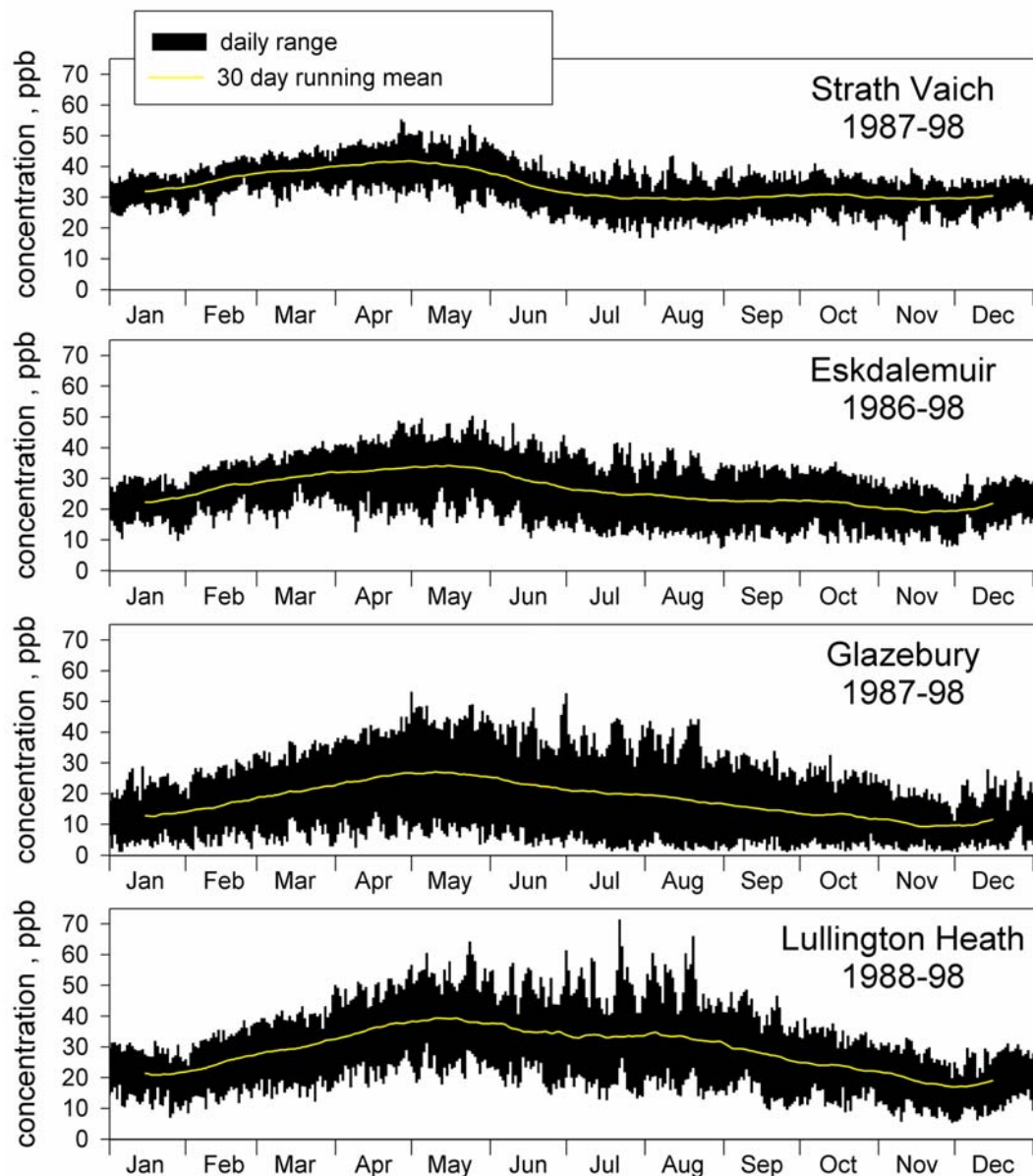


Figure 1.5 Examples of seasonal cycles observed across the UK, from a remote rural site in the north (Strath Vaich) to a more polluted site in the south (Lullington Heath) (Figure originally presented in NEG-TAP, 2001).

### 1.3.2 Local Scale and the Diurnal Cycle

A diurnal cycle in ozone concentration is typically observed, and in rural areas of the UK this has a mid-afternoon peak and night-time minimum, as shown in Figure 1.6a (Garland and Derwent, 1979). The cycle is governed by changes in the PBL and free troposphere, although photochemical production also plays a part. During the daytime, turbulent mixing in the PBL, induced by both wind shear and thermal convection, lead to entrainment of ozone from the free troposphere (Stull, 1989). In sunny weather the presence of NO<sub>x</sub> and VOC emissions can also lead to photochemical production throughout the troposphere and so enhanced ozone concentrations. These processes produce an afternoon peak in ozone concentration when the atmosphere is most turbulent and UV levels are at a maximum. During the night and early morning the lower regions of the boundary layer become thermally stratified and stable as the surface cools, greatly reducing entrainment of ozone from the free troposphere. The ozone concentration decreases rapidly as losses to dry deposition are not replenished by mixing from above and photochemical production cannot occur. The minimum concentration is usually reached between midnight and dawn, although increases may be observed over short periods when sporadic turbulence breaks through the stable layer and mixes down ozone from the free troposphere (Corsmeier, *et al.*, 1997; Garland and Derwent, 1979).

In warm anti-cyclonic conditions the diurnal cycle is most pronounced and large amounts of precursor emissions can lead to episodes of high ozone concentration across large areas of the country, often reaching or exceeding air quality standards. During the daytime concentrations build up as photochemical production of ozone is enhanced in the precursor-rich, slow-moving air and increased convective mixing brings ozone down from the free-troposphere. Strong temperature inversions occur during the night as the surface rapidly loses heat to clear skies. A large drop in concentration occurs at the surface as nocturnal ozone deposition removes ozone; high concentrations remain above the inversion and are mixed down the following day. Thus concentrations can build over several days and an ozone episode occurs.

There are also two other influences on the shape of a local diurnal cycle: site windiness and proximity to the coast:

1. The degree to which the nocturnal boundary layer stabilises and becomes isolated from the rest of the troposphere depends on the local topography and meteorology. Low lying sites tend to experience more nocturnal depletion as the winds become light and calm at night and surface cooling may produce a very stable inversion layer. By contrast, on hill-tops the night-time decrease in ozone is reduced as, although the lower layers of the atmosphere cool, it remains more turbulent as cold air flows down-slope and is replaced by relatively ozone rich air from above. However, the magnitude and timing of the mid-afternoon peak is very similar at all sites, showing that rural concentrations may be comparable over a wide geographical area during this period (Weston, *et al.*, 1994; Coyle, *et al.*, 2002).
2. The deposition velocity of ozone to water surfaces is  $< 1 \text{ mm s}^{-1}$  (Chang, *et al.*, 2004), so that vertical gradients of ozone concentration in the maritime boundary layer are small. A larger vertical gradient near the surface evolves as air crosses a coast and moves over the land-surface with a far greater deposition rate. Thus there is a difference in the exposure to ozone between the coast and inland during on-shore flow, with essentially a flat diurnal cycle at the coast (PORG, 1998). Entwistle *et al.*, (1997) used observations of ozone concentration from suitable coastal sites and a simple model to quantify this coastal effect. They showed that it extends  $\sim 5$  km inland and, at the coast, daily mean ozone concentrations may be enhanced by 2-5 ppb depending on the degree of exposure to onshore breezes.

The diurnal cycle is most clearly observed in the countryside as in urban areas, or close to combustion sources, ozone concentrations are depleted by titration with NO (see equation 1). The plot in Figure 1.6b is of typical urban cycles and the minimum caused by rush-hour traffic is clearly observed. This process also leads to ozone concentrations being generally lower in and around densely populated areas, so in this respect ozone is a rural pollution problem. Figure 1.7 is a map of 2001 summer mean ozone in the region around London, extracted from a 1 km by 1 km map for the UK (Coyle, *et al.*, 2002). A map of NO<sub>x</sub> concentration is used to account for urban ozone depletion (Stedman, *et al.*, 1997; Stedman, 2003) and so the influence of dense traffic levels in London and on surrounding motorways are clearly visible in Figure 1.7. However, reductions

in NO emissions are currently causing urban ozone to increase and during photochemical episodes urban concentrations often reach or exceed rural values, as illustrated by the data plotted in Figure 1.6c.

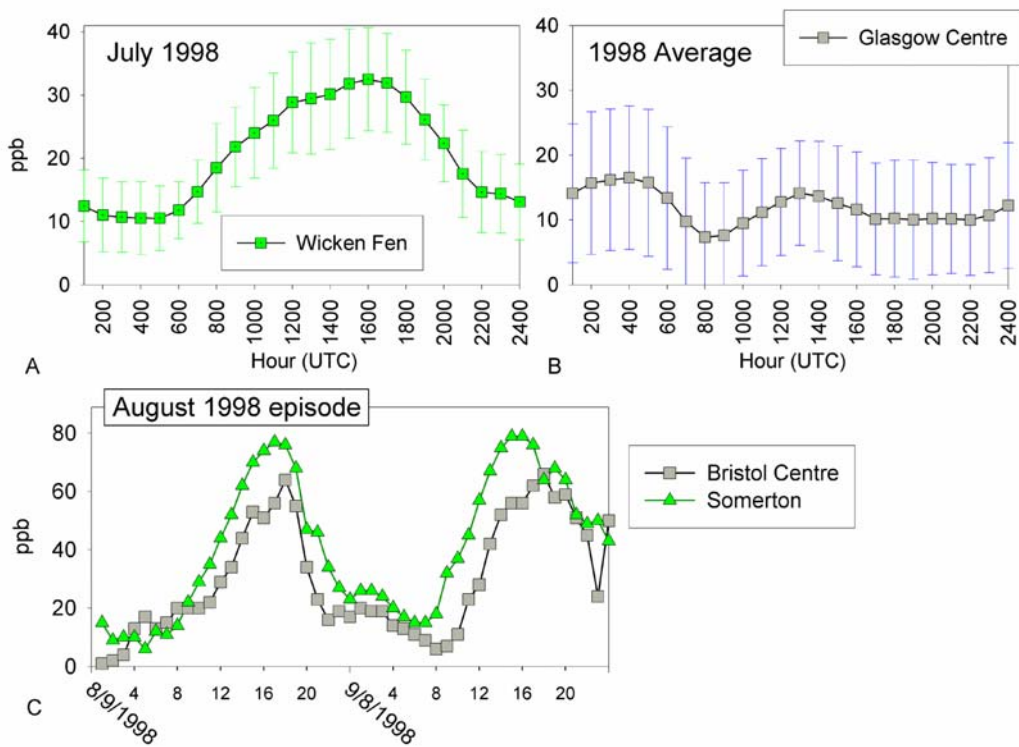


Figure 1.6 Examples of diurnal cycles in ozone concentration at (a) a rural site, (b) a city centre site and (c) at an urban and nearby rural site during a photochemical episode. Error bars show the standard deviation of hourly means. (Originally presented in NEGAP, 2001).

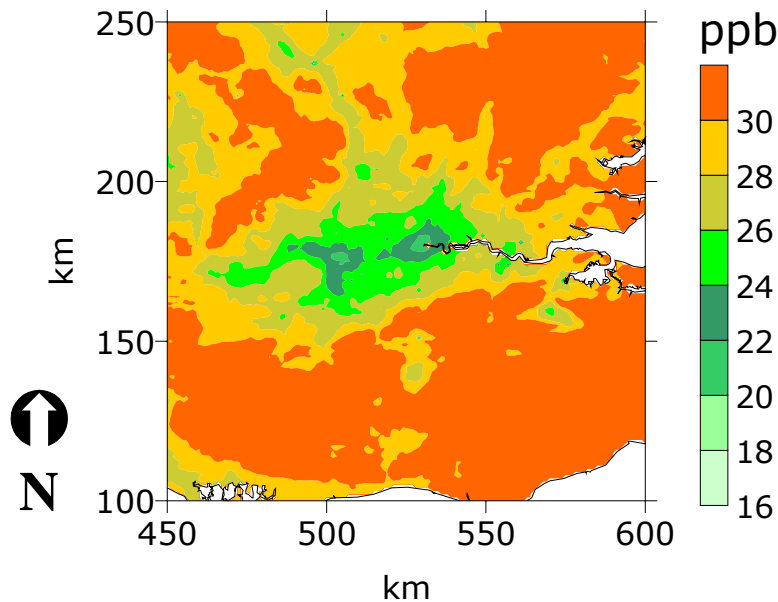


Figure 1.7 2001 summer mean ozone concentrations in the region around London, extracted from a 1 km by 1 km map of ozone across the UK (Coyle, *et al.*, 2002)

## ***1.4 Effects of ozone on human health, vegetation and materials***

Ozone is an unstable molecule and reactive oxidant, thus it readily deposits onto most surfaces, including biological tissues ie lungs, eyes or plant membranes. Although ozone is a natural constituent of the atmosphere, and many organisms have evolved mechanisms to protect against oxidative damage, ozone concentrations now regularly exceed the ability of these mechanisms to cope and effects can be observed.

### **1.4.1 Effects on Vegetation: thresholds and critical levels**

Although plants have evolved protective mechanisms to prevent ozone damage, there is a threshold ozone concentration above which the plant's detoxification processes can no longer cope (Karenlampi and Skarby, 1996). The effects that occur include reductions in crop yield and quality, growth reductions, changes in morphology and physiology, visible injury, and early senescence (Ball *et al.*, 1998; Bungener *et al.*, 1999; Davison and Barnes 1998; Finnan *et al.*, 1996; Gimeno *et al.*, 2004; Kollner and Krause, 2000; Pleijel *et al.*, 2004; Sellden and Pleijel, 1995; Soja and Soja, 1995). The images in Figure 1.8 show examples of some of the effects that are observed. Although the detoxification threshold varies with local conditions and from species to species, concentrations observed across Europe are currently very close to those likely to cause damage to many types of vegetation (Benton *et al.*, 2000; Fowler *et al.*, 1999; Fuhrer *et al.*, 1997).

In 1994 the UNECE set critical levels for forests, crops and semi-natural vegetation based on atmospheric concentrations of ozone at the top of a plant canopy (Fuhrer and Achermann, 1994). Although it was known that the ozone entering the plant through their stomata actually caused the damage, current knowledge was not sufficient to recommend critical levels based on stomatal uptake. A cut-off concentration for effects of 40 ppb was set based on the results of many experiments and the indices are calculated as an accumulated concentration over the threshold (AOT40), i.e. the differences between an hourly mean in excess of 40 ppb and 40 ppb are summed over a specified period for each vegetation type.



Figure 1.8 Examples of damage to vegetation caused by ozone: top left to right show visible injury on *potentilla*, *carex* and *dryas*; the bottom image shows early senescence (left) induced in *Lolium perenne*. All images were obtained from experiments in controlled chambers with a range of ozone concentrations (Buse, *et al.*, 2003; Van Oijen, *et al.*, 2003).

In the USA a similar index called SUM06 is used, where the hourly averages over 60 ppb are summed over a defined period. The AOT40 (and in some regions the SUM06) has been adopted by researchers around the world to assess vegetation effects, as it is relatively simple to calculate and can use data from monitoring stations (e.g. Pochanart, *et al.* 2002; Zheng, *et al.* 1998). More recently, the UNECE has updated their assessment and new levels have been set for some vegetation types based of Accumulated Stomatal Flux ( $AF_{st}$ ) (ICP, 2004). All the indices are outlined in Table 1.1.

The stomatal flux-based critical levels ( $CL_{ef}$ ) for ozone take into account the varying influences of temperature, water vapour pressure deficit ( $vpd$ ), radiation (sunlight), soil water potential ( $SWP$ ), ozone concentration and plant development (phenology) on the stomatal flux of ozone. They therefore provide an estimate of the critical amount of ozone entering through the stomata and reaching the sites of action inside the plant. This is an important new

development in the derivation of critical levels because, for example, for a given ozone concentration, the stomatal flux in warm, humid conditions with moist soil can be much greater than that in hot, dry conditions with dry soil because the stomatal pores will be more widely open. Concentration-based critical levels do not differentiate between such climatic conditions and would not indicate the increased risk of damage in warm, humid conditions.

Table 1.1 Indices for assessing the effects of ozone on vegetation.

Approach		Crops	(Semi-) Natural Vegetation	Forest Trees
Stomatal flux-based critical level	<b>CL<sub>ef</sub>*</b>	<i>Wheat</i> : An AF <sub>st</sub> 6 of 1 mmol m <sup>-2</sup> PLA <sup>#</sup> <i>Potato</i> : An AF <sub>st</sub> 6 of 5 mmol m <sup>-2</sup> PLA	Not defined	<i>Birch and beech</i> : Provisionally AF <sub>st</sub> 1.6 of 4 mmol m <sup>-2</sup> PLA
	<b>Time period</b>	<i>Wheat</i> : Either 970 °C days, starting 270 °C days before mid-anthesis (flowering) or 55 days starting 15 days before mid-anthesis <i>Potato</i> : Either 1130 °C days starting at plant emergence or 70 days starting at plant emergence		One growing season
	<b>Effect</b>	Yield reduction		Growth Reduction
Concentration-based critical level	<b>CL<sub>ec</sub>*</b>	<i>Agricultural crops</i> : An AOT40 of 3 ppm h <i>Horticultural crops</i> : An AOT40 of 6 ppm h	An AOT40 of 3 ppm h	An AOT40 of 5 ppm h
	<b>Time period</b>	<i>Agricultural crops</i> : 3 months <i>Horticultural crops</i> : 3.5 months	3 months (or growing season, if shorter)	Growing season
	<b>Effect</b>	Yield reduction for both agricultural and horticultural crops	Growth reduction in perennial species and growth reduction and/or seed production in annual species	Growth reduction
VPD-modified concentration-based critical level	<b>CL<sub>ec</sub></b>	An AOT30 <sub>VPD</sub> of 0.16 ppm h	Not defined	Not available
	<b>Time period</b>	Preceding 8 days		
	<b>Effect</b>	Visible injury to leaves		

\*CL<sub>ef</sub> - Flux-based critical level of ozone; CL<sub>ec</sub> - Concentration-based critical level of ozone  
#PLA - Projected Leaf Area

However, as the CL<sub>ef</sub> are based on the flux rather than simple concentrations they are more difficult to evaluate at a national scale. There are very few sites where the necessary data are collected to directly calculate the stomatal flux, and so some modelling is required. The UNECE has already developed methods

to map  $AF_{st}$  across Europe using a new deposition module in the EMEP model (Emberson 2002; Simpson *et al.*, 2003b; Tuovinen *et al.*, 2004). The provision of a model suitable for use in the UK was one of the motivations for this research and the measurements from our field site will be used to develop a site-specific model with a view to scaling it up to the UK.

#### 1.4.2 Effects on Human Health: thresholds and critical levels

The effects of ozone on human health have been extensively studied since the 1960s, as it is considered to be one of the most irritant of common air pollutants. The mechanism for ozone effects in humans is quite well understood and involves inflammation of the respiratory tract and lungs induced by the oxidation of ozone (Figure 1.9).

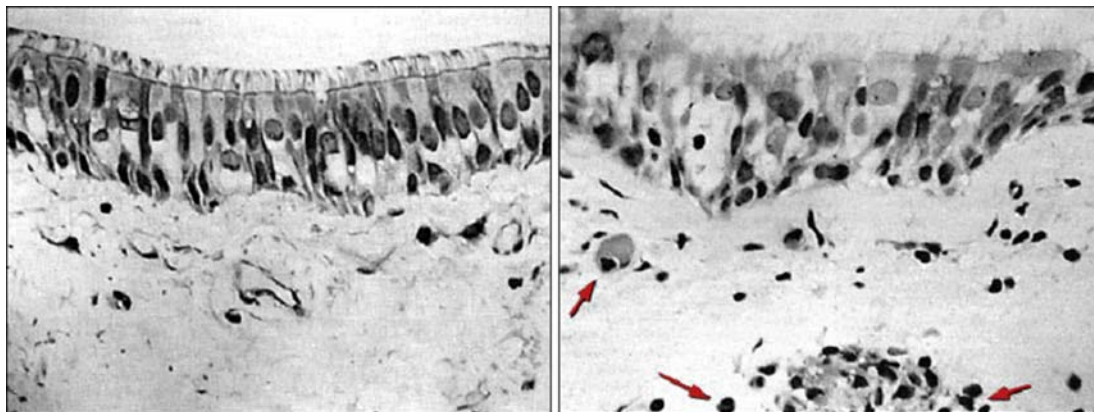


Figure 1.9 Microscopic views of human lung tissue (epithelium, or lining) show damage resulting from exposure to relatively low levels of ozone. In the control image (left) from the lung of a person exposed only to air, the tiny cilia that clear the lungs of mucus appear along the top of the image in a neat and regular row. In the lung exposed to 20 ppb of ozone added to the air for four hours during moderate exercise, many cilia appear missing and others appear misshapen. Arrows point to tiny bodies called neutrophils in the ozone-exposed subject (right hand image). The presence of neutrophils indicates inflammation. Magnification: x400. (Aris *et al.*, 1993; NASA, 2004)

A threshold for effects has been found in some studies, although it varies between individuals and the ozone exposure regime used (PORC, 1993). The UK Expert Panel on Air Quality Standards (EPAQS) had recommended an eight hour running mean (8hrm) of 50 ppb as the critical level for ozone effects. The government adopted this as its air quality standard, with the objective that by the end of 2005, the 97<sup>th</sup> percentile of daily maximum 8hrm should not exceed 50 ppb (DoE, 1997). However, more recently the opinion on there being a threshold for effects has changed and a zero threshold is now being used (Mudway and Kelly, 2003). The Committee on the Medical Effects of Air Pollution

(COMEAP) have recommended using the annual average of the daily maximum 8 hour running mean to assess health effects, although a critical level or objective has not been set for this index.

Other countries and regions have set air quality guidelines or standards to protect human-health. For example, under the UNECE-convention of Long-Range Transboundary Air Pollution an AOT60 is used to assess health effects, based on the WHO Air Quality Guideline for ozone of  $120 \mu\text{g m}^{-3}$  (60 ppb) eight-hour mean value. However, as with COMEAP, WHO has recently reassessed the ozone issue and found that severe effects of ozone may also occur at levels significantly lower than 60 ppb. Therefore, new concepts are currently being developed to account for effects of ozone on human health.

### 1.4.3 Effects on Materials: thresholds and critical levels

The mechanisms of damage to materials by ozone and the concentrations at which they occur are not well defined as yet (PORG, 1998), although research programmes have been undertaken (Lee, *et al.*, 1995; Leith and Cape, 1998). In general, ozone degrades materials such as paints, plastic and rubber but the rate of deterioration can be reduced by adding "anti-ozonants" to the material, for example N-isopropyl-N-phenyl-p-phenylene diamine may be added to natural and synthetic rubber. The images in Figure 1.10 show examples of some of the effects on rubber observed during open-top chamber experiments at CEH Edinburgh (Leith, 2005). A provisional level of an annual mean  $\text{O}_3$  concentration of 20 ppb was set for an acceptable rate of materials deterioration at a UNECE workshop in 1993 (UNECE, 1993).

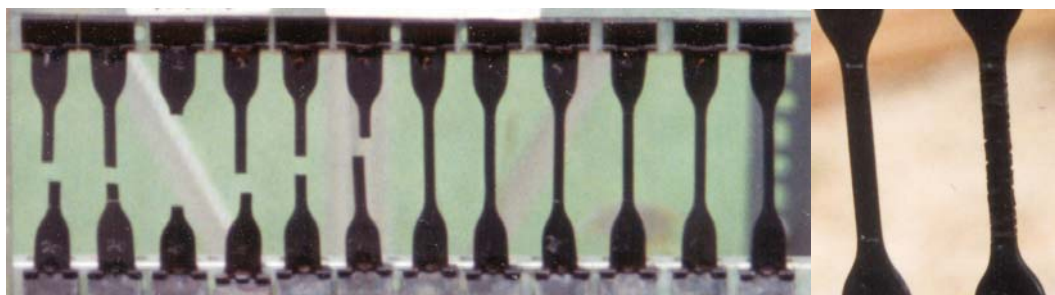


Figure 1.10 The effects of ozone on rubber samples under mild tension, with varying degrees of anti-ozonant protection (Leith, 2005). The samples with less protection show more damage. The right-hand image shows a close-up of a samples with (left) and without (right) protection. The unprotected sample is cracked along its length.

## 1.5 Global and UK Ozone Trends

### 1.5.1 Precursor Emissions

As has been described above, ozone is not directly emitted, but is a secondary pollutant, generated via photochemical reactions with man-made and natural precursor compounds such as NO<sub>x</sub> and VOC. The relative balance of these compounds determine whether ozone is produced or destroyed and the atmosphere is often termed NO<sub>x</sub>-limited or VOC-limited, depending on which is more important (Sillman, 1999). Thus changes in the emissions of these precursor compounds are important when considering trends in ozone.

Emissions from natural sources make some contribution, in particular biogenic VOCs can play an important role in regional ozone formation (Solmon *et al.*, 2004; Thunis and Cuvelier, 2000; Mendoza-Dominguez *et al.*, 2000). The main natural source of NO<sub>x</sub> is from soils but it is difficult to estimate on a large scale as many factors influence emission rates; for example temperature, soil water, inputs of fertilizer and N deposition. Simpson *et al.*, (1999) reported total European soil-NO<sub>x</sub> emissions ranging from 140 Gg-N y<sup>-1</sup> to 1500 Gg-N y<sup>-1</sup>, depending on the methodology used. Lightning and forest-fires are another, smaller, source, estimated to be ~20 Gg-N y<sup>-1</sup> and 9 Gg-N y<sup>-1</sup> respectively (*ibid*). This natural NO<sub>x</sub> is estimated to contribute about 10-30% of the tropospheric ozone budget (Lelieveld and Dentener, 2000).

Many plant species emit VOCs, such as isoprene, terpenes and alpha/beta-pinene, although forests are the most important source. Globally, biogenic VOCs (BVOCs) are a large component of total VOCs emissions (~60-70%) although regionally they may be more or less important depending on the balance of industry, urbanisation, agriculture and natural vegetation (Owen *et al.*, 2003; Simpson *et al.*, 1995). Guenther *et al* (1995) estimated global emissions of, at least, 1150 Tg C y<sup>-1</sup> which is about 7 times greater than estimates of man-made emissions. However as with natural NO<sub>x</sub> emissions, estimates of total emissions vary and earlier studies predicted emissions to be 400 to 500 Tg C y<sup>-1</sup> (*ibid*). The impact of BVOCs on ozone varies as some compounds deplete as well as produce ozone (alpha-pinene for example; Bell and Ellis 2004; Diem 2000; Han *et al.*, 2005). Some studies have also found ozone affects the amount of emission for vegetation (Rinnan *et al.*, 2005 and Vuorinen *et al.*, 2004).

The man-made emissions of ozone precursors are more reliably estimated, as most countries have statistics on industrial, commercial and domestic activity which can be used to calculate outputs. In many industrialised countries, emissions are also monitored at source which provides data to check the modelled estimates; for example the UK National Atmospheric Emission Inventory (<http://www.naei.org.uk/>) provides estimates of the emissions of many gases from measurements and modelling, including the ozone precursors.

#### **1.5.1.1 Trends in Emissions**

The efforts made by many industrialised countries to reduce air pollution since the 1960s has led to dramatic decrease in the emissions of several compounds; mainly SO<sub>2</sub> but also the ozone precursors. However, at the same time emissions from other parts of the world have continued to increase and biogenic emissions are largely uncontrollable. Overall, the present day trend is for a continuing, but slower, decrease in man-made NO<sub>x</sub> and VOC emissions from Europe and N America, and a rise in emissions from (re)developing countries such as China, Russia and SE Asia. Estimating current or future natural emissions is more uncertain and many models assume they remain constant. However, it is likely that climate change will affect emissions of BVOCs as they are sensitive to temperature and the soil water balance.

#### **1.5.2 Historical Trends**

As has been discussed, ozone would have been present in the pre-industrial "unpolluted" atmosphere due to its formation from natural emissions of NO<sub>x</sub> and VOCs. Several studies have attempted to model ozone concentrations in this period (Berntsen *et al.*, 2000; Hauglustaine and Brasseur, 2001; Lelieveld and Dentener, 2000) and there are some measurements from *ca* 1870's: Montsouris (Paris-France; Volz and Kley, 1988), Pic du Midi (SW France; Marenco *et al.*, 1994), and Moncalieri (N Italy; Anfossi *et al.*, 1991), for example. There were also measurements made on Ben Nevis (Scotland; Roy, 2005) during the 1880s but these are lost in the Royal Meteorological Society's archive and so have not been examined or published. All these studies indicate that since the early 1900s NH and European annual mean concentrations have roughly doubled or even tripled, from ~10 to ~30 ppb (Volz and Kley, 1988, Anfossi and Sandroni, 1997, Pavelin *et al.*, 1999) while SH concentrations have increased by only ~50% (from ~10 to ~15 ppb) to date (Sandroni and Anfossi, 1994).

### 1.5.3 Current and Future Trends

Since the late 1960s several countries have instigated networks of sites to make continuous measurements of air pollution. In the UK, routine measurements began in the early 1970s with measurement campaigns for short periods and a national network of ~16 rural monitoring stations was established in 1986 (PORG, 1998). These data, as well as modelling studies, have been used to assess current and future ozone trends.

With more than two decades of data available we would anticipate that trends due to reductions in precursor emissions and changes in the global-background ozone concentration would be easily discernible. Many factors influence ozone concentrations and so trends can be difficult to interpret, for example: local site characteristics such as ozone dry deposition rates and NO<sub>x</sub> emissions vary; annual large scale meteorological patterns, such as the prevalence of anti-cyclonic conditions, affect the long-range transport of ozone and precursor emissions. However, several studies using measurements and models have clearly demonstrated:

1. Decreases in peak ozone concentrations in industrialised regions as precursor emissions have been reduced, although the trends are not linear with emissions, as might be expected with ozone's complicated chemistry (Bellanger and Tomassone, 2004; Derwent *et al.*, 2003; Metcalfe *et al.*, 2002; Solberg *et al.*, 2005).
2. Increases in the global background ozone concentration of ~0.2 ppb y<sup>-1</sup>, mainly in the NH, due to global increases in precursor emissions (Ashmore *et al.*, 2003; Simmonds *et al.*, 2004; Vingarzan, 2004).

To predict trends into the future models must be used, although measurements can also be incorporated (Ashmore *et al.*, 2003). Several factors influence the realism of modelled future ozone concentrations, but the main driving factors are emissions and meteorology. The baseline emission estimates used by many researchers are from the IPCC (Nakicenovic *et al.*, 2000), although there are other data sets that can be used, such as RAINS (Regional Air Pollution Information and Simulation, IIASA, 2005). These emission data sets usually provide a range of emission estimates based on different scenarios of future activity, such as industrialisation, global population, methods of energy production etc. In most studies where a business-as-usual (BAU) emission scenario is used, global background ozone concentrations continue to increase,

reaching levels that could cause major damage to crops and human health in some parts of the world. For example Prather *et al.*, 2003 compiled the results from 10 global models using a predefined set of IPCC emission scenarios and produced average predictions of future ozone levels upto 2100. Figure 1.11 shows one of the resulting maps of the change in ozone concentrations across the globe from the year 2000 to 2100, based on the A2 high emission scenario, and Figure 1.12 shows a plot of the measured annual mean at a site in the UK and modelled values from a range of emission scenarios. There are many uncertainties in such estimates of future ozone levels but the consensus is that in future concentrations will be greater than at present unless dramatic reductions in emissions occur globally.

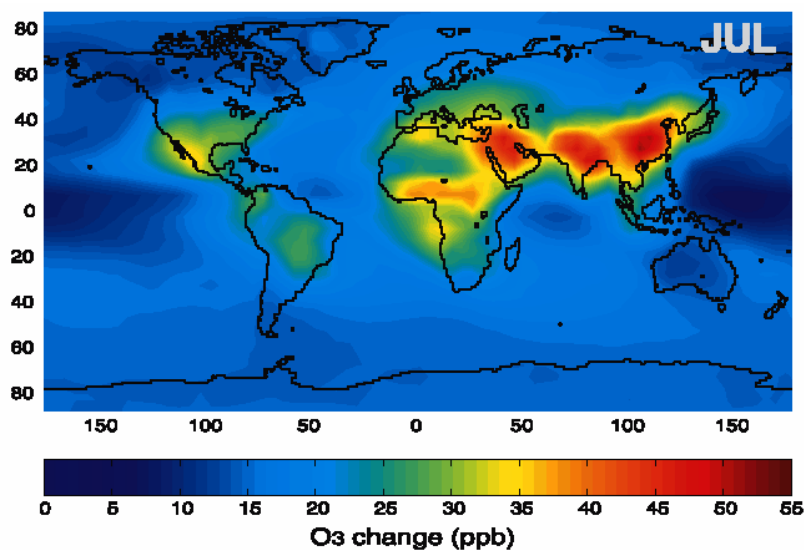


Figure 1.11 Monthly mean surface ozone increase (ppb) July from Y2000 to Y2100 following scenario A2x. Prather *et al.*, 2003.

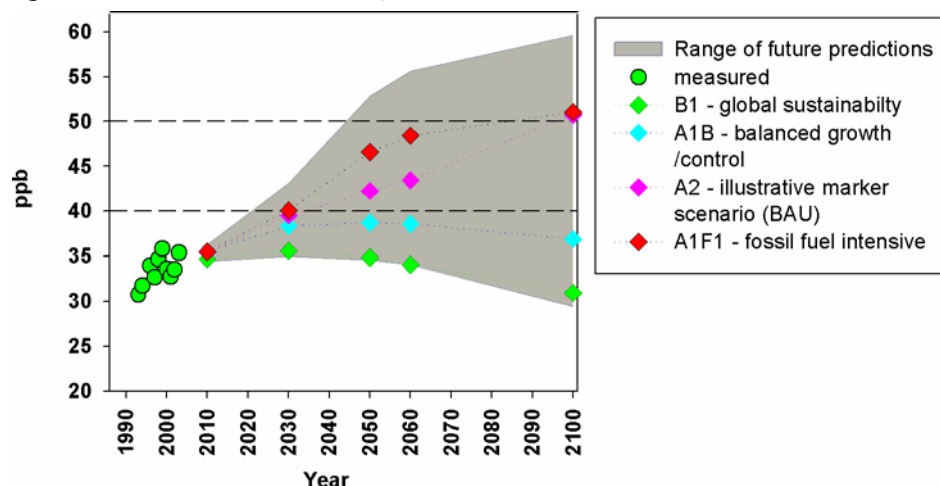


Figure 1.12 The current measured annual mean ozone concentration at Dunslair Heights, a hill-top site in the Scottish Border, and predictions of future concentrations derived from the results of Prather *et al.*, 2003 using the methodology described in Ashmore *et al.*, 2003.

Another question often asked is the likely impact of future ozone concentrations on vegetation but this is quite difficult to answer. The model estimates are themselves subject to uncertainties as climate change is likely to affect the distribution of plant types and their physiology, as well as VOC emissions. However, if there is a threshold ozone concentration of  $\sim 20$ - $30$  ppb for effects to begin in vegetation we can assume that predictions of average concentrations in the range 40 to over 100 ppb by 2100 are likely to cause significant damage (Ashmore *et al.*, 2002, 2003). An assessment of possible changes in the AOT40 across the UK indicated substantial increases in this index by the year 2050 (Figure 1.13).

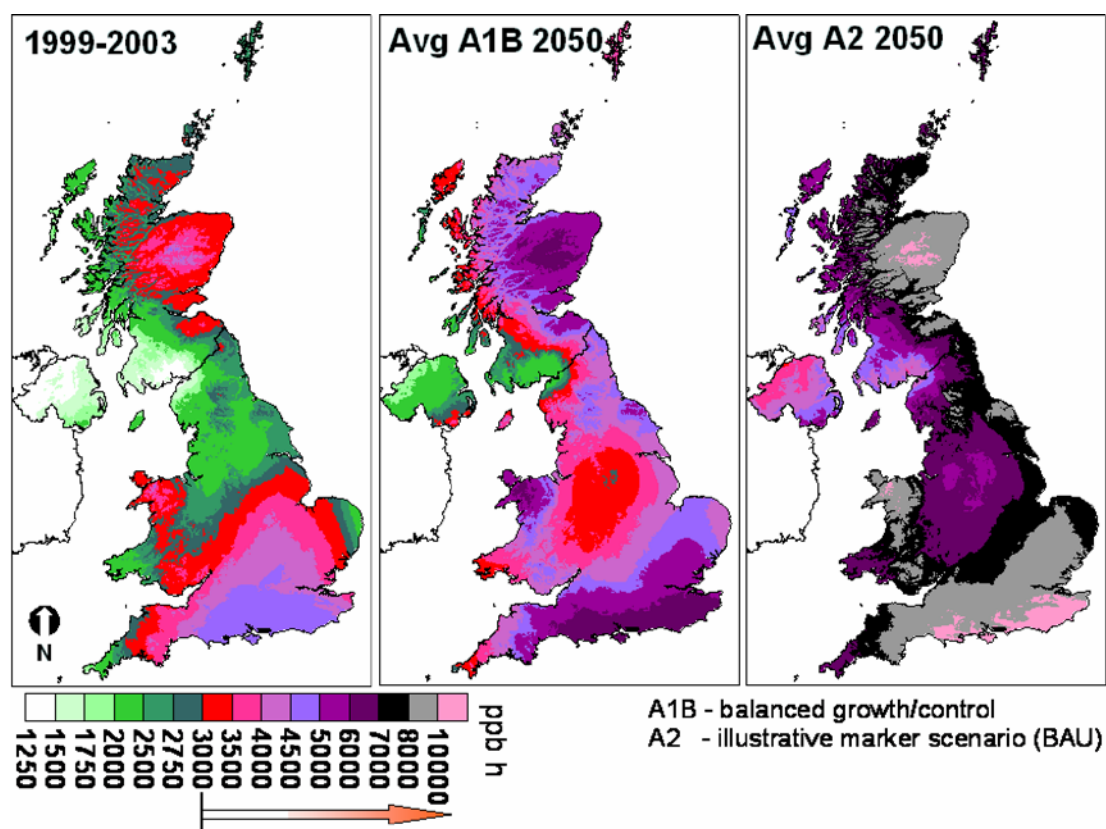


Figure 1.13 1 km x 1km maps of the current AOT40 for crops and semi-natural vegetation across the UK (Coyle *et al.*, 2004), and predictions of future levels in 2050 derived from data for the UK monitoring sites and the results of Prather *et al.*, 2003, using the methodology described in Ashmore *et al.*, 2003 and Coyle *et al.*, 2002. The arrow indicates the colour range that exceeds the critical level of 3,000 ppbh.

## ***1.6 Hypothesis, Objectives and Thesis Plan***

The concentrations, budgets and trends in tropospheric ozone have been described in this chapter. It is a trace gas that plays many roles in the atmosphere from its beneficial effects in the stratosphere to its detrimental effects on human health and vegetation in the boundary layer. The focus of this thesis is the gaseous exchange of ozone at the Earth's surface and understanding the complex process by which it is deposited on and absorbed by vegetation.

As will be described in the following chapters, the downward flux of ozone can be easily measured in the field using micrometeorological methods but distinguishing the different deposition pathways, eg stomata, leaf cuticle or soil, is more difficult. It is possible to separate the stomatal and total non-stomatal pathways by considering only night-time measurements or measuring and modelling the stomatal flux. Previous work using both of these approaches has identified surface temperature, solar radiation, surface wetness and relative humidity as possible controlling mechanisms on the non-stomatal flux (Coe *et al.*, 1995; Fowler *et al.*, 2001; Rondon *et al.*, 1993; Zhang *et al.*, 2002).

Increasing surface temperature and solar radiation increase the ozone flux to dry surfaces. It has been hypothesised that this is due to the thermal decomposition of ozone or photolytic/photochemical destruction of ozone; mediated by compounds on, or emitted by, leaf surfaces.

The effect of surface wetness and humidity is less clearly defined as some studies found the ozone flux increased when the surface was wet while others that it decreased. In some circumstances surface water may block the pathway for ozone deposition as ozone has a low solubility in water and so the flux decreases. However if the chemistry of the surface water allowed significant uptake of ozone by aqueous phase reactions then the flux may increase.

The hypothesis that the processes outlined above control non-stomatal deposition are examined by:

1. Measuring ozone deposition over grassland for an extended period using micrometeorological methods – this vegetation was chosen as the canopy is almost entirely one species and it has a fairly homogenous physical

structure, which simplifies the analysis and interpretation of the measurements.

2. Quantifying the amount of ozone the vegetation directly absorbs through its stomata, using standard methods of measuring and modelling stomatal conductance to water-vapour.
3. Examining variations in the amount of ozone deposited to non-stomatal parts of the canopy and surface – this aspect of the surface exchange process is currently poorly understood which limits our ability to correctly model and estimate the boundary layer ozone budget. This issue was recently highlighted by Erisman *et al.*, (2005) as a target for further research.
4. Defining a parameterisation for the non-stomatal process that could be implemented in regional ozone model (assuming controlling factors can be clearly identified).
5. Testing the new parameterisation and comparing the results to the field measurements, using a simple multiplicative type “big-leaf” deposition model.

These objectives are met as follows:

Chapter 2: The underlying theory of micrometeorology and methods of implementing it in the field are described, as well as the deposition resistance analogy which is used to interpret the results.

Chapter 3: Current methods of modelling ozone concentrations and deposition at the global, regional and local scale are reviewed and the methods that will be applied to the grassland are described.

Chapter 4: In this chapter the field measurements are described, giving a thorough overview of the basic structure of the canopy, the instrumentation employed, and the site’s meteorology.

Chapter 5: The trace-gas flux measurements are described, giving a thorough review of the data treatment and quality processing that is required to obtain the final datasets. An overview of the results is given and some aspects of ozone

deposition are examined such as the effects of silage harvests and the difference between daytime and night-time fluxes.

Chapter 6: In this chapter the process of ozone deposition to the canopy is examined in detail. The stomatal conductance models are parameterised, allowing stomatal deposition to be quantified, and the results are compared to the measured stomatal component. The stomatal term is then separated from the total using both the measurements and models. The processes controlling this residual non-stomatal deposition then examined and parameterised. Finally the new non-stomatal parameterisation is tested in a simple canopy deposition model for the site.

Chapter 7: The errors and uncertainties in the measurements and derived values are described and quantified in this chapter.

Chapter 8: This chapter gives a synthesis of the results, conclusions and possible avenues for further research.



## **2 Measuring the Ozone Flux: Micrometeorological Theory and Methods**

### ***2.1 Introduction***

Dry deposition and trace gas emission occurs at the Earth's surface in the lowest part of the troposphere, the planetary boundary layer (PBL). In the PBL air flow is modified by aerodynamic friction with the surface and thermal stratification, which determines the air density gradient. The depth of the boundary layer can vary from  $\sim 100$  m to  $\sim 3$  km depending on conditions. Within the boundary layer entities such as momentum, heat, water vapour and trace gases are mainly transported horizontally by wind and vertically by turbulence. These processes operate on relatively small temporal and spatial scales hence their study is included in the field of micrometeorology.

Vertical transport between the atmosphere and the surface primarily occurs via the swirling motions of air known as eddies, which are variable in size but are generally smaller towards the surface. Kinetic energy transfer occurs on 3 scales: large eddies are approximately the same size as the depth of PBL and receive energy from large-scale atmospheric processes such as thermals or wind shear; in the middle size range larger eddies transfer energy to smaller eddies in a process sometimes called an energy cascade (Garratt, 1992); for smaller eddies of a few millimetres in size, viscous damping becomes the dominant energy loss mechanism. Although it is possible to write down a complete set of equations describing the dynamics and thermodynamics of the boundary layer, they are complex and have no exact analytical solution (known as the closure problem; Stull, 1989 and Garratt, 1992). In the case of measuring fluxes of trace gases in the lower part of the boundary layer, several assumptions and mathematical techniques are employed to reduce the problem to a relatively simple set of equations, as described in the following sections.

### ***2.2 Structure of the PBL***

It is possible to identify 2 layers within the PBL (Figure 2.1):

1. The outer (Ekman) layer, where air flow is largely independent of the surface and the Coriolis force, due to the Earth's rotation, is more important. This

layer is sometimes called the *Ekman layer* as Ekman first examined the effects of rotation on boundary layer flow (Garratt, 1992).

2. The inner or surface layer where the atmosphere is mainly dependent on the surface characteristics.

It is only the surface layer, where the atmosphere is closely coupled to the surface, in which we are interested. This region is normally defined as that in which fluxes vary by less than 10% with height. It is often called the constant flux layer, as fluxes within it can be described by measurements at a single height. The surface layer itself has structure, as very close to the surface wakes are produced by rough surface elements, leading to a roughness sub-layer as shown in Figure 2.1. Above this is the inertial sub-layer where fluxes are constant with height and can be readily deduced from measurements.

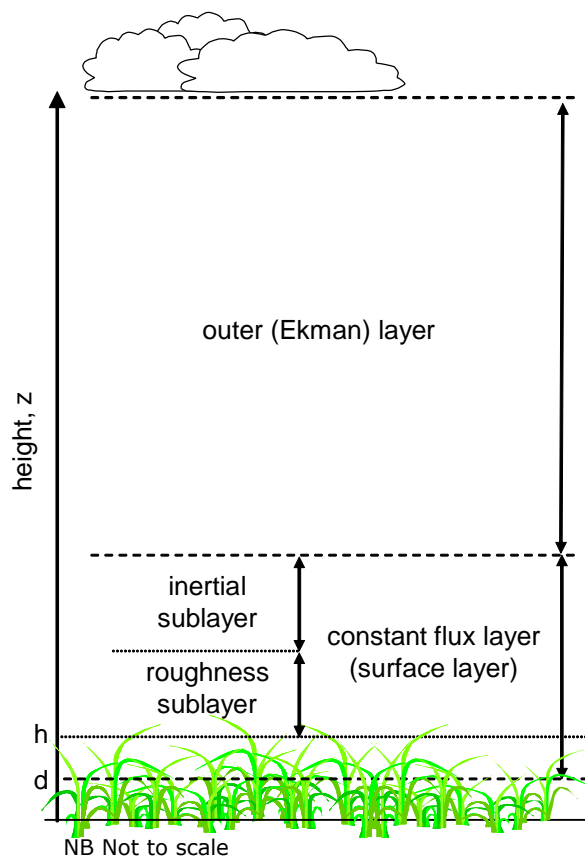


Figure 2.1 Structure of the PBL and constant flux layer (its depth is ca. 15% of the PBL).

## **2.3 Gradients and Stability in the Surface Layer**

The change in an entity with height above the surface of a crop, or other uniform vegetation, is called its profile or gradient. The profile of wind-speed in the surface layer is modified by thermal stratification as well as turbulence. Changes in the thermal stratification of air above the ground arise from the daily variation in solar heating and radiative cooling of the ground, as discussed in relation to the diurnal cycle of ozone. The surface layer is often described as being neutral, unstable or stable depending on which factors are controlling the degree of turbulence within the layer and so the shape of the wind-speed profile.

### **2.3.1 Neutral Conditions (Fully-Forced Convection)**

Neutral conditions typically occur on windy and overcast days when thermal stratification is at a minimum and turbulence is mainly driven by wind shear and surface friction. In a neutral atmosphere there is no gradient in virtual potential temperature ( $\theta_v$ ),  $\partial\theta_v/\partial z = 0$ , wind speed increases logarithmically with height and the eddies are roughly circular (Figure 2.2a). The rate of turbulent diffusion for momentum is the same as heat, water vapour and trace gases as the latter are also transported vertically by eddies alone.

### **2.3.2 Unstable (Mixed or Free Convection)**

During sunny daytime conditions, sunlight heating the ground results in a negative vertical gradient in the absolute temperature of moist air,  $T$ . If this decrease in temperature exceeds the dry adiabatic lapse rate ( $\Gamma = 9.8 \text{ }^\circ\text{C km}^{-1}$ ), equivalent to a negative vertical gradient in  $\theta_v$ , (i.e.  $\partial\theta_v/\partial z < 0$ ), the adiabatic cooling of a rising air parcel allows it to remain warmer, hence lighter, than the surrounding air, and the ascent is sustained through buoyancy. Conversely, an air parcel descending from a higher level would be colder and denser than surrounding air and so tend to descend further. Such conditions are termed unstable because air parcels tend to continue moving in the same direction and away from their original position when set in motion. Turbulence generated by the friction of wind blowing horizontally over a rough surface can therefore be greatly enhanced in unstable conditions, resulting in a well-mixed boundary layer and large rates of turbulent diffusion. The amount of enhancement increases as wind shear decreases and eddies are progressively stretched with height, as illustrated in Figure 2.2b. In this case, the rate of turbulent diffusion of

momentum is less than that for heat (and water vapour and trace gases), as there is a preferential upwards transport of heat.

### 2.3.3 Stable (Damped or No Convection)

Positive vertical gradients in virtual potential temperature ( $\partial\theta_v/\partial z > 0$ ) may occur in which temperature increases with height up to a level in the atmosphere where the gradient then changes sign. The level at which the gradient changes to a decrease with height is typically 1 m to 1 km in UK conditions and is referred to as a temperature inversion. These occur primarily at night due to the long-wave radiative cooling of the ground and indirect cooling of the air close to the ground. Vertical transport within the surface layer is reduced as any parcel of air forced up or downwards will then tend to revert to its former position. In these circumstances, friction-driven turbulence is reduced or even suppressed and diffusional mixing is small, leading to large pollutant concentrations and vertical gradients. The turbulent eddies tend to be compressed towards to the surface, as illustrated in Figure 2.2c

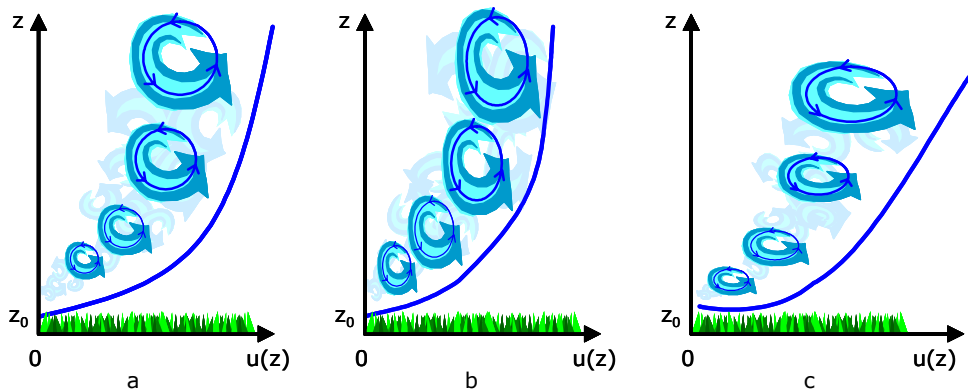


Figure 2.2 Illustration of wind speed profiles and turbulent eddy structure in different stability regimes, (a) neutral, (b) unstable and (c) stable (after Thom, 1975).

## 2.4 Describing the Surface Layer and Measuring Fluxes

As noted above, it is not possible to provide exact analytical equations to describe the dynamics of turbulence and heat in the surface layer. However measurement campaigns over the last 60 years or so have shown that observations have repeatable and consistent characteristics, allowing empirical relationships to be developed. Similarity theory is a method of organizing the variables of interest into dimensionless groups and deriving relationships

between them. In the case of the surface layer, Monin-Obukhov similarity theory is used, which only works when winds are not calm, and friction velocity ( $u_*$ ) is not zero (Stull, 1989).

It is the tangential forces or shearing stress, acting on air passing over a rough surface that disrupts the laminar flow and generates eddies of air so that the flow becomes turbulent. This turbulence leads to random fluctuations in wind-speed and other entities on the scale of the eddies. The horizontal and vertical wind-speeds ( $u$  and  $w$  respectively) can be equated to a mean over time plus the instantaneous departure from the mean, commonly written:

$$u = \bar{u} + u' \quad (9.)$$

where  $\bar{u}$  = mean with time,  $u'$  = instantaneous deviation from the mean value

Some other common variables and parameters that will be used are:

- $T$  = absolute temperature in °C or K
- $\theta$  = potential temperature
- $\theta_v$  = virtual potential temperature
- $\chi_s$  = concentration of trace gas S
- $k$  = von Karman's constant<sup>1</sup> = 0.41, which is independent of the surface type
- $g$  = 9.81 ms<sup>-2</sup>, gravitational acceleration
- $q$  = specific humidity of air  
(mass of water vapour per unit mass of moist air)
- $e$  = partial pressure of water vapour in air
- $e_s[T]$  = saturation vapour pressure of water at temperature T.
- $d$  = vapour pressure deficit (*vpd*) or saturation deficit,  $e_s[T]-e$
- $\rho$  = air density, normally in kg or g m<sup>-3</sup>
- $c_p$  = specific heat at constant pressure for moist air, 1.01 J kg<sup>-1</sup> K<sup>-1</sup>
- $\lambda$  = latent heat of vaporisation of water, 2470 J kg<sup>-1</sup> K<sup>-1</sup>
- $z$  = height above ground, normally in m
- $h$  = crop height (m)
- $d$  = zero plane displacement height; the height at which canopy effectively becomes closed and all momentum is dissipated (m; typically 60 to 80% of the canopy height<sup>2</sup>)
- $z_0$  = aerodynamic roughness length, the height at which the extrapolated vertical profile in windspeed = 0, typically about 0.1 h.
- $z_0'$  = height of apparent sink for heat and water vapour ( $z_0' < z_0$ )

The relevant scaling parameters for Monin-Obukhov theory are:

$$u_* = (-\overline{u'w'})^{0.5}, \text{ friction velocity} \quad (10.)$$

$$L = \frac{-\overline{\theta u_*^3}}{kg(\overline{w'\theta'})}, \text{ Monin-Obukhov length} \quad (11.)$$

---

<sup>1</sup> There has been some debate as to the exact value of  $k$  as although a constant of 0.40 is measured in the laboratory, in the field it appears to vary with Reynolds number (Frenzen and Vogel, 1995). A value of 0.41 is generally accepted as being the most suitable for short vegetation and is used in this study.

$$\theta_* = -\frac{\overline{w'\theta'}}{u_*}, \text{ potential temperature scale} \quad (12.)$$

$$q_* = -\frac{\overline{w'q'}}{u_*}, \text{ humidity scale} \quad (13.)$$

$$\chi_{s*} = -\frac{\overline{w'\chi_s'}}{u_*}, \text{ trace-gas (s) scale} \quad (14.)$$

The parameter  $L$  depends on the ratio of frictional to buoyancy forces and so can be used to characterise the condition of the surface layer. The flux of an entity can be found from (Thom, 1975):

$$F_s[z] = a_s u_* \chi_* \quad (15.)$$

where  $a_s$  = scaling factor for trace gas  $S$

There are three methods that are commonly used to measure trace-gas fluxes in the surface layer. The first, eddy-correlation or covariance, is a direct method whereas the other two (aerodynamic gradient and Bowen ratio) are indirect and rely on the measurement of mean values.

### 2.4.1 The Eddy-Correlation Method

In all conditions the average vertical flux of momentum ( $\tau$ ) or shearing stress is defined as:

$$\tau = -\rho \overline{u'w'} = \rho u_*^2 \quad (16.)$$

By analogy with this equation the fluxes of sensible heat ( $H$ ), latent heat ( $\lambda E$ ) and a trace gas ( $F_s$ ) can be written as:

$$H = \rho c_p \overline{w'\theta'} \quad (17.)$$

$$\lambda E = \lambda \overline{w'q'} \quad (18.)$$

$$F_s = \overline{w'\chi_s'} \quad (19.)$$

Hence measurements of the turbulent fluctuations of each component can be used to determine fluxes. This method has the advantage of being quite simple and direct but the turbulent fluctuations occur very rapidly so fast response instruments are required. Sensors must be capable of responding to signals with a frequency of 0.1 Hz to 10 Hz. The practical application of this technique to measuring fluxes over grassland is described in Sections 4.5.3 and 5.2.2.

---

<sup>2</sup>  $d$  is calculated from the measurements at Easter Bush in Section 6.2.4.

## 2.4.2 The Aerodynamic Gradient Method

Where the turbulent fluctuations ( $u'$ ,  $w'$  etc) are not directly measured further assumptions and simplifications must be made to estimate the fluxes. In the case of the gradient method,  $u$ ,  $T$ ,  $e$  and  $\chi$  are measured at a series of heights above the surface giving their profiles in the surface layer.

In neutral conditions the wind-speed profile is logarithmic and the eddies rotate at a uniform tangential velocity (the friction velocity) so that  $u_* = u' = w'$ . The logarithmic wind-speed profile is:

$$u = \frac{u_*}{k} \ln\left(\frac{z-d}{z_0}\right) \quad (20.)$$

and differentiating this gives:

$$\frac{\partial u}{\partial z} = \frac{u_*}{k(z-d)} \quad (21.)$$

The diameter of the eddies increase with height and is known as the mixing length ( $l$ ):

$$u_* = u' = w' = l \partial u / \partial z \quad (22.)$$

In unstable conditions  $w' > u'$  and  $l > k(z-d)$ , whereas in stable conditions  $w' < u'$  and  $l < k(z-d)$ . This tends to cause the wind-speed profile to diverge from its logarithmic shape as height increases. The differential wind-speed profile (19) can therefore be rewritten in a more general form as:

$$\frac{\partial u}{\partial z} = \frac{u_*}{k(z-d)} \Phi_m \quad (19')$$

where  $\Phi_m$  is a dimensionless stability function with a value larger or smaller than one in stable or unstable conditions respectively

and the mixing length as:

$$l = \frac{k(z-d)}{\phi_m} \quad (23.)$$

The first-order closure approximation known as K-theory assumes that the time averaged flux is related to its local gradient (i.e.  $-\overline{u'w'} \propto \partial u / \partial z$ ), giving an equation similar to Fick's Law of diffusion:

$$F_s[z] = a_s K[z] \partial \chi_s / \partial z \quad (24.)$$

where  $a_s$  = scaling factor for  $S$   
 $K[z]$  = eddy diffusivity<sup>3</sup>

<sup>3</sup> K is also known as eddy viscosity, eddy-transfer coefficient, turbulent-transfer coefficient, gradient-transfer coefficient or any other variation on these themes.

Applying this formula to equations 16 to 19 for the fluxes of momentum, sensible heat, latent heat and a trace gas ( $m$ ,  $H$ ,  $E$  and  $F_s$  respectively) gives:

$$\tau = \rho K_m \partial u / \partial z \quad (16')$$

$$H = -K_H \rho c_p \partial T / \partial z \quad (17')$$

$$E = -K_E \lambda \partial q / \partial z \quad (18')$$

$$F_s = -K_s \partial \chi / \partial z \quad (19')$$

From equations (16) and (16') it can be shown that:

$$K_m = \frac{k(z-d)u_*}{\Phi_m} \quad (25.)$$

and similar functions can be derived for  $K_H$ ,  $K_E$  and  $K_s$  containing the stability correction functions  $\Phi_H$ ,  $\Phi_E$  and  $\Phi_s$  respectively.

$$K_H = \frac{k(z-d)u_*}{\Phi_H} \quad (26.)$$

In neutral conditions  $K_m = K_H = K_E = K_s$ ; in stable conditions  $K_m \approx K_H$  and  $K_H = K_E = K_s$ ; in unstable conditions  $K_m < K_H$  and  $K_H = K_E = K_s$ . However, as will be shown below, it is more convenient to express the flux in terms of frictional values ( $u_*$ ,  $\theta_*$ ,  $q_*$ , and  $\chi_*$ ) so that the equation (15) can be used to calculate the fluxes. From equation (19') it follows that:

$$u_* = \frac{k(z-d)}{\Phi_m} \frac{\partial u}{\partial z} \quad (27.)$$

and similarly

$$\theta_* = \frac{k(z-d)}{\Phi_H} \frac{\partial \theta}{\partial z} \quad (28.)$$

$$q_* = \frac{k(z-d)}{\Phi_H} \frac{\partial q}{\partial z} \quad (29.)$$

$$\chi_* = \frac{k(z-d)}{\Phi_H} \frac{\partial \chi}{\partial z} \quad (30.)$$

The parameters  $L$  and  $Ri$  depend on the ratios of buoyant thermal forces to frictional turbulent forces and are most commonly used to describe the state of the atmosphere.

$$L = -\frac{\overline{(u'w')^2}^3}{k(g/\theta)\overline{(w'\theta')}} = -\frac{\rho c_p \theta u_*^3}{kgH} \quad (11')$$

$$Ri = \frac{g\theta^{-1} \frac{\partial \theta}{\partial z}}{\left(\frac{\partial u}{\partial z}\right)^2} \quad (31.)$$

Several parameterisations for  $K$  and  $\Phi$  using  $L$  and  $Ri$  to quantify different stability conditions have been derived from experiments over the years. The most commonly used and accepted (Paulson, 1970 for example) are those developed by Dyer and Hicks, (1970), Businger *et al.*, (1971) and Webb (1970):

In unstable conditions,  $Ri < 0.1$ :

$$\Phi_m^2 = \Phi_H = \Phi_E = \Phi_X = \left(1 - 16 \frac{z-d}{L}\right)^{-0.5} = (1 - 16Ri)^{-0.5} \quad (32.)$$

and in stable to slightly unstable conditions,  $-0.1 \leq Ri \leq 1$ :

$$\Phi_m = \Phi_H = \Phi_E = \Phi_X = \left(1 - 5.2 \frac{z-d}{L}\right) = (1 - 5.2Ri) \quad (33.)$$

The effect of  $\Phi$  on non-neutral wind-speed profiles is to effectively linearise them on a log scale and move them towards the neutral profile. The simplest approach to quantifying the wind-speed profile and fluxes which was often used in the past (Garland, 1977 for example) treats  $\Phi$  as a constant in the integration of equation (19'). However, this approach leads to some non-linearity in non-neutral conditions as  $\Phi_m$  does vary with height (as a function of  $(z-d)/L$ ). The most commonly used approach in gradient measurements now includes  $\Phi_m$  in the integration (equation 34), leading to the following equations for the corrected wind-speed profile (35) and equivalent relationships for the other scalars (36 to 38) (Sutton, *et al.*, 1993).

$$U[z-d] = \frac{u_*}{k} \int_0^z \frac{\Phi_m(\zeta)}{z-d} \partial z \quad \text{where } \zeta = (z-d)/L \quad (34.)$$

$$U[z-d] = \frac{u_*}{k} \left[ \ln\left(\frac{z-d}{z_0}\right) - \Psi_m(\zeta) \right] \quad (35.)$$

$$\theta[z-d] = \frac{\theta_*}{k} \left[ \ln\left(\frac{z-d}{z_\theta}\right) - \Psi_H(\zeta) \right] \quad (36.)$$

$$q[z-d] = \frac{q_*}{k} \left[ \ln\left(\frac{z-d}{z_q}\right) - \Psi_H(\zeta) \right] \quad (37.)$$

$$\chi[z-d] = \frac{\chi_*}{k} \left[ \ln\left(\frac{z-d}{z_x}\right) - \Psi_H(\zeta) \right] \quad (38.)$$

$$\text{where } \Psi_m[\zeta] = \int_0^{\zeta/L} \frac{1 - \Phi_m}{\zeta} \partial \zeta \quad (39.)$$

$$\psi_H[\zeta] = \int_0^{\zeta/L} \frac{1 - \Phi_H}{\zeta} d\zeta \quad (40.)$$

and the constants of integration,  $z_\theta$  etc, are the heights above  $d$  at which the scalars are zero.

In stable conditions

$$\psi_m[\zeta] = \psi_H[\zeta] = -5.2 \zeta = -5.2 \frac{z-d}{L} \quad (41.)$$

In unstable conditions, integrating with equation (27) gives (Paulson, 1970):

$$\psi_m[\zeta] = 2 \ln\left(\frac{1+\chi}{2}\right) + \ln\left(\frac{1+\chi^2}{2}\right) - 2 \tan^{-1}(\chi) + \frac{\pi}{2} \quad (42.)$$

$$\psi_H[\zeta] = 2 \ln\left(\frac{1+\chi^2}{2}\right) \quad (43.)$$

$$\text{where } \chi = (1-16\zeta)^{0.25}$$

Thus having calculated values of  $\psi_m[\zeta]$  or  $\psi_H[\zeta]$  at each measurement height simple linear regression of each quantity (temperature, wind speed or trace-gas concentration) with  $\ln(z-d) - \psi[\zeta]$  provides  $u^*$ ,  $\theta^*$  and  $\chi^*$  from which the fluxes can be calculated using equation (15) with appropriate scaling parameters.

This approach has some advantages over the eddy-correlation technique as it allows  $z_0$  to be estimated directly in non-neutral conditions and provides a check on the stability correction since it is possible to examine the improvement in linearity of the wind-speed profile. The practical application of the aerodynamic-gradient method to measuring fluxes in the surface layer is discussed in Sections 4.5.2 and 5.2.1.

### 2.4.3 The Bowen Ratio

The Bowen Ratio method uses the formula describing the energy balance of the surface to derive fluxes:

$$R_n - G = H + \lambda E \Rightarrow \lambda E = (R_n - G)/(1+\beta) \quad (44.)$$

where  $R_n$  = net radiation  
 $G$  = soil heat flux  
 $\lambda E$  = latent heat flux  
 $\beta$  = Bowen Ratio,  $H/\lambda E$

Assuming that the transfer coefficients of heat and water vapour are the same,  $\beta$  can be found from measurements of temperature ( $T$ ) and vapour pressure ( $e$ ) at a series of heights, using  $\beta = H/\lambda E = \gamma \partial T / \partial e$  where  $\gamma$  = psychrometer constant. The psychrometer constant is defined as:

$$\gamma = \frac{c_p p}{\lambda \varepsilon} \quad (45.)$$

where  $p$  is atmospheric pressure (Pa) and  $\varepsilon$  is the ratio of the molecular weight of water to dry air (18/29),  $\gamma$  has a value of 66 Pa K<sup>-1</sup> at 0°C and 101.3 kPa, (Monteith and Unsworth, 1990).

Using K-theory the latent heat flux may be written as:

$$\lambda E = - \frac{\rho c_p}{\gamma} K_E \partial e / \partial z \quad (46.)$$

From equations (15") and (31) the energy balance (29) can be written as:

$$R_n - G = -\rho c_p K_H \left( \frac{\partial \theta}{\partial z} + \frac{\partial e}{\gamma \partial z} \right) \quad (47.)$$

Hence from measurements of  $R_n$ ,  $G$ , temperature and vapour pressure,  $K_H$  can be determined and used to estimate  $K_\chi$ . The Bowen Ratio method performs best when energy fluxes ( $H$  and  $\lambda E$ ) are large and more poorly when they are small. In these circumstances or when stability corrections are large, it may be preferred to the eddy-correlation or gradient methods. On the other hand it does not perform well close to dawn or dusk, during overcast days, periods of intermittent cloud or at night-time when ( $R_n - G$ ) tends towards zero.

The measurements required to use this method are described in Chapter 4. However, in this study the Bowen Ratio method has not been used to calculate fluxes but the data are used as a check on the quality of the gradient and eddy-correlation measurements. From equation (44) the net balance of incoming and outgoing energy should be zero and a plot of  $R_n - G$  against  $H + \lambda E$  form a straight line, with a slope of 1 and zero intercept. In practice the energy balance is never zero and most measurements achieve closure within the range of 10 - 30% (Twine, *et al.*, 2000; Wilson, *et al.*, 2002).

## 2.4.4 Practical Consideration and Limitations of Micrometeorological Methods

### 2.4.4.1 Fetch

As described above, flux measurements are made in the inertial sub-layer where it can be assumed that fluxes are reasonably constant with height. However to allow the surface layer to develop and stabilise the surface must be fairly flat, homogeneous and extensive. Thus measurements must be made at some distance downwind of the last major obstacle to flow, termed the fetch (Figure 2.3). Over short vegetation a ratio of measurement height to fetch of

approximately 1:100 is required (Monteith and Unsworth, 1990). It is possible to calculate the flux footprint of each measurement and so check that the results only include the surface area of interest, as described in Section 5.2.3.

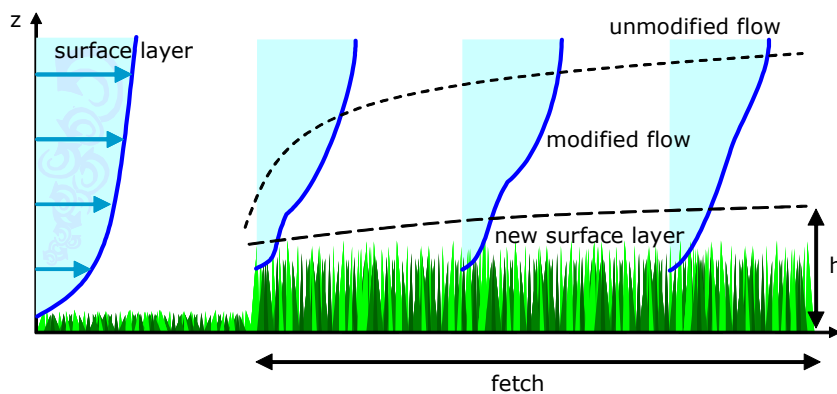


Figure 2.3. Illustration of the development of a new surface layer as air moves from one surface to another (after Monteith and Unsworth, 1990 p 233). For micrometeorological flux measurements the ratio of fetch to  $h$  should be approximately 100:1.

#### 2.4.4.2 Stationarity and Homogeneity

Although the assumption that fluxes are constant with height in the inertial sub-layer (Section 2.2) is generally accepted, it is only true if conditions at the measuring location are “stationary”. In practice a range of processes may introduce non-stationarities including: (1) chemical reactions within the air column, (2) changes in trace-gas concentration or meteorological variables with time and (3) horizontal gradients in concentration. These factors may lead to a change in the flux with height known as flux divergence. For a reactive trace gas, such as ozone, a conservation equation may be written as (Fitzjarrald and Lenschow, 1983):

$$\frac{\partial \chi}{\partial t} + u \frac{\partial \chi}{\partial x} + w \frac{\partial \chi}{\partial z} + \frac{\partial \overline{w' \chi'}}{\partial z} = Q_x \quad (48.)$$

where  $u$  and  $w$  are mean horizontal and vertical wind velocities, respectively, and  $Q_x$  represents the sum of internal chemical sources and sinks within the air column. Assuming that the mean vertical wind speed is zero, the vertical gradient in trace gas flux (or flux divergence) is given by (Fowler and Duyzer, 1989):

$$\frac{\partial F}{\partial z} = Q_x - \frac{\partial \chi}{\partial t} - u \frac{\partial \chi}{\partial x} \quad (49.)$$

### 1) Chemical Reactions

Chemical interactions may lead to large errors in measured fluxes when the timescales of reactions are similar to the timescales of turbulent mixing (Vila-Guerau de Arellano *et al.*, 1993). Ozone reacts rapidly with nitric oxide (NO) which can result in a large divergence, particularly for the flux of NO and NO<sub>2</sub> (Gao and Wesely, 1994; Gao *et al.*, 1991; Heal *et al.*, 2001; Lenschow and Delany, 1987). However in un-polluted rural environments, although there may potentially be interference from soil NO emissions, the effect on ozone fluxes is small and can be neglected (Flechard 1998a; Gao *et al.*, 1991; Walton *et al.*, 1997).

Emissions of volatile organic compounds can also cause non-stationarity, for example Utiyama *et al.*, (2004) reported observations of ozone production just above a pine forest in central Japan which they attributed to biogenic emissions of VOCs from the canopy.

### 2) Changes with Time (Non-Stationarity): Storage Errors

Changes in the trace gas concentration with time in the air column below the measurement point (storage) may be caused by other factors and the vertical gradient in flux due to storage may be expressed as:

$$\frac{\partial F_{stor}}{\partial z} = -\frac{\partial \chi}{\partial t} \quad (50.)$$

which results in a storage error,  $\Delta F_{stor}$ :

$$\Delta F_{stor} = \int_0^{z-d} \frac{\partial \chi}{\partial t} dz \approx (z-d) \frac{\partial \chi}{\partial t} \quad (51.)$$

The magnitude of the storage error increases linearly with height (Fowler and Duyzer, 1989) and may therefore be kept to a minimum by reducing the maximum measurement height, although this reduces the area for which the flux is representative.

### 3) Horizontal Gradients (Inhomogeneity): Advection Errors

Horizontal concentration gradients may occur when there is an emission source of a trace gas within the fetch or a sudden change in conditions brings in an air mass with a different gas concentration. As for storage errors, advection errors are largest for micrometeorological flux measurements taken at higher levels

above the surface. However as ozone is not emitted, advection errors are not normally a significant issue.

Measured fluxes should, whenever possible, be corrected for the effects of chemical reactions, storage and advection errors. However for ozone, chemical reactions are only an issue in high NO<sub>x</sub> or VOC environments (Section 5.2.6) and advection errors cannot be accounted for when measuring at a single point. Corrections may be applied for storage errors calculated from the time series of ozone concentrations, as described in Section 5.2.5.

#### *2.4.4.3 Flux Attenuation, Sampling Frequency and Measurement Averaging Period*

The sampling frequency and averaging time used for any of the 3 micrometeorological methods have to be carefully considered to ensure reliable characterisation of the fluxes. Gradient and Bowen ratio measurements both give time-averaged values and the choice of averaging period is a matter of instrumentation and a judgement of the timescale over which the most relevant processes occur. For measurements close to the ground an averaging period of 15 to 60 minutes is typical. This allows for a reasonable number of measurements to be made within the response time of most instruments and should capture the main components of the flux.

In the case of eddy-correlation measurements, theory is based on the assumption that turbulent fluctuations are captured on all scales, ie from the smallest to largest (or fastest to slowest) eddies within the sampling height. In practice instruments place a limit on the range of frequencies that can be sampled and may distort the sample. The averaging time must be chosen to minimise the loss of low frequency variation in the flux. These factors can lead to attenuation of the measured flux at either end of the turbulent frequency distribution.

The main characteristics required of a sensor for eddy-correlation are that it can sample the fastest frequencies occurring at the measurement height and that any distortion of the turbulent flow is minimised. For measurements close to the surface of short-vegetation a response time of at least 0.1 s (10 Hz) is required whereas for rougher surfaces such as forests, 1 s may be adequate. Flow distortion is minimised by careful design and mounting of instruments, for example sonic anemometers generally have very open sensing heads mounted

on narrow bases (Figure 5.18) and are orientated away from the mean flow. In the case of closed-path sensor where an air sample is drawn down a tube to the sensor some distortion is inevitable. However as long as the tube dimensions and flow rate are chosen to ensure the flow remains turbulent, errors in the resulting flux estimates are minimised (Lenschow and Raupach, 1991).

Both the sensor response time, flux attenuation and the optimum averaging period can be checked by examining the power spectra and co-spectra of the measurements, as described in Section 5.2.2.

#### 2.4.4.4 Co-ordinate Systems

The equations above describe events that occur in three dimensions and so the co-ordinate system used must be consistent with them. In some applications the Cartesian co-ordinate system with  $x$ ,  $y$ ,  $z$  axis (with associated wind-speed vectors,  $u$ ,  $v$  and  $w$ ) aligned east, north and up might be used but in micrometeorology it is often more convenient to rotate  $x$  and align it with the some other aspect of the system, such as the streamlines of the mean flow.

Micrometeorological theory is also based on the assumption that measurements are made over a flat, horizontal surface using a sensor in perpendicular alignment with the  $x$ - $y$  plane and the streamlines. In the case of gradient and Bowen ratio measurements which normally use simple cup-anemometers (see Chapter 5), no information on the 3D structure of the turbulence is obtained so errors can only be limited by ensuring that anemometers are as well aligned as possible. However when a 3D sonic anemometer is used each wind vector ( $u$ ,  $v$  and  $w$ ) is resolved and rotating the co-ordinates also allows misalignment and sloping terrain to be accounted for.

The procedure most commonly applied uses the measured wind to define an orthogonal vector for each measurement period to which all the fluxes are transformed, known as the natural wind system (Lee *et al.*, 2004). Essentially it is assumed that there is no correlation between the vertical and lateral wind velocities ( $\overline{v'w'} = 0$ ). Transformation occurs by a two-step rotation along the  $uv$  and  $uw$  planes, with 3 rotation angles. This aligns the  $u$  axis to the streamlines at the measurement point and effectively corrects for any tilt in the orientation of the anemometer being used to measure wind. However the assumption that

$\overline{v'w'} = 0$ , although appropriate over "ideal" surfaces in fair weather conditions, is not always true when measurements are made continuously at less-ideal sites.

More recently Wilczak *et al.*, (2001) proposed a planar-fit rotation scheme that attempts to overcome the limitations of the natural wind system. In this method the z-axis is perpendicular to the mean streamline plane and the y-axis is perpendicular to the plane in which the current velocity vector,  $\vec{\bar{u}}$ , and z-axis lie. The mean streamline plane is determined by fitting a plane ( $\bar{w} = b_0 + b_1\bar{u} + b_2\bar{v}$ ) through an ensemble of  $\bar{u}$ ,  $\bar{v}$  and  $\bar{w}$  measurements. The regression coefficients ( $b_1$  and  $b_2$ ) of the streamline plane are used to calculate the angles of rotation around the y-axis (pitch) and x-axis (roll). The final rotation around the z-axis (yaw) is found from transformed streamline wind-velocities,  $\bar{u}'$  and  $\bar{v}'$ . A full description of the methodology can be found in Wilczak *et al.*, (2001) and Lee *et al.*, (2004). This co-ordinate scheme has the advantage that it is stable with time and the x-y plane is more or less parallel to the surface. It also allows information on the 2- and 3-dimensional nature of the flow field, such as the mean vertical velocity, to be recovered from measurements at a single point (Lee *et al.*, 2004).

In practice great care must still be taken to align a sonic-anemometer perpendicularly to the surface as Wilczak *et al.*, (2001) showed that for a 1° tilt the error in the momentum flux is typically ~10%. The application of this method to the Easter Bush site is described in Section 5.2.2.2.

## ***2.5 Ozone Deposition and the Resistance Analogy***

Although measurements of boundary layer fluxes are of intrinsic interest and have greatly improved our understanding of the deposition process, they do not reveal much about the underlying processes or how vegetation are responding to the atmosphere. A useful method of visualising and analysing trace-gas transfer between the atmosphere and the interaction at surface is the resistance analogy (Monteith, 1981). Ohm's Law states that the electron flux density (or current,  $I$ ) in an electrical conductor is directly proportional to the potential difference (or voltage,  $V$ ) between its two ends. The constant of proportionality in this relationship is termed the resistance  $R$  and so:

$$V = IR$$

Ohm's Law

By analogy if we consider a trace gas flux,  $F_s$  ( $\text{g m}^{-2} \text{s}^{-1}$ ), to be equivalent to current and the voltage to be the difference between the gas's concentration at two heights ( $\chi_{z_1}$  and  $\chi_{z_2}$ , in  $\text{g m}^{-3}$ ) we can write:

$$R_{z_1, z_2} = \frac{\chi_{z_1} - \chi_{z_2}}{F_s} \text{ where } R \text{ has units of } \text{s m}^{-1} \quad (52.)$$

Resistances can be combined in series or parallel using the same rules as for electric circuits (Figure 2.5) resulting in a network of resistances that determine the transfer rate between the atmosphere and the surface.

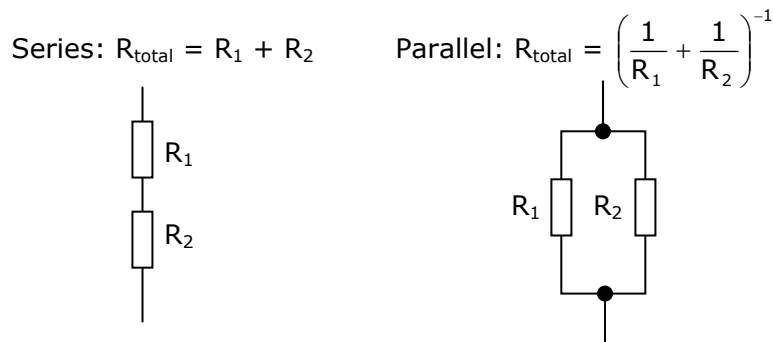


Figure 2.4. The rules for adding resistances in series or parallel.

If we take  $z_2$  to be  $z_0'$  (the height above  $d$  at which heat and trace-gases are exchanged) the concentration is zero for some trace gases (such as  $\text{O}_3$  or  $\text{SO}_2$ ) as they are totally absorbed at this height. Thus equation (52) can be used to calculate the total surface-layer resistance ( $R_t$ ) to exchange of an entity from its flux and concentration at a single height, usually the reference height  $z - d = 1$  m. In the case of gases which are emitted by the surface, as well as deposited to it,  $\chi(z_0') > 0$  and more complex models are required. These usually involve a "compensation point" to account for the point at which vegetation switches from emission to deposition and vice-versa (Smith, *et al.*, 2000; Sutton, *et al.*, 1998). As ozone is only deposited ( $\chi(z_0') \approx 0^4$ ) this type of bi-directional exchange will not be considered further.

The inverse of  $R_t$  is often considered by micrometeorologists to be the deposition velocity,  $v_d$  ( $\text{m s}^{-1}$ ), and was introduced by Chamberlain (1966) as a useful way of parameterising the deposition process:

$$v_d(z-d) = F_s(z-d)/\chi(z-d) = 1/R_t \quad (53.)$$

<sup>4</sup>  $\chi(z_0')$  is normally assumed to be zero for ozone but there is some evidence that this is not always the case (Kollist, *et al.*, 2000; Wang, *et al.*, 1995).

$1/R$  may also be taken to be a conductance, by analogy with electrical resistance and this approach is often taken by plant physiologists who measure the ability of stomata to take in or release gases as a stomatal conductance in  $\text{mol-gas m}^{-2} \text{s}^{-1}$ , as will be discussed in Sections 4.4.4.

Measurements of deposition over a completely closed vegetation canopy, such as grassland, or over more patchy vegetation such as savannah or even an individual plant leaf, will require different parameterisations and combinations of resistances. There are two atmospheric resistances which describe the transfer of a gas from a height in the atmosphere to a point just above the surface (Figure 2.5):

### 1. The aerodynamic atmospheric resistance, $R_a[z-d]$

The roughness length can be interpreted as the height below which molecular diffusion takes over from turbulent diffusion as the main vertical transfer process. Thus the aerodynamic resistance describes transfer between  $z_0$  and a reference height, normally  $z-d = 1$  m. If the eddy diffusivity is regarded as conductivity the resistance can be found by integrating  $1/K$  over the height range:

$$R_a[z-d] = \int_{z_0}^{z-d} K_m^{-1} dz = \int_{z_0}^{z-d} \frac{1}{u_*^2} \partial u = \frac{u(z-d)}{u_*^2} \text{ as } u(z_0) = 0 \quad (54.)$$

Substituting in equation (35) yields:

$$R_{am}[z-d] = \frac{\ln\left(\frac{z-d}{z_0}\right) - \Psi_m\{\zeta\}}{ku_*} \text{ as } u(z_0) = 0 \quad (55.)$$

This equation is suitable for all entities in neutral and stable conditions as  $\Psi_m = \Psi_H$ , however as  $\Psi_m \neq \Psi_H$  in unstable conditions it is more useful to define a general form that can be used at all times (Garland, 1977):

$$R_a[z-d] = \frac{\ln\left(\frac{z-d}{z_0}\right) - \Psi_H\{\zeta\}}{ku_*} = \frac{u\{z-d\}}{u_*^2} - \frac{\Psi_H\{\zeta\} - \Psi_m\{\zeta\}}{ku_*} \quad (56.)$$

### 2. Sub-laminar boundary-layer resistance, $R_b$ .

The transfer of momentum to the surface is governed by  $R_a$  as momentum is totally absorbed at  $z = d + z_0$ , due to both frictional and form drag. However only frictional drag is involved in the flux of heat, water-vapour and trace-

gases and so exchange appears to occur at a lower height,  $z = d + z_0'$  ( $z_0' < z_0$ ). At this height the surface elements are surrounded by a "quasi-laminar viscous sub-layer" immediately in contact them, where viscous forces dominate and molecular diffusion is the main transfer process. This results in an additional resistance for heat and other entrained entities, called the laminar boundary-layer resistance<sup>5</sup>,  $R_b$ . It can be defined in a similar way to  $R_a$  (Equation 49):

$$R_b = \frac{\ln\left(\frac{z_0}{z_0'}\right) - \Psi_H\{\zeta\}}{ku_*} \quad (57.)$$

However, in practice  $z_0'$  is estimated using  $R_b$  where  $R_b$  has been calculated using one of the semi-empirical formula that can be found in the literature, based on the methodology initially developed by Chamberlain (1966). In the case of field-scale micrometeorological measurements over fairly smooth and homogeneous vegetation, such as wheat, equation (58) maybe adequate (Monteith and Unsworth, 1990).

$$R_b = 6.2 u_*^{-0.67} \quad \text{for } 0.1 < u_* < 0.5 \text{ m s}^{-1} \quad (58.)$$

For more rigid and rough vegetation, such as needle leafed trees or moorland, the parameterisation developed by Garland (1977) and references therein is more suitable:

$$R_b = u_*^{-1} \left( 1.45 \left( \frac{z_0 u_*}{\nu} \right)^{0.24} (Sc_s)^{0.8} \right) \quad (59.)$$

$$\text{where } Sc = \text{Schmidt number} = \frac{\nu}{D_s}$$

$\nu$  = kinematic velocity of air =  $14.2 \times 10^{-6} \text{ m}^2 \text{ s}^{-1}$  at  $10^\circ\text{C}$ ,  $D_s$  =  
molecular diffusivity of entity  $s$  (eg  $22.7 \times 10^{-6} \text{ m}^2 \text{ s}^{-1}$  for water vapour  
in air at  $10^\circ\text{C}$ )

Other workers and some regional-scale modelling studies have used the formula derived by Hicks *et al.*, (1987) (Fuentes *et al.*, 1992, Simpson *et al.*, 2003b and Smith *et al.*, 2000 for example):

$$R_b = \frac{2}{ku_*} \left( \frac{Sc_s}{Pr} \right)^{2/3} \quad (60.)$$

where  $Sc_s$  and  $Pr$  are the Schmidt (as above) and Prandtl numbers respectively,  $Pr = 0.71$  (for air, Monteith and Unsworth, 1990)

---

<sup>5</sup> It may also be called simply the boundary-layer resistance

Where deposition to a single leaf is being considered the formula given by Monteith and Unsworth (1990) for mass exchange at the surface of a flat plate ( $r_b$ ), can be used:

$$r_b = \frac{\delta}{D_s Sh_s} \quad (61.)$$

where  $\delta$  = mean leaf-length in the direction of the wind,  $D_s$  = molecular diffusivity and  $Sh_s$  = Sherwood number,  $Sh_s = 0.66Re^{0.5}Sc_s^{0.33}$ ,  $Re = u[z-d] \cdot \delta/\nu$ , ( $u[z-d]$  = wind-speed at the canopy height)

### 3. Canopy Resistance, $R_c$

The final part in the resistance network is the surface component, which in the case of deposition to vegetation is termed the canopy or surface resistance,  $R_c$ . The degree of complexity used for parameterising  $R_c$  depends on the application. In large scale regional or global models a single surface resistance may be used, which simply varies with  $LAI$  (leaf area index) and wind-speed, for example. Whereas in more mechanistic local scale models several resistances may be used to account for deposition to each component of the canopy such as leaf cuticles, stomata, and soil, and may even be split into layers to account for the vertical structure of the canopy. The modelling of surface deposition is described in more detail in Chapter 3.

The resistance network most commonly used for interpreting measurements of the deposition of ozone to vegetation uses  $R_a$ ,  $R_b$  and a total canopy resistance  $R_c$  with three components, stomatal ( $R_{c1}$ ), external plant surfaces ( $R_{c2}$ ) and soil ( $R_{c3}$ ) resistances, as shown in Figure 2.5. In some circumstances, for open or sparse canopies, additional sub-canopy aerodynamic resistance may be added in series with  $R_{c3}$ . It has also been suggested that the ozone concentration within the stomatal cavity is not zero and so an additional mesophyll resistance maybe added in series with  $R_{c1}$ .

Thus where the total flux is measured,  $R_c$  can be calculated from equation (62). Separating  $R_c$  into its three components requires more detailed measurements or modelling as described below in Section 2.5.1, although at night when most plants close their stomata,  $R_c$  can be assumed to be the combination of  $R_{c2}$  and  $R_{c3}$ .

$$R_c = \frac{\chi_s(z-d)}{F_s(z-d)} - (R_a + R_{b_s}) = \frac{1}{v_{ds}} - (R_a + R_{b_s}) \quad (62.)$$

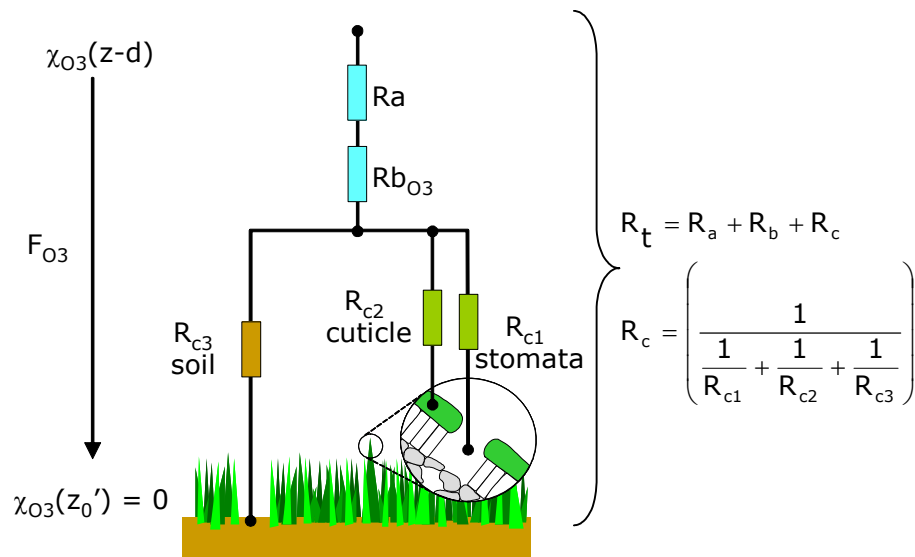


Figure 2.5. The deposition resistance analogy for ozone.

## 2.5.1 Measuring the Components of Total Canopy Resistance

Micrometeorological measurements of  $O_3$  flux, on their own, only provide information of the bulk surface characteristics ( $R_c$ ). Therefore unless the surface consists of a single substance, eg water or bare soil, additional data are required to examine different components of the canopy ( $R_{c1}$ ,  $R_{c2}$ ,  $R_{c3}$ ). The flux of water-vapour can readily be measured using micrometeorological methods and this provides a route to separating out the stomatal component.

### 2.5.1.1 Plants and the Atmosphere

In order to carry out photosynthesis, most plants exchange carbon dioxide, oxygen and water-vapour with their external environment through pores called stomata. During the day  $CO_2$  enters the plant for photosynthesis and water-vapour is released (transpired). To balance the amount of water they lose by transpiration against carbon uptake and therefore optimise growth rates, stomatal opening is closely controlled.

The stomata consist of a pair of guard cells that form an opening in the epidermis of a leaf and allow gases to enter the mesophyll and be absorbed by the moist spongy cells, as illustrated in Figure 2.6. A plant may have only have stomata on one side of its leaves (hypostomatous) or both (amphistomatous). Stomatal opening is controlled by a change in the water pressure (turgor) within the guard cells. The inner wall of each guard cell is thick and elastic. When turgor increases within the two guard cells flanking a stoma, the thin outer walls

bulge out and force the inner walls into a crescent shape. This opens the stoma. When the guard cells lose turgor, the elastic inner walls regain their original shape and the stoma closes.

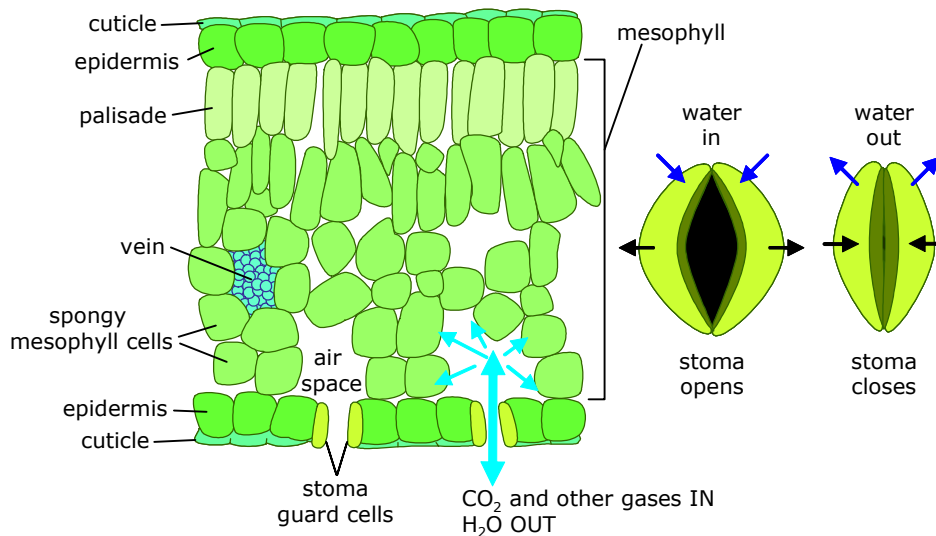


Figure 2.6. Diagram showing a typical leaf's cross-section and illustration of a stoma opening and closing.

Guard cell turgor is controlled by the flow of ions into and out of the cells. The ion flow rate is determined via signalling by plant chemicals (phytochemicals), such as abscisic acid (ABA), phaseic acid, cytokinins and gibberellins (Larcher, 2001). Abscisic acid increases the rate of ion diffusion out of the guard cells, so they lose turgor and the stoma closes. Stomatal opening occurs when  $K^+$  is transported from subsidiary cells into the guard cells and so turgor increases. The chemical and physical processes involved are very complex as phytochemical concentrations can be influenced by many environmental factors, including exposure to atmospheric pollutants. For example, ozone induces the production of anti-oxidants, such as ascorbate which in turn induces secondary stress responses and affects ABA concentrations. Prolonged exposure to stress such as drought or pollutants can permanently damage the guard cells, restricting their ability to open and close, as well as having other detrimental effects (Padu *et al.*, 2005; Scebbba *et al.*, 2003; van Hove *et al.*, 2001; Zheng *et al.*, 2000). The main environmental factors that influence stomatal opening are described below.

- Light

In general stomata open during the day and close at night. Although the reverse occurs in CAM plants to reduce water-loss as they are adapted to hot

climates (Larcher, 2001). The wavelength of light is also relevant as red to blue wavelengths are important for photosynthesis. Blue light also has an additional effect on stomatal activity, independent of its role in photosynthesis as it stimulates starch breakdown.

- Carbon Dioxide Concentration

The concentration of CO<sub>2</sub> in the mesophyll exerts some control. It tends to be low during the day, when stomata are open and it is used for photosynthesis but higher at night when it is produced during respiration and stomata are closed. During the day, stomata open or close to optimise the CO<sub>2</sub> concentration.

- Plant Water Content

This is the prevailing and overriding control and there are two mechanisms by which water loss regulates stomatal closure, one is active and the other passive:

1. Hydropassive Control - simply put, as the plant loses water, the turgidity of the leaf cells, including guard cells, decreases and this results in stomatal closure (phytochemicals are not inducing the stomatal closure, it is simply the consequence of drying out).
2. Hydroactive Control - When the water potential in the leaf or stem drops below some critical level, it triggers the release of phytochemicals such as ABA which close the stomata. ABA is normally present in very low concentrations but increases very rapidly after water stress (within minutes).

- Temperature

In most conditions an increase in temperature increases stomatal opening, mainly to enhance evaporative cooling. However, if the temperature becomes too high the stomata close due to water stress and increased CO<sub>2</sub> concentration (from respiration).

- Wind

Air flow around the plant may cause stomatal closure because it brings in CO<sub>2</sub> enriched air or increases the rate of transpiration that causes water stress. Although in some cases, wind causes stomata to open and increase transpiration.

Other factors can affect stomatal opening although not as directly as those listed above: the age of a plant has an influence as older cells become damaged and are less quick to respond to stimuli; pollutant gases or aerosols can damage the guard cells or block stomata; surface water blocks stomata; nutrient levels in the soil will affect plant function.

The various processes that control stomatal functioning have been extensively studied over the years in the field and laboratory (Ball *et al.*, 1987; Collatz *et al.*, 1991; Kim and Verma, 1991; Mott and Buckley, 1998; Tardieu and Davies, 1992; 1993; Turner, 1991), leading to a variety of models with different degrees of complexity. Methods of measuring stomatal opening are reviewed in Section 2.5.1.2 below while modelling methods are discussed in Chapter 3.

### 2.5.1.2 *Stomatal Resistance, $R_{c1}$ , or Conductance, $g_s$*

The ease with which gases can diffuse into the stomata is controlled by the degree of stomatal opening and, as with atmospheric fluxes, can be thought of as a resistance. The inverse of resistance is conductance (as resistance increases, conductance decreases) and by convention this variable is normally used by plant scientists.

There are several different methods that may be used to measure stomatal resistance. The size of a stoma's aperture can be directly observed and measured under a microscope. However this is not possible under natural conditions so an impression of the stomata can be made by applying a quick-drying substance to the leaf surface. Measuring the rate of infiltration of substances with known viscosity can also be used but this method, although cheap and simple, is not very accurate (Beadle *et al.*, 1993). The approach most commonly used in the field today is based on measuring the transfer of water-vapour (transpiration) either of an individual leaf or the whole canopy:

#### • **Individual Leaf - Diffusion Porometers**

This type of instrument directly measures conductance of an individual plant and consists of a small chamber which is attached to a leaf or leaves. The chamber may be ventilated or sealed and transpiration is calculated from either:

- The time taken for humidity to increase by a certain amount;

- The increase in humidity of air flowing through the chamber at a constant rate;
- The rate of inflow of dry air required to maintain humidity in the chamber at a constant level (null-balance).

The first two types of porometer maybe relatively simple but are markedly affected by temperature making them difficult to calibrate. The later type of instrument is preferred as:

- Humidity is constant during a measurement which is important as plants respond to changes in humidity. Modern instruments allow measurements to be made at ambient humidity and so determine real-time behaviour.
- Where stomatal response is being examined the humidity balance point can be varied.
- Calibration is simple and less dependant on assumptions and uncertainties, such as the instruments temperature response.

The stomatal conductance is calculated using a null-balance porometer as follows (Beadle *et al.*, 1993):

$$E = f q_s / a \quad (63.)$$

where  $E$  = transpiration rate (or water-vapour flux) in  $\text{kg m}^{-2} \text{s}^{-1}$   
 $f$  = dry air inflow rate in  $\text{m}^3 \text{s}^{-1}$   
 $q_s$  = water vapour density (humidity) in  $\text{kg m}^{-3}$  at the balance point  
 $a$  = area of leaf enclosed by the chamber ( $\text{m}^2$ )

At a steady state  $E$  can be written as:

$$E = (q_i - q_s) / r_{c1w} \quad (64.)$$

where  $q_i$  = water vapour density at the saturation vapour pressure corresponding to leaf temperature  
 $r_{c1w}$  = resistance to water vapour flow =  $r_{c1} + r_b$

As the chamber is ventilated  $r_b$  is small and can be either neglected or determined by replacing the leaf with wet blotting paper (or something similar). Also, if the leaf and air temperatures are similar  $q_i/q_s$  becomes  $1/RH$ , the reciprocal of relative humidity and stomatal resistance for water-vapour can be found as:

$$r_{c1w} = \frac{\left( \frac{1}{RH} - 1 \right) a}{f} - r_{bw} \quad (65.)$$

The units of  $r_{c1w}$  from equation (65) are  $\text{s m}^{-1}$  and so  $g_{sw}$  is  $\text{m s}^{-1}$ , however in studies of plant physiology molar units of  $\text{mol m}^{-2} \text{s}^{-1}$  are commonly used, where the unit surface is leaf area (*LAI*). Conversion between the units is given by:

$$g_{sw} (\text{m s}^{-1}) = g_{sw}(\text{mol m}^{-2} \text{s}^{-1}) \times \frac{8.314T}{p} \quad (66.)$$

where  $T$  = chamber temperature in K  
 $p$  = chamber pressure in Pa

Measurements of leaf level stomatal resistance ( $r_{c1w}$ ) are useful when studying the responses of plants to various stimuli. However in the context of field scale micrometeorology they must be scaled in some way to obtain values representative of the total canopy ( $R_{c1w}$ ). Various methods have been developed to do this as will be discussed in Chapter 3.

- **Canopy Scale – Water-vapour Flux**

The micrometeorological methods described above can be used to measure water-vapour flux with suitable instrumentation and determine a bulk-canopy stomatal resistance,  $R_{c1w}$ . The standard formula used is known as the Penman-Monteith equation (67). In 1948, Penman combined the energy balance (Bowen ratio) with mass transfer formulae and derived an equation to compute the evaporation from an open water surface from measurements of radiation, temperature, humidity and wind speed. This so-called combination method was further developed by Monteith and extended to vegetated surfaces by introducing resistance factors.

$$\lambda E = \frac{\Delta(Rn - G) + \rho C_p (e_s[T_z] - e[z]) / (R_a + R_b)}{\Delta + \gamma \left( 1 + \frac{(R_a + R_b)}{R_{cw}} \right)} \quad (67.)$$

where  $\Delta$  = rate of change in saturation vapour pressure with temperature ( $\partial e_s[T] / \partial T$ )

If transpiration is the only source of water vapour from the surface, ie the surface is completely dry and stomata are open, then  $R_{cw}$  can be assumed to be  $R_{c1w}$ . A simpler, more direct, formulation of (67) can be used when the canopy surface temperature ( $T[z_0]$ ) and vapour pressure at  $d + z_0$ ,  $e[z_0]$  are calculated from  $R_a$ ,  $R_b$ , the latent heat flux and the sensible heat flux (Coe *et al.*, 1995):

$$T[z_0] = T[z-d] + \frac{H}{\rho C_p} (Ra[z-d] + Rb) \quad (68.)$$

$$e[z_0] = e[z-d] + \frac{Ep}{\rho \varepsilon} (Ra[z-d] + Rb) \quad (69.)$$

$$R_{c1w} = \frac{\rho \varepsilon}{p} \frac{e_s[T(z_0)] - e(z_0)}{E} \quad (70.)$$

where  $\varepsilon$  = ratio of the molecular weight of water to that of dry air  
 $\approx 0.62$

These values of stomatal resistances are for unit ground area (rather than leaf area) and water-vapour, which experiences no resistance within the mesophyll. Where other gases are being considered that can be assumed to have zero mesophyll resistance their stomatal resistance can be calculated by simply scaling  $R_{c1w}$  for their molecular diffusivities ie:

$$R_{c1w} D_w = R_{c1\chi} D_\chi \text{ where } D = \text{molecular diffusivity} \quad (71.)$$

The value of  $D$  for different gases varies with temperature and pressure, as described by Massman (1998). If  $D$  at standard temperature and pressure is known (STP: 0°C and 101.325 kPa) then other values can be calculated from:

$$D(T,p) = D_{STP} (p_0/p)(T/T_0)^\alpha \quad (72.)$$

where  $p_0 = 101.325$  kPa,  $T_0 = 273.15$  K,  $p <$  critical gas pressure  
 $1.5 \leq \alpha \leq 2.0$

Table 2.1 below gives values for various atmospheric trace gases at STP and at 10°C, 101.325 kPa using  $\alpha = 1.81$ .

*Table 2.1* Molecular diffusivities ( $\text{cm}^2 \text{s}^{-1}$ ) for several important atmospheric trace gases

Gas	STP	10°C, 101.325 kPa
H <sub>2</sub> O	0.2178	0.2324
CO <sub>2</sub>	0.1381	0.1474
NO	0.1802	0.1923
NO <sub>2</sub>	0.1361	0.1453
O <sub>3</sub>	0.1444	0.1541

Thus, from Table 2.1 the ratio for ozone is 1.51 and this is used here. However as  $D_{O_3}$  has not been measured the value used does vary from study to study, for example Grunhage and Haenel, (1997) used 1.51 whereas Wesely (1989) used 1.6 (at 298 K) and Fowler *et al.*, (2001) used 1.67. The stomatal resistance has been extensively studied because of its relevance to subjects such as photosynthesis, carbon sequestration and crop production. The other two components,  $R_{c2}$  and  $R_{c3}$ , are far less well known and their relative importance is often open to question. In many cases it has been assumed that they are essentially constant although some studies have shown variations with water-vapour and temperature, as described in Section 2.5.1.4. One of the objectives of this thesis is to examine these resistances at our grassland site.

### 2.5.1.3 *Separating the Components of $R_c$ in Field Measurements*

Once  $R_{c1}$  has been determined from measurements of transpiration (canopy water-vapour flux in dry day-light conditions), the sum of  $R_{c2}$  and  $R_{c3}$  (non-stomatal,  $R_{ns}$ ) can be calculated as the residual term:

$$R_{ns} = \left( \frac{1}{R_c} - \frac{1}{R_{c1}} \right)^{-1} \quad (73.)$$

Whether it is possible to separate the components of  $R_{ns}$  ( $R_{c2}$  – external surfaces or  $R_{c3}$  – soil) depends on the nature of the measurement site and canopy. In the case of grassland it is reasonable to neglect  $R_{c3}$  when the canopy is fully grown and completely closed, so  $R_{ns} \approx R_{c2}$ .

### 2.5.1.4 *External Plant Surfaces Resistance, $R_{c2}$ and Soil or Ground Surface Resistance, $R_{c3}$*

For simplicity  $R_{c2}$  will be referred to as cuticular but it includes deposition to all external plant surfaces, such as bark in the case of trees or stems in herbaceous plants. When measuring ozone flux over vegetation in the field it is not normally possible to distinguish the cuticle from other non-stomatal components such as the soil. Where fluxes are measured using cuvettes that enclose only plant tissues  $R_{c2}$  can be calculated as the residual of the total resistance minus the stomatal component. Some studies have reported such measurements for trees, for example Rondon *et al.*, (1993) found minimum values for  $R_{c2}$  of 200-330  $\text{s m}^{-1}$  for Norway spruce and Scots pine. The estimates of  $R_{c2}$  available in the literature are listed and summarised in Table 2.2.

As with cuticular resistance, it is not normally possible to distinguish the soil from other components. However for many arable crops there are periods when the field will be bare and in some climates plants completely die back in the dry season, leaving mainly bare soil and dead plant matter. Measurements made in these circumstances or results from controlled chamber studies can be used to estimate  $R_{c3}$ . Some typical values reported in the literature are given in Table 2.2 along with some estimates of resistances to water and snow for reference. Where a plant canopy is completely closed, such as fully grown grass, it can be assumed that no ozone reaches the surface and so  $R_{c3}$  can be neglected.

Table 2.2 Estimates of the non-stomatal resistance for ozone to snow, water, soil and plant surfaces.

Reference	Type	Surface	$R_{ns}$ , s m <sup>-1</sup>
Chang <i>et al.</i> , 2002	chamber	Agricultural soil (no data on moisture content)	ca 625 ca 475
Wesely <i>et al.</i> , 1981	Field $\mu$ met	Wet bare soil	1000 $\pm$ 100 (370 - 2100)
		Snow -11°C	2000 $\pm$ 200
		-5°C	3500 $\pm$ 200
		-1 to 2 °C	3300 $\pm$ 300
		Lake water	9000 $\pm$ 300
Sanchez <i>et al.</i> , 1997	Field $\mu$ met	Semi-arid steppe (wet and dry)	Dry 275 Wet 437
Rondon <i>et al.</i> , 1993	Field chambers	Coniferous trees	200 - 330
Granat and Richter, 1995	Field chambers	Pine	500 - 2500
Coe <i>et al.</i> , 1995	Field $\mu$ met	Sitka spruce	ca 133
Fowler <i>et al.</i> , 2001	Field $\mu$ met	Dry moorland	200 - 400
Grantz <i>et al.</i> , 1995	Field $\mu$ met	Wet and dry grape	Dry 1020 Wet 292 <sup>a</sup>
Grantz <i>et al.</i> , 1997	Field $\mu$ met	Wet and dry cotton	Dry 770 Wet 3030
Zhang <i>et al.</i> , 2002 <sup>b</sup>	Field $\mu$ met	Wet and dry:	
		Mixed forest	244 - 970
		Deciduous forest	397 - 1831
		Corn	308 - 1332
		Soyabean	137 - 735
		Pasture	571 - 879
McKay <i>et al.</i> , 1992 and references therein	Laboratory chambers and field	Sea water & saline solutions	650 - 6600
Gallagher <i>et al.</i> , 2001	Field $\mu$ met	Coastal waters	950 $\pm$ 70

a from data reported in Grantz *et al.*, 1997

b data derived from references therein

The literature reviewed above reported estimates of  $R_{ns}$  although most do not examine possible controlling factors. However in some studies surface factors affecting ozone deposition, other than stomatal uptake, have been considered. The bulk of them have focussed on the effects of surface water and found both positive and negative effects on deposition rates. The remainder also considered solar radiation or surface temperature and found deposition rates increased with both variables.

- **Effects of surface water**

Wesely *et al.*, (1981) stated that the resistance of a water layer to the uptake of ozone by dissolving and diffusing the gas is very large and calculated values of  $3 \times 10^5$  to  $8 \times 10^5 \text{ s m}^{-1}$ . Therefore they (*ibid*) concluded that the far lower values found in their measurements (Table 2.2) resulted from surface chemical reactions, which has been supported by further work since then. Although the deposition velocity of ozone to open water is generally small,  $\sim 0.001$  to  $0.04 \text{ cm s}^{-1}$ , Wesely *et al.*, (1981) and Chang *et al.*, (2004) reported that deposition velocities to sea water increased with disturbance to the surface and McKay *et al.*, (1992) showed that increasing concentrations of chemical surfactants in the seawater also enhanced deposition (see Table 2.2 for typical resistance values). These results indicate that although deposition rates to water are generally small they can be significant if other reactive compounds are present in the water, a conclusion also supported by measurements to wet vegetated canopies.

In Fuentes *et al.*, (1992) enhanced deposition to a mixed deciduous forest (mainly aspen and maple) was measured with wet surfaces caused by dew, rain or drizzle, whereas in a controlled chamber study, Fuentes (1992) showed that while surface wetness enhanced the ozone flux to maple leaves, for poplar surface wetness had little effect, slightly decreasing deposition immediately after wetting. Examination of the chemistry of water films taken from both tree species gave little indication of what chemicals may be involved as, although total organic compound concentrations were larger in the maple samples, no specific ozone-reacting compounds could be found. However, the inclusion of wetness dependant surface resistances in a simple model improved results when compared to field measurements of ozone deposition.

Other studies have also reported different responses to surface wetness, depending on vegetation type: Padro (1994) found that wetting by dew enhanced deposition to a deciduous forest, whereas rainfall suppressed it, and suggested this was due to a difference in water chemistry; Grantz *et al.*, (1995) reported substantial increases in deposition to wet grape vines and suggested that this may be due to their hypostomatous leaves on which dew formation increased ozone reactivity on the upper surface without occluding the stomata on the bottom; Pleijel *et al.*, (1995) also found surface wetness increased deposition to a pasture canopy by  $\sim 40\%$  in controlled chamber studies; in contrast Grantz *et al.*, (1997) measured decreased deposition rates to wet cotton

plants and concluded that this was due to stomatal conductance being reduced by water blocking upper stomata on their amphistomatous leaves.

Despite this variation in reported results for the effect of surface wetness Zhang *et al.*, (2002) proposed a parameterisation based on night-time measurements of canopy resistance from five field sites. The measurements indicated that  $R_{ns}$  is reduced by increased humidity or the presence of surface water:

For dry canopies,

$$\frac{1}{R_{ns}} = \frac{1}{R_{inc0} u_*^{-2} LAI^{0.25} + R_{c3}} + \frac{1}{R_{c20\_dry} e^{-0.03RH} LAI^{-0.25} u_*^{-1}} \quad (74.)$$

For wet canopies:

$$\frac{1}{R_{ns}} = \frac{1}{R_{inc0} u_*^{-2} LAI^{0.25} + R_{c3}} + \frac{1}{R_{c20\_wet} LAI^{-0.5} u_*^{-1}} \quad (75.)$$

where:  $R_{inc0}$  is an in-canopy aerodynamic resistance ( $50 \text{ s m}^{-1}$  for pasture),  $R_{c3} = 200 \text{ s m}^{-1}$  for pasture,  $R_{c20\_dry} = 4000 \text{ s m}^{-1}$ ,  $R_{c20\_wet} = 200 \text{ s m}^{-1}$ ,  $RH$  is given as a percentage, wet conditions are defined as when dew or rain are present and dry conditions all other times (regardless of humidity levels).

Incorporation of these relationships into a full resistance model gave reasonably good agreement with night day-time measurements of total canopy resistance.

#### • Solar Radiation and Surface Temperature

As has been described, ozone is a reactive gas and deposits quite readily on most surfaces simply by oxidative reactions (Grontoft, 2004). However many studies have concluded that stomatal uptake is the main factor controlling ozone deposition to vegetated surfaces, although some results have shown non-stomatal deposition is also significant (the studies above being a few examples). Given its reactive nature it is not unreasonable to suppose the surface temperature may have some influence on  $R_{ns}$  and indications of such an effect were first reported by Rondon *et al.*, (1993). In their (*ibid*) measurements of ozone deposition to a coniferous forest they found that the surface resistance to ozone was much lower than that predicted by stomatal conductance alone and the residual term ( $R_{ns}$ ) varied with air temperature, radiation and stomatal conductance. It was proposed that this effect was due to temperature increasing the reaction rates of ozone with organic compounds on the canopy surface. Coe *et al.*, (1995) found similar results in measurements of ozone uptake by Sitka spruce. Granat and Richter, (1995) also reported that although  $R_{ns}$  varied with stomatal conductance it could also be explained by other diurnally varying

processes such as light intensity. More recently, Fowler *et al.*, (2001) analysed four years of continuous ozone and water-vapour flux measurements to a Scottish moorland and explicitly examined the stomatal and non-stomatal flux. Their results showed a clear reduction in  $R_{ns}$  with total solar radiation ( $St$ ), from  $\sim 400 \text{ s m}^{-1}$  with  $\sim 100 \text{ W m}^{-2}$  of solar radiation to  $\sim 150 \text{ s m}^{-1}$  at  $800 \text{ W m}^{-2}$ . It was concluded that this was due to thermal decomposition of ozone at the surface, as temperature is closely related to  $St$ . However the relationship between temperature and  $R_{ns}$  was more complex due to the differing thermal and chemical properties of the surface in wet and/or cold conditions, and so the effect was quantified using the relationship with  $St$ :

$$R_{ns} = -1.29.9\ln(St)+989.1 \quad (76.)$$

An Arrhenius type plot of  $\ln(v_d)$  against  $1/RT$  gave an activation energy of  $36 \text{ kJ mol}^{-1}$  for the process.

Methods of examining  $R_{ns}$  using night-time field measurements or stomatal conductance measurements have been described above. However as estimates of  $R_{c1w}$  are limited to daylight periods when the canopy is dry the latter data sets are quite limited in the conditions they represent. Examining only night-time data can give further information but it is often useful to also model  $R_{c1w}$  so that more extensive periods of data can be considered. The following chapter reviews modelling methods and outlines those that will be applied to our field measurements.

### 3 Modelling the Dry Deposition of Ozone

The deposition of ozone can be modelled at a range of scales, from individual plant leaves, where complex physiological processes may be simulated, to grid squares encompassing 100 km<sup>2</sup> of the Earth's surface which have to greatly simplify natural processes. This chapter provides a brief introduction to some of the models most commonly used today and describes the approaches that will be taken to model our grassland measurements.

#### 3.1 Current Ozone Models

##### 3.1.1 Global Ozone Models

Several global models provide estimates of boundary layer ozone concentration, some being developed specifically to do so and others as a consequence of investigating another process, such as OH or CH<sub>4</sub> chemistry. Prather *et al.*, (2003) co-ordinated an ozone model comparison experiment for the IPCC, which incorporated several of the major models in use today. These models are summarised in Table 3.1 which also gives a brief description of the surface deposition scheme where it was available. These models are parameterised at very large scales and so surface deposition is treated quite simply, often with no differentiation between land cover other than water or ground for example; although in some cases variations in surface roughness are accounted for. Some efforts are now being made to incorporate more detailed surface vegetation schemes so that climate change/CO<sub>2</sub>/O<sub>3</sub> interactions can be examined; for example Mike Sanderson at the UK MetO is currently testing a new version of the STOCHEM model which includes deposition to several different vegetation types which are dynamically modelled so they vary with season.

Table 3.1 Summary of global models used to estimate ozone concentrations as given in Prather *et al.*, (2003)

Model Name ( <i>ibid</i> )	Institution
HGIS <sup>1</sup>	Harvard University
Resolution	4°lat×5°lon, 9 levels, surface to 10 hPa
Advection	second-order moments <sup>2</sup>
Surface deposition scheme	Not available
References	1. Mickley, <i>et al.</i> , 1999 2. Prather, 1986

Table 3.1 Summary of global models used to estimate ozone concentrations as given in Prather *et al.*, (2003)

Model Name ( <i>ibid</i> )	Institution
<b>IMAGES</b> - Intermediate Model of Global Evolution of Species (IASB) IAS/Belgium	
Resolution	5°×5°, 25 levels, surface to 50 hPa
Advection	semi-Lagrangian <sup>1</sup>
Surface deposition scheme	Deposition velocity: $v_d = 1/(R_a + R_s)$ where $R_s$ is a species dependent surface resistance and $R_a = 50 \text{ s m}^{-1}$ . A geographic distribution of surface resistance for ozone is used with average deposition velocities ( $O_3$ ) in $\text{mm s}^{-1}$ : water/ice/snow = 0.75; bare ground and grass = 4; savanna = 0.5; tropical forest = 10; non-trop forest = 6 Diurnal variation is also taken into account. <sup>2</sup>
References	1. Smolarkiewicz and Rasch, 1991 2. Muller, 1992, Muller, 1993
<b>TM3</b> (adapted from model TM2) (KNMI) KNMI/IMAU Utrecht	
Resolution	4°lat × 5°lon, 19 levels, surface to 10 hPa
Advection	slopes scheme <sup>1</sup>
Surface deposition scheme	No tropospheric chemistry is included Dry deposition at surface is applied with constant surface dependant dry deposition velocities for 11 categories, based on the RADM scheme <sup>2,3</sup> .
References	1. Russell and Lerner, 1981 2. Wauben, <i>et al.</i> , 1998 3. Wesely, 1989
<b>MOZART</b> (MOZ1 & MOZ2) <sup>1</sup> NCAR/CNRS	
Resolution	2.8° × 2.8°, 25 levels, surface to 3 hPa
Advection	semi-Lagrangian <sup>2</sup>
Surface deposition scheme	Mass conservation with a diffusion operator (D) that takes into account surface emission and dry deposition
References	1. Muller and Brasseur, 1995 2. Williamson and Rasch, 1989 Hauglustaine and Brasseur, 2001
<b>TOMCAT</b> (UCAM) University of Cambridge	
Resolution	5.6° × 5.6°, 31 levels, surface to 10 hPa
Advection	second-order moments <sup>1</sup>
Surface deposition scheme	A range of deposition velocities are specified for different surface types , based on the RADM scheme <sup>2, 3,4</sup>
References	1. Prather, 1986 2. Valentin, 1990 3. Giannakopoulos, 1994 4. Walcek, <i>et al.</i> , 1986
<b>UCI</b> University of California, Irvine	
Resolution	8°lat × 10°lon, nine levels, surface to 10 hPa
Advection	second-order, moments <sup>1</sup>
Surface deposition scheme	Dry deposition velocities at 1 m are specified for different vegetation types and surfaces <sup>2</sup> .
References	1. Prather, 1986 2. Hough, 1991

Table 3.1 Summary of global models used to estimate ozone concentrations as given in Prather *et al.*, (2003)

Model Name ( <i>ibid</i> )	Institution
<b>CTM (UIO1)<sup>1</sup></b>	University of Oslo
Resolution	8°lat × 10°lon, nine levels, surface to 10 hPa
Advection	second-order moments <sup>2</sup>
Surface deposition scheme	Dry deposition velocities for ozone at 1 m are specified for 3 surfaces: land 6, sea 1, ice/snow 0.5 mm s <sup>-1</sup> (see references 3, 4).
References	1. Prather, <i>et al.</i> , 1987 2. Prather, 1986 3. Hough, 1991 4. Berntsen and Isaksen, 1997
<b>STOCHEM (UKMO)<sup>1, 2, 3</sup></b>	UK Met. Office
Resolution	5° × 5°, nine levels: surface to 100 hPa
Advection	Lagrangian
Surface deposition scheme	Constant land surface dependant deposition velocities are used <sup>4</sup> . Only land and ocean are distinguished (ie sea ice and Antarctica is classified as ocean, other ice areas as land).
References	1. Stevenson, <i>et al.</i> , 1998b 2. Stevenson, <i>et al.</i> , 1998a 3. Collins, <i>et al.</i> , 2000 4. Hough, 1991
<b>ULAQ</b>	University of L'Aquila
Resolution	10°lat×22.5° lon 26 levels, surface to 0.04 hPa
Advection	Eulerian
Surface deposition scheme	Not specified
References	Pitari, <i>et al.</i> , 2002

### 3.1.2 Regional Ozone Models

To investigate the potential for effects of ozone on specific populations or environments models covering an individual country or group of countries are required. As these operate at smaller scales (typically 50 x 50 to 1 x 1 km) the full depth of the boundary layer can be considered and more detailed land surface schemes used, incorporating vegetation specific stomatal resistances with temporal variability for example. Although some models focus on predicting ozone episodes for their impacts on human health and so, as with the global models, surface processes are not considered in detail, (Metcalf *et al.*, 2002 for example). The methods used to model deposition are often similar to that used for site-specific models, as described in Sections 3.1.3 and 3.2 below, although the parameterisation has to be generalised for the models spatial scale. Table 3.2 gives some examples of typical models and summarises their deposition schemes.

Table 3.2 Summary of some typical regional models that predict ozone concentrations.

<b>CEH</b>	
<b>CEH Edinburgh, UK</b>	
Resolution	5 km x 5 km across the UK
Surface Deposition Scheme	Land-use dependant deposition velocities, using a "big-leaf" canopy model, with light and temperature dependant stomatal conductances for 4 vegetation types (grassland, arable, moorland, forest).
References	Smith, <i>et al.</i> , 2000
<b>EMEP</b>	
<b>Unified Eularian Model – EMEP MSC-W</b>	
Resolution	50 x 50 km across Europe
Surface Deposition Scheme	Land-use dependant deposition velocities, with a "big-leaf" canopy model and multiplicative type stomatal conductance scheme for several vegetation types. Stomatal conductance is dependant on light, temperature, vpd and soil moisture to capture the range in variation of climate across Europe.
References	Emberson, <i>et al.</i> , 2000a; Simpson, <i>et al.</i> , 2003b; Tuovinen, <i>et al.</i> , 2004 <a href="http://www.emep.int/index_model.html">http://www.emep.int/index_model.html</a>
<b>MODELS-3</b>	
<b>US-EPA Community Multiscale Air Quality (CMAQ)</b>	
Resolution	2 to 20 km (dependant on meteorological input)
Surface Deposition Scheme	Different models can be incorporated depending on the application. In general the "big-leaf" Wesely, 1989 RADM scheme is used where bulk-canopy stomatal resistance is parameterised as a function of light and temperature for several vegetation types.
References	EPA, 1999 Wesely, 1989 <a href="http://www.epa.gov/asmdnerl/CMAQ/CMAQscienceDoc.html">http://www.epa.gov/asmdnerl/CMAQ/CMAQscienceDoc.html</a>
<b>EURAD</b>	
<b>European Dispersion Air Pollution Model</b>	
Resolution	~2 to ~60 km (dependant on meteorological input)
Surface Deposition Scheme	The "big-leaf" Wesely, 1989 RADM scheme is used where bulk-canopy stomatal resistance is parameterised as a function of light and temperature for several vegetation types.
References	<a href="http://www.eurad.uni-koeln.de/index_e.html">http://www.eurad.uni-koeln.de/index_e.html</a> Hass, <i>et al.</i> , 1993 Wesely, 1989
<b>LOTOS</b>	
<b>Long-Term Ozone Simulation</b>	
Resolution	0.25 x 0.5° (can be nested to higher resolutions)
Surface Deposition Scheme	As EMEP
References	Erisman, <i>et al.</i> , 2005 Hass, <i>et al.</i> , 1997

### 3.1.3 Local Scale Models

Where measurements have been made at an individual site it is common for a specific deposition model to be derived to assist in the interpretation of the measurements. These models are then used to derive more general deposition schemes for use in regional or global scale modelling, for example Erisman, *et*

*al.*, (1994) summarised the results a workshop on “Models and Methods For the Quantification of Atmospheric Input to Ecosystems” (Lovblad, *et al.*, 1993) into a surface resistance model that uses simple meteorological input data. In some cases plant physiology is the focus and so a very detailed stomatal resistance or photosynthesis scheme may be used with less emphasis on atmospheric processes (Tuzet, *et al.*, 2003, Zeller and Nikolov, 2000).

Many models are based on the “big-leaf” assumption where the canopy is treated as a single big-leaf with an area equal to the canopy leaf area index (*LAI*). The fine structures within the surface, such as variations in the vertical and horizontal distribution of stomata or patterns of sunlight across and within the canopy, are not explicitly characterised. The factors controlling deposition are considered to be entirely homogenous and can be treated in terms of the overall process, thus spatial variations average out. This approach is most suited to simple short canopies such as grassland or dense arable crops such as wheat. Where the canopy has more structure (in forests or scrub for example), or where a model for application to different sites is required, more detail can be included by considering several vertical layers. In these cases processes such as sub-canopy aerodynamics or variations of light intensity can be parameterised. Table 3.3 lists some typical local-scale models, and Section 3.2 describes some of the techniques they employ.

*Table 4.3* Examples of local-scale and site-specific vegetation/atmosphere models.

PLANTIN	
Surface Deposition Scheme	A single layer “big-leaf” type model where stomatal conductance is estimated for a leaf using a multiplicative approach then scaled to the canopy depending on the proportion of sunlit to shaded leaves. $R_{c2}$ is found using the methodology of Wesely, 1989 where surface water is assumed to increase resistance. In canopy aerodynamics and soil resistances are included.
References	Grunhage and Haenel, 1997
NOAA-MLM (multi-layer model)	
Surface Deposition Scheme	20 layers with $R_b$ , $R_{c1}$ and $R_{c2}$ evaluated for each vegetated layer using vertical profiles of the relevant variables (such as light intensity). At the ground a surface the soil latent heat flux is estimated as well as in canopy $R_a$ and soil $R_b$ .  The original stomatal resistance scheme <sup>1</sup> used a multiplicative approach whereas the latest version uses photosynthesis <sup>2</sup> . 15 vegetation types are parameterised, including grasses.
References	1. Meyers, <i>et al.</i> , 1998 2. Wu, <i>et al.</i> , 2003

Table 4.3 Examples of local-scale and site-specific vegetation/atmosphere models.

FORFLUX	
	A multi-layer "big-leaf" type model where stomatal conductance is estimated for a leaf layer using a photosynthesis model then integrated across the layers. The light and photosynthetic capacity is estimated for each layer. $R_{c2}$ is calculated for the whole canopy by scaling a constant resistance for LAI. In canopy aerodynamics and soil resistances are included.
References	Nikolov and Zeller, 2003; Zeller and Nikolov, 2000

## 3.2 Methods of Treating of Dry Deposition and Proposed Models for the Grassland Site

### 3.2.1 Parameterising Aerodynamic Resistance, $R_a$

The calculation of  $R_a$  from measurements was described in Section 2.5 above and the methods use to model it are very similar, requiring an estimate of wind speed, friction velocity, zero-plane displacement ( $z_0$ ) and Monin-Obukov length ( $L$ ). Equation (56) is a standard formula used in many models (77), although a slightly different form is used in some (Simpson *et al.*, 2003a, Erisman *et al.*, 1994):

$$R_a[z-d] = \frac{1}{ku_*} \left[ \ln \left( \frac{z-d}{z_0} \right) - \psi_H \left\{ \frac{z-d}{L} \right\} + \psi_H \left( \frac{z_0}{L} \right) \right] \quad (77.)$$

In other cases a very simple formula may be used, by assuming stable conditions (Smith *et al.*, 2000):

$$R_a[z-d] = \frac{u(z-d)}{u_*^2} \quad (78.)$$

or conversely a more complex parameterisation with different formula for stable or unstable conditions is used by MODELS-3:

$$\text{stable, } R_a[z-d] = \frac{Pr_0}{ku_*} \left[ \ln \left( \frac{z}{z_0} \right) + \beta_H \frac{z-z_0}{L} \right] \quad (79.)$$

$$\text{unstable, } R_a[z-d] = \frac{Pr_0}{ku_*} \left[ \ln \left( \frac{\left( -1 + \sqrt{1 + \frac{\gamma_H z}{L}} \right) \left( 1 + \sqrt{1 + \frac{\gamma_H z_0}{L}} \right)}{\left( 1 + \sqrt{1 + \frac{\gamma_H z}{L}} \right) \left( -1 + \sqrt{1 + \frac{\gamma_H z_0}{L}} \right)} \right) \right] \quad (80.)$$

where  $Pr_0 = 0.95$ , neutral Prandtl number  
 $\beta_H = 8.21$  stable profile coefficient for heat  
 $\gamma_H = 11.60$  unstable profile coefficient for heat

In the case of the Easter Bush grassland site, a generalised approach will be taken and  $R_a$  is calculated from equation (56). In multi-layer “big-leaf” models an in-canopy aerodynamic resistance ( $R_{inc}$ ) may also be included, for example the EMEP model uses equation (81) to account for the transfer of gases between the top of the canopy and soil (Emberson *et al.*, 2000b). However for grassland,  $R_{inc}$  is assumed to be negligible and so is not included at Easter Bush or in the EMEP model for this vegetation type.

$$R_{inc} = \frac{b.LAI.h}{u_*} \quad (81.)$$

where  $b$  = an empirical constant of  $14 \text{ s m}^{-1}$   
 $h$  = canopy height

### 3.2.2 Parameterising Boundary-Layer Resistance, $R_b$

As with  $R_a$ ,  $R_b$  is modelled in the same way as measurement derived values. The specific formula used depends on the aspect of the vegetation being examined; if it is the bulk-canopy scale, equation (60) is most commonly applied whereas when deposition to an individual leaf is considered (61) is more appropriate.

In the case of the grassland the equation for the bulk-canopy, (60) is used. However, equation (61) is more appropriate when the new stomatal uptake based effects indices for ozone, AFst (see Section 1.4.1), are being calculated, as they are currently defined for sunlit “big-leaf” at the top of the canopy.

### 3.2.3 Modeling Stomatal Resistance, $R_{c1}$

There are three approaches that have commonly been used to model stomatal resistance:

- “Jarvis-type” multiplicative schemes which are based on empirical relationships between stomatal resistance and environmental variables
- “Ball-Berry type” photosynthesis schemes which are more mechanistic but semi-empirical, based on the relationships between physiological parameters such as net photosynthesis and carbon dioxide concentration
- “Tardieu-type” physiological schemes based on guard cell function; abscisic acid (ABA) regulates guard cell turgor and stomatal conductance can be related to its concentration in the xylem sap (Farquhar *et al.*,

1980; Tardieu and Davies, 1993; Tuzet *et al.*, 2003; Yu *et al.*, 1998; Gao *et al.*, 2002; Buckley *et al.*, 2003).

Each has its own advantages and disadvantages, for example Jarvis-type models can be fairly simple to apply as they only require knowledge of some basic meteorological variables and a few vegetation specific parameters, whereas other types of model may require more detailed parameterisation and input variables that are not always available. The first two methods will be applied to our grassland site and are summarised below.

### 3.2.3.1 *Jarvis: Multiplicative Stomatal Resistance*

A simple model relating stomatal resistance to water-vapour ( $R_{c1w}$ ) to PAR, ambient CO<sub>2</sub> concentration, leaf-air vapour pressure difference, leaf temperature and leaf water status was proposed by Jarvis (1976). The response of  $R_{c1w}$  to all these variables is not independent so that the value of  $R_{c1w}$  expected at a particular value of one variable may be reduced due to the influence of another. However if enough measurements are available, the limit of a scatter diagram of  $R_{c1w}$  with a variable can be used to define its response. For example, Figure 3.1 shows plots of the relative value of  $R_{c1w}$  for potato with various parameters. Stomatal resistance can then be calculated using a series of such relationships (Figure 3.1) to scale the minimum potential resistance or maximum conductance, ie:

$$R_{c1w}^{-1} = [R_{c1w\_min}^{-1} (f_a f_b \times \dots f_z)] = [g_{max} (f_a f_b \times \dots f_z)] \quad (82.)$$

where  $f_a$  to  $f_z$  are functions relating the relative to value of  $R_{c1w}$  to an environmental variable and so they vary between 0 to 1  
 $R_{c1w\_min}$  = minimum stomatal resistance (s m<sup>-1</sup>)  
 $g_{max}$  = maximum stomatal conductance (m s<sup>-1</sup>)

Jarvis (1976) noted that this approach was not wholly satisfactory as the parameters have limited physiological meaning. Nevertheless, although understanding of physiological processes has advanced over the years (and more mechanistic models are now available), it has proved to be a useful way of using simple field measurements to model stomatal responses. Several different forms and parameterisations of the scaling functions have been derived using this technique, depending on the data available for a particular study. The relationships that will be used for the Easter Bush site are based on the EMEP deposition module (Emberson *et al.*, 2000a) and are outlined below (their full parameterisation will be considered in Chapter 6).

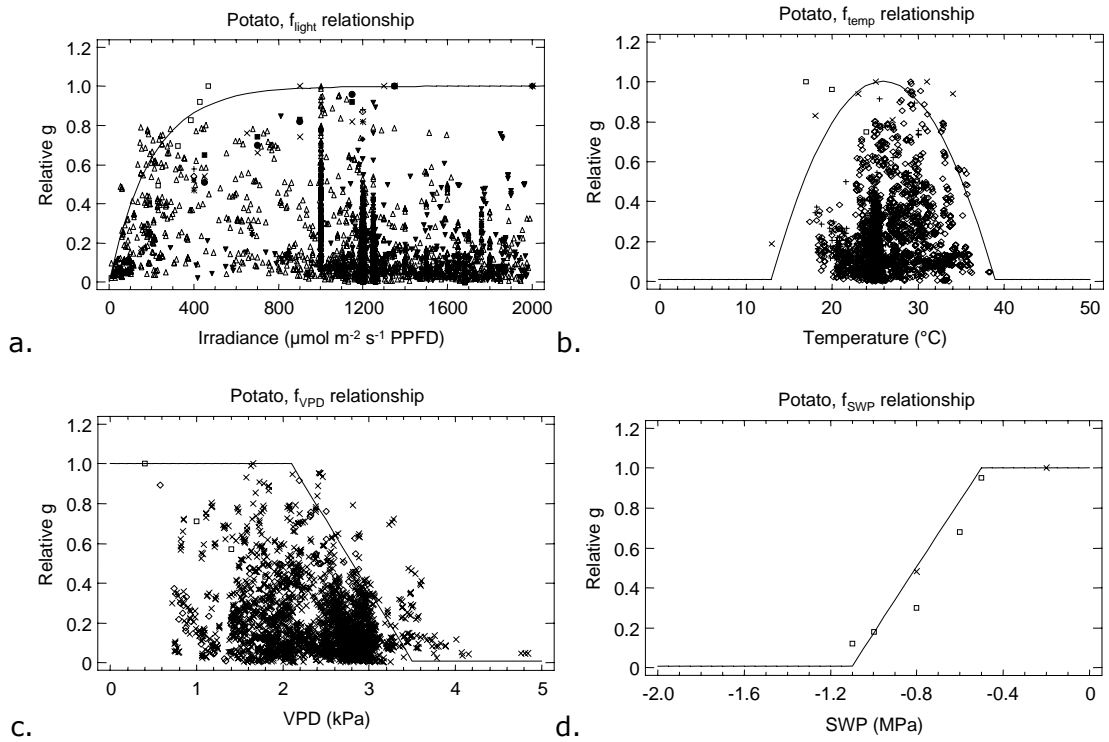


Figure 3.1. Examples of the variation of the stomatal conductance of potatoes which environmental parameters (a. photosynthetically active radiation, b. temperature, c. vapour pressure deficit and d. soil water potential), measured using leaf-level porometers in the field or controlled chambers (ICP, 2004). The scaling functions, fitted using a boundary line approach, are shown as solid lines.

In order to model stomatal conductance throughout the year seasonal variations in canopy characteristics must be incorporated in the model as well as the response of stomata to environmental variables. The basic formula used for total canopy resistance is:

$$R_c = \left[ \frac{LAI}{R_{c1}} + \frac{SAI}{R_{c2}} + \frac{1}{R_{c3}} \right]^{-1} \quad (83.)$$

$LAI$  is the leaf area index and  $SAI$  is a surface area index, set equal to  $LAI$  when the canopy height is greater than 6.4 cm (the height at which  $LAI \approx 1$ ) and 1 at other times. The non-stomatal resistances are considered in Section 3.2.4. and  $R_{c1}$  is modelled using:

$$R_{c1\_O3} = 1.51 \left[ \frac{g_{max} \cdot f_{pot} (\text{maximum}(f_{min}, (f_{light} \cdot f_T, f_{VPD}, f_{SWP})))}{a_w} \right]^{-1} \quad (84.)$$

where  $a_w$  is the conversion factor for  $\text{mol m}^{-2} \text{s}^{-1}$  to  $\text{m s}^{-1}$  from equation (66)

**Leaf-Age,  $f_{pot}$ :** The maximum stomatal conductance that a leaf can achieve varies throughout the year as the plant grows in the spring then senesces in the autumn (termed phenology). However at the Easter Bush site, growth is also

influence by harvesting and grazing. A “temperature sum” approach generally gives the most realistic representation of phenology but in the absence of a suitable parameterisation for *Lolium perenne*, a simple step function is used which increases linearly at the start of the year to a maximum then decreases in the autumn (Figure 3.2). Although some grasses die back completely over the winter, the fields at Easter Bush remained green throughout the year indicating that the plants were still active and so  $f_{pot}$  goes to a minimum of 0.5. The harvests and grazing generally occur during the summer months and are accounted for in the scaling for leaf area index (LAI) in equation (83).

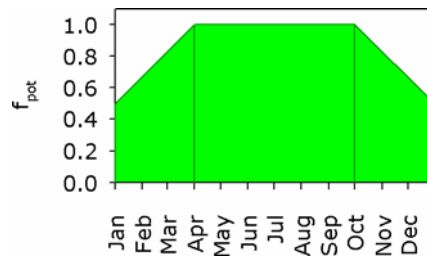


Figure 3.2. Example of the phenology function,  $f_{pot}$ , used to represent the variation of maximum potential stomatal conductance with leaf age.

**Light,  $f_{light}$ :** Stomatal conductance increases rapidly with light levels (Figure 3.1a, measured as photosynthetically active radiation, PAR) and so an exponential function is used:

$$f_{light} = (1 - \exp^{-\alpha PAR}) \quad (85.)$$

where  $\alpha$  is a constant

However, this function is representative of a sunlit leaf at the top of the canopy and not all leaves will be fully exposed to the radiation. As a single layer is being used to represent the whole canopy, differences in stomatal conductance caused by shading of individual leaves must be accounted for. A method to describe radiation transfer within a canopy was developed by Norman, (1982) which estimates the amount of the direct and diffuse radiation incident on sunlit and shaded leaves. Various parameterisations have been proposed based on this type of analysis (Baldocchi *et al.*, 1987, Nikolov and Zeller 2003 and Smith *et al.*, 2000) and the EMEP scheme is used for here (Jakobsen *et al.*, 1996):

$$LAI_{sun} = \left[ 1 - \exp\left(-0.5 \frac{LAI}{\sin \beta}\right) \right] 2 \sin \beta, \quad LAI_{shade} = LAI - LAI_{sun} \quad (86.)$$

$$PAR_{sun} = I_{dir} \cos \zeta / \sin \beta + PAR_{shade} \quad (87.)$$

$$PAR_{shade} = I_{diff} \exp(-0.5 LAI^{0.7}) + 0.07 \cdot I_{dir} (1.1 - 0.1 LAI) \exp(-\sin \beta) \quad (88.)$$

$PAR_{sun}$  is dependant on the mean angle between leaves and the sun,  $\zeta$  which is assumed to have a spherical distribution with a constant value of  $60^\circ$ .  $\beta$  is the complement of the solar zenith angle,  $\delta$ . The equation for  $PAR_{shade}$  (88) is a semi-empirical function derived by Norman, (1982).  $I_{dir}$  and  $I_{diff}$  are the direct and diffuse components of  $PAR$  at the top of the canopy. Weiss and Norman, (1985) proposed a methodology to estimate  $I_{dir}$  and  $I_{diff}$  from measurements of total solar radiation and  $PAR$ , and a similar method is used here:

$$\text{direct radiation, } I_{dir} = PAR_{meas} \cdot \exp(-B \sec \delta \frac{p}{p_0}) \quad (89.)$$

where  $PAR_{meas}$  is the measured  $PAR$  in  $W m^{-2}$  or  $\mu mol m^{-2} s^{-1}$

$$B = -0.7 \times 10^{-9} Jd^3 - 1 \times 10^{-6} Jd^2 + 0.0006 Jd + 0.1218 \quad (90.)$$

$$\sec \delta = 1/\cos \delta$$

$$\cos \delta = \sin\left(\frac{d\pi}{180}\right) \sin\left(\frac{lat\pi}{180}\right) + \cos\left(\frac{d\pi}{180}\right) \cos\left(\frac{lat\pi}{180}\right) \cos\left(\frac{h_r\pi}{180}\right) \quad (91.)$$

$$\sin \beta = \sin\left(\frac{lat\pi}{180}\right) \sin\left(\frac{d\pi}{180}\right) + \cos\left(\frac{lat\pi}{180}\right) \cos\left(\frac{d\pi}{180}\right) \quad (92.)$$

$$d = \text{solar declination} = 23.5 \frac{\pi}{180} \sin\left(\frac{2\pi(Jd - 80)}{365 + ly}\right) \quad (93.)$$

$$h_r = \text{hour angle (degrees)} = (\text{hour} + lon_c) \left( \frac{2\pi}{24} + lon_{radians} \right) \quad (94.)$$

$$lon_c = \text{longitude correction} = 4(lon_s - lon) \quad (95.)$$

$Jd$  = Year day number (1 to 365 or 366),  $ly$  = 1 for leap years

$lat$  = site latitude in degrees,  $lon$  = site longitude,  $lon_s$  = standard longitude = 0,  $p$  = pressure,  $p_0$  = 101.3 kPa

$$\text{diffuse radiation, } I_{diff} = C \cdot I_{dir} \quad (96.)$$

$$\text{where } C = -0.6 \times 10^{-9} Jd^3 - 9 \times 10^{-7} Jd^2 + 0.0004 Jd + 0.0881 \quad (97.)$$

The final value of  $f_{light}$  is calculated from a combination of  $f_{light\_sun}$  and  $f_{light\_shade}$ :

$$f_{light\_sun} = (1 - \exp^{-\alpha PAR_{sun}}), f_{light\_shade} = (1 - \exp^{-\alpha PAR_{shade}}) \quad (98.)$$

$$f_{light} = f_{light\_sun} \frac{LAI_{sun}}{LAI} + f_{light\_shade} \frac{LAI_{shade}}{LAI} \quad (99.)$$

Zhang *et al.*, (2001) reviewed methods of estimating in-canopy radiation and recommended the use of a slightly modified exponential term in equation (88) ( $LAI^{0.8}$  instead of  $LAI^{0.7}$ ). However a test of this revision in the Easter Bush model

showed it had an insignificant effect on estimates of canopy conductance and the model was more sensitive to other parameters.

**Temperature,  $f_T$ :** The response to temperature is usually represented as a parabola; Figure 3.1b shows the symmetrical function used by the EMEP model (equation (100)). A commonly used asymmetrical formula (101) (Baldocchi *et al.*, 1987 or Smith *et al.*, 2000) is applied to Easter Bush.

$$f_T = 1 - \left[ \frac{T - T_{opt}}{T_{opt} - T_{min}} \right]^2 \quad (100.)$$

$$f_T = \left[ \frac{T - T_{min}}{T_{opt} - T_{min}} \right] \left[ \frac{T_{max} - T}{T_{max} - T_{opt}} \right]^{\left[ \frac{T_{max} - T_{opt}}{T_{opt} - T_{min}} \right]} \quad (101.)$$

where  $T_{opt}$  = optimum temperature for stomatal opening  
 $T_{min}$  and  $T_{max}$  are the minimum and maximum temperatures at which stomata open

**Vapour Pressure Deficit ( $vpd$ ),  $f_{vpd}$ :**  $vpd$  influences stomatal opening as high values indicate a dry environment and so plants tend to reduce their stomatal conductance to preserve water. The response to  $vpd$  is a simple step function which declines linearly above a fixed value of  $vpd$  ( $vpd_{max}$ ) as shown in Figure 3.1c.

**Soil Water Potential (SWP),  $f_{SWP}$ :** The effect of soil water potential is a mirror image of that for  $vpd$ , in that stomatal conductance declines linearly below a fixed value of SWP ( $SWP_{min}$ ) (Figure 3.1c).

### 3.2.3.2 Ball-Berry: Photosynthesis Derived Stomatal Resistance

Ball, (1988) and Ball *et al.*, (1987) proposed a simple equation to describe the response of stomatal conductance to the net rate of CO<sub>2</sub> uptake ( $A_n$ ), the relative humidity (as a ratio,  $RH_s$ ) and CO<sub>2</sub> concentration at the leaf surface:

$$g_s = m \frac{A_n RH_s}{\chi_{CO_2}(z_{0'})} + b \quad (102.)$$

Where  $m$  and  $b$  are the linear regression coefficients obtained from a plot of the ratio ( $A_n RH_s / \chi_{CO_2}$ ) with measurements to stomatal conductance, normally made using a leaf porometer. For accurate parameterisation, the day-time respiration rate of the leaf ( $R_d$ ) should be taken into account ( $A_n = A_g - R_d$ ). This is often

taken to be a constant derived from measurements, following the methodology of Farquhar *et al.*, (1980). Although some good results have been obtained using this simple relationship, it has been expanded on to improve the response to atmospheric water content as stomata respond to vapour pressure deficit at the leaf surface ( $vpd_{ls}$ ) rather than humidity (Leuning, 1995):

$$g_s = m \frac{A_n}{\chi_{CO_2}(z_{0'})} f(vpd_{ls}) + b \quad (102')$$

where various forms of  $f(vpd_{ls})$  have been proposed:  $f(vpd_{ls}) = 1 - vpd_{ls}/vpd_o$  (Jarvis, 1976);  $f(vpd_{ls}) = vpd_{ls}^{-2}$  (Lloyd, 1991);  $f(vpd_{ls}) = (1 + vpd_{ls}/vpd_o)^{-1}$  (Lohammer, *et al.*, 1980). To allow the model to also estimate stomatal conductance at low  $CO_2$  concentrations (where  $\chi_{CO_2}$  approaches the compensation point,  $\Gamma_{CO_2}$ , conductance approaches maximum values but  $A_n \rightarrow 0$ ) Leuning, (1990) proposed an additional modification:

$$g_s = g_o + m \left[ \frac{A_n}{\chi_{CO_2}(z_{0'}) - \Gamma_{CO_2}} \right] f(vpd_{ls}) + b \quad (102'')$$

Ball-Berry type equations have been incorporated into canopy scale models for water-vapour flux and trace gas exchange (Ronda, *et al.*, 2001 and Wu *et al.*, 2003 for example) and further developed to include responses driven by ABA (Gutschick and Simonneau, 2002).

As with the multiplicative method, this approach is based on estimating  $g_s$  for a single leaf and one of its limitations is that for modelling ecosystem trace-gas exchange, estimates of bulk-canopy net  $CO_2$  assimilation rate are required. Plant physiological models for leaf  $A_n$  and  $R_d$  are available (Collatz *et al.*, 1992) but scaling up such estimates to the whole canopy can require complex formula and parameterisations, see Ronda *et al.*, (2001) for example. However the measurements available for the Easter Bush site allow a simple form of equation (102) to be derived that estimates bulk-canopy stomatal conductance, as described in Chapter 6. The approach used has the advantage that a single relationship is fitted which implicitly includes factors such as phenology and  $LAI$ .

### 3.2.4 Models for Non-Stomatal Resistance, $R_{ns}$

In the majority of deposition models  $R_{c2}$  is essentially treated as a constant, only varying with a structural aspect of the canopy such as surface area, as in equation (80), although  $R_{c3}$  may include some temperature or wetness dependence. For example the EMEP model (Simpson *et al.*, 2003a) uses a constant value of  $2500 \text{ s m}^{-1}$  for  $R_{c2}$  and  $R_{c3} = R_{g0} + R_{low} + 2000\delta_{snow}$ , where  $R_{g0} = 1000 \text{ s m}^{-1}$  for grasslands,  $\delta_{snow} = 1$  when snow is present and 0 at all other times,  $R_{low}$  is an adjustment to increase  $R_{c3}$  at low temperatures ( $R_{low} = 1000\exp(-T-4)$ ).

As discussed in Section 2.5.1.3, some studies have found that  $R_{ns}$  is controlled by other variables such as surface wetness, solar radiation or temperature and two parameterisations have been proposed in the literature. The influence of temperature and radiation, as well as surface wetness, will be examined at our grassland site and compared to these parameterisations. As the grass canopy is closed for much of the time, soil resistance is assumed to be unimportant when the canopy is fully developed and  $1000 \text{ s m}^{-1}$  at other times, as described in Chapter 6.

## **4 Measurements of Ozone Flux to Grassland: Experimental Setup and Characterisation of the Field-site**

### ***4.1 Introduction***

The measurements and models required to examine the deposition of ozone to vegetation have been described in the preceding chapters. This chapter describes the practical application of these techniques to the measurement of deposition over a grassland site in central Scotland and characterises the site by summarising the meteorological and vegetative results.

The measurements of ozone deposition began in May 2001, stopped over the winter of 2001/02, and continue to the present. Results from May 2001 to December 2004 are presented here. The grassland site was chosen as: there are no long-term measurements of ozone deposition to this important fodder crop; the vegetation is predominately *Lolium perenne* (perennial rye-grass) which simplifies interpretation of the measurements; several other experiments were being undertaken at the site allowing for a sharing of resources and measurements; during three years the grass was cut for silage, allowing us to examine the effect on deposition.

### ***4.2 Site Location and Topography***

The site is located at a university owned experimental farm (Easter Bush) in southern Scotland (3°12' W, 55° 52' N, elevation 190 m above sea level), close to CEH-Edinburgh (Figure 4.1a). The field-site consists of two grassland fields of approximately five ha each, named 'SW' and 'NE' field from now on. The measurement equipment was placed on the boundary of the two fields (Figure 4.1b) which runs NW to SE. This enabled measurements to be conducted over one field in SW wind directions and the other field in NE wind directions.

The site is in the foothills of the Pentlands and so gently slopes down from the NW to SE. There is a step in the slope of the SW field, roughly halfway across in a line parallel to the NW boundary (Figure 4.1b). Another feature is a very slight ridge along the fence line separating the two fields, which could potentially affect the gradient measurements by compressing the streamlines as they cross over.

This ridge also adds to the uncertainty in the measurements of canopy and instrument heights.

### 4.3 Site Management: Harvests, Grazing, Experiments

During 2001 and 2002 the fields were intensively managed to provide silage as fodder for the farms' animals. Several applications of fertilisers were made and

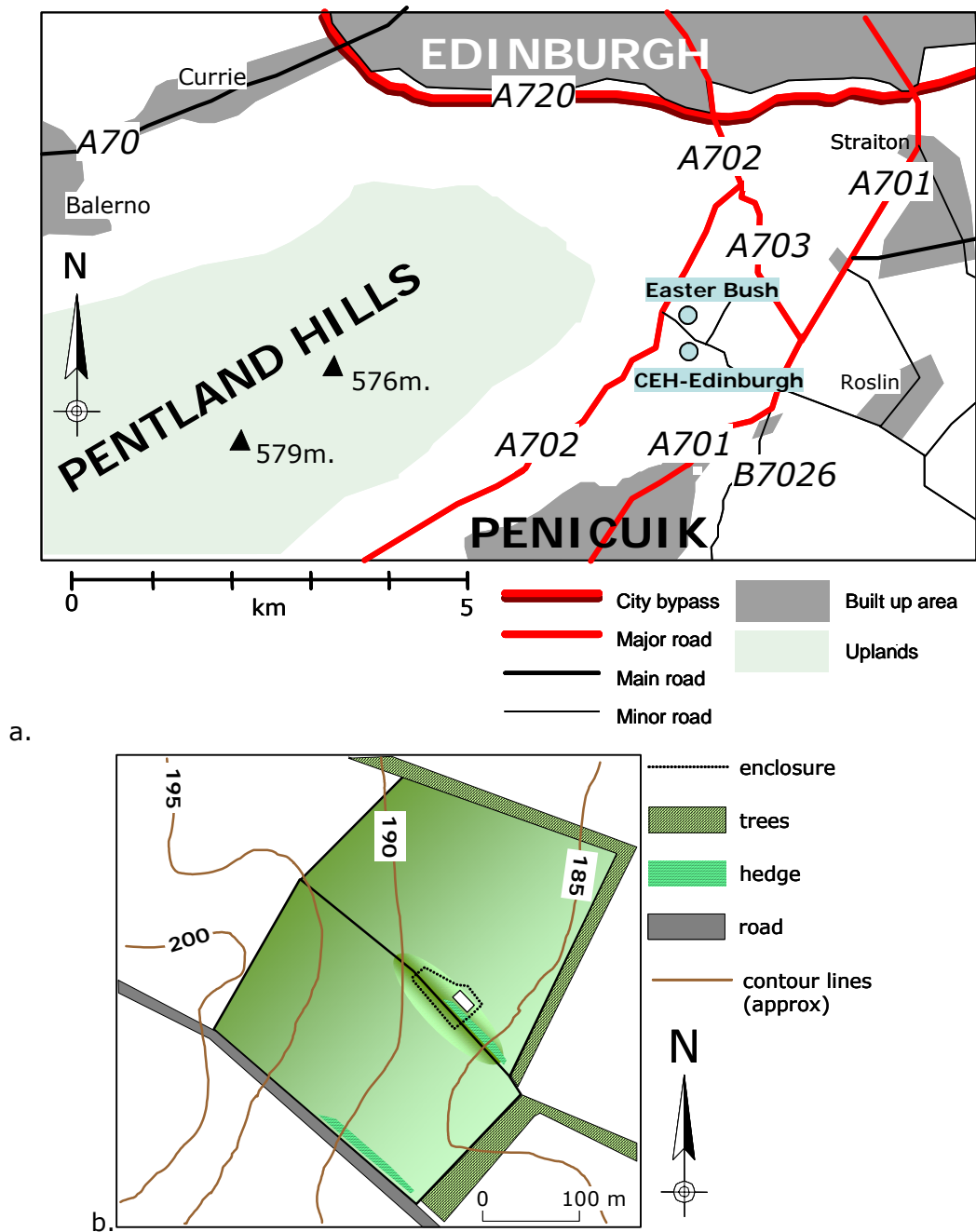


Figure 4.1. a. The location of Easter Bush and CEH Edinburgh. b. A sketch of Easter Bush giving an indication of topography and the location of the equipment enclosure.

each field was cut at least once each year and grazed at the end of the summer. In 2003 the farmer decided to use the fields for grazing only and so, although fertiliser applications continued only one silage cut occurred in the SW field, at our request. In 2004 the fields were grazed by sheep throughout the year. The events are summarised in Table 4.1 and Figure 4.3 shows the grazing periods. As the management of both fields is similar the data are analysed as a whole, although field specific canopy heights are used dependent on wind direction.

*Table 4.1* Major events occurring at the Easter Bush field site

<b>Date</b>	<b>Event</b>
26/05/2001	Core equipment installed and operational
01/06/2001	Both fields harvested for silage
03/06/2001	Cut grass lifted
25/07/2001	Both fields harvested for silage
26/07/2001	Cut grass lifted
20/08/2001	NE field waterlogged
01/10/2001	Ozone gradient removed for winter
21/03/2002	Ozone gradient reinstalled and fully functional
01/06/2002	Both fields harvested for silage
04/06/2002	Cut grass lifted
18/07/2002	New cabin in place and instrumentation back on.
05/08/2002	SW field harvested for silage
22/10/2002	Heavy rain, equipment flooded, all power off
06/03/2003	Ozone gradient pump fault detected (it was repaired but problems continued until it was replaced with a new pump)
20/05/2003	Gradient data logger replaced
29/05/2003	SW field harvested for silage
11/09/2003	Ozone gradient pump fault detected
07/10/2003	New PTFE pump installed on gradient
28/09/2004	Slurry spread in SW field

The field-site was not only used for ozone deposition measurements as several other projects shared the facility. This resulted in many measurements being made that are useful for interpreting the ozone results but could not have been resourced by the ozone project alone, Table 4.2 briefly summarises the major concurrent projects and any data that they provided. The ozone equipment was maintained by Mhairi Coyle throughout the measurement period although colleagues assisted with other systems, such as the sonic anemometers, Bowen ratio and water-vapour/CO<sub>2</sub> analysers.

Table 4.2 Major experiments at Easter Bush

Experiment	Time Period		People	Description and Data ( <i>used for ozone</i> )
	Start	End		
Quantification and validation of the total annual UK nitrous oxide budget (GANE funded)	07/06/02	21/06/03	Chiara DiMarco	N <sub>2</sub> O flux measurements using Eddy Correlation Tuneable Diode Laser (TDL) spectrometer used for N <sub>2</sub> O concentration operating at 10 Hz. <i>Metek sonic anemometer</i>
IFO3 Grassland	2001	2002	Marcel van Ojien Gina Mills Felicity Hayes Peter Levy Maureen Murray	In O3GRASSLAND, the solardomes at CEH-Bangor were used for detailed measurements of damage caused by ozone to grass ( <i>Lolium perenne</i> ) and clover ( <i>Trifolium repens</i> ). Measurements of O <sub>3</sub> , CO <sub>2</sub> and H <sub>2</sub> O fluxes were made at Easter Bush, as well as photosynthesis and gas exchange of individual plants. A simulation model that accounts for the four damage mechanisms triggered by ozone was constructed and applied to the field site.
GREENGRASS and CARBOEUROPE	2001	ongoing	Celia Milford Eiko Nemitz Claire Campbell Margaret Anderson Chiara Di Marco	Sources and sinks of greenhouse gases from managed European grasslands and mitigation strategies. These are very large collaborative projects, studying greenhouse gas exchange, which provided the resources for much of the vegetative and CO <sub>2</sub> /H <sub>2</sub> O flux measurements. <i>Gill sonic, LICORS</i>

## 4.4 Vegetation Measurements

As part of some of the GREENGRASS/CARBOEUROPE experiments outlined above regular samples of vegetation were taken and analysed for *LAI*, biomass and chemical content (Nitrogen for example). As part of the IFO3 Grassland experiment, leaf gas exchange was measured on a few days in 2001 and 2002, to parameterise a physiological model of *lolium perenne* growth and response to ozone. A survey of plant species was also undertaken in July 2002 and regular measurements of canopy height were made.

### 4.4.1 Vegetation Survey

The plant survey followed standard protocols and species numbers within 50 randomly selected (by throwing) 0.5 m quadrats were counted in each field. The

dominant plant is *Lolium perenne* (Ryegrass) which covers >90% of each field but there are a few other species present as indicated by the data in Table 4.3.

#### 4.4.2 Canopy Height ( $h$ )

Measurements of canopy height ( $h$ ) were made using a “Herbomètre” (Figure 4.2) which gives a consistent result. To capture the variation in canopy height measurements were made at 10 pseudo-random locations in each field and the maximum, minimum and average recorded. The data analysis requires a continuous time series of  $h$  so a set of curves were fitted to each years data to best fit the samples, allowing for some variation due to an individuals sampling preference. Different people measured on different days which caused some variation in the average  $h$  from day to day. The plots shown in Figure 4.4 show the resulting time series; the are peaks around the cutting periods are due to the grass being left in piles across the field for period before they were removed (Figure 4.5). These time series are used to estimate the micrometeorological height,  $d = 2/3 h$  as discussed in Chapters 2 and 5 .



Figure 4.2. Photo of the “Herbomètre”, the bottom of the black pole is placed on the soil and the green plate, which is attached to the yellow tube and ruler, sits on top of the vegetation. The vegetation height can then be read from the ruler.

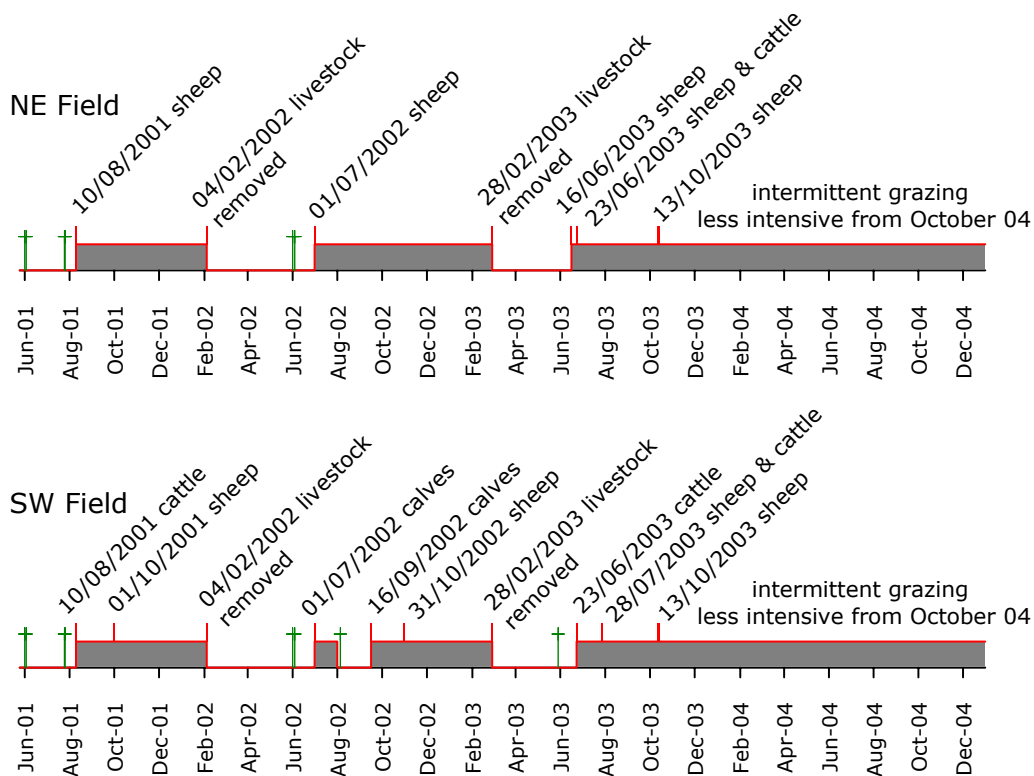


Figure 4.3. Timelines of grazing periods (shaded blocks) and silage harvests (crosses) in each field.

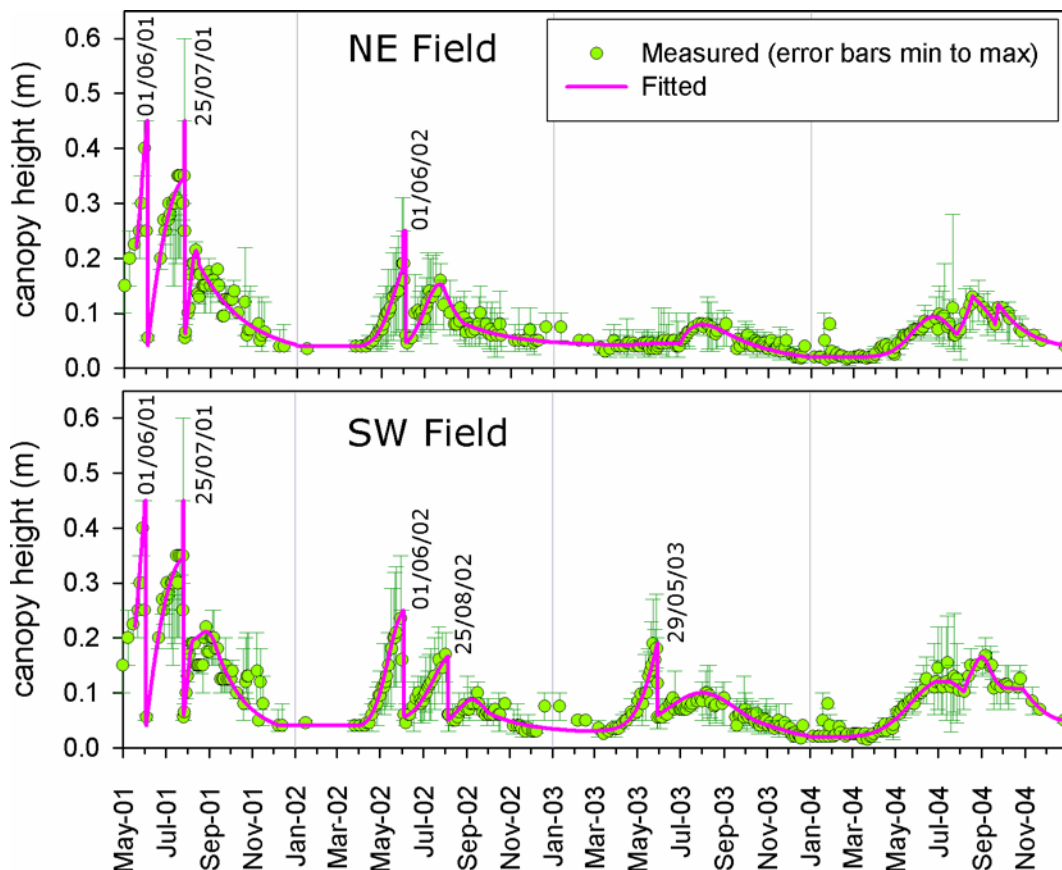


Figure 4.4. Time series of measured and fitted canopy height in each field (NE top and SW bottom plot respectively). The dates indicate silage harvests; the rest of the variation is due to grazing and plant growth/senescence.

Table 4.3 Easter Bush Field Survey 18/07/02

SW Field		
Species		Mean % Cover
<i>Lolium perenne</i> (Ryegrass)		96.44
<i>Phleum pratense</i> (Timothy)		1.66
<i>Poa annua</i> (annual meadow grass)		0.20
<i>Ranunculus repens</i> (buttercup)		0.98
<i>Trifolium repens</i> (white clover)		0.26
<i>Rumex obtusifolia</i> (broad leaved dock)		0.10
<i>Taraxacum officinale</i> (dandelion)		0.14
<i>Veronica pratense</i> (field speedwell)		0.04
<i>Chaerophyllum temulum</i> (Chervil)		0.10
<i>Dactylis glomerata</i> (cock's foot)		0.04
<i>Holcus lanatus</i> (Yorkshire Fog)		0.02
NE Field		
Species		Mean % Cover
<i>Lolium perenne</i> (Ryegrass)		92.46
<i>Phleum pratense</i> (Timothy)		1.40
<i>Poa annua</i> (annual meadow grass)		0.44
<i>Ranunculus repens</i> (buttercup)		2.24
<i>Trifolium repens</i> (white clover)		0.16
<i>Rumex obtusifolia</i> (broad leaved dock)		3.00
<i>Taraxacum officinale</i> (dandelion)		0.02
<i>Veronica pratense</i> (field speedwell)		0.00
<i>Chaerophyllum temulum</i> (Chervil)		0.06
<i>Dactylis glomerata</i> (cock's foot)		0.20
<i>Bellis perennis</i> (daisy)		0.02

**Summary**

Both fields are composed of more than 90% Rye grass (*Lolium perenne*) with around 1-2 % Timothy (*Phleum pratense*), 1-2 % buttercup (*Ranunculus repens*) and up to 3% dock (*Rumex obtusifolius*).



Figure 4.5. The SW field on 30/5/2003 after cutting but before lifting.

### 4.4.3 LAI – Leaf Area Index

A study of the effects of ozone on plant chemistry is not within the scope of this project and so these measurements are not described here, however the *LAI* measurements are of interest. Although *LAI* is not used in the calculation of flux it is required by deposition models to quantify stomatal and cuticular resistances. *LAI* is found from samples of vegetation by placing individual leaves on the bed of a *LAI* meter, ensuring that they are as flat as possible. The meter effectively scans the leaves in a similar way to a document scanner and uses the number of dark and light pixels to estimate area.

Vegetation samples were taken from the SW field in 2002 (IFO3 project), 2003 and 2004 (GREENGRASS project) on a total of 16 days and their *LAI* measured. However, as continuous time series of *LAI* are required a relationship between *LAI* and *h* was used, as derived by Milford (2004) from measurements in 1999 (equation 103). The estimated *LAI* was constrained to a minimum of 0.25 at canopy heights less than ~2 cm and during the periods when the grass was cut but left lying on the field. The measurements made during 2002 to 2004 agree fairly well with this relationship as shown in Figure 4.6.

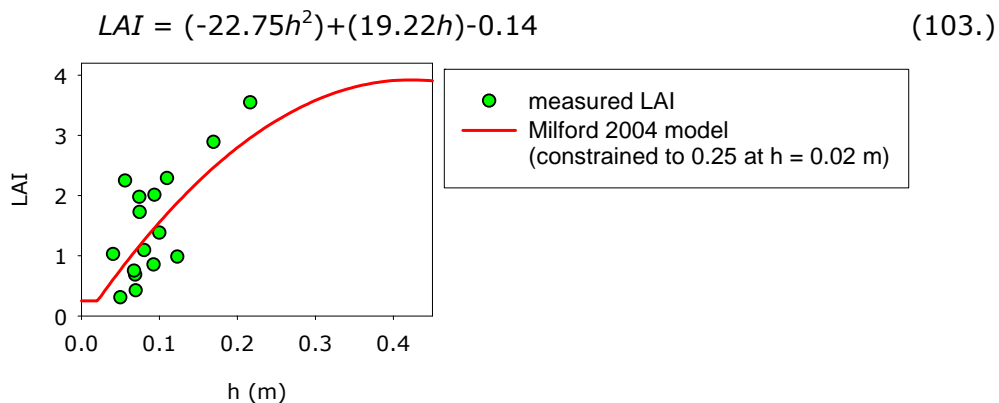


Figure 4.6. The relationship between *h* and *LAI* for *lolium perenne* as derived by Milford, 2004 and measurements for 2002 to 2004.

### 4.4.4 Photosynthesis – Stomatal Resistance

On a number of days in summer 2001 and 2002, leaf photosynthesis and stomatal conductance were measured (by Peter Levy and Maureen Murray, CEH Edinburgh) using a closed gas exchange system (LI 6200, Li Cor, Lincoln, NB, USA). The measurements were only carried out on upper leaves in the sward, as the lower leaves could not be reached because of the size of the measurement chamber. Measurements were of two types: 1. those made rapidly after

enclosing the leaf with the chamber, so as to be representative of the ambient functioning of the leaf; or 2. those made over a number of minutes, during which chamber conditions were altered, so as to derive the response of photosynthesis to changes in internal CO<sub>2</sub> concentration ( $C_i$ ) or photosynthetic photon flux density ( $PAR$ ). Each individual measurement was made over 15 seconds, achieving a CO<sub>2</sub> differential of around 5 ppm with 4 cm<sup>2</sup> of leaf area enclosed. A consecutive pair of measurements was made each time to check for errors.

The first type of measurement, representative of the ambient functioning of the leaf will be used to assess the performance of the different stomatal resistance models, albeit for limited conditions, as described in Chapter 6. The second set of measurements was used to parameterise a photosynthesis-type vegetation model for the IFO3 project.

## ***4.5 Instrumentation: Setup and Operation***

The instruments were setup along the boundary between the two fields, as shown in Figure 4.7. The configuration and operation of the instruments are considered below in groups that perform specific tasks<sup>6</sup> and listed in Table 4.4. At the start of the experiment a tow-a-van was used to house the equipment, such as ozone analysers, pcs and data-loggers, which did not have their own weather-proof enclosures. The mains power supply was via an armoured cable connected to a mains socket at a tree nursery ~400 m away. In 2002 a significant investment was made in the site and a new port-a-cabin was installed (July 2002) along with a dedicated mains power supply (May 2002).

### **4.5.1 Standard Meteorological Measurements and Energy Balance (BR system)**

At the start of measurements in May 2001 a Campbell Scientific Bowen-Ratio mast was setup at one end of the enclosure to measure the energy balance (Section 2.4.3) and provide a platform for other meteorological measurements. A photograph of the mast is shown in Figure 4.8. Data were processed and stored every 15 minutes using a Campbell Scientific 21X data-logger. As the logger overwrites the earliest data when its memory capacity is exceeded this logger required downloading at least once a week to ensure there was no loss of data. The instruments included in this setup are described in this section.

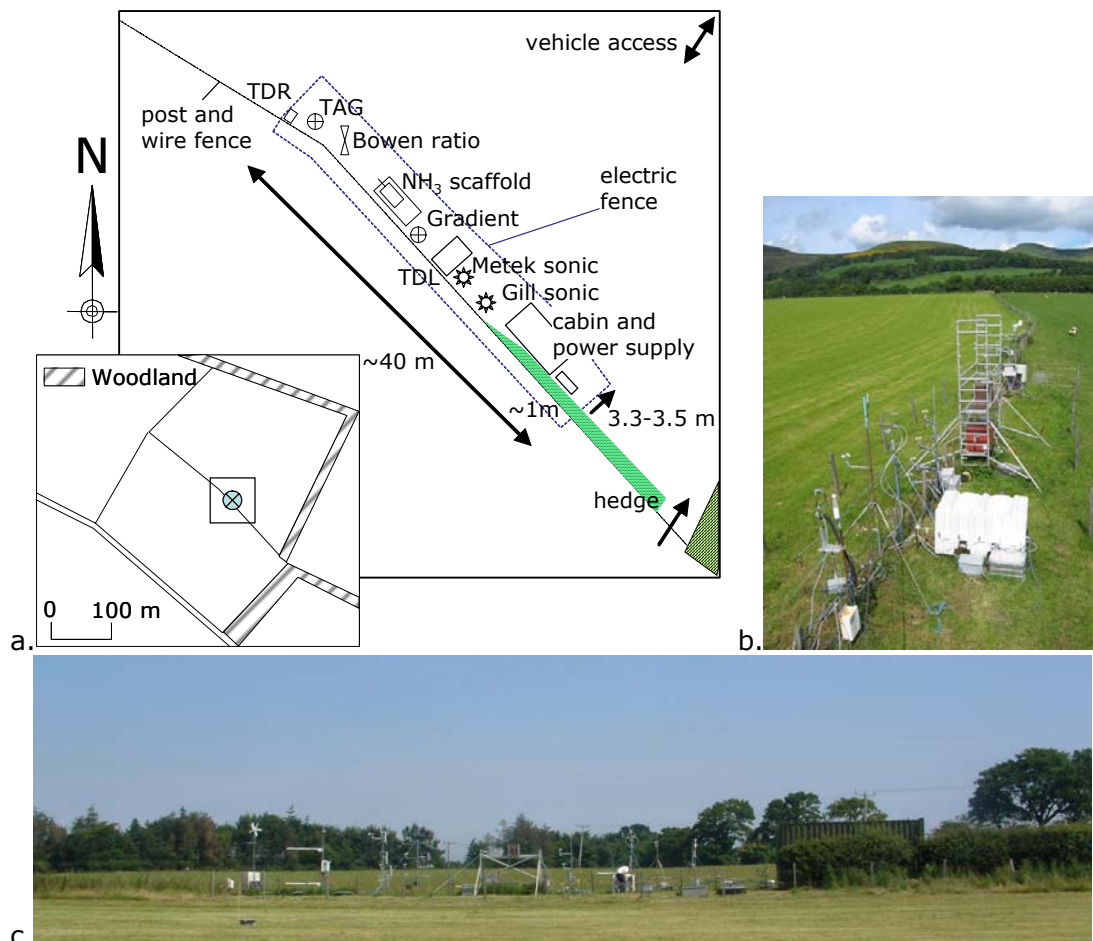


Figure 4.7. (a) A sketch of Easter Bush showing the location of major equipment and instruments (TDR = Time Domain Reflectometer, TAG<sup>7</sup> = Time Averaged Gradient, TDL = Tunable Diode Laser). Photographs of all the equipment on (b) 14/6/2003 and (c) 06/08/2002.

- **Fine-wire Type-E thermocouples at 2 heights ( $T_u$ ,  $T_l$ )**

Initially these were supplied by Campbell Scientific and when they failed they were replaced using home-made probes. A thermocouple consists essentially of two strips or wires made of different metals and joined at one end. Changes in the temperature at that junction induce a change in electromotive force (voltage) between the other ends. As temperature goes up, this output voltage of the thermocouple rises, though not necessarily linearly. In type-E thermocouples the wires are made of Nickel-Chromium (Ni-Cr) and Copper-Nickel (Cu-Ni) and respond to temperatures in the range  $-270$  to  $1000$  °C, giving an output voltage over this range of  $-9.8$  to  $76.4$  mV.

<sup>6</sup> Contact details for all the manufacturers of instrumentation mentioned can be found in the Appendices

<sup>7</sup> These instruments, the TAG and TDL, are not used for the ozone experiment and so are not described further.

Table 4.4 Instrumentation employed at Easter Bush.

System Group	Components	Parameter and Label	Start Date	End Date
Bowen Ratio	2 Fine-wire type-E thermocouples	Air temperature gradient $T_l, T_u$	18/5/01	ongoing
	2 Soil Heat Flux plates	Soil Heat Flux (G) $HF_{s1}, HF_{s2}$	18/5/01	
	Averaging temperature probes	Soil temperature $T_s$	18/5/01	
	RH/T probe	Relative humidity and air temperature $RH, T$	3/4/03	
	Pyranometer	Total solar radiation, $St$	18/5/01	
	PAR sensor	Photosynthetically active radiation, $PAR$	3/4/03	
	2 Net radiation sensors	Net radiation, $Rn_1, Rn_2$	18/5/01	
	Surface Wetness PCB	Presence and duration of surface wetness $SW$	8/6/01	
	Tipping bucket	Rainfall	18/5/01	
Gradient	3 Fine-wire type-E thermocouples	Air temperature gradient $T_1, T_3, T_5$	22/5/01	ongoing
	5 cup-anemometers	Wind-speed gradient $U_1$ to $U_5$		
	ozone analyser	Average ozone concentration gradient, $\chi_{O_3 1}$ to $\chi_{O_3 5}$		
Eddy-correlation	2 sonic anemometers	Turbulence parameters and wind direction $u', w', v'$ etc and $Wd$ .	15/5/01	ongoing
	LICOR CO <sub>2</sub> /H <sub>2</sub> O analysers	CO <sub>2</sub> and H <sub>2</sub> O flux and concentration $\chi_{CO_2}, \chi_{CO_2}$ $\chi_{H_2O}, \chi_{H_2O}$		ongoing
	GFAS/ROFI fast-ozone sensors	Ozone flux $\chi_{O_3}$	Jun-Aug 01, Mar-Apr 02, Jun 02 – Sep 03	
Other	TDR – time domain reflectometer	Soil water content at 4 locations in each field $SWC_{SW1}$ to $SWC_{SW4}$ , $SWC_{NE1}$ to $SWC_{NE4}$	25/6/02	ongoing

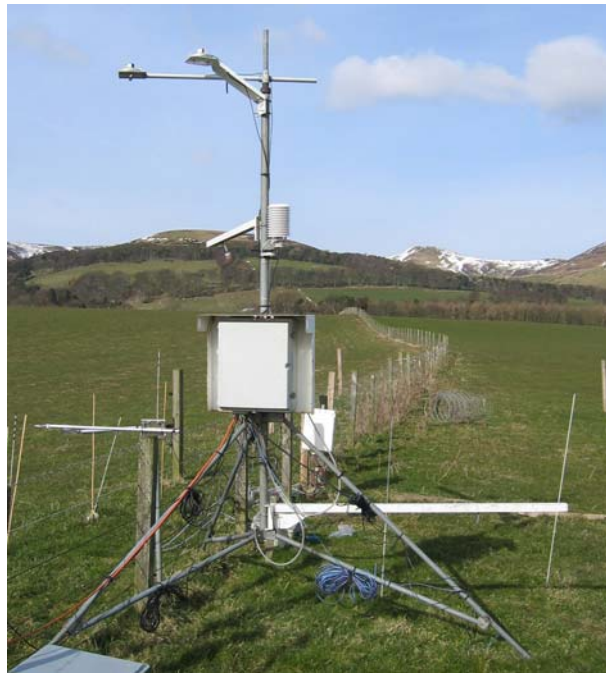


Figure 4.8. Photograph of the Bowen ratio mast. The two top arms hold the solar radiation and *PAR* sensors; the white “beehive” shelters the *RH/T* probe; the two long white arms hold the thermocouples and dewpoint sensor inlets; to the left are the two net radiometers; the two thin white sticks on the right indicate the location of the soil heat flux plates and temperature probes.

The thermocouple probes supplied by Campbell consist of very fine wires which are capacitatively soldered to form 2 junctions (Figure 4.9). The homemade probes use pre-made fine-wire (0.075 mm/0.003”) thermocouples supplied by Omega (CHCO-003) which are carefully threaded into a probe assembly (Figure 4.9). The specification of the Omega thermocouples is given below and the Campbell sensor is assumed to be similar.

The probes are mounted on arms extending from the mast at two heights: lower, 0.64 m and upper, 1.95 m.

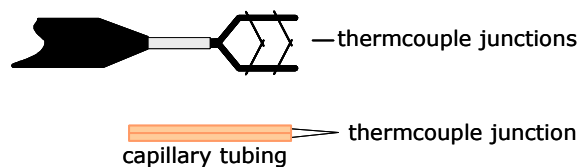


Figure 4.9. A sketch of Campbell (top) and home-made (bottom) fine-wire thermocouples.

*Specification:*

- Response time < 0.08 s
- Standard limits of error, greater of 1.7 °C or 0.5%

- **Dewpoint sensor**

In the Campbell BR System a dewpoint sensor is included to measure the dewpoint temperature of the air at two heights and so calculate the latent heat flux. However, this sensor continually caused problems as the Peltier block tended to over-cool and ice-up the sensor head. When it completely failed on 05/07/03 it was not repaired and the data are not included in this analysis. The eddy-correlation measurements of latent heat flux are used throughout the data analysis.

- **Relative humidity and temperature (*RH/T*)**

A Vaisala 50Y Temperature and Relative Humidity probe, uses a 1000  $\Omega$  platinum resistive thermometer (PRT) to measure temperature and a Vaisala capacitive humidity sensor (INTERCAP®) to measure relative humidity (*RH*). Internal signal conditioning provides an output of 0 to 1000mV for both variables.

*Specification:*

Temperature Measurement:

Range: (for the specified accuracy) -10°C to +60°C

Accuracy:  $\pm 0.35^\circ\text{C}$  at -10°C,  $\pm 0.6^\circ\text{C}$  at +60°C

Relative Humidity:

Range: (for the specified accuracy) 10% to 90%

Accuracy:  $\pm 2\%$  at 10%,  $\pm 3\%$  at 90%,  $\pm 6\%$  at 90–100%

Typical Long-Term Stability: Better than  $\pm 1.0\%$  per year

Measurements began on 03/04/2003 11:15 but an intermittent fault with the probe led to poor capture of *RH* until 29/01/2004 14:00 when a new probe was installed. The temperature measurements are used as an additional measure of ambient air temperature and *RH* is used to check the operation of the eddy-correlation water-vapour measurements (described below).

- **Average soil temperature (*Ts*)**

This is measured using a set of 4 thermocouple probes which are connected together and so their output voltage is an average of all 4 signals (TCAV, Figure 4.10). *Ts* is used in the calculation of soil heat flux to account for the heat storing properties of soil, as described in Section 4.6. The installation of this sensor along side the soil heat flux plates is illustrated in Figure 4.11.



Figure 4.10. Campbell TCAV soil averaging thermocouple assembly.

- **Soil heat flux plates ( $HF_{s1}$ ,  $HF_{s2}$ )**

HFP01 Soil Heat Flux plates provided by Campbell Scientific were used throughout the measurements. The HFP01 is a conventional heat flux plate consisting of a thermopile which measures the differential temperature across its plastic body. Operating in a completely passive way, it generates a small output voltage that is proportional to this differential temperature. Assuming that the heat flux is steady, that the thermal conductivity of the body is constant and that the sensor has negligible influence on the thermal flow pattern, the signal of the HFP01 is directly proportional to the local heat flux. The millivolt output voltage is measured then converted to a heat flux in  $W m^{-2}$  by dividing by the calibration constant for the flux plate (supplied with each sensor). In order to measure soil heat flux at the surface ( $G$ ), two HFP01SCs are used to measure the soil heat flux at a depth of  $\sim 10$  cm and a TCAV Averaging Soil Thermocouple measures the temporal change in temperature of the soil layer above them. Figure 4.11 illustrates how the heat flux plates and temperature probes are installed and the method used to calculate surface heat flux ( $G$ ) is described in Section 6.4.

*Specification:*

Expected accuracy: +/-20% for daily totals over a thermal conductivity range 0.1 to 1.7 W/mK and temperature range of -30 to +70°C.  
 Expected sensor output in meteorological applications: -25 to +25 mV  
 Sensitivity (nominal): 50  $\mu V/W m^{-2}$  (the exact figure is supplied on the calibration certificate supplied with each sensor)  
 Range : + 2000 to - 2000  $W m^{-2}$   
 Non stability: < 1% change per year under normal meteorological use  
 Sensor thermal conductivity (estimated): 0.8 W/mK

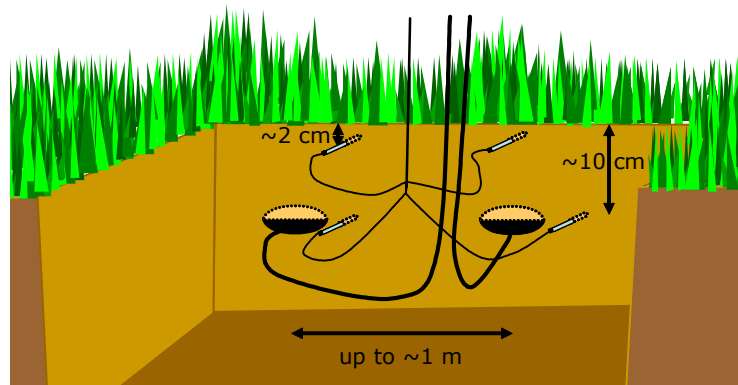


Figure 4.11. Sketch of heat flux plate and soil temperature probe installation; the sensors are fully inserted into the soil then the hole back filled.

- **Net radiation ( $R_n$ )**

Net radiometers have an upwards facing sensor which measures the solar energy and far infra-red energy (0.3 to 30  $\mu\text{m}$ ) that is received from the entire hemisphere (180° field of view) and a downwards facing sensor which measures the energy received from the surface of the ground. The two readings are automatically subtracted and the result converted to a single output signal. This output represents the net radiation, (which can be interpreted as meaning the radiative energy that is absorbed by the ground surface) and is normally expressed in Watts per square metre ( $\text{W m}^{-2}$ ).

At the start of the experiment a REBS Q7 net radiometer was installed by the BR mast to measure  $R_n$ . This instrument consists of two thermopile sensors which are protected by plastic domes (Figure 4.12a).

*Specification:*

Spectral response 0.25 to 60  $\mu\text{m}$

Detector type: Thermopile

Calibration factors: 9.6  $\text{W m}^{-2} \text{mV}^{-1}$  for positive values; 11.9  $\text{W m}^{-2} \text{mV}^{-1}$  for negative values

Time constant: Approximately 30 seconds

Uncorrected wind effect: up to 6% reduction @ 7  $\text{m s}^{-1}$  for positive fluxes  
up to 1% reduction @ 7  $\text{m s}^{-1}$  for negative fluxes

On 06/08/2003 15:00 a second sensor, Kipp-Zonen NrLite, was installed in parallel to the Q7. This sensor has the advantage that the sensing heads are not protected by plastic domes (Figure 4.12b), which can be damaged or be obscured by condensation. However its readings may be affected by wind as described in Section 4.6 below.

*Specification:*

Spectral range: 0.2 to 100  $\mu\text{m}$   
Detector type: Thermopile  
Directional error (0 - 60° at 1000  $\text{Wm}^{-2}$ ): <30  $\text{Wm}^{-2}$   
Sensor asymmetry:  $\pm 5\%$  typical, ( $\pm 10\%$  worst case)  
Working temperature: -30 to +70°C  
Temperature dependence: 0.12%/°C

The two radiometers are shown in place at Easter Bush in Figure 5.11c. Both are  $\sim 1$  m above the surface. During 2004 the NR-Lite developed an intermittent fault and sections of data had to be discarded.

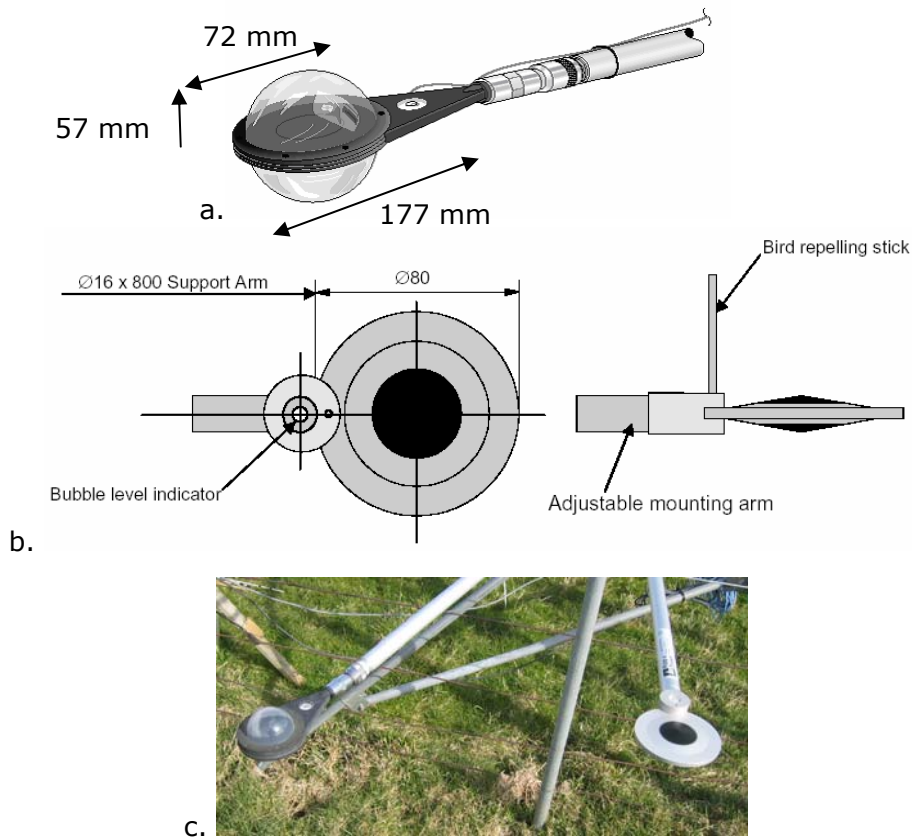


Figure 4.12. (a) The REBS Q7 net radiometer, (b) the NR-LITE and (c) both instruments in place in the field.

• **Total Solar Radiation ( $S_f$ )**

A Skye SP1110 is used to measure total solar radiation. The cosine corrected head contains a special high grade silicon photocell sensitive to light between wavelengths of 350 and 1100 nm. The head is completely sealed and can be left indefinitely in exposed conditions. The sensor is calibrated under open-sky conditions against reference pyranometers, and is hence referenced to the World Radiometric Reference. The calibration thus refers to solar energy in

the waveband 300 nm to 3000 nm, i.e. the acceptance band of thermopile pyranometers.

*Specification:*

Sensitive to light between wavelengths of 350 nm and 1100 nm  
Output 1mV per 100 Wm<sup>-2</sup>  
Absolute accuracy ±5% (typically <±3%)  
Cosine corrected head (typical errors zero 0-70°, <10% 85-90°)  
Operating temperature -35 °C to +75 °C

- **PAR (Photosynthetically Active Radiation)**

A Skye SKP215 radiation sensor was installed on, 03/04/2003 11:15, to measure incident quanta between 400 and 700 nm. Light in this waveband is used for photosynthesis and is often referred to as 'PAR' (Photosynthetically Active Radiation). Quanta below 400 nm are not generally used in photosynthesis and those above 700 nm have insufficient energy for the process. The head of the sensor is completely sealed and can be left indefinitely in exposed conditions. The sensor is calibrated against standard quartz halogen lamps traceable to NPL<sup>8</sup> reference lamps. Absolute errors are always within 5%, and typically much better than 3%. The calibration is given in units of μmol m<sup>-2</sup> s<sup>-1</sup>. A μmol is one millionth of Avagadro's number of quanta or photons.

*Specification:*

Sensitive to light between 400 nm and 700 nm wavelength  
Output 1 mV per 100 μmol m<sup>-2</sup> s<sup>-1</sup>  
Absolute accuracy ±5% (typically <±3%)  
Cosine corrected head (typical errors zero 0-70°, <10% 85-90°)  
Operating temperature -35 °C to +75 °C

- **Surface Wetness**

A Campbell Scientific 237 Wetness Sensing Grid is used to indicate surface wetness. It is an artificial leaf, consisting of a rectangular circuit board (63 mm wide, 76 mm long) with interlacing gold-plated copper fingers (Figure 4.13). Condensation on the sensor lowers the resistance between the fingers, and this change is measured by the datalogger. AC excitation is used to prevent degradation of the sensor. Resistance varies from above 3000 kΩ (dry) to about 1 kΩ (wet). The transition point of an uncoated sensor is normally between 50 and 200 kΩ. A disadvantage of this type of sensor is

---

<sup>8</sup> NPL – National Physical Laboratory <http://www.npl.co.uk/>

that they do not mimic the thermal properties of leaves and tend to only detect significant wetting events, such as precipitation or heavy dew.



Figure 4.13. Photograph of the Campbell wetness sensing grid in place at Easter Bush.

An alternative method of sensing surface wetness, developed by Burkhardt and Gerchau (1994), uses clips that attach directly to the vegetation, the conductivity between the prongs is measured and this increases with wetness. They have the advantage that wetness is directly measured and they can detect non-precipitation events such as the recondensation of transpired water-vapour (Burkhardt *et al.*, 1999). However they are more labour intensive to use, as they require regular calibration (ideally daily) to account for movement of the vegetation between the clips and were not employed at Easter Bush.

- **Tipping bucket**

A standard mercury tilt-switch type tipping bucket is used to measure rainfall amounts. Rainfall is funnelled into a small 2 sided basin which tips to one side when it is full, emptying the basin, triggering the switch and bringing the other side of the basin up to be filled (Figure 4.14). The number of tips are counted by the data logger and a calibration factor used to convert this to mm of rainfall. A spare bucket was obtained from CEH-Edinburgh but as it is quite old the manufacturer's details and specifications are not available. The instrument is manufactured so that the area of the top of the bucket is equivalent to the tip size in millimetres. The tip size of 0.3084 mm was estimated by measuring the width of the top of the bucket and then confirmed by testing with a known volume.

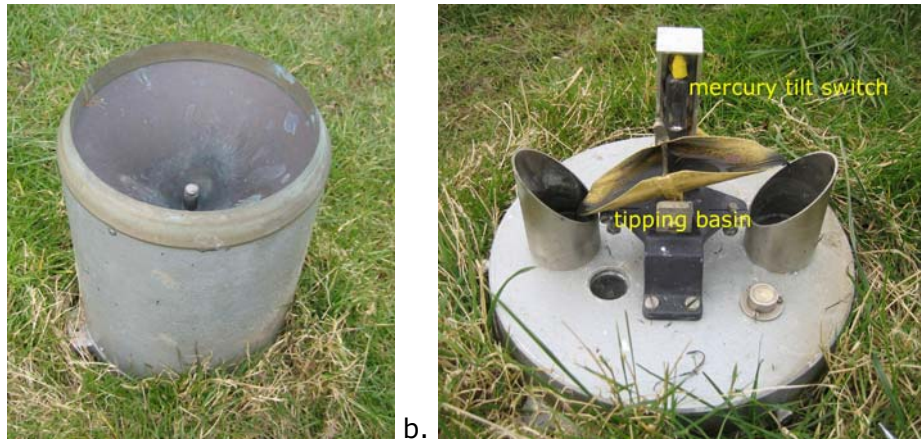


Figure 4.14. Photo of the tipping bucket in place at Easter Bush with it's (a) cover on and (b) off, which shows the basin and switch.

#### 4.5.2 Ozone, Wind-speed and Temperature Gradient

The ozone gradient measurements are made on a fixed mast at 5 heights (Figure 4.15). Air is drawn down ptfе tubing to a standard UV-photometric ozone analyser (described below) by a ptfе pump. A Campbell 21X data-logger controls solenoid-valves at the bottom of the mast which switch the air-intakes, as well as processing and storing the ozone concentration, wind-speed and temperature data. The data logger controls switching of the solenoid valves using solid-state relays, so that each gas inlet is sampled in turn, once every 15 minutes. The cycle was setup to allow for a 60 s purge time to clear the tubing of air from the previous height and allow for the ozone analysers response time. As a result each height is measured for 2 minutes in every 15 and the data must be adjusted to account for this sequential sampling, as described in Section 5.2.1.

In 2001 (22/5/01 to 1/10/01) 3 cup-anemometers and fine-wire thermocouples (as described in Section 5.5.1) were included to provide a measure of atmospheric stability and allow the calculation of  $d$  (Section 5.2.4). From 21/3/02 onwards another 2 cup-anemometers were added to improve sampling of the wind speed profile.

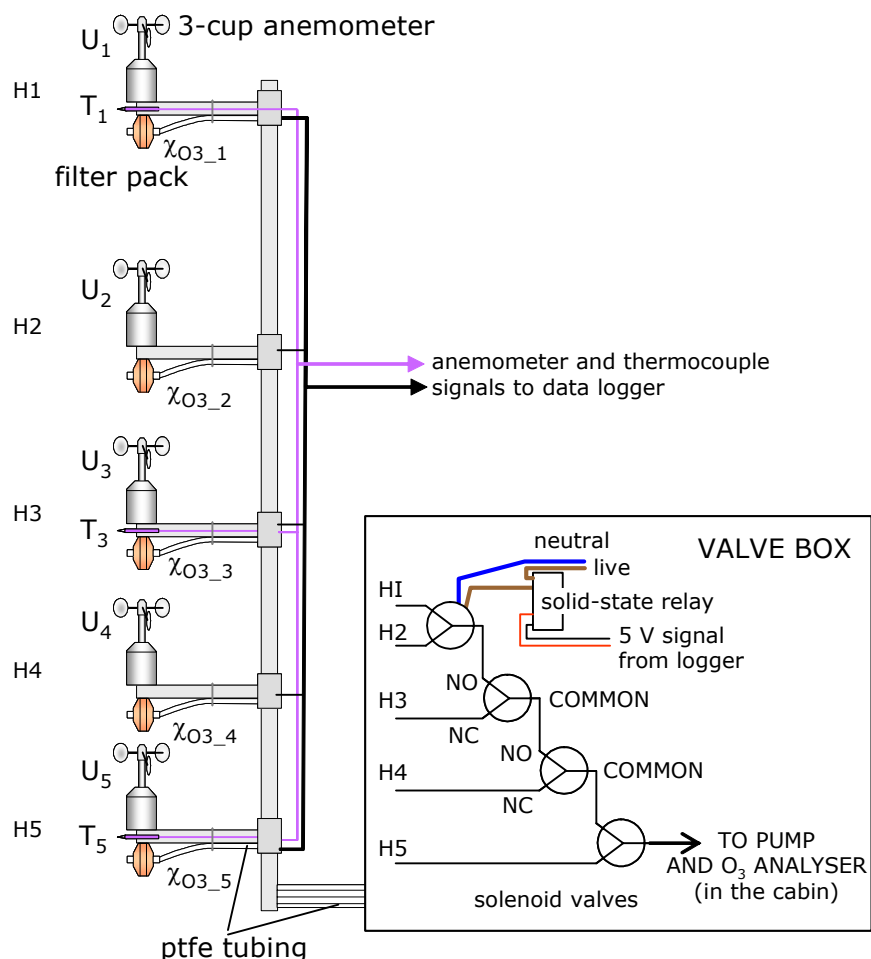


Figure 4.15. Sketch of gradient setup.

The arms for mounting the gas inlets, anemometers and thermocouples are positioned to give logarithmically equal spacing. In 2001 they were moved up and down as the canopy height changed but in the following years they stayed at the same height. This was mainly due to the bottom mount becoming completely jammed so it could not be moved. Table 4.5 lists the heights of each sensor and Figure 4.16 illustrates the log spacing.

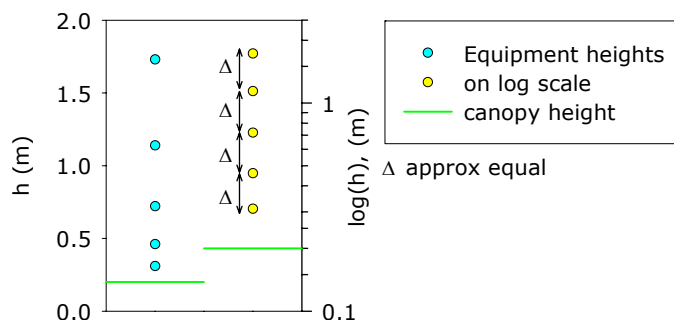


Figure 4.16. Illustration of log spacing.

Table 4.5 Heights of inlets and sensors on the gradient mast.

Start	End	Sensor	Top				
			1 [m]	2 [m]	3 [m]	4 [m]	5 [m]
22/05/2001 12:00	01/06/2001 10:15	Gas Inlets	2.07	1.47	1.04	0.74	0.52
		Anemometers	2.28		1.07		0.69
		Thermocouples	2.09		1.04		0.74
01/06/2001 10:30	05/06/2001 15:30	Gas Inlets	1.75	1.28	0.94	0.66	0.46
		Anemometers	2.00		1.17		0.69
		Thermocouples	1.82		1.00		0.50
05/06/2001 16:00	28/06/2001 11:45	Gas Inlets	1.75	1.22	0.98	0.59	0.41
		Anemometers	2.00		1.08		0.64
		Thermocouples	1.82		0.91		0.45
28/06/2001 12:30	1/10/2001 15:00	Gas Inlets	1.75	1.14	0.75	0.49	0.32
		Anemometers	2.00		1.08		0.64
		Thermocouples	1.82		0.91		0.45
21/03/2002 16:45	Present	Gas Inlets	1.73	1.14	0.72	0.46	0.31
		Anemometers	1.98	1.39	0.97	0.70	0.56
		Thermocouples	1.82		0.91		0.45

- **Ozone Analysers ( $\chi_{O_3}$ )**

The basic operation of continuous ozone monitors is based on absorption of UV light. The ozone molecule has an absorption maximum at 254 nm, coincident with the principal emission wavelength of a low-pressure mercury lamp. Few other molecules found at significant concentrations in the atmosphere absorb at this wavelength. However interference, from organic compounds containing aromatic rings for example, can occur in highly polluted air.

Figure 4.17 is a schematic diagram of the ozone monitor. Ozone is measured based on the attenuation of light passing through an absorption cell fitted with quartz windows. A low-pressure mercury lamp is located on one side of the absorption cell, and a photodiode is located on the opposite side. The photodiode has a built-in interference filter centred on 254 nm, the principal wavelength of light emitted by the mercury lamp. An air pump draws sample air into the instrument at a flow rate of approximately  $1 \text{ l min}^{-1}$ . In basic instruments a single cell is used and a solenoid valve alternately directs this air through an ozone scrubber and into the absorption cell. The intensity of light at the photodiode is measured in air that has passed through the ozone scrubber ( $I_0$ ) and air that has not passed through the scrubber ( $I$ ). Ozone

concentration is calculated from the measurements of  $I_0$  and  $I$  according to the Beer-Lambert Law (Equation 104). In more accurate instruments a pair of absorption cells are used which alternate between zero air and the sample.

$$\chi_{O_3} = \frac{1}{\sigma l} \ln\left(\frac{I_0}{I}\right) \quad (104.)$$

where  $l$  is the pathlength and  $\sigma$  is the absorption cross section for ozone at 254 nm ( $1.15 \times 10^{-17} \text{ cm}^2 \text{ molecule}^{-1}$  or  $308 \text{ atm}^{-1} \text{ cm}^{-1}$ ), which is known with an accuracy of approximately 2%.

In most instruments the pressure ( $P_{cell}$ ) and temperature ( $T_{cell}$ ) within the absorption cell(s) are measured so that the ozone concentration can be expressed as a mixing ratio in parts-per-billion by volume (ppbV) or nano-moles per mol ( $\text{nmol mol}^{-1}$ ):

$$\chi_{O_3} = \frac{1}{\sigma l} \ln\left(\frac{I_0}{I}\right) \left(\frac{T_{cell}}{P_{cell}}\right) \quad (105.)$$

where  $T_{cell}$  is the absolute temperature in Kelvin and  $P_{cell}$  is the cell pressure in Torr.

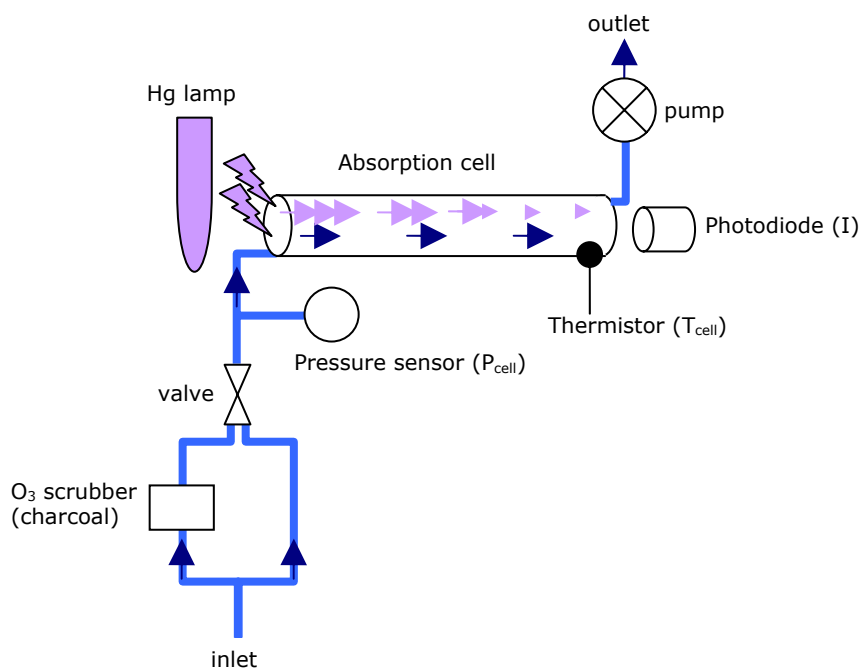


Figure 4.17. Schematic of an  $O_3$  analyser.

Throughout the four years of measurement 4 different instruments were employed. All of them had specifications suitable for measuring the ozone gradient with a 15 minute time-step and were regularly calibrated using a transfer standard or the ML9811 as a calibrator.

22/05/01 - 01/10/01      **Analysis Automation Limited 427 (equivalent to a Thermo Electron 8810)**

Specification:

Range 0 to 1 ppm  
Zero drift <0.5% per month  
Span drift <1% per month  
Precision  $\pm 0.002$  ppm  
Linearity  $\pm 0.001$  ppm  
Noise  $\pm 0.001$  ppm  
Response time 20 s  
Flow rate 1 - 3 lpm  
Operating temperature 0 - 45 °C

22/03/02 - 26/03/02      **Thermo Electron 8810 (developed fault)**

Specification:

Range 0 to 1 ppm (adjustable)  
Zero drift <1 ppb per day  
Span drift 2 ppb per week  
Precision  $\pm 0.002$  ppm  
Linearity <1% ppm  
Noise  $\pm 0.001$  ppm  
Response time 20 s  
Flow rate 0.5 - 1 lpm  
Operating temperature 5 - 40 °C

26/03/02 - 24/09/02      **Monitor Labs 9811 (calibration standard instrument)**

Specification:

Range 0 to 20 ppm (adjustable)  
Zero drift 0.1 ppb per °C (temperature dependant)  
Span drift 0.1 ppb per °C (temperature dependant)  
Precision  $\pm 0.001$  ppm or 0.1% (whichever greatest)  
Linearity  $\pm 0.001$  ppm or 0.1% (whichever greatest)  
Noise  $\pm 0.00025$  ppm or 0.1% (whichever greatest)  
Response time 10 - 60 s  
Flow rate 0.5 lpm  
Operating temperature 5 - 40 °C

19/07/02 - to date      **Thermo Electron 49C (brand new instrument)**

*Specification:*

Range 0 to 200 ppm (adjustable)  
Zero drift <1 ppb per day or <2 ppb per week  
Span drift <1% per month  
Precision  $\pm 0.001$  ppm  
Linearity  $\pm 1\%$  full scale  
Noise  $\pm 0.0005$  ppm  
Response time 10 - 60 s  
Flow rate 1 - 3 lpm  
Operating temperature 0 - 45 °C

- **Wind-speed Gradient ( $U_1$  to  $U_5$ ) - Cup-Anemometers**

Vector Instruments A100R anemometers were used at each height on the mast. A magnet turns with the rotor spindle producing a varying field which causes a mercury wetted reed switch to make and break contact once per revolution of the rotor. The contacts are bounce free, and no power is required apart from that necessary to detect contact closure. The rotor is tested by comparison with a rotor calibrated at the UK National Physical Laboratory, and a calibration figure is provided with each instrument. The anemometers used at Easter Bush were fully calibrated and serviced by Vector Instruments before being used at the site.

*Specification:*

Stalling Speed:  $0.2 \text{ ms}^{-1}$

Max. Speed:  $>75 \text{ ms}^{-1}$

Accuracy:  $\pm 0.1 \text{ ms}^{-1}$  ( $0.3\text{-}10 \text{ ms}^{-1}$ );  $\pm 1\%$  ( $10\text{-}55 \text{ ms}^{-1}$ );  $\pm 2\%$  ( $>55 \text{ ms}^{-1}$ )

Calibration: 0.80 revolutions per metre (1 pulse per 1.25 metres)

Switch Life: Rated  $25 \times 10^9$  operations minimum ( $>20$  years)

Temperature Range:  $-30^\circ\text{C}$  to  $+70^\circ\text{C}$

- **Temperature Gradient ( $T_1$  to  $T_5$ ) – Type-E Thermocouples**

In 2001 three thermocouples were attached at the top, middle and bottom heights. At this time fine-wire probes were not available and so heavier grade pre-made junctions from Omega were used with a small sun-shield to reduce interference from solar heating of the junction. They tended to give slightly higher temperature readings on average but the gradient was similar to that measured by the Bowen Ratio probes.

In the following years the homemade fine-wire probes were used and their reading were more comparable to the other sensors. However a fault with one of the input channels on the Campbell 21X data logger caused an intermittent error on the bottom thermocouple. In general readings were far more variable than normal, leading to the temperature gradient being overestimated. The logger was replaced on the 20/05/2003 15:00, with a unit that had recently been service by Campbell Scientific, resulting in much more consistent readings. All data from the bottom thermocouple during 21/03/02 to 20/05/03 are discarded.

### 4.5.3 Eddy-Correlation: Turbulence, CO<sub>2</sub>, Water-vapour, Ozone

The eddy-correlation instruments all operate at frequencies of at least 10 Hz so that they can capture the rapid variations in wind-speed or gas concentration caused by the turbulent eddies. Variations in wind-speed are measured using 3D sonic-anemometers, CO<sub>2</sub> and water-vapour using open and closed path LICOR instruments and O<sub>3</sub> using an optical sensor, the operation of each is described below.

- **Sonic Anemometers ( $u'$ ,  $v'$ ,  $w'$ )**

The basic principle of operation of sonic anemometers is the measurement of the difference in the transit time of sound waves between pairs of transducers. A pair of transducers acts alternatively as transmitters and receivers, sending pulse of high frequency ultrasound between them. The time of flight in each direction ( $t_1$  and  $t_2$ ) is measured and used to calculate the wind-speed and the speed of sound, which is related to the air temperature.

$$t_1 = \frac{L}{c+v}, t_2 = \frac{L}{c-v} \quad (106.)$$

where  $L$  = distance between transducers,  $c$  = speed of sound,  
 $v$  = velocity of any air flow along the line of the transducers

From equation (107)  $v$  and  $c$  can be found independently of  $c$  or any other parameters such as temperature which may interfere with the signal:

$$v = 0.5L\left(\frac{1}{t_1} - \frac{1}{t_2}\right) \quad (107.a) \quad c = 0.5L\left(\frac{1}{t_1} + \frac{1}{t_2}\right) \quad (107.)$$

There is little effect on  $t_1$  or  $t_2$  from any air flow perpendicular to the line of the transducers and so  $v$  represents the vector component of flow along it. If 3 pairs of transducers are arranged in different orientations they can be used to capture wind-speed variations in all directions. The pairs do not have to be orientated along Cartesian axis and a non-orthogonal arrangement is commonly used for optimum undisturbed air flow.

The rapid variations in air temperature can also be calculated from  $c$  and this is used in the calculation the sensible heat flux from (Equation 17). Although an average air temperature can also be calculated it is not the most accurate measure as  $c$  is affected by humidity.

Two sonic anemometers were employed at Easter Bush:

1. From the start of the experiment in May 2001, a Solent Research ultra-sonic anemometer (1012RA, Gill Instruments, Lymington, UK) was used alongside an open path CO<sub>2</sub>/H<sub>2</sub>O sensor (described below). Figure 5.18a includes a photograph of the instruments.

*Specification:*

Wind-speed range: 0-60 m s<sup>-1</sup>

Wind-speed accuracy (10 s average): <30 m s<sup>-1</sup> ±1.5%  
>30 m s<sup>-1</sup> ±3%

Wind-speed offset: ±0.02 m s<sup>-1</sup>

Instantaneous accuracy: <30 m s<sup>-1</sup> ±3%  
(incident wind not within ±10° of spar)

Direction accuracy (10 s average): <30 m s<sup>-1</sup> ±2°  
>30 m s<sup>-1</sup> ±3°

Sampling rate: 168 s<sup>-1</sup>

These accuracies are specified for operating temperatures within 5°C to 35°C and wind incident within ±10° of horizontal.

This instrument is relatively old (purchased *ca.* 1990) and although it is very reliable for measuring  $u_*$ ,  $H$ ,  $L$  etc, only one pair of transducers is used in the measurement of  $T$  so its average air temperature values are not used.



Figure 4.18. (a) The Gill sonic and LICOR 7500 in place at Easter Bush; (b) Metek sonic in place at Easter Bush.

2. On the 29/05/02 a brand new Metek USA-1 sonic anemometer was installed to measure turbulence alongside the TDL instrument and a closed path CO<sub>2</sub>/H<sub>2</sub>O sensor (LICOR 7000, described below). Both instruments became fully operational on the 06/06/02. Figure 5.18b includes a photograph of the instruments.

*Specification:*

Wind-speed range: 0-50 m s<sup>-1</sup>

Wind-speed components range: -50 - 50 m s<sup>-1</sup>

Temperature range: -30 - 50 °C

Wind-speed resolution: ±0.01 m s<sup>-1</sup>

Wind-speed components resolution: ±0.01 m s<sup>-1</sup>

Direction resolution: ±0.4°

Temperature resolution: ±0.01 K

Sampling rate: 0.004 to 25 Hz

- **GFAS/ROFI ( $\chi_{O_3}$ )**

It is also possible to measure the ozone flux using eddy-correlation, although there are only a limited number of sensors available commercially. For tall canopies such as forests which do not require very fast sampling rates the Unisearch LUMINOX instrument can be used; it uses a wet chemical reaction to measure O<sub>3</sub> concentrations. However its response time is too slow for use with short-vegetation such as grassland.

In the early 90s Hans Guesten developed a very fast-response ozone sensor based on the fluorescence of a laser-dye (Coumarin-1) in the presence of ozone (Gusten, *et al.*, 1992). The principle of operation is very simple, air is drawn down a sample line at a high flow rate and passes over a small disk which has been coated with the ozone sensitive dye. Photons emitted by the dye are detected by a photomultiplier tube (PMT) whose output signal varies with the number of photons emitted. The number of photons is proportional to the ozone concentration and so the rapid variations in ozone concentration due to atmospheric turbulence are measured. However, it is not an absolute method so a standard O<sub>3</sub> analyser has to be used alongside to measure the average concentration. It was developed into a commercial instrument and manufactured by a company called GFAS but they went out of business in the late 90s.

At Easter Bush a GFAS sensor (borrowed from the University of Manchester Atmospheric Science Research Group) was used for some of the measurement period. When this was returned to UMIST, custom made fast-ozone sensors (called the ROFI – Rapid Ozone Flux Instrument) were constructed<sup>9</sup> using off-the shelf components and a simple housing with light baffles at the inlet and outlets (Figure 19a). The ROFI is designed to have the same specification as the GFAS in terms of gas flow rate and volume. The two instruments were

---

<sup>9</sup> Nicholas Weir of Scitech assisted in the design of the ROFI and constructed three sensors.

tested alongside one another for a short period (20/01/2003 to 27/01/2003) with one connected to the Gill and the other to the Metek. Figure 19b shows a photo of ROFI2 connected to the Gill system. Initial results indicated that both sensors worked well but as the measurements are currently being reprocessed they are not discussed further in this thesis.

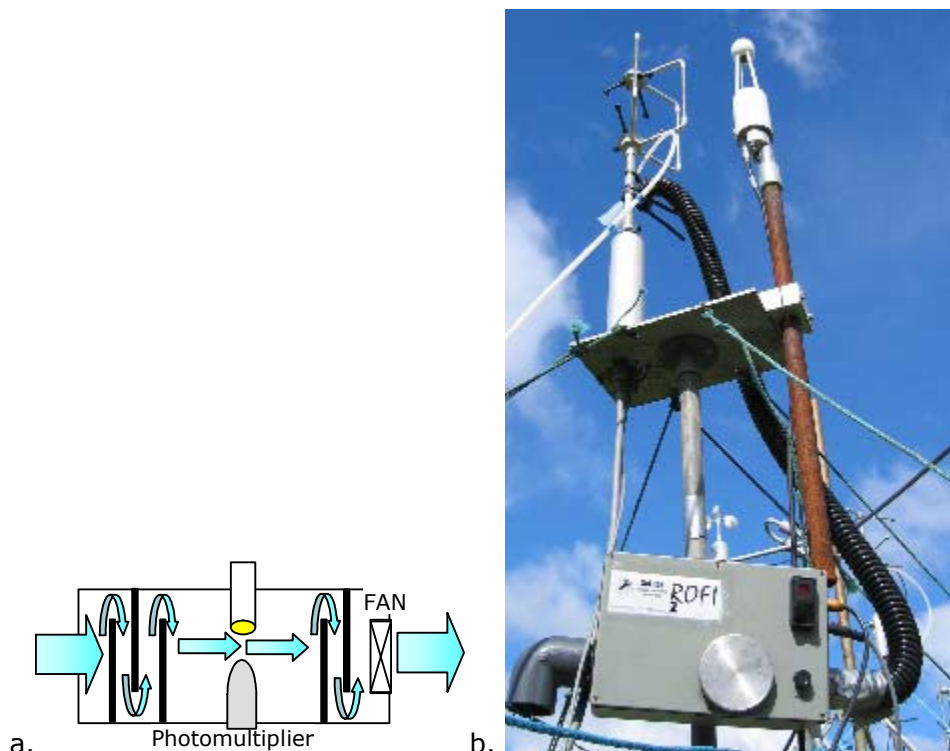


Figure 4.19. The (a) ROFI internal structure and (b) use in the field.

- **LICORs**

As noted above two CO<sub>2</sub>/H<sub>2</sub>O sensors were employed each with its own advantages and disadvantages. Both instruments are manufactured by LICOR, a leading manufacturer of these types of sensors, and employ the same basic principle of operation. In a similar way to ozone, CO<sub>2</sub> and H<sub>2</sub>O-vapour absorb electromagnetic radiation at particular wavelengths, in this case in the infra-red at ~4.25 and 2.59 μm respectively. However, unlike O<sub>3</sub> in the UV-band, infra-red absorption is more dependant of the partial pressures of gases in a mix. Infrared absorption (or any other wavelength) is due to energy-induced changes in vibrational and rotational states of molecules or atoms. Such energy states are altered by intermolecular collisions which increase in number as pressure increases. The kinetic theory of gases and quantum mechanics predicts that absorption band widths increase with pressure, and it

is observed that broad band infrared absorption increases as pressure increases at constant absorber concentration. Not all gases are equally effective in causing pressure induced line broadening. Therefore, how much radiation a particular gas will absorb depends not only on its mole fraction, but also on the mole fractions of all the other gases, especially those of similar structure such as CO<sub>2</sub> and H<sub>2</sub>O. The equations used to calculate CO<sub>2</sub> and H<sub>2</sub>O concentrations are therefore quite involved and not described here<sup>10</sup>.

1. The first instrument used is a LICOR 7500 open-path sensor. As its name implies the concentrations of CO<sub>2</sub> and H<sub>2</sub>O are measured in place as the infra-red radiation path is exposed to the atmosphere. To protect the internal electronics from the weather the light passes through sapphire windows which are translucent at infra-red frequencies. The diagram and photos in Figure 18a show its configuration and use in the field. It is recommended that it is placed downwind of the sonic anemometer at a slight angle, to allow water to run-off the transducer windows.

The LICOR 7500 can output data as both in serial and analogue forms. For this experiment the analogue outputs were connected to the analogue input channels on the Gill sonic.

The atmospheric pressure is also measured by this instrument, as it is required for calculating the gas concentrations, and can be output separately. The enclosure includes a pressure port so the internal pressure will be representative of ambient conditions. The pressure sensor has a range of 15-115 kPa and accuracy (between temperatures of 0-85 °C) of ±1.5%.

This instrument is very stable and so its calibration coefficients do not change much with time. However, to ensure good quality data were obtained it was calibrated once a month, for most of the measurement period.

2. A LICOR 7000 was also installed and connected to the Metek system from 13/03/03 09:30. This is a closed-path type instrument where air is sampled by pumping it down a tube to the analyser which remains undercover. The infrared beam passes through two optical cells, one of

---

<sup>10</sup> See Appendices for information on where to find the LICOR instrument manuals which describe

which measures air with a known CO<sub>2</sub> and H<sub>2</sub>O concentration (reference cell A) and the other the sampled air (sample cell B). Figure 18b shows the inlet funnel positioned close to the sonic anemometer.

The LICOR 7000 can also output data as both in serial and analogue forms. For this experiment the analogue outputs were connected to the analogue input channels on the Metek sonic. As the air has to be drawn down the sample line a time delay is introduced between the wind-speed ( $w'$ ) and concentration variations ( $\chi'$ ), known as the time-lag ( $t_l$ ). An optimum time-lag can be calculated from the pump flow-rate and sample-line volume but in practice it tends to vary with ambient conditions. Data-logging and reanalysis programmes therefore need to calculate the actual time-lag by finding the optimum correlation coefficient for  $w'$  with  $\chi'$ .

For optimum operation this instrument requires weekly calibration which was done using a cylinder of CO<sub>2</sub> at a known concentration and a dew-point generator to provide different water-vapour concentrations. The zero was checked using the dew-point generator as this can provide air with both CO<sub>2</sub> and water-vapour removed.

As described above there are essentially two sets of eddy-correlation measurements, those with the Gill sonic and the other with the Metek. Both sensors allow analogue signals (from the LICORS for example) to be measured alongside the turbulence. Each set was connected to its own pc, using serial communication, and the data logged and processed using a Labview<sup>11</sup> programme (written by Eiko Nemitz). The logging programme stores the raw data as well as calculating the fluxes and turbulence parameters in real-time at 15-minute resolution. This allows the operation of the instruments to be monitored and any problems to be dealt with efficiently. Throughout the measurements this system was maintained and calibrated by other workers at the field site (Celia Milford, Eiko Nemitz, Margaret Anderson, Claire Campbell, Daniela Famulari and Chiara DiMarco).

---

their operation in detail.

<sup>11</sup> Labview is a graphical data acquisition and processing programme from National Instruments.  
<http://www.ni.com/>

#### 4.5.4 Other Measurements: Soil Water Content, Present Weather

- **TDR ( $SWC_{SW1}$  to  $SWC_{SW4}$ ,  $SWC_{NE1}$  to  $SWC_{NE4}$ )**

Soil water content was measured from 25/06/2002 15:15 using a Campbell Scientific TDR100 (Time Domain Reflectometry) system. TDR100 generates a very short rise time electro-magnetic pulse that is applied to a TDR probe (Figure 4.20) embedded in the soil, and then samples and digitizes the resulting reflection waveform. The elapsed travel time and pulse reflection amplitude contain information used by the on-board processor to quickly and accurately determine soil volumetric water content or soil bulk electrical conductivity. A sample pit was dug in the field in 2002, as part of the GREENGRASS project, which indicated the maximum rooting depth was ~30 cm. Therefore the eight probes were installed, four in each field, at depths of 3.5, 7.5, 15 and 30 cm (depths 1 to 4 respectively), in accordance with the GREENGRASS protocols. An average of both the 7.5 cm probes is used to calculate  $G$ , as described in Section 4.6.

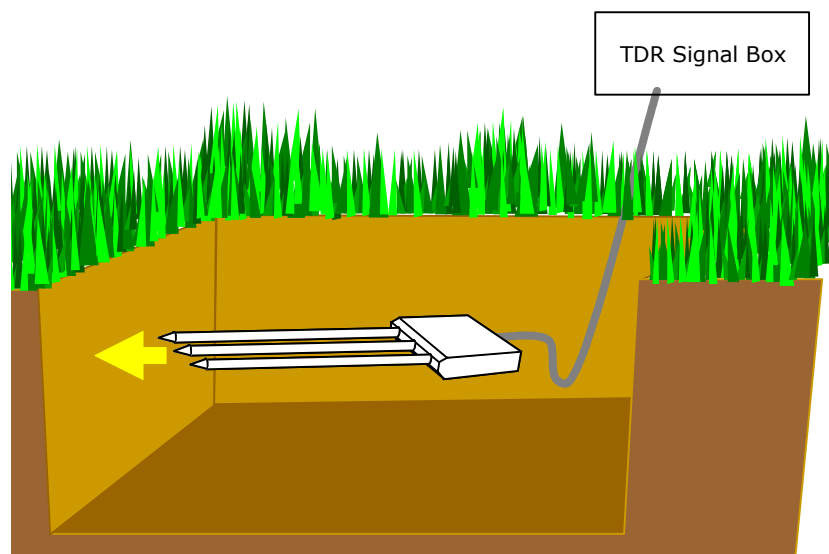


Figure 4.20. Sketch of a TDR probe.

- **Present Weather**

A Vaisala FD12P Weather Sensor was installed and became fully operational on 23/05/2003 14:20 (Figure 4.21). Its main purpose was to measure atmospheric visibility and assist in the interpretation of aerosol measurements but it also provides a duplicate measure of rainfall. The sensor combines the functions of a forward scatter visibility meter and a present weather sensor. In addition, the sensor can measure the intensity and amount of both liquid

and solid precipitation. Precipitation water content is measured with a capacitive device and combines this information with optical scatter and temperature measurements. These three independent measurements together provide data sufficient for an accurate evaluation of current visibility and weather type.

The FD12P was configured to automatically determine the visibility and precipitation related weather codes in the World Meteorological Organization (WMO) standard SYNOP and METAR messages every minute. This extensive data set has still to be fully processed and will not be considered further here.

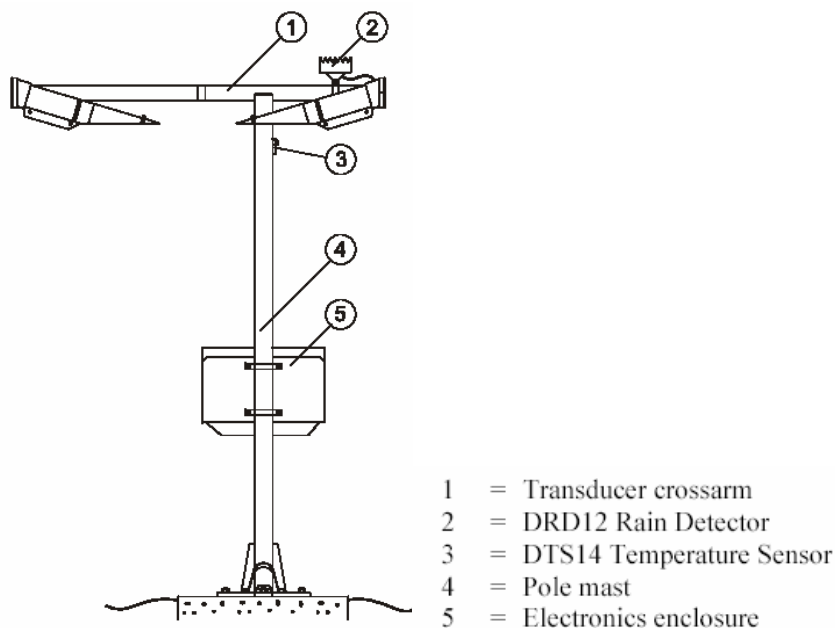


Figure 4.21. Sketch of the Vaisala Present Weather Sensor.

#### ***4.6 Data Treatment (QA/QC) and Preliminary Analysis***

Such a large suite of instruments requires regular maintenance and checks to ensure their reliable operation; although inevitably some data is lost due to instruments faults. Throughout the 4 years of measurements different individuals took on the role of "site-operator" and made regular visits to the site; filling in a standard form which ensured checks were made on all instruments, the data were download, livestock numbers estimated and the canopy height measured. This provided the information for the first stage of treating the data, mainly removing periods where an instrument was faulty or the power supply had failed.

This initial screening provides the “raw” data set for further checking, calibration and filtering.

Several power failures occurred during the 4 years of measurements, on some occasions this was due to a local mains fault but more often water entering equipment or other faults caused the problem. The most severe event occurred on the 22<sup>nd</sup> of October 2002 when very heavy rains caused the site to flood, Figure 4.22.



Figure 4.22. A very soggy fieldsite, Easter Bush 24/10/2002.

Each component of the measurements requires different treatment; this is described for the gradient and eddy-correlation data in Section 5.2 and the rest of the data here. Concurrent measurements of air temperature, atmospheric pressure, wind-speed, wind direction and ozone concentration are made at CEH-Edinburgh (Bush), only a ~300 metres away and so these are used to check the data and gap-fill some data sets where appropriate. However, Bush is not a standard UKMO site as the sensors are placed at the top of a 10 m mast and there are tall trees to the NE, which has some influence of the measurements. Table 4.6 summarises the data capture achieved for each system and dataset discussed in this section. Where data capture is given for 2001 and 2002 this is from the start of measurements in May and March respectively.

- **Gradient Wind-speed**

The cup-anemometers have a stalling speed of  $0.2 \text{ m s}^{-1}$ , at wind-speeds around this value they will cease to turn or will not start turning from rest. The data-logger reads the wind-speed every second and stores a 15 minute average, if the anemometer has stalled it will read  $0.25 \text{ m s}^{-1}$  thus the 15 minute average will not be the true value. To remove such points from the

final dataset all values below  $0.8 \text{ m s}^{-1}$  are discarded; the annual data capture for each anemometer is given in Table 4.7 below. A minimum of three points are required to characterise the wind-speed profile.

Table 4.6 Summary data capture for each data set (specific data capture for some individual elements may vary slightly from these figures).

	2001	2002	2003	2004
Soil Heat Flux (G)	97	66	88	87
$T_{ur}, T_l$	91	82	99	96
$St$	ND	8	99	91
$T_s$	97	83	99	87
$RH$	ND	ND	74	89
$PAR$	ND	ND	74	96
$R_n$ (NrLite)	97	78	99 (40)	98 (94)
surface wetness	76	83	99	98
rainfall	34	83	99	92
$T_{1r}, T_{3r}, T_{5r}$	57	66	90	95
$U_1$ to $U_5$	See Table 5.7			
Sonic Wind Dir.	95	90 (52)	92 (86)	86 (86)
LICOR 7000 P	83	90	90	90
$SWC_{SW1}$ to 4, $NE1$ to 4	ND	45	99	98
<b>Collated Data</b>				
$T_a$	100	100	100	100
$P$	100	100	100	100
$St$	100	100	100	100
Rainfall	100	99	100	99
Wind Direction	100	100	100	100

ND = No Data

Table 4.7 Annual %data capture for each anemometer on the wind-speed gradient.

	$U_1$ - top	$U_2$	$U_3$	$U_4$	$U_5$
31/5/01 to 1/10/01	78.01		70.01		70.19
21/3/02 onwards	75.22	73.01	69.28	58.12	61.90
2003	81.05	73.64	69.47	68.99	64.21
2004	77.01	72.47	67.59	65.01	62.59

#### • Air Temperature

Air temperature is measured by several different sensors in different locations (fine-wire thermocouples on the Bowen ratio and gradient masts;  $RH/T$  probe on the Bowen ratio mast; two sonic anemometers for the eddy-correlation system), each with its own characteristics and uncertainties.

It is useful to have a measure of ambient air temperature,  $T_a$ , to calculate density for example, and so the data sets are combined to give a continuous time series. The BR was taken as our baseline dataset as it has the most complete time series and had the same configuration throughout. As temperature is measured at two heights they are averaged to give  $T_a$ .

Different data sets are available to fill the gaps and were used in the following order of precedence: Gradient (average of all heights), RH/T probe, Metek sonic, Bush. Figure 4.23 shows the correlation and regression statistics for each data set with the BR average temperature; the Gill sonic temperature is not used as it is less reliable (Section 4.3.3) and does not compare as well with the other data sets. The resulting time series is plotted in Figure 4.31 and Table 4.8 summarises the gap filling.

Table 4.8 Percentage of the Ta time series<sup>1</sup>.

	2001	2002	2003	2004
<b>BR</b>	90.96	81.57	98.35	95.53
<b>RH/T</b>	ND <sup>2</sup>	ND	0.03	4.37
<b>Gradient</b>	6.48	4.40	0.98	0.01
<b>Metek</b>	ND	7.14	0.31	0.00
<b>Bush</b>	2.56	6.89	0.33	0.09

1. Gap filling results in 100% data capture overall each year, 2. ND = no data

As noted above, the 21X logger for the Gradient system was replaced on the 20/05/2003 as it had a fault. The amount of scatter between the average Gradient and BR temperature measurements is reduced after this date with the R<sup>2</sup> value between the Gradient and BR being 0.87 for 01/01/2003 to 20/5/2003 and 0.97 thereafter.

- **Atmospheric Pressure (P)**

There are two measures of atmospheric pressure (used in the calculation of air density), one from the LICOR 7500 and the other at Bush. The two data sets are very similar and so the data sets are simply combined using the LICOR in preference to Bush, Table 4.9 gives regression statistics and the percentage of time each data set is used.

Table 4.9 Regression statistics; overall data capture for P and % of time each data set used.

	2001	2002	2003	2004
<b>Slope</b>	1.001	0.998	0.999	0.999
<b>Intercept</b>	-0.160	0.098	0.106	0.107
<b>R<sup>2</sup></b>	0.999	0.999	0.999	0.999
<b>Combined %DC</b>	99.97	100	100	99.95
<b>LICOR%</b>	83.96	89.98	89.93	89.70
<b>Bush%</b>	16.04	10.02	10.07	10.30

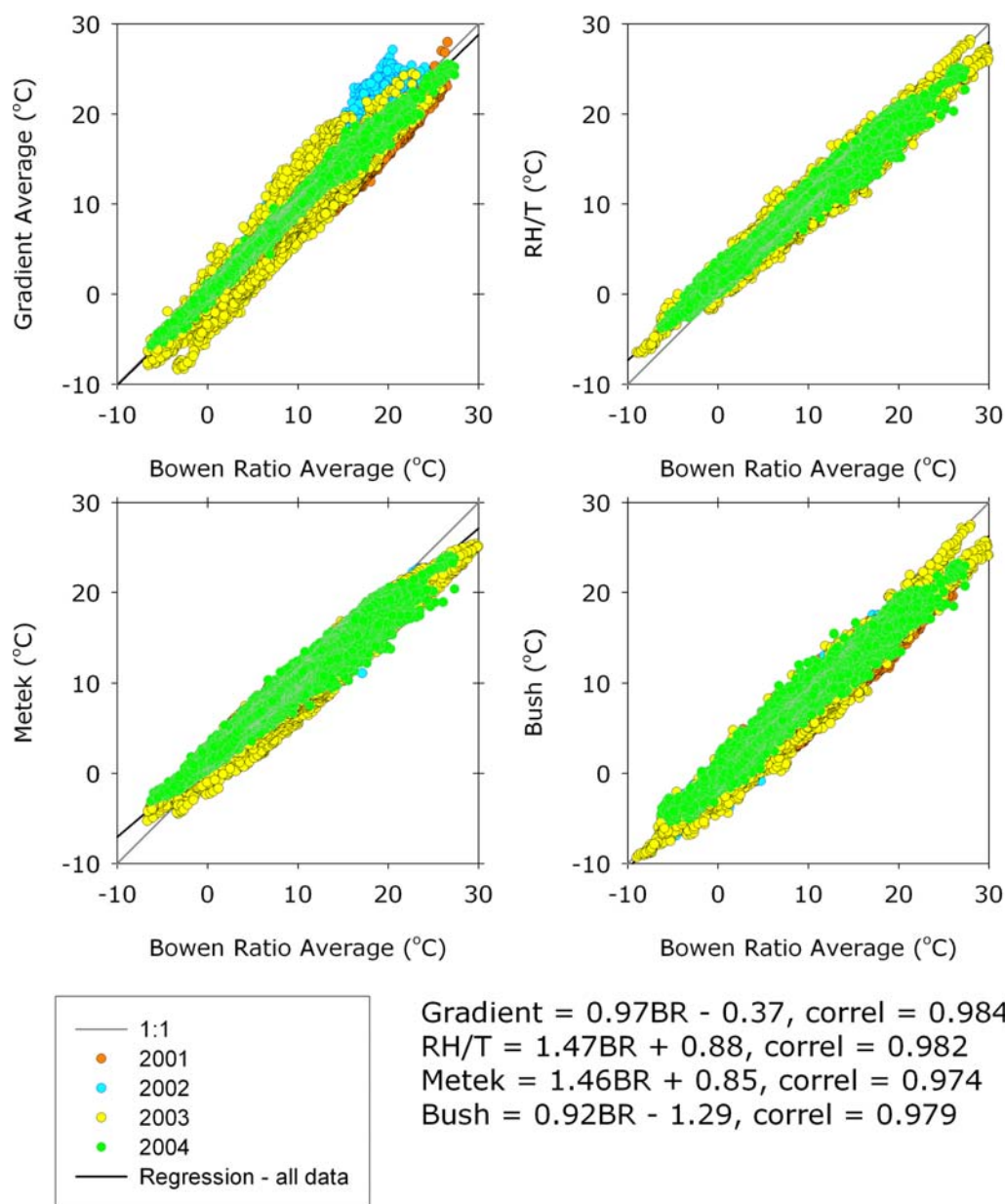


Figure 4.23. The correlation between different measures of ambient air temperature at Easter Bush and Bush.

- **Rainfall**

The tipping bucket at Easter Bush operated continuously, apart for some periods when the cable was accidentally cut when strimming the grass or when its was being tested. The data from Bush are used to gap fill the time series, as in general the two measurements agree well. The plot in Figure 4.24 shows the monthly total rainfall measured at each site. During 2001 and 2002 there was an intermittent fault with the Bush tipping bucket which led to poorer agreement between the sites, however Bush is only used to fill a small percentage of the data as indicated in Table 4.10.

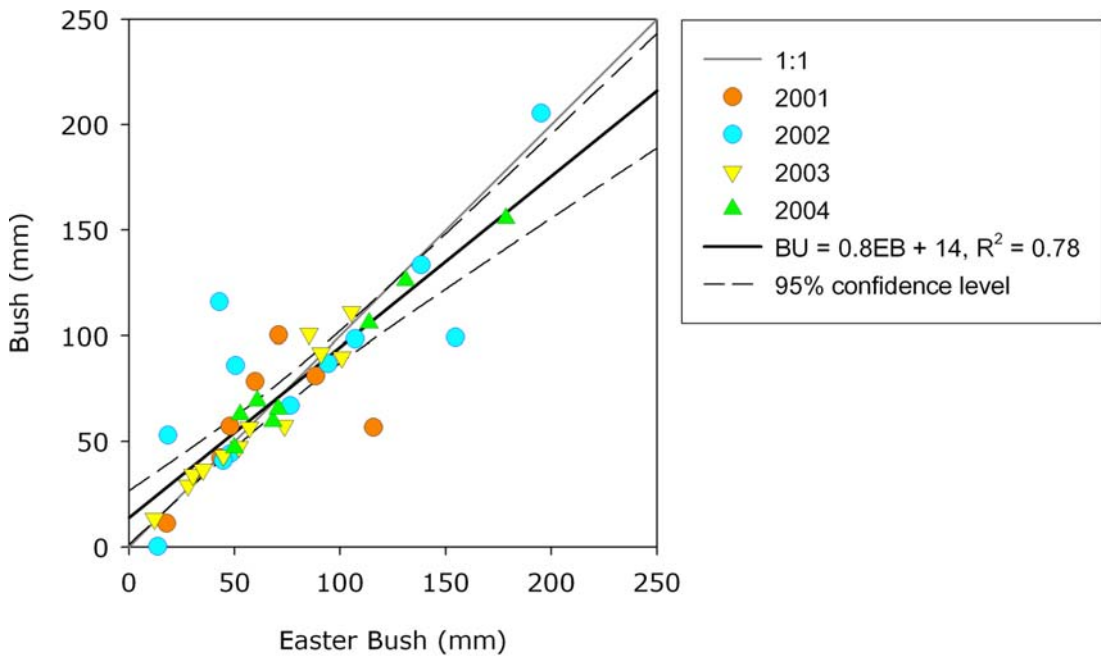


Figure 4.24. Comparison of monthly total rainfall amounts measured at Easter Bush and Bush.

Table 4.10 Overall data capture for rainfall and % of time each data set used.

	2001	2002	2003	2004
<b>Combined %DC</b>	100.00	99.39	99.99	99.12
<b>Easter Bush%</b>	94.00	84.01	99.33	92.66
<b>Bush%</b>	6.00	15.99	0.67	7.34

- **Wind Direction (*Wd*)**

There are three measures of wind direction, one from each sonic anemometer and the third from the wind-vane at Bush. To compare the three data sets the cosine of the angle between each is calculated (as wind-direction is a vector),  $\Delta Wd = \cos(Wd_1 - Wd_2)$ ; when they are identical  $\Delta Wd = 1$ , perpendicular  $\Delta Wd = 0$  or anti-parallel  $\Delta Wd = -1$ . The difference between the two sonics is between 0.9 to 1 for over 90% of the time, and so the Gill instrument is used as the baseline dataset (it has a longer and more complete time series).

The annual frequency distribution of wind directions in  $15^\circ$  sectors is also calculated and shown in the plots in Figure 4.25. A shift in wind direction of  $\sim 15^\circ$  between Easter Bush and Bush is clearly visible in the plots. This is probably due to a localised effect of the tall trees that surround Bush. The median  $\Delta Wd$  for Gill vs Bush is  $10^\circ$ ,  $11^\circ$ ,  $13^\circ$ ,  $15^\circ$  for 2001 to 2004 respectively and  $12^\circ$  on average overall, thus the Bush readings are shifted by  $12^\circ$  (as shown on Figure 4.25) to match the Gill and Metek.

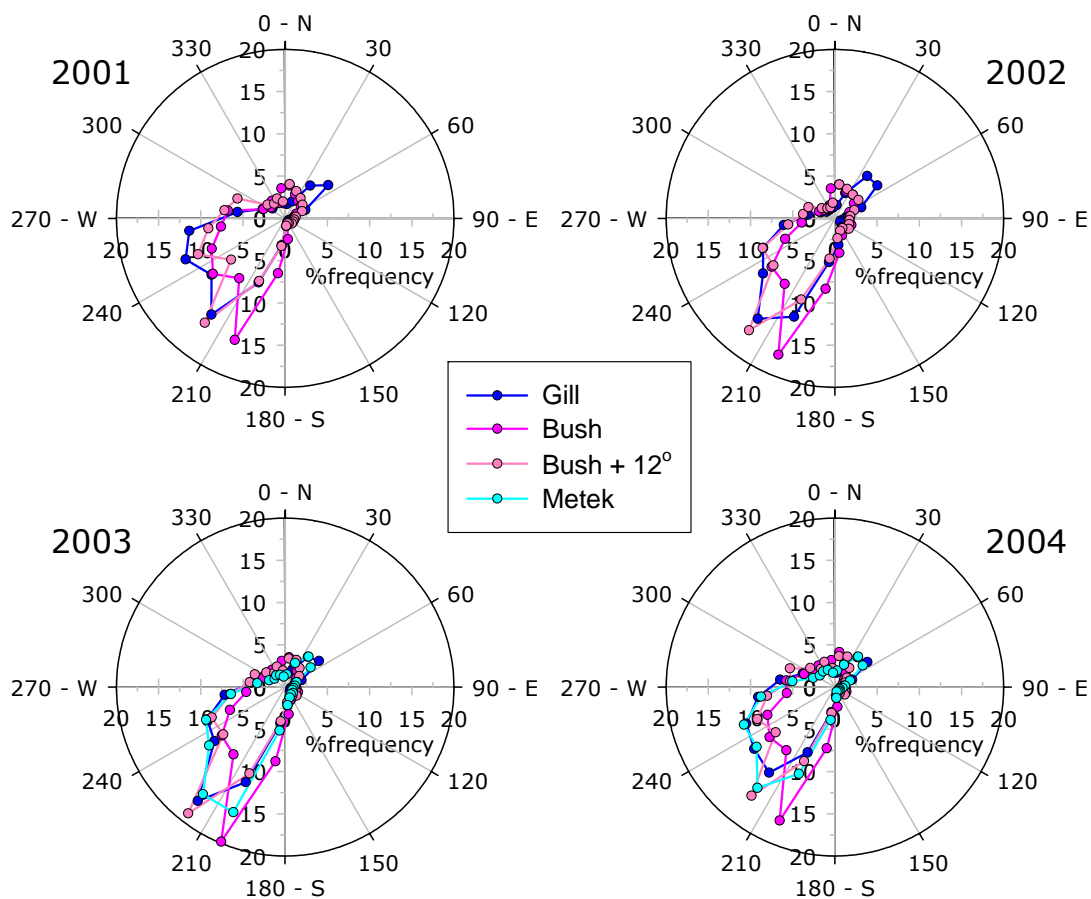


Figure 4.25. 15-minute average wind direction frequency plots for each data set 2001 to 2004.

The three data sets are combined in the following order of precedence Gill, Metek, Bush, resulting in 100% data capture for each year. The percentage of each dataset used is shown in Table 4.11.

Table 4.11 Percentage of the Wd time series.

	2001	2002	2003	2004
<b>Gill</b>	93.74	90.58	92.63	90.12
<b>Metek</b>	ND <sup>1</sup>	ND	3.94	5.30
<b>Bush</b>	6.26	9.42	3.42	4.58

1. ND = no data

- **Total Solar Radiation (*St*)**

At the start of measurements in 2001 until 27/11/02 09:15, the pyranometer on the Bowen Ratio mast was measured with the wrong voltage range on the logger input channel. This resulted in a loss of resolution, particularly at low light levels, and measurements from Bush are used for all of this period, as well as for gap filling the subsequent data. Table 4.12 gives the regression statistics between the two data sets and the percentage of data used each year.

Table 4.12 Regression statistics and percentage of the St time series used from each dataset.

	2001	2002	2003	2004
<b>Slope</b>	1.05	0.96	1.01	0.94
<b>Intercept</b>	11.60	13.63	8.65	4.24
<b>R<sup>2</sup></b>	0.97	0.85	0.98	0.96
<b>Bowen Ratio</b>	0	7.62	99.33	95.54
<b>Bush</b>	100	92.38	0.67	4.46

- **Soil Heat Flux ( $G$ )**

The soil heat flux plates measure the soil heat flux at their particular location, in the case of at Easter Bush ~10 cm below the ground surface. To estimate the energy balance this needs to be adjusted to a ground surface value,  $G$ , by adding the change in energy stored in the layer above the heat flux plates during the measurement period (storage correction,  $S$ ). The specific heat of the soil and the change in soil temperature,  $\Delta T_s$ , over the output interval,  $t$ , are required to calculate the change in stored energy. This calculation of  $S$  requires site specific inputs for bulk density ( $Bd$ ), volume basis soil water content ( $SWC$ ), and the specific heat of the dry soil ( $c_s$ ).

$$S = \frac{((SWC \cdot c_w) + c_s) \cdot Bd \cdot d}{t} \quad (108.)$$

Where: Specific heat water,  $c_w = 4190 \text{ J kg}^{-1} \text{ K}^{-1}$   
 Specific heat dry soil (site specific),  $c_s = 840 \text{ J kg}^{-1} \text{ K}^{-1}$   
 Programme output interval (programme specific),  $t = 900 \text{ s}$   
 Depth of soil heat flux plates (site specific),  $d = 0.1 \text{ m}$   
 Soil bulk density (site specific),  $Bd = 1000 \text{ kg m}^{-3}$   
 Soil water content (Vol H<sub>2</sub>O/Bulk soil vol.), (site specific)  
 Up to 25/06/2002 15:15  $SWC = 0.2$   
 From 25/06/2002 15:30  $SWC = \text{Average}(SWC_{SW2}, SWC_{NE2})$

$$G = \text{Average}(HF_{s1}, HF_{s2}) + S \quad (109.)$$

Some data was lost from this time series due to breaks in the sensor cables, overall data capture is given in Table 4.6.

- **Net Radiation ( $R_n$ )**

Up to the 06/08/2003 15:00 measurements from the Q7 net radiometer are used, after this date measurements from the NR-Lite are also available. An initial comparison of the two data sets shows that the instruments record broadly similar values and are well correlated (98%) but the NR-Lite tends to read lower than the Q7 (Figure 4.26). Despite filtering the obviously erroneous data, in 2004 there is also more scatter between the data sets due to a fault with the NR-Lite.

The NR-Lite is slightly affected by wind-speed in that its sensitivity decreases with increasing wind-speed. This decrease in sensitivity is less than 1% per  $\text{m s}^{-1}$  wind speed, and the effect is essentially independent of the radiation level. Readings can be corrected using the factor,  $1 + 0.0082u$ , where  $u$  is the wind-speed at the sensor level in  $\text{m s}^{-1}$ . The middle anemometer of the gradient system is at approximately the same height as the NR-Lite and so this is used to apply the correction. This slightly improves the correlation between the two data sets with the slope going from 0.92 to 0.94 in 2003 and 0.91 to 0.94 in 2004 (Figure 4.26), but for consistency only the Q7 dataset is used throughout.

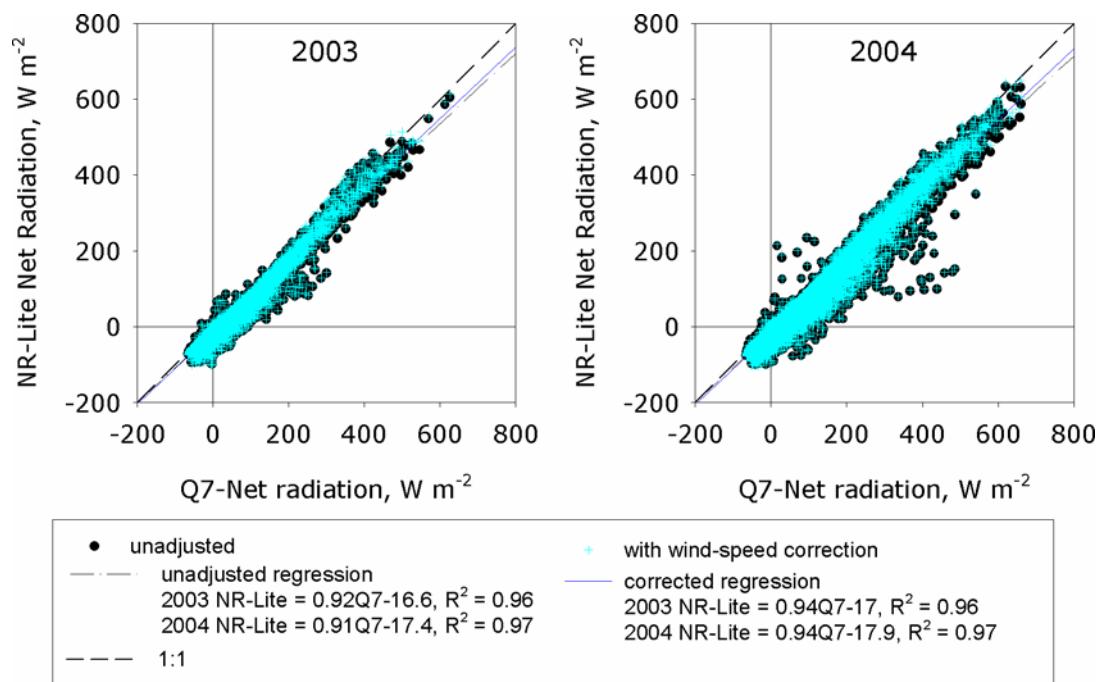


Figure 4.26. Comparison of the Q7 net radiometer with un-adjusted and wind-speed corrected data from the NR-Lite net radiometer.

- **TDR, Soil Water Content ( $SWC_{SW1}$  to  $SWC_{SW4}$ ,  $SWC_{NE1}$  to  $SWC_{NE4}$ )**

The TDR probes give soil moisture content as a fraction of volume, however many models require soil water potential as a pressure in kPa. The conversion between the two units requires information on how the soil retains and releases moisture, known as the soil water release curve (SWRC). Such data have not been obtained for the Easter Bush site but a previous study has been made by SAC of the same type of soil from a nearby field (O'Sullivan, 2003). This data was used to fit a SWRC and convert the  $SWC$  to  $SWP$  in kPa (Figure 4.27).

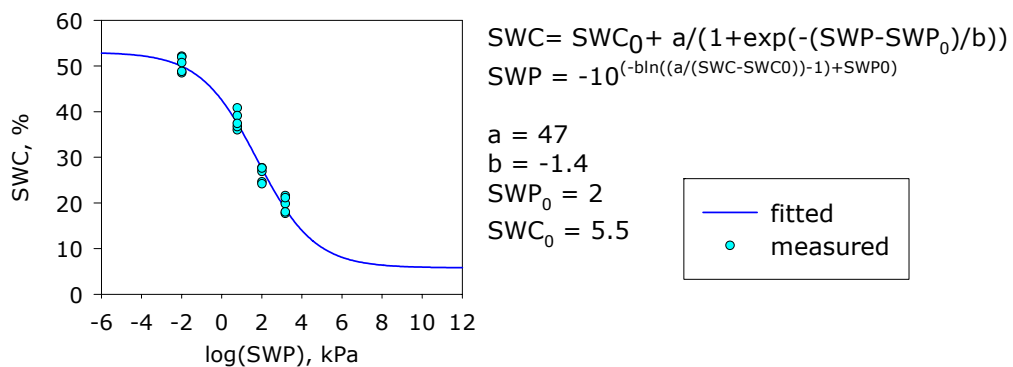


Figure 4.27. Measured *SWP* and *SWC* at a site with Macmerry series soil, close to Easter Bush, and the fitted soil water release curve.

## 4.7 Site Meteorology

The ozone flux is influenced by many aspects of the weather, for example: wind-speed, wind-direction, latent and sensible heat fluxes which change the turbulence; temperature, humidity, soil water content and PAR control stomatal activity; surface wetness and temperature may influence the non-stomatal ozone flux. With almost four years of measurements the inter-annual variability of the weather will have had a great influence on the measured fluxes. Some of the relevant parameters are summarised in this Section and will be referred to in the following Chapters.

### 4.7.1 Wind Direction

The prevailing wind direction at the site is South Westerly ( $180^\circ - 270^\circ$ N; Figure 4.25), with winds coming from this direction ( $180 - 270^\circ$ ) for 60% of the time, which is typical of the UK. The other main sector is the North Easterly ( $0^\circ - 90^\circ$ N) with  $\sim 19\%$  of the data and  $\sim 3\%$  comes from the fence-line ( $130^\circ - 150^\circ, 305^\circ - 315^\circ$ N). There is some variation from month to month and year to year which has an impact on the amount of flux data that can be obtained. The pie charts in Figure 4.28 show the monthly frequency of wind directions from the main sectors for each year. Although some months are quite similar from year to year, such as June and July, others are more variable, such as September and December.

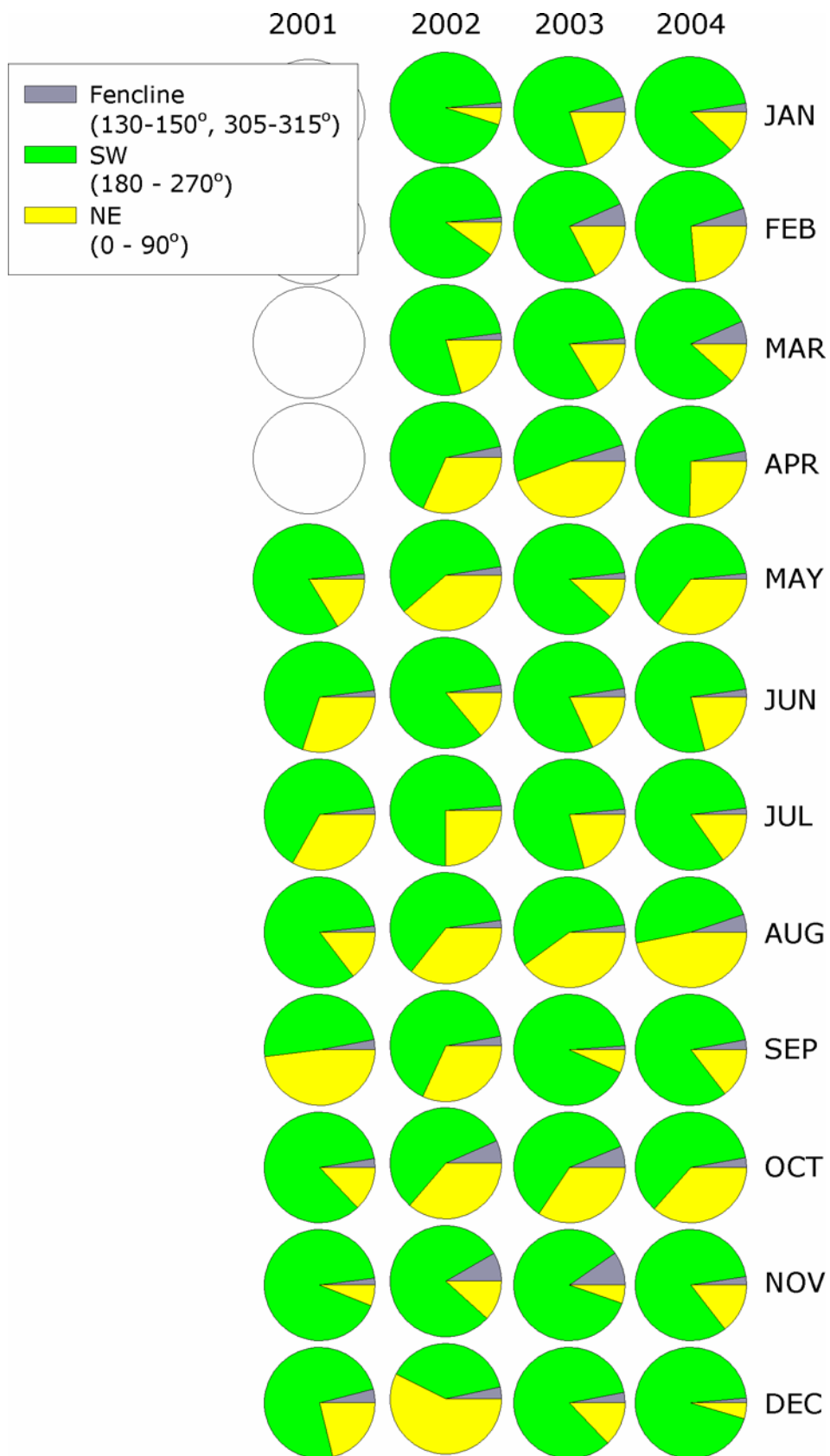


Figure 4.28. Monthly frequency pie charts for the combined wind direction dataset, showing the fraction of data from the along the fence-line and SW or NE sectors.

## 4.7.2 Wind-speed

There are several different measurements of wind-speed at the site, however as they are all at different heights they cannot be simply combined at this point. As part of the analysis of fluxes, the wind speed at the reference height of 1 m is calculated for each system and a comparison of these data is given in Section 5.2. Results from the Gill sonic are used here to give a general description of annual weather conditions. The overall average wind-speed at the site is  $3.2 \text{ m s}^{-1}$  (median  $2.9 \text{ m s}^{-1}$ ) with a standard deviation of  $2.2 \text{ m s}^{-1}$ , which is typical of such a location in the UK. However, there is a seasonal cycle in wind speed with the larger values in the autumn and winter months. Figure 4.29a shows a plot of the 15 minute average measured wind-speeds and Figure 4.29b summarises the data in a monthly box plot.

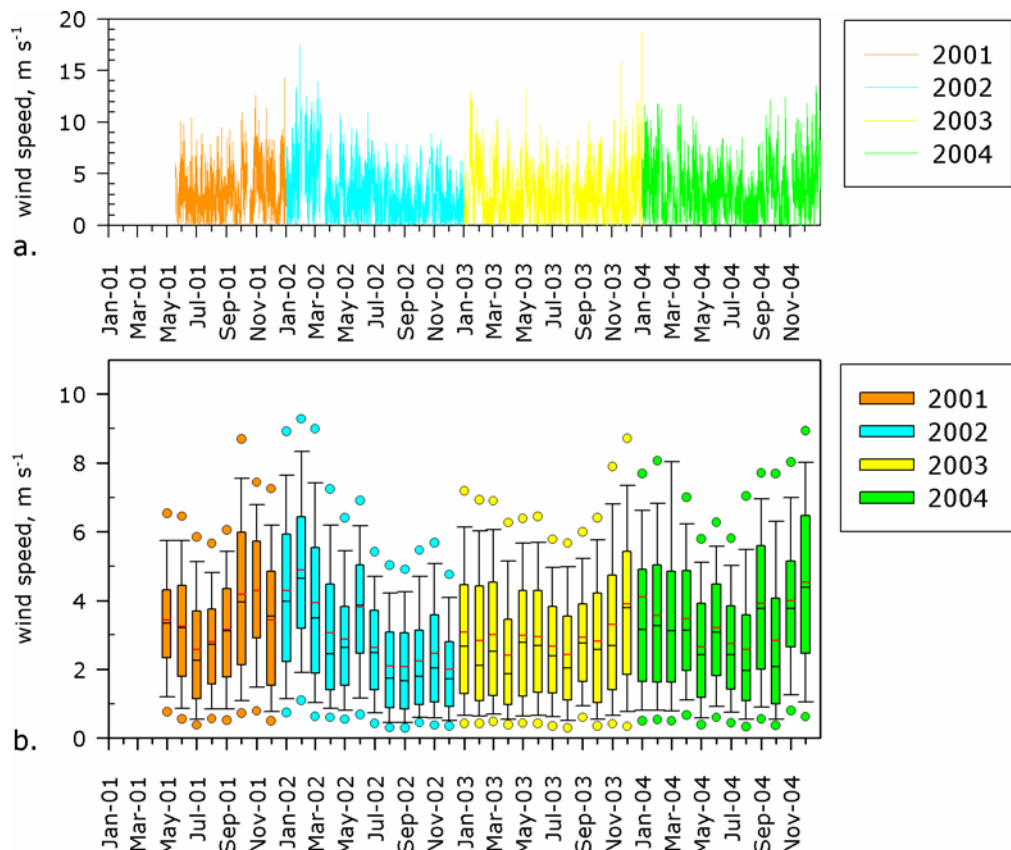


Figure 4.29. a) Time series of 15 minute average wind speed measured by the Gill sonic (2.15 m) and b) monthly summary statistics of the 15 minute wind speed: the box indicates the 75<sup>th</sup> and 25<sup>th</sup> percentiles; the black bar is the median; the red bar the average; the whiskers the 90<sup>th</sup> and 10<sup>th</sup> percentiles; the dots are the outliers at the 95<sup>th</sup> and 5<sup>th</sup> percentiles.

The wind-direction also influences the observed wind speed with the SW sector tending to be windier throughout the year. The plots in Figure 4.30 show the monthly statistics for the two main wind-sectors.

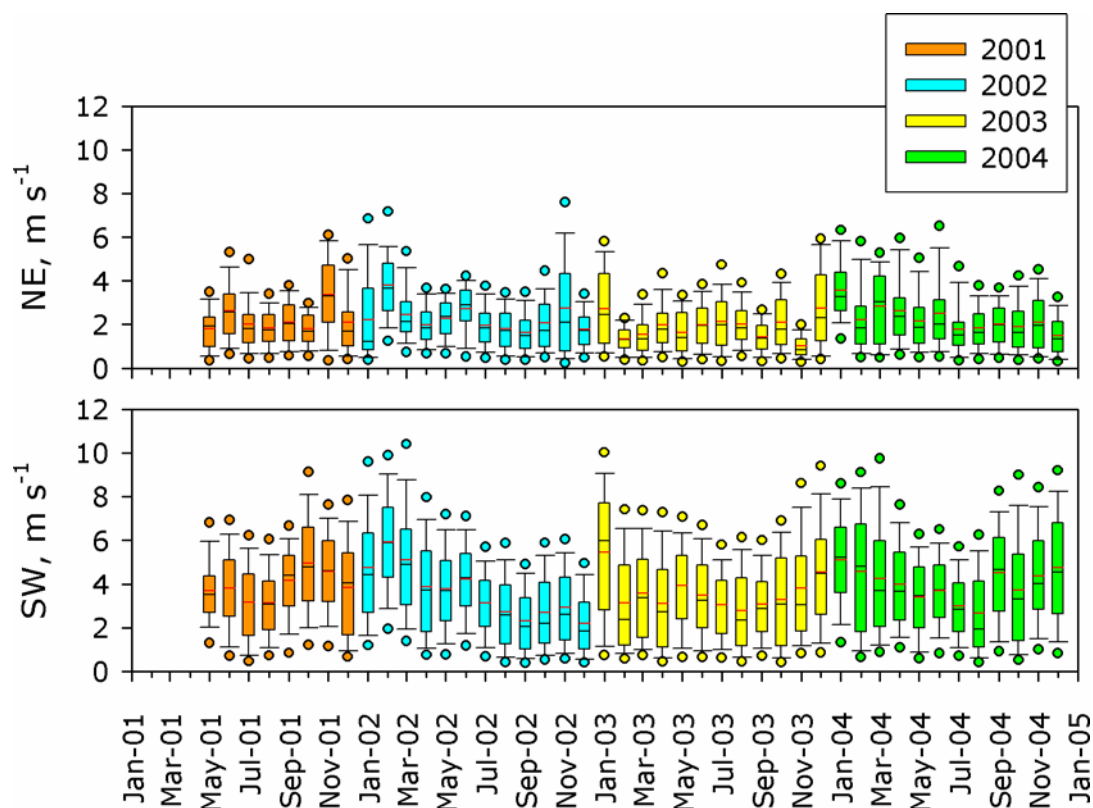


Figure 4.30. Annual monthly summary statistics of the 15 minute wind speeds from each sector: the box indicates the 75<sup>th</sup> and 25<sup>th</sup> percentiles; the black bar is the median; the red bar the average; the whiskers the 90<sup>th</sup> and 10<sup>th</sup> percentiles; the dots are the outliers at the 95<sup>th</sup> and 5<sup>th</sup> percentiles.

### 4.7.3 Ambient Air Temperature

The overall annual mean temperature is 9.5 °C with a standard deviation of 5.3 °C which is slightly higher than the regional average of 8 °C reported by the UK Meteorological Office (Met, 2004). There is some variation between the years with 2002 being relatively cool whereas 2001 and 2003 were particularly hot during the summer months; the plots in Figure 4.31 show the 15 minute time series and monthly summary statistics. There is little difference between the two main wind sectors as shown in Figure 4.33.

Temperature is an important factor in controlling stomatal conductance and photosynthesis as plants are only active at temperatures within a certain range (Figure 3.1b). The optimum temperature for *Lolium perenne* to function with, potentially, its maximum stomatal conductance is between 16 to 20°C; Figure 4.32 shows the monthly frequency distribution for each year with percentage of time temperature is within this range indicated.

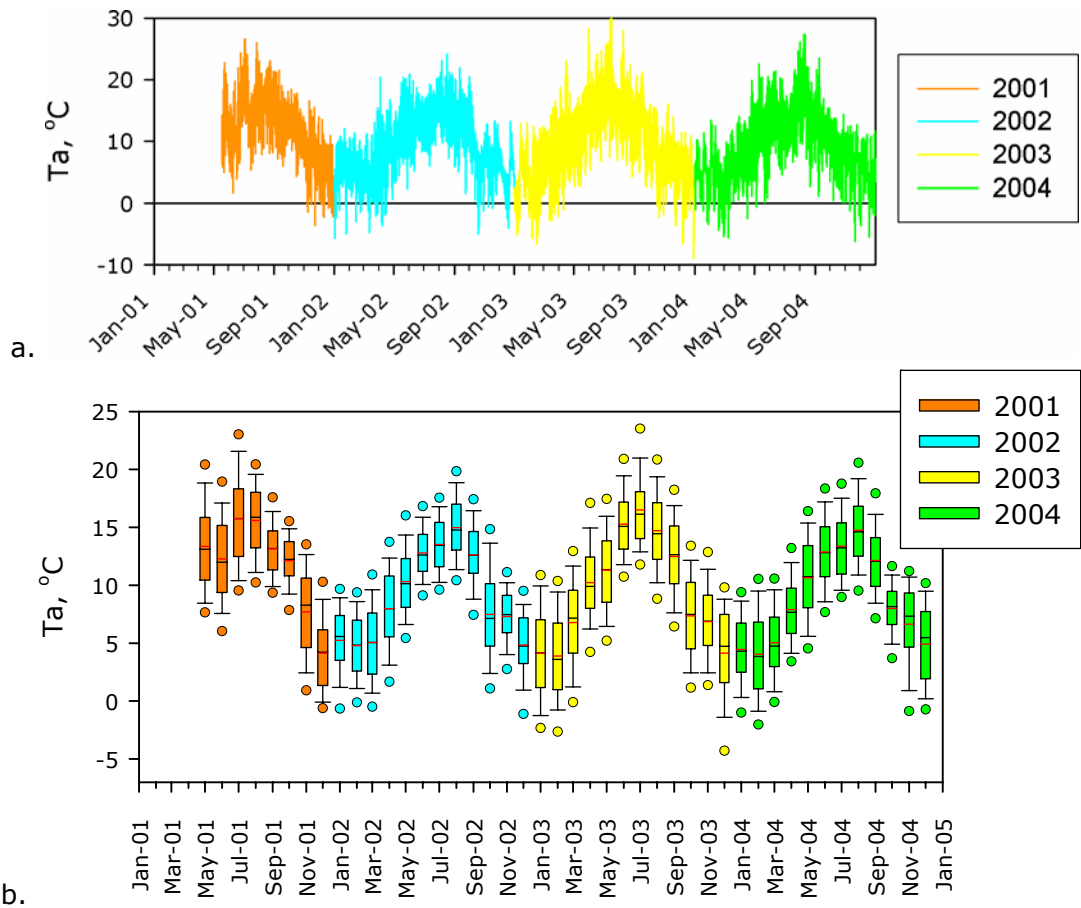


Figure 4.31. (a) Time series of combined 15-minute average ambient air temperatures and (b) monthly box plot of the data plotted in (a) the box indicates the 75<sup>th</sup> and 25<sup>th</sup> percentiles; the black bar is the median; the red bar the average; the whiskers the 90<sup>th</sup> and 10<sup>th</sup> percentiles; the dots are the outliers at the 95<sup>th</sup> and 5<sup>th</sup> percentiles.

#### 4.7.4 Total Solar Radiation ( $St$ ) and $PAR$

Total solar radiation is a major controlling factor on the sensible heat flux and turbulence. Vegetation is sensitive to radiation in the  $PAR$  wavelength range of 400 to 700 nm, thus both total solar radiation and  $PAR$  are measured at Easter Bush. The fraction of total solar radiation reaching the ground surface that is in the  $PAR$  range can vary. However the  $PAR$  content of total extraterrestrial radiation is 0.45 and this factor is commonly used to estimate  $PAR$  from measurements of  $St$  (Monteith and Unsworth, 1990). Although  $St$  is normally measured in  $W m^{-2}$ ,  $PAR$  is often expressed as a photon flux density in  $\mu mol m^{-2} s^{-1}$ , as photosynthetic rates are more closely related to the quantum rather than energy content of the radiation. An exact conversion of  $W m^{-2}$  to  $\mu mol m^{-2} s^{-1}$  would require measurements of the energy density distribution and knowledge of the frequency response of the radiation sensors; the manufacturer of the  $PAR$  sensor recommends using  $PAR[\mu mol m^{-2} s^{-1}] = 4.6PAR[W m^{-2}]$ .

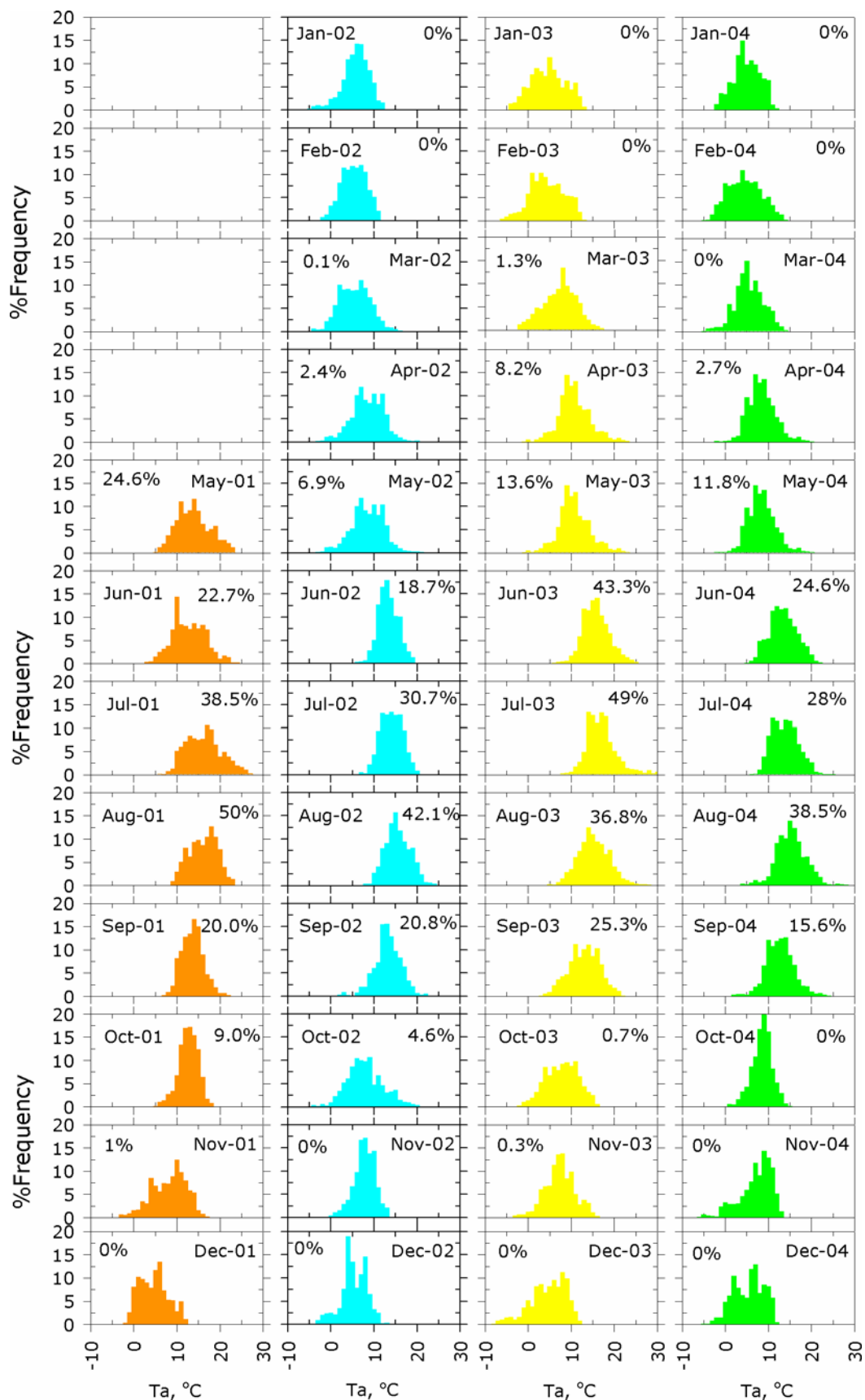


Figure 4.32. Monthly frequency distributions of 15-minute ambient air temperature observed each year.

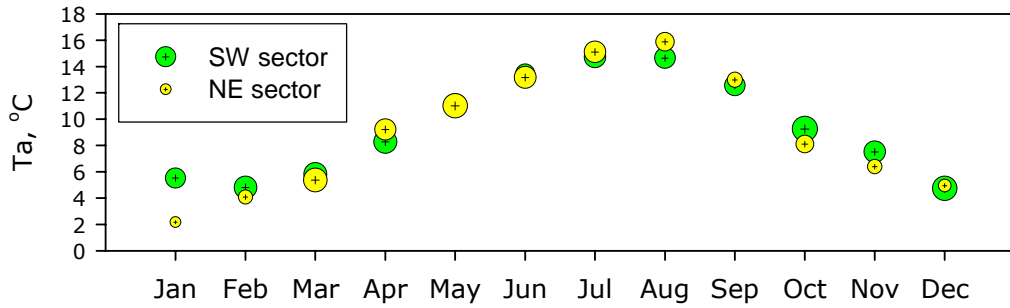


Figure 4.33. Overall (2001 to 2004) monthly mean ambient temperature for the two main wind sectors; the size of the symbols indicates the standard deviation.

In general, plants become active during daylight hours when total solar radiation exceeds  $\sim 50 \text{ W m}^{-2}$  ( $PAR$  of  $\sim 104 \mu\text{mol m}^{-2} \text{ s}^{-1}$ ). Photosynthesis rates for temperate grasses reach a maximum at a  $St$  of  $\sim 500 \text{ W m}^{-2}$  or  $PAR$  of  $\sim 1035 \mu\text{mol m}^{-2} \text{ s}^{-1}$ . Both total solar radiation and  $PAR$  levels vary considerably throughout the year as shown by the plots of 15-minute  $St$  and  $PAR$  in Figure 4.34a (for 2001 and 2002  $PAR$  is assumed to be  $0.45 \cdot St$ ). To summarise the data, Figure 4.34b shows monthly box plots of the  $St$  time series.

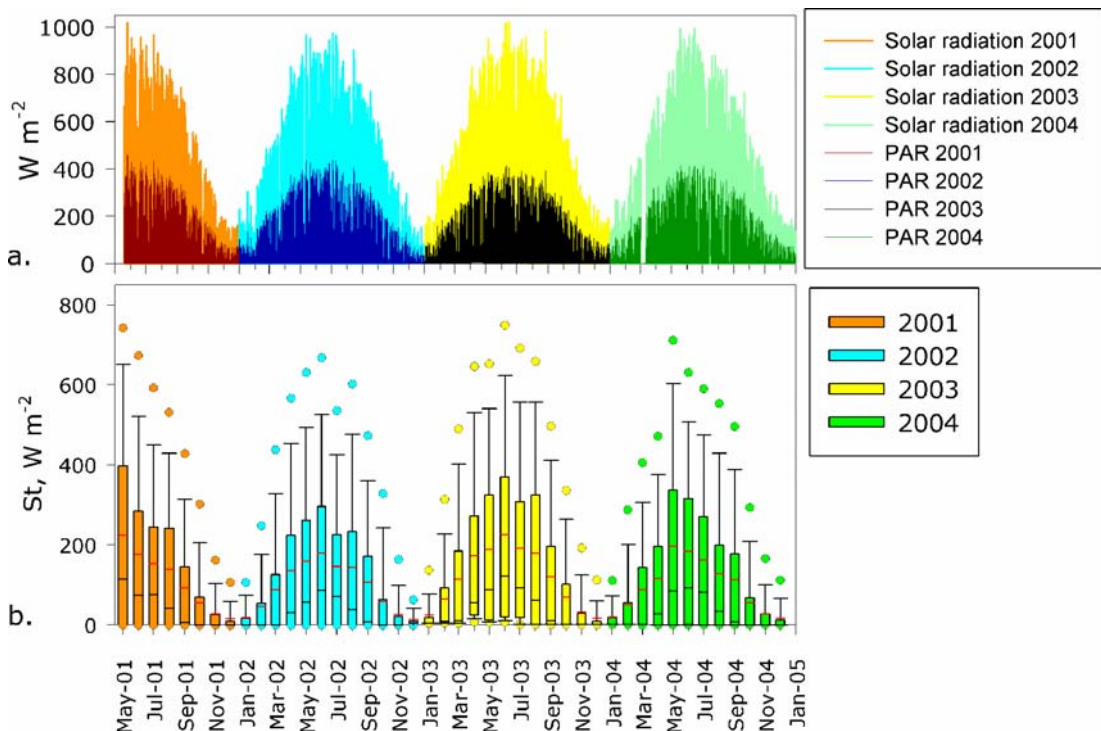
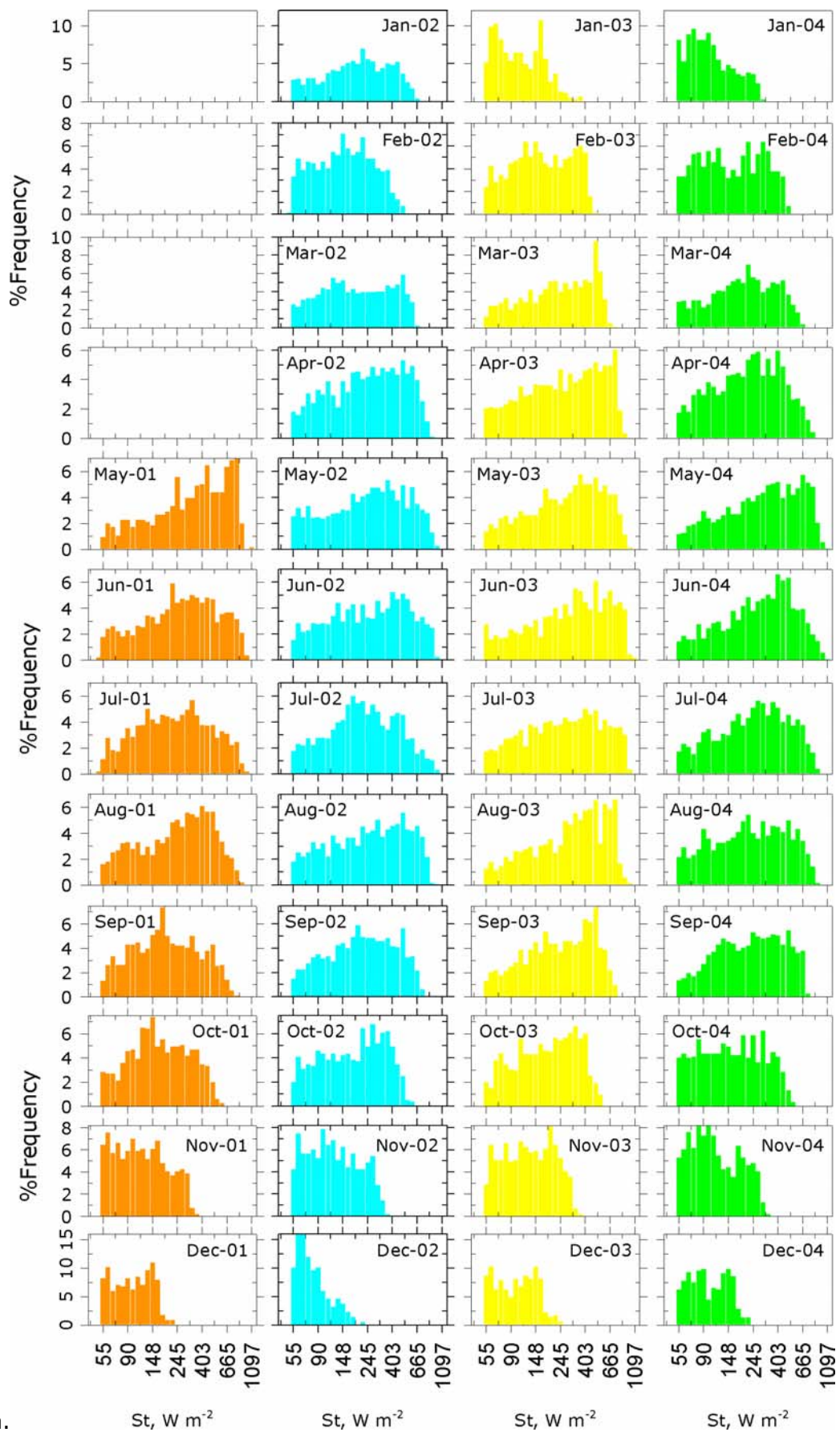
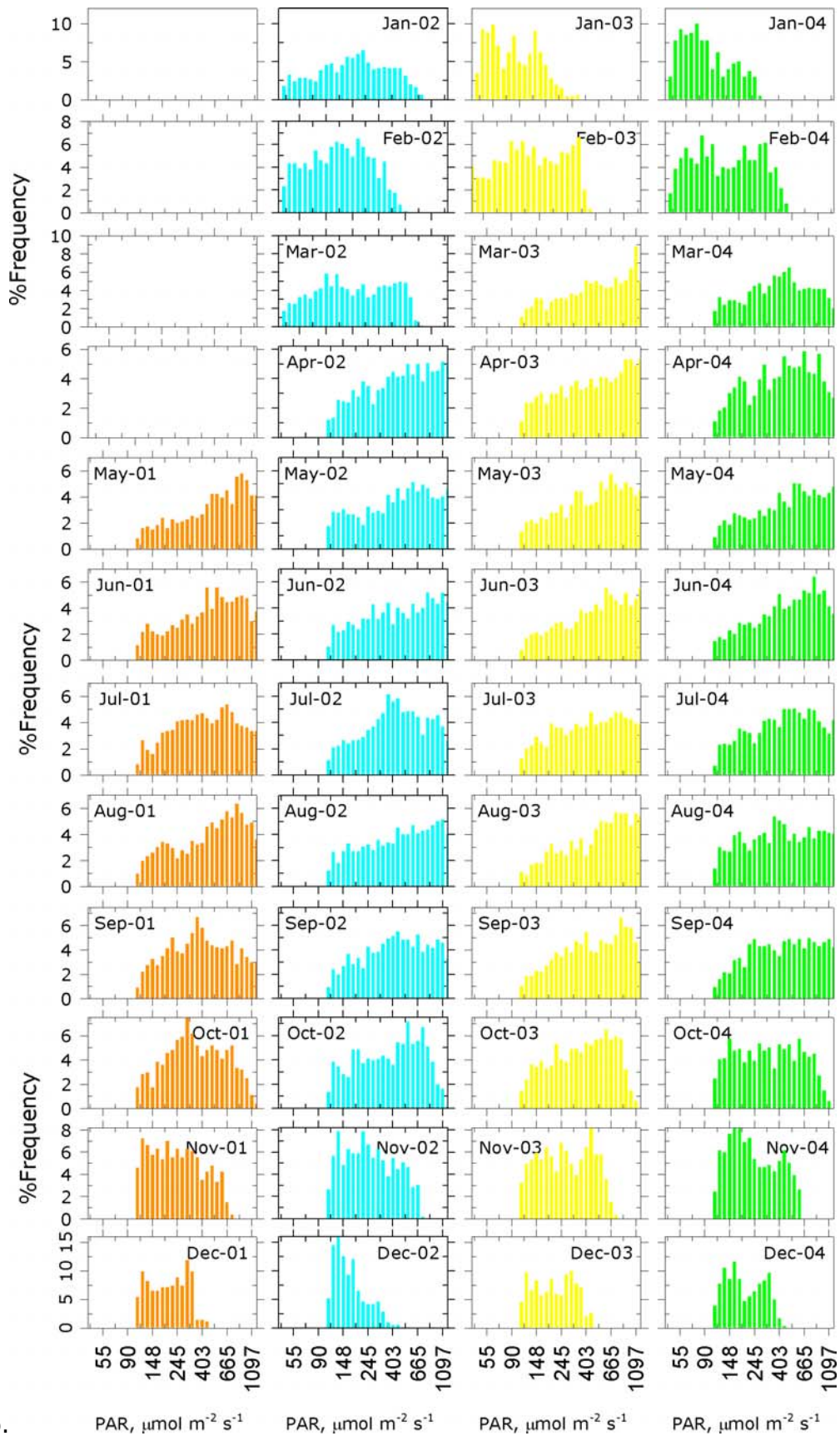


Figure 4.34. a. Time series of  $St$  and  $PAR$  measured at Easter Bush. b. Monthly box plot of  $St$  measured at Easter Bush; the box indicates the 75<sup>th</sup> and 25<sup>th</sup> percentiles; the black bar is the median; the red bar the average; the whiskers the 90<sup>th</sup> and 10<sup>th</sup> percentiles; the dots are the outliers at the 95<sup>th</sup> and 5<sup>th</sup> percentiles.





b. PAR,  $\mu\text{mol m}^{-2} \text{s}^{-1}$  PAR,  $\mu\text{mol m}^{-2} \text{s}^{-1}$  PAR,  $\mu\text{mol m}^{-2} \text{s}^{-1}$  PAR,  $\mu\text{mol m}^{-2} \text{s}^{-1}$   
 Figure 4.35. Frequency distributions of (a)  $St$  and (b)  $PAR$  above the daylight thresholds of  $50 \text{ W m}^{-2}$  and  $104 \mu\text{mol m}^{-2} \text{s}^{-1}$  respectively.

As with  $T_a$ , radiation levels show little variation with wind sector. Figure 4.35 shows monthly frequency distributions of radiation levels above the approximate daylight hour thresholds of  $50 \text{ W m}^{-2} St$  and  $104 \mu\text{mol m}^{-2} \text{ s}^{-1} PAR$ . Considering the number of days during May to September when  $St$  exceeded  $500 \text{ W m}^{-2}$ , 2003 was a particularly sunny year with 131 days compared to 102, 116 and 119 in 2001, 2002 and 2004 respectively.

#### **4.7.5 Rainfall, Surface Wetness and Soil Water Content**

The input of water to the site is relevant for several reasons: rainfall interferes with the operation of the open-path LICOR 7500; stomatal resistance cannot be measured when the surface is wet; surface wetness may influence the non-stomatal ozone deposition rate as will be examined in Section 6.4.3; soil water content exerts a strong influence on stomatal resistance as plants close stomata in response to drought and may be damaged by water-logging.

The plot in Figure 4.36a shows the monthly and annual total rainfall; for 2002 to 2004 the annual totals are slightly lower than the regional values reported by the Meteorological Office; Easter Bush 1183, 732, 1167 mm compared to 1440, 842 and 1236 mm from the MetO (Met, 2004). Figure 4.36b is a plot of the rainfall in the main sectors, over all there is little difference with a total of 1495 mm from the SW and 1338 mm from the NE, although in some months one sector dominates. In particular the flood of October 2002 was caused by weather systems from the NE sector and particularly intense rainfall events tend to occur from this sector.

The measurements of soil moisture content and surface wetness are closely related to rainfall, as might be expected, although not always in a linear manner. The surface wetness reading drops rapidly when rainfall starts but may take a while to increase (dry out) after the event. The sensor may indicate a wet surface in the absence of rain as it responds to dew fall events. Also on a few occasions the sensor remains dry even though the tipping bucket has recorded a tip. This is probably due to the wetness sensor drying out rapidly in warm weather, particularly if the tip is caused by a brief shower adding to previously accumulated water in the tipping bucket. The data obtained from the Vaisala Present Weather Sensor will allow for an interesting study of the performance of the wetness sensor by providing detailed information on rainfall duration and intensity.

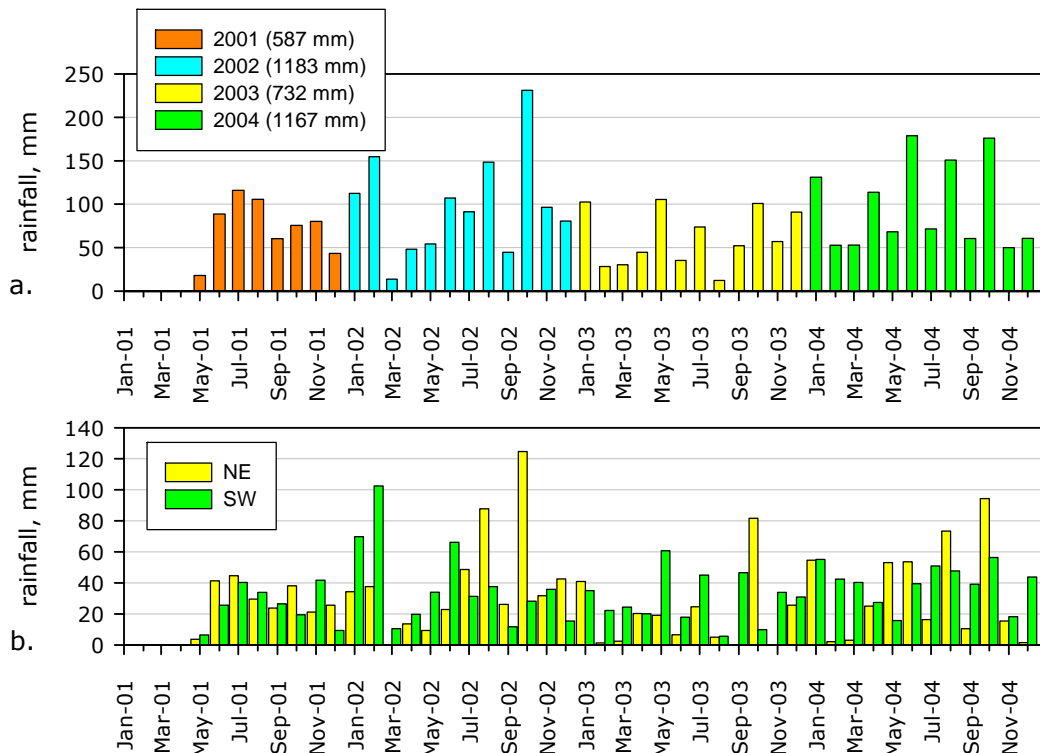


Figure 4.36. a) Monthly total rainfall and (b) monthly total rainfall in the main wind sectors.

As discussed in Section 2.5.1.4, surface wetness may have either a positive or negative influence on non-stomatal ozone deposition rates. Observation of the sensor's readings indicates that there is significant surface water when values less than 4000 are recorded, ~50% of the time. The plot in Figure 4.37 shows the monthly frequency of such wetness events.

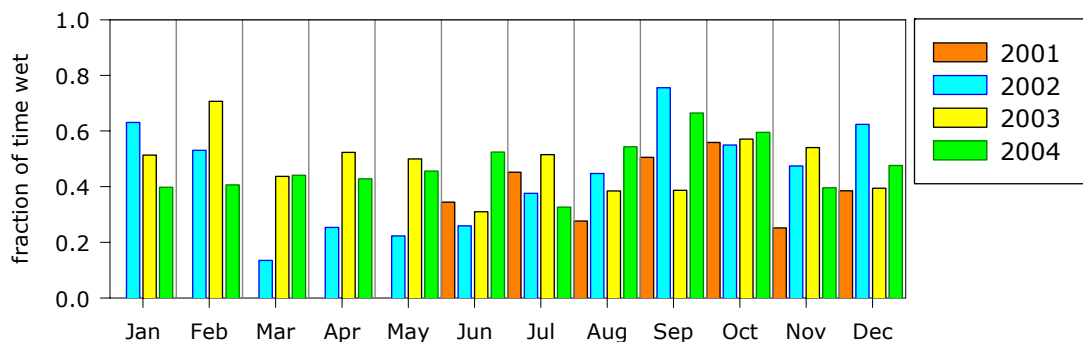


Figure 4.37. Monthly fraction of the time the wetness sensor indicates a wet surface.

Soil water content increases during rainfall events and the field at Easter Bush often reaches its capacity of ~50-60%, during a 15 minute period. The soil becomes more compacted with depth and so it tends to hold less moisture. Thus the lowest depth responds quite slowly to changes at the surface, unless breakthrough occurs, whereas in the top layer wetting and drying occur quite quickly. Some interesting processes can be observed, such as the breakthrough

of water to different depths and the gradual depletion of water content through the profile during dry periods. For example of the 7<sup>th</sup> of September 2002 a fairly heavy rain shower caused a large increase in *SWC* at 3.5 and 7.5 cm whereas there was only a slight increase at 15 and 30 cm (Figure 4.38). However on the 9<sup>th</sup> of September a further shower caused water to breakthrough into the lower layers and *SWC* reached ~40% at all levels.

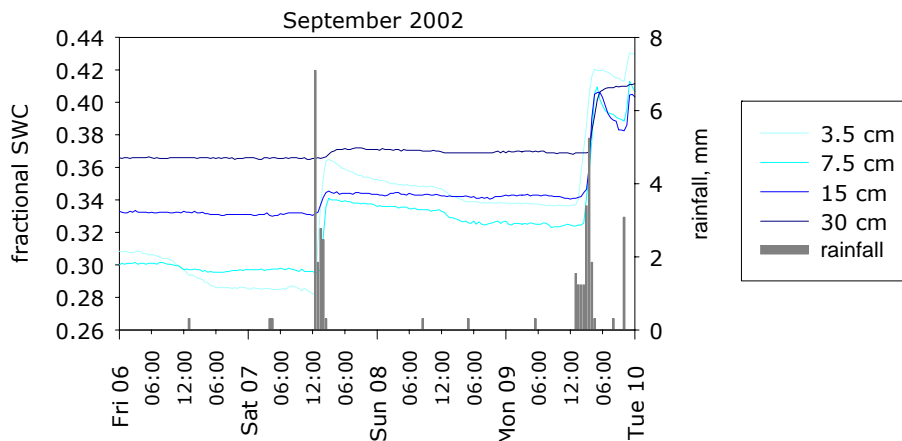


Figure 4.38. Rainfall and soil water content in the SW field during 6<sup>th</sup> September 2002 to the 9<sup>th</sup> of September 2002.

With these data it would be possible to develop a fairly detailed soil water model, however its main use is for input to stomatal conductance models and calculation of soil heat flux (Section 4.6). For modelling purposes *SWC* at the approximate maximum rooting depth of 30 cm is used and it starts to impact on stomatal conductance at daily mean values below ~25% (-300 kPa *SWP*). The plots in Figure 4.39 show daily mean soil water content at each depth in either field. The relatively dry and sunny weather in 2003 clearly caused the soil to dry out quite significantly and will have caused some drought stress in the plants. For the rest of the period there was sufficient water available for the plants to maintain their optimum levels of activity. The heavy rains in October 2002 caused the fields to be waterlogged with *SWC* exceeding 40% at all depths. Detrimental effects such as yellowing, and browning at the tips, of the grass was observed, however, this effect is not accounted for in most stomatal conductance models.

For the period, without *SWC* measurements, it is assumed that the fields retained adequate water levels for the plants to avoid drought stress, given the amount of rainfall.

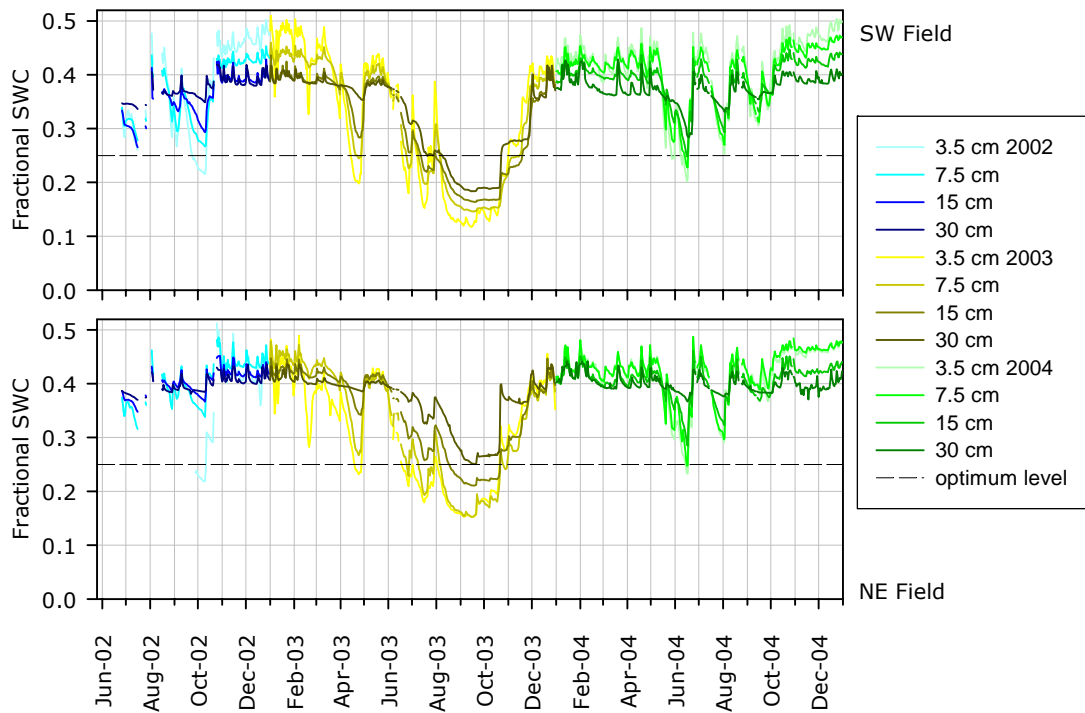


Figure 4.39. Daily mean soil water content (SWC) of the SW and NE fields.

### 4.8 Summary

The measurements systems and instrumentation employed at the Easter Bush field site have been described in this chapter and an overview of its climate has been made. To provide a final summary and reference data set, monthly statistics of canopy height, *LAI*, wind speed, temperature, solar radiation, rainfall, surface wetness, humidity and soil water content are given in Appendix C. The measurements of trace-gas fluxes are described in the following chapter.



# 5 Measurements of Ozone Flux to Grassland

## 5.1 Introduction

As described in Chapter 4, a comprehensive and extensive data set has been gathered to examine ozone fluxes to grassland. Chapter 5 focussed on the basic meteorological and vegetative data and instrumentation whereas this chapter will describe the measured fluxes. The factors controlling ozone deposition are also examined with a focus on the non-stomatal component.

It should be noted that in Chapter 2, the description of micrometeorological theory, the potential temperature,  $\theta$  was used rather than simple air temperature,  $T$ . However in practice, when measuring less than a few metres above the surface  $T$  can be used, as  $\Gamma$  (dry adiabatic lapse rate  $\approx 0.01 \text{ K m}^{-1}$ ) will be small relative to the magnitude and uncertainty of the temperature measurement (Monteith and Unsworth, 1990).

## 5.2 Data Treatment and Quality

Either the gradient or eddy-correlation data can be used to calculate the basic turbulence statistics and energy fluxes that are required to calculate deposition from the ozone gradient data. Therefore, as with the basic meteorological data, the gradient and eddy-correlation data sets are reviewed and combined for further analysis. The final data capture achieved for the main components is given in Table 5.15.

### 5.2.1 Gradient Data

The quality checks and filtering applied to the raw wind-speed and temperature measurements are described in Section 4.6. For the ozone measurements the first stage of processing is to remove data for periods of calibration, mast maintenance or known equipment faults. Any necessary calibration adjustments are then applied by correcting for zero then span offsets. In general the ozone analysers are very stable, requiring few adjustments. As a final check, the data set is visually compared to measurements at the Bush site. Any odd data that can be attributed to an event, such as an unusually long analyser warm-up after a power cut or maintenance on other equipment that may have interfered with the ozone for example, are discarded. There were problems with the ptfе pump

in 2003 (split diaphragms and stiff bearings) which will have affected the quality of the gradient data. However these periods could not be clearly seen in a visual examination of the measurements so all the data are retained and the subsequent filtering should remove any poorly defined gradients. The raw and final data-capture percentages are given in Table 5.15.

As discussed in Section 4.5.2, a single ozone analyser measures each height on the gradient mast in sequence, for 2 minutes in every 15. The data therefore have to be adjusted for any change in the concentration during each 15 minute period. It is assumed that concentration changes are independent of height and the top height is used as a reference. For most of the four years of measurement the inlets were sampled in the order: Top (1), bottom (5), middle (3), 2<sup>nd</sup> from top (2), 2<sup>nd</sup> from bottom (4). A correction for sequential sampling is applied using the formula:

$$\chi'_i = \chi_i - (a * \frac{\Delta\chi_{i,i-1}}{\Delta t}) \quad (110.)$$

where:  $a$  is the time period between sampling from the reference height and the current height, for example if sampling from top to bottom on the mast at Easter Bush,  $a = 5.5$  minutes.

$\frac{\Delta\chi_{i,i-1}}{\Delta t}$  is the rate of change of concentration from the previous sample ( $\chi_i$ ) to the previous ( $\chi_{i-1}$ ), so in the case of Easter Bush  $\Delta t = 15$  minutes.

Overall the correction results in a very small change in concentration of  $\pm 1\%$  on average, although on occasion it can exceed  $\pm 100\%$ . Periods when the correction is large are mainly due to non-stationarity or poorly developed turbulence and so will be filtered from the final dataset.

As 30 minute fluxes will be analysed (see Section 5.2.2) the fifteen minute values are averaged to give half-hourly ozone concentrations (only periods with two 15-minute readings are included). The wind-speed and temperature data are also averaged to 30 minutes and Table 4.6 gives the final data capture for their 30 minute averages.

### 5.2.1.1 *Turbulent Conditions and Stationarity*

As was described in Chapter 2, micrometeorological methods can only be applied when surface-layer is turbulent and so a filter must be used to ensure this condition is met. For gradient measurements tests are based on checking the

magnitude of  $u_*$ , stability conditions, and the regression coefficient of gradients. The following filter was applied to the Easter Bush data:

1. discard flux data where  $u_* < 0.08 \text{ m s}^{-1}$
2. discard flux data where  $|L| < 2 \text{ m}$  (indicates strong stability or instability)
3. discard  $\partial u / \partial [\ln(z - d) - \Psi_m] > 2.5$  (see section 5.2.5)
4. discard  $|\partial T / \partial [\ln(z - d) - \Psi_H]| > 2.0$  (see section 5.2.5)
5. flag data poor where the  $R^2$  of linear regression for wind-speed  $< 0.9$ ,  $T < 0.8$  or ozone concentration is  $< 0.60$

However, as eddy-correlation measurements allow more rigorous checks to be applied, these data are mainly used to calculate  $u_*$  and  $H$ , with any gaps are filled by the gradient results, as described in Section 5.4.2.1.

## 5.2.2 Eddy-correlation Data

Although the eddy-correlation data are analysed and stored in real-time the raw-data must be reanalysed to provide the final data set, as variables such as  $T_a$ ,  $d$  and  $z_0$  are not accurately quantified in real-time. The reanalysis is performed using another Labview programme, similar to the data acquisition and analysis programme (Section 4.5.3), written by Eiko Nemitz. Some post-measurement quality checks and filters are also applied to the data.

### 5.2.2.1 Averaging Period

As discussed in Section 2.4.4.3, the averaging period used is important, if it is too short some longer wavelength contributions to the flux may be missed. A simple way to check that the chosen time period is adequate is to examine ogive curves. These are the integral under the cospectral curve of a flux (111) and show the cumulative contribution of eddies of increasing frequency. If the curve reaches an asymptote at some period this indicates that there is no more flux beyond that point.

$$Og_{w,s}[f_0] = \int_{-\infty}^{f_0} Co_{w,s}[f]df \quad (111.)$$

where  $f$  = frequency  
 $Co_{w,s}$  = cospectra of the vertical wind velocity and a scaler  $s$

Although the measurements were initially made with a 15 minute averaging period, reanalysis was performed over 30 minutes. This was to conform to the analysis and data reporting requirements of the GREENGRASS project but proved to be an appropriate time period for the site, as well as reducing the volume of data. The ogive curves of  $wT$  and  $wCO_2$  were examined for the Gill system in 2001 to 2003 and in general all reached an asymptote by 30 minutes; the plot in Figure 5.1 shows example curves.

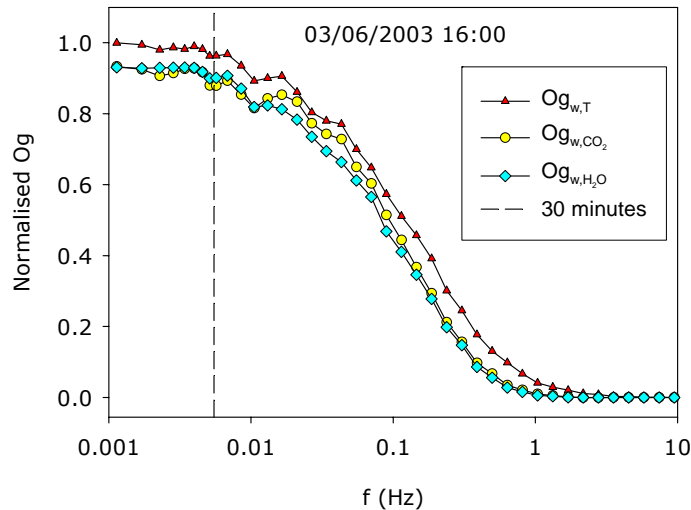


Figure 5.1. Examples of ogive curves for  $wT$  and  $wCO_2$

### 5.2.2.2 Planar Fit Co-ordinates

As discussed in Section 2.4.4.4, the data co-ordinates are rotated to align the measurements with the mean flow and correct for any tilt in the anemometer relative to the surface. The planar fit method of rotation is used and this requires the definition of the mean streamline plane by fitting a surface to a plot of  $\bar{u}$ ,  $\bar{v}$  and  $\bar{w}$ . This procedure was completed by a colleague (Claire Campbell) as part of the GREENGRASS project. At Easter Bush the sloping nature of the terrain led to planes being fitted for up to four different wind sectors and two sets of planes had to be found, one for each sonic. As the Gill remained in the same position throughout a single fit was required, however the Metek sonic was removed and reinstalled on occasion, requiring three different fits. Table 5.1 gives the fit parameters for both the sonic anemometers. The plot in Figure 5.2 shows an example of the data and fitted planes for the Gill sonic in August 2004.

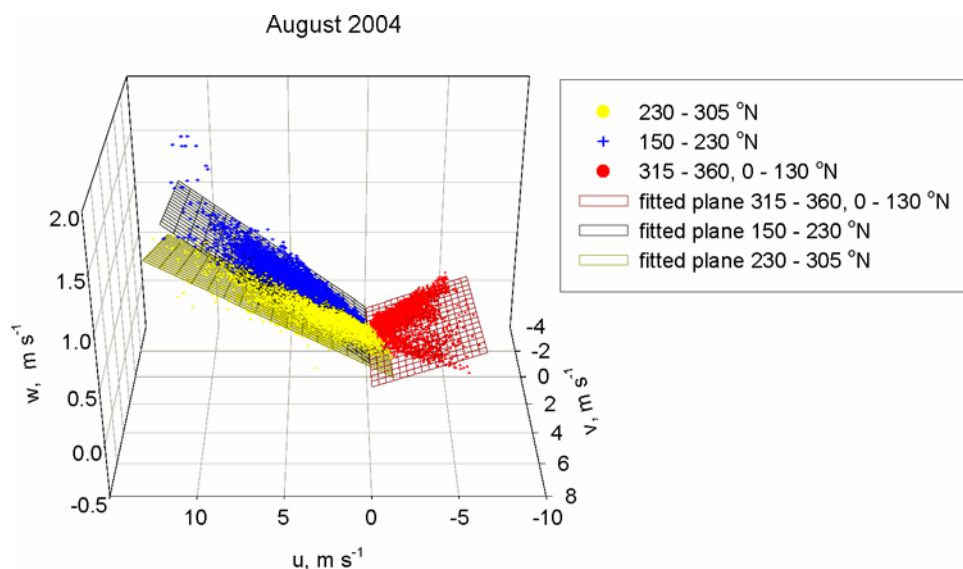


Figure 5.2. Example of the planar fit to  $\bar{u}$ ,  $\bar{v}$  and  $\bar{w}$  from the Gill sonic during August 2004.

Table 5.1 Planar fit parameters ( $b_0$ ,  $b_1$ ,  $b_2$ ) and rotation angles ( $a$ ,  $b$ )

Gill Sonic, All Data							
Wind Directions							
150 - 230		230 - 315		315 - 360, 0 - 80			
$b_0$	-0.0333	$b_0$	0.00564	$b_0$	3.20E-03		
$b_1$	0.1064	$b_1$	0.075	$b_1$	-0.0493		
$b_2$	0.0615	$b_2$	0.0822	$b_2$	0.0388		
$a$	-6.06	$a$	-4.27	$a$	2.82		
$b$	3.52	$b$	4.70	$b$	2.22		
Metek Sonic							
Up to Oct-3: Wind Directions							
280 - 110		110 - 190		190 - 280			
$b_0$	0.0663	$b_0$	0.0346	$b_0$	0.0235		
$b_1$	0.0788	$b_1$	-0.0050	$b_1$	-0.0511		
$b_2$	-0.0196	$b_2$	-0.1292	$b_2$	-0.0382		
$a$	-4.50	$a$	0.28	$a$	2.92		
$b$	-1.12	$b$	-7.36	$b$	-2.19		
From Oct-03: Wind Directions							
280 - 70		110 - 190		190 - 280		70 - 11	
$b_0$	0.0803	$b_0$	0.0597	$b_0$	0.0528	$b_0$	0.0171
$b_1$	0.0809	$b_1$	0.0241	$b_1$	-0.0295	$b_1$	0.0879
$b_2$	-0.0286	$b_2$	-0.1508	$b_2$	-0.0165	$b_2$	0.0567
$a$	-4.62	$a$	-1.37	$a$	1.69	$a$	-5.02
$b$	-1.64	$b$	-8.58	$b$	-0.95	$b$	3.25
From Apr-04: Wind Directions							
167 - 280		280 - 90		90 - 167			
$b_0$	0.0078	$b_0$	0.0498	$b_0$	0.0334		
$b_1$	-0.0440	$b_1$	0.0524	$b_1$	0.0692		
$b_2$	-0.0052	$b_2$	0.0054	$b_2$	0.0160		
$a$	2.52	$a$	-3.00	$a$	-3.96		
$b$	-0.30	$b$	0.31	$b$	0.92		

### 5.2.2.3 Flux Attenuation

As described in Section 2.4.4.3, although in theory the eddy-correlation measurements should capture all the flux-carrying turbulent eddies in practice some are missed, leading to an underestimation of the true fluxes (ie flux attenuation). In general, physical limitations of instruments and digital processing tend to put a limit on the smallest eddies that can be resolved; whereas the necessity of choosing a finite averaging period restricts the size of the largest eddies sampled. The appropriate averaging period for Easter Bush was found to be 30 minutes from examination of the co-spectral density, as described in Section 5.2.2.1 above. However, the loss of high frequency (small) eddies must also be accounted for.

Loss of the high frequency component occurs due to: slow sensor response times; noisy electronic data acquisition systems or poorly resolved analogue to digital conversion; spatial separation of the sonic anemometer and scalar sensor; and in the case of closed path instruments, damping of turbulence in the inlet tubing. In the case of the Easter Bush measurements, the methodology of Horst, (1997) was used, in which it is assumed that the major loss occurs due to the limitations of the scalar sensors, ie the LICOR CO<sub>2</sub>/H<sub>2</sub>O instruments, rather than any other factor such as the sonic anemometers response time or electronics. As we are measuring at only ~2 m above a relatively smooth canopy and the data acquisition system used was more than adequate, this assumption is valid. The co-spectra of the sensible heat flux ( $Co_{w,T}(f)$ ) can then be taken to represent the true flux and is used to correct the LICOR measurements.

The measured flux of a scalar ( $s$ ),  $\overline{w' \chi'_s}$ , is the integral over frequency ( $f$ ) of the cospectrum,  $Co_{w,T}(f)$ , and including a transfer function,  $H_s(f)$ , to account for sensor induced high frequency losses, can be written as:

$$\overline{w' \chi'_s} = \int_0^{\infty} H_s(f) Co_{w,s} df \quad (112.)$$

The transfer function of many gas analysers and temperature sensors typically takes the form of a simple low-pass RC (resistor/capacitor) filter (Bentley, 1988; Horst, 1997), with the form:

$$H_s(f) = \frac{1}{1 + (2\pi f \tau_s)^{2a}} \quad (113.)$$

where,  $\tau_s$  = sensor response time,  $a$  = filter order

This function can then be fitted to the ratio of an average measured co-spectra of  $w'T'$  with that of  $w'\chi_{CO_2}'$  or  $w'\chi_{H_2O}'$  (Figure 5.3a) and so estimate the amount of damping in  $Co_{w,s}$  relative to  $Co_{w,T}$ . The formula is then used in the reanalysis programme to adjust the covariance of  $w'\chi_{CO_2}'$  or  $w'\chi_{H_2O}'$  so that they match that of  $w'T'$  and any high frequency loss is accounted for (Figure 5.3b). As the LICORs should have a first order response the parameter 'a' was fixed at 1. The fitting procedure therefore provides an estimate of their response times which were found to be different for CO<sub>2</sub> and H<sub>2</sub>O in the closed-path LICOR7000 but the same for the open-path LICOR7500. They also vary slightly from year to year as shown in Table 5.2.

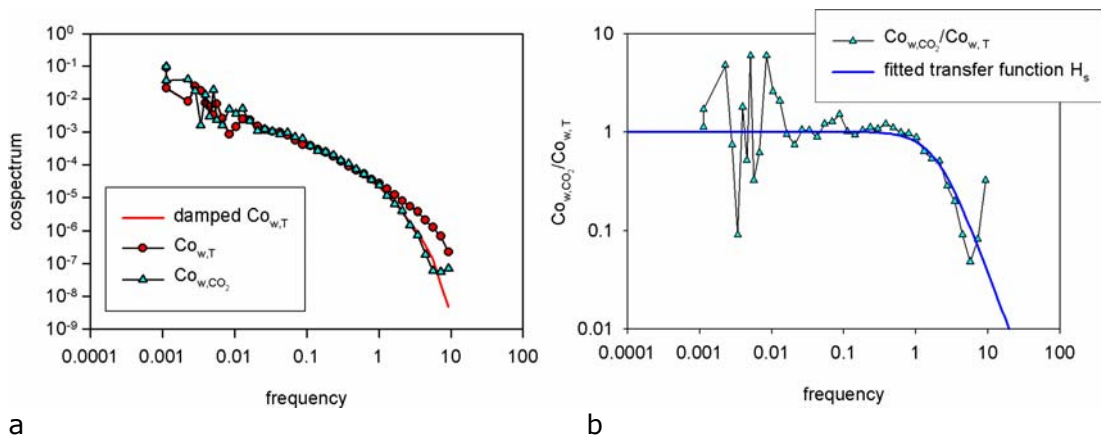


Figure 5.3. Example of attenuation correction for  $wCO_2$ .

#### 5.2.2.4 Webb Correction

When sensible and latent heat fluxes are non-zero they cause vertical gradients in the air density which result in an apparent vertical flow of air (Fowler and Dyer, 1989). Therefore if the concentration of a gas is measured as a mass per unit volume (rather than mixing ratio) it will vary because of the variation in density rather than turbulence. This effect was described by Webb, *et al.*, (1980) and can be corrected for using equation (114) below.

$$F_s = \overline{w' \chi'_s} + \left( \frac{\chi_s}{\rho} \right) \left[ \frac{\mu}{1} + \mu \sigma_{wa} (1 + \mu \sigma_{wa}) \right] E + \left( \frac{\chi_s}{\rho} \right) \frac{H}{c_p T} \quad (114.)$$

where  $\mu = 1/\epsilon$ , the ratio of the molecular weight of dry air to water vapour  
 $\sigma_{wa}$  = the ratio of the density of water vapour to the density of air ( $\rho$ )

In the case of the Easter Bush measurements the correction was only required for the CO<sub>2</sub> and H<sub>2</sub>O fluxes measured by the open-path LICOR7500, and in general was quite small.

Table 5.2 Response times used for the LICOR flux attenuation correction low-pass filter.

LICOR 7500 Date	H <sub>2</sub> O and CO <sub>2</sub> $\tau$	LICOR7000 Date	CO <sub>2</sub> $\tau$	H <sub>2</sub> O $\tau$
Jun-01	0.07	Jul-03	0.07	0.10
Jun-02	0.09	Dec-03	0.15	0.25
01/01/03 - 24/01/03	0.10	Apr-04	0.15	0.25
28/01/03 - 15/08/03	0.10			
Jun-04	0.08			

### 5.2.2.5 Turbulent Conditions - Integral Turbulence Characteristic

As with the gradient measurements, atmospheric conditions must be tested to ensure that the turbulence is sufficient to ensure the validity of the micrometeorological equations. In the case of eddy-correlation measurements flux variance similarity (where the ratio of the standard deviation of a turbulent parameter to its flux is nearly constant or a function of stability) is used to test the development of turbulent conditions (Foken, *et al.*, 2004). The integral turbulence characteristic (*ITC*) is calculated using equations (115) and (116) below. When it is less than 30% well developed turbulence can be assumed, and so 30 minute periods where it is greater than 30% at Easter Bush are discarded.

$$ITC = \left| \frac{\left(\frac{\sigma_w}{u_*}\right)_{model} - \left(\frac{\sigma_w}{u_*}\right)_{measurement}}{\left(\frac{\sigma_w}{u_*}\right)_{model}} \right| \quad (115.)$$

$$\left(\frac{\sigma_w}{u_*}\right)_{model} = 0.21 \cdot \ln\left(\frac{z_+ \cdot f}{u_*}\right) + 3.1 \quad z_+ = 1 \text{ m} \quad (116.)$$

where  $f = \text{Coriolis parameter} = 2\Omega\sin\lambda$   
 $\Omega = \text{angular velocity of the Earth} = 7.2921 \times 10^{-5} \text{ rad s}^{-1}$   
 $\lambda = \text{site latitude (radians)}$   
 Easter Bush  $\lambda = 55.86^\circ\text{N}$ ,  $f = 1.2 \times 10^{-4}$

### 5.2.2.6 Stationarity

As described in Section 2.4.4.2, various factors may cause non-stationarity so that fluxes may vary within the 30 minute averaging period, causing an error in the final result. Several different methods have been developed to test eddy-covariance measurements for non-stationarity, most of which are based on checking for variations in a parameter over the whole averaging period and sub divisions within it. For example Foken, *et al.*, (2004) proposed the following formula, where the covariance of a parameter (*s*) with the vertical wind speed

( $w$ ) over the whole period (117) is compared with that over  $M$  shorter intervals (118) containing  $N$  samples (for 30 minute averaging  $M = 6$  is recommended):

$$\overline{(s'w')}_b = \frac{1}{M(N-1)} \left[ \sum_i \left( \sum_j s_j w_j \right)_i - \frac{1}{MN} \sum_i \left( \sum_j s_j \sum_j w_j \right)_i \right] \quad (117.)$$

$$\overline{(s'w')}_i = \frac{1}{N-1} \left[ \sum s_j w_j - \frac{1}{N} \sum_j s_j \sum_j w_j \right]; \quad \overline{s'w'} = \frac{1}{M} \left[ \sum_i \overline{(s'w')}_i \right] \quad (118.)$$

The difference between the covariances is then:

$$RN_{cov} = \left| \frac{\overline{(s'w')} - \overline{(s'w')}_b}{\overline{(s'w')}_b} \right| \quad (119.)$$

and if  $RN_{cov}$  is less than 30% the time series is steady state.

An alternative approach is to consider a time integrated covariance function (essentially the inverse of the ogive function), as described by Nemitz, *et al.*, (2002) and Dutuar, (1998):

$$\Lambda(t) = \frac{1}{T} \int_0^t w' s' dt \quad \text{where } T = \text{the averaging time and } 0 \leq t \leq T \quad (120.)$$

In stationary conditions  $\Lambda(t)$  should be close to linear and so linear regression can be performed and the standard deviation of  $\Lambda(t)$  from the straight line ( $\sigma_\Lambda$ ) calculated. A relative stationarity coefficient (RSC) is then defined as:

$$RSC_s = 2\sigma_\Lambda / \overline{w' s'} \quad (121.)$$

However, at present, no thresholds for  $RSC$  have been defined so to filter a measurement data set the choice of a limiting value is slightly arbitrary.

As  $RSC$  is calculated for the Easter Bush measurements, as part of the reanalysis programme, it was used for the stationarity test on  $\tau$ ,  $H$ ,  $F_{CO2}$  and  $F_{H2O}$ . To define its threshold, the ogive function (calculated for the Gill system in 2001 and 2003) was used as a secondary test. Following the analysis of Foken, *et al.*, (2004) that  $RN_{cov}$  should be less than 30%, the relative value of  $Og_{w,s}$  should be greater than 70% at 0.0033 Hz ( $\sim 5$  minutes) ie only 30% of the flux occurs at frequencies lower than this (Nemitz, 2005). It was found from analysis of the 2001 and 2003 measurements that, in general, this condition on  $Og_{w,s}$  was met for  $\sim 90\%$  of the time so the  $RSC$  threshold was chosen to exclude  $\sim 10\%$  of the measurements every year for both the Gill and Metek systems. The values used varied from year to year and are given in Table 5.3.

Table 5.3 Thresholds for the RSC to exclude ~10% of the Easter Bush measurements

	Gill System				Metek System			
	$\tau$	H	$F_{CO_2}$	$F_{H_2O}$	$\tau$	H	$F_{CO_2}$	$F_{H_2O}$
2001	0.05	1.8	4.1	2.5				
2002	0.05	0.6	5.0	4.5	0.10	1.0	90.0	20.0
2003	0.06	1.0	4.5	3.2	0.10	1.0	20.0	4.5
2004	0.3.0	2.1	7.9	3.0	0.05	1.0	4.6	4.5

### 5.2.2.7 Number of Data Points

The reanalysis programme may on occasion run on and include too many data points in a half-hourly average or not find enough data to provide an accurate half-hourly value. However the programme does output a record of the number of data points it has used ( $N$ ) and so invalid data is removed using a simple filter that checks for  $(N_i - 25\%) < N < (N_i + 25\%)$ , where  $N_i$  is the correct number of points for a half-hourly period at the sampling frequency ie  $N_i = 37494$  for the Gill sonic sampling at 20.83 Hz.

### 5.2.2.8 Gill and Metek Systems $U$ , $u_*$ , $H$ , $e$ and $\lambda E$

Both sonic anemometers give similar results overall (Table 5.4) although the data are quite scattered, as shown in Figure 5.4. The degree of scatter is typical for measurements made by two instruments separated by more than a meter (Hogstrom and Smedman, 2004).

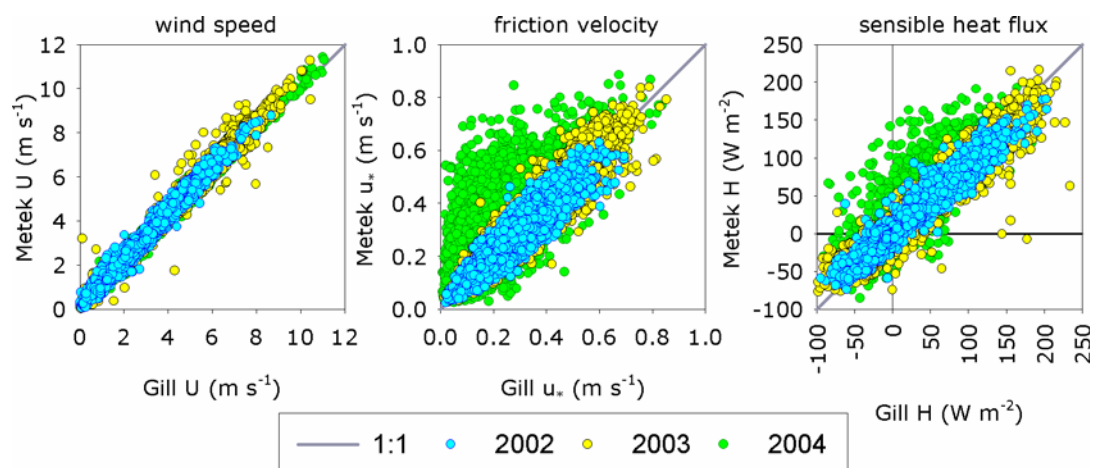


Figure 5.4. Comparison of wind-speed,  $u_*$  and  $H$  readings from the Gill and Metek sonics.

It is noted that the comparison between the two instruments is poorer in 2004 with the Gill giving a lower readings than the Metek. Table 5.5 gives the summary statistics for each data set, including the gradient system, and when all three are considered it would appear there is a problem with the Gill system

in 2004. The reasons for this require investigation but a detailed analysis is out-with the scope of this thesis.

*Table 5.4* Regression statistics for  $U$ ,  $u_*$  and  $H$  from the Metek against the Gill sonic.

		2002	2003	2004	All
U	Slope	1.05	1.07	1.04	1.06
	Intcp <sup>1</sup>	0.09	0.10	0.08	0.09
	R <sup>2</sup>	0.98	0.98	0.99	0.98
	Slope <sup>2</sup>	1.08	1.09	1.05	1.07
$u_*$	Slope	0.91	0.95	0.77	0.80
	Intcp <sup>1</sup>	0.02	0.02	0.16	0.09
	R <sup>2</sup>	0.86	0.89	0.43	0.62
	Slope <sup>2</sup>	0.96	1.00	1.30	1.06
H	Slope	0.86	0.86	0.96	0.88
	Intcp <sup>1</sup>	1.14	1.87	8.12	4.06
	R <sup>2</sup>	0.92	0.92	0.72	0.85
	Slope <sup>2</sup>	0.86	0.87	1.02	0.91

1. In units of  $\text{m s}^{-1}$  and  $\text{W m}^{-2}$  for  $U$  or  $u_*$  and  $H$  respectively

2. Slope with the intercept forced through zero.

The estimates of vapour pressure and latent heat flux,  $\lambda E$ , from the open-path LICOR 7500 must be filtered to remove periods of rainfall or high humidity which may have interfered with the infra-red beam or obscured the windows. This is done using the coefficient, known as the AGC value, reported by the instrument which indicates the degree of attenuation of the detected infra-red beam. The nominal value is 75%, although it was found to drift upwards during the four years of measurement (mainly due to degradation of the windows). A variable baseline AGC value was chosen by examining the time series of the AGC and  $\text{CO}_2/\text{H}_2\text{O}$  data discarded when this baseline was exceeded.

The closed-path LICOR 7000 was calibrated regularly and data for these periods was removed. In general the instrument operated well but some data was lost due to a fault with the pump that draws air down the inlet line and also the inlet filter becoming blocked.

Once they have been filtered for all the factors described above the water-vapour pressure ( $e$ ) measurements from the two instruments compare reasonably well (Figure 5.5, Table 5.6). The latent heat flux ( $\lambda E$ ) results do not agree so well with the closed-path instrument giving lower readings than the open-path. There were some problems with the pump used to sample with the LICOR-7000 which may have led to some attenuation of the flux in the sampling line (Lenschow and Raupach, 1991; Massman, 1991; Zeller, 2000). However, in 2004 in particular, the differences in  $u_*$  from the Gill and Metek sonics are

possibly a major factor. Given these differences<sup>12</sup> and that the LICOR-7500 was operating for most of period only its data are used to examine stomatal resistance.

Table 5.5 Summary statistics for U, u\* and H calculated from the Gill, Metek and Gradient data. All datasets area matched so they contain values for the same 0.5h.

		H, W m <sup>-2</sup>			U(1m), m s <sup>-1</sup>			u*, m s <sup>-1</sup>		
		Gill	Metek	Grad.	Gill	Metek	Grad.	Gill	Metek	Grad.
2001	Average	12.1		12.4	2.96		3.16	0.35		0.31
2002	Average	-0.7	-1.0	16.0	2.22	2.38	2.38	0.26	0.24	0.24
2003	Average	3.9	4.5	26.3	3.02	3.25	3.20	0.31	0.31	0.35
2004	Average	13.2	5.0	9.4	3.28	3.29	3.29	0.23	0.32	0.32
2001	Median	1.1		-3.2	2.77		2.94	0.34		0.29
2002	Median	-7.0	-7.8	-1.5	2.02	2.16	2.06	0.25	0.22	0.23
2003	Median	-8.9	-8.0	-3.5	2.82	3.00	2.85	0.30	0.29	0.33
2004	Median	-6.7	-6.2	-1.5	2.96	2.95	2.88	0.21	0.30	0.31
2001	1 <sup>st</sup> %tile	-81.8		-147.6	0.88		1.11	0.10		0.02
2002	1 <sup>st</sup> %tile	-72.4	-58.7	-102.2	0.50	0.32	0.91	0.04	0.04	0.01
2003	1 <sup>st</sup> %tile	-92.6	-62.9	-105.5	0.40	0.38	0.95	0.04	0.04	0.02
2004	1 <sup>st</sup> %tile	-84.7	-60.8	-107.9	0.60	0.37	0.95	0.03	0.05	0.02
2001	99 <sup>th</sup> %tile	191.3		334.6	6.59		7.01	0.73		0.74
2002	99 <sup>th</sup> %tile	136.9	117.3	428.3	5.60	5.81	5.67	0.57	0.55	0.72
2003	99 <sup>th</sup> %tile	167.6	146.1	645.3	7.76	8.03	7.93	0.70	0.70	1.02
2004	99 <sup>th</sup> %tile	121.7	140.4	299.2	8.77	8.49	8.58	0.58	0.72	0.83
2001	Stdev	55.6		87.4	1.26		1.38	0.14		0.14
2002	Stdev	40.3	34.0	114.2	1.27	1.32	1.17	0.12	0.12	0.15
2003	Stdev	344.4	45.6	132.7	1.81	1.81	1.76	0.16	0.16	0.21
2004	Stdev	1374.3	56.5	73.2	2.01	1.83	1.82	0.15	0.15	0.19

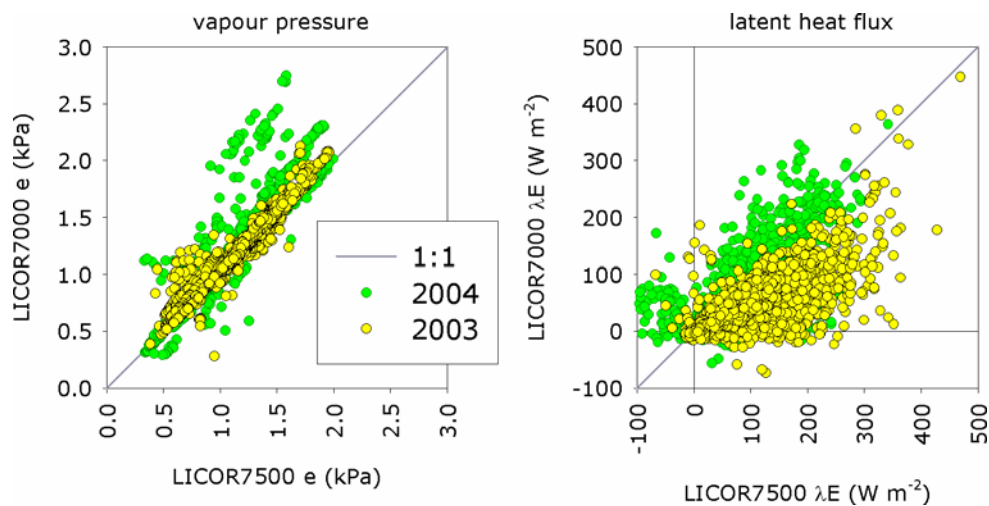


Figure 5.5. Comparison of vapour pressure and latent heat fluxes measured by the LICOR7500 and LICOR7000 and logged on the Gill and Metek systems respectively.

<sup>12</sup> The LICOR data were reanalysed by a colleague and so further collaboration is required to examine the differences in the data sets. Subsequent investigation, post submission of this thesis, has found an error in the reanalysis of the closed-path data which is currently being rectified.

Table 5.6 Regression statistics for  $e$  and  $\lambda E$  from the closed-path (LICOR7000) against the open-path (LICOR75000) instrument.

	$e$ (kPa) 2003	$e$ (kPa) 2004	$e$ (kPa) All	$\lambda E$ (W m <sup>-2</sup> ) 2003	$\lambda E$ (W m <sup>-2</sup> ) 2004	$\lambda E$ (W m <sup>-2</sup> ) All
Slope	0.98	1.13	1.06	0.44	0.66	0.50
Intcpt	0.06	-0.06	-0.01	-1.39	6.71	5.15
R <sup>2</sup>	0.95	0.86	0.89	0.56	0.52	0.47

### 5.2.3 Wind Direction and Fetch

Both the gradient and eddy-correlation data must be filtered to ensure measurements are representative of the grassland. The first stage of filtering simply removes data from the direction of the fence line, 130 to 150°N and 305 to 315°N. This effectively accounts for disruptions caused by other instrumentation and the cabin, as they are all located along the fence line. As these wind-directions occur infrequently only 2.7% of data is removed over all.

The second stage of filtering checks the flux footprint to ensure measurements are representative of the required fetch. The extent of an upwind area affecting a flux measurement changes with wind direction, wind speed, surface roughness and stability. Schmid, (2002) reviewed the existing footprint modelling approaches and provides a summary of the development of the footprint concept. The footprint is defined as "the upwind area most likely to affect a downwind flux measurement at a given height  $z$ ". Schuepp, *et al.*, (1990) provided analytical solutions of the diffusion equation and defined the cumulative normalized contribution to the flux measurement ( $CNF$ ) at height  $z$  and upwind distance  $x_L$  as:

$$CNF(x_L) = \int_0^{x_L} f(x) dx = \int_0^{x_L} \frac{U}{u_* k x^2} \exp\left(\frac{-U}{k u_* x}\right) dx = \exp\left(-\frac{U}{k u_* x_L}\right) \quad (122.)$$

where  $U$  is defined as the average wind-speed between the surface and the measurement height  $z$  assuming a logarithmic wind-speed profile, ie neutral conditions.

The integrand,  $f(x)$  is the cross-wind integrated flux at a distance  $x$  and height  $(z-d)$ . Although the footprint is actually 3 dimensional this 1-dimensional form is adequate for assessing a relatively simple site such as Easter Bush. Where more complex terrain is being considered, with changes in vegetation type for example,  $f(x)$  may be expanded into 2 or 3 dimensions with more detailed modelling. To account for non-neutrality Schuepp, *et al.*, (1990) also proposed an approximate adjustment to equation (81) of multiplying  $U/u_*$  by the momentum stability correction function ( $\Phi_m$ ).

Various other studies have developed footprint analysis methods, for example: Haenel and Grunhage, (1999); Horst and Weil, (1994); Kljun *et al.*, (2004); Leclerc *et al.*, (1997); Savage *et al.*, (1996). Kormann and Meixner, (2001) proposed an analytical model for the footprint, which more directly accounts for non-neutral stratification. They calculate the CNF at upwind distance  $x_L$  and height  $(z-d)$  using:

$$CNF(x_L) = \int_0^{x_L} f(x) dx = \int_0^{x_L} \frac{1}{\Gamma[\mu]} \frac{\xi^\mu}{x^{1+\mu}} e^{-\xi} dx \quad (123.)$$

where  $\Gamma[\mu]$  is the value of the standard Gamma function at  $\mu$

$$\xi = \frac{U_c}{K_c} \frac{(z-d)^r}{r^2}$$

$$\mu = (1 + m)/r$$

$r = 2 + m - n$ , known as the "shape factor"

$$m = \frac{u_* \Phi_m}{kU[z-d]}, \text{ which is the exponent in the wind-speed profile}$$

equation:

$U[z-d] = U_c (z-d)^m$ ,  $U_c = U/(z-d)^m$ ,  $U[z-d]$  is found from equation (35) and  $\Phi_m$  from equation (32) or (33) depending on stability conditions

$$n = \begin{cases} \frac{1}{1 + 5 \frac{L}{(z-d)}} & \text{for } L > 0 \\ \frac{L}{1 - 24 \frac{(z-d)}{L}} & \\ \frac{L}{1 - 16 \frac{(z-d)}{L}} & \text{for } L < 0 \end{cases} \quad \text{where } L \text{ is found from (11'),}$$

and  $n$  is the exponent in the eddy-diffusivity equation:

$$K_H [z-d] = K_c(z-d)^n, K_c = K_H/(z-d)^n, \text{ is found from equation (26)}$$

This method (Kormann and Meixner, 2001) is applied to the Easter Bush field site by calculating *CNF* for each 30 minute average from the gradient and eddy-correlation systems.  $x_L$  is the distance from the measurement point to the field boundary in the current wind direction. The Excel analysis spreadsheet and coordinates used to define the field dimensions were taken from an earlier experiment that studied ammonia fluxes at the site (Figure 5.6, Milford, 2004). Data are excluded when *CNF* < 65% which results in excluding 10% to 30% of the data each year. The plots in Figure 5.7 show the *CNF* results from the Gill (2001 to 2003) and Metek (2004) by wind direction. For much of the time the *CNF* is between 60 to 80% in the main wind sectors.

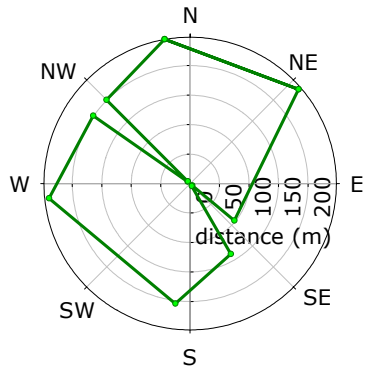


Figure 5.6. Dimensions (m) of the fetch at Easter Bush.

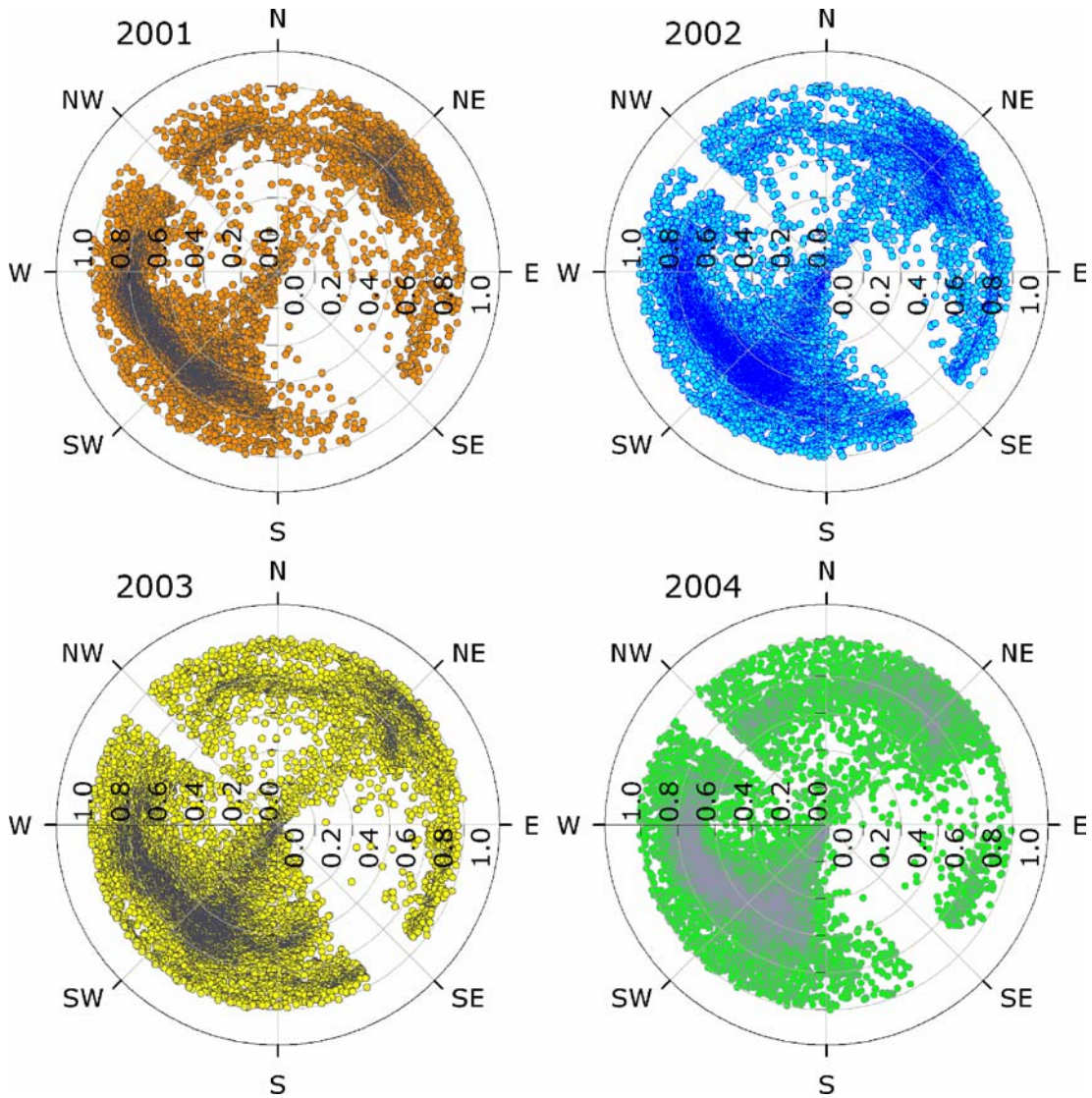


Figure 5.7. The CNF from the Gill sonic in 2001 to 2003 and Metek in 2004, plotted by wind direction.

## 5.2.4 Displacement Height, $d$

In neutral conditions the log-linear wind-speed profile should be a straight line. If  $d$  is overestimated the profile will curve downwards whereas if it is underestimated the profile will curve upwards (Thom, 1975). In the absence of profile measurements it is common to assume that  $d = 2/3 h$ , where  $h$  is the canopy height. However where measurements are available the correct value for  $d$  can be found by optimising the linearity of the profile in neutral conditions.

At Easter Bush, data for strongly neutral conditions ( $|Ri| < 0.007$ ) were selected from the filtered data set, giving 4321 profiles. Each profile was optimised by varying  $d$  from  $0.01h$  to  $0.99h$  and finding the value that gave the highest  $R^2$  value for the linear regression of  $u$  with  $\ln(z-d)$ , the effect of varying  $d$  is shown for a typical profile in Figure 5.8. The value found for  $d$  varied between the full test range, with  $2/3h$  and  $0.99h$  occurring most frequently (50% and 42% of profiles respectively). Examination of the results found no controlling factors and so the standard value of  $2/3h$  was used in the analysis of ozone deposition.

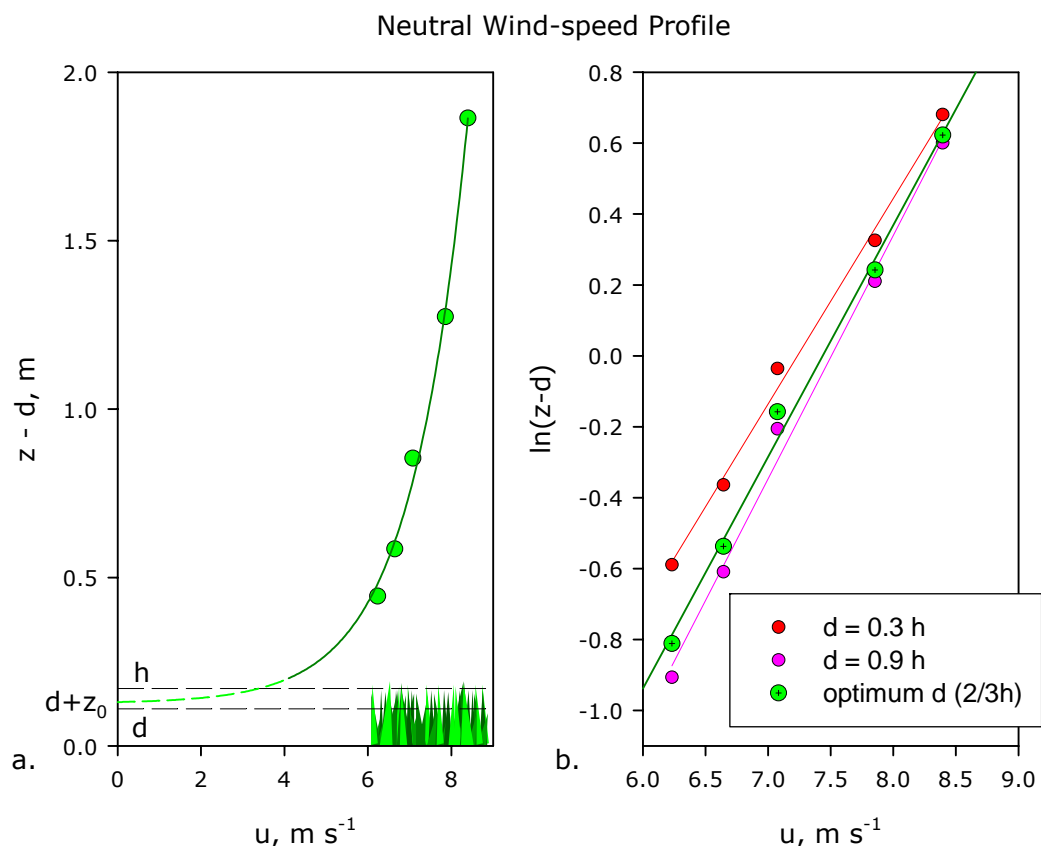


Figure 5.8. (a) An example of a neutral wind-speed profile (14/05/2002 18:00) and (b) the effect of different  $d$  values on the log-linear profile.

### 5.2.5 Storage Correction

The storage error described in Section 2.4.4.2 is corrected for using formula (124) and is applied to the ozone fluxes. It could also be applied to the water-vapour and carbon-dioxide fluxes but in these cases the correction is so small it is insignificant, for example for the water-vapour flux it is only 0.001% on average.

$$F_{\chi'} = F_{\chi} + \frac{\Delta\chi_{i,i-1}}{\Delta t} \quad (124.)$$

where  $t$  is the averaging time in seconds,  
ie for the Easter Bush data 1800 s.

In general the correction is also small for the ozone fluxes, averaging 1.2% (median 0.03%) but when fluxes are small ( $\pm 4 \text{ ng m}^{-2} \text{ s}^{-1}$ ) it can be exceed 100%.

### 5.2.6 O<sub>3</sub>/NO<sub>x</sub> or VOC Chemistry

The tests outlined above check for any non-stationarity in the measurements no matter the source. For the ozone data there is the possibility that some periods of non-stationarity are due to chemical reactions occurring on the same time-scale as the fluxes. As the Easter Bush field-site is generally in a quite clean atmosphere, it was assumed that other chemicals were normally at too low concentration to interfere with the ozone and they were not measured onsite.

Concurrent measurements of NO<sub>x</sub> are made at the nearby Bush site which would allow this assumption to be checked, however fully QA/QC'd data for the whole period are not available at this time. The NO<sub>x</sub> measurements at the site became part of the national monitoring network in 2003 and so the ratified data from the National Air Quality Archive<sup>13</sup> are considered here.

The wind-rose plots in Figure 7.9a and b show the annual median NO and NO<sub>2</sub> concentrations measured at Bush from the 9<sup>th</sup> of October 2003 to the end 2004. There are no large peaks visible which would indicate significant vehicle emissions, although concentrations are slightly enhanced from the direction of the major urban areas (Edinburgh to the N-NE, Dalkeith to the NE-E, and Penicuik to the S-SW). Overall, NO<sub>x</sub> concentrations are low, particularly in the main wind-sector, and being well-mixed throughout the surface layer they do not significantly affect the results.

---

<sup>13</sup> <http://www.airquality.co.uk/>

Some studies have measured VOC emission from freshly cut grass (de Gouw, *et al.*, 1999; Kirstine and Galbally, 2004) which raises the possibility of interference when the fields were cut for silage. There are indications of such emissions in the time series of ozone deposition as will be examined in Section 5.6.

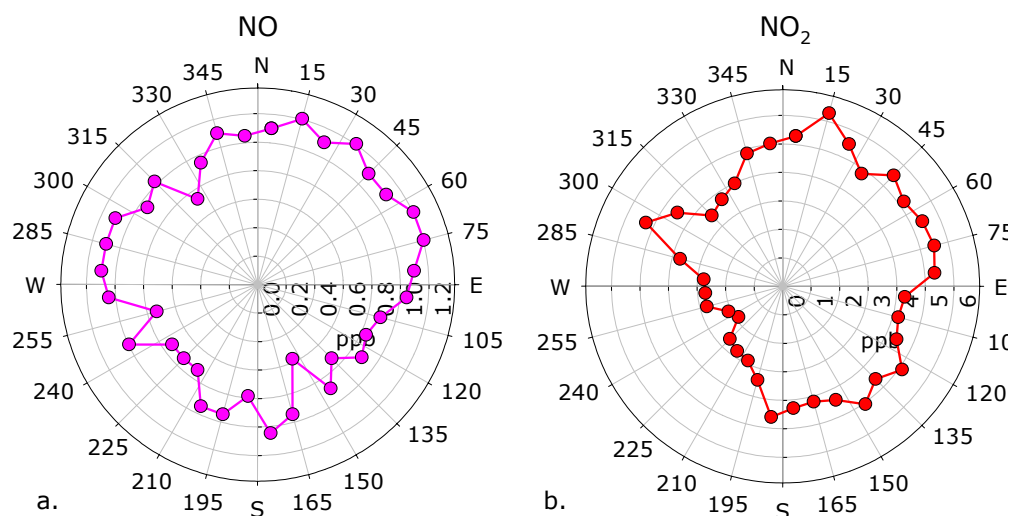


Figure 5.9. Median (a) NO and (b) NO<sub>2</sub> concentrations by wind-direction at Bush. Calculated from hourly gas concentration data and wind direction measurements at Bush.

### 5.2.7 Gradient vs. Eddy-correlation Results for $u_*$ and $H$ .

It is possible that for some of the time the upper or lower points on the gradient mast are out-with the surface-layer. An additional filter was applied to the gradient data to exclude the most extreme points by examining gradients ( $\partial u / \partial [\ln(z-d) - \Psi_m]$  and  $\partial T / \partial [\ln(z-d) - \Psi_H]$ ) using  $\Psi$  calculated from the eddy-correlation data. The range of values found indicated that for  $u$  the gradient should be less than 2.5 and for  $T$  the absolute value of the gradient should be less than 2. This resulted in the exclusion of only a small percentage of the data (0.28% of  $u$  and 0.30% of  $T$ ) and the resulting data sets are compared below.

In general the gradient method tends to underestimate  $u_*$  and overestimate  $H$  with respect to both the eddy-correlation data sets, although at times they agree very well. Table 5.7 gives the annual regression statistics and Table 5.5 the summary statistics for each data set; in general the Gill and gradient are most closely matched but as with the Metek and Gill, the agreement is poorer in 2004. The plots in Figure 5.10 show the regression plot of each fully filtered data set. It is likely that differences in each sensors' fetch is responsible for some of these differences but a comprehensive study of micrometeorological methods is not

within the scope of this thesis and so the reasons for these differences are not examined further.

The Gill data are used in preference to the Metek then gradient in 2001 to 2003 and in 2004 the Metek is used in preference to the gradient then the Gill. Ozone fluxes calculated with each data are compared in Section 5.4 below.

## 5.2.8 Closing the Energy Balance

As discussed in Section 2.4.3, the energy balance of the surface can be used to indicate the quality of the measurements. If the systems are performing well ( $H + \lambda E$ ) should equal  $(R_n - G)$ , and a plot of  $(H + \lambda E)$  against  $(R_n - G)$  should form a straight line with slope 1 and intercept 0. However this criterion becomes less certain during periods when energy fluxes are low and so times when  $St < 50$   $W m^{-2}$  are excluded.

Table 5.7 Regression coefficients for the Gradient  $u^*$  and H in comparison to the Gill or Metek sonics

Year	Statistic	Gradient vs Gill		Gradient vs Metek	
		$u^*$	H	$u^*$	H
2001	Slope	0.78	1.21		
2002	Slope	0.80	1.00	0.81	1.21
2003	Slope	0.89	1.06	0.74	1.18
2004	Slope	0.65	1.54	0.75	1.26
2001	$R^2$	0.59	0.55		
2002	$R^2$	0.58	0.59	0.47	0.56
2003	$R^2$	0.58	0.50	0.48	0.48
2004	$R^2$	0.24	0.60	0.47	0.67
2001	Intercept	0.05	0.80		
2002	Intercept	0.05	3.36	0.07	1.77
2003	Intercept	0.08	8.61	0.13	7.71
2004	Intercept	0.22	9.70	0.09	0.26
2001	Slope <sup>2</sup>	0.89	1.21		
2002	Slope <sup>2</sup>	0.92	1.01	0.99	1.22
2003	Slope <sup>2</sup>	1.08	1.09	1.05	1.22
2004	Slope <sup>2</sup>	1.33	1.54	0.96	1.26

1. In units of  $m s^{-1}$  and  $W m^{-2}$  for  $u^*$  and H respectively
2. Slope with the intercept forced through zero.

Considering the combined eddy-correlation and gradient data, for some periods this criteria is met with the ratio of  $(H + \lambda E)/(R_n - G)$  being close to 1, but overall the slope of regression for the is 0.82 (with a small intercept of 1.57) indicating that ~20% of the energy is not being accounted for. As may be expected there is some seasonal variation, with more periods close to closure in the summer months when fluxes are larger. Given that losses of 10-30% are

typical for most field experiments this figure of 20% shows that we have a good quality data set and the bulk of the data can be taken to be reliable.

The plots in Figure 5.11 show the annual regression of each system and although there is some scatter and a few large outliers, in general the points are close to the 1 to 1 line, indicating that each system is performing well. Despite having some of the largest outliers, with the exception of 2002 the gradient is best overall as indicated by the regression statistics in Table 5.8.

*Table 5.8* Linear regressions statistics for the energy balance,  $(H + \lambda E)$  vs  $(Rn - G)$ , from each measuring system and the combined data set, at Easter Bush. In all cases  $\lambda E$  is given by the open-path LICOR7500. The slope with intercept forced through zero is given in brackets.

<b>2001</b>	<b>Gradient</b>	<b>Gill</b>	<b>Metek</b>	<b>Combi.</b>
Slope	1.09 (1.04)	0.90 (0.91)	ND	0.91 (0.92)
R <sup>2</sup>	0.57	0.66	ND	0.66
Intercept	-12.32	3.12	ND	2.45
<b>2002</b>	<b>Gradient</b>	<b>Gill</b>	<b>Metek</b>	<b>Combi.</b>
Slope	0.77 (0.78)	0.88 (0.88)	0.89 (0.83)	0.79 (0.78)
R <sup>2</sup>	0.01	0.56	0.56	0.02
Intercept	1.23	0.26	-13.97	-2.41
<b>2003</b>	<b>Gradient</b>	<b>Gill</b>	<b>Metek</b>	<b>Combi.</b>
Slope	1.06 (0.94)	0.87 (0.83)	0.85 (0.80)	0.80 (0.82)
R <sup>2</sup>	0.45	0.63	0.62	0.84
Intercept	-27.72	-9.77	-11.31	16.13
<b>2004</b>	<b>Gradient</b>	<b>Gill</b>	<b>Metek</b>	<b>Combi.</b>
Slope	0.88 (0.92)	0.60 (0.67)	0.68 (0.80)	0.88 (0.79)
R <sup>2</sup>	0.47	0.26	0.37	0.51
Intercept	9.63	15.88	27.04	-16.38
<b>All Data</b>	<b>Gradient</b>	<b>Gill</b>	<b>Metek</b>	<b>Combi.</b>
Slope	0.95 (0.91)	0.82 (0.83)	0.77 (0.80)	0.82 (0.82)
R <sup>2</sup>	0.09	0.52	0.50	0.12
Intercept	-9.00	2.30	8.47	1.57

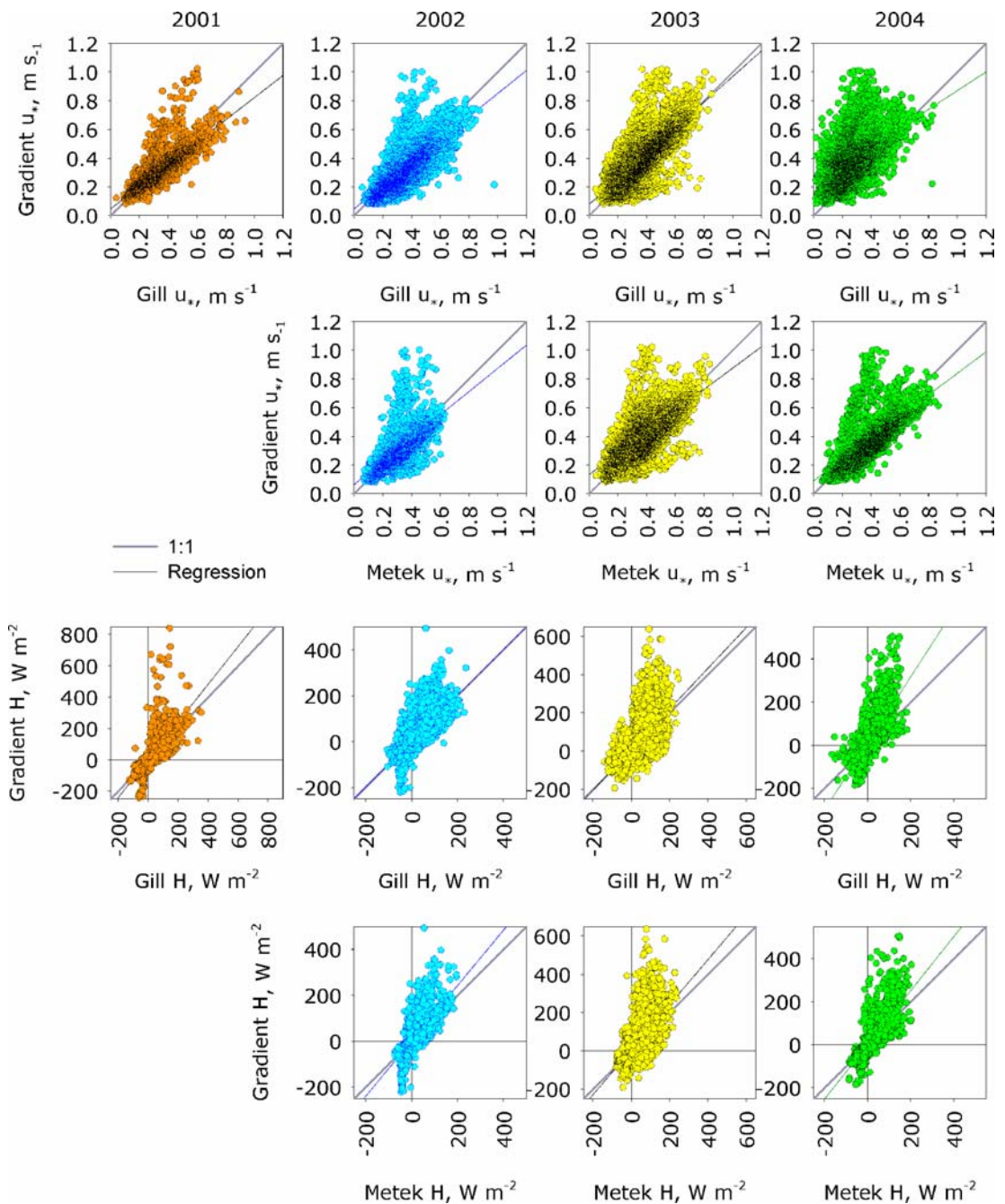


Figure 5.10. Comparison the  $u_*$  and  $H$  measured by the gradient and eddy-correlation systems.

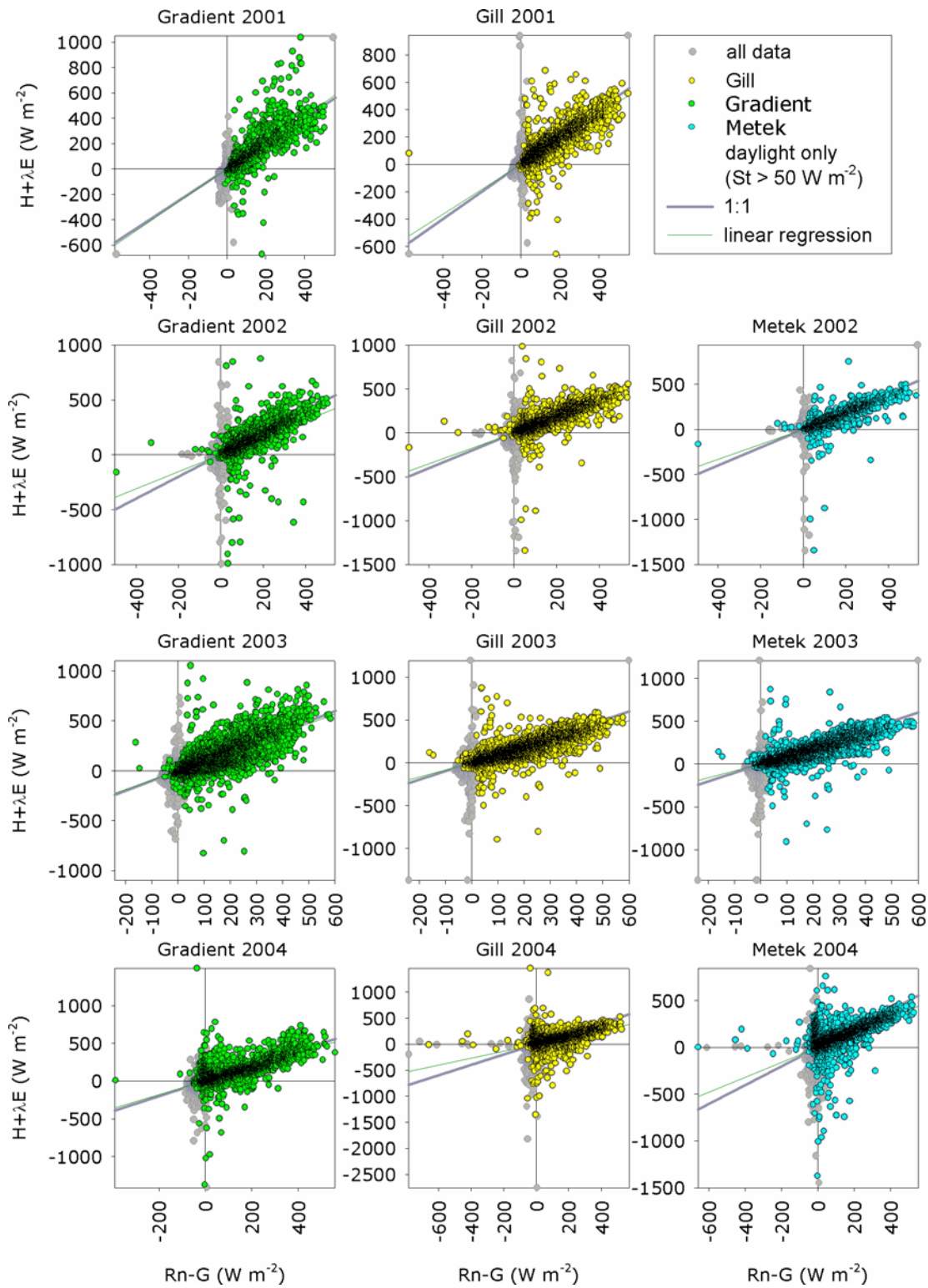


Figure 5.11. Annual energy balance regression plots for each measurements system.

### 5.3 Aerodynamic Resistance, $R_a$ and Boundary Layer Resistance, $R_b$

The aerodynamic atmospheric resistance,  $R_a$  and boundary layer resistance,  $R_b$  are calculated using equations (56) and (59) respectively with the combined data set. As is common in micrometeorological studies  $R_a$  is reported for the standard height of 1 m (i.e.  $z - d = 1$ ). Results, summarised in Tables C9 and C10, are typical of measurements over fairly smooth vegetation, varying with meteorology and surface roughness. Both  $R_a$  and  $R_b$  are log-normally distributed, as shown in Figure 5.12, and so median values are used when summarising the 30 minute data.

The plot in Figure 5.13 shows the diurnal cycle of  $R_a$  as a median for the whole data set and as seasonal, October to March and April to September, medians.  $R_a$  is at a minimum ( $\sim 25 \text{ s m}^{-1}$ ) during the day when the atmosphere is most turbulent and increases ( $\sim 35 \text{ s m}^{-1}$ ) at night when winds tend to be calmer. During the summer when the grass is long and sensible heat fluxes large,  $R_a$  reaches a low daytime minimum whereas in the winter the surface is smoother and the diurnal cycle is small.

The magnitude of  $R_b$  partly depends on the entity being considered, for example the  $R_b$  for ozone tends to be larger than that for water-vapour as the lighter water molecules more readily diffuse through the sub-laminar boundary layer. As with  $R_a$ , the magnitude of the diurnal cycle varies with the season as surface characteristics and meteorology change (Figure 5.14).

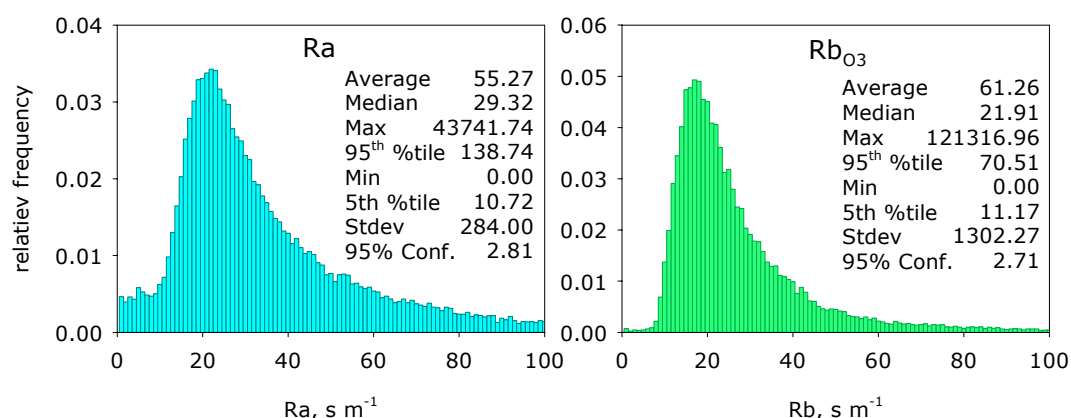


Figure 5.12. Normalised frequency distributions for (a)  $R_a$  and (a)  $R_{b_{O_3}}$ .

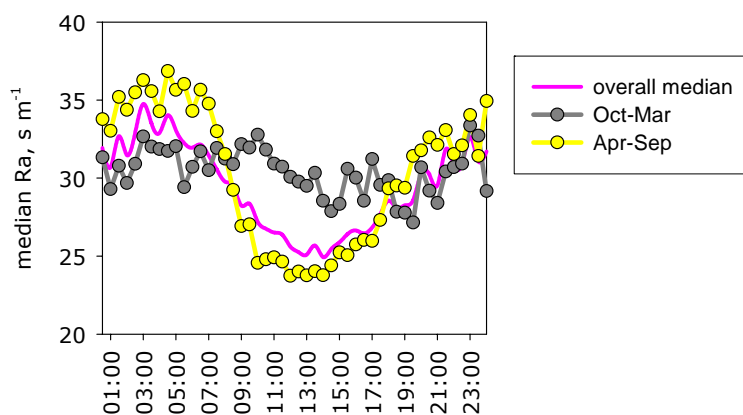


Figure 5.13. Diurnal cycles of (a) overall median and (b) seasonal median  $R_a$  for Easter Bush (2001 to 2004).

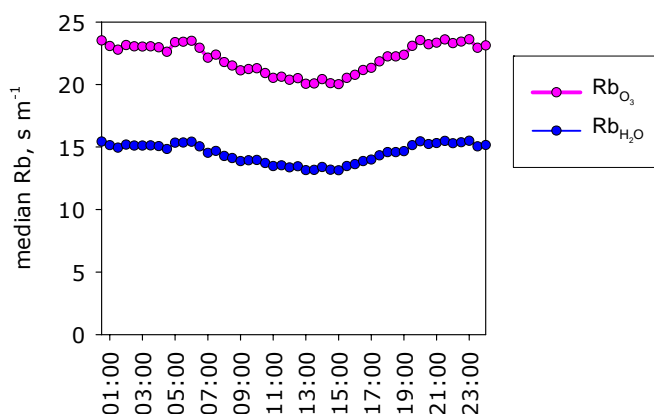


Figure 5.14. Diurnal cycles of overall median  $Rb_{O_3}$  and  $Rb_{H_2O}$  at Easter Bush.

## 5.4 Ozone Concentration and Flux

There are few measurements of deposition to grassland in literature and the majority of those are for fairly short periods of a few days to months. Table 5.9 summarises the available literature and their results.

### 5.4.1 Ozone Concentrations

As discussed in Chapter 1 many factors influence ambient ozone concentrations and many of them are evident in the measurements at Easter Bush. Such a comprehensive data set would allow a thorough and lengthy description of the site characteristics, however only the main features are outlined below.

The Easter Bush site is generally classified as rural although  $NO_x$  emissions from Edinburgh, and the surrounding roads, do have a very small influence. It is also quite exposed on the edge of the Pentland Hills and so it is often quite windy.

Table 5.9. Summary of publications discussing field measurements of ozone deposition to grassland.

Reference	Location	Canopy	Measurements
Garland and Derwent, 1979	Southern England	Chalk grassland, 10 cm tall	Gradient 9 <sup>th</sup> 12 September 1974
<i>Results</i>	Day-time $v_{dO_3}$ 5.8 mm s <sup>-1</sup> , $R_{CO_3}$ 120 s m <sup>-1</sup> Night-time $v_{dO_3}$ 2.9 mm s <sup>-1</sup> , $R_{CO_3}$ 250 s m <sup>-1</sup>		
Colbeck and Harrison, 1985	Stodday, Lancaster, England	Grass, 5- 15 cm tall	Gradient January to October 1983
<i>Results</i>	$v_{dO_3}$ 0.8 to 9.1 mm s <sup>-1</sup>		
Pederson, <i>et al.</i> , 1995	San Joaquin Valley, California, USA	Dry annual grassland (senescent & desiccated, LAI 0.18, 0.20 m tall), soil & rock	4 weeks of eddy-correlation O <sub>3</sub> fluxes etc in July – August 1990 and 1991
<i>Results</i>	very little diurnal variation $v_{dO_3}$ ~0 to 5 mm s <sup>-1</sup>		
Padro, 1996; Padro, <i>et al.</i> , 1994	As above	As above	As above but for 15 <sup>th</sup> July to 3 <sup>rd</sup> August, 1991
<i>Results</i>	$v_{dO_3}$ night-time ~0.5, day-time ~2 mm s <sup>-1</sup>		
Massman, <i>et al.</i> , 1994	As above	As above	As above but for 8 <sup>th</sup> July to 7 <sup>th</sup> August, 1991
<i>Results</i>	$F_{O_3}$ ~-100 ng m <sup>-2</sup> s <sup>-1</sup> to -1000 ng m <sup>-2</sup> s <sup>-1</sup> $v_{dO_3}$ <0.5 to ~5.5 mm s <sup>-1</sup>		
Grunhage, <i>et al.</i> , 1994	Braunschweig, Germany	Intensively managed grassland (grazing and silage)	Gradient May – September 1990 and 1991
<i>Results</i>	$v_{dO_3}$ night-time 0.25 – 2 mm s <sup>-1</sup> , day-time 3 – 10 mm s <sup>-1</sup>		
Horvath, <i>et al.</i> , 1994	Hungary	fescue grass (dry and brown in Sept.)	Gradient 19 <sup>th</sup> – 30 <sup>th</sup> June 1993 3 <sup>rd</sup> – 28 <sup>th</sup> Sept. 1990
<i>Results</i>	$v_{dO_3}$ summer day-time 5.3 mm s <sup>-1</sup> , night-time 1.2 mm s <sup>-1</sup> $v_{dO_3}$ autumn 1.7 mm s <sup>-1</sup>		
Meyers, <i>et al.</i> , 1998	Sand Mountain, Alabama, USA	Pasture (fescue, blue grass, white colver), well watered, LAI 1.0 to 2.3, 10 – 30 cm tall	Eddy correlation 15 <sup>th</sup> April – 13 <sup>th</sup> June 1995
<i>Results</i>	$F_{O_3}$ ~-220 ng m <sup>-2</sup> s <sup>-1</sup> ng m <sup>-2</sup> s <sup>-1</sup> $v_{dO_3}$ 2.4 mm s <sup>-1</sup> (~1 to 4 mm s <sup>-1</sup> )		

Table 5.9. Summary of publications discussing field measurements of ozone deposition to grassland.

Reference	Location	Canopy	Measurements
De Miguel and Bilbao, 1999	Castile & Leon, Central Spain	Green grassland (~40 cm tall)	Gradient 6 days (19-24 <sup>th</sup> July 1995)
<i>Results</i>	$F_{O_3} \sim -100 \text{ ng m}^{-2} \text{ s}^{-1}$ to $-1600 \text{ ng m}^{-2} \text{ s}^{-1}$ $v_{dO_3} < 1$ to $14 \text{ mm s}^{-1}$ $R_{CO_3} \sim 25 \text{ s m}^{-1}$ to $200 \text{ s m}^{-1}$		
Sorimachi, <i>et al.</i> , 2003	Beijing, China	Summer – green grass (~10 cm tall) Winter – senescent grass	Gradient 10 days in September and November 2001
<i>Results</i>	Summer $F_{O_3} -100 (\pm 70) \text{ ng m}^{-2} \text{ s}^{-1}$ , $v_{dO_3} 2 (\pm 2) \text{ mm s}^{-1}$ , $R_{CO_3} 340 (\pm 420) \text{ s m}^{-1}$ Winter $F_{O_3} -80 (\pm 60) \text{ ng m}^{-2} \text{ s}^{-1}$ , $v_{dO_3} 4 (\pm 3) \text{ mm s}^{-1}$ , $R_{CO_3} 270 (\pm 450) \text{ s m}^{-1}$		
Pio, <i>et al.</i> , 2000	Aveiro, Portugal	Grassland Growth period – autumn to spring (Nov-Apr) Dry/senescent - July to August	Eddy-correlation November 1994 to October 1995
<i>Results</i>	$v_{dO_3} 1 \text{ mm s}^{-1}$ – night, $2-5 \text{ mm s}^{-1}$ – day $R_{CO_3} 500 \text{ s m}^{-1}$ – night, $200 \text{ s m}^{-1}$ – day		
Droppo, 1985	Champaign, Illinois, USA	Grassland (~25 30 cm tall)	Gradient and eddy-correlation 2 days (June 26 <sup>th</sup> -27 <sup>th</sup> 1982)
<i>Results</i>	Average deposition velocities 26 <sup>th</sup> June-82: $1.9$ to $4.1 \text{ mm s}^{-1}$ 27 <sup>th</sup> June-82: $3.8$ to $6.2 \text{ mm s}^{-1}$		

Seasonal mean diurnal cycles of ozone observed at the site are plotted in Figure 5.15 and show both influences. In the autumn to spring months (October to March)  $O_3$  concentrations are slightly reduced in the “rush-hour” periods as weather conditions cause  $NO_x$  concentrations to be slightly higher than average. This small effect of urban emissions can also be seen in a wind-rose plot of the seasonal data (Figure 5.16) as the autumn-spring average is slightly lower in the “urban” wind directions (as indicated by Figure 5.9). During the summer months (April to September) the diurnal cycle is typical of a mid-altitude rural location (Coyle *et al.*, 2002), with a fairly pronounced mid-afternoon peak (see Section 1.3.2) and concentrations are almost constant with wind direction (Figure 5.16).

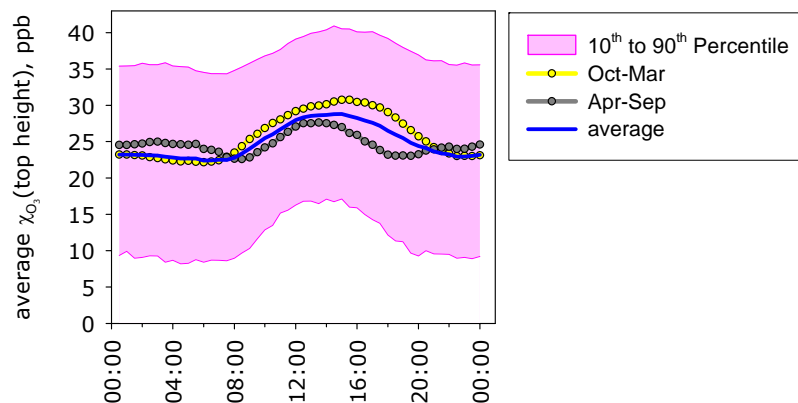


Figure 5.15. Average diurnal cycle in ozone concentrations observed at Easter Bush during October to March and April to September, 2001 to 2004; Calculated using the 30 minute average concentrations from the top height of the gradient mast.

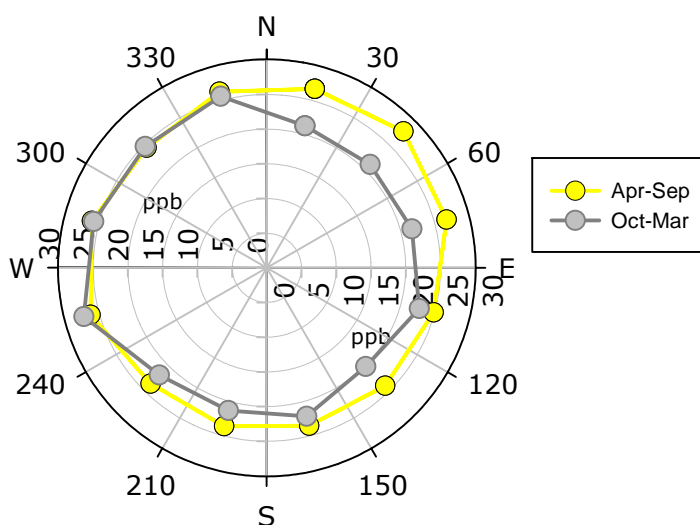


Figure 5.16. Average ozone concentrations in 15° wind sectors during April to September and October to March 2001 to 2004; Calculated using the 30 minute average concentrations from the top height of the gradient mast..

Upland or coastal sites where the diurnal cycle is generally small tend to have almost normal frequency distributions; urban sites, where concentrations are regularly depleted by NO emissions, tend to have distributions skewed towards being log-normal; intermediate sites in rural or suburban areas usually have more pronounced diurnal cycles and distributions skewed slightly towards lower values. The frequency distribution at Easter Bush is almost a normal form, with a slight skew to lower values, which would be expected from the location. The plots in Figure 5.17 show the overall frequency distribution in comparison to the equivalent normal distribution as (a) a curve and (b) accumulated. In Figure 5.18 the annual frequency distribution of the concentrations measured at each height on the gradient mast are plotted. Although these data have not been

filtered for stability conditions, they show the propensity of ozone to be removed at the surface as the bottom height tends to measure slightly lower concentrations than the top.

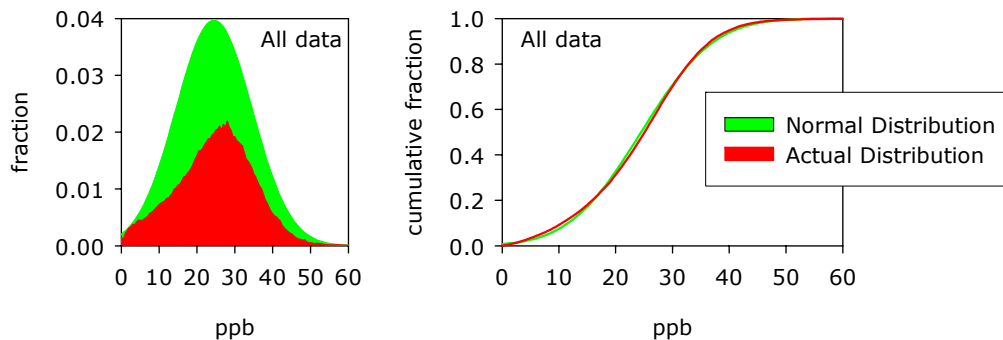


Figure 5.17. Overall frequency distribution of 30 minute ozone concentrations measured at the top height of the gradient mast.

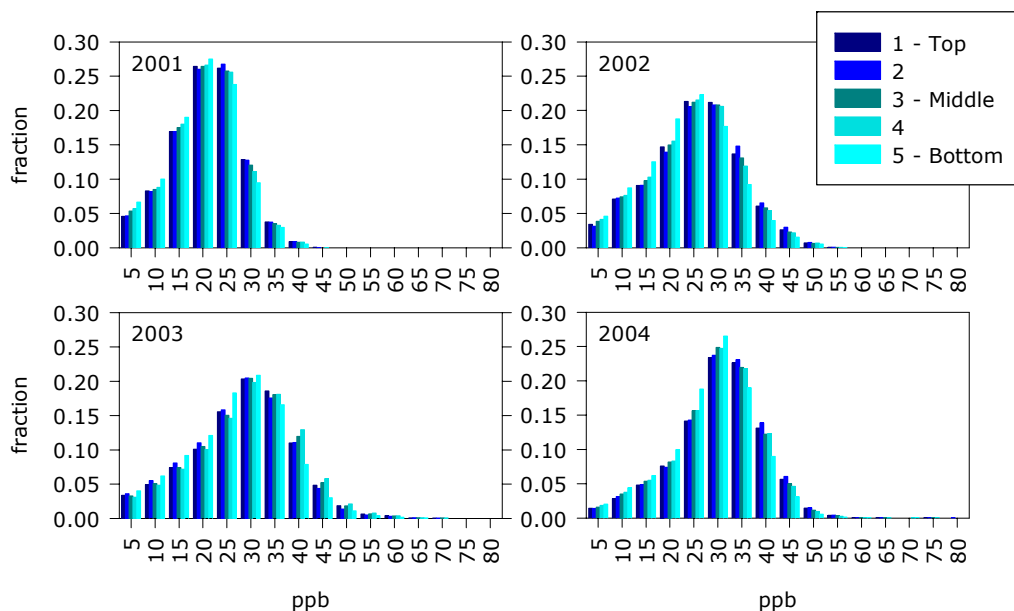


Figure 5.18. Annual frequency distributions of 30 minute ozone concentrations at each height on the gradient mast.

Some inter-annual differences are also indicated by the annual frequency distributions. An examination of the seasonal cycle and the number of ozone episodes (concentrations above 50 – 60 ppb) helps explain some of the variation. Figure 5.19a shows a plot of the annual monthly averages from the top height and the time series of 30 minute averages is plotted in Figure 5.19b: in 2001 there is not enough data to comment on the form of the cycle but there are few episodes; 2002 was particularly cold and wet so summer-time photochemical was suppressed, few episodes occurred and concentrations peaked in April which is typical of northerly background ozone concentrations;

2003 was very warm and fairly sunny so there was plenty photochemical ozone production which is reflected in the frequent episodes and later peak in June; in 2004 concentrations were generally slightly higher than in the previous years but there were fewer episodes, indicating that this was due to background concentrations being enhanced over the whole region, this is also reflected in the peak occurring in April as this is typical of northerly background cycles. There is an upward trend in the monthly average concentrations of  $ca. 0.06 \text{ ppb } y^{-1}$  which is typical of rural sites in the UK and Europe (NEG-TAP, 2001, Simmonds *et al.*, 2004; Vingarzan, 2004). It is possible that this trend is part of the general increase observed in background concentrations in the Northern hemisphere but more detailed analysis and comparison to other sites would be required to confirm this.

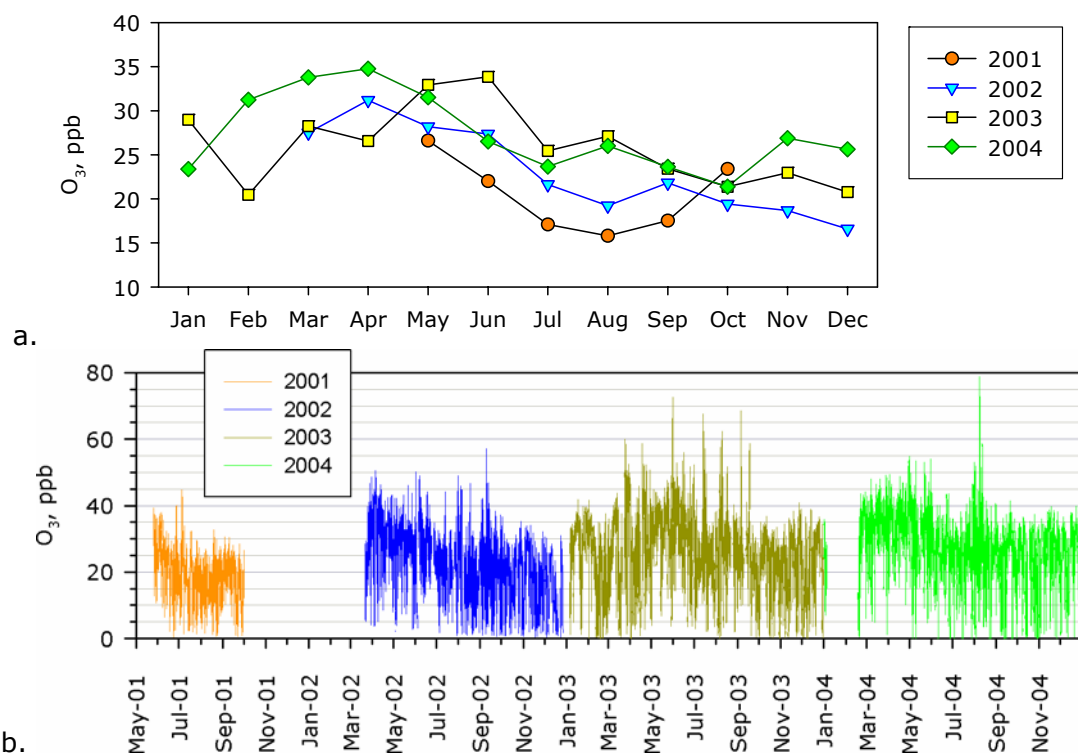


Figure 5.19.(a) Monthly average concentration measured at the top height on the gradient mast every year. (b) Time series of 30 minute average concentrations measured at the top height.

The ozone concentrations measured at Easter Bush are therefore typical of its location, indicating a fairly exposed rural site with minimal interference from local pollution sources. There is also some evidence in the data of increasing background ozone concentrations, due to a combination of a general increase in Northern hemisphere background concentrations and a local reduction in  $NO_x$  emissions.

## 5.4.2 Total Ozone Fluxes

The ozone fluxes are calculated from each estimate of  $u_*$  and  $H$  using the methodology described in Chapter 2. To allow comparison with the literature fluxes are reported at 1 m and in the standard unit of  $\text{ng m}^{-2} \text{s}^{-1}$ . Ozone concentrations must be converted from ppb to  $\mu\text{g m}^{-3}$  and although it is common to use a constant conversion factor (eg  $1 \text{ ppb} = 2 \mu\text{g m}^{-3}$  at  $20^\circ\text{C}$  and  $1013 \text{ hPa}$ ), the data are available to calculate a more accurate factor using equation (125) below.

$$\chi_{\mu\text{g m}^{-3}} = \chi_{\text{ppb}} \frac{M}{22.41} \frac{T_0}{T_a} \frac{p_0}{p} \quad (125.)$$

where  $M$  = molecular weight of ozone,  $48 \text{ g mol}^{-1}$   
 $T_0$  = reference temperature  $273.15 \text{ K}$   
 $p_0$  = reference pressure  $1013 \text{ hPa}$   
 $T_a$  = ambient air temperature in  $\text{K}$  (see section 5.6)  
 $p$  = atmospheric pressure in  $\text{hPa}$  (see section 5.6)

This gave a conversion factor that varied from 1.97 to 2.28 and averaged 2.11.

### 5.4.2.1 Final Filtering and Combination of Data Sets

As described above we have three data sets that can be used to calculate the flux from the ozone gradient measurements. The time series plots in Figure 5.20 (a), (b) and (c) show the raw 30 minute average fluxes calculated from each system with the filtered time series superimposed. The filtering applied at this stage accounts for wind direction, fetch, turbulence and stationarity, which removes some of the positive and more extreme negative values.

By convention, deposition is given as a negative flux and emission as a positive value, however for ozone we would not expect to see any emission. Small positive values ( $\leq 50 \text{ ng m}^{-2} \text{ s}^{-1}$ ) are observed fairly often in all three data sets ( $\sim 3\%$ ,  $1.5\%$ ,  $8\%$  and  $2\%$  of values in 2001 to 2004 respectively) but these occur when the measurements are least certain and the standard error exceeds  $100\%$ . There are some periods where far larger positive fluxes are found, particularly during 2003 which had over 1000 values over  $50 \text{ ng m}^{-2} \text{ s}^{-1}$  whereas, at most, 87 were recorded in other years. As we do not expect to see ozone emission, these points may be due to unusual advection (or other meteorological events) reversing the ozone gradient although in 2003 they are most likely due to problems with the equipment. It would be interesting to investigate these periods in detail but as it is the surface deposition processes that are being

examined here all negative resistances or deposition velocities are simply excluded from the final analysis.

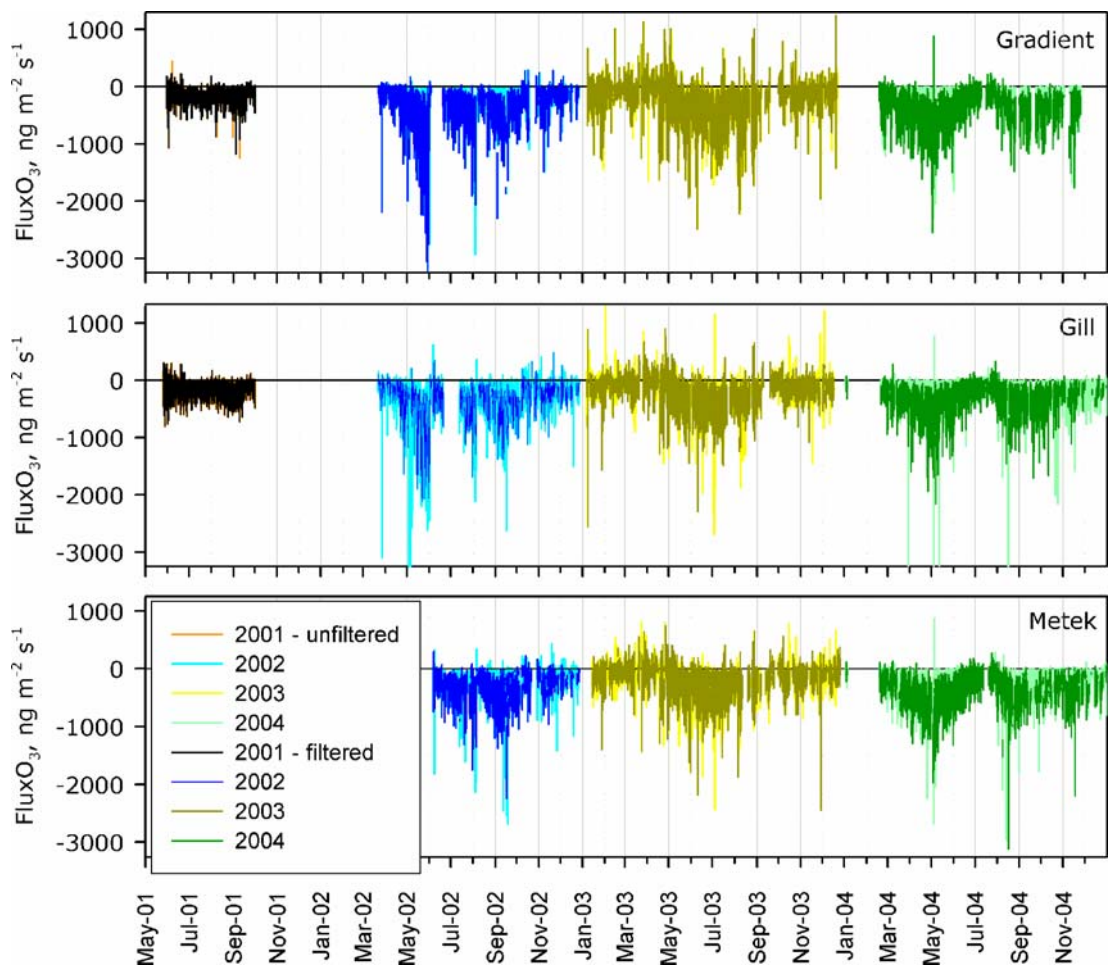


Figure 5.20. Time series of 30 minute average ozone flux calculated from (a) the gradient system (b) the Gill  $u_*$ , H etc and ozone gradient and (c) the Metek  $u_*$ , H etc and ozone gradient.

The gradient data were flagged as being uncertain when the  $R^2$  of their linear regression was lower than a specified value (Section 5.2.1.1). If these data are discarded then the majority of the large positive fluxes and remaining negative outliers are also removed, however large amounts of potentially useful data are also lost (~70% of available data in 2001, 2002, 2004 and 95% of 2003). This filter is particularly harsh in 2003 as the ozone gradient was affected by a low flow rate and/or leaking valves in a faulty pump for some of the time. The criteria could be relaxed in 2003 but to avoid an excessive loss of data overall, a more subjective filtering was applied: obvious erroneous values that were identified by the  $R^2$  filter are discarded, such as the positive spike in the gradient data on the 05/04/2004 11:00, a total of 21, 5 and 14 points were removed from the gradient, Gill and Metek data sets respectively; the average maximum

positive value recorded by all three systems in 2001, 2002 and 2004 is then  $318 \text{ ng m}^{-2} \text{ s}^{-1}$  and so all values greater than this are discarded. This filtering does slightly bias the data but as the large positive values will not be used for the analysis of surface deposition processes it is not significant.

Considering all four years of data as a whole it appears that the fluxes are very high in 2002, particularly prior to the first silage harvest, although they follow the expected seasonal and diurnal patterns. The filtering processes did not identify any particular problem with the gradient during this period and a thorough examination of the data did not identify a specific cause. However it was noted that there was a step change in the ozone gradient value on the 18<sup>th</sup> of October 2002. At this time the system was changed to allow the measurement of  $\text{SO}_2$  gradients which requires the inlet tubing to be heated (avoiding the loss of  $\text{SO}_2$  to any condensation within the tubing). A new valve box was installed with all stainless steel solenoid valves; previously two ptfе valve had been used to switch the bottom/middle and 2<sup>nd</sup> top/2<sup>nd</sup> bottom heights. Although no leaks were detected, the ptfе valves are more prone to such problems than the stainless steel type so it is possible that there was a fault. Also, from around the end of April the canopy height was more uncertain than usual due to very uneven growth in the fields, so it was possible that the bottom inlet was within the roughness sublayer. Reanalysis of the data, excluding measurements from the bottom inlet from the 20/04/2002 to 18/10/2002, systematically reduces the flux values (Figure 5.21). Although there are still some unusually large outliers and the gradient is less well defined, this data set is used in the subsequent analysis.

A comparison of these three fully filtered data sets gives results consistent with those for  $u_*$  and  $H$ , in that the gradient and Gill are better correlated during 2001 to 2003 than in 2004, and the Metek is in closer agreement with the gradient in 2004 (Table 5.5). Thus the data are combined in the following order of precedence: 2001 to 2003, Gill, Metek then gradient; 2004, Metek, gradient then Gill. The final data set is plotted in Figure 5.22 as a time series of 30 minute values and a monthly summary box plot. Some annual variation is immediately obvious, in that fluxes in 2001 appear to be smaller than in later years and larger in 2004. Unlike in 2002, reanalysis of the data by removing heights from the gradient did not indicate a systematic problem and the data are retained as they are. There are also unusually small fluxes during July and August 2004,

although overall values are larger (Figure 5.22). A statistical summary and some general features of the data are described in the following paragraphs while the seasonal differences (and some other features of the data) will be discussed in more detail in Chapter 6.

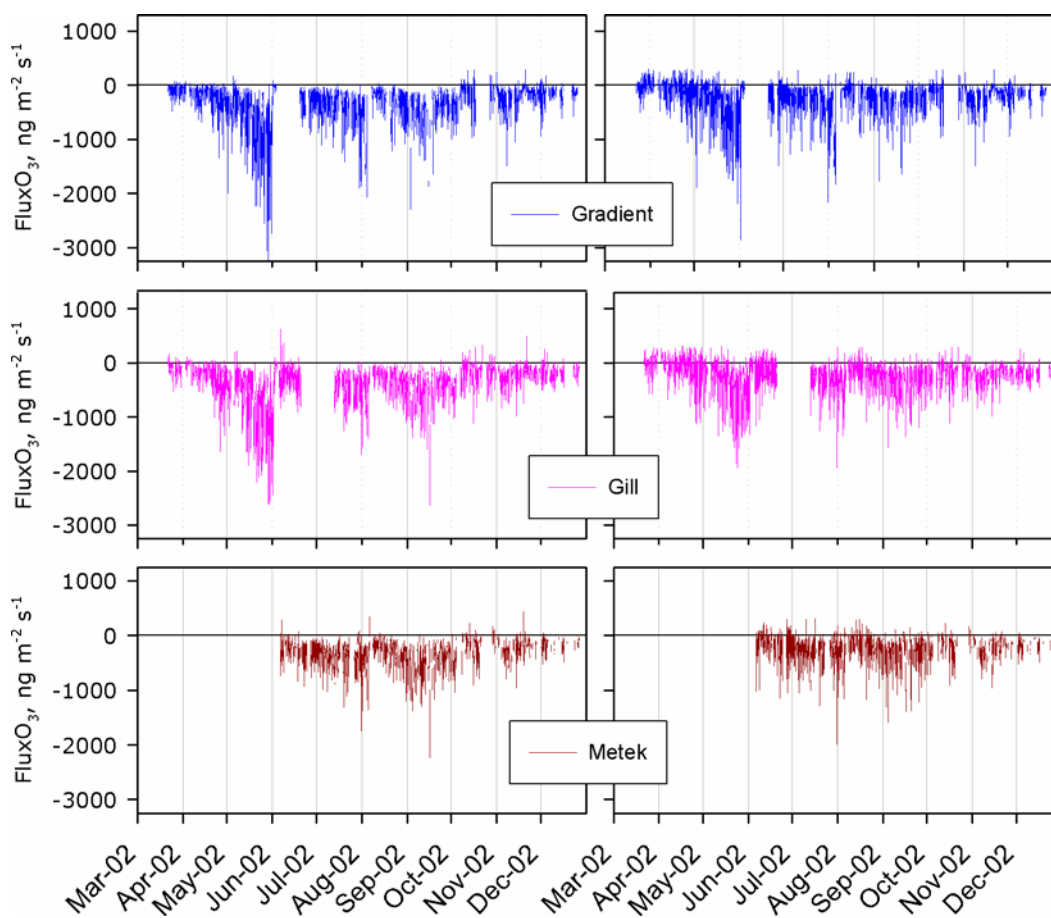


Figure 5.21..Comparison of original and revised 2002 flux measurements from each system.

Table 5.10. Regression statistics for the three ozone flux data sets.

	Year	Slope	R <sup>2</sup>	Intercept	Slope <sup>1</sup>
<b>Grad. - Gill</b>	2001	0.87	0.80	-36.30	1.02
<b>Grad. - Gill</b>	2002	0.88	0.91	-67.72	0.96
<b>Grad. - Metek</b>	2002	0.79	0.82	-75.68	0.93
<b>Gill - Metek</b>	2002	0.94	0.93	-13.54	0.97
<b>Grad. - Gill</b>	2003	0.73	0.87	-28.12	0.78
<b>Grad. - Metek</b>	2003	0.70	0.87	-27.43	0.75
<b>Gill - Metek</b>	2003	0.95	0.96	-4.00	0.96
<b>Grad. - Gill</b>	2004	0.68	0.71	-39.22	0.75
<b>Grad. - Metek</b>	2004	0.82	0.79	-70.30	0.94
<b>Gill - Metek</b>	2004	0.95	0.78	-73.54	1.11

1. Slope with the intercept forced through zero.

The final ozone flux data set is log-normally distributed with an overall median of  $-175 \pm 2.4 \text{ ng m}^{-2} \text{ s}^{-1}$ , as shown in Figure 5.23a. The ozone concentration is calculated from interpolation of the ozone gradient to the reference height of 1 m, and (as for the measured concentrations) the result is normally distributed as shown in Figure 5.23b. Therefore, when summarising the 30 minute results, the median of ozone fluxes and arithmetic mean of ozone concentrations are used.

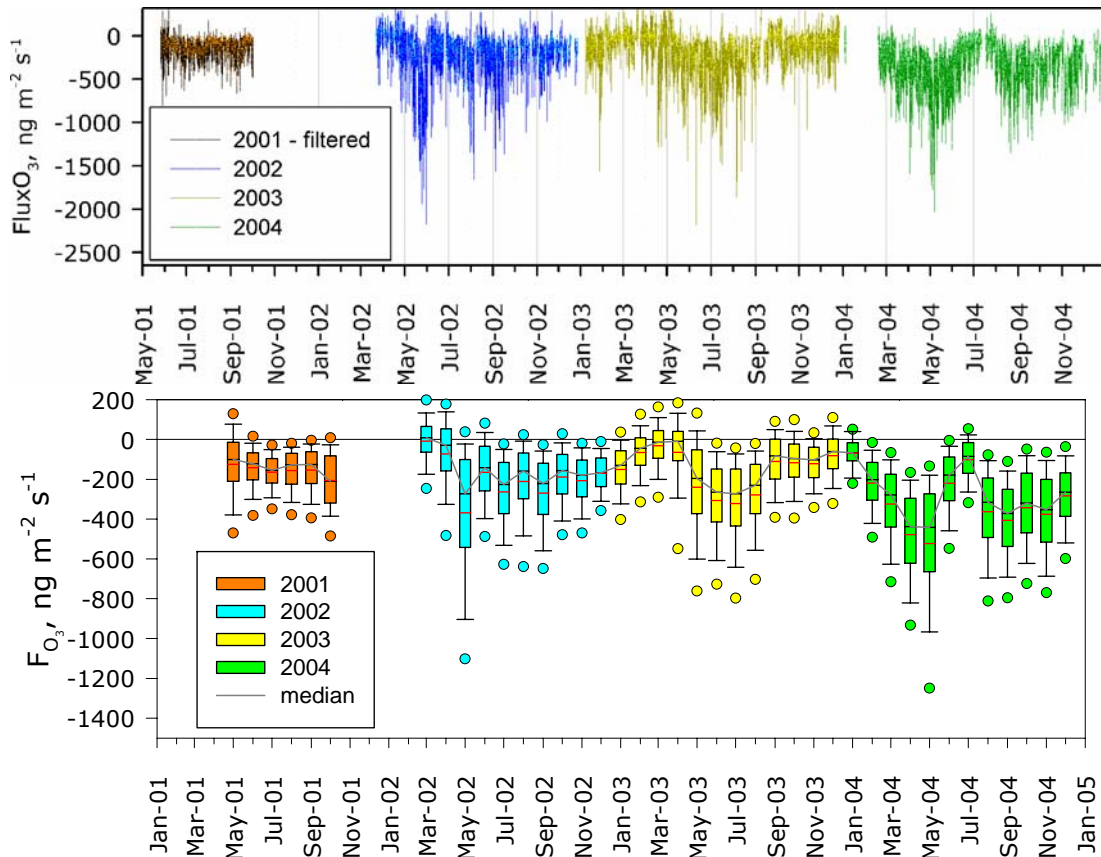


Figure 5.22. Final combined time series (Gill, Metek then gradient in 2001 to 2003 and Metek, gradient then Gill in 2004).

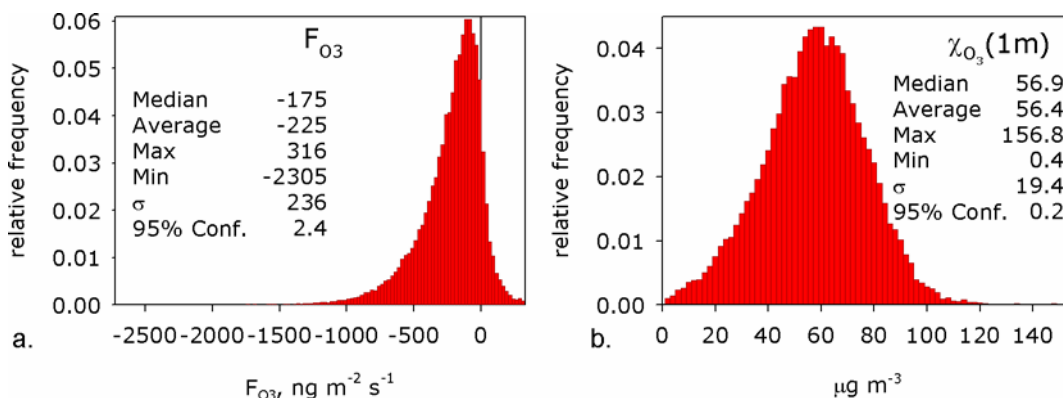


Figure 5.23. Frequency distribution of (a) the final ozone flux data set and (b) the ozone concentration at 1m.

The diurnal cycle in ozone flux is typical of that observed in many studies, with an afternoon peak and reduced night-time deposition. As with the diurnal cycle in ozone concentration this is partly driven by changes in atmospheric stability but vegetation also plays a part. During the summer months when vegetation is most active and stomatal uptake of ozone is significant, the diurnal cycle is most pronounced whereas during the winter when aerodynamic and non-stomatal resistances are the main controlling factors, the cycle is smaller.

The plots in Figure 5.24 a to d show annual-seasonal median fluxes, as Oct01-Mar02 only contains a few points it is not plotted. The Apr-Sep 2001 fluxes are noticeably smaller than in the following years and in 2004 both seasons are larger.

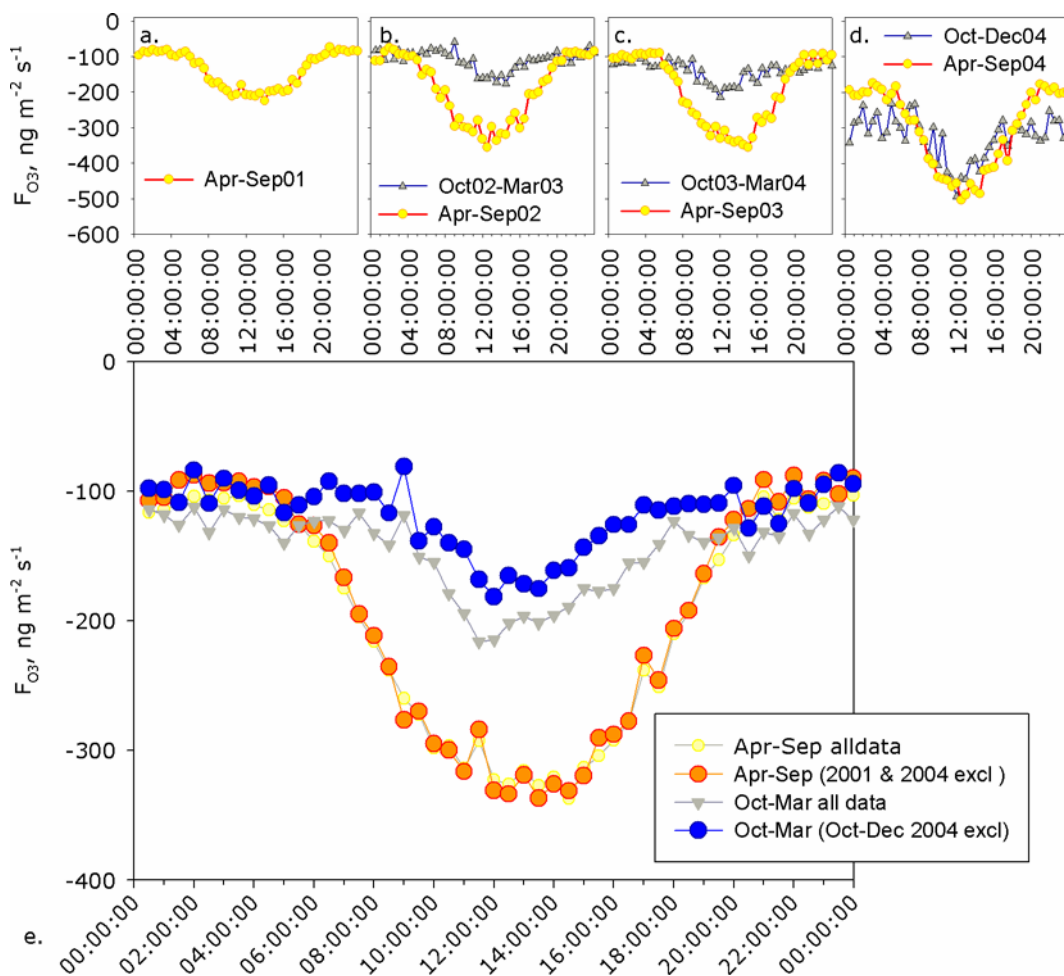


Figure 5.24. (a) to (d) Individual seasonal mean diurnal cycles in the total ozone flux. (e) Overall median cycles in the ozone flux, the small pale symbols show the results using all the data whereas the large symbols exclude the unusual seasons in 2001 and 2004.

Figure 5.24e therefore shows overall seasonal cycles for the whole dataset and with these unusual periods excluded, although this has little impact in the

summer months. In the summer day-time fluxes peak at *ca.*  $-336 \text{ ng m}^{-2} \text{ s}^{-1}$  whereas in the winter the minimum is *ca.*  $-180 \text{ ng m}^{-2} \text{ s}^{-1}$ , a change of  $\sim 50\%$ . During the night-time fluxes decline to similar values of *ca.*  $-95 \text{ ng m}^{-2} \text{ s}^{-1}$  in both seasons. The day-time versus night-time differences are considered in more detail below, in the context of examining the non-stomatal deposition process.

### 5.4.3 Total Canopy Resistance and Deposition Velocity

The total canopy resistance to ozone deposition ( $R_c$ , in units of  $\text{s m}^{-1}$ ) and the deposition velocity ( $v_{dO_3}(1\text{m})$  in units of  $\text{mm s}^{-1}$ ) are calculated using equations (63) and (52) respectively. As a final check on the validity of the measurement  $v_{d\text{max}}$  is calculated from:

$$v_{dO_3\text{max}} = \frac{1000}{Ra + Rb_{O_3}} \quad (126.)$$

Any periods where  $v_{dO_3}$  exceeds  $v_{d\text{max}}$  are excluded from the final analysis, as are negative values of  $v_d$  or  $R_c$ , which avoids the conceptual inconsistency of ozone emission.

The frequency distribution of  $v_d$  and  $R_c$  is log-normal (as shown in Figure 5.25a and b). Figures 5.26 and 5.27 summarise the data while Tables C13 and C14 give the monthly statistics. As with the ozone flux, the diurnal cycles of  $R_c$  and  $v_d$  reflect changes in atmospheric stability and vegetation. These seasonal variations in  $R_c$  and  $v_d$  are considered in more detail in Chapter 6 in the context of factors controlling the surface exchange process of ozone.

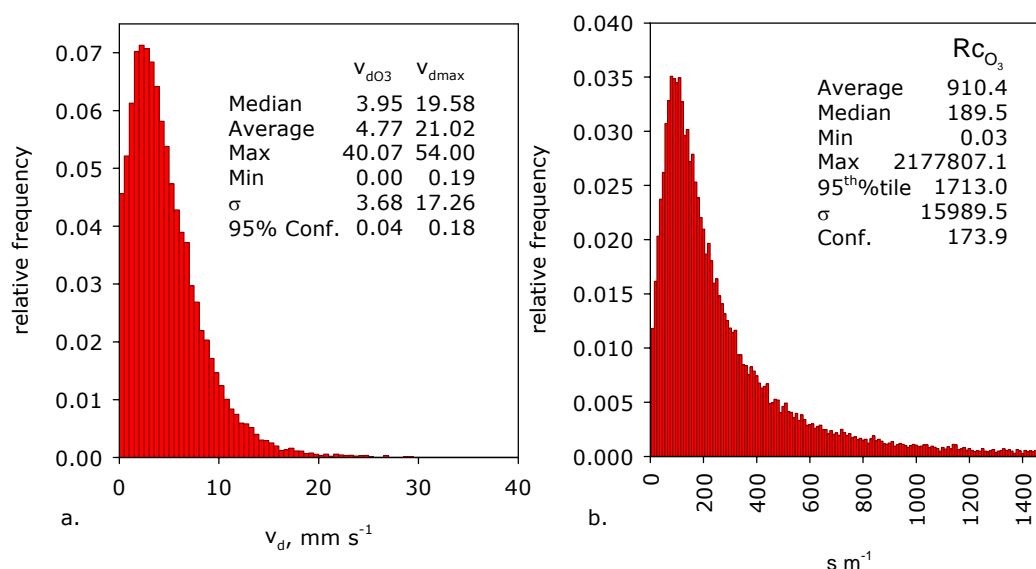
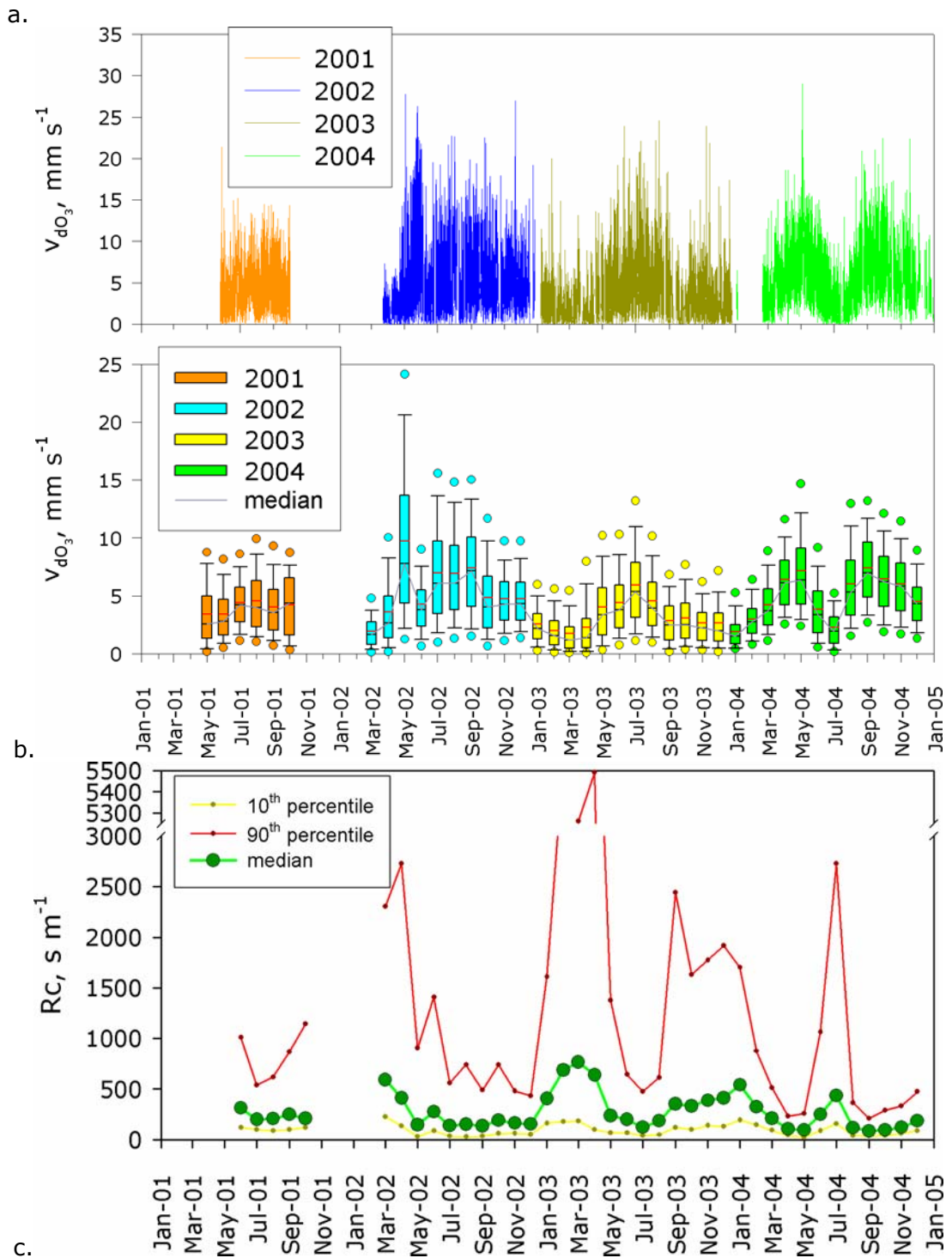


Figure 5.25. The normalised frequency distributions of (a) deposition velocity  $v_{dO_3}$  and (b) total canopy resistance,  $R_{cO_3}$ .



c. Figure 5.26. (a) Time series of 30 minute median  $v_d$ , (b) monthly box plot of  $v_d$  (the box indicates the 75<sup>th</sup> and 25<sup>th</sup> percentiles; the black bar is the median; the red bar is the average; the whiskers the 90<sup>th</sup> and 10<sup>th</sup> percentiles; the dots are the outliers at the 95<sup>th</sup> and 5<sup>th</sup> percentiles) and (c) monthly median  $R_c$  with the bars indicating the 90<sup>th</sup> and 10<sup>th</sup> percentiles.

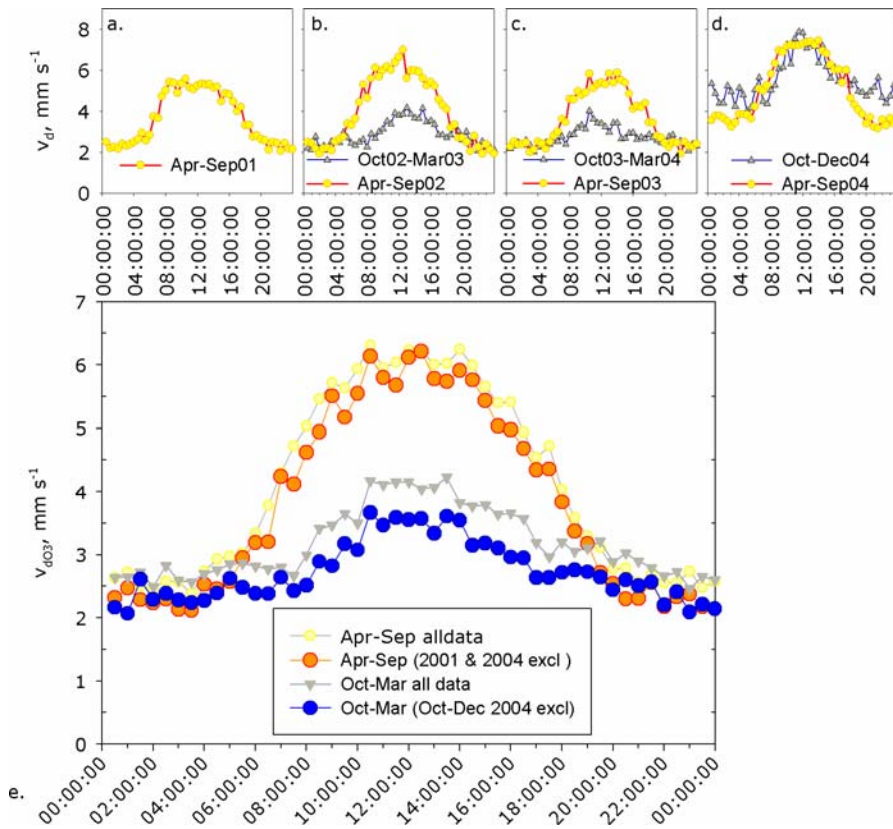


Figure 5.27. Seasonal diurnal cycles in  $v_d$ .

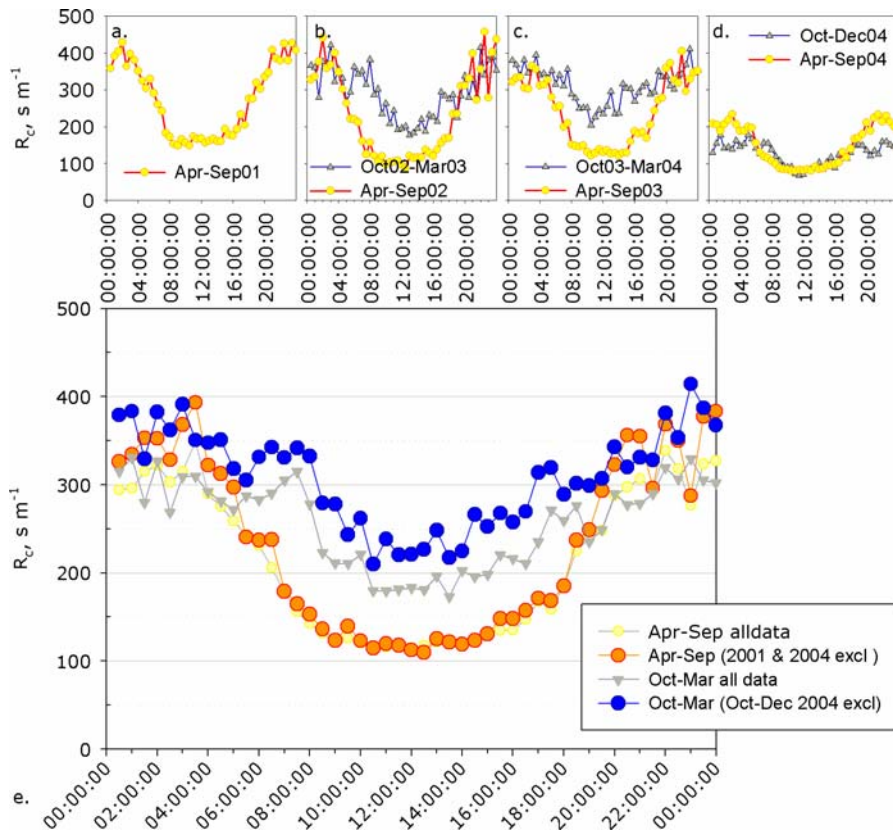


Figure 5.28. Seasonal diurnal cycles in  $R_c$ .

## 5.5 CO<sub>2</sub> and Water-vapour Fluxes, Stomatal Conductance and Rc<sub>1</sub>

The whole time series of CO<sub>2</sub>, vapour pressure and their respective fluxes are plotted in Figures 5.29 to 5.32, along with summary monthly box plots. As with the ozone measurements, the concentration values (taking vapour pressure to represent the water-vapour concentration) are normally distributed while the fluxes are log-normal (Figures 5.33 and 5.34) so average concentration and median fluxes are used when summarising the data. There is a gap in the frequency distribution CO<sub>2</sub> flux just below zero which is caused by the instrumentation filters. This indicates a possible limitation of the open-path sensor but data in the “missing” period require more detailed examination.

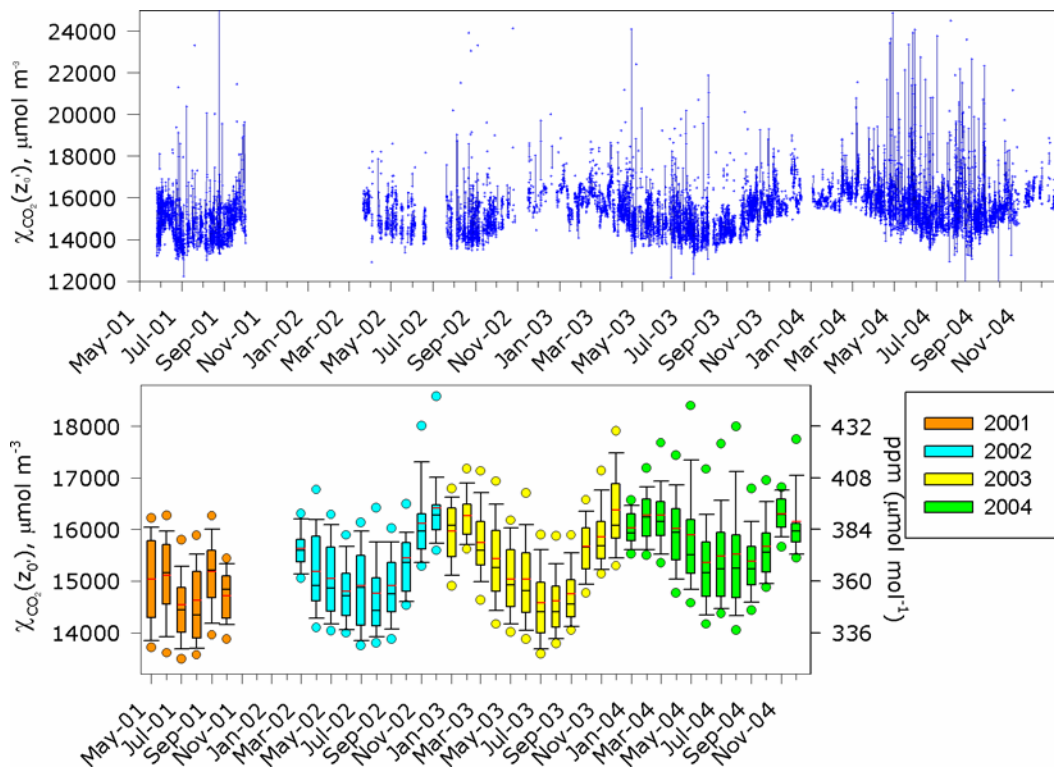


Figure 5.29. The upper plot shows the complete time series of CO<sub>2</sub> concentrations, calculated at  $z_0'$  and the lower a summary box plot of the data (the box indicates the 75<sup>th</sup> and 25<sup>th</sup> percentiles; the black bar is the median; the red bar the average; the whiskers the 90<sup>th</sup> and 10<sup>th</sup> percentiles; the dots are the outliers at the 95<sup>th</sup> and 5<sup>th</sup> percentiles).

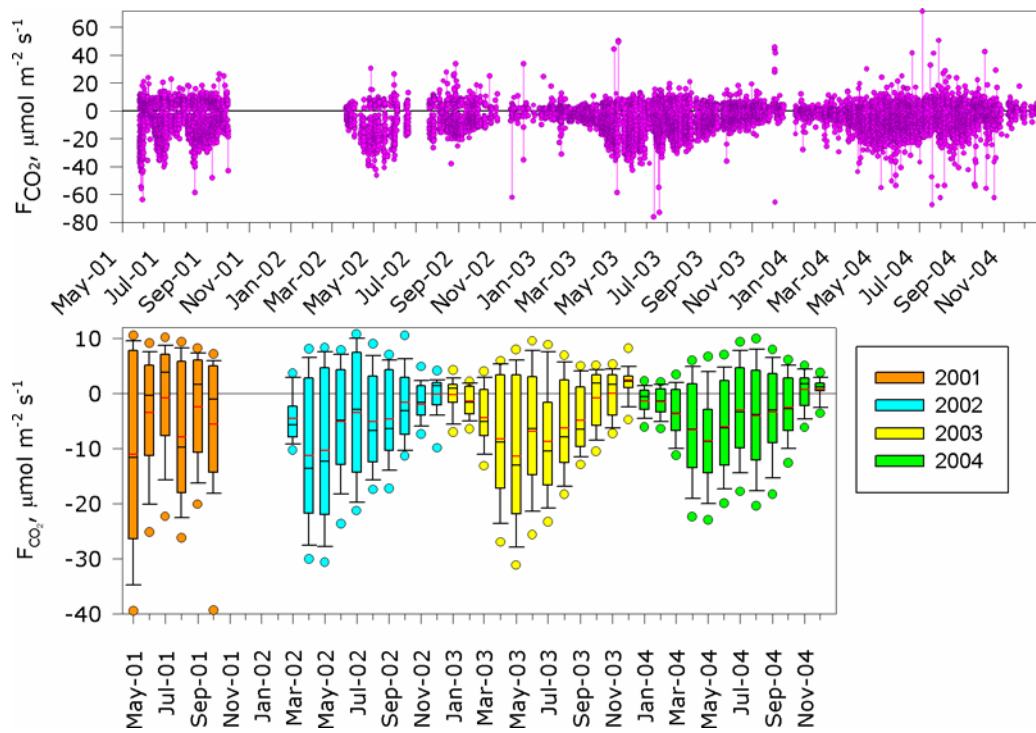


Figure 5.30. The upper plot shows the complete time series of CO<sub>2</sub> fluxes, measured at  $\sim 2.15$  m and the lower a summary box plot of the data.

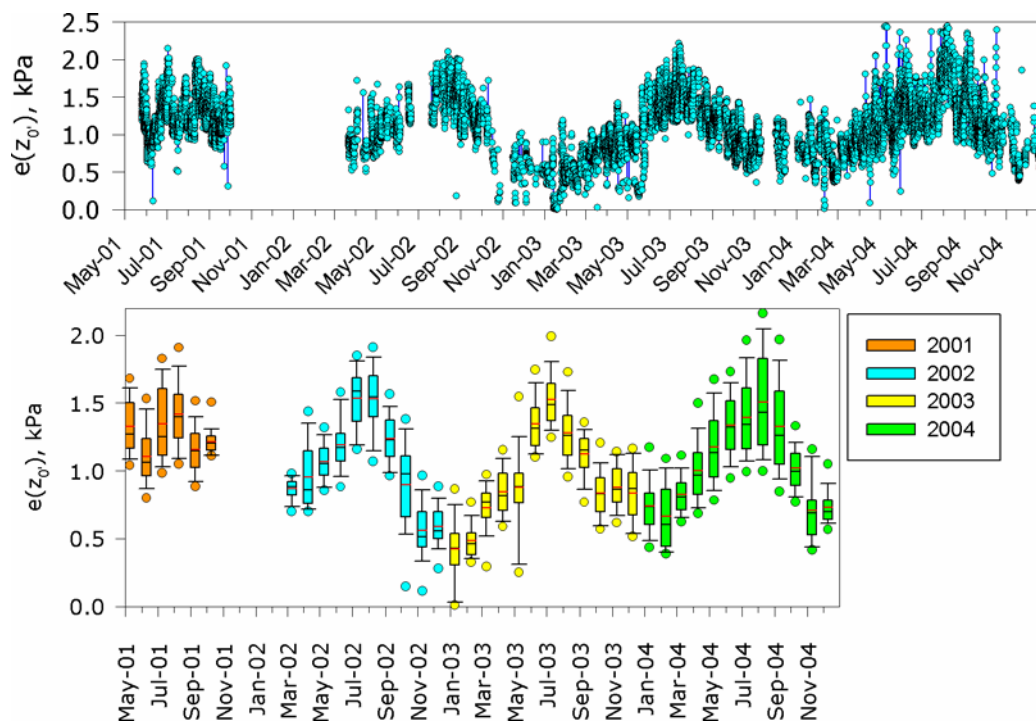


Figure 5.31. The upper plot shows the complete time series of vapour pressure, calculated at  $z_0'$  and the lower a summary box plot of the data (the box indicates the 75<sup>th</sup> and 25<sup>th</sup> percentiles; the black bar is the median; the red bar the average; the whiskers the 90<sup>th</sup> and 10<sup>th</sup> percentiles; the dots are the outliers at the 95<sup>th</sup> and 5<sup>th</sup> percentiles).

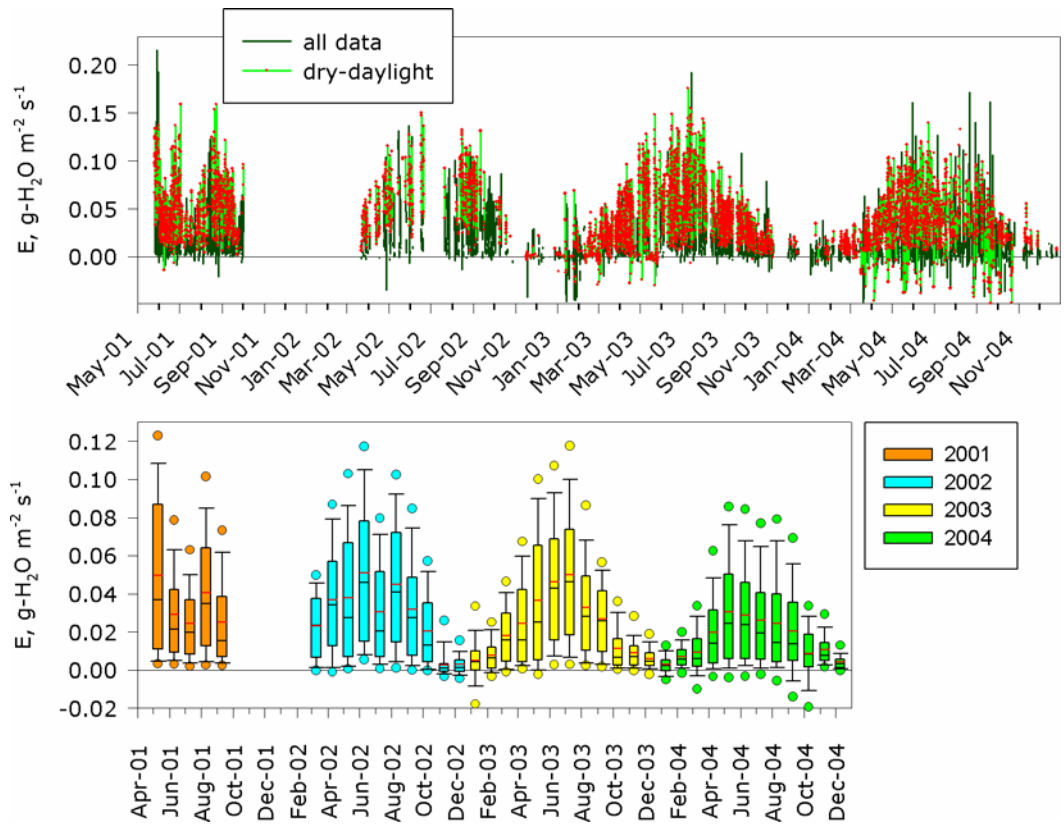


Figure 5.32. The upper plot shows the complete time series of water-vapour flux measured at  $\sim 2.15\text{m}$  and the time series filtered for dry-daylight condition. The lower a summary box plot of the complete time series (the box indicates the 75<sup>th</sup> and 25<sup>th</sup> percentiles; the black bar is the median; the red bar the average; the whiskers the 90<sup>th</sup> and 10<sup>th</sup> percentiles; the dots are the outliers at the 95<sup>th</sup> and 5<sup>th</sup> percentiles).

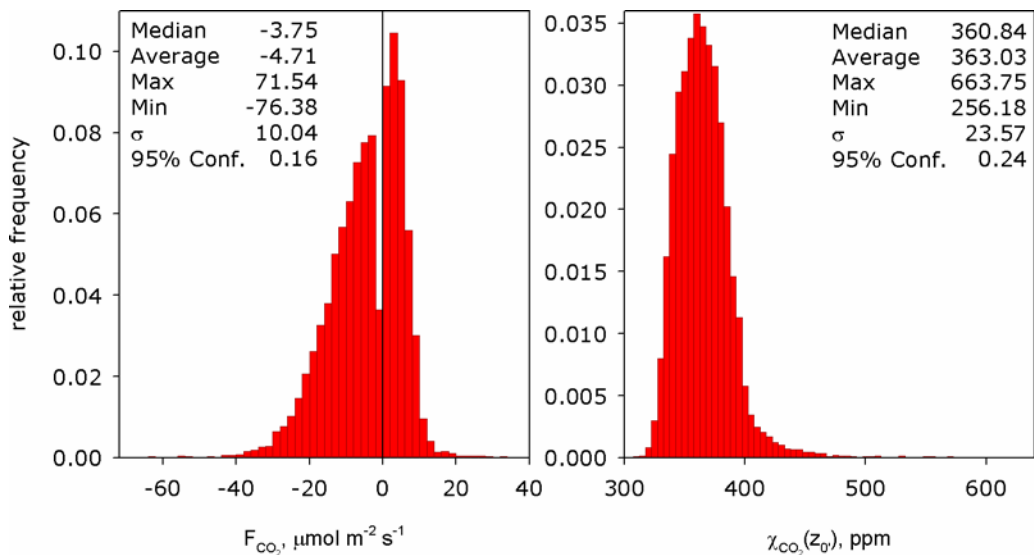


Figure 5.33. The normalised frequency distribution of  $\text{CO}_2$  flux and concentration.

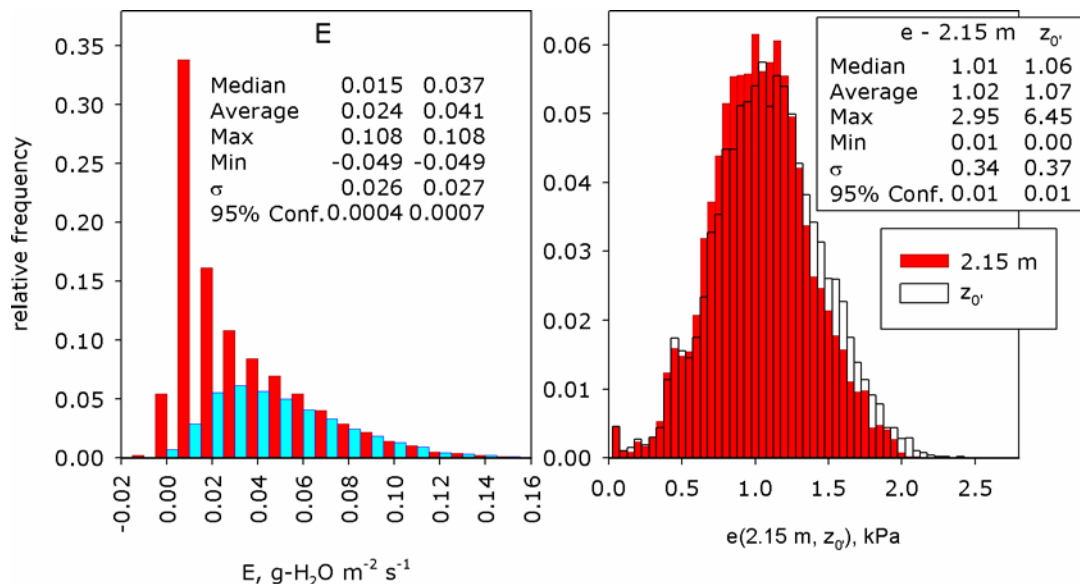


Figure 5.34. The left hand plot shows the normalised frequency distribution of water-vapour flux for the whole data set (red bars) and filtered for dry-daylight conditions (blue bars). The right hand plot is the normalised frequency distribution of vapour pressure measured at  $\sim 2.15$  m and calculated at the canopy surface ( $z_0$ ).

The magnitude of the  $\text{CO}_2$  flux reflects the productivity of the vegetation as it gradually declines over the four years of measurement. As described in Sections 4.3 and 4.4, the intensity of grazing increased over the period leading to a reduction in maximum canopy height and LAI. Weather conditions also contributed to this decline: 2002 was relatively dull overall with quite a wet period early in the year which reduced the amount of growth prior to first silage harvest, the remainder of the year was also cool, wet and dull so re-growth was suppressed; the spring and summer of 2003 on the other hand were warm and sunny but also particularly dry which led to continued poor growth throughout the year; the weather in 2004 was more "average" and towards the end of the year the vegetation appears to have recovered and productivity began to increase (the minimum flux in September 2001 to 2004 is  $-48$ ,  $-20$ ,  $-36$  and  $-54 \mu\text{mol m}^{-2} \text{s}^{-1}$  respectively).

The bulk canopy resistance to water-vapour (stomatal resistance  $R_{c1w}$ ) is calculated from the water-vapour flux and surface vapour pressure using equation (70) during dry-daylight conditions only (no rainfall, surface wetness  $> 4000$ ,  $RH < 70\%$ ), as described in Section 2.5.1.2. The resulting time series is plotted in Figure 5.35, during the spring and summer when the vegetation is most active  $R_{c1w}$  is  $\sim 100 \text{ s m}^{-1}$  and increases to  $\sim 200 \text{ s m}^{-1}$  in the winter. However in the winter months when canopy is sparser and some soil is exposed the resistance may be underestimated. Also despite filtering for dry conditions

some water-vapour release from the soil may occur particularly on relatively warm sunny days. Therefore for the stomatal conductance modelling only data where the *LAI* exceeded 1.5 are used (as described in Chapter 7), although this results in a relatively small data set (Figure 5.35).

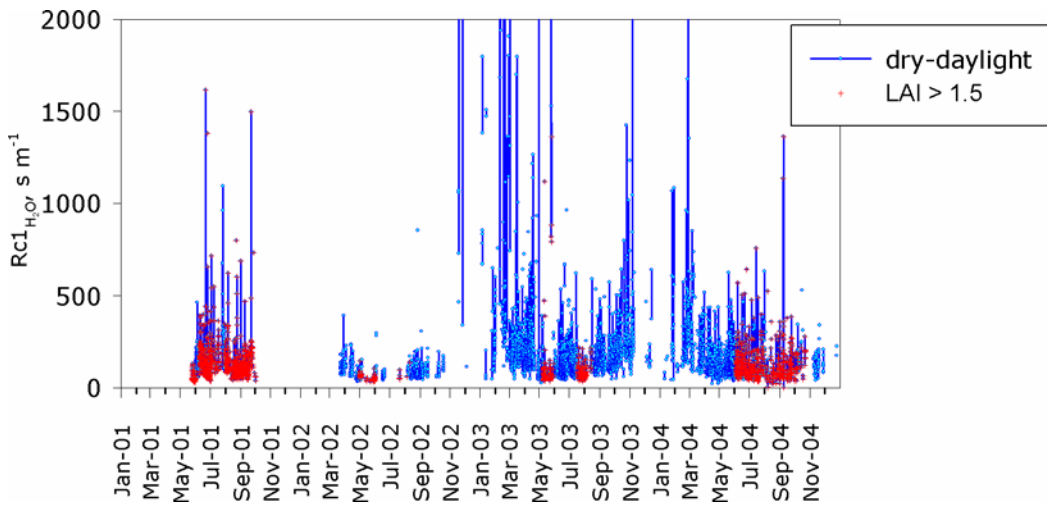


Figure 5.35. The complete time series of  $R_{c1H_2O}$  measurements with periods with *LAI* > 1.5 highlighted.

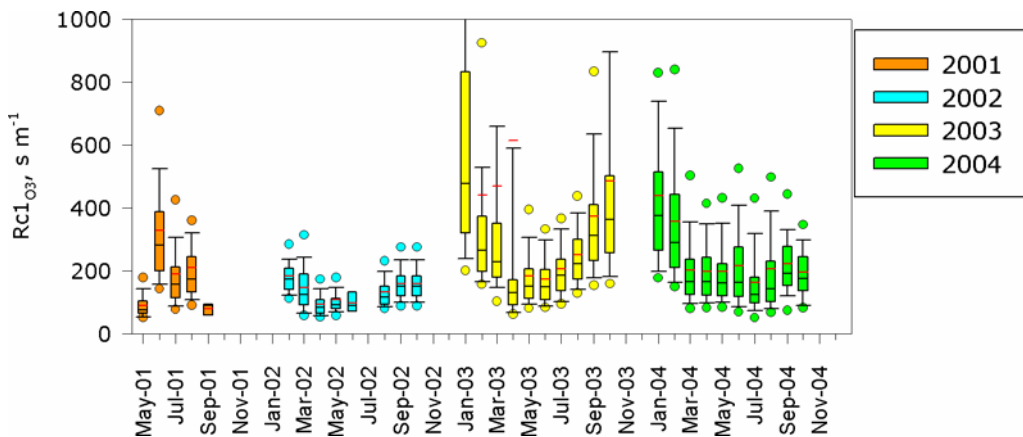


Figure 5.36. Summary box plot of the stomatal resistance for ozone, calculated from the dry-daylight results for water-vapour (the box indicates the 75<sup>th</sup> and 25<sup>th</sup> percentiles; the black bar is the median; the red bar the average; the whiskers the 90<sup>th</sup> and 10<sup>th</sup> percentiles; the dots are the outliers at the 95<sup>th</sup> and 5<sup>th</sup> percentiles).

## 5.6 Silage Harvests

A total of five silage harvests (01/06/01, 25/07/01, 01/06/02, 05/08/02, 29/05/03) occurred during the measurement period and their effects on surface conditions and fluxes are considered here. For the last two harvests only the SW field was cut and only data from this sector are used. The series of plots in Figures 5.37 and 5.38 show the following variables for a week (7 days) before and after two of the harvests (25/07/01 and 29/05/03): canopy height ( $h$ ), LAI, wind direction (with the SW sector indicated), ambient temperature ( $T_a$ ),  $v_{pd}$  at  $\sim 1.5$  m, rainfall, solar radiation ( $St$ ), the ozone concentration at 1 m ( $\chi_{O_3}(1m)$ ), the ozone flux ( $F_{O_3}$ ), deposition velocity ( $v_{dO_3}$ ), the energy budget ( $R_n$ ,  $H$ ,  $\lambda E$  and  $G$ ), the flux of  $CO_2$  ( $F_{CO_2}$ ) and finally the stomatal conductance for ozone ( $R_{c1_{O_3}}$ , the modelled values are also plotted and will be discussed in Chapter 6).

The general pattern is as anticipated, ie deposition and trace-gas fluxes are reduced after each cut and the loss of active vegetation is evident in the energy balance, as the major component changes from being dominated by water-vapour loss and hence latent-heat  $\lambda E$ ; to a surface energy balance dominated by sensible heat loss ( $H$ ). The plots in Figure 5.39 show the deposition velocity and canopy resistances for ozone, calculated from the measurements 6 days before and after the grass being cut then lifted. With exception of the 1<sup>st</sup> of June 2001,  $v_d$  clearly decreases (by 30 to 80%) and  $R_c$  increases post-harvest and examining the data split into day and night time periods (Figure 5.39c) shows the changes are largest during the day, reflecting the loss of the stomatal uptake component of deposition.

However in 2001 the decrease in ozone flux is less marked despite the taller canopy pre-harvest (Figure 5.39). Large emissions of oxygenated VOCs have been measured from freshly cut vegetation (Kirstine *et al* 1998, 2004; De Gouw *et al* 2000; Karl *et al* 2001a, b) and, in particular, grasses release hexenyl compounds when physically damaged which have sufficiently fast reaction rates with ozone to cause non-stationarity and enhance the measured ozone flux. For example, Kirstine *et al* (1998) measured total VOC emissions of 33 to 830  $\mu\text{g-C g}^{-1} \text{h}^{-1}$  (as dry weight) from freshly cut *Lolium perenne* of which over 70% were hexenyl compounds. The emission declined over  $\sim 3$  hours with a linear decay rate of 30% per hour. Other studies have measured similar peaks and a second longer peak as the cut vegetation dried although the hexenyl content of this

tends to be smaller (~22-40%; Kirstine and Galbally 2004; Figure 5.40) than that of the initial peak. The VOC emissions mainly arise from the harvested grass, although some comes from the wounds on the live plants left in the ground. Enzyme activity is responsible for hexenyl production (Kirstine and Galbally, 2004) and so temperature and solar radiation affect the amount of emission. As the emissions arise from a physiological process the health and vitality of the vegetation may also have some influence.

From the measurements of Kirstine *et al* (1998) and those at Easter Bush just after the harvest on the 1<sup>st</sup> of June 2001 (summarised in Table 5.11), the apparent ozone flux due to VOC chemistry during the first silage harvest (01/06/01) is estimated to be -30 to -1500 ng-O<sub>3</sub> m<sup>-2</sup> s<sup>-1</sup>, depending on the amount of hexenyl emission (23 to 581 µg-C g<sup>-1</sup> h<sup>-1</sup>). The experiments of Kirstine *et al* (1998) were done on sunny days with temperatures of ~30°C. Although each harvest at Easter Bush occurred on sunny days the temperatures were lower, 12°C to 20°C, and so it is likely that VOC emissions would be at the lower end of the range. However, there could still be sufficient chemistry occurring to account for the small change in ozone deposition observed after the harvests in 2001. The effect was not seen in 2002 or 2003 which may have been partly due to the smaller biomass as the canopy was shorter when cut.

Table 5.11. Data used to estimate the potential flux due to O<sub>3</sub> reacting with VOCs emitted by cut *Lolium perenne*.

Hexenyl-O <sub>3</sub> reaction rate cm <sup>3</sup> molecule s <sup>-1</sup> at 23°C	(Z)-3-hexen-1-ol 6.4 x 10 <sup>-7</sup> (Z)-3-hexenyl acetate 5.4 x 10 <sup>-7</sup> Used 6 x 10 <sup>-7</sup>
Emissions of hexenyls µg-C g <sup>-1</sup> h <sup>-1</sup>	23; 50 to 500 interval 50; 581
Silage yield <sup>14</sup>	25 t ha <sup>-1</sup> ; 500 g m <sup>-2</sup>
v <sub>d_max</sub> (1m), cm s <sup>-1</sup>	4 Used to estimate χ <sub>VOC</sub> (1 m)
R <sub>a</sub> (1 m), s m <sup>-1</sup>	11.7
R <sub>b_hexenyl acetate</sub> , s m <sup>-1</sup>	12.4
Hexenyl and O <sub>3</sub> concentrations are calculated every 10 cm from the surface to 1 m and integrated to estimate the apparent O <sub>3</sub> flux.	
Estimated F <sub>O<sub>3</sub></sub> due to VOC, ng m <sup>-2</sup> s <sup>-1</sup>	-30 to -1500 ng-O <sub>3</sub> m <sup>-2</sup> s <sup>-1</sup> -131 per 50 µg-C g <sup>-1</sup> h <sup>-1</sup> emitted
F <sub>O<sub>3</sub></sub> , ng m <sup>-2</sup> s <sup>-1</sup>	-240

<sup>14</sup> This an estimate given by the farmer as actual yields are not recorded.

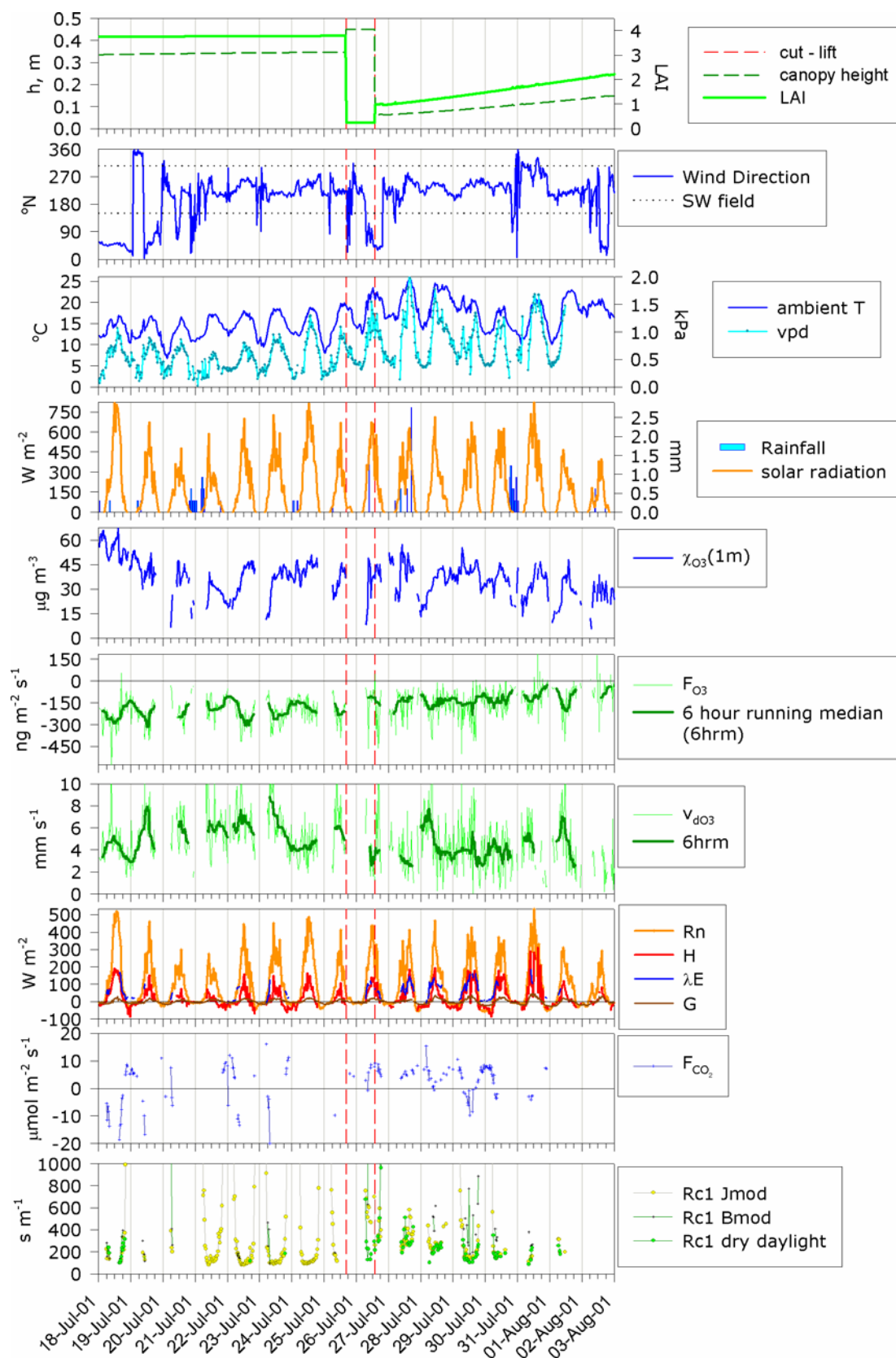


Figure 5.37. Summary of measurements pre and post the silage harvest in both fields on the 25/07/2001 (cut and lifting times are approximate).

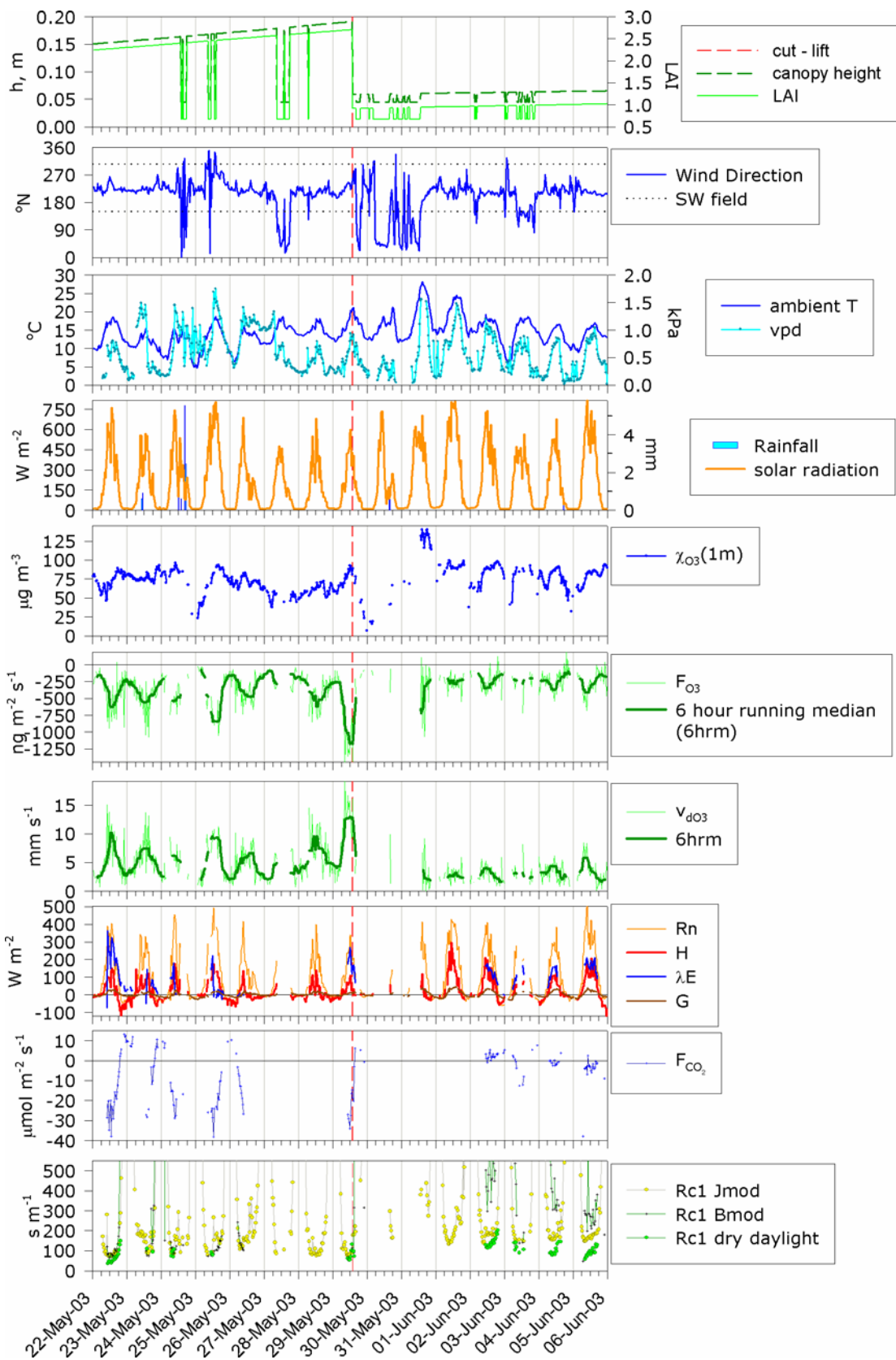


Figure 5.38. Summary of measurements pre and post the silage harvest in both fields on the 25/05/2003 (the time of cutting is approximate).

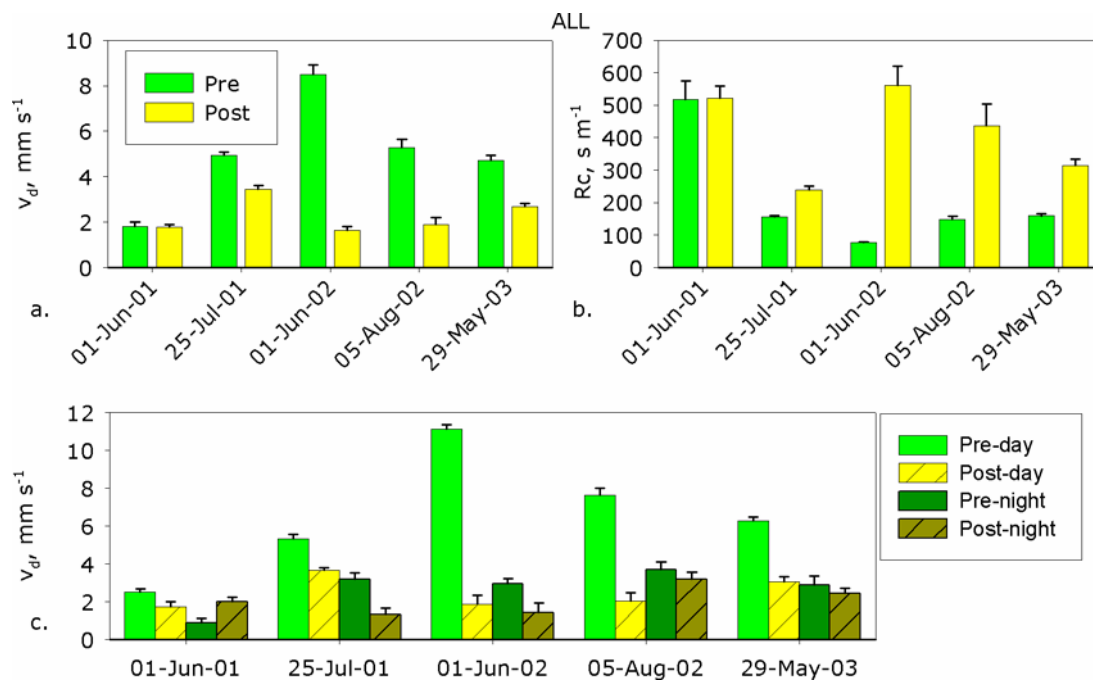


Figure 5.39 The deposition velocity (a) and canopy resistances (b) measured pre and post harvest for all hours and (b) the data split into day and night-time periods.

## 5.7 Day-time vs. Night-time Deposition

The autumn/winter diurnal cycles in ozone flux, deposition velocity and canopy resistance (Figures 5.24, 5.27 and 5.28) all show some daily variation, despite the low activity of vegetation at these times of year (even in December some variation is evident as shown in Figure 5.40). This raises the question of there being some factor other than stomata influencing deposition, as if the non-stomatal resistance decreases with increased temperature such a signal would also be seen.

In the absence of measured or modelled stomatal resistances it is common practice to use night-time measurements to examine the non-stomatal flux (Zhang, *et al.*, 2003 for example), as it can be assumed that stomata are closed. The Easter Bush data are split into day and night periods using sunrise and sunset times for the site (obtained from the US Naval Observatory's online calculator, [http://aa.usno.navy.mil/data/docs/RS\\_OneDay.html](http://aa.usno.navy.mil/data/docs/RS_OneDay.html)). Measurements 1 hour before sunrise and after sunset are allocated to the night-time whereas 1 hour after sunrise and before sunset are allocated to day-time. This excludes the twilight periods where the sun is below the horizon but light levels may still be large enough to influence stomatal opening.

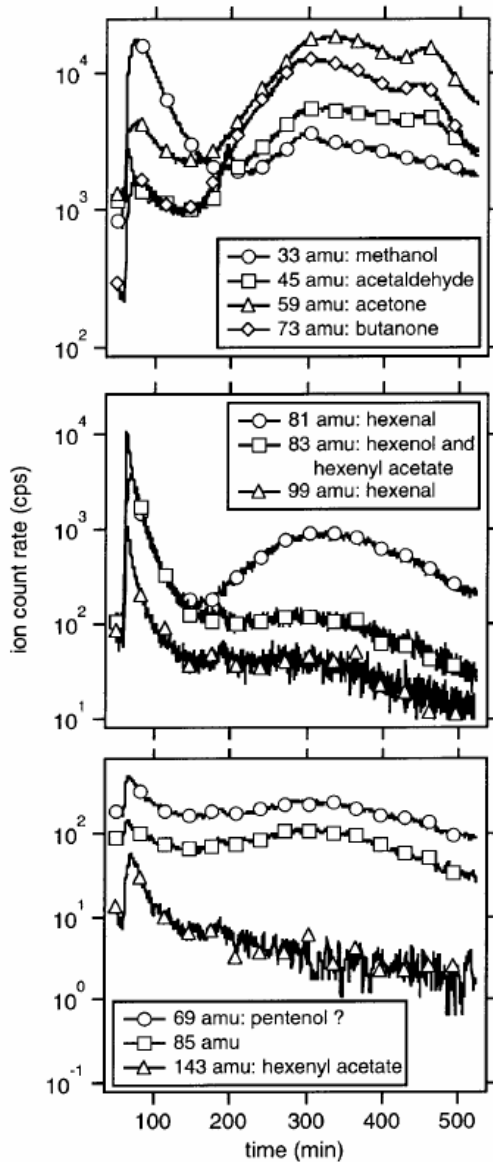


Figure 5.40. VOC emissions from freshly excised clover during the drying process as measured with the PT-CIMS instrument. A sample of clover stems and leaves was cut and immediately placed in the flux chamber for VOC analysis during subsequent drying (from de Guow *et al* 2000).

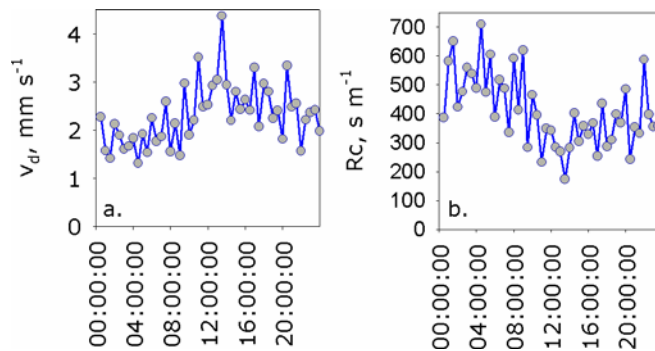


Figure 5.41. Diurnal cycles in deposition velocity and canopy resistance during December, calculated from median ozone fluxes and average concentrations in 2002 and 2003.

The day and night-time fluxes and concentrations are summarised in Table 5.11 whereas Table 5.12 shows the monthly deposition velocities and canopy resistances calculated from these data. The day-time deposition velocity tends to be about twice the night-time value during the summer months and the difference decreases during the autumn and winter (Figure 5.41). This is partly due to the influence of vegetation as during the summer LAI increases and a larger non-stomatal surface area is available for ozone to deposit too. The minimum deposition rates occur *ca.* December to February when temperatures and radiation levels are lowest, raising the question of their influence as well.

To investigate this further the canopy resistance is plotted against surface temperature (in the day and night) and solar radiation (during daylight hours) in Figure 5.42. As may be expected the day-time canopy resistance decreases markedly as temperature and radiation increase due to the stomata opening in response to both these variables.

During the night-time it is harder to see a pattern but resistance is definitely larger at low temperatures and may decrease slightly at higher values. The signal can be detected more clearly by blocking into the data into temperature bands and recalculating the surface resistance, as shown in Figure 6.43. The resistance increases markedly at temperatures below zero and a double exponential function is fitted to achieve the degree of curvature. As the surface is likely to be frozen or at least wet at low temperatures this is not unexpected and resistances of  $\sim 3000 \text{ s m}^{-1}$  have been reported at other sites in these conditions (Wesely, *et al.*, 1981). However these data are more uncertain as there are few data points available to calculate the block value. Where no error bars are shown the standard error could not be calculated as there was only one point in the sample. At higher temperatures, above  $\sim 25^\circ\text{C}$ , there are also fewer data points as indicated by increased or missing standard error (Figure 5.43a).

Table 5.12 Monthly summary of median ozone fluxes and average concentrations measured during the day and night (standard deviation).

	<b>Day</b> $\chi_{O_3}(1m)$ $\mu g m^{-3}$	<b>Day</b> $F_{O_3}$ $ng m^{-2} s^{-1}$	<b>Night</b> $\chi_{O_3}(1m)$ $\mu g m^{-3}$	<b>Night</b> $F_{O_3}$ $ng m^{-2} s^{-1}$
May-01	56.2 (12.1)	-140.4 (195.5)	54.0 (13.9)	-47.7 (95.5)
Jun-01	49.0 (12.9)	-145.6 (131.6)	47.8 (11.5)	-97.3 (68.4)
Jul-01	39.4 (11.8)	-178.8 (97.8)	38.2 (14.2)	-103.0 (62.5)
Aug-01	36.1 (9.6)	-187.8 (114.9)	33.6 (10.7)	-70.6 (58.2)
Sep-01	39.3 (11.2)	-190.3 (130.6)	39.8 (10.8)	-82.1 (84.8)
Oct-01	50.6 (4.2)	-279.4 (131.3)	52.6 (3.7)	-90.5 (88.1)
Mar-02	65.6 (14.7)	-128.3 (110.7)	66.6 (21.8)	-54.8 (57.4)
Apr-02	70.9 (13.4)	-156.6 (201.8)	70.7 (14.6)	-13.2 (110.3)
May-02	62.9 (11.1)	-426.7 (381.2)	63.3 (11.1)	-98.8 (138.8)
Jun-02	59.0 (15.8)	-168.6 (209.4)	58.4 (18.4)	-85.8 (116.0)
Jul-02	47.7 (11.3)	-304.0 (208.1)	46.7 (14.0)	-121.7 (105.2)
Aug-02	45.0 (15.8)	-231.8 (243.9)	40.1 (14.9)	-92.5 (111.8)
Sep-02	53.4 (13.3)	-310.5 (214.4)	49.6 (19.9)	-134.2 (109.8)
Oct-02	45.6 (15.4)	-242.1 (180.8)	48.4 (14.2)	-117.0 (122.7)
Nov-02	44.6 (15.0)	-236.0 (166.3)	44.4 (16.2)	-162.3 (129.4)
Dec-02	38.6 (15.7)	-186.6 (133.3)	39.4 (15.3)	-158.6 (96.9)
Jan-03	63.7 (13.6)	-162.6 (177.1)	66.9 (13.2)	-122.0 (127.4)
Feb-03	51.4 (19.7)	-47.7 (109.1)	51.9 (22.4)	-11.0 (97.6)
Mar-03	68.4 (24.7)	-31.7 (152.6)	65.6 (21.9)	-6.6 (105.0)
Apr-03	67.2 (21.9)	-44.0 (260.5)	57.2 (24.0)	7.2 (91.4)
May-03	72.5 (14.6)	-287.7 (273.1)	70.3 (14.8)	-44.1 (158.9)
Jun-03	73.5 (14.9)	-327.7 (229.9)	66.2 (15.0)	-162.0 (140.7)
Jul-03	54.9 (17.2)	-358.2 (238.7)	46.2 (13.9)	-143.1 (93.9)
Aug-03	61.8 (17.1)	-299.3 (238.4)	53.0 (16.4)	-134.1 (99.4)
Sep-03	53.9 (19.8)	-100.1 (171.6)	50.0 (18.0)	-62.0 (106.3)
Oct-03	50.9 (13.0)	-112.2 (170.2)	50.2 (13.8)	-92.7 (129.4)
Nov-03	55.7 (13.4)	-127.1 (127.8)	52.3 (17.9)	-90.2 (109.8)
Dec-03	48.1 (18.9)	-66.2 (137.1)	52.2 (18.3)	-53.4 (146.2)
Jan-04	51.8 (9.2)	-95.1 (59.6)	50.2 (6.2)	-49.9 (95.4)
Feb-04	74.5 (15.2)	-226.6 (147.8)	77.6 (12.9)	-168.5 (132.1)
Mar-04	77.9 (12.3)	-345.8 (210.2)	73.9 (13.0)	-226.5 (188.9)
Apr-04	76.3 (13.9)	-558.8 (238.4)	72.0 (16.4)	-329.0 (170.9)
May-04	71.7 (15.1)	-542.3 (353.4)	65.8 (15.6)	-242.8 (195.5)
Jun-04	59.1 (13.8)	-232.7 (170.0)	55.1 (13.8)	-84.5 (88.3)
Jul-04	57.8 (11.9)	-123.9 (121.2)	52.6 (13.9)	-15.2 (68.3)
Aug-04	64.6 (19.7)	-403.6 (233.8)	58.3 (22.0)	-215.8 (136.8)
Sep-04	54.5 (13.5)	-464.5 (229.5)	55.4 (14.5)	-303.6 (151.2)
Oct-04	54.3 (13.9)	-399.6 (228.6)	49.2 (15.6)	-259.9 (177.4)
Nov-04	58.9 (15.5)	-437.4 (292.2)	62.7 (11.2)	-339.0 (182.5)
Dec-04	60.7 (15.3)	-328.8 (227.4)	67.1 (13.5)	-260.9 (143.5)
ALL	58.1 (18.9)	-239.2 (260.6)	55.3 (19.2)	-118.8 (161.9)

Table 5.13 Monthly deposition velocities and canopy resistance calculated from the data in Table 6.9 and the monthly median Ra and Rb. The standard errors given are calculated as described in Appendix A.

	Day	Day	Night	Night
	$V_d$ $\text{mm s}^{-1}$	$R_c$ $\text{s m}^{-1}$	$V_d$ $\text{mm s}^{-1}$	$R_c$ $\text{s m}^{-1}$
May-01	2.5±0.3	366±39	0.9±0.3	1093±325
Jun-01	3.0±0.1	292±10	2.0±0.1	441±23
Jul-01	4.5±0.1	170±4	2.7±0.1	306±16
Aug-01	5.2±0.1	145±4	2.1±0.1	416±21
Sep-01	4.8±0.1	163±5	2.1±0.1	437±23
Oct-01	5.5±0.7	157±19	1.7±0.5	554±171
Mar-02	2.0±0.1	457±30	0.8±0.1	1147±121
Apr-02	2.0±0.1	404±20	0.2±0.1	5318±2924
May-02	6.8±0.2	104±3	1.6±0.2	590±57
Jun-02	2.9±0.1	309±14	1.5±0.2	631±66
Jul-02	6.4±0.2	103±3	2.6±0.2	314±21
Aug-02	5.2±0.2	133±6	2.3±0.2	360±30
Sep-02	5.8±0.2	114±4	2.7±0.2	284±17
Oct-02	5.3±0.2	135±6	2.4±0.1	353±21
Nov-02	5.3±0.2	129±6	3.7±0.1	220±8
Dec-02	4.8±0.3	146±9	4.0±0.1	181±7
Jan-03	2.6±0.2	357±25	1.8±0.1	510±22
Feb-03	0.9±0.1	1013±123	0.2±0.1	4670±2070
Mar-03	0.5±0.1	2106±454	0.1±0.1	9937±8047
Apr-03	0.7±0.2	1470±353		
May-03	4.0±0.1	211±7	0.6±0.1	1536±354
Jun-03	4.5±0.1	177±4	2.4±0.2	342±23
Jul-03	6.5±0.2	104±3	3.1±0.2	242±12
Aug-03	4.8±0.2	152±5	2.5±0.1	329±18
Sep-03	1.9±0.2	486±40	1.2±0.1	739±89
Oct-03	2.2±0.2	406±29	1.8±0.1	491±31
Nov-03	2.3±0.1	387±22	1.7±0.1	528±27
Dec-03	1.4±0.2	674±95	1.0±0.1	933±112
Jan-04	1.8±0.3	488±92	1.0±0.3	947±294
Feb-04	3.0±0.2	284±15	2.2±0.1	411±23
Mar-04	4.4±0.1	182±5	3.1±0.1	277±11
Apr-04	7.3±0.1	89±2	4.6±0.1	163±5
May-04	7.6±0.2	84±2	3.7±0.2	208±12
Jun-04	3.9±0.1	212±5	1.5±0.1	603±44
Jul-04	2.1±0.1	416±15	0.3±0.1	3386±1097
Aug-04	6.2±0.2	99±3	3.7±0.2	202±10
Sep-04	8.5±0.2	69±2	5.5±0.2	131±4
Oct-04	7.4±0.2	84±3	5.3±0.2	121±5
Nov-04	7.4±0.3	92±4	5.4±0.1	142±4
Dec-04	5.4±0.4	142±11	3.9±0.2	218±9
ALL	4.1±0.05	243±2	2.1±0.03	465±6

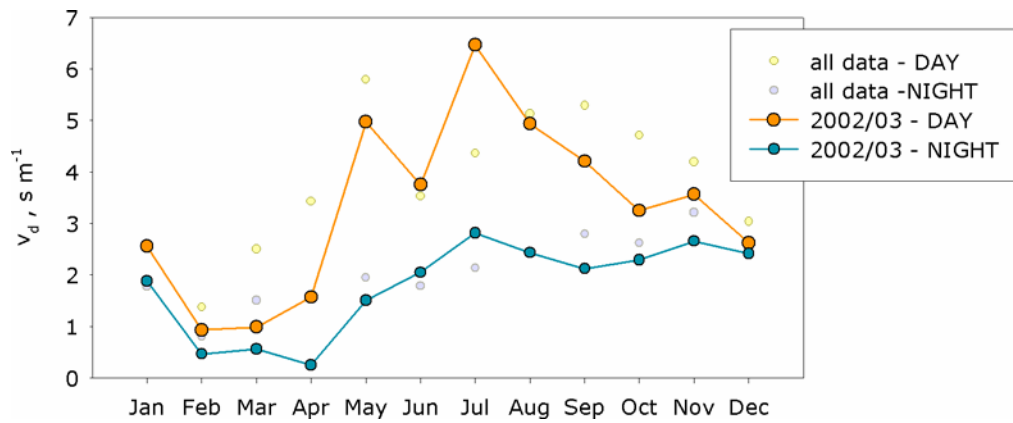


Figure 5.42. Overall summary of monthly deposition velocity observed during the day and night at Easter Bush.

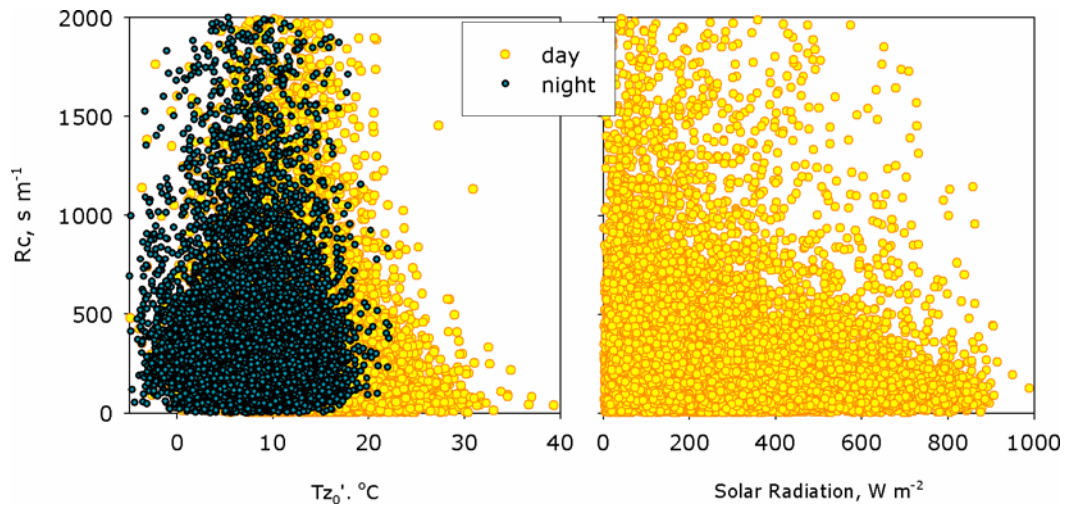
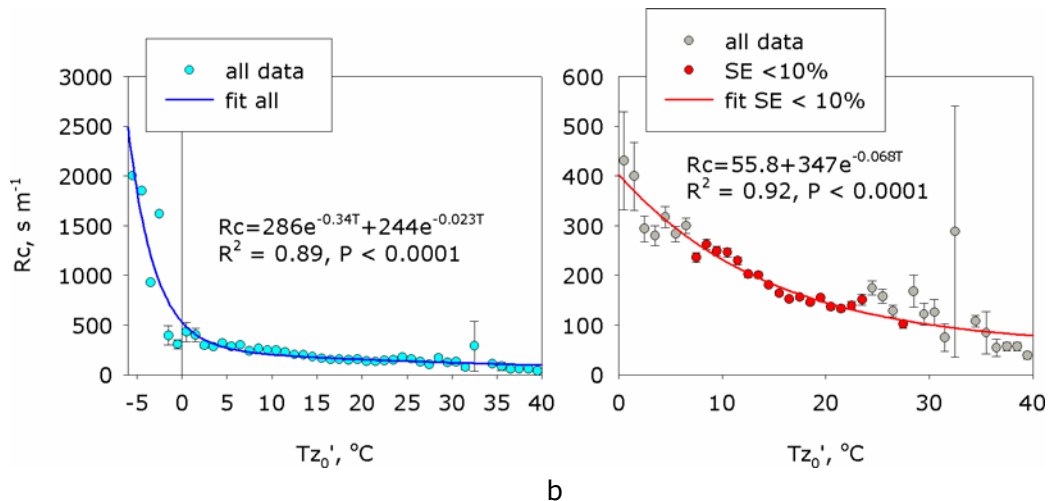


Figure 5.43. The canopy resistance measured during day and night periods versus surface temperature (left hand plot) and daytime value versus solar radiation (right hand plot).



a b  
Figure 5.44. The night-time canopy resistance calculated from measurements blocked by 1°C surface temperature increases. The left hand plot shows the relationship fitted to all points including temperatures below zero and with standard errors (SE > 10%). The right hand plot shows the same data with a fit restricted to points above zero and with SE < 10%.

Given the different behaviour in the surface at sub-zero temperatures only points above zero and where the standard error is less than 10% are plotted in Figure 5.45b. This shows the temperature response more clearly and the night-time canopy resistance clearly decreases with temperature from  $\sim 400 \text{ s m}^{-1}$  near  $0^\circ\text{C}$  to  $\sim 100 \text{ s m}^{-1}$  above  $20^\circ\text{C}$ . It was noted earlier that the flux measurements in 2001 and 2004 appear unusual in comparison with the other two years, particularly during the late summer and winter of 2004. However analysing each year individually gives similar results to the whole dataset, as shown from the fit parameters in Table 5.13. Although the magnitude of the temperature response varies from year to year this can be explained by the weather patterns and differences in LAI, as will be discussed below, and the data will be treated as a whole in the subsequent analysis.

Table 5.14 Results of fitting  $R_c = y_0 - a \cdot \exp(-bT)$  to  $1^\circ\text{C}$  blocked values of  $R_{c\_night}$  at Easter Bush (with standard errors for the fitted parameters).

	$y_0$	a	b	Rc at $0^\circ\text{C}$	at $30^\circ\text{C}$	$R^2$
All data	$56 \pm 54$	$347 \pm 27$	$0.07 \pm 0.03$	403	101	0.91
2001	$146 \pm 11$	$1709 \pm 588$	$0.23 \pm 0.04$	1855	148	0.94
2002	$74 \pm 65$	$330 \pm 34$	$0.09 \pm 0.06$	404	94	0.76
2003	$\rightarrow 0$	$1290 \pm 247$	$0.10 \pm 0.04$	1290	63	0.75
2004	$114 \pm 6$	$144 \pm 12$	$0.18 \pm 0.02$	260	115	0.93
All Dry Data	$\rightarrow 0$	$736 \pm 484$	$0.10 \pm 0.17$	736	37	0.88
All Wet Data	$395 \pm 287$	$-152 \pm 258$	$0.07 \pm 0.24$	243	376	0.14

‡ As negative resistances are not realistic for ozone  $y_0$  is restricted to being greater than zero.

The temperature relationship is very similar to that found by Fowler, *et al.*, (2001) for non-stomatal resistance and solar radiation at a moorland site in the Scottish Borders. Although they (*ibid*) fitted a logarithmic function, in this case a single exponential is used; conceptually it agrees better with the results, in that it does not go to infinity at zero and reaches an asymptote at high temperatures. It was also noted (*ibid*) that the relationship with temperature was more complex due to different surface properties in dry and wet conditions. To examine the effect of surface wetness the data are split into wet and dry conditions using the same criteria as for the stomatal resistance calculation:

1. DRY low humidity: no rainfall, wetness  $> 4000$  and RH  $< 70\%$
2. WET: rainfall, wetness  $< 4000$  and RH  $> 70\%$

Out of the 11555 0.5-hourly measurements of night-time ozone flux available, only 626 (5%) occur in dry condition when relative humidity is also low and 6317 (54%) occur in wet conditions when humidity is high. Zhang *et al.*, (2002)

also included a fourth criteria where the surface was dry, according to a wetness sensor, and relative humidity was high (>80%) but such conditions never occurred during the night Easter Bush. It is noted that even when the measurements indicate a dry surface the surface wetness sensor does not accurately mimic the physical properties of the leaves and there is likely still be some water present as the leaf cuticle generally does not completely dry out until humidity is below 40% (Klemm *et al.*, 2002).

Despite the small sample for dry conditions the temperature response is clearly discernible (Figure 5.44a) and gives a similar response to that using all the data (although not statistically significant). In wet conditions with high humidity the response is not found (Figure 5.44b), implying that temperature response does not arise from a wet chemical process and is more likely to be caused by the simple thermal decomposition of ozone at the surface (as suggested by Fowler, *et al.*, 2001). If data for all humidity levels but dry surfaces are examined the response is also suppressed supporting this conclusion.

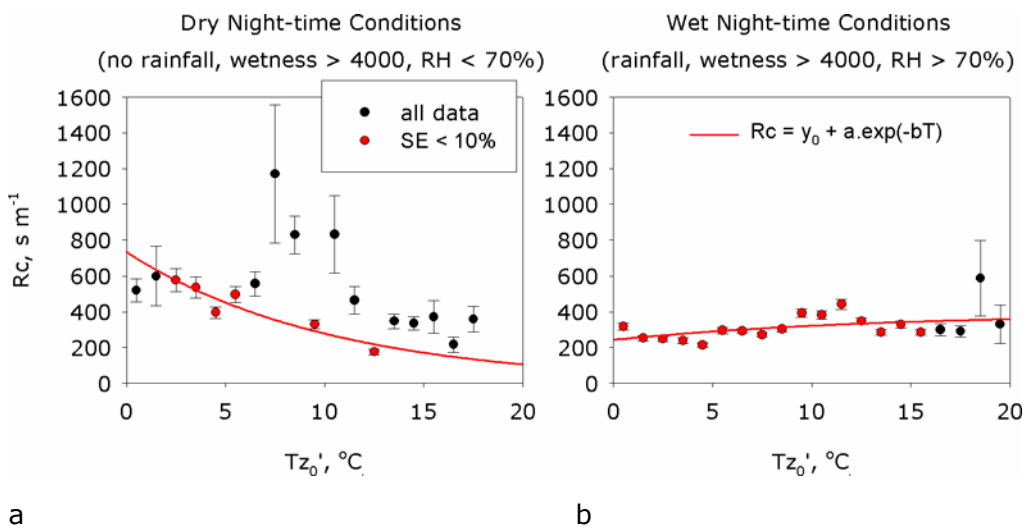


Figure 5.45. The response of night-time  $R_c$  to temperature in very dry and wet conditions. The results of curve fitting are given in Table 6.14.

Using the same approach, the relationship of  $R_{c\_night}$  with humidity is also examined using the night-time data set as a whole and with dry or wet surfaces only. A decrease in  $R_{c\_night}$  with humidity above ~60% is found in all conditions (Figure 5.46, Table 5.15) which is slightly more pronounced in dry conditions and less in wet, although the differences are not statistically significant. The relationship is similar to that found by Zhang, *et al.*, (2002) for dry surface conditions over pasture in N America ( $R_{c\_night} = 1501\exp^{-0.8RH}$ ) but temperatures were not reported in this study.

Table 5.15 Results of fitting  $R_c = y_0 - a \cdot \exp(-bRH)$  to 5% blocked values of  $R_{c\_night}$  at Easter Bush (with standard errors for the fitted parameters).

	$y_0$ ( $\times 10^{-6}$ )	A	b	$R_c$ at 20%	at 100%	$R^2$
All data	$1.65 \pm 1487$	$1020 \pm 405$	$1.35 \pm 5.78$	778	263	0.59
All Dry Data	$4.73 \pm 3045$	$1157 \pm 730$	$1.38 \pm 10.56$	877	290	0.34
All Wet Data	$0.97 \pm 798$	$527 \pm 552$	$1.04 \pm 3.09$	428	185	0.60

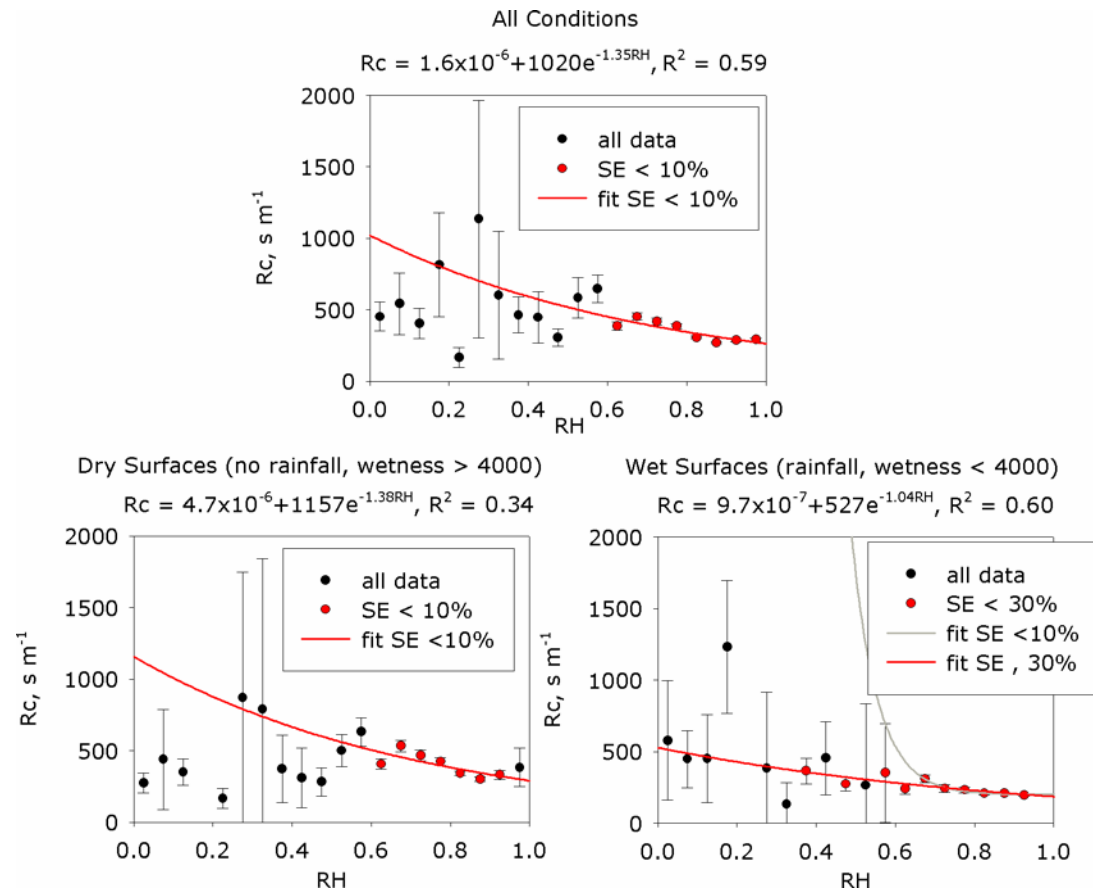


Figure 5.46. The response of night-time  $R_c$  to relative humidity (RH) in all conditions, when the surface is dry and when the surface is wet.

The seasonality in the temperature response also shows that the variation in  $R_{c\_night}$  is mitigated by weather conditions but temperature is the main driver of the response: 2001 and 2003 had the warmest and driest summers and the temperature response is larger in these years; 2002 and 2004 were generally quite dull and wet in the latter half of both years and although a significant decline in  $R_{c\_night}$  with temperature is seen, the curve is much smaller than in the drier years. These differences are mainly due to the value of  $R_{c\_night}$  at low temperatures (0 to 5°C) which can be explained by considering the data in Figure 5.46. When the surface is cold and dry resistances are relatively large

( $\sim 800 \text{ s m}^{-1}$ ) but when it is cold and wet (but not below zero  $^{\circ}\text{C}$ ) values are smaller  $\sim 350$  to  $400 \text{ sm}^{-1}$ .

Overall these results indicate that in dry conditions temperature is a major factor in controlling night-time and hence non-stomatal deposition at Easter Bush. There may also be a temperature threshold,  $\sim 0^{\circ}\text{C}$ , below which  $R_{c\_night}$  is relatively large ( $\sim 1000 \text{ s m}^{-1}$ ) but above which it decreases rapidly. When the surface is saturated with water  $R_{c\_night}$  is largely independent of temperature and humidity and has a value of 200 to  $400 \text{ s m}^{-1}$ .

## 5.8 Summary

This chapter had described the analysis of the flux measurements and examined some features of the final datasets. In general the results are what would be expected in that the effects of vegetation on the energy balance of the environment and trace gas fluxes can be clearly seen. There are some unusual features during some periods such as the small effect of the 2001 harvests on deposition rates and the enhanced ozone fluxes seen during the autumn and winter of 2004. For reference, summary tables of  $R_a$ ,  $R_{bO_3}$ ,  $V_{dO_3}$ ,  $R_{cO_3}$  as well as the fluxes and concentrations of ozone,  $\text{CO}_2$  and water-vapour are provided in Appendix C. Analysis of the day-time/night-time canopy resistance has revealed a consistent picture of a response of  $R_{ns}$  to temperature.

$$R_{c\_night} = 56 + 347e^{-0.07T(z0)} \quad (127.)$$

The measured and modelled stomatal resistances are used in the following chapter to expand the range of conditions which can be studied and further examine  $R_{ns}$ .

Table 5.16 Summary of raw and final data capture (%) for the main components of the trace-gas flux measurements.

	$u^*, H$ (Gradient, Gill, Metek, Combined)		$\text{O}_3$ (Gradient, Gill, Metek, Combined)		$\text{H}_2\text{O}$ (dry daylight)		$\text{CO}_2$	
	Raw	Final	Raw	Final	Raw	Final	Raw	Final
2001	72, 96, ND	84	72, 95, ND	39	97	53 (43)	97	41
2002	62, 88, 64	76	61, 79, 56	55	88	74 (14)	88	14
2003	69, 89, 83	89	68, 80, 79	74	86	57 (29)	86	30
2004	65, 92, 85	79	53, 78, 76	65	93	64 (29)	92	28
Overall		78		69		26 (10)		26



## 6 What Controls Ozone Deposition to the Canopy?

Subsequent to completion of this thesis an inconsistency was found in the method used to analyse  $R_{ns}$  described in Section 6.4.2. It does not change the conclusions but does modify the curve fitting results and so the final model. A full description can be found in the Addendum at the end of this chapter.

### 6.1 Modelling Fluxes at Easter Bush

#### 6.1.1 Introduction

As was described in Section 2.5.1.3 non-stomatal deposition can also be investigated by separating the stomatal from non-stomatal component. This is achieved by using the measurements of water-vapour flux to calculate the bulk-canopy stomatal resistance to water-vapour ( $R_{c1w_c}$ ) and hence ozone from equation (71). This method is restricted to day-light periods when the canopy is dry and so to examine the non-stomatal resistances over a wider range of conditions, two simple models of bulk-canopy stomatal resistance to water-vapour are derived (the first based on the Jarvis approach (denoted by Jmod) and the second on Ball-Berry (denoted by Bmod)). A second Jarvis-type model is also described (JmodG) which follows the more general methodology where stomatal conductance is estimated at the leaf level then scaled up to canopy (as discussed in Chapter 3). In the final section of this chapter JmodG is used to test the parameterisations for  $R_{ns}$  that were described in Section 2.5.1.4 and new formula developed in Section 6.4. As *Lolium perenne* is the dominant species at Easter Bush some vegetation specific parameters are based on the leaf-level measurements of stomatal conductance (Section 4.4.4) and consideration of values for other species reported in the literature.

#### 6.1.2 Parameters for *Lolium Perenne*

Little information on the required model parameters for *Lolium perenne* could be found in the literature, despite its being a common species in the UK and Europe. As part of the IFO3-Grassland project (Van Oijen *et al.*, 2003) measurements of leaf photosynthesis and stomatal conductance were made in the field (Section 4.4.4) and solardomes (a controlled environment facility at CEH-Bangor: Rafarel and Ashenden, 1991; Rafarel *et al.*, 1995). The measurements include PAR (field only), air temperature, leaf temperature, humidity, vapour pressure, internal and external CO<sub>2</sub> concentration, gross leaf

CO<sub>2</sub> assimilation rate (flux) and stomatal conductance to water-vapour ( $g_s$ ). However as they were intended to parameterise a Farquhar *et al.*, (1980) type model of plant growth which estimates daily carbon assimilation (van Oijen *et al.*, 2004; van Oijen *et al.*, 1998) they represent a limited range of conditions and cannot explicitly parameterise Jmod. They could be used to develop a leaf-level stomatal conductance model based on physiology and photosynthesis, and hence a process based model of ozone flux. However, as non-stomatal processes are the focus of this thesis such a complex model is not used here and the data simply provide some basic model parameters while the field measurements provide an independent test for the model results.

The data were used to estimate a value of 3.5  $\mu\text{mol-CO}_2 \text{ m}^{-2} \text{ s}^{-1}$  for the day-time leaf respiration rate ( $R_d$ ) for *lolium perenne* (to be used in Bmod, Levy, 2005) and 30  $\text{mmol-H}_2\text{O m}^{-2} \text{ s}^{-1}$  for the minimum stomatal conductance ( $g_{min}$ , in all 3 models). A maximum stomatal conductance is required by Jmod and the largest value measured was 1899  $\text{mmol-H}_2\text{O m}^{-2} \text{ s}^{-1}$  for a leaf growing in the solardomes, although the median of all values was only 342  $\text{mmol-H}_2\text{O m}^{-2} \text{ s}^{-1}$ . Using a  $g_{max}$  of 1899  $\text{mmol-H}_2\text{O m}^{-2} \text{ s}^{-1}$  would lead to an overestimation of the bulk-canopy stomatal conductance in Jmod so a value of 985  $\text{mmol-H}_2\text{O m}^{-2} \text{ s}^{-1}$  was used, as shown below. For JmodG, where leaf conductance is being estimated a value 1350  $\text{mmol-H}_2\text{O m}^{-2} \text{ s}^{-1}$  was used, which is the 95<sup>th</sup> percentile of the measurements.

### 6.1.3 Parameterising the Jarvis Type Models (Jmod and JmodG)

These models are normally parameterised using a boundary line analysis of variations in leaf-level stomatal conductance with the relevant variables, as described in Section 3.2.3.1. However, as bulk-canopy scale conductance is required the analysis is done using the micrometeorological measurements of water-vapour flux across the whole field. The need for up-scaling from leaf to canopy is therefore avoided at this stage and equation (85) is used for the light response. Normally the relationships would be fitted around the maximum values, however as we are using bulk-canopy data, where despite filtering there may be some interference from non-transpired water-vapour and the 95<sup>th</sup> percentile is used.

The canopy-scale values of  $R_{c1w}$  described in Section 5.5 are converted into conductance ( $g_{s_c}$ ) in  $\text{mmol-H}_2\text{O m}^{-2} \text{ s}^{-1}$  and plotted against PAR,  $T_{z0}$ , vpd, SWP and LAI in Figure 6.1a to e, to derive the relevant scaling relationships (equation 84).

To ensure the data are only representative of the water-vapour flux from the stomata, measurements during dry, daylight conditions when LAI > 1.5 are used. The plots show scatter typical of such analysis (Avisar, 1993; ICP, 2004) and the response functions are fitted by blocking the data and taking 95<sup>th</sup> percentiles. The function for the light response,  $f_{light}$ , was fitted using non-linear regression and gave a value for  $g_{max}$  of  $985 \text{ mmol-H}_2\text{O m}^{-2} \text{ s}^{-1}$  which is used in the final model.

The measurements are representative of the bulk-canopy (with LAI > 1.5) and so it is not necessary to scale the modelled  $g_{s_j}$  for LAI, as is done in JmodG (equation (83)). However, when the canopy is cut or grazed, conductance will be reduced due to there being less green leaf material and a  $f_{LAI}$  function is required to account for this. The plot of  $g_{s_c}$  with LAI in Figure 6.2 shows a decrease below LAI  $\sim 2$  but as soil may also be exposed these measurements slightly overestimate  $g_{s_c}$ .  $f_{LAI}$  is therefore fitted as a simple step function that decreases linearly below LAI = 2 with a slightly steeper slope than that indicated by the data.

$$R_{c1\_O3J} = 1.51 \left[ \frac{g_{max} f_{pot} \left( \text{maximum} \left( g_{min}, \left( f_{light} \cdot f_T \cdot f_{vpd} \cdot f_{SWP} \cdot f_{LAI} \right)^{-1} \right) \right)}{a_w} \right]^{-1} \quad (128.)$$

where  $a_w$  is the conversion factor for  $\text{mol m}^{-2} \text{ s}^{-1}$  to  $\text{m s}^{-1}$  from equation (66)

The time series of water-vapour and CO<sub>2</sub> flux measurements were examined to estimate the parameter values for  $f_{pot}$ . The minimum value was set at 0.5, as although the canopy did not grow during the winter there was still significant activity when the weather was mild. The growing season start and end days for the phenology function,  $f_{pot}$  (Figure 3.2) were simply set at day 1 and 365 as this best reflected the changes in the flux data. The relevant parameters are shown on each plot in Figure 6.1 and summarised in Table 6.1.

Although no equivalent parameter values could be found in the literature for comparison they are within the range typically reported for temperate species. For example the values used by the EMEP model for grassland were derived from

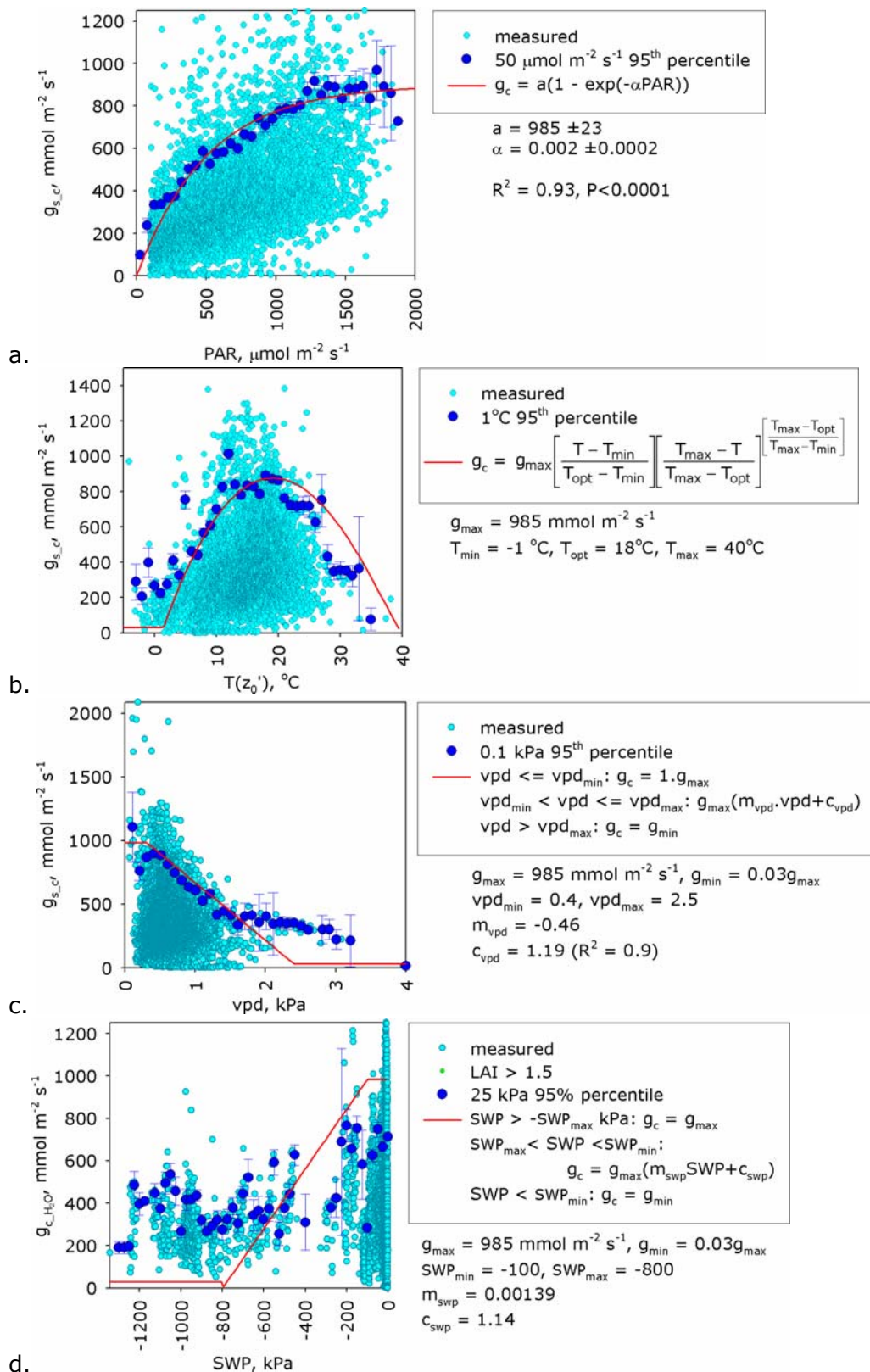


Figure 6.1. Data used in the parameterisation of Jmod, bulk-canopy scale  $R_{c1w}$  plotted as conductance ( $g_{s,c}$ ) against (a) measured total PAR, (b) surface temperature,  $T_{z_0'}$ , (c) vpd, and (d) SWC. Both the 30 minute average values and 90<sup>th</sup> percentiles are shown. The error bars show the 95% confidence level for each blocked value. The response curves are fitted to the 90<sup>th</sup> percentiles and the resulting parameter values are also shown.

clover and wheat data and are shown in Table 6.2. As the EMEP model has to operate across a wide range of climates, from the Mediterranean to Scandinavia, the parameters are greatly generalised.

For JmodG ideally the analysis would be repeated with leaf-level measurements however as sufficient data are not available, the same parameter values as Jmod were for  $f_{min}$ ,  $f_{pot}$ ,  $f_T$ ,  $f_{vpd}$  and  $f_{SWP}$ . To more closely follow the normal practice of using the outer boundary line of the light response,  $g_{max}$  was increased to 1350  $\text{mmol-H}_2\text{O m}^{-2} \text{s}^{-1}$  (95<sup>th</sup> percentile of the leaf measurements) and  $\alpha$  was also increased to -0.004 which results in a steeper response curve. The leaf-level measurements are plotted with the scaling functions in Figure 6.3. The resulting values of  $R_{cL\_JG}$  were used in a full ozone deposition model with total canopy resistance calculated according equation (83) with different estimates of  $R_{ns}$ .

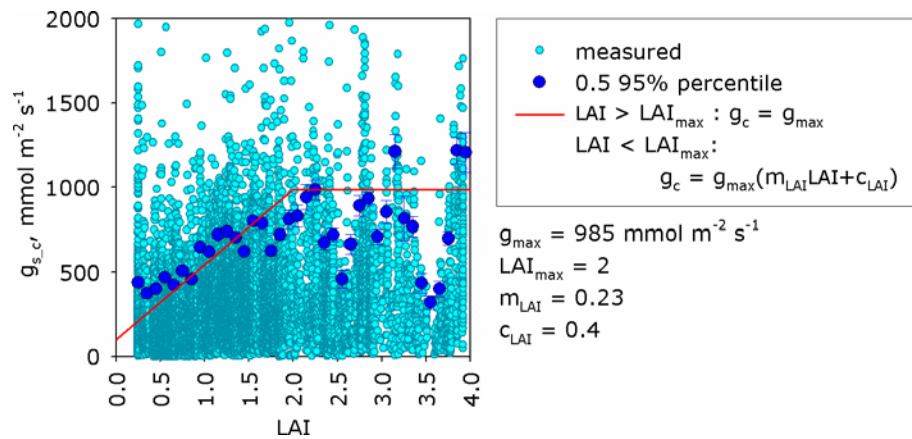


Figure 6.2. Bulk-canopy scale  $R_{c1w}$  plotted as conductance ( $g_{s,c}$ ) LAI and the fitted response curve. Both the 30 minute average values and 90<sup>th</sup> percentiles are shown. The error bars show the 95% confidence level for each blocked value. The response curve is fitted to the 90<sup>th</sup> percentiles and the resulting parameter values are also shown.

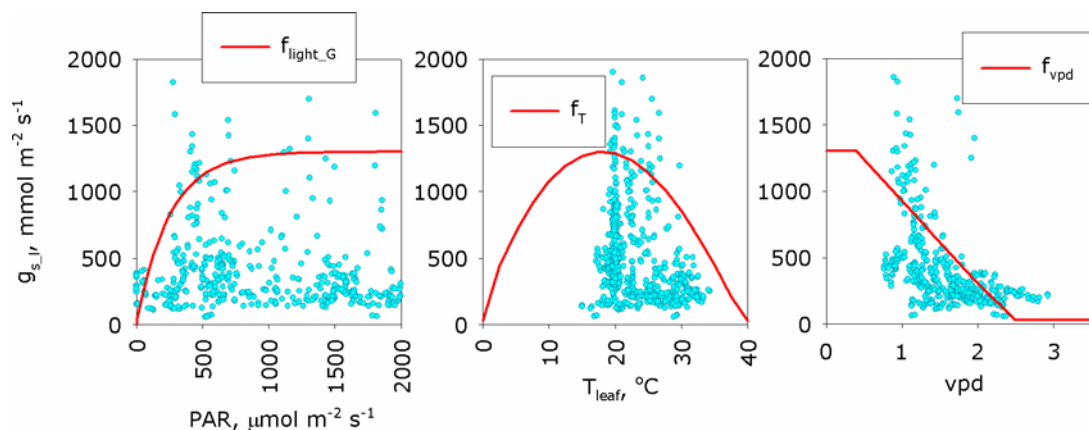


Figure 6.3. Leaf-porometer measurements of leaf stomatal conductance ( $g_{s,l}$ ) in the field and solardomes plotted with the response curves used for JmodG.

Table 6.1 Parameters for Jmod and JmodG

	Jmod		JmodG	
$g_{\max}$	985		1350	
$f_{\min}$	0.033		0.0033	
	$\alpha$		$\alpha$	
$f_{\text{light}}$	-0.002		-0.004	
$f_T$	$T_{\min}$	$T_{\text{opt}}$	$T_{\max}$	
	-1	18	40	
$f_{\text{vpd}}$	$\text{vpd}_{\min}$	$\text{vpd}_{\max}$		
	0.4	2.5		
$f_{\text{SWP}}$	$\text{SWP}_{\min}$	$\text{SWP}_{\max}$		
	-800	-100		
$f_{\text{LAI}}$	$g_{\min}$	$\text{LAI}_{\max}$		
	0.11	2		
$f_{\text{pot}}$	Day number			
	Start Growth	End Growth	Start Senescence	End Senescence
	1	91	274	365
	$f_{\text{potmin}}$	0.5		

Table 6.2 Parameters used by the EMEP model

	Grassland		
$g_{\max}$	407		
$f_{\min}$	0.01		
	$\alpha$		
$f_{\text{light}}$	-0.009		
$f_T$	$T_{\min}$	$T_{\text{opt}}$	$T_{\max}$
	12	26	40
$f_{\text{vpd}}$	$\text{vpd}_{\min}$	$\text{vpd}_{\max}$	
	1.3	3.0	
$f_{\text{SWP}}$	$\text{SWP}_{\min}$	$\text{SWP}_{\max}$	
	-1500	-490	

### 6.1.3.1 Ball-Berry Type (Bmod)

The final model to be parameterised is Bmod. As we have measurements of  $\text{CO}_2$  flux and an estimate of  $R_d$ , its derivation is less empirical than Jmod or JmodG. The field scale measurements of  $\text{CO}_2$  flux include the non-stomatal components,  $R_d$  (day-time leaf respiration) and soil respiration ( $A_s$ ). As part of the GREENGRASS project, measurements of soil respiration were made on almost monthly intervals from January 2003 to March 2005 (ongoing). The measurements were made using a portable respiration meter which has small opaque chamber. This chamber is placed over a patch of ground where the grass had been trimmed down to the soil level, and measurements recorded over several minutes. The results showed typical seasonal variation in soil respiration, with higher levels during the summer than winter, as increased soil temperature

stimulates microbial activity. For Bmod these measurements were simply collated into monthly means to provide a monthly estimate  $A_s$ , which varied from  $\sim 2 \mu\text{g-CO}_2 \text{ m}^{-2} \text{ s}^{-1}$  in the winter to a peak of  $10 \mu\text{g-CO}_2 \text{ m}^{-2} \text{ s}^{-1}$  in August (Figure 6.4).

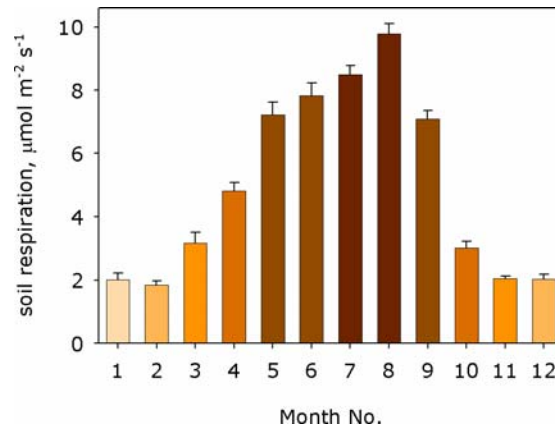


Figure 6.4. Monthly average soil respiration measured at Easter Bush.

To estimate  $g_{s\_c}$  the measured values were plotted against the Ball-Berry ratio, in the form (Figure 6.5):

$$g_{s\_c} = m \frac{(A_n - A_s - R_d)RH_s}{\chi_{CO_2}(z_0')} + b \quad (129.)$$

where  $A_n$  is the measured  $\text{CO}_2$  flux,  $A_s$  is the estimated soil respiration and  $R_d = 3.5 \mu\text{mol-CO}_2 \text{ m}^{-2} \text{ s}^{-1}$

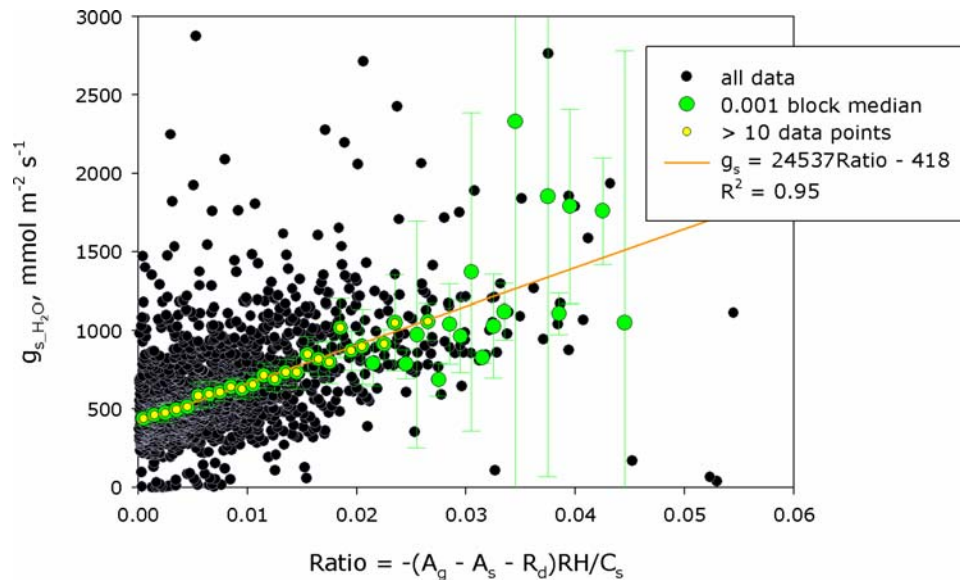
$$\chi_{CO_2}(z_0) = \chi_{CO_2}(z-d) + A_n(R_a(z-d) + R_{bCO_2})$$


Figure 6.5. The Ball-Berry relationship for bulk-canopy respiration and stomatal conductance measured at Easter Bush. The error bars show the 95% confidence level for each median value. The line is fitted to the median ratio  $((-A_g - A_s - R_d)RH/C_s)$  values.

There is some scatter in the relationship and so linear regression was performed on block medians of the data. The resulting model was used to directly estimate  $g_{s_c}$  when  $PAR > 5 \mu\text{mol m}^{-2} \text{s}^{-1}$  ( $PAR < 5 \mu\text{mol m}^{-2} \text{s}^{-1}$ ,  $g_{s_c} = 30 \text{ ng m}^{-2} \text{s}^{-1}$ ), the results of which are considered in the following sections.

## ***6.2 Comparison of Measured and Modelled Stomatal Conductance***

### **6.2.1 Leaf-level measurements in the field**

The leaf-level measurements made using the portable porometer in the field during 2001 are used to assess the performance of each model. However as they are made for short periods they are averaged over each half-hour during which they occur, with from 2 to 10 samples per half hour period. Additionally, as they are for the leaf ( $g_{s_l}$ ) they must be scaled up-to the canopy for comparisons with JMod and BMod. The ambient measurements were made immediately after the porometer's chamber was attached to the leaf, ie they should be representative of the current temperature, vpd, SWP and phenological state. Taking the Jmod approach, only the effects of canopy light levels need be accounted for to estimate  $g_{s_c}$ , and so this was done using the concurrent values of  $f_{light}$  from JModG.

Bearing in mind that the leaf level measurements represent a very small sample and stomatal conductance can vary from leaf to leaf within an individual plant as well as from plant to plant, it is anticipated that this type of comparison will give mixed results. The plots in Figure 6.6 show each estimate of  $g_{s_c}$  and this is indeed the case. It cannot be said the agreement is good although they are all within the same order of magnitude and some individual estimates match quite closely. On 8<sup>th</sup> of June, with the exception of the first point from BMod, all the values are larger than the leaf measurement but as this was a few days after the first silage harvest an uncut plant was sampled on the field boundary which is likely to be very different from the field as a whole. On the 21<sup>st</sup> and 2<sup>nd</sup> of June the canopy was taller and plants within the fetch of the micrometeorology instruments were sampled. The results are quite variable on these days which may reflect a high degree of inhomogeneity across the fields as the plants were re-growing. The best agreement is on the 18<sup>th</sup> of July, a few days before the second cut, when the canopy had grown substantially and was more homogenous. These results, summarised in Table 6.3, illustrate the complexity

of the processes controlling stomatal conductance but demonstrate that bulk-canopy measurements and simple models are capable of making representative estimates of canopy conductance.

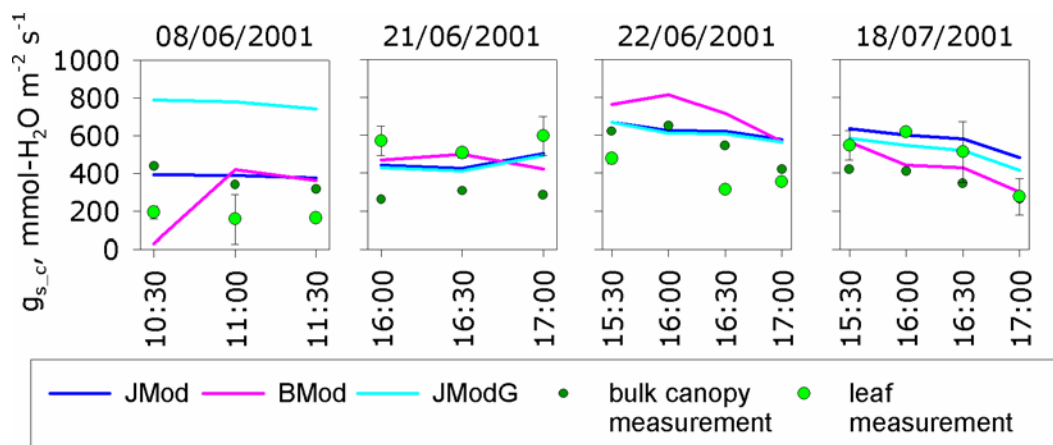


Figure 6.6. Comparisons of leaf-level and canopy level measurements of bulk-canopy stomatal conductance with estimates from JMod, BMod and JModG (the error bars show the standard deviation of the leaf level measurements).

Table 6.3 Summary of measured and modelled estimates of stomatal conductance on days when leaf-level conductance was measured.

**A. Summary Statistics**

2001	LAI	Average Leaf-scaled	Stdev	N	Average			
					Bulk-Canopy	Jmod	Bmod	JModG
<b>8<sup>th</sup> May</b>	1.5							
	10:30	194.5	33.3	6	439.5	393.3	30.0	791.1
	11:00	157.7	130.2	10	341.2	390.4	421.0	780.1
	11:30	164.3	8.1	4	317.6	377.3	362.8	741.8
<b>21<sup>st</sup> May</b>	2.8							
	16:00	571.1	78.0	10	260.2	442.9	469.8	429.4
	16:30	507.8	27.6	8	306.8	424.2	498.3	411.1
	17:00	596.7	102.6	6	284.7	503.1	423.7	494.3
<b>22<sup>nd</sup> May</b>	2.9							
	15:30	477.3	28.5	2	621.5	668.2	764.0	668.8
	16:30	312.4	8.0	2	545.5	622.8	714.7	608.7
	17:00	353.7	10.1	2	419.9	579.2	566.9	564.7
<b>18<sup>th</sup> July</b>	3.7							
	15:30	545.5	77.8	4	419.5	635.9	563.9	584.4
	16:00	616.8	22.6	3	410.2	599.6	440.9	545.8
	16:30	511.9	160.5	5	345.7	581.1	427.2	520.9
	17:00	275.0	95.5	6	263.7	481.2	298.7	415.4
<b>8<sup>th</sup> May</b>	1.5	172.1	64.4	6	366.1	387.0	271.3	771.0
<b>21<sup>st</sup> May</b>	2.8	558.5	38.2	10	283.9	456.7	463.9	444.9
<b>22<sup>nd</sup> May</b>	2.9	634.7	22.7	4	562.3	632.1	720.7	626.2
<b>18<sup>th</sup> July</b>	3.7	487.3	56.8	10	359.8	574.5	432.7	516.6

Table 6.3 Summary of measured and modelled estimates of stomatal conductance on days when leaf-level conductance was measured.

<b>B. %Difference from leaf measurement</b>				
<b>2001</b>	<b>Bulk-Canopy</b>	<b>Jmod</b>	<b>Bmod</b>	<b>JModG</b>
<b>8<sup>th</sup> May</b>				
10:30	-126%	-102%	85%	-307%
11:00	-116%	-148%	-167%	-395%
11:30	-93%	-130%	-121%	-352%
<b>21<sup>st</sup> May</b>				
16:00	54%	22%	18%	25%
16:30	40%	16%	2%	19%
17:00	52%	16%	29%	17%
<b>22<sup>nd</sup> May</b>				
15:00	59%	52%	47%	51%
15:30	-30%	-40%	-60%	-40%
16:00				
16:30	-75%	-99%	-129%	-95%
17:00	-19%	-64%	-60%	-60%
<b>18<sup>th</sup> July</b>				
15:30	23%	-17%	-3%	-7%
16:00	33%	3%	29%	12%
16:30	32%	-14%	17%	-2%
17:00	4%	-75%	-9%	-51%
<b>8<sup>th</sup> May</b>	-113%	-125%	-58%	-348%
<b>21<sup>st</sup> May</b>	49%	18%	17%	20%
<b>22<sup>nd</sup> May</b>	11%	0.4%	-14%	1%
<b>18<sup>th</sup> July</b>	26%	-18%	11%	-6%

### 6.2.2 Results for the canopy-scale

As the models are derived from all the measurements where LAI > 1.5 they are not entirely independent of each other, however comparing the complete data sets does give an indication of how well the models perform. The results show considerable variability but BMod appears to follow the bulk-canopy measurements more closely than JMod or JModG. The plots in Figure 6.7 show scatter plots of each modelled data set with the measured values. There is a lot of scatter in both estimates of  $g_{s_c}$  with Jmod and JmodG showing a tendency to underestimate the larger values. The scatter in Jmod/JModG is typical of such models (Finkelstein *et al.*, 2000) and is due to the use of the fixed  $g_{max}$  which places an upper limit on  $g_{s_c}$ . However, JModG generally over predicts while JMod slightly under predicts, due to the different values of  $g_{max}$  used in each. Bmod appears to perform better in that it predicts some of the larger values, but it also tends to overestimate. The summary and comparison statistics of these data are given in Table 6.4, they have been calculated using points where there is an estimate from all three models to allow cross-comparisons.

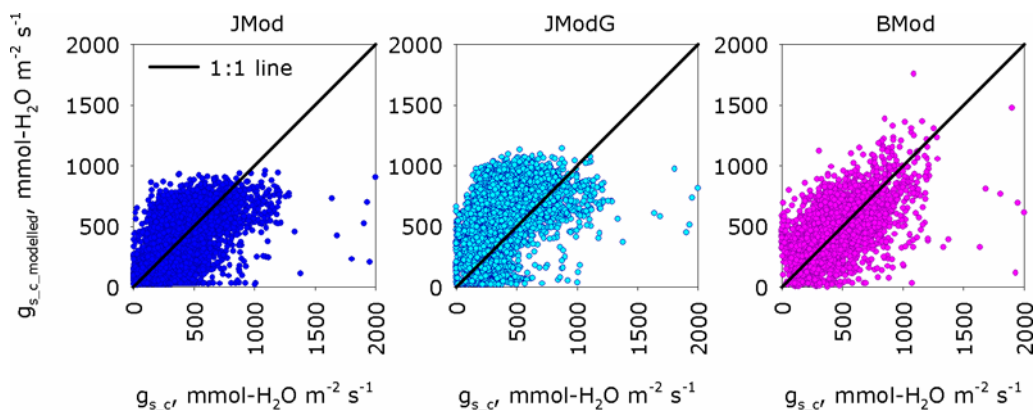


Figure 6.7. Scatter plots of measured vs modelled estimates of bulk-canopy conductance to water-vapour.

Considering the time series of data, there are seasonal patterns in each model's performance as shown in Figure 6.8. JMod and JModG underestimate  $g_s$  in the winter months, due to the simple phenology function they use, whereas BMod overestimates. This could be due to the soil respiration rate being too small which would lead to  $g_s$  being over predicted. All three models most closely agree with the measurements in the summer months although there is a lot of inter-year variability. There is also variability from day to day and period to period, with one model agreeing well for a period then another on the next (as illustrated in Figure 6.9), which make it difficult to judge which performs best overall.

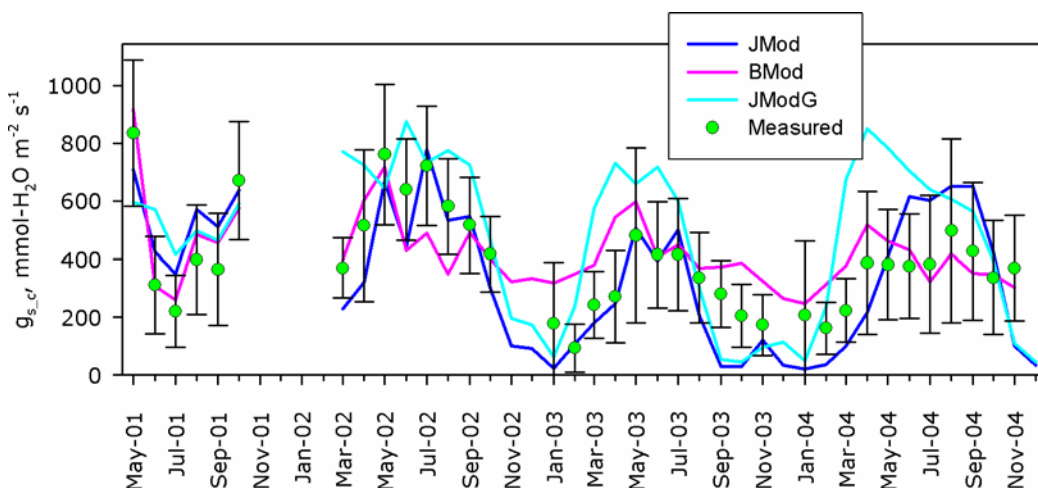


Figure 6.8. Monthly median estimates of bulk canopy conductance to water-vapour. NB the data sets are matched to include 30 minute periods where all 4 estimates are available and thus represent day-time dry periods only.

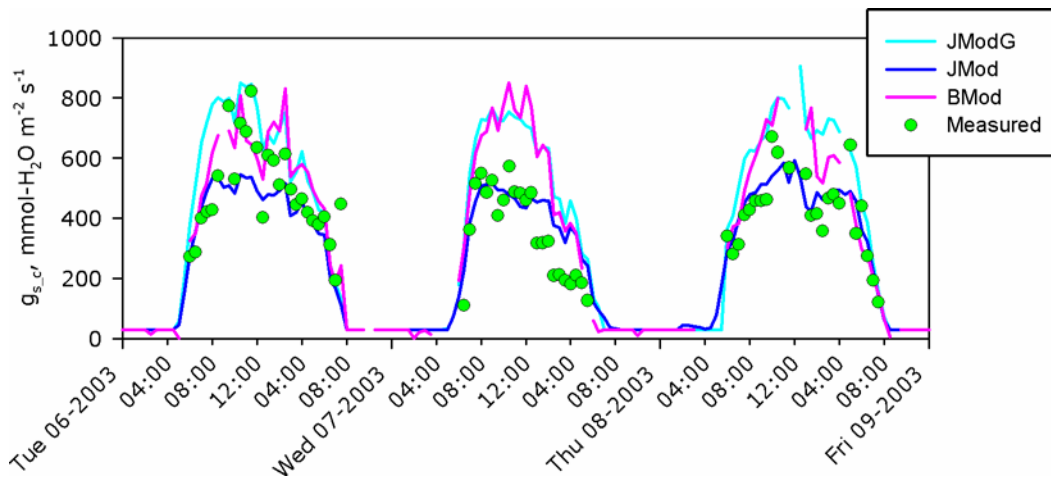


Figure 6.9. Example of  $g_{s,w}$  estimated from measurement and models of a series of days in 2003.

Table 6.4 Summary of measured and modelled estimates of canopy conductance to water-vapour ( $\text{mmol-H}_2\text{O m}^{-2} \text{s}^{-1}$ ).

	Measured	JMod	JModG	BMod
Average	393	366	539	435
Median	352	363	581	410
Stdev	223	228	264	198
Max	1999	955	1143	2429
Min	0.59	17	21	0.14
10 <sup>th</sup> Percentile	153	30	27	211
90 <sup>th</sup> Percentile	688	670	808	686
Median Residual		27	-146	-42
Average Residual		21	-164	-61

However, considering that the models are using simple methods to simulate a wide range of conditions, they represent the variation in conductance with environmental factors reasonably well and yield useful estimates of  $R_{cl_{O_3}}$ . Their performance could be improved in several ways for example: using seasonal parameterisations in each model; a temperature sum based phenology function in JMod/JModG; the inclusion of the  $\text{CO}_2$  compensation point in BMod and more detailed estimates of soil respiration.

The ozone flux measurements appear to be small during June-July 2004 then large during the autumn and winter which is a feature of the data that has no obvious cause. There is a similar pattern in the  $\text{CO}_2$  flux measurements although values are not so small in June-July or enhanced during November and December. In Figure 6.8 it appears that the estimates of stomatal conductance from the water-vapour flux measurements and BMod are large over the autumn-

winter period. From these results it would appear that there may be a problem with the baseline turbulence data from the Metek sonic or that some unusual factors caused the plants to reduce their activity then become very active. Given that the former is more likely, the data from the 8<sup>th</sup> of June 2004, when the ozone flux started to decline, are excluded from further analysis.

### **6.3 Stomatal vs Non-stomatal Flux**

The JMod and BMod values of  $g_{s_w}$  are converted into resistances using equation (66) and then converted for ozone using a factor of 1.51. Results from JModG are not used here as it has been setup to test any parameterisation for  $R_{ns}$  that arise from the following analysis and use the more typical method of scaling leaf conductance to the bulk-canopy.

A comparison of the JMod and BMod estimates of  $R_{c1_{O3}}$  with the measured values indicated that the models were performing well when the residual between measurement and model was  $\pm 100 \text{ s m}^{-1}$ . However to avoid any bias in the final estimate of  $R_{ns}$  the measured time series was gap-filled using data when the 7 day running median residual was less than  $\pm 50 \text{ s m}^{-1}$ , this effectively excluded the periods when the model performance was very poor. The non-stomatal resistance to ozone uptake could then be calculated as the residual of  $R_c$  and  $R_{c1_{O3}}$  as described in Section 2.5. However, there were some points where  $R_{c1_{O3}}$  was found to be smaller than  $R_c$  which gave a negative value for  $R_{ns}$ . These tended to be during the summer months when the stomatal flux is a larger component of the total and so the method is most sensitive to uncertainties in the estimates of  $R_c$  or  $R_{c1}$ . The resulting data set covers 17% of the measurement period (compared to only 4% using the measurements alone) with 9277 samples: 23% are derived from measurements, 20% from BMod and 57% from JMod.

Overall the flux is dominated by the non-stomatal component with 64% of the total overall being non-stomatal and 36% stomatal. During the day-time the stomatal flux increases to >60% in the summer and is only ~20% in the winter, whereas during the night-time the non-stomatal flux is always 85-90% of the total (Figure 6.10). Although stomatal conductance is reduced at night both types of model do not predict zero conductance to account for the stomata not fully closing and so there is still a small fraction of stomatal flux at night.

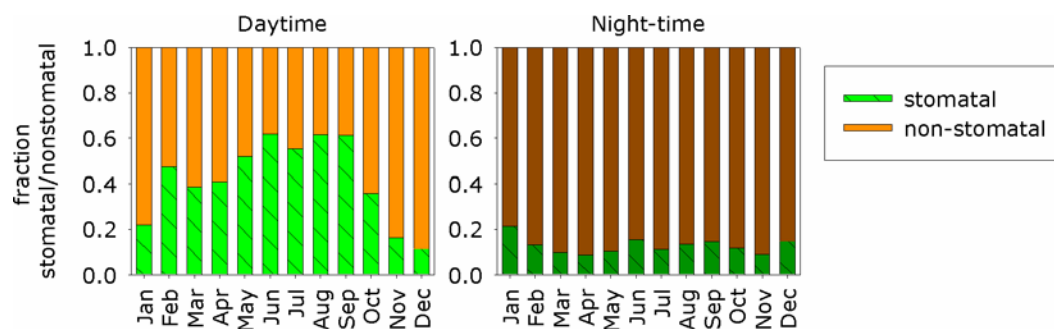


Figure 6.10. Proportion of the monthly median ozone flux that is either stomatal or non-stomatal during the day and night.

## 6.4 What Controls Non-Stomatal Resistance

The stomatal resistance to ozone has been calculated from the measurements of water-vapour flux ( $R_{cl\_c}$ ) and by the application of two simple models with the measured data ( $R_{cl\_Jmod}$  and  $R_{cl\_Bmod}$ ). It was shown in Section 5.7 that the night-time resistance (which is assumed to be the non-stomatal) decreases as surface temperature increases, and the response is suppressed when the surface is wet. The non-stomatal component of surface resistance ( $R_{ns}$ ) is now separated from the total using equation (73) and its response to various environmental variables examined.

### 6.4.1 Measured $R_{ns}$ in Dry-Daylight Conditions

As has been described  $R_{cl\_c}$  is only calculated in dry daylight periods to ensure the water-vapour flux is from the stomata. As an additional filter to exclude interference from soil moisture, measurements where LAI is less than 1.5 are also excluded. The resulting estimates of  $R_{ns\_c}$  are summarised in Figure 5.36 and plotted against LAI, surface temperature and solar radiation in Figure 6.11a to c respectively. The data are quite scattered but patterns are visible:  $R_{ns\_c}$  decreases slightly with increasing LAI as there will be a larger surface area for ozone to deposit to; there is a decrease with increasing surface temperature (as was found for  $R_{c\_night}$ ) and solar radiation. The relative importance of solar radiation or surface temperature is difficult to judge as they are closely coupled. High radiation levels lead to high surface temperatures directly through surface heating. However, given that  $R_{c\_night}$  responds quite clearly to temperature, ie in the absence of solar radiation, it is assumed that temperature is the main controlling factor. It is also possible that the observed relationship with  $T_{z0}'$  is being confounded by LAI.  $R_{ns}$  will decrease as LAI increases due to the increased

surface area available for deposition and the largest increases in LAI values occur in the summer months when temperatures are also high. Figure 6.11d shows the results of plotting measured  $R_{ns}/LAI$  against  $T_{z0}'$  and the response is still visible. To quantify the relationship the data are blocked into 1 °C bands  $R_{c1\_c}$ ,  $R_c$  and  $R_{ns\_c}$  recalculated for each. The results are shown in Figure 6.12a and the curve parameters are given in Table 6.5 Set 1.

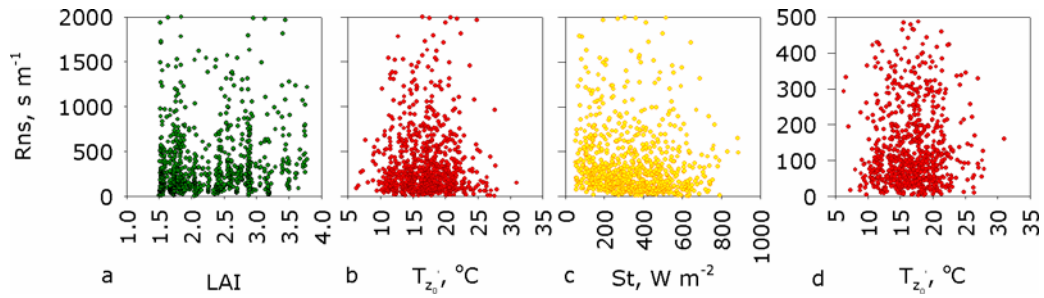


Figure 6.11. The variation of  $R_{ns\_c}$  (dry-daylight conditions where  $LAI > 1.5$ ) with LAI, surface temperature and solar radiation.

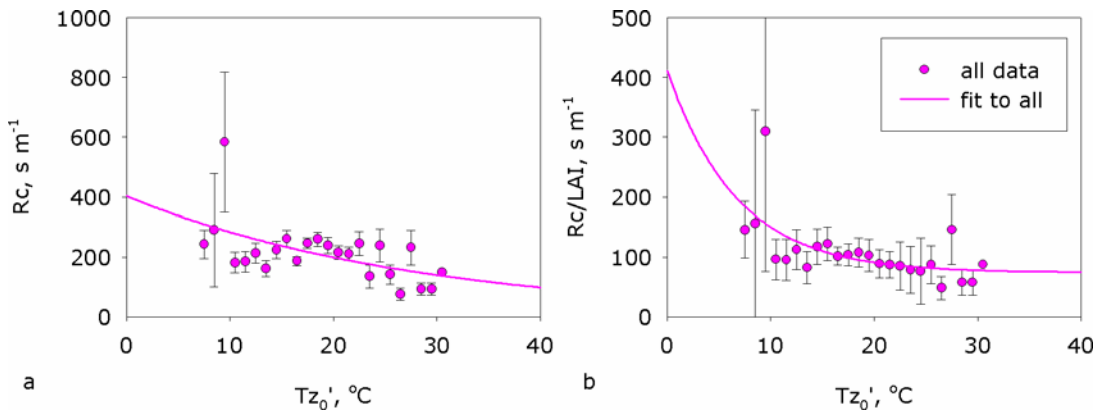


Figure 6.12. (a) The response of  $R_{ns\_c}$  (dry-daylight conditions where  $LAI > 1.5$ ) to surface temperature and (b) the data normalised for average LAI.

This data set is limited to quite specific conditions resulting in a relatively small sample size (2823) that represent periods when the stomatal resistance is likely to be a large component of the total and the estimates of  $R_{ns}$  are therefore more uncertain. Despite this restriction the temperature response is clearly evident and normalising the points for LAI improves the fit (Figure 6.12b), with both curves being similar to the results for  $R_{c\_night}$ . To more clearly define the temperature response in a wider range of conditions and examine the effects of surface wetness, the dataset is now expanded to include all the measured  $R_{c1}$  results and the modelled values from JMod and BMod.

### 6.4.2 The $R_{ns}$ Temperature Response

As in the preceding analysis the data are blocked in fixed ranges of the variable being investigated and the  $R_{ns}$  values recalculated for each range. However as a starting point, plots of the three data sets against the relevant variables ( $T_{z0}$ ,  $St$ , LAI and RH) are shown in Figure 6.13. The measured values of  $R_{ns}$  in Figure 6.8d have only been filtered for rainfall and surface wetness to show the variation with humidity, so there may be some interference from non-transpired water-vapour. Despite the different sources of the three estimates of  $R_{ns}$  (although they are ultimately derived from the same water-vapour flux data) they all show very similar variation. Making a purely qualitative comparison the BMod data resemble the measurements, in terms of the range of variation and response to each variable. The JMod results tend to give larger values, due to the nature of the model and the wider range of conditions they represent (Section 6.2.2), but overall the variation with each parameter is similar.

The results of blocking each dataset with temperature are summarised in Table 6.5 Set 2. In this analysis the median values of only  $R_{ns\_cr}$ ,  $R_{ns\_Jmod}$  and  $R_{ns\_Bmod}$  used as this does not significantly affect the results. The curve fitting is limited to points where the standard error is less than 20% and is repeated with  $R_{ns}$  normalised for the average LAI ( $R_{nsn} = R_{ns}/LAI$  where  $LAI > 1$ ). The initial fits yielded a stronger temperature response from the BMod data due to high  $R_{ns}$  values at low temperatures. However, when the data are normalised for LAI this difference is reduced slightly (Table 6.5 Set 3), and all three decline to similar values at 30°C.

The gap-filled time series of  $R_{ns}$  is now used (Section 6.3) and as there is no straightforward way to recalculate  $R_{cl}$  (and so  $R_{ns}$ ) from this combined data set the medians of  $R_{ns}$  in each variable block are used. In the following discussion the combined data set is taken to be our best estimate of the true non-stomatal resistance and is simply referred to as  $R_{ns}$ .

The individual data sets all yielded a clear temperature response and, as would be expected, the combined data does also. The blocked data are shown in Figure 6.5 and the results of curve fitting in Table 6.5. As before, normalising for LAI improves the relationship (standard errors are reduced and  $R^2$  increases) and indicates a slightly higher value for  $R_{ns}$  at low temperatures and lower value at high temperatures.

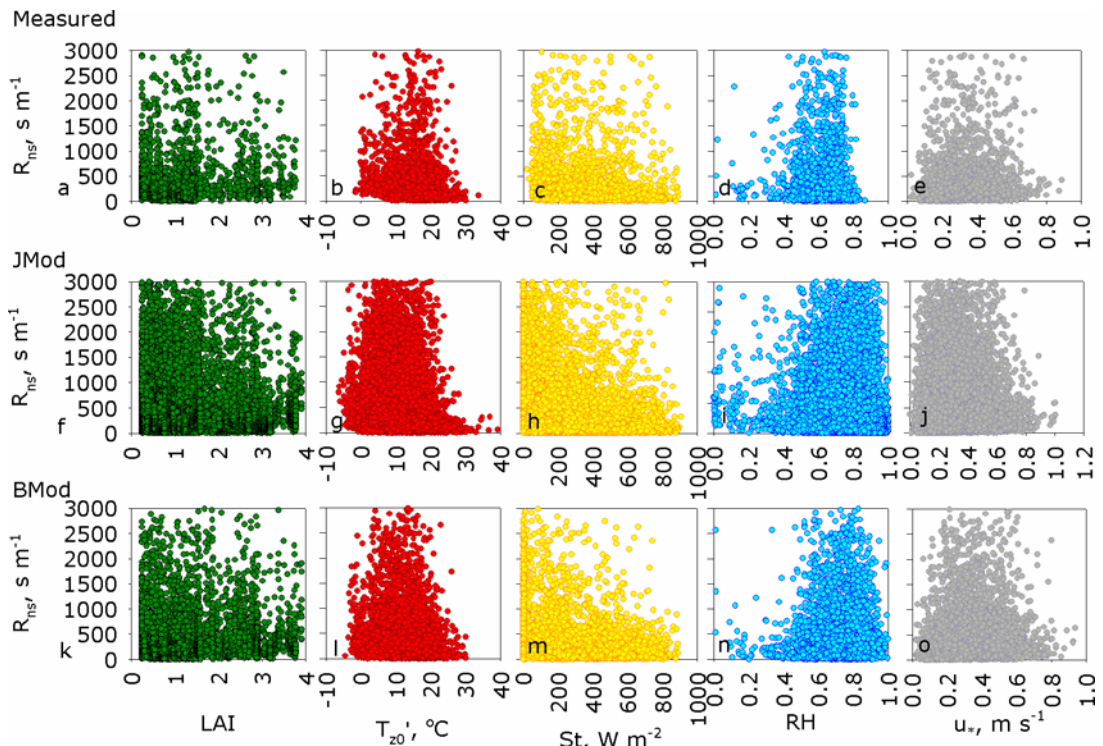


Figure 6.13. The variation of measurement and model derived estimates of  $R_{ns}$  with LAI, surface temperature ( $T_{20'}$ ), solar radiation ( $St$ ), relative humidity ( $RH$ ) and friction velocity ( $u_*$ ).

Table 6.5 Results of fitting  $R_{ns} = y_0 - a \exp(-bT)$  to  $1^\circ\text{C}$  blocked values of  $R_{ns}$  at Easter Bush (in units of  $\text{s m}^{-1}$ , with standard errors for the fitted parameters). For reference the results for  $R_{c\_night}$  are also given.

$R_{ns}$ Data Set	$y_0$	$a$	$b$	$R_{ns}$ at $0^\circ\text{C}$	at $30^\circ\text{C}$	$R^2$
1 Measured	$7.28 \times 10^{-7} \pm 672$	$403.6 \pm 503.3$	$0.035 \pm 0.112$	404	140	0.23
Dry, LAI > 1.5						
Norm. LAI	$74.2 \pm 25.2$	$337.5 \pm 312.3$	$0.15 \pm 0.12$	412	78	0.31
2 All Measured	$101.3 \pm 37.0$	$423.1 \pm 37.3$	$0.09 \pm 0.03$	524	126	0.81
JMod	$2.6 \times 10^{-6} \pm 198$	$321.6 \pm 187.6$	$0.03 \pm 0.03$	322	128	0.82
BMod	$2.1 \times 10^{-6} \pm 204$	$334.6 \pm 192.4$	$0.03 \pm 0.03$	335	134	0.80
3 All Meas./LAI	$62.8 \pm 33.6$	$493.3 \pm 37.9$	$0.11 \pm 0.02$	556	83	0.86
JMod/LAI	$16.5 \pm 27.5$	$323.9 \pm 23.6$	$0.06 \pm 0.01$	340	69	0.97
BMod/LAI	$56.9 \pm 22.3$	$299.5 \pm 19.7$	$0.08 \pm 0.01$	356	83	0.95
4 $R_{ns}$	$164 \pm 39$	$293 \pm 51$	$0.11 \pm 0.04$	457	176	0.63
$R_{nsN}$	$127 \pm 13$	$388 \pm 32$	$0.18 \pm 0.03$	514	128	0.90
5 $R_{nsN}$ -Dry	$61 \pm 94$	$477 \pm 79$	$0.07 \pm 0.03$	538	114	0.80
$R_{nsN}$ -Wet	$159 \pm 9$	$191 \pm 100$	$0.33 \pm 0.17$	350	159	0.53
$R_{nsN}$ -Wet (all)	$145 \pm 27$	$90 \pm 25$	$0.11 \pm 0.10$	235	148	0.49
$R_{c\_night\_alldata}$	$56 \pm 54$	$347 \pm 27$	$0.07 \pm 0.03$	403	101	0.91
$R_{c\_night\_dry}$	$\rightarrow 0$	$736 \pm 484$	$0.10 \pm 0.17$	736	37	0.88
$R_{c\_night\_wet}$	$395 \pm 287$	$152 \pm 258$	$0.07 \pm 0.24$	243	376	0.14

In the analysis of  $R_{c\_night}$ , it was found that the surface resistance was reduced at low temperatures during wet conditions and the temperature response was suppressed for fully wetted canopies; whereas in dry conditions the effect was enhanced, although the relationship was very uncertain due to the low sample size. The  $R_{ns}$  time series is therefore split into dry and wet periods using the same criteria and  $R_{nsN}$  is examined. The estimate of stomatal resistance relies entirely on the models in wet conditions as it cannot be measured when the surface is wet. The models do not explicitly include any effect of surface wetness although it is possible that the presence of substantial water films may block the diffusion pathway through stomata and so increase resistance. However, as rainfall events normally occur during periods when JMod will increase resistance in response to other environmental factors, such as temperature or radiation, and BMod uses the CO<sub>2</sub> flux measurements which will reflect the real stomatal conductance, the effect on estimates of  $R_{ns}$  is assumed to be minimal. Also, *Lolium perenne* only has stomata on the lower leaf surface (hypostomatous) and the stomata are less likely to be blocked when the surface is wet.

These segregated data sets indicate the response of  $R_{nsN}$  is again more pronounced for the dry canopy in that it is large at low temperatures ( $\sim 538 \text{ s m}^{-1}(\text{m}^2\text{m}^{-2})$ ) but decreases exponentially with temperature, to a minimum of  $\sim 110 \text{ s m}^{-1}(\text{m}^2\text{m}^{-2})$  at 30°C. The results of fitting the curve to all the available data points and only those with standard errors less than 100% are shown in Figure 6.14a but as they are very similar only the latter is given in Table 6.5 Set 5. For very wet canopies  $R_{nsN}$  is also slightly larger at low temperatures ( $\sim 350 \text{ s m}^{-1}(\text{m}^2\text{m}^{-2})$ ) but declines more quickly and is virtually constant at  $\sim 159 \text{ s m}^{-1}(\text{m}^2\text{m}^{-2})$  above 15°C. This initially seems a slightly small resistance value for wet surfaces but if it is scaled for a typical LAI of 2.5, *ie*  $375 \text{ s m}^{-1}$ , it compares well with other values reported for wet canopies (Table 2.2). However, this result is more uncertain as, despite the smaller standard errors, the fitted curve is slightly different if all data point points are used. In this case the resistance at low temperatures is smaller at  $\sim 235 \text{ s m}^{-1}(\text{m}^2\text{m}^{-2})$  although it declines to a similar value of  $\sim 150 \text{ s m}^{-1}(\text{m}^2\text{m}^{-2})$  above 15°C.

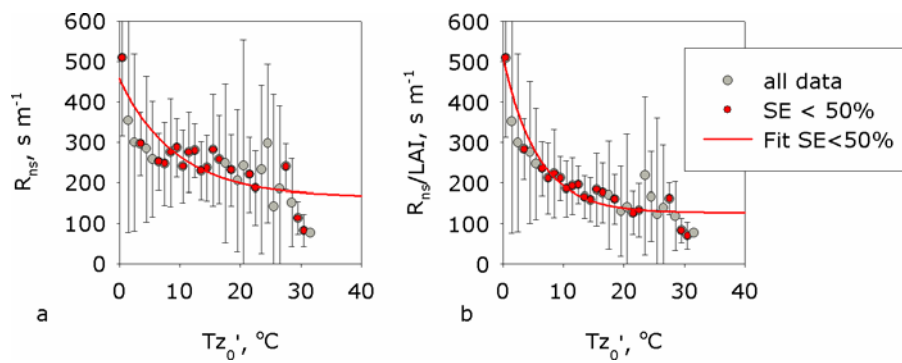


Figure 6.14. (a) The temperature response of  $R_{ns}$  during all conditions and (b) normalised for LAI.

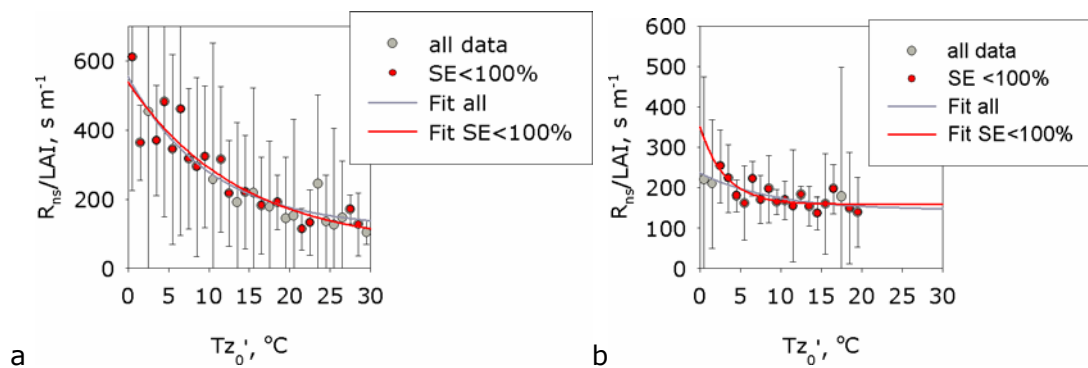


Figure 6.15. (a) The temperature response of  $R_{nsN}$  in very dry and (b) very wet conditions.

$R_{ns}$  is generally smaller in wet than it is in dry conditions, up to temperatures of  $\sim 20^\circ\text{C}$  when  $R_{ns\_dry}$  continues to decline whereas  $R_{ns\_wet}$  is constant. This suggests that when surface water is present, ozone reacts with chemicals in the water at a low temperature until the reaction reaches equilibrium; when the surface is dry the temperature response is consistent with simple thermal decomposition of ozone at the surface which increases with increasing temperature. If this is the case the activation energy for the process over wet surfaces should be smaller than that for dry surfaces. The non-stomatal deposition velocities ( $v_{d\_dry} = 1/R_{nsN\_dry}$  and  $v_{d\_wet} = 1/R_{nsN\_wet}$ ) can be taken to be the reaction rate for the processes and Arrhenius plots of each data set reveals the activation energies ( $E_a$ ), as shown in Figure 6.15. The  $E_a$  for the dry surface is  $\sim 36 \text{ kJ mol}^{-1}$  whereas for the wet surface it is only  $15 \text{ kJ mol}^{-1}$ , which supports this conclusion. The result for dry canopies is consistent with that of Fowler *et al.*, (2001) who also reported a value of  $36 \text{ kJ mol}^{-1}$  for a dry moorland canopy, and implies that the effect may be largely independent of vegetation type. As was noted above, the response during wet conditions is more uncertain and if all the data are included  $E_{a\_wet}$  increases to  $\sim 19 \text{ kJ mol}^{-1}$ .

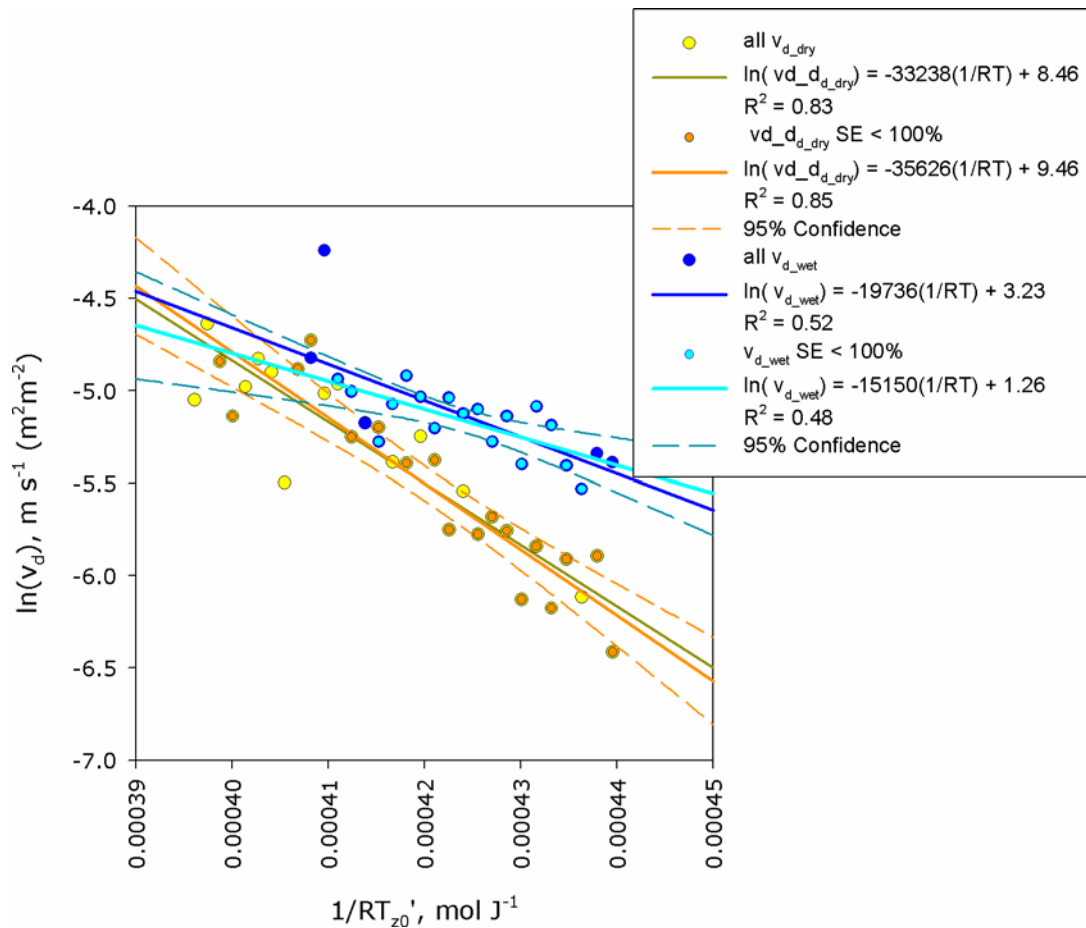


Figure 6.16. The natural logarithm of  $v_d$  for wet and dry surfaces against  $1/RT$ , which estimates the activation energy of the deposition process to the surfaces in each condition as the intercept of linear regression to each set of points. Regression lines fitted to both all the data and only those points with a standard error less than 100% are shown.

It is noted that LAI was not accounted for in the analysis of  $R_{c\_night}$  which showed little response to temperature for wet surfaces. However as changes in LAI appear to reduce the observed temperature responses and the non-normalised  $R_{ns\_wet}$  data also have a smaller response to temperature, the basic interpretation of the results is not affected.

#### • Sub-Zero Temperatures

It was noted in Section 5.7 that the surface will have different characteristics at sub-zero temperatures than those above zero. At temperatures down to about  $-5^\circ\text{C}$  water may be present as a liquid and snow remains "wet", below this threshold the surface of snow dries out. There only 43 estimates available of  $R_{ns}$  at temperatures ranging from  $-3.5$  to just below  $0^\circ\text{C}$  and these give an average value of  $1875 \pm 1460 \text{ s m}^{-1} (\text{m}^2 \text{m}^{-2})$ . The large standard error reflects the scatter in the data as values range from  $\sim 200 \text{ s m}^{-1}$  at  $-1^\circ\text{C}$  for a wet surface to over

2000 s m<sup>-1</sup> for a dry surface. There is some indication that a cold wet surface may have a lower resistance than a dry surface down to about -2°C, where they both increase, but the data set is too small to be conclusive. The data do confirm that  $R_{ns}$  is large at low temperatures with a value of  $\sim 2000$  s m<sup>-1</sup> (m<sup>2</sup>m<sup>-2</sup>).

### 6.4.3 Other Factors Influencing $R_{ns}$

To assess the ability of the fitted temperature response curves to predict  $R_{nsN}$  the dry and wet relationships (Table 6.5 Set 5) are used to calculate 0.5 hourly values of  $R_{nsN}$ . The residuals ("measured" – predicted) are shown in Figure 6.17 plotted against temperature and the other variables that may influence  $R_{ns}$  (all dry or wet data across the full range of relative humidity are shown in the final plots whereas the others show only RH<70% for dry and RH>70% for wet). The predicted values for  $R_{ns}$  are most often larger than the measurements (negative residuals), although they are also significantly too small on occasion (positive residuals). The residual tends to decrease to zero with temperature in dry conditions which implies that additional factors interact with temperature and are influencing  $R_{ns}$  at lower temperatures. In wet conditions the residual is more evenly scattered, indicating that the temperature response is reasonably well characterised.

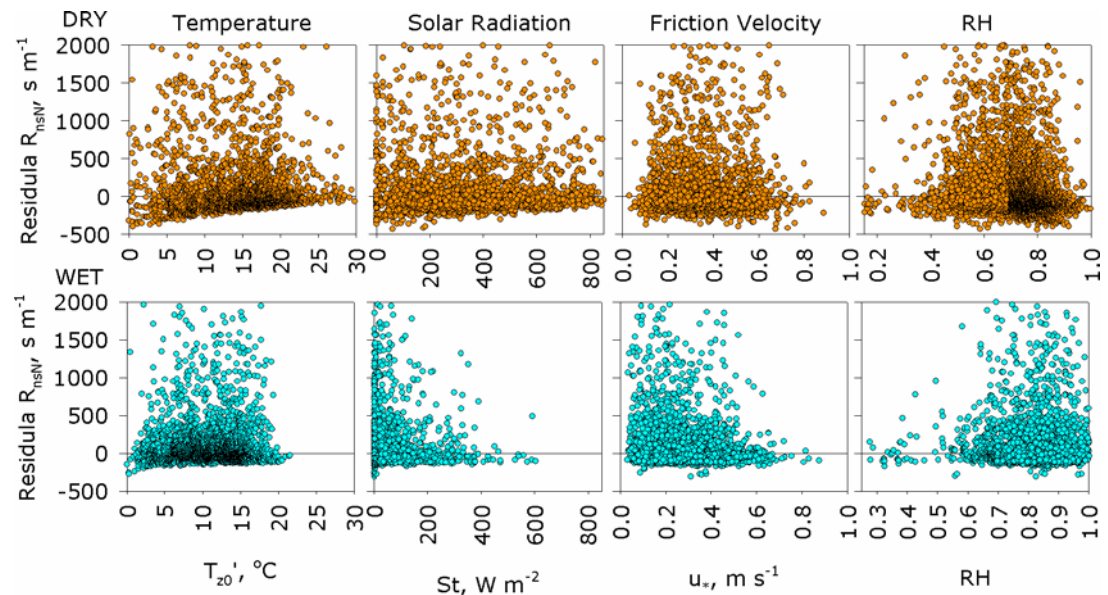


Figure 6.17. The residuals of  $R_{nsN}$  predicted using the fitted temperature response in dry (top plots) and wet conditions (bottom plots).

Surface temperature is closely coupled to solar radiation, as was discussed in Section 6.41, and this is evident in Figure 6.17 with the residual during dry

conditions also declining slightly with  $St$ . To examine the variation in  $R_{ns}$  with solar radiation the median of  $R_{nsN\_dry}$  is calculated for  $20 \text{ W m}^{-2}$  blocks and an exponential curve fitted as shown in Figure 6.18a.

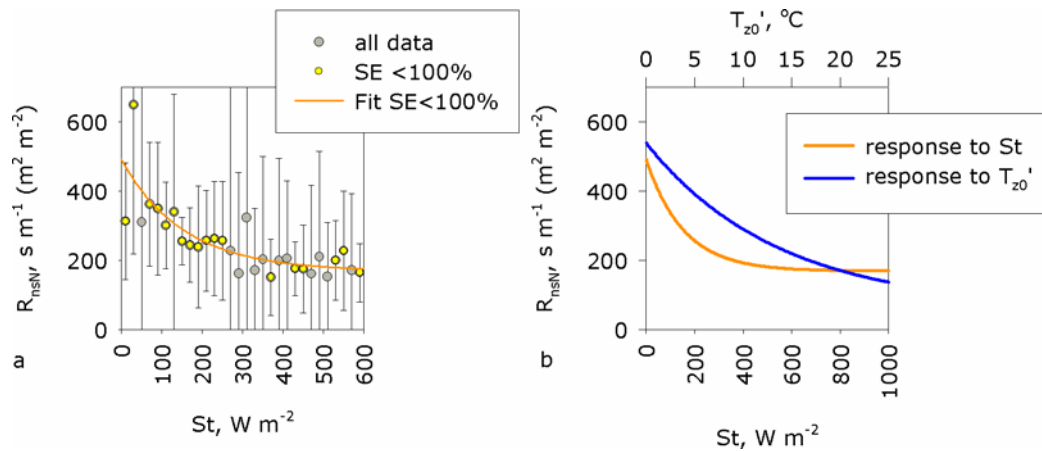


Figure 6.18. (a) The response  $R_{nsN\_dry}$  to solar radiation and (b) the fitted curve compared to the response of  $R_{nsN\_dry}$  to temperature.

The data set is more scattered than that for temperature but a decline in  $R_{ns}$  is clearly evident.  $R_{nsN}$  has a slightly lower value at low radiation levels than that found for low temperatures ( $492 \text{ s m}^{-1} (\text{m}^2 \text{m}^{-2})$ ) and there is a faster decline. The two curves are plotted together (Figure 6.18b), where  $20^{\circ}\text{C}$  was found to be equivalent to  $\sim 800 \text{ W m}^{-2}$  of radiation from a plot of  $T$  against  $St$  (Figure 6.20).

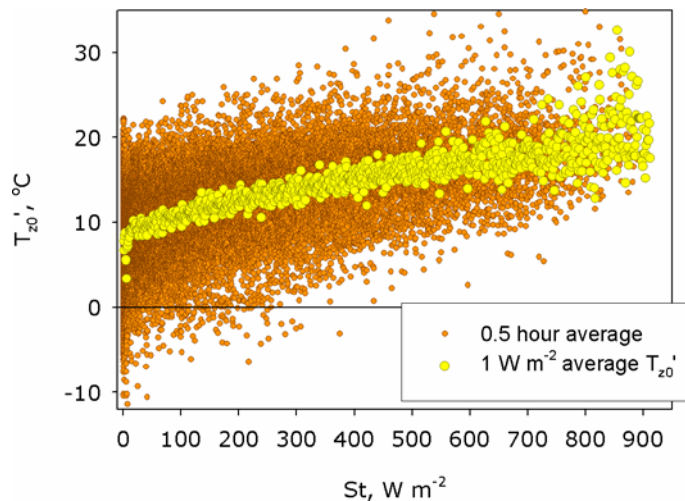


Figure 6.19. The variation in surface temperature with solar radiation.

The difference between the two curves in Figure 6.18b between  $5\text{-}10^{\circ}\text{C}$  is approximately  $100 \text{ s m}^{-1} (\text{m}^2 \text{m}^{-2})$  which is similar to the median residual of  $-90 \text{ s m}^{-1} (\text{m}^2 \text{m}^{-2})$ . It is possible that the response to solar radiation is simply an interaction with temperature as increasing radiation correlates with increasing

surface temperature (Figure 6.19). However, the two curves are clearly different and the  $R_{ns}(St)$  response declines more steeply than  $R_{ns}(T)$  at low radiation or temperature levels. This implies that there is an additional influence of solar radiation on  $R_{ns}$ , initiated by relatively low light levels. This may be due to either the photolysis of ozone mediated by compounds on the leaf cuticle or the reaction of ozone with photochemically produced compounds, as hypothesised by Rondon *et al.*, (1993). This would also account for the larger canopy resistances found during night-time dry conditions (Figure 5.44).

As VOC emissions from vegetation increase with increasing temperature and solar radiation (Kirstine and Galbally, 2004) it is possible that these compounds are responsible for the observed reponse of  $R_{ns}$ . Kirstine *et al* (1998) reported typical midday emissions of  $\sim 2 \mu\text{g-C g}^{-1} \text{ m}^{-2} \text{ h}^{-1}$  from *Lolium perenne* although most of the compounds do not react quickly with ozone enough to affect of the ozone flux (3-4% hexanal). Using the approach summarised in Table 5.11 with emissions of  $0.1 \mu\text{g-C g}^{-1} \text{ m}^{-2} \text{ h}^{-1}$  (dry weight) and a dry biomass density of  $100 \text{ g m}^{-2}$ , gives an apparent ozone flux of only  $-0.05 \text{ ng m}^{-2} \text{ s}^{-1}$  which is too small to account for the observed results. However as a small fraction of the VOCs emitted were not identified, and there are few other studies of emissions from grasses (De Gouw *et al* 2000; Karl *et al* 2001a, b, 2005), their role in ozone deposition to dry surfaces cannot be discounted at present.

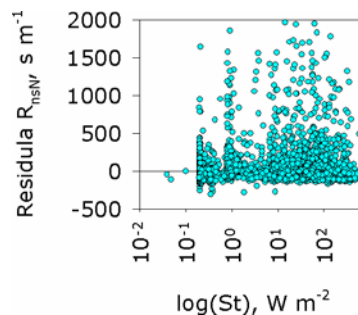


Figure 6.20. The variation of the residuals of  $R_{ns\_wet}$  with  $\log(St)$ .

The residuals for wet conditions show far less variation with temperature which indicates that although the relationship may overestimate  $R_{ns}$ , the response to temperature is not significantly influenced by other factors. It would appear that the residuals decline markedly with solar radiation in wet conditions but this trend is an artefact of the narrow range of radiation levels (wet or damp weather normally coincide with overcast conditions and low radiation levels) this data set represents. If the data are plotted on a logarithmic scale it is evident that there is little variation in the residual with  $St$  in wet conditions (Figure 6.20). This is

confirmed by plotting the response of  $R_{nsN\_wet}$  to solar radiation as shown in Figure 6.21a. The curve is very similar to the temperature response (Figure 6.21b) and so could simply be an interaction with temperature. However, smaller  $R_{ns}$  values are predicted by the solar radiation relationship ( $120 \text{ s m}^{-1}$  at  $200 \text{ W m}^{-2}$  and  $170 \text{ s m}^{-1}$  at  $8^\circ\text{C}$ ), which would account to the negative residuals from the temperature response. It therefore remains possible that there are also photochemical reactions occurring in the surface water. That the night-time resistance is slightly larger ( $\sim 300 \text{ s m}^{-1}$ ) and showed no response to temperature (although this data was not normalised for LAI) supports this hypothesis.

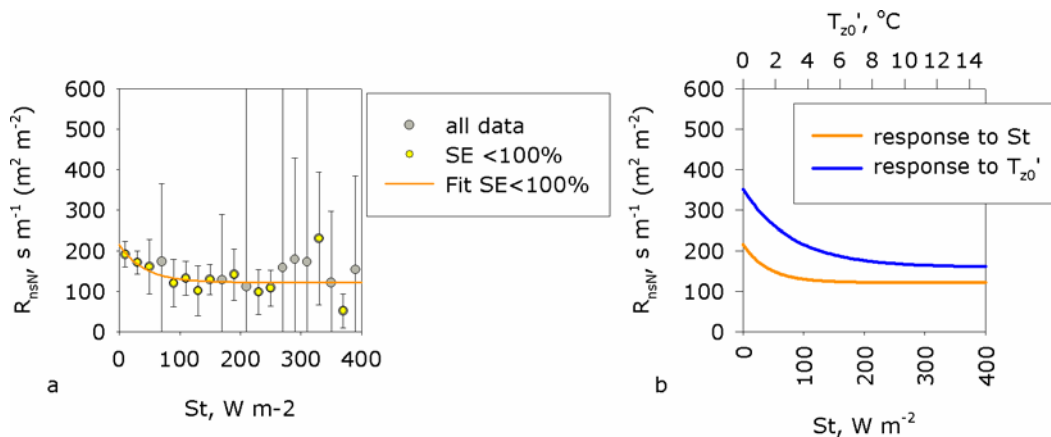


Figure 6.21. (a) The response  $R_{nsN\_wet}$  to solar radiation and (b) the fitted curve compared to the response of  $R_{nsN\_wet}$  to temperature.

The residuals of  $R_{nsN\_dry}$  also show some slight variation with friction velocity; although in-canopy aerodynamic effects are assumed to be negligible for a fully developed grass canopy, they will still have some effect as with larger friction velocities ozone will be able to penetrate further in to the canopy. However a plot of  $R_{nsN\_dry}$  blocked by  $0.02 \text{ m s}^{-1}$  does not suggest any clear influence of  $u_*$  (Figure 6.22a). This would be the case if dry conditions generally occur during the summer when the canopy is taller and LAI larger. If the data where LAI is less than 0.3 are selected (187 values) a small effect can be detected, although the data are quite scattered (Figure 6.22b).  $R_{nsN\_dry}(LAI < 0.3)$  declines with increasing  $u_*$  and if a single exponential function is fitted the result is quite similar to that reported by Zhang *et al.*, (2002) for night-time measurements over a pasture ( $R_{nsN\_dry}(u_*) = 504e^{-0.60u_*}$  and  $R_{c\_night\_dry} = 406e^{-0.48u_*}$ ).

During wet conditions the residuals clearly decline with friction velocity and a plot of  $R_{nsN\_wet}$  blocked with  $u_*$  shows a decreases from  $\sim 250 \text{ s m}^{-1}$  at  $< 0.1$

$\text{m s}^{-1}$  to  $\sim 150 \text{ s m}^{-1}$  at  $0.5 \text{ s m}^{-1}$  (Figure 6.22c). It was suggested above that the range LAI represented by dry conditions could explain the lack of a response of  $R_{\text{nsN}_{\text{dry}}}$  to  $u_*$  and so it would follow that during wet conditions LAI should more frequently be smaller. However the two data sets actually have very similar distributions of LAI and so this cannot explain the observed  $u_*$  responses. An alternative hypothesis is that in-canopy aerodynamic resistance is indeed insignificant for the grass canopy and the response is due to the effect of faster winds increasing mixing in the layer of surface water and so enhancing the chemical reactions. Such effects of wind speed enhancing ozone deposition to open water have been reported in the literature (Chang *et al.*, 2004; Gallagher *et al.*, 2001) and Padro, (1994) also noted that night-time resistance appeared to decrease with wind speed over a wet deciduous forest.

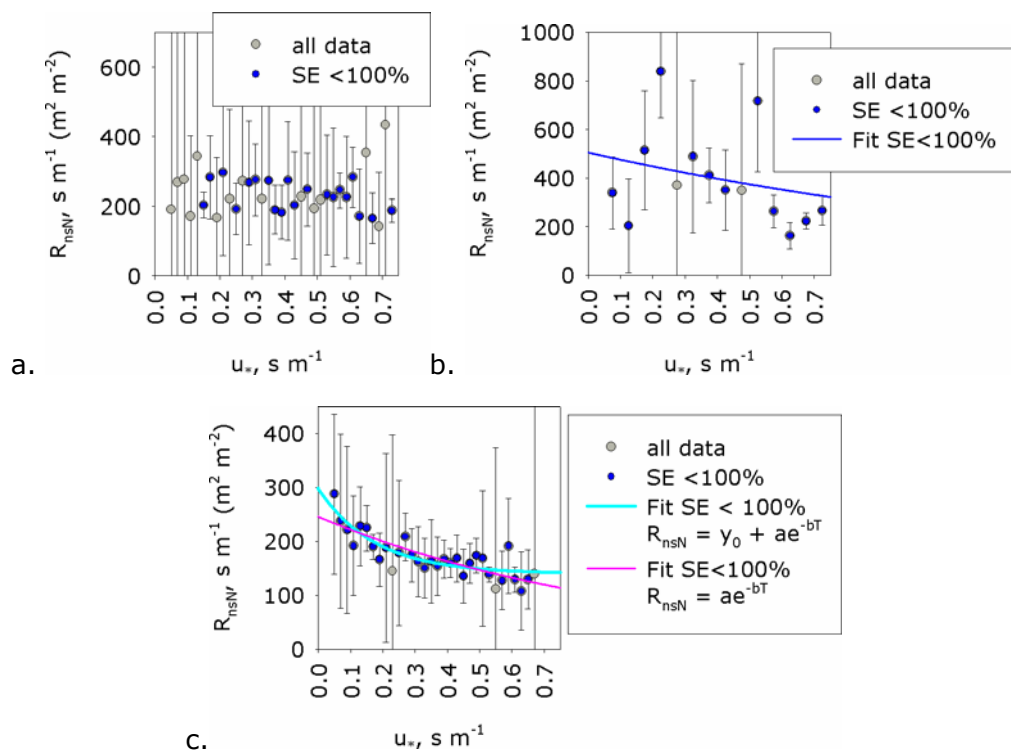


Figure 6.22. (a) The variation in all  $R_{\text{nsN}_{\text{dry}}}$  data, (b)  $R_{\text{ns}_{\text{dry}}}$  when LAI < 0.3 and (c)  $R_{\text{nsN}_{\text{wet}}}$  with friction velocity,  $u_*$ .

The relationship between  $u_*$  and temperature is quite complex and not easily discernible from a plot of 0.5 hourly measurements of surface temperature with  $u_*$  (Figure 6.23). The calculation of surface temperature using equation (68) includes the aerodynamic resistances,  $R_a$  and  $R_b$ , as well as the sensible heat flux (H). Thus although at faster friction velocities  $R_a$  and  $R_b$  may be smaller and so reduce  $T_{z_0}'$ , if the sensible heat flux is large their influence will be small. This in

reflected in Figure 6.23 as below  $\sim 0.4 \text{ m s}^{-1}$  the temperature data are fairly evenly scattered but above this appear to converge to  $\sim 10^\circ\text{C}$ . As the  $R_{nsN\_wet}(T)$  residuals are fairly evenly scattered it can be assumed that this  $R_{nsN\_wet}$  relationship with  $u_*$  has a minimal effect on the temperature response but further analysis is required to quantify the co-dependency of  $R_{ns\_wet}$  on  $u_*$  and  $T_{z0}'$ .

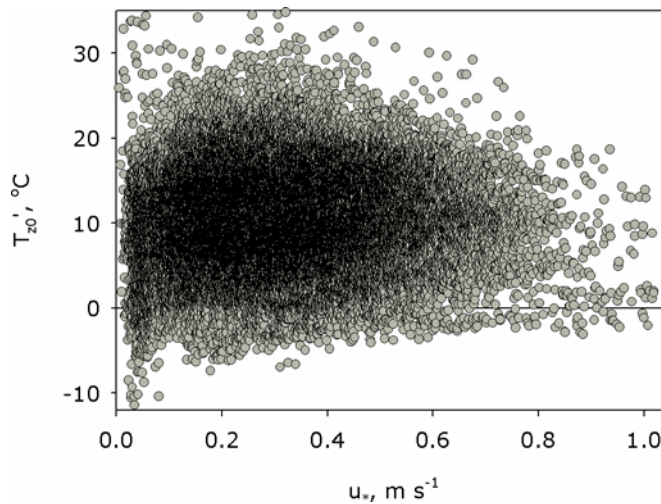


Figure 6.23. The variation of surface temperature ( $T_{z0}'$ ) with friction velocity ( $u_*$ ).

A response of  $R_{c\_night}$  to relative humidity (RH) was discussed in Section 5.7 and was found to be small for the normal range of humidity experienced at Easter Bush. It is possible that the effect is also an interaction with temperature as they often both increase at the same time in the damp Scottish climate. Examining the  $R_{nsN}$  data split into very dry conditions (surface wetness = 6999 and no rainfall) or very wet (surface wetness < 3000 and/or rainfall) for all humidity levels produces similar results. Above  $\sim 40\%$  humidity there is a decline in  $R_{nsN}$  in both wet and dry conditions (Figure 6.24) although the curves are poorly defined when the standard errors are considered (Table 6.6).

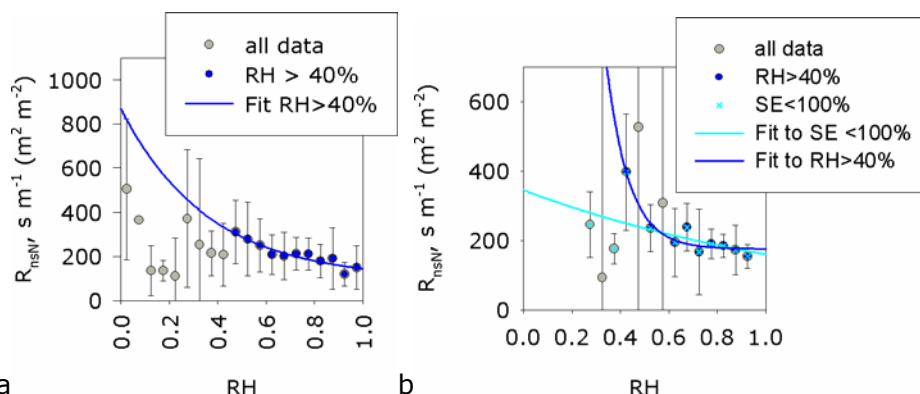


Figure 6.24. (a) The variation in  $R_{nsN\_dry}$  and (b)  $R_{nsN\_wet}$  with relative humidity, RH.

It is more difficult to account for the effect of RH on the temperature response as there is no clear relationship between RH and  $T$  (Figure 6.25). If the  $R_{nsN}(RH)$  and  $R_{nsN}(T)$  responses are plotted alongside each other, with RH increasing with  $T$  this shows that the RH response tends to predict larger values for  $R_{nsN}$  (Figure 6.26) and this may account for some of the positive residuals found from the temperature response.

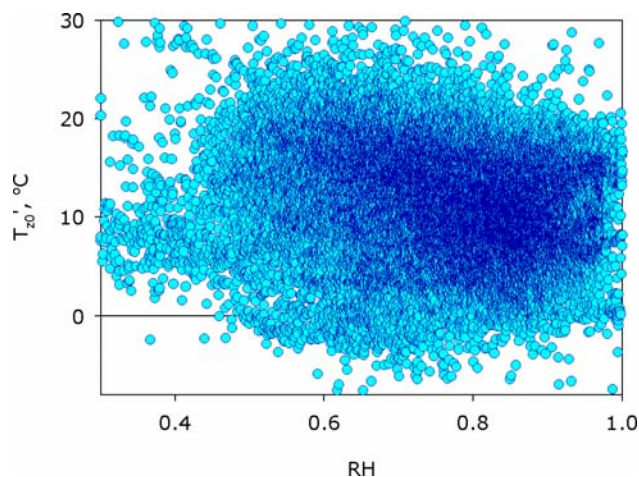


Figure 6.25. The variation in surface temperature with humidity.

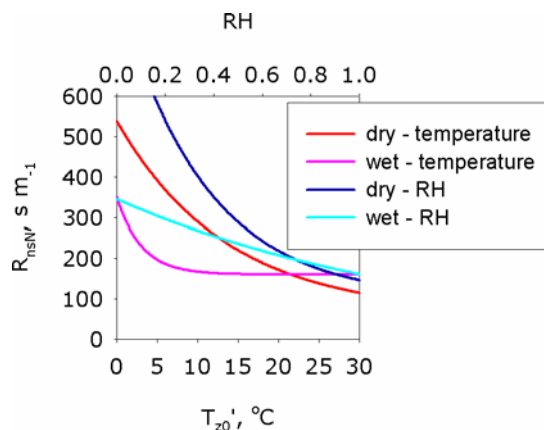


Figure 6.26. The response curves of  $R_{nsN}$  with temperature and humidity in wet and dry conditions, plotted with  $T$  and RH increasing together.

However, although absolute humidity increases with temperature, the saturation vapour pressure also increases and so RH actually declines. Therefore the response curves are also plotted with opposing axis in Figure 6.27. In dry conditions with low temperatures ( $<10^{\circ}C$ ) and high humidity ( $>70\%$ ), it is likely that although the surface wetness sensor reads dry, surface water is present on the vegetation. In a study of leaf wetness using "Burkhardt" type wetness sensor clips (Section 5.5.1, Burkhardt and Gerchau, 1994), Klemm, *et al.*, (2002) showed that the PCB type sensor tends to predict a higher frequency of dry

surfaces than the clips. This was attributed to the PCB having a different heat capacity and conductivity to the vegetation which biased the exchange pattern of humidity with the atmosphere (*ibid*). Thus when temperatures are low and humidity high, there may be sufficient water on the vegetation to allow the wet surface reactions to occur and hence reduce  $R_{ns}$ . In intermediate conditions, when humidity is 30-60% and temperature between about 10 to 20°C, there may still be some surface water present but this would generally take the form of a fine film. In this case the reactions responsible for  $R_{nsN\_dry}(T)$  may be inhibited but there is insufficient water for the wet reactions to be significant and so  $R_{ns}$  increases.

Table 6.6 Results of fitting  $R_{nsN} = y_0 - a \cdot \exp(-bx)$  to values of  $R_{nsN\_dry}$  and  $R_{nsN\_wet}$  blocked by solar radiation, friction velocity and relative humidity (with standard errors for the fitted parameters).

	$y_0$	a	b	$R_{ns}$ at $0 \text{ W m}^{-2}$	at $600 \text{ W m}^{-2}$	$R^2$
$R_{nsN\_dry}(\text{St})$	$169 \pm 46$	$322 \pm 65$	$6.5 \pm 3.2 \times 10^{-3}$	491	176	0.57
$R_{nsN\_wet}(\text{St})$	$121 \pm 20$	$97 \pm 72$	$0.024 \pm 0.035$	215	121	0.07
				$0 \text{ m s}^{-1}$	$1 \text{ m s}^{-1}$	
$R_{nsN\_wet}(u^*)$	$140 \pm 11$	$158 \pm 23$	$5.7 \pm 1.92$	298	141	0.72
$R_{nsN\_dry}(u^*)$ LAI < 0.3	$3.87 \times 10^{-6} \pm 665$	$505 \pm 6475$	$0.6 \pm 10.3$	505	277	0.01
				20% RH	100% RH	
$R_{nsN\_dry}(\text{RH})$	$87 \pm 79$	$773 \pm 498$	$2.79 \pm 2.01$	529	134	0.84
$R_{nsN\_wet}(\text{RH})$	$5.8 \times 10^{-6} \pm 1809$	$345 \pm 1596$	$0.77 \pm 6.33$	296	160	0.12

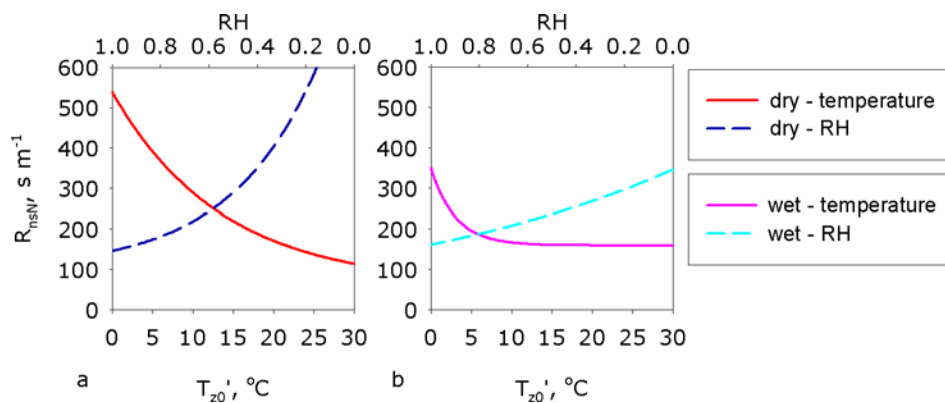


Figure 6.27. The response curves of  $R_{nsN}$  with temperature and humidity in (a) dry and (b) wet conditions, plotted with  $T$  increasing as RH decreases.

Some studies have shown that the source of surface water can determine whether ozone deposition is enhanced or reduced (Section 2.5.1.4). In wet conditions it is unclear why  $R_{ns}$  should also respond to humidity as the surface is already wet and in this case it may simply be an interaction with temperature. These patterns are reflected in the overall medians of the datasets as  $R_{nsN\_wet}$  in all humidity conditions is larger than for RH > 70% only, whereas  $R_{nsN\_dry}$  is

smaller in all humidity conditions and increases when only RH>70% are excluded (Table 6.7).

Table 6.7 Summary statistics of each  $R_{nsN}$  data set ( $s\ m^{-1}$ ).

	All	Wet (all RH)	Wet (RH>70%)	Dry (all RH)	Dry (RH<70%)
Median	196	180	173	217	227
Average	632	524	404	729	803
Stdev	2046	1960	1272	2115	2389
90 <sup>th</sup> %Tile	1128	877	684	1384	1547
10 <sup>th</sup> %Tile	65	60	66	70	70
Count	9277	4382	3027	4895	2263

Overall these results show that surface temperature is a major factor controlling non-stomatal deposition during dry and wet conditions. In wet conditions friction velocity also reduces  $R_{ns}$  and should also be considered but in dry conditions its influence appears to be negligible. There are also interactions with solar radiation and humidity for both wet and dry surfaces. As the former is positively correlated with temperature and causes a decrease in  $R_{ns}$  its influence can be neglected in most circumstances; although it does raise the possibility that there are photochemical reactions occurring at the surface. The interaction with humidity is more complex and confounded by the use of the PCB type wetness sensor which does not accurately mimic conditions on plant surfaces. At high humidity (>70%) although the sensor indicates a dry surface there may be sufficient surface water for the wet chemical reactions to be significant and reduce  $R_{ns}$ . Whereas when humidity is lower there may be surface water present but as a thin film which inhibits the reactions responsible for the "dry" surface's temperature response.

### **6.5 A Model of Total Canopy Canopy Resistance**

The focus of most ozone modelling exercises has been the parameterisation of stomatal conductance as it was taken to be the main factor controlling diurnal variations in ozone deposition to vegetated surfaces. The results described above illustrate the complexity of the surface deposition process and that stomata are not always the most important factor. The non-stomatal ozone flux is often the largest component of the total, particularly in the autumn to spring period, and assuming  $R_{ns}$  is a simple of function of LAI greatly underestimates its variability. A new parameterisation of non-stomatal resistance based on variations with temperature over wet and dry surfaces in described in the following section and incorporated into a simple Jarvis-type big-leaf model of

total canopy resistance. The modelled results are then compared to the measurements from Easter Bush. This type of model is commonly used in global and regional models at present, as it is simpler to parameterise and scale predictions of leaf-level stomatal conductance to the whole canopy.

### 6.5.1 Parameterisation of $R_{ns}$ in JModG

The stomatal resistance component of JModG has already been described in Section 6.1. The temperature response is assumed to exert the strongest influence of  $R_{ns}$  for dry surfaces, although there are also interactions with humidity, solar radiation and friction velocity. For wet surfaces the influence of temperature was smaller and  $R_{ns}$  was constant above  $\sim 15^\circ\text{C}$ , but  $u_*$  caused a significant decline. Two functions are therefore proposed, one for dry conditions and one for wet, based on the curve fitting results reported in Section 6.4:

$$R_{ns\_dry} = \text{SAI}(61 + 477e^{-0.07Tz0'}) \quad (130.)$$

$$R_{ns\_wet} = \text{SAI}(159 + 191e^{-0.33Tz0'})u_*^{-1} \quad (131.)$$

where SAI is the surface area, set equal to LAI or to 1 when LAI < 1.

Although the effect of soil resistance ( $R_{c3}$ ) could not be separated from the total it is assumed that  $R_{ns} \approx R_{c2}$  and so in the final model  $R_{c3}$  is simply set to  $1000 \text{ s m}^{-1}$ :

$$R_C = \left[ \frac{\text{LAI}}{R_{c1}} + \frac{1}{R_{ns}} + \frac{1}{R_{c3}} \right]^{-1} \quad (132.)$$

where:

$R_{c1}$  is calculated using the methodology and parameterisation described in Sections 3.2.3.1 and 6.1.3 respectively

$R_{ns}$  was calculated using equation (130) with dry conditions taken as zero rainfall and wetness > 4000, and (131) with wet conditions taken as rainfall or wetness < 4000. The parameterisations used in EMEP (with  $\delta_{\text{snow}} = 0$  at all times, Section 3.3.2.1, Emberson *et al.*, 2000b) and those based on humidity from Zhang *et al.*, (2002) (with  $R_{inc} = 0$ ,  $R_{c3} = 1000 \text{ s m}^{-1}$  and LAI = SAI, Section 2.5.1.4) were also implemented for comparison.

## 6.5.2 Measured and Modelled Total Canopy Resistance

Incorporating this first form of the new parameterisation of  $R_{ns}$  does improve the ability of the model to estimate the total canopy resistance in that it more closely follows variation in the measurements, especially at night; however in terms of overall statistics the results are mixed. The plots in Figure 6.27 summarise the results as seasonal diurnal cycles for wet and dry periods from the new model (NMod), the Zhang parameterisation and the standard (EMEP) parameterisation. In all cases the summer daytime resistance is underestimated due to the stomatal conductance being too large, as described in Section 6.2.1. The standard model significantly underestimates the canopy resistance during the winter months, particularly during wet periods (Figure 6.27c).

During wet periods the NMod and Zhang both perform better and although NMod gives a slightly larger median resistance (Table 6.8), its residual is smaller than that for Zhang. During the winter agreement is very good for both models and in the summer NMod does well at night. The Zhang model appears to give a better estimate of  $R_c$  during dry periods at all times of year, although NMod is an improvement on the standard version. This indicates that humidity is an important factor in regulating  $R_{ns}$  in dry conditions and should be included in the model.

Table 6.8 Summary of preliminary model results compared to the measurements and estimates from Zhang, *et al.*, 2002 and EMEP type models.

DRY	Residuals						
	Measured	NMod	Zhang	EMEP	NMod	Zhang	EMEP
Median	208	78	99	105	91	56	52
10 <sup>th</sup> Percentile	61	31	34	33	-46	-185	-324
90 <sup>th</sup> Percentile	1030	250	454	635	800	622	676
Average	972	118	187	232	824	675	710
Stdev	8794	91	173	242	9305	8619	9302
<b>WET</b>							
Median	244	263	239	360	2	11	-52
10 <sup>th</sup> Percentile	70	54	52	56	-244	-241	-461
90 <sup>th</sup> Percentile	1145	433	430	690	509	532	443
Average	1185	252	239	357	543	555	438
Stdev	16093	144	141	238	9593	9593	9518

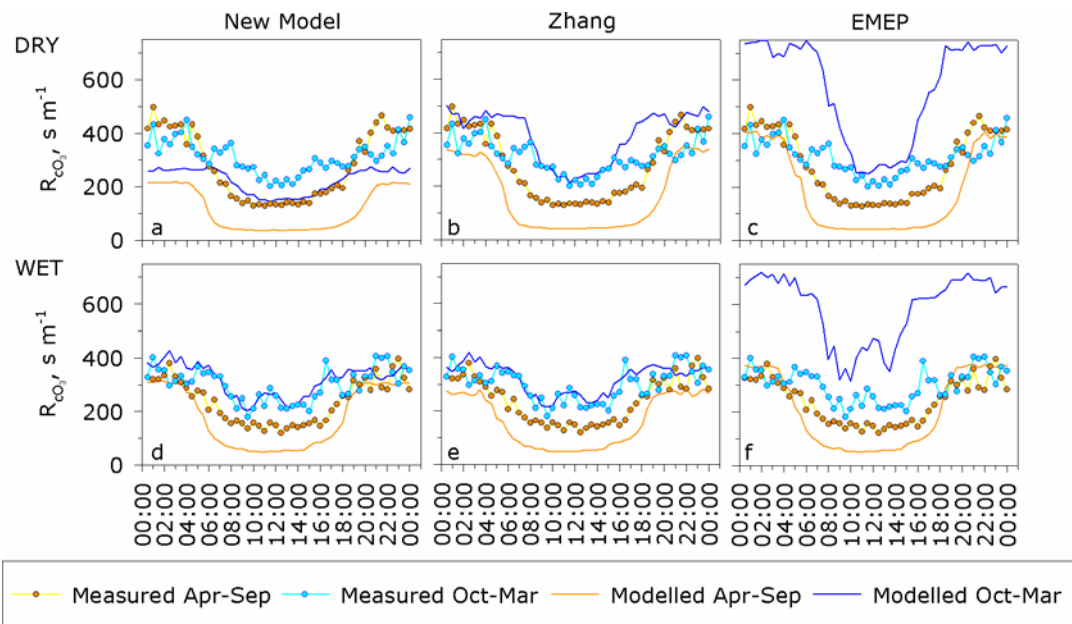


Figure 6.28. Diurnal cycles during the summer and winter from the measurements and three different canopy resistance models.

## Addendum

Subsequent to the completion of this thesis an inconsistency in the analysis was found. In Section 6.4.2 the  $R_{ns}$  data set is normalised for LAI by dividing ( $R_{nsN} = R_{ns}/LAI$  where  $LAI > 1$ ), however in the final model this results in  $R_{ns}$  increasing with increasing  $LAI$  which is incorrect ( $R_{ns} = R_{nsN} \times LAI$ ).

In principle  $R_{ns}$  should decrease with increasing  $LAI$  as the surface area available for ozone to deposit to increases and initial analysis of the data appeared to indicate it did so (Figure a1). In order to normalise for this effect the division with  $LAI$  was used however this is incorrect and it should have been a multiplication. The data have been reanalysed in light of this error. It was found that the normalisation is not necessary, and although the parameterisations of the  $R_{ns}$  relationships have changed the overall conclusion of this thesis remains valid.

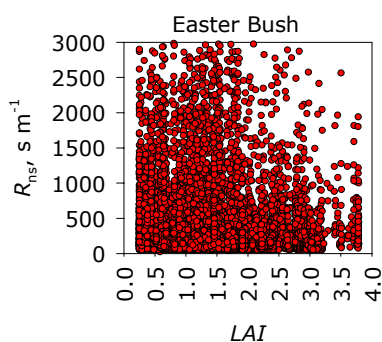


Figure a1. Scatter plot of the final (measured and modelled)  $R_{ns}$  data with  $LAI$ .

## Re-analysis

In Figure a1 it appears that  $R_{ns}$  decreases with increasing  $LAI$  however taking block medians of  $R_{ns}$  with 0.1  $LAI$  shows no clear relationship between them, Figure a2. If it is assumed that some normalisation for LAI is required and  $R_{nsN} = R_{ns} \cdot LAI$  is used then this appears to over estimate an effect so that  $R_{nsN}$  increases with  $LAI$ , Figure a2. The two data sets ( $R_{ns}$  and  $R_{nsN}$ ) were used to fit  $T_{z0}$  relationships for wet and dry surfaces (Figure a3), as described in Section 6.4.2, which were then used to predict  $R_{ns}$  values and the residual between measured and modelled calculated. The original functions are also used but the residuals are almost identical for each, Figure a4, indicating that they give similar estimates of  $R_{ns}$ .

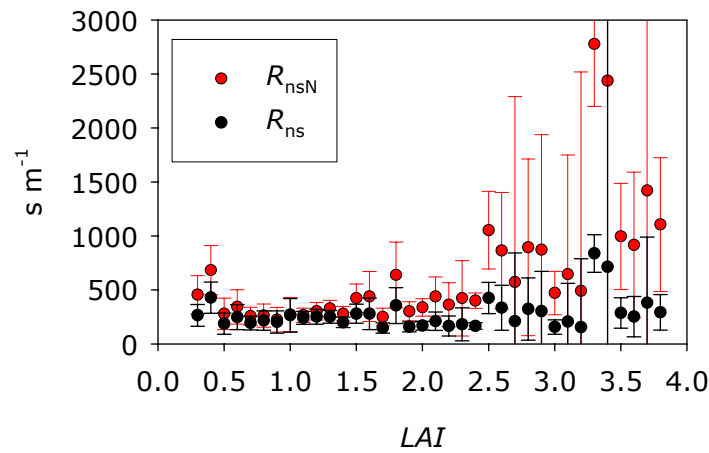


Figure a2. 0.1 LAI block medians of  $R_{ns}$  and  $R_{nsN}$  ( $= R_{ns} \cdot LAI$ ), the error bars show one standard deviation.

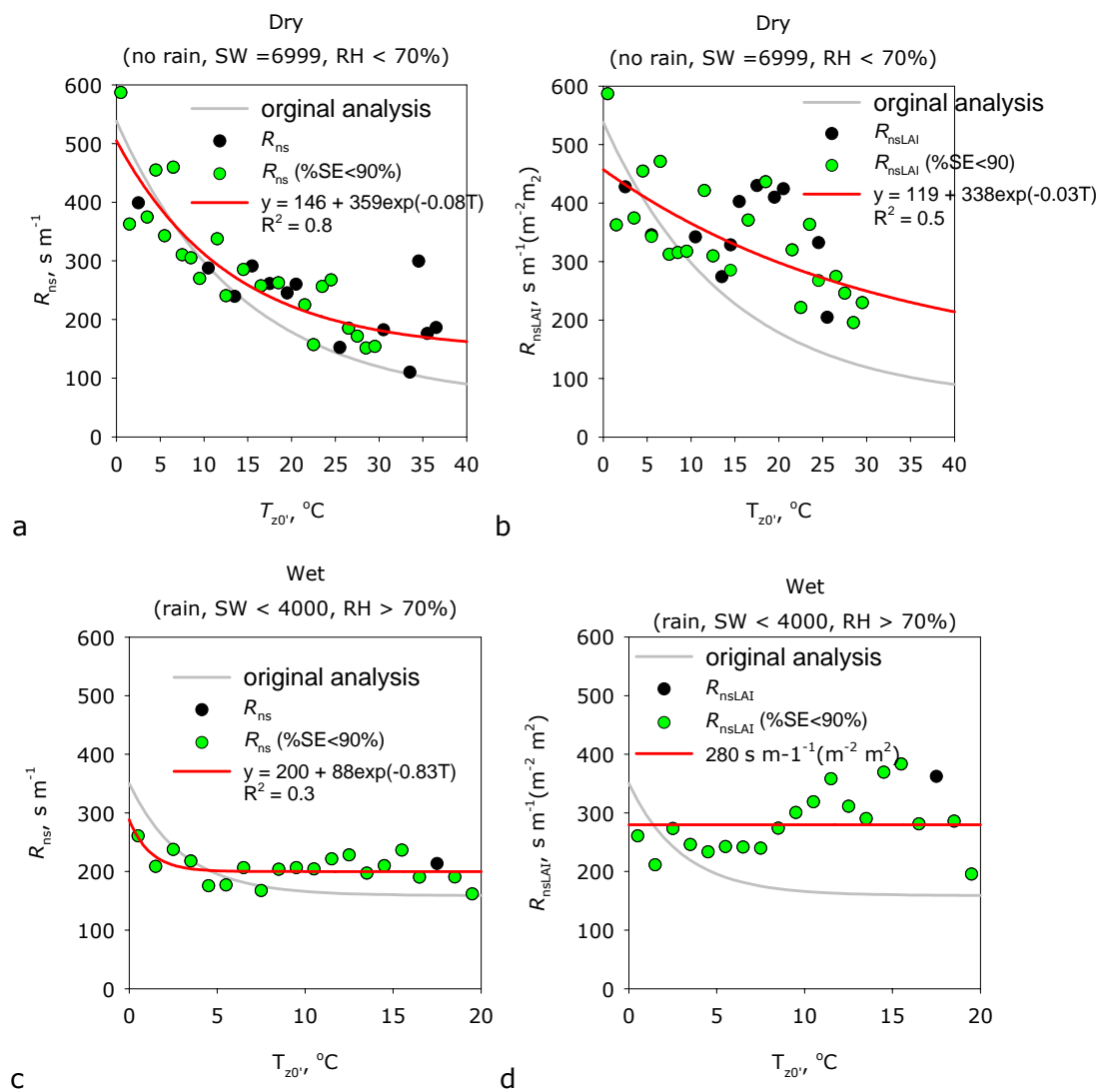


Figure a3. Revised  $R_{ns}(T_{z0'r})$  relationships for wet and dry conditions using (a) and (c)  $R_{nsr}$ , (b) and (d)  $R_{nsN} = R_{ns} \cdot LAI$ . The curves fitted in the original analysis with  $R_{nsN} = R_{ns}/LAI$  are shown for comparison.

The grass canopy at Easter Bush is quite dense and when tall, tends to flop to one side. Therefore it is possible that the surface area exposed to the atmosphere remains fairly constant. If this was true we would also expect to see little variation in  $R_{ns}$  with wind speed or friction velocity over a dry surface which is indeed the case, Figure a5a. As in the original analysis, there is a decrease in  $R_{ns}$  (Figure a5b) with increasing  $u_*$  over wet surfaces and this is attributed to enhanced mixing of the surface water leading to an increase in the aqueous reactions that are removing ozone from the atmosphere. It was therefore concluded that no normalisation for  $LAI$  is required for the Easter Bush data and any relationship with  $LAI$  is masked by variability due to other factors.

In conclusion, the error in the original analysis does not change the interpretation of the data and the mechanisms for non-stomatal ozone deposition discussed are still valid. However it does highlight the uncertainty in deriving models for the process and further work is necessary to refine the relationships. The outcome of this will be published in a peer reviewed journal as soon as possible.

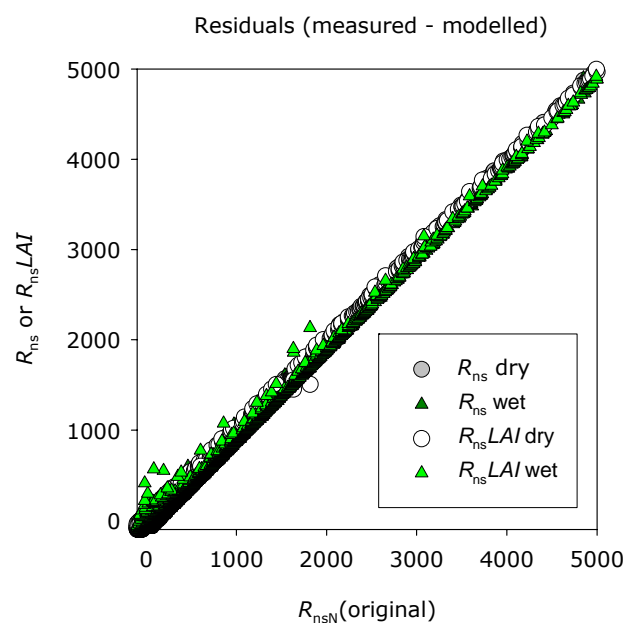
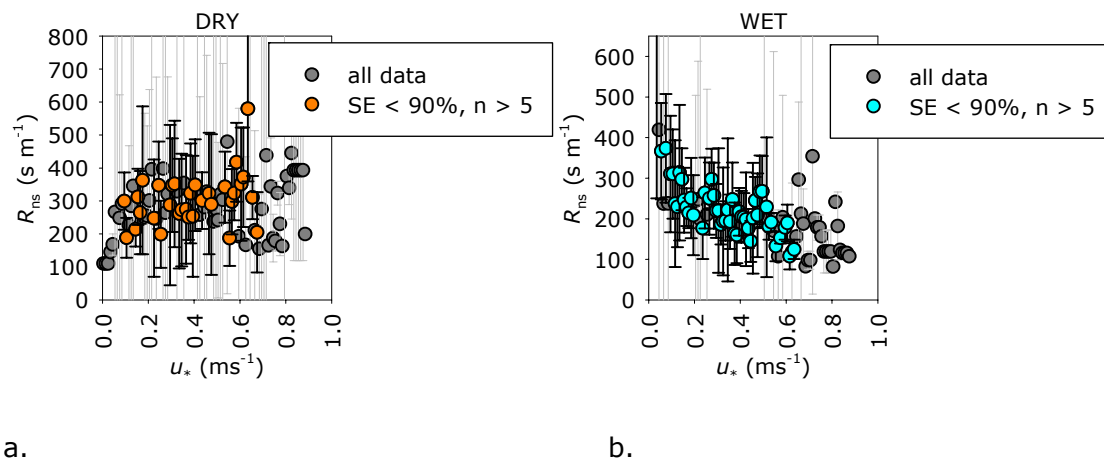


Figure a4. Residuals of measured – modelled  $R_{ns}$  values where  $R_{ns}$  has been estimated using relationships based on  $R_{ns}/LAI$  (original analysis),  $R_{ns}$  and  $R_{ns}\cdot LAI$ .



a. b.  
 Figure a5. The variation of  $R_{ns}$  with  $u^*$  over dry and wet surfaces at Easter Bush.

## 7 Errors and Uncertainties

There are several different sources of error and uncertainty in all the measured and derived variables that have been discussed in this thesis. In the case of most sensors the manufacturer will report its precision and accuracy which accounts for some of the error however there are other systematic and random errors that must be considered.

### *7.1 Systematic Errors*

These errors arise because of some definable factor in the measurement or analysis that leads to an uncertainty in the result. The accuracies reported for instruments (measurement errors) are typical of this but in the case of micrometeorology there are also the limitations discussed in Section 2.4.4, mainly stationarity and homogeneity, as well as uncertainties due to the use of empirical functions.

The most significant measurement error is that in the ozone concentration measurement as this can have a large effect on the resulting gradient, particularly when concentrations are low. All the analysers used are designed to measure small ambient concentrations (<50 ppb) and taking into account the calibration procedures, an accuracy of  $\pm 5\%$  is estimated with an associated precision of  $\pm 2$  ppb. Thus when concentrations are small or the difference between the top and bottom ozone concentration on profile is small ( $\ll 2$  ppb), even with 5 points, the resulting gradient may be very uncertain.

The application of the stability correction to the measurement heights also adds some uncertainty to the gradient. However a study of corrected and uncorrected gradients by Sutton and Fowler, (1992) showed that even a 10% error in the stability correction would give only a 0.2 to 0.3% error in the flux.

Changes in the trace-gas concentration between the surface and the measurement height are known as the storage error and were considered in Section 6.2.5. The storage correction to the ozone flux is normally very small,  $\sim 1.2\%$  on average, and so is not a significant factor in the over all error. Chemical interactions of ozone with NO<sub>x</sub> or VOC are a possible source of non-stationarity and divergence in ozone flux measurements but as was shown in Section 6.2.6, this was not significant for the Easter Bush site.

## 7.2 Random Errors

Random errors are essentially the uncertainty in a measurement that is left after systematic errors have been accounted for. They may arise from ambiguities in the measurement process or fluctuations which are too fast or irregular to be observed (Barford, 1985). In some cases it may be appropriate to use the accuracy reported by an instrument's manufacturer, ie for the fine wire thermocouples

$$SE_x = \text{greater of } 1.7^\circ\text{C or } 0.5\% \text{ of } x$$

or where an average is calculated the standard error is given by:

$$SE_x = \frac{\sigma_x}{\sqrt{(n-1)}} \quad (133.)$$

where  $\sigma_x$  = the standard deviation of  $x$ ,  $n$  = number of values

For quantities calculated from a sum or general product of other variables (with their associated uncertainties) the combined error can be estimated using the following general expressions.

$$SE_{xy} = \sqrt{SE_x^2 + SE_y^2} \text{ for } f(xy) = x + y \text{ or } x - y \quad (134.)$$

or

$$\frac{SE_{xy}}{f(xy)} = \sqrt{\frac{a^2 SE_x^2}{x^2} + \frac{b^2 SE_y^2}{y^2}} \text{ for } f(xy) = x^a y^b \quad (135.)$$

Equation (91) is known as the fractional or relative error as it is expressed as the error in  $f(xy)$  divided by  $f(xy)$ .

In the case of the measurements used here Flechard, (1998b) and Sutton and Fowler, (1992) showed that the errors in  $F_{O_3}$ ,  $v_{dO_3}$  and  $Rt_{O_3}$  can be from:

$$\frac{SE_{F_{O_3}}}{F_{O_3}} = \sqrt{\left[ \frac{SE_{u_{\text{slope}}}}{u_{\text{slope}}} \right]^2 + \left[ \frac{SE_{O_3_{\text{slope}}}}{O_3_{\text{slope}}} \right]^2} \text{ for the gradient system} \quad (136.)$$

or

$$\frac{SE_{F_{O_3}}}{F_{O_3}} = \sqrt{\left[ \frac{SE\left(\frac{u_*}{k}\right)}{\frac{u_*}{k}} \right]^2 + \left[ \frac{SE_{O_3_{\text{slope}}}}{O_3_{\text{slope}}} \right]^2} \text{ for eddy-correlation} \quad (137.)$$

where  $SE(u_*/k)$  can be taken to be a constant from the anemometer specifications ie 1.5% for the Gill and Metek

and

$$\frac{SE_{v_{dO_3(1m)}}}{v_d(1m)} = \frac{SE_{Rt(1m)}}{Rt(1m)} = \sqrt{\left[\frac{SE_{F_{O_3}}}{F_{O_3}}\right]^2 + \left[\frac{SE_{\chi_{O_3(1m)}}}{\chi_{O_3}}\right]^2} \quad (138.)$$

The error in the canopy resistance,  $R_c$ , could be calculated from equation (138) below but as the errors in  $R_a$  and  $R_b$  are generally negligible compared to that in  $R_t$  they may be ignored (Sutton and Fowler, 1992) so that:

$$SE_{R_c} = \sqrt{SE_{R_t}^2 + SE_{R_a}^2 + SE_{R_b}^2} \approx SE_{R_t} \approx SE_{v_{dO_3}} \quad (139.)$$

The concentration at a given height can be found from either the interpolation of the concentration gradient or

$$\chi_{O_3}[z_i] = \chi_{O_3}[z-d] + F_{O_3}(R_a + R_{bO_3}) \quad (140.)$$

In the case of the former  $SE_{\chi_{O_3}[z_i]}$  could be found by transforming the points so that the intercept on the y-axis is at  $\chi_{O_3}[z_i]$  and so the standard error in the intercept is  $SE_{\chi_{O_3}[1\text{ m}]}$ . However, Flechard, 1998b noted that the standard error in interpolated and extrapolated concentrations varies with the square of the distance to the mean measurement height. Therefore the error on  $\chi_{O_3}[1\text{m}]$  will be much smaller than that on  $\chi_{O_3}[0]$  and so  $SE_{\chi_{O_3}[0]}$  can be taken as the maximum uncertainty. In the latter case  $SE_{\chi_{O_3}[1\text{ m}]} \approx \sqrt{SE_{\chi_{O_3}}^2 + SE_{F_{O_3}}^2}$ , where the standard error in the concentration is taken to be the accuracy of the measurement, ie  $\pm 5\%$ . Similar expression can be derived to find the errors in the quantities such as the latent heat flux and  $R_{c1}$ .

### **7.3 Errors in the Easter Bush Results**

The main focus of this analysis of the Easter Bush data is the estimates of  $R_{ns}$ . These were derived from measurements and modelling, so many factors contribute to their uncertainty. In order to quantify this uncertainty each component is considered individually then incorporated into an overall value, Table 7.1 summarises the uncertainties in each component.

#### **7.3.1 Measurements**

For each variable that is measured there is a systematic error associated with the sensor and some random error. For an individual 15 or 30 minute value the main error is given by the sensors' accuracy and precision. Although there will also be a random error associated this value being an average (or in the case of rainfall, sum) of individual samples these are not retained by the datalogger and

so a standard error is not available for some variables. In the case of the eddy-correlation measurements the raw 10 Hz data are retained and so some uncertainty calculations are possible for these data.

- **Windspeed**

*Sonic anemometers*

The Gill sonic has a quoted accuracy of  $\pm 3\%$  for instantaneous values and  $\pm 1.5\%$  for 10 s averages. An accuracy value is not given for the Metek sonic but it has a quoted precision of  $\pm 0.1 \text{ m s}^{-1}$ . For both sensors the uncertainty on the 30-minute windspeeds ( $u$ ,  $v$  and  $w$ ; equation. 133) is calculated, then the combined random and instrumentation error is given by equation (134).

For the Gill sonic the uncertainty is inbetween  $-1.5\%$  to  $1.5\%$ ,  $-2\%$  to  $2\%$  and  $-3\%$  to  $3\%$  for over 90% of measurements of  $u$ ,  $v$ , and  $w$  respectively. Figure 7.1 shows the relative distribution of the uncertainty as a percentage  $u$ ,  $v$  and  $w$ . The median on  $w$  ( $1.7\%$ ) is slightly larger than that on  $u$  and  $v$  ( $1.5\%$ ) as this wind speed vector tends to be smaller than the other two.

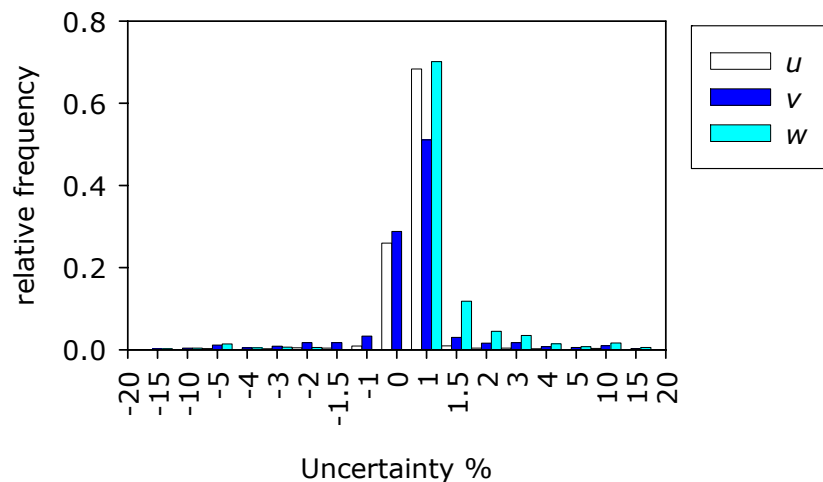


Figure 7.1. Relative frequency distribution of the percentage uncertainties in  $u$ ,  $v$  and  $w$  measured by the Gill sonic anemometer.

For the Metek

The relative frequency distribution of the uncertainty (as a percentage) for the Metek is similar to that for the Gill and the uncertainty is

inbetween -1.5% to 1.5%, -1.5% to 1.5% and -4% to 4% for over 90% of measurements of  $u$ ,  $v$ , and  $w$  respectively.

#### *Cup-anemometers*

The cup-anemometers have a quoted accuracy of  $\pm 0.1 \text{ m s}^{-1}$  with wind speeds of 0.3 to 10  $\text{m s}^{-1}$  and  $\pm 1\%$  within 10 to 55  $\text{m s}^{-1}$ . These values are used for the overall uncertainty as the standard deviation of the individual measurements was not logged and so a standard error cannot be calculated. The percentage uncertainty declines exponentially with windspeed up to 10  $\text{m s}^{-1}$  where it remains constant at  $\pm 1\%$ .

- **Temperature**

#### *Thermocouples*

The standard error of the fine-wire thermocouples supplied by Omega is the greater of  $1.7^\circ\text{C}$  or  $0.5\%$  of the measurement for temperatures greater than  $0^\circ\text{C}$  or  $1.7^\circ\text{C}$  or  $1\%$  when the temperature is less than  $0^\circ\text{C}$ . Thus for the range of temperatures measured on the Bowen Ratio or Gradient systems at Easter Bush the error is usually  $\pm 1.7^\circ\text{C}$ .

#### *RH/T Probe*

The Vaisala 50Y RH/T probe has a specified accuracy of  $\pm 0.35^\circ\text{C}$  at  $-10^\circ\text{C}$  and  $\pm 0.6^\circ\text{C}$  at  $+60^\circ\text{C}$ , therefore a linear function is used for the instrumentation error on temperature:

$$\text{Error} = 0.00357T + 0.39,$$

giving a median uncertainty of  $\pm 4\%$ .

#### *Sonic Anemometers*

As discussed in Section 5.5.3, although the sensible heat flux from the Gill sonic is used the temperature measurement is more uncertain and is discarded. The Metek sonic temperature is used and this has a resolution of  $\pm 0.01 \text{ K}$  which represents the instrumentation error. The combined standard and instrument error is less than  $0.2\%$  for  $80\%$  of the measurements.

- **Air pressure,  $p$**

Ambient air pressure is measured by the LICOR 7500 and a sensor at the Bush monitoring site. No information is available on the accuracy of the Bush sensor but the LICOR has a specified accuracy of  $\pm 1.5\%$ . As the LICOR is used for the majority of the time ( $>80\%$ ) this value is used for the error in  $p$ .

- **Ozone concentration**

Several different ozone analysers were used throughout the measurement period however for simplicity the specification of the longest running instrument is applied: resolution of  $\pm 1$  ppb and a linearity of  $\pm 1\%$  full scale. The instrument error is therefore taken to be the larger of 2 ppb or 1%. As the standard deviation of individual measurements is not logged the standard error cannot be calculated. The data area also adjusted to account for the sequential sampling of the gradient mast (Section 6.2.1) which introduces another unquantified error. The average change in concentration due to the correction for sequential sampling is  $\pm 1\%$  and so an uncertainty of  $\pm 0.5\%$  is added to the instrument error.

The median percentage uncertainty is  $\pm 3.8\%$  but can be over 100% when concentrations are less than  $\sim 2$  ppb, hence the ozone gradient will be most uncertain when concentrations are small.

- **Water-vapour and CO<sub>2</sub> concentration**

LICOR, the manufacturer of the CO<sub>2</sub>/H<sub>2</sub>O analysers, states that the accuracy of the instruments only depends on the accuracy of the calibration standards used, ie if the CO<sub>2</sub> span gas is 351 ppm  $\pm 5$  ppm then  $\pm 5$  ppm is the accuracy of the CO<sub>2</sub> concentration measurement. At Easter Bush both LICOR instruments were calibrated using the same standards: CO<sub>2</sub>  $\pm 5$  ppm; H<sub>2</sub>O – LICOR-610 Portable dew point generator,  $\pm 0.2$  °C dew point  $\approx 0.62$  kPa. However as the LICOR7500 measurements alone were used to examine ozone deposition only its data are considered here.

The uncertainty in the CO<sub>2</sub> concentration is therefore a combination of the standard error and the instrument error giving a median value of  $\pm 1.4\%$  which is mainly due to the instrument. The water-vapour data are analysed as latent-heat flux fluxes ( $\lambda E$ ) rather than vapour pressure ( $e$ ) or concentration ( $q$ ) and so their uncertainty is discussed below in Section 7.3.2. However the dew-point calibrator does provide an instrumentation error for the vapour

pressure and water-vapour concentration measurements with a median of  $\pm 61\%$  and  $\pm 1\%$  respectively.

### 7.3.2 Derived Values

#### *Ambient temperature, $T_a$*

The ambient air temperature will make a small contribution to the overall uncertainty as it is used to calculate parameters such as the conversion factor from ppb to  $\mu\text{g m}^{-3}$ , air density ( $\rho$ ) and Monin-Obukhov length ( $L$ ). The data set used is a combination of measurements from the Bowen Ratio, Gradient and Metek systems as well as a small amount of data from the Bush monitoring site (Section 5.6). The errors for the Easter Bush instruments have been discussed above and the sensors quoted accuracy of  $\pm 0.2$  °C is used for Bush. The median uncertainty in the final  $T_a$  dataset is  $\pm 24\%$  which is mainly due to the quoted accuracy of the thermocouple probes used on the Bowen Ratio and Gradient systems.

Given the relatively poor accuracy of the thermocouple probes it may have been better to use an alternative measure of  $T_a$  (ie only the sonic anemometer or RH/T probe). However, as  $T_a$  should characterise the average air temperature of the whole fetch and the four data sets used compare reasonably well (Section 5.6), its uncertainty is neglected where it makes a large contribution to the total.

$$\text{Friction velocity, } u_* = \sqrt{|u'w'|} = k \frac{du[z-d]}{\ln(z-d) - \psi_m}$$

#### Sonic anemometers

In this case the uncertainty in  $u_*$  is the combination of  $u'$  and  $w'$  using equation (135) which gives a median value of  $\pm 2.2\%$  for the Gill and  $\pm 1.1\%$  for the Metek.

#### Cup-anemometers

Using the gradient approach to find  $u_*$  adds additional uncertainty from the estimation of the stability correction  $\psi_m$ , however Sutton and Fowler, (1992), showed that this only has a small impact on the final estimate of flux. There will also be a small contribution from the  $(z-d)$  term.

In order to assess the uncertainty in  $u_*$  due to  $\Psi_m$ , uncorrected and corrected values of  $u_*$  are compared. The median change in  $u_*$  is -1.6%, although it can be over  $\pm 100\%$  in very stable or unstable conditions. An uncertainty of  $\pm 5\%$  is therefore included in the total.

The error in the measurement of  $z$  is assumed to be  $\pm 0.01$  m and for  $d$ ,  $\pm 1.5\%$  which is the median difference between  $d = 2/3h$  and optimised  $d$  in neutral conditions (Section 5.2.4).

The total uncertainty is therefore a combination of the errors in  $u$ ,  $\Psi_m$ ,  $z$  and  $d$ , which gives a median value of  $\pm 27\%$ . This compares to a median standard error in the slope of linear regression of only 7.9%.

$$\text{Sensible Heat Flux, } H = \rho c_p w' T' = -k u_* \rho c_p \frac{dT[z - d]}{\ln(z - d) - \Psi_H}$$

The specific heat capacity of air,  $c_p$ , is a constant and is assumed to have no uncertainty. The air density,  $\rho$ , is found using equation (141) and so contributes the uncertainty in  $H$  through the errors in  $p$  and  $T_a$ .

$$\rho = \frac{p}{R_m T_a} \text{ where } T \text{ is in K and } R_m = R/M = 287 \text{ J mol}^{-1} \text{ K}^{-1} \text{ kg}^{-1} \text{ (141.)}$$

Sonic anemometers

The uncertainty in  $H$  is the combination of  $w'$ ,  $T'$  and the error in  $\rho$ , using equation (135) which gives a median value of  $\pm 21\%$  for the Gill and  $\pm 25\%$  for the Metek (0.7% and 6.3% when the uncertainty in  $\rho$  is neglected).

Gradient

The uncertainty in  $H$  using the gradient approach is a combination of the errors in  $T$ ,  $u_*$ ,  $\Psi_H$ ,  $z$  and  $d$ . In order to assess the uncertainty in  $H$  due to  $\Psi_H$ , uncorrected and corrected values of  $H$  are compared. The median change in  $H$  is -1.4%, although it can be over  $\pm 100\%$  in very stable or unstable conditions. An uncertainty of  $\pm 5\%$  is therefore included in the total. This gives a total value of  $\pm 51\%$  in comparison to a median standard error in the slope of linear regression of only 4.4%.

Latent heat flux,  $\lambda E = \overline{\lambda w' q'}$

$\lambda$  is calculated using an empirical formula ( $\lambda = 3147.5 - 2.76T_a$ ), fitted to a series of values of  $\lambda$  and  $T$  given in Monteith and Unsworth (1990) and so the uncertainty in  $T_a$  should be included in the total.

The Webb correction, which adjusts  $\text{CO}_2$  and  $\text{H}_2\text{O}$  concentrations for vertical gradients in air density (Section 6.2.2.4) results in a small change  $\lambda E$  of about  $\pm 4\%$  and so an uncertainty of  $\pm 5\%$  is also included.

As the standard deviation of  $\lambda E$  rather than  $q$  is given by the reanalysis program this is used to calculate a percentage standard error and combined with the uncertainty due to  $T_a$  and the Webb correction. This gives a median value of  $\pm 20\%$  which is mainly due to  $T_a$  as excluding it gives only  $\pm 5\%$ .

$\text{CO}_2$  Flux (photosynthesis),  $A_n = \overline{w' \chi'_{\text{CO}_2}}$

The  $\text{CO}_2$  flux is also adjusted using the Webb correction, resulting in a change in  $A_n$  of  $\pm 19\%$ . The uncertainty in  $A_n$  is therefore a combination of  $\pm 20\%$  for the Webb correction and the uncertainties in  $w'$  and  $\chi'_{\text{CO}_2}$ , which gives a total of  $\pm 20\%$ . In this case the uncertainty is dominated by the Webb correction term.

$\text{O}_3$  Flux,  $F_{\text{O}_3} = -ku \ast a \frac{d\chi_{\text{O}_3}[z-d]}{\ln(z-d) - \psi_H}$

The uncertainty in the  $\text{O}_3$  flux can be calculated using equation (136) for the gradient and (137) for the sonic data as discussed above. The combined flux data set (Section 6.4.2) is analysed using the appropriate equation for each 0.5 hourly value, giving a median error of  $\pm 45.7\%$ .

However other terms may be included to account for additional uncertainties. There are uncertainties in  $p$  and  $T_a$ , associated with the conversion factor,  $a$ , for ppb to  $\mu\text{g m}^{-3}$  (equation 125) and the stability correction  $\psi_H$  ( $\pm 5\%$ ). The storage correction is applied to this data set (Section 6.2.5) and adds a small uncertainty of  $\pm 1\%$ . These increase the total uncertainty to  $\pm 54\%$  (or  $\pm 46\%$  when  $T_a$  is excluded).

The uncertainty on individual flux estimates can be very large, >100%, particularly when fluxes are small, this is mainly due to poorly defined ozone concentration gradients. If gradients where the  $R^2$  of the linear regression are less than 0.6 are excluded the median uncertainty decreases to  $\pm 29\%$ . The plot in Figure 7.2 shows the total uncertainty (excluding  $T_a$ ) plotted against the ozone flux; there is a lot of scatter but the uncertainty tends to get smaller as deposition increases and taking block medians of the data shows that the median uncertainty is less than 30% when fluxes are less than  $-200 \text{ ng m}^{-2} \text{ s}^{-1}$ .

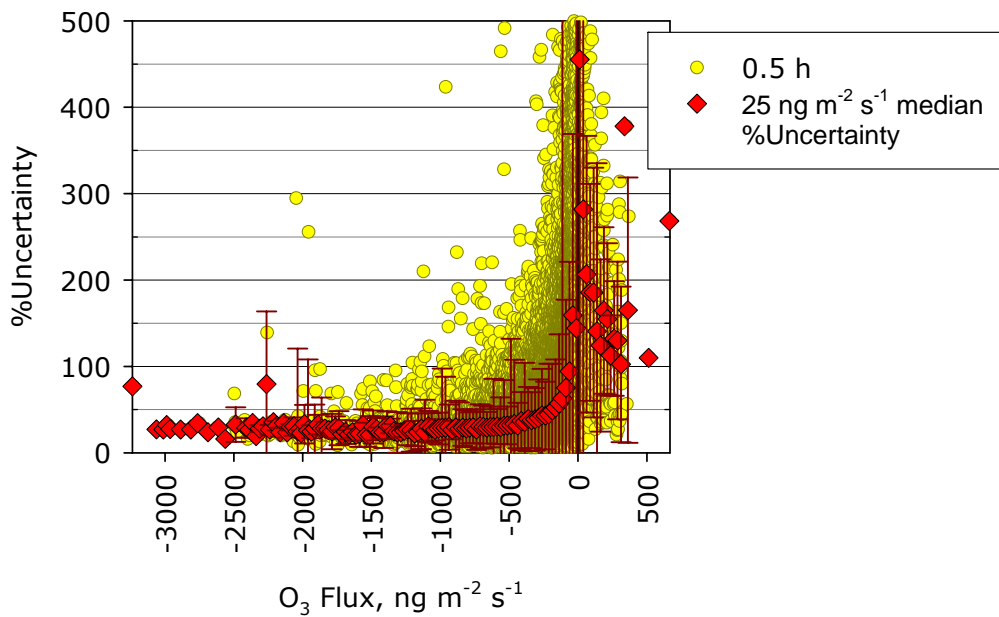


Figure 7.2. The 0.5 hourly percentage uncertainties in the ozone flux and  $25 \text{ ng m}^{-2} \text{ s}^{-1}$  block medians plotted against the flux (error bars show the standard deviation of each  $25 \text{ ng m}^{-2} \text{ s}^{-1}$  block).

$z_0$  and  $u[1\text{m}]$

$$z_0 = \exp\left(\ln(z-d) - \psi_m(z-d) - k \frac{u(z-d)}{u_*}\right)$$

The uncertainty in the combined  $z_0$  data set (gradient and sonics) is  $\pm 6\%$ , which is combination of the uncertainties in  $z$ ,  $d$ ,  $\psi_m$ ,  $u_*$  and  $u(z-d)$ .

$$u[1 \text{ m}] = \frac{u_*}{k} \left( \ln\left(\frac{z-d}{z_0}\right) - \psi_m\left(\frac{z-d}{L}\right) \right) = -\frac{u_*}{k} (\ln(z_0) - \psi_m(1 \text{ m}))$$

The uncertainty in the combined  $u[1\text{m}]$  data set (gradient and sonics) is  $\pm 8\%$ , which is combination of the uncertainties in  $z_0$ ,  $\psi_m$ , and  $u^*$ .

Quantities at 1 m and  $z_0$

As discussed above in Section 7.2, the random error in an estimate of  $S$  at a height less than 1 m, derived from gradient data, can be taken to be the standard error on the zero intercept of the slope. Where the value has been estimated using a form of equation (140) the error is:  $SE_{\chi_{S[1\text{ m}]}] \approx \sqrt{SE_{\chi_s}^2 + SE_{F_s}^2}$ .

The following variables are used in the analysis of  $R_{ns}$  and their uncertainties are calculated as described above with the addition of other parameters as required:

$T[z_0]$  (equation 68; includes  $\rho$ ) -  $\pm 20\%$  excluding  $T_a$  ( $\pm 33\%$  including)

$e[z_0]$  (equation 69; includes  $\rho$  and  $p$ ) - the percentage uncertainty in  $E$  is assumed to be the same as that in  $\lambda E$  and for  $e$  the dewpoint calibrator's accuracy of 0.62 kPa is used, giving  $\pm 61\%$  which is mainly due to  $e$ .

$\chi_{\text{CO}_2[z_0]}$  (as equation 140) -  $\pm 20\%$

$\chi_{\text{O}_3[z_0]}$  and  $\chi_{\text{O}_3[1\text{ m}]}$  (equation 140 or gradient) -  $\pm 47\%$

Resistances

$R_a$  and  $R_b$

As discussed in Section 7.2, it is often assumed that the random error in these two resistances is small. Taking the approach of combining the errors in each component of equations (56) and (59) using equation (135), gives an uncertainty of  $\pm 6.9\%$  and  $\pm 6.4\%$  in  $R_a$  and  $R_b$  respectively.

$R_{c\text{O}_3}$

Equation (168), combined with the errors in  $R_a$  and  $R_b$ , is used to estimate the uncertainty in  $R_{c\text{O}_3}$ , giving a median value of  $\pm 51\%$  (or  $\pm 45\%$  excluding  $R_a$  and  $R_b$ ).

$R_{c1}$

The canopy-resistance for water-vapour ( $R_{c1w}$ ) is calculated using equation (70) and then scaled for ozone ( $R_{c1O3}$ ) using equation (71). The uncertainty is therefore a combination of  $T[z_0]$ ,  $e[z_0]$ ,  $E$ ,  $p$ ,  $\rho$  and  $D_x/D_w$ ; the uncertainty in  $D_x/D_w$  is assumed to be  $1.51 \pm 10\%$ . This gives a total of  $\pm 69\%$  which is mainly due to the large instrumentation error on the measurement of vapour pressure ( $e[z_0]$ ); excluding this the uncertainty is only  $\pm 33\%$ .

### 7.3.3 Models

Quantifying uncertainty in modelled values can be very difficult as so many factors contribute, for example: the relationships and parameter values used to represent different components of the system may be very empirical and tuned to best fit the measured data; changing the value of one parameter may or may not greatly influence the final result; the measured or modelled data used as inputs will have their own associated uncertainties.

The models presented in this thesis have not been thoroughly evaluated, although a comparison to the measured data showed that they gave reasonable results. The uncertainty in the modelled  $R_{c1O3}$  is therefore estimated using the residuals of the measured versus the modelled values. The mean residual, as a percentage of the measurements, is 6%, -17% and -43% for JMod, BMod and JModG respectively, although it can be over  $\pm 100\%$  for individual values. Only JMod and BMod are used in the analysis of  $R_{ns}$  and an uncertainty of  $\pm 25\%$  is assumed for both. This value is greater than the median residuals and so gives a reasonable indication of the uncertainty in the modelled values. The plot in Figure 7.3 shows an example of the measured and modelled values (as shown in Figure 6.9) with the error bars indicating the uncertainty.

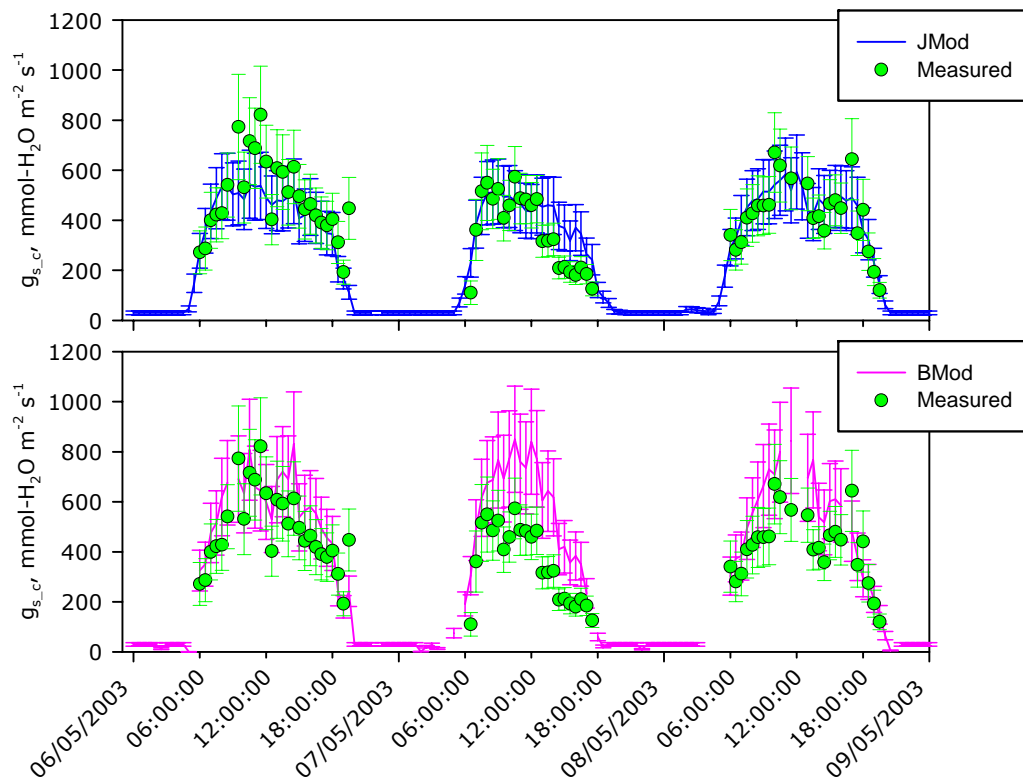


Figure 7.3. An example of measured stomatal conductance ( $g_s$ ) compared to modelled values (JMod top plot; BMod bottom plot). The error bars show the uncertainty in  $\text{mmol-H}_2\text{O m}^{-2} \text{s}^{-1}$ .

### 7.3.4 Overall Uncertainty in $R_{ns}$

$R_{ns}$  is calculated using equation (75):

$$R_{ns} = \left( \frac{1}{R_c} - \frac{1}{R_{c1\_O3}} \right)^{-1}$$

and so its uncertainty is a combination of the errors in  $R_{cO3}$  and  $R_{c1\_O3}$ . The value for  $R_{c1\_O3}$  will depend on the data set used (measured or modelled) and the median-total uncertainty in  $R_{ns}$  is  $\pm 63\%$ , or  $\pm 52\%$  excluding the errors in  $e$ ,  $R_a$  and  $R_b$ . This is quite a large value but reflects the difficulty in making accurate micrometeorological measurements of some variables (ozone gradients for example) and the associated uncertainty in values derived from them.

The standard error of the block medians used to derive the relationships between  $R_{ns}$  and meteorological variables was calculated using equation (133). These values tend to be similar to the uncertainty estimated here, for example

Figure 7.4 shows the dry temperature response with the standard error and uncertainties plotted.

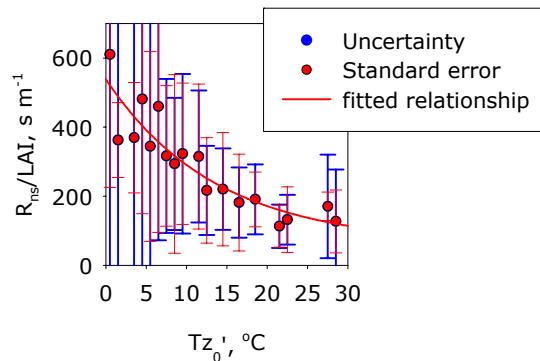


Figure 7.4. The uncertainty in 1 °C block medians of dry  $R_{ns}$  with  $T_{z0}$  where the error bars are calculated using either the standard error of the block values or the median total uncertainty derived from the data sets.

Table 7.1 Summary of errors in each measurement and the main derived values.

Instrument or Data Set	Variable	Notes	Median	Average	StDev	10th %tile	90th %tile
Gill	$u$		1.5	1.9	6.4	1.5	1.6
Gill	$v$		1.5	13.1	1594	1.5	2.5
Gill	$w$		1.7	4.3	90.5	1.6	3.2
Metek	$u$		-0.4	1.1	182.2	-2.0	1.3
Metek	$v$		-0.3	0.8	133.1	-1.6	1.4
Metek	$w$		5.8	13.2	1126	2.4	18.3
Gradient	$u$ Top 1		3.2	4.0	2.4	1.6	7.6
Gradient	$u$ Top 2		3.5	4.2	2.4	1.7	7.8
Gradient	$u$ Mid 3		3.7	4.4	2.4	1.9	8.0
Gradient	$u$ Mid 4		3.9	4.6	2.5	1.9	8.4
Gradient	$u$ Bot 5		4.1	4.8	2.5	2.1	8.6
Bowen Ratio	$T_{lower}$		17.7	77.0	1608	10.3	62.5
Bowen Ratio	$T_{upper}$		17.3	68.5	1820	10.4	55.6
Gradient	$T1$		17.9	64.3	1190	10.9	56.4
Gradient	$T3$		18.8	63.0	767.1	11.1	64.3
Gradient	$T5$		17.2	60.0	947.8	10.3	57.5
Vaisala RH/T	$T$		4.2	11.8	207.3	2.7	9.9
Metek	$T_s$		0.1	0.2	5.4	0.1	0.2
LICOR7500/ Bush	$\rho$		1.5	1.5	1.5	1.5	1.5
Gradient	$O_3$ 1		3.7	4.6	24.9	2.6	6.3
Gradient	$O_3$ 2		3.7	4.5	6.3	2.6	6.4
Gradient	$O_3$ 3		3.7	4.5	6.0	2.7	6.4
Gradient	$O_3$ 4		3.7	4.6	6.1	2.7	6.5
Gradient	$O_3$ 5		4.0	4.9	5.5	2.8	7.1
LICOR7500	$CO_2$		1.4	1.4	0.1	1.3	1.4
LICOR7500	$e$		61.1	87.8	349.2	42.6	102.0
LICOR7500	$H_2O$		0.8	0.9	0.3	0.5	1.2

Table 7.1 .....

Instrument or Data Set	Variable	Notes	Median	Average	StDev	10th %tile	90th %tile
	$T_a$		23.9	113.2	2417	14.3	78.2
Gill	$u^*$		2.2	14.0	1594	2.1	3.4
Metek	$u^*$		1.1	7.0	225	0.5	5.9
Gradient	$u^*$		26.8	33.7	17.7	16.5	63.7
Combined	$u^*$		2.2	15.6	1637	0.9	9.4
Gill	$H$		21.5	82.8	1724	13.9	54.6
Metek	$H$		25.4	135.0	2596	15.2	74.6
Gill	$H$		0.7	3.8	98.6	0.5	3.1
Metek	$H$		6.3	37.8	1137	2.8	22.4
Gradient	$H$		50.9	166.0	2222	32.8	130.7
LICOR7500	$\lambda E$	Incl. $T_a$	20.4	92.7	2098	13.8	53.4
LICOR7500	$\lambda E$	Excl. $T_a$	5.0	5.0	1.5	5.0	5.0
	$A_n$		20.0	21.4	77.6	20.0	20.1
	$F_{O_3}$	Incl. $T_a$	54.8	179.7	2451	28.0	236.4
	$F_{O_3}$	Excl. $T_a$	46.4	136.4	2079	19.0	204.7
	$F_{O_3}$	Slope of regression	28.6	32.0	236.2	15.4	43.2
	$z_0$		6.0	25.4	1643	5.5	40.3
	$u(1m)$		8.1	32.3	2324	7.5	42.2
	$T_{z0'}$	Incl. $T_a$	32.6	134.9	2585	17.9	99.1
	$T_{z0'}$	Excl. $T_a$	20.0	83.4	1461	10.6	82.3
	$e_{z0'}$		61.4	88.1	349.1	42.9	102.1
	$CO_2(z_{0'})$		20.1	21.5	77.6	20.0	20.2
	$O_3(z_{0'})$		46.6	136.0	2107	19.5	204.9
	$R_a$		6.9	45.9	3287	5.4	76.4
	$R_+$		6.4	33.9	2324	5.6	55.0
	$R_{CO_3}$	Incl. $T_a$	50.9	80.7	738.7	28.9	107.1
	$R_{CO_3}$	Excl. $T_a$	44.6	63.4	375.9	26.2	74.6
	$R_{CH_2O}$	Incl. $T_a$	5.1	5.1	1.5	5.0	5.2
	$R_{CH_2O}$	Excl. $T_a$	10.6	21.5	99.4	9.4	40.4
	$R_{c1O_3}$	Incl. $T_a$	69.1	210.5	3303	48.4	139.0
	$R_{c1O_3}$	Excl. $T_a$	33.0	152.8	3283	21.9	88.2
	$R_{ns}$	Incl. $T_a$	62.8	88.6	468.9	40.6	115.0
	$R_{ns}$	Excl. $T_a$	52.5	71.1	444.3	36.8	79.6



## 8 Synthesis and Conclusions

Ozone is an important trace-gas as it plays a central role in tropospheric chemistry and has detrimental effects on plants, animals and materials at the surface. Many studies have shown that ozone readily deposits on most materials and the dry deposition of ozone at the Earth's surface represents the largest sink for ozone in the planetary boundary layer.

The micrometeorological methods used to measure trace-gas exchange at the surface are well established and have been employed in many studies of ozone deposition to plant canopies. The majority of experiments have been for short time periods and many have focussed on the influence of stomatal uptake on ozone deposition as this was assumed to be the main controlling factor and it is this uptake that causes most damage to vegetation (Buse *et al.*, 2003; Fuhrer *et al.*, 1997; Grunhage and Jager, 2003). However it has been shown that non-stomatal deposition can also be significant and in terms of the mass budget of deposited ozone it is the largest component.

Most models of ozone deposition assume that non-stomatal deposition is constant and only varies with surface area, although some account may be taken of increased resistance over frozen surfaces (Simpson *et al.*, 2003a). Where non-stomatal deposition has been examined in more detail it is clear that it is not constant and can vary depending on surface wetness, humidity, temperature and solar radiation (Fowler *et al.*, 2001; Rondon *et al.*, 1993; Zhang *et al.*, 2002). Thus most models may under or over estimate the non-stomatal uptake of ozone and this will affect their ability to predict surface concentrations in the atmosphere.

This study has described the measurement of ozone, water-vapour and carbon-dioxide fluxes, as well as many other canopy and meteorological variables, over a grassland canopy in Central Scotland. The grass canopy was chosen as this provides a relatively homogenous and simple surface over which to study the ozone deposition process. Although non-stomatal ozone deposition cannot be measured directly it can be estimated as the residual from the total canopy resistance and stomatal resistance ( $R_{ns} = (1/R_{canopy} - 1/R_{stomatal})^{-1}$ ). The measurements of water-vapour flux were used to calculate  $R_{stomatal}$  using the Penman-Monteith equation. Two models were also developed using the water-

vapour and carbon-dioxide flux measurements, which estimated  $R_{stomatal}$  when it could not be measured. The resulting estimates of  $R_{ns}$  were not constant and it was found to vary with all the factors mentioned above (surface wetness, humidity, temperature and solar radiation). A clear distinction between wet and dry surfaces was found, resulting in two new model parameterisations for non-stomatal resistance. An overview of the results is given below.

### **8.1.1 Ozone Deposition and Water-vapour/CO<sub>2</sub> Fluxes over Grassland**

Measurements were made almost continuously for 4 years (26<sup>th</sup> May to 1<sup>st</sup> October 2001 and 21<sup>st</sup> March 2002 to 31<sup>st</sup> December 2004) which resulted in a substantial data set of about 31700 0.5 hourly ozone flux values and 15000 of H<sub>2</sub>O/CO<sub>2</sub>, as well as almost complete time series of the main meteorological parameters (wind direction, temperature and solar radiation).

The temporal patterns and, in general, the magnitude, of all the measurements were typical of the location and comparable with results from other experiments reported in the literature. Ozone and CO<sub>2</sub> deposition increased over the spring and summer as the canopy grew then declined in the autumn and winter, while the water-vapour flux followed the same pattern but for emission rather than deposition. The grass was harvested for silage of five occasions which highlighted the effect of vegetation on the energy balance of the surface. When active vegetation is present most of the incoming energy used in emitting water-vapour, as the latent-heat flux is large relative to that of sensible heat, whereas when the grass is cut the energy balance is dominated by the sensible heat flux. Fluxes of ozone and CO<sub>2</sub> also show this as they are normally much smaller after the grass is removed (Figure 5.38).

A period of heavy rainfall and flooding during 2002 followed by very dry weather in 2003, appeared to adversely affect the vegetation as it did not grow as well during 2002-2004 as it had during 2001, despite similar applications of fertilizer. This was reflected in the CO<sub>2</sub> fluxes which were smaller in 2002-2003 and only showed signs of increasing in the latter half of 2004 (Figure 5.30). The ozone flux did not reflect this trend as clearly. Fluxes were slightly smaller in 2001 than the following years and the largest deposition rates occurred in 2002, although deposition also increased in 2004 (Figure 5.22). This highlights the fact that

stomatal conductance is not the only factor controlling ozone deposition and other variables must be examined.

The influence of stomata can clearly be seen in the data when seasonal summaries are made and Figure 8.1 shows the seasonal ozone flux, deposition velocity and total canopy resistance. The ozone flux is larger in the summer months and during the daytime when the vegetation is most active and stomata open to allow the exchange of CO<sub>2</sub> and water-vapour. This is also reflected in the deposition velocity and total canopy resistance which are larger and smaller during the summer daytime respectively. These plots also show the importance of the non-stomatal sink as significant deposition occurs during the winter and at night in all months, when plants are inactive or senescent.

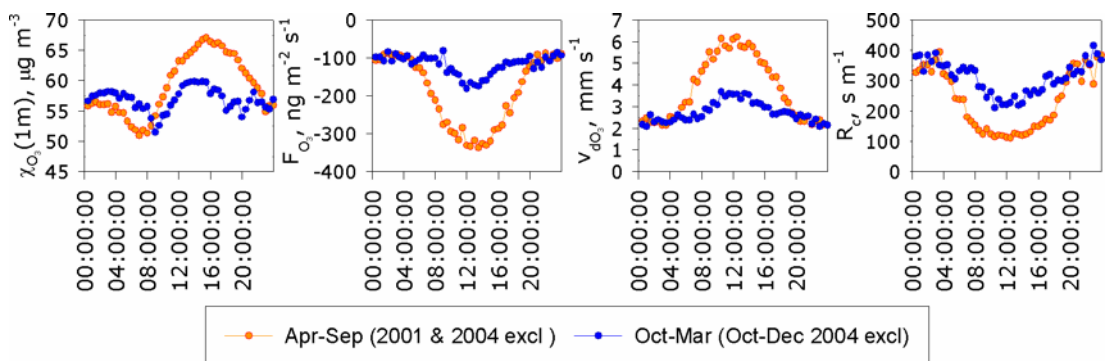


Figure 8.1. The seasonal diurnal cycles of (from left to right) average ozone concentration, median ozone flux, deposition velocity and resistance. Only data for 2002 and 2004 are included due the uncertainties in the 2001 and 2004 data, which are discussed in Chapters 5 and 6.

This non-stomatal sink is clearly not constant as there is additional variability and this was examined by selecting data for night-time only (Section 5.7). The night-time canopy resistance ( $R_{c\_night}$ ) was found to decline exponentially with temperature (and, to some extent, humidity) and the effect was suppressed when the canopy was very wet. It was suggested that this may be due to the simple thermal decomposition of ozone on warm surfaces. In order to investigate this further and include daylight conditions the measurements of water-vapour and CO<sub>2</sub> flux were used to estimate stomatal resistance and so estimate the non-stomatal term.

### 8.1.2 Measured and Modelled Stomatal Resistance - $R_{c1}$

The water-vapour and sensible heat flux measurements were used to calculate the stomatal resistance to water-vapour which was then scaled for ozone, as described in Section 2.5.1.2. This methodology can only be applied during

daylight when the canopy is completely dry so that the water-vapour flux is only from the stomata and not evaporation from soil or external surfaces of the foliage. As an additional filter to exclude evaporation from non-stomatal sources only data when  $LAI > 1.5$  were selected. The resulting data set is therefore relatively small and does not represent all conditions. However it was used to calculate values of non-stomatal resistance ( $R_{ns\_c}$ ) which also decreased with temperature, in a similar manner to  $R_{c\_night}$ .

To extend the range of conditions that could be examined, two models of stomatal resistance ( $R_{cl}$ ) were used, although they are parameterised in terms of stomatal conductance ( $g_s = 1/R_{cl}$ ) as this is commonly used in studies of plant physiology. Most stomatal conductance models are designed from the bottom up by first estimating  $g_s$  for an individual leaf then scaling this up to the whole canopy. The two approaches often used for studies of trace-gas exchange are: the multiplicative method (JMod; originally developed by Jarvis, 1976), where a maximum conductance is scaled for the effects of several environmental variables; and a more mechanistic photosynthesis based approach (BMod; originally developed by Ball, *et al.*, 1987) where  $g_s$  is related to the ratio of  $CO_2$  flux and the  $CO_2$  concentration at the surface. With both methods scaling their estimates of leaf conductance to the whole canopy increases their complexity and, to some extent, the uncertainty in their results. However by using the measurements of water-vapour and  $CO_2$  flux for the whole canopy, two simple models based on both these methods were parameterised. These gave estimates of the bulk-canopy stomatal conductance (Section 6.1) which are all that was required. If the purpose of the models had been to the accumulated stomatal flux effects indices (Section 1.4.1) then the more traditional bottom-up approach would have been more appropriate as this allows the flux to a sunlit leaf to be distinguished from that to the whole canopy.

The modelled values of  $g_s$  compared reasonably well with the measurements, although there was substantial variability with one model performing better than the other one day then the other on the next. It was assumed that as the photosynthesis based model is more mechanistic it more accurately reflects variations in  $g_s$ . These values were used to gap-fill the measured  $R_{cl}$  data but a filtering process was included to ensure modelled values were only included when the models were performing well in comparison to the measurements. This extended time series was then used to calculate  $R_{ns}$ .

### 8.1.3 Processes Controlling $R_{ns}$ and a New Model Parameterisation

Both the night-time canopy resistance ( $R_{c\_night}$ ) and the non-stomatal resistance ( $R_{ns\_c}$ ), calculated from the measurements in dry-daylight conditions, were found to decline with surface temperature ( $T_{z0}$ ).  $R_{ns\_c}$  also tends to decrease with increasing LAI as there is a larger surface for ozone to deposit to, and so the values were normalised for LAI using  $R_{nsN} = R_{ns\_c}/LAI$ , when  $LAI > 1$ . This improved the definition of the temperature response by reducing the scatter in the data and the standard errors in the parameters of the fitted curve.

The analysis was repeated for the individual data sets of  $R_{ns}$  and  $R_{nsN}$  ( $R_{ns\_cr}$  including all LAI,  $R_{ns\_JMod}$ ,  $R_{ns\_BMod}$ ) and similar temperature responses were found in each. The gap-filled time series of  $R_{ns}$  was therefore used to further examine the non-stomatal deposition process. In previous studies surface wetness has been found to affect ozone deposition rates and so the data were split into dry and wet periods. Several interesting differences were found:

- **Dry Surfaces**

The temperature response,  $R_{nsN\_dry}(T_{z0})$ , in dry conditions takes the form of a steady exponential decline from  $\sim 500 \text{ s m}^{-1}$  ( $\text{m}^2\text{m}^{-2}$ ) at  $0^\circ\text{C}$  to  $128 \text{ s m}^{-1}$  at  $30^\circ\text{C}$ . The simplest interpretation of this observation is that ozone is being destroyed at the surface by thermal decomposition, mediated by compounds on the warm leaf surfaces. However  $R_{nsN\_dry}$  was also found to be slightly smaller during the daytime than at night and exponentially decline with solar radiation ( $R_{ns\_dry}(St)$ ). Temperature and solar radiation are positively correlated and so the response to  $St$  may be partly due this coupling. However given that  $R_{ns\_dry}(St)$  is smaller than  $R_{ns\_dry}(T_{z0})$  and shows a step decline as radiation levels increase from zero to  $\sim 200 \text{ W m}^{-2}$  (Figure 6.18b) it was suggested that an additional photochemical or photolytic process is involved.

A decline with  $R_{nsN\_dry}$  with increasing  $u^*$  was also anticipated as increased turbulence would allow more air to penetrate the canopy and bring ozone down to the soil surface. However no clear trend was found in the data set as a whole and a small decrease was only seen when LAI was less than 0.3. It was therefore concluded that in-canopy aerodynamics has a minimal effect on  $R_{ns\_dry}$ .

A response to relative humidity (RH) above ~40% was also found but as the relationship between RH and  $T_{z0}'$  is not straightforward it was more difficult to separate the two effects on  $R_{nsN\_dry}$ . At temperatures above ~10°C with humidity <70%,  $R_{nsN\_dry}(RH)$  gave larger values than  $R_{nsN\_dry}(T_{z0}')$ . This would be consistent with a thin film of water being present on leaf surfaces, although the wetness sensor is dry (Klemm *et al.*, 2002), and occluding the sites for the thermal or photochemical reactions. At low temperatures and high humidity there may be sufficient water present for the surface to “wet” even though the wetness sensor is dry.

- **Wet Surfaces**

When the surface was wet,  $R_{nsN}$  was smaller than in dry conditions (by ~40% up to temperatures ~20°C) and a decrease at low temperatures was found ( $R_{nsN\_wet}$  declined from ~300 s m<sup>-1</sup> to ~160 s m<sup>-1</sup> between 0 to 10°C).  $R_{nsN\_wet}$  was also found to decrease slightly with solar radiation and it was concluded that aqueous phase reactions of ozone with compounds in the surface water occurred that are enhanced by additional photochemical reactions in the water during the daytime. A small response to humidity was observed which may simply be an interaction with temperature.

Ozone can act as an oxidising agent for SO<sub>2</sub> in water but this reaction is self limiting and quickly saturates when the pH is less than 6. However if ammonia is present at sufficient concentrations it can increase the pH and allow the SO<sub>2</sub> reaction to continue. In these circumstances this could represent a significant sink for ozone.

A simple model of the surface water chemistry (see Appendix D for more details) indicates that with 35 ppb of O<sub>3</sub>, 1 ppb of SO<sub>2</sub> and 1 ppb of NH<sub>3</sub> the pH of surface water would be ~6. This leads to ozone uptake rates of a few hundred ng m<sup>-2</sup> s<sup>-1</sup> depending on the thickness of the water layer, eg ~250 ng m<sup>-2</sup> s<sup>-1</sup> for 0.5 mm layer. If NH<sub>3</sub> concentrations are larger, 10 ppb, then the final pH is around 7, leading to uptake rates of several µg m<sup>-2</sup> s<sup>-1</sup>. However in practice, as ozone is relatively insoluble and the reaction rates very fast, uptake would be limited by diffusion within the liquid. For example, if only the top 10 µm contributed, the absolute removal rate would be only ~100 ng m<sup>-2</sup> s<sup>-1</sup> even at pH 7.2.

Measurements of SO<sub>2</sub> and NH<sub>3</sub> are available from Bush and Easter Bush as summarised in Table 8.1 below. For much of the time concentrations are too small to account for a significant amount of ozone removal but there are periods where both may be present in sufficient quantities to allow the removal of ozone by this route. More complex modelling is required to quantify the contribution this process may make to total ozone deposition.

*Table 8.1 Summary statistics for NH<sub>3</sub> and SO<sub>2</sub> concentrations observed at Easter Bush (NH<sub>3</sub>) and Bush (SO<sub>2</sub>) during 30<sup>th</sup> June – 30<sup>th</sup> Sept 2002 and 1<sup>st</sup> June to 31<sup>st</sup> August 2003.*

	Median	Average	Max	Min	Stdev	5 <sup>th</sup> %tile	95 <sup>th</sup> %tile
NH <sub>3</sub> (1 m)	1.01	1.35	12.71	0.01	1.11	0.22	3.52
SO <sub>2</sub> (10 m)	0.13	0.77	76.30	0.00	2.81	0.01	3.06

Unlike dry surfaces, a clear decrease in  $R_{ns\_wet}$  with increasing  $u_*$  was found. As it seemed unlikely that in-canopy aerodynamics are significantly different for a wet or dry canopy, it was concluded that this was due to the increased turbulence enhancing mixing in the water film and so increasing the rate of the chemical reactions.

The different response of  $R_{ns}$  to temperature in wet or dry conditions is summarised in Figure 8.2a which shows plots of the fitted curves;  $R_{nsN\_wet}$  is smaller than  $R_{nsN\_dry}$  up to temperatures of ~20oC where  $R_{nsN\_wet}$  is roughly constant while  $R_{ns\_dry}$  continues to decline. The two distinct behaviours indicate two chemical processes are occurring, one with a low activation energy on wet surfaces and another with a larger activation energy in dry conditions. This was confirmed by an Arrhenius plot (Figure 8.2b) where the deposition velocity ( $v_d = 1/R_{nsN}$ ) was taken to be the reaction rate for each process. The activation energy for the dry process of 36 kJ mol<sup>-1</sup> which is the same as the value reported by Fowler *et al.*, (2001) for a moorland canopy which implies the process may be independent of vegetation type.

These results were incorporated into a simple model of total canopy resistance which improved its ability to predict night-time resistances, particularly during wet periods and the winter. However comparison with the humidity based parameterisation of  $R_{ns}$  developed by Zhang *et al.*, (2002), indicated that humidity is an important factor during dry periods and should be included alongside the temperature response.

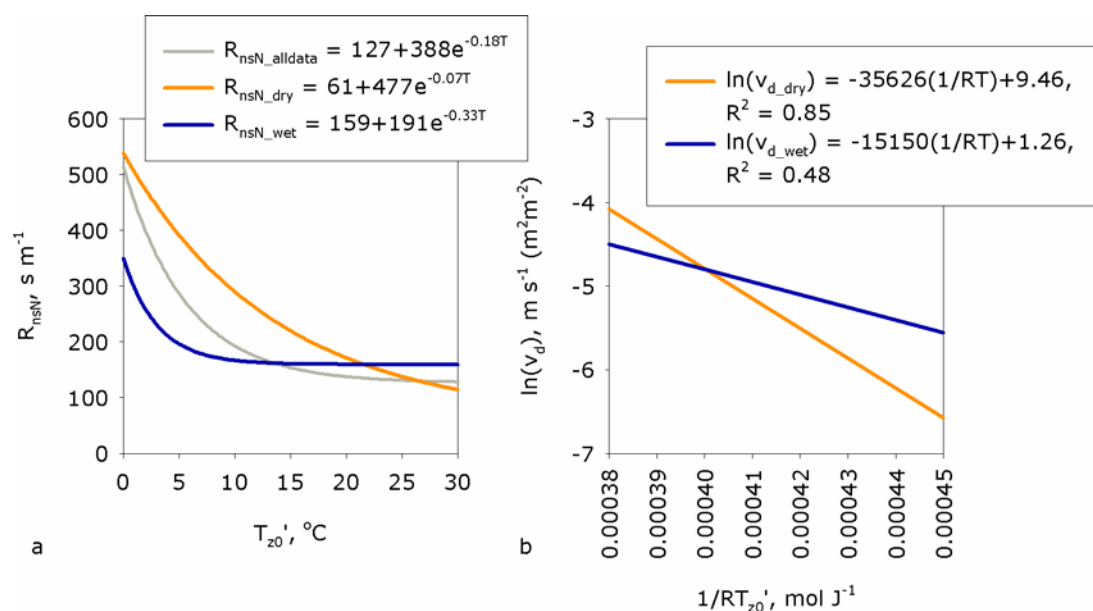


Figure 8.2. (a) The curves fitted to the response of  $R_{nsN\_dry}$  and  $R_{nsN\_wet}$  to surface temperature. (b) Arrhenius plots of the two temperature response curves.

### 8.1.4 Conclusions

Non-stomatal ozone deposition is a major component of the total, amounting to ~60% of the total budget, although the stomatal uptake of ozone does have a significant influence on daytime deposition during the summer. Some studies have found that non-stomatal deposition varies with factors such as surface wetness, humidity, temperature or radiation although the underlying mechanisms are currently poorly understood. The results presented have shown that in dry conditions, surface temperature is a major influence on  $R_{ns}$ . This is consistent with the thermal decomposition of ozone, mediated by chemicals on leaf surfaces. In the presence of sunlight additional reactions may take place that further reduce  $R_{ns}$ , these could either be the photolysis of ozone via compounds on the cuticle or the reaction of ozone with photochemically generated compounds at the surface. As the emission of VOCs from vegetation increases with temperature and solar radiation these compounds may be responsible. These reactions appear to be suppressed by humidity which would occur if a thin layer of water was deposited in these conditions and this occluded the reaction sites. The effects of temperature and humidity should be included in the model parameterisation as using the temperature response alone appeared to underestimate  $R_{ns}$ .

Although it is often assumed that wet surfaces will inhibit ozone deposition this was not found to be the case. The non-stomatal resistance of wet surfaces found to decrease with temperature and was lower than that in dry conditions up to a temperature of  $\sim 20^{\circ}\text{C}$ . As the solubility of ozone decreases with increasing temperature (as it does for most compounds) aqueous phase reactions must be removing ozone from the atmosphere. It was also found  $R_{ns}$  decreased as friction velocity increased over wet surfaces although it did not over dry. This is attributed to increased mixing in the water layer enhancing the chemical reactions by increasing the rate that the compounds involved are replenished (either from the cuticle or atmosphere).

The chemical properties of any plant canopy are complex with waxes present on the surface of the leaf cuticle as well as water, micro-organisms, dust particles and pollutants. Thus the exact mechanisms causing the observed variation in  $R_{ns}$  cannot be identified from field measurements alone where so many factors are uncontrolled, although some aspects of leaf water chemistry could be tested. The field measurements have however highlighted some possible processes that could be investigated further using controlled chamber studies.

### 8.1.5 Future Work

The analysis presented here has raised many questions regarding the non-stomatal deposition process for ozone, some of which may only be answered using controlled chamber studies. However some aspects could be investigated further:

1. Measurements of ozone deposition can be made alongside other trace gases, such as  $\text{SO}_2$  and  $\text{NH}_3$  which would allow possible interactions over wet surfaces to be investigated. There are measurements of  $\text{SO}_2$  and  $\text{NH}_3$  fluxes, concurrent with the ozone, available at Easter Bush which could be used to test a model of surface water chemistry.
2. Any effect of the source of surface water was not investigated as different types of wetting events could not be distinguished. However the data from the FD12P Present Weather Sensor will allow periods of dewfall, fog, drizzle, snow etc to be clearly identified and could be used to further examine  $R_{ns\_wet}$ .

3. The co-dependence of  $R_{ns\_dry}$  on surface temperature and humidity should be investigated further to allow both effects to be included in the model parameterisation.
4. Laboratory studies to identify the specific reactions that occur with ozone on leaf surfaces are required. In a chamber experiment all the individual factors such as humidity, temperature and radiation could also be controlled and their influence more clearly described.
5. Although it is assumed that the mesophyll resistance for ozone is zero there is some evidence that this is not the case (Kollist *et al.*, 2000; Wang *et al.*, 1995). It is possible that some of the effects observed in this study are due to interactions within the mesophyll and any data that are available data should be reviewed to assess its likely importance.

Some other developments that would improve the interpretation of the field measurements include:

1. Analysis of the eddy-correlation measurements of ozone flux (Section 4.5.3) to validate the gradient measurements and characterise the performance of the new ROFI instrument.
2. Include Burkhardt and Gerchau, (1994) type wetness sensing clips in future field measurements, to better characterise surface conditions.
3. Refinement of the gap-filling stomatal conductance models:
  - JMod - tune the parameters by season and use a temperature sum based phenology function.
  - BMod - use a temperature based estimate of soil respiration, derived from the night-time CO<sub>2</sub> flux measurements and include the CO<sub>2</sub> compensation point.
  - Account for stomatal blocking by surface water in both models.
4. Develop a full photosynthesis based stomatal conductance model for use in a complete model of the canopy resistance to ozone for grassland (*Lolium perenne*). This would ultimately be used for the gap-filling process.
5. Review available models of surface wetness that could be included in a model of total canopy resistance and allow  $R_{ns}$  to be calculated when suitable measured data are not available.

## **Appendix A Suppliers and Manufactures of Instrumentation**

Campbell Scientific Ltd.  
Campbell Park  
80 Hathern Road  
Shephed  
Loughborough, LE12 9GX  
United Kingdom  
Phone: +44 (0) 1509 601141  
Fax: +44 (0) 1509 601091  
<http://www.campbellsci.co.uk/>

Gill Instruments Ltd  
Saltmarsh Park  
67 Gosport Street  
Lymington, Hampshire  
England, SO41 9EG  
Tel: +44 (0)1590 613500  
Fax: +44 (0)1590 613501  
<http://www.gill.co.uk/>

LI-COR Biosciences  
4421 Superior St.  
Lincoln, NE 68504  
USA  
Phone 800-447-3576 (U.S. &  
Canada)  
Phone 402-467-3576 (International)  
Fax 402-467-2819  
<http://www.licor.com/env/>

METEK GmbH  
Fritz-Straßmann-Str. 4  
25337 Elmshorn  
Germany  
Phone +49 (0) 4121 4359 - 0  
Telefax +49 (0) 4121 4359 - 20  
<http://www.metek.de/>

Monitor Labs - Teledyne Monitor  
Labs-Englewood  
35 Inverness Drive East  
Englewood, CO, Denver USA  
80112  
Phone: (303) 792-3300  
Fax: (303) 799-4853  
<http://www.teledyne-ml.com/>

OMEGA Engineering Limited  
One Omega Drive  
River Bend Technology Centre  
Northbank  
Irlam  
Manchester M44 5BD  
United Kingdom  
Tel: +44(0) 161 777 6611  
Fax: +44(0) 161 777 6622  
<http://www.omega.co.uk/>

Skye Instruments Ltd.  
21, Ddole Enterprise Park,  
Llandrindod Wells,  
Powys  
LD1 6DF  
UK  
Phone +44 (0)1597 824811  
Fax + 44 (0)1 597 824812  
<http://www.skyeinstruments.com/>

ThermoElectron Corporation  
<http://www.thermo.com/>

Vaisala Ltd  
Newmarket Office  
Unit 9, Swan Lane  
Exning  
Newmarket  
Suffolk CB8 7FN, UK  
Phone: +44 1638 576 200  
Fax: +44 1638 576 240  
<http://www.vaisala.com/>

Windspeed Limited (trading as Vector  
Instruments)  
115 Marsh Road, RHYL,  
LL18 2AB,  
United Kingdom.  
Tel: 01745 350700  
Fax: 01745 344206  
<http://www.windspeed.co.uk/>



## Appendix B Tables of Summary Data

Table B.1 Canopy height (h)

	Average	Median	Max	Min	98 <sup>th</sup> %Tile	10 <sup>th</sup> %Tile	Stdev
May-01	0.38	0.38	0.43	0.33	0.42	0.34	0.03
Jun-01	0.19	0.18	0.45	0.04	0.27	0.07	0.10
Jul-01	0.28	0.32	0.45	0.06	0.34	0.09	0.09
Aug-01	0.19	0.20	0.21	0.12	0.21	0.16	0.02
Sep-01	0.15	0.14	0.21	0.11	0.20	0.11	0.03
Oct-01	0.12	0.12	0.12	0.12	0.12	0.12	0.00
Mar-02	0.04	0.04	0.04	0.04	0.04	0.04	0.00
Apr-02	0.06	0.05	0.10	0.04	0.09	0.04	0.02
May-02	0.16	0.17	0.24	0.08	0.24	0.09	0.05
Jun-02	0.09	0.07	0.25	0.05	0.25	0.05	0.06
Jul-02	0.13	0.13	0.16	0.09	0.15	0.10	0.02
Aug-02	0.08	0.08	0.17	0.05	0.13	0.06	0.03
Sep-02	0.08	0.07	0.09	0.06	0.09	0.07	0.01
Oct-02	0.06	0.06	0.06	0.05	0.06	0.05	0.00
Nov-02	0.05	0.04	0.06	0.04	0.05	0.04	0.00
Dec-02	0.04	0.05	0.05	0.03	0.05	0.04	0.01
Jan-03	0.04	0.03	0.05	0.03	0.05	0.03	0.01
Feb-03	0.03	0.03	0.04	0.03	0.04	0.03	0.01
Mar-03	0.03	0.03	0.04	0.03	0.04	0.03	0.00
Apr-03	0.05	0.04	0.07	0.04	0.06	0.04	0.01
May-03	0.11	0.11	0.19	0.04	0.17	0.04	0.04
Jun-03	0.07	0.07	0.09	0.04	0.08	0.04	0.01
Jul-03	0.09	0.09	0.10	0.05	0.10	0.07	0.01
Aug-03	0.09	0.09	0.10	0.06	0.10	0.07	0.01
Sep-03	0.07	0.07	0.09	0.05	0.08	0.06	0.01
Oct-03	0.05	0.05	0.06	0.03	0.06	0.04	0.01
Nov-03	0.03	0.03	0.04	0.03	0.04	0.03	0.00
Dec-03	0.02	0.02	0.03	0.02	0.03	0.02	0.00
Jan-04	0.02	0.02	0.02	0.02	0.02	0.02	0.00
Feb-04	0.02	0.02	0.02	0.02	0.02	0.02	0.00
Mar-04	0.02	0.02	0.03	0.02	0.03	0.02	0.00
Apr-04	0.04	0.04	0.05	0.02	0.05	0.02	0.01
May-04	0.07	0.07	0.09	0.04	0.09	0.05	0.01
Jun-04	0.11	0.11	0.12	0.08	0.12	0.09	0.01
Jul-04	0.11	0.12	0.12	0.06	0.12	0.08	0.02
Aug-04	0.12	0.12	0.17	0.08	0.16	0.09	0.03
Sep-04	0.13	0.13	0.17	0.09	0.16	0.10	0.02
Oct-04	0.10	0.11	0.11	0.07	0.11	0.07	0.01
Nov-04	0.08	0.08	0.10	0.05	0.10	0.06	0.01
Dec-04	0.05	0.05	0.06	0.04	0.06	0.05	0.00

Table B.2 Leaf Area Index (LAI)

	Average	Median	Max	Min	98 <sup>th</sup> %Tile	10 <sup>th</sup> %Tile	Stdev
May-01	3.9	3.9	3.9	3.7	3.9	3.8	0.1
Jun-01	2.2	2.4	3.9	0.3	3.3	0.8	0.9
Jul-01	3.2	3.6	3.8	0.3	3.8	1.3	1.0
Aug-01	2.7	2.8	2.9	1.9	2.9	2.3	0.2
Sep-01	2.2	2.1	2.9	1.6	2.8	1.7	0.4
Oct-01	1.8	1.8	1.9	1.8	1.9	1.8	0.0
Mar-02	0.6	0.6	0.6	0.6	0.6	0.6	0.0
Apr-02	0.9	0.8	1.6	0.6	1.3	0.6	0.3
May-02	2.3	2.4	3.2	1.2	3.1	1.4	0.6
Jun-02	1.0	1.0	3.2	0.3	1.3	0.7	0.4
Jul-02	1.9	2.0	2.3	1.4	2.3	1.5	0.3
Aug-02	1.3	1.2	2.4	0.8	1.9	0.9	0.4
Sep-02	1.2	1.2	1.4	1.0	1.4	1.1	0.1
Oct-02	0.9	0.9	1.0	0.7	1.0	0.8	0.1
Nov-02	0.7	0.7	0.9	0.6	0.8	0.6	0.1
Dec-02	0.6	0.7	0.8	0.5	0.8	0.5	0.1
Jan-03	0.5	0.5	0.7	0.4	0.7	0.4	0.1
Feb-03	0.5	0.4	0.7	0.4	0.6	0.4	0.1
Mar-03	0.5	0.5	0.6	0.4	0.6	0.4	0.1
Apr-03	0.7	0.6	1.1	0.5	1.0	0.6	0.2
May-03	1.7	1.7	2.7	0.6	2.5	0.7	0.6
Jun-03	1.1	1.1	1.3	0.7	1.3	0.7	0.2
Jul-03	1.4	1.5	1.6	0.8	1.6	1.2	0.2
Aug-03	1.3	1.4	1.6	1.0	1.6	1.1	0.2
Sep-03	1.1	1.1	1.3	0.7	1.3	1.0	0.2
Oct-03	0.7	0.7	0.9	0.5	0.9	0.5	0.1
Nov-03	0.5	0.5	0.6	0.3	0.6	0.4	0.1
Dec-03	0.3	0.3	0.4	0.3	0.4	0.3	0.0
Jan-04	0.3	0.3	0.3	0.3	0.3	0.3	0.0
Feb-04	0.3	0.3	0.3	0.3	0.3	0.3	0.0
Mar-04	0.3	0.3	0.4	0.3	0.4	0.3	0.0
Apr-04	0.5	0.5	0.7	0.3	0.7	0.3	0.1
May-04	1.0	1.1	1.5	0.5	1.4	0.7	0.2
Jun-04	1.6	1.7	1.8	1.2	1.8	1.5	0.2
Jul-04	1.7	1.8	1.8	1.0	1.8	1.3	0.2
Aug-04	1.9	1.9	2.4	1.2	2.4	1.4	0.3
Sep-04	2.0	1.9	2.4	1.4	2.4	1.6	0.3
Oct-04	1.5	1.7	1.7	1.0	1.7	1.1	0.2
Nov-04	1.2	1.2	1.6	0.7	1.5	0.9	0.2
Dec-04	0.8	0.8	1.0	0.6	0.9	0.8	0.1

Table B.3 Wind-speed (u(1m))

	Average	Median	Max	Min	98 <sup>th</sup> %Tile	10 <sup>th</sup> %Tile	Stdev
May-01	1.17	1.09	4.74	0.49	1.73	0.71	0.45
Jun-01	1.24	0.89	8.63	0.00	2.50	0.36	1.27
Jul-01	0.98	0.81	5.90	0.00	1.92	0.24	0.80
Aug-01	1.21	0.96	5.44	0.01	2.46	0.40	0.85
Sep-01	1.24	0.95	6.29	0.00	2.57	0.33	1.08
Oct-01	1.88	1.67	7.69	1.02	2.03	1.37	1.13
Mar-02	1.92	1.02	6.79	0.02	4.30	0.36	1.64
Apr-02	1.16	0.99	8.28	0.00	2.06	0.22	1.04
May-02	1.08	0.95	6.18	0.00	1.96	0.39	0.70
Jun-02	1.07	0.92	5.78	0.01	1.54	0.42	0.79
Jul-02	0.94	0.73	5.85	0.00	2.02	0.23	0.81
Aug-02	0.64	0.51	4.86	0.00	1.20	0.10	0.61
Sep-02	0.68	0.55	3.54	0.00	1.21	0.12	0.60
Oct-02	1.10	0.86	6.11	0.00	2.22	0.25	1.03
Nov-02	1.29	0.93	6.35	0.00	2.83	0.38	1.11
Dec-02	0.90	0.66	5.34	0.00	2.16	0.25	0.81
Jan-03	1.76	1.27	10.96	0.00	3.54	0.55	1.78
Feb-03	1.34	0.83	6.91	0.01	3.85	0.28	1.43
Mar-03	1.15	0.83	7.93	0.00	2.78	0.25	1.12
Apr-03	0.79	0.68	7.68	0.00	1.41	0.19	0.62
May-03	1.25	0.95	10.24	0.00	2.32	0.35	1.28
Jun-03	0.91	0.78	4.51	0.00	1.62	0.23	0.70
Jul-03	0.77	0.66	5.14	0.00	1.21	0.24	0.65
Aug-03	0.87	0.58	6.60	0.00	1.51	0.14	1.06
Sep-03	0.96	0.70	8.44	0.01	1.54	0.27	1.09
Oct-03	1.01	0.87	4.57	0.00	1.78	0.33	0.72
Nov-03	1.60	1.02	11.35	0.00	3.65	0.46	1.63
Dec-03	1.64	1.12	6.76	0.00	3.75	0.43	1.27
Jan-04	4.24	4.21	9.57	0.14	6.63	1.92	1.83
Feb-04	3.66	3.51	9.95	0.01	6.61	1.07	2.11
Mar-04	3.55	3.22	10.04	0.04	6.87	0.98	2.19
Apr-04	3.22	2.95	9.29	0.03	5.54	1.17	1.71
May-04	2.48	2.31	6.37	0.02	4.55	0.65	1.47
Jun-04	2.94	2.89	7.00	0.01	4.90	1.10	1.43
Jul-04	2.33	2.18	6.81	0.01	4.00	0.97	1.21
Aug-04	2.05	1.73	6.81	0.01	3.97	0.50	1.36
Sep-04	3.73	3.62	9.47	0.00	6.38	1.14	1.96
Oct-04	2.83	2.43	10.86	0.02	5.87	0.52	2.11
Nov-04	3.57	3.36	9.15	0.01	6.20	1.10	1.84
Dec-04	4.11	4.16	9.24	0.02	6.61	1.12	1.98

Table B.4 Ambient air temperature (Ta)

	Average	Median	Max	Min	98 <sup>th</sup> %Tile	10 <sup>th</sup> %Tile	Stdev
May-01	13.44	13.18	20.92	7.75	18.28	9.92	3.09
Jun-01	12.27	12.05	23.86	1.69	17.07	7.62	3.91
Jul-01	15.74	15.72	26.44	5.66	21.52	10.41	4.11
Aug-01	15.58	15.86	22.98	8.32	19.55	11.12	3.19
Sep-01	13.15	13.16	21.21	6.09	16.28	9.86	2.50
Oct-01	13.13	12.61	15.68	11.53	15.30	11.61	1.49
Mar-02	6.76	6.97	15.34	-1.89	11.35	1.15	3.75
Apr-02	7.97	8.00	20.20	-3.50	12.32	3.13	3.76
May-02	10.32	10.15	19.91	2.47	14.33	6.61	3.10
Jun-02	12.79	12.61	20.72	5.23	15.86	10.11	2.34
Jul-02	13.60	13.51	19.93	6.11	16.79	10.31	2.52
Aug-02	14.98	14.78	23.81	7.31	18.88	11.36	2.86
Sep-02	12.62	12.56	21.94	1.72	16.44	8.80	3.11
Oct-02	7.65	7.16	19.64	-4.82	13.60	3.11	4.04
Nov-02	7.31	7.48	13.30	-0.74	10.21	4.02	2.47
Dec-02	4.85	4.75	12.79	-3.95	8.35	1.01	3.02
Jan-03	4.13	4.18	13.05	-4.96	9.92	-1.26	3.98
Feb-03	3.88	3.63	12.15	-6.36	9.47	-0.81	3.92
Mar-03	6.77	7.18	16.45	-2.71	11.63	1.26	3.89
Apr-03	10.23	9.92	22.88	-1.04	15.01	6.28	3.70
May-03	11.32	11.35	28.16	2.77	15.86	6.46	3.86
Jun-03	15.28	15.07	24.53	5.40	19.42	11.78	3.07
Jul-03	16.50	16.14	29.91	6.95	20.92	12.89	3.55
Aug-03	14.72	14.43	27.90	4.22	19.30	10.25	3.66
Sep-03	12.49	12.62	21.14	2.69	16.93	7.69	3.54
Oct-03	7.36	7.44	16.01	-2.22	12.18	2.51	3.74
Nov-03	6.85	6.92	15.93	-3.47	11.32	2.48	3.42
Dec-03	4.13	4.74	11.45	-8.63	8.78	-1.40	4.12
Jan-04	4.45	4.28	11.32	-3.32	8.60	0.30	3.07
Feb-04	4.03	3.83	13.37	-5.33	9.47	-0.89	3.81
Mar-04	5.03	4.73	13.62	-5.33	9.59	0.79	3.30
Apr-04	7.90	7.66	19.47	-2.36	11.93	4.14	3.16
May-04	10.65	10.75	22.16	-0.04	15.33	5.60	3.79
Jun-04	12.87	12.81	21.17	4.66	17.27	8.63	3.16
Jul-04	13.37	13.29	25.38	5.97	17.51	9.56	3.03
Aug-04	14.74	14.64	27.09	2.82	19.18	10.87	3.47
Sep-04	12.15	12.09	22.84	1.43	16.12	8.42	3.27
Oct-04	7.99	8.15	13.97	0.21	10.86	4.93	2.32
Nov-04	6.64	7.35	12.57	-6.07	10.68	0.93	3.67
Dec-04	4.91	5.47	11.55	-5.30	9.48	0.22	3.53

*Table B.5 Solar Radiation (St)*

	Average	Median	Max	98 <sup>th</sup> %Tile	Stdev
May-01	218.9	108.8	860.0	647.1	250.9
Jun-01	175.6	79.0	903.0	510.7	216.4
Jul-01	153.4	75.6	950.5	453.9	192.6
Aug-01	138.7	41.8	790.0	424.5	182.1
Sep-01	92.2	6.9	653.4	311.3	142.3
Oct-01	168.1	114.2	454.5	420.5	178.9
Mar-02	108.5	6.7	612.2	403.1	165.8
Apr-02	135.9	33.2	767.0	449.8	188.0
May-02	158.9	58.8	897.0	488.2	206.3
Jun-02	180.0	90.6	904.5	522.8	217.2
Jul-02	146.0	70.4	858.5	421.2	180.5
Aug-02	143.5	39.3	801.5	479.5	198.2
Sep-02	105.9	8.0	698.5	364.3	157.0
Oct-02	58.5	0.5	529.9	234.5	108.2
Nov-02	25.9	0.5	327.4	98.7	56.8
Dec-02	13.7	5.1	189.5	42.2	22.8
Jan-03	24.9	5.2	347.0	77.7	43.9
Feb-03	65.5	9.3	446.3	227.6	98.9
Mar-03	113.4	11.7	652.5	403.9	160.5
Apr-03	173.0	55.4	826.5	522.9	206.1
May-03	188.8	92.6	869.5	531.7	212.9
Jun-03	226.4	127.0	910.0	612.9	241.8
Jul-03	192.2	94.1	890.0	550.2	223.3
Aug-03	179.8	64.8	966.5	545.4	221.6
Sep-03	120.4	12.8	694.7	410.9	169.1
Oct-03	69.3	1.1	509.9	260.0	113.1
Nov-03	32.3	1.0	324.4	128.0	62.2
Dec-03	16.8	1.0	221.2	63.2	35.9
Jan-04	20.4	1.0	250.2	73.6	42.0
Feb-04	50.9	1.0	459.4	205.3	94.2
Mar-04	87.7	1.7	605.5	297.6	134.7
Apr-04	116.6	30.1	736.0	376.9	160.1
May-04	197.4	87.1	988.5	585.8	237.9
Jun-04	184.4	94.3	914.5	505.1	212.0
Jul-04	163.4	86.3	854.5	460.5	192.9
Aug-04	128.5	35.4	771.5	421.9	180.4
Sep-04	112.4	8.9	675.7	393.9	163.8
Oct-04	55.3	0.4	480.3	211.4	97.9
Nov-04	27.7	0.4	285.5	101.5	54.5
Dec-04	17.2	0.2	202.3	66.5	36.3

Table B.6 Relative Humidity (RH)

	Average	Median	Max	Min	98 <sup>th</sup> %Tile	10 <sup>th</sup> %Tile	Stdev
May-01	0.80	0.83	1.00	0.47	0.91	0.66	0.10
Jun-01	0.71	0.73	0.99	0.11	0.88	0.52	0.14
Jul-01	0.73	0.74	1.00	0.45	0.86	0.60	0.10
Aug-01	0.77	0.78	1.00	0.44	0.90	0.61	0.11
Sep-01	0.76	0.76	1.00	0.26	0.90	0.62	0.11
Oct-01	0.79	0.81	0.87	0.67	0.86	0.70	0.06
Mar-02	0.71	0.70	0.94	0.45	0.84	0.56	0.10
Apr-02	0.69	0.70	1.00	0.29	0.82	0.53	0.11
May-02	0.74	0.76	1.00	0.38	0.87	0.60	0.11
Jun-02	0.76	0.77	1.00	0.46	0.90	0.60	0.11
Jul-02	0.83	0.83	1.00	0.55	0.95	0.70	0.09
Aug-02	0.83	0.85	1.00	0.38	0.95	0.69	0.10
Sep-02	0.78	0.78	0.96	0.47	0.88	0.66	0.09
Oct-02	0.75	0.77	1.03	0.11	0.86	0.62	0.11
Nov-02	0.45	0.43	0.93	0.09	0.65	0.34	0.13
Dec-02	0.67	0.67	0.87	0.09	0.80	0.48	0.12
Jan-03	0.46	0.54	0.86	0.00	0.69	0.03	0.24
Feb-03	0.52	0.55	0.76	0.14	0.68	0.34	0.13
Mar-03	0.59	0.62	0.85	0.03	0.74	0.46	0.16
Apr-03	0.59	0.58	0.91	0.13	0.71	0.48	0.10
May-03	0.67	0.70	0.98	0.10	0.85	0.45	0.18
Jun-03	0.72	0.73	1.00	0.28	0.86	0.58	0.10
Jul-03	0.79	0.80	1.00	0.32	0.97	0.62	0.13
Aug-03	0.77	0.79	1.00	0.37	0.93	0.58	0.13
Sep-03	0.71	0.72	0.98	0.44	0.87	0.54	0.12
Oct-03	0.68	0.68	0.98	0.43	0.79	0.57	0.09
Nov-03	0.80	0.82	0.98	0.36	0.91	0.67	0.10
Dec-03	0.86	0.87	1.00	0.42	0.96	0.72	0.10
Jan-04	0.85	0.87	1.00	0.52	0.95	0.74	0.08
Feb-04	0.77	0.81	1.00	0.01	0.93	0.56	0.15
Mar-04	0.79	0.80	0.99	0.45	0.89	0.66	0.09
Apr-04	0.80	0.82	0.98	0.13	0.93	0.65	0.11
May-04	0.77	0.79	0.98	0.02	0.93	0.59	0.13
Jun-04	0.80	0.82	1.00	0.43	0.92	0.65	0.11
Jul-04	0.80	0.82	1.00	0.47	0.91	0.64	0.11
Aug-04	0.85	0.88	1.00	0.47	0.97	0.69	0.11
Sep-04	0.83	0.85	1.00	0.48	0.95	0.70	0.09
Oct-04	0.86	0.87	0.99	0.45	0.96	0.76	0.08
Nov-04	0.84	0.86	0.98	0.21	0.93	0.71	0.08
Dec-04	0.85	0.86	1.00	0.63	0.92	0.78	0.05

Table B.7 Soil Water Content at Rooting Depth (SWC)

	Average	Median	Max	Min	98 <sup>th</sup> %Tile	10 <sup>th</sup> %Tile	Stdev
May-01	ND	ND	ND	ND	ND	ND	ND
Jun-01	ND	ND	ND	ND	ND	ND	ND
Jul-01	ND	ND	ND	ND	ND	ND	ND
Aug-01	ND	ND	ND	ND	ND	ND	ND
Sep-01	ND	ND	ND	ND	ND	ND	ND
Oct-01	ND	ND	ND	ND	ND	ND	ND
Mar-02	ND	ND	ND	ND	ND	ND	ND
Apr-02	ND	ND	ND	ND	ND	ND	ND
May-02	ND	ND	ND	ND	ND	ND	ND
Jun-02	35.72	35.70	36.60	34.89	36.45	35.10	0.52
Jul-02	34.27	34.70	35.75	32.20	35.13	32.88	0.91
Aug-02	38.16	37.94	48.26	36.73	39.19	37.10	1.16
Sep-02	37.53	37.41	41.95	36.06	38.43	36.58	0.93
Oct-02	38.52	38.61	43.39	34.80	42.50	35.10	2.81
Nov-02	40.37	40.01	43.54	39.02	41.81	39.64	0.93
Dec-02	40.53	40.20	51.46	38.91	42.05	39.46	1.15
Jan-03	41.06	40.80	43.74	39.60	42.43	40.00	0.98
Feb-03	40.27	39.96	42.51	38.16	41.78	39.54	0.85
Mar-03	39.87	39.88	42.20	38.66	40.60	39.01	0.65
Apr-03	36.82	37.05	39.51	34.10	39.10	34.34	1.85
May-03	39.56	39.63	40.76	36.75	40.20	38.90	0.57
Jun-03	35.16	35.35	38.86	30.64	38.41	30.93	2.70
Jul-03	29.11	28.41	33.16	26.16	32.05	26.58	2.19
Aug-03	25.55	25.26	32.70	21.58	29.38	22.14	2.70
Sep-03	20.80	20.75	28.49	20.00	21.21	20.26	0.48
Oct-03	23.51	21.23	30.80	20.79	28.49	21.08	3.34
Nov-03	30.70	29.53	39.41	28.49	33.18	29.35	2.06
Dec-03	38.81	37.91	51.68	35.98	41.55	37.04	1.83
Jan-04	40.83	40.46	51.31	38.30	43.03	39.10	1.45
Feb-04	40.60	40.05	50.79	37.56	43.31	39.03	1.52
Mar-04	39.33	38.86	52.20	38.09	40.75	38.54	1.24
Apr-04	39.58	39.10	53.73	38.19	41.19	38.59	1.28
May-04	38.42	38.51	50.91	34.64	40.61	35.64	1.93
Jun-04	35.18	34.46	87.52	29.38	40.72	31.00	3.90
Jul-04	37.81	37.55	87.52	33.70	41.05	34.34	2.96
Aug-04	38.57	39.41	87.52	32.85	41.84	34.16	2.98
Sep-04	37.36	37.43	45.81	35.88	38.21	36.24	0.74
Oct-04	41.02	41.21	48.15	37.15	43.00	37.55	1.69
Nov-04	40.86	40.70	87.52	38.23	41.33	40.08	2.85
Dec-04	41.28	41.09	87.53	36.33	42.75	40.29	1.58

Table B.8 Rainfall and surface wetness

	Sum (mm)	Max (mm) in 0.5h	%Wet
May-01	13.86	4.31	ND
Jun-01	88.65	3.39	0.34
Jul-01	115.81	4.93	0.45
Aug-01	105.64	4.62	0.28
Sep-01	60.24	3.08	0.50
Oct-01	0.62	0.31	0.56
Mar-02	0.00	0.00	0.14
Apr-02	48.05	2.77	0.25
May-02	54.23	3.39	0.22
Jun-02	107.18	2.77	0.26
Jul-02	91.29	3.00	0.38
Aug-02	148.44	6.79	0.45
Sep-02	44.71	7.09	0.76
Oct-02	231.16	5.55	0.55
Nov-02	96.32	4.94	0.47
Dec-02	80.69	2.47	0.62
Jan-03	56.00	3.39	0.51
Feb-03	13.25	1.85	0.71
Mar-03	15.42	3.08	0.44
Apr-03	23.74	3.08	0.52
May-03	65.05	5.55	0.50
Jun-03	15.42	2.78	0.31
Jul-03	45.63	4.32	0.52
Aug-03	2.77	1.23	0.38
Sep-03	36.39	5.55	0.39
Oct-03	75.55	5.24	0.57
Nov-03	37.92	4.93	0.54
Dec-03	59.19	2.78	0.39
Jan-04	131.01	8.94	0.40
Feb-04	52.70	3.39	0.41
Mar-04	52.97	2.25	0.44
Apr-04	113.75	4.93	0.43
May-04	68.13	4.94	0.46
Jun-04	178.78	3.70	0.52
Jul-04	71.60	8.02	0.33
Aug-04	150.76	4.94	0.54
Sep-04	60.40	2.47	0.67
Oct-04	176.03	4.94	0.60
Nov-04	49.93	1.85	0.40
Dec-04	60.72	3.39	0.48

Table B.9 Aerodynamic resistance at 1 m ( $R_a(1\text{ m})$ ,  $s\text{ m}^{-1}$ )

	Average	Median	Max	Min	98 <sup>th</sup> %Tile	10 <sup>th</sup> %Tile	Stdev
May-01	19	16	49	8	30	11	8
Jun-01	34	26	711	0	61	14	34
Jul-01	46	27	3073	3	72	15	114
Aug-01	47	28	4403	0	68	15	169
Sep-01	43	24	4804	2	64	14	160
Oct-01	16	14	52	7	22	11	7
Mar-02	59	45	1051	1	104	23	68
Apr-02	49	26	1756	1	83	13	113
May-02	33	22	1315	0	55	12	64
Jun-02	33	24	423	1	54	16	30
Jul-02	47	34	3004	0	78	18	98
Aug-02	60	36	1067	0	121	17	86
Sep-02	76	38	2031	0	142	18	151
Oct-02	54	30	802	0	98	10	86
Nov-02	43	30	530	0	83	13	45
Dec-02	56	38	827	0	105	16	68
Jan-03	39	23	826	1	62	14	64
Feb-03	82	40	2694	0	151	14	169
Mar-03	69	33	3077	0	117	16	169
Apr-03	62	32	2688	0	99	13	137
May-03	40	25	1280	0	69	15	67
Jun-03	49	28	1276	0	95	14	72
Jul-03	52	33	1134	0	98	18	74
Aug-03	61	33	1370	1	107	16	106
Sep-03	51	35	1043	3	83	21	64
Oct-03	45	28	1610	0	78	14	79
Nov-03	52	32	923	0	88	17	76
Dec-03	53	30	1605	0	94	14	99
Jan-04	96	36	1882	11	116	23	253
Feb-04	57	29	1508	2	80	8	140
Mar-04	54	28	6972	0	85	13	221
Apr-04	47	32	4003	1	77	16	123
May-04	97	28	43742	1	78	15	1305
Jun-04	36	23	4080	1	58	13	119
Jul-04	54	30	7551	2	74	15	264
Aug-04	75	34	5496	1	105	12	254
Sep-04	52	33	1612	0	83	17	103
Oct-04	70	36	5104	1	122	17	203
Nov-04	56	24	7171	3	95	15	282
Dec-04	118	24	19936	0	63	17	1046

Table B.10 Boundary layer resistance for ozone ( $R_{bo3}$  s m<sup>-1</sup>)

	Average	Median	Max	Min	98 <sup>th</sup> %Tile	10 <sup>th</sup> %Tile	Stdev
May-01	20	20	39	10	27	13	5
Jun-01	26	21	1474	8	38	14	45
Jul-01	40	25	6084	9	50	15	203
Aug-01	30	23	2176	0	39	16	68
Sep-01	27	22	758	0	37	15	29
Oct-01	23	17	211	10	38	11	24
Mar-02	23	17	206	2	37	12	18
Apr-02	26	22	154	2	42	13	16
May-02	31	24	2861	4	41	15	85
Jun-02	24	19	1146	9	38	13	37
Jul-02	32	25	1195	1	46	17	43
Aug-02	48	29	5311	7	73	17	208
Sep-02	61	29	8364	1	74	18	334
Oct-02	37	27	2485	5	59	15	96
Nov-02	36	26	1488	10	56	15	66
Dec-02	37	27	1666	8	58	17	67
Jan-03	27	14	8525	7	30	10	263
Feb-03	52	23	7244	1	65	12	315
Mar-03	35	20	6276	0	48	12	199
Apr-03	37	26	1508	2	58	14	68
May-03	29	21	1526	2	45	14	47
Jun-03	32	23	3671	5	48	14	106
Jul-03	37	24	3515	4	54	15	114
Aug-03	36	25	4070	5	54	14	128
Sep-03	27	22	197	9	42	13	19
Oct-03	44	23	6473	3	57	14	213
Nov-03	41	20	8336	4	52	12	276
Dec-03	27	17	5256	1	32	11	173
Jan-04	29	19	120	0	64	11	26
Feb-04	25	20	112	3	41	14	16
Mar-04	24	18	667	0	41	10	29
Apr-04	26	20	2741	0	40	12	77
May-04	41	24	9677	0	58	15	276
Jun-04	27	21	189	0	42	14	18
Jul-04	34	27	1265	0	50	16	50
Aug-04	46	30	9633	0	64	16	289
Sep-04	24	17	258	3	40	10	23
Oct-04	36	23	1486	0	66	11	63
Nov-04	26	19	382	0	41	12	27
Dec-04	23	16	415	0	38	11	30

Table B.11 Ozone concentration at 1 m ( $\chi_{O_3}(1\text{ m})$ ,  $\mu\text{g m}^{-3}$ )

	Average	Median	Max	Min	98 <sup>th</sup> %Tile	10 <sup>th</sup> %Tile	Stdev
May-01	55.1	56.1	77.3	26.5	71.7	34.6	13.2
Jun-01	49.3	51.1	79.7	2.6	64.3	32.5	12.5
Jul-01	39.3	39.8	90.4	4.7	54.5	22.8	12.4
Aug-01	35.2	36.0	66.6	4.7	47.7	22.3	10.1
Sep-01	39.3	41.3	63.3	1.4	51.5	23.7	11.0
Oct-01	41.0	40.1	57.6	23.4	55.0	28.8	10.1
Mar-02	65.3	67.7	104.9	11.1	87.5	43.3	17.8
Apr-02	71.0	70.5	107.8	20.4	88.6	54.5	13.7
May-02	62.9	63.0	93.5	10.0	77.2	50.1	11.1
Jun-02	58.9	59.5	101.7	8.8	78.9	40.4	16.5
Jul-02	47.4	47.2	93.3	4.2	60.8	33.5	11.8
Aug-02	43.4	43.3	94.2	3.8	62.6	23.9	15.6
Sep-02	51.9	52.2	117.5	2.3	69.7	34.5	15.3
Oct-02	47.1	50.2	77.3	4.1	63.6	25.3	14.9
Nov-02	44.3	45.0	74.8	1.8	64.5	22.1	15.8
Dec-02	39.2	42.0	67.1	2.8	57.5	16.6	15.2
Jan-03	65.7	67.9	92.7	3.4	80.2	49.2	13.6
Feb-03	51.5	56.4	92.4	0.6	76.4	20.1	21.4
Mar-03	67.0	70.8	126.3	3.2	94.2	31.5	23.4
Apr-03	64.3	64.9	118.3	4.5	93.8	33.9	23.3
May-03	71.7	74.0	140.0	9.8	84.8	55.0	14.9
Jun-03	71.9	71.5	111.8	8.5	91.4	54.5	15.6
Jul-03	52.8	51.9	130.2	4.4	70.9	34.3	17.0
Aug-03	59.4	58.9	121.2	1.7	78.6	41.1	17.5
Sep-03	52.3	50.4	138.7	4.5	69.6	32.2	19.2
Oct-03	50.4	52.4	75.1	0.4	65.6	32.9	13.5
Nov-03	53.8	56.1	89.3	0.4	72.1	31.7	16.2
Dec-03	51.1	55.7	84.7	0.5	72.8	23.4	18.7
Jan-04	51.0	52.4	61.6	24.7	57.4	41.5	7.2
Feb-04	75.7	79.1	95.3	5.0	90.6	57.7	15.0
Mar-04	75.8	76.9	104.0	15.1	90.0	60.6	12.6
Apr-04	74.6	74.9	114.4	23.2	92.8	54.1	15.2
May-04	70.0	71.6	109.1	7.3	88.4	48.0	15.5
Jun-04	58.0	58.7	93.7	16.9	75.4	40.3	13.6
Jul-04	56.1	56.3	97.8	13.9	70.8	41.3	12.5
Aug-04	62.7	59.6	156.8	4.8	86.8	41.6	20.7
Sep-04	54.4	56.9	88.3	2.2	69.6	35.1	14.1
Oct-04	51.8	55.3	77.8	0.6	67.7	28.8	14.9
Nov-04	60.9	63.5	84.6	2.0	75.2	44.0	13.4
Dec-04	65.0	67.9	86.7	0.7	77.8	49.0	14.1

Table B.12 Ozone flux ( $F_{O_3}$  ng m<sup>-2</sup> s<sup>-1</sup>)

	Average	Median	Max	Min	98 <sup>th</sup> %Tile	10 <sup>th</sup> %Tile	Stdev
May-01	-125.7	-105.4	306.1	-806.2	76.7	-370.6	182.1
Jun-01	-142.7	-123.4	301.7	-773.7	-20.7	-298.5	123.2
Jul-01	-168.0	-157.9	53.6	-577.4	-56.9	-294.9	94.6
Aug-01	-153.4	-126.7	185.1	-609.9	-40.1	-308.2	109.6
Sep-01	-155.1	-127.0	125.3	-726.6	-24.9	-329.1	124.5
Oct-01	-168.5	-127.8	22.6	-486.5	-33.8	-332.2	123.1
Mar-02	-105.3	-84.1	160.1	-529.5	-3.6	-230.8	99.0
Apr-02	-128.2	-99.0	293.7	-1131.0	72.9	-353.6	193.2
May-02	-385.3	-282.6	301.8	-1944.6	-25.5	-951.0	367.3
Jun-02	-169.4	-143.6	296.0	-1327.8	34.1	-405.3	195.9
Jul-02	-266.1	-229.0	308.4	-1935.1	-51.7	-532.9	202.2
Aug-02	-211.5	-159.0	285.2	-1268.3	-9.9	-488.0	218.0
Sep-02	-272.9	-232.3	177.5	-1213.8	-62.3	-551.8	203.5
Oct-02	-187.8	-156.9	303.1	-821.8	-17.2	-408.7	162.9
Nov-02	-207.3	-180.3	284.2	-991.4	-42.9	-398.7	146.6
Dec-02	-170.2	-167.0	257.9	-576.5	-45.4	-308.8	108.3
Jan-03	-149.7	-129.4	270.7	-1572.2	-3.7	-318.4	145.5
Feb-03	-36.6	-25.8	297.0	-651.9	74.5	-170.1	106.7
Mar-03	-29.8	-13.6	314.5	-577.4	110.0	-192.8	130.4
Apr-03	-66.7	-11.6	312.3	-1289.3	129.9	-309.3	222.8
May-03	-234.7	-194.6	316.4	-1447.4	43.6	-592.0	265.6
Jun-03	-303.2	-264.7	192.3	-2184.7	-62.1	-590.5	221.0
Jul-03	-316.0	-264.4	267.2	-1492.2	-67.8	-634.8	231.8
Aug-03	-272.7	-227.5	300.1	-1682.0	-56.9	-534.2	220.3
Sep-03	-100.0	-71.8	304.9	-819.3	55.6	-309.5	150.6
Oct-03	-114.5	-93.7	304.3	-816.9	41.3	-307.2	147.4
Nov-03	-119.4	-101.4	292.1	-609.2	3.8	-268.0	117.3
Dec-03	-79.7	-60.2	315.6	-884.3	67.8	-246.8	142.7
Jan-04	-69.5	-66.4	118.4	-330.1	33.8	-193.9	84.8
Feb-04	-214.9	-195.2	114.0	-949.7	-55.5	-400.5	142.6
Mar-04	-324.2	-278.4	198.6	-1147.2	-102.8	-628.1	204.2
Apr-04	-482.4	-446.1	94.9	-1392.2	-208.9	-819.6	237.1
May-04	-514.7	-440.9	-6.1	-2305.0	-179.2	-933.2	340.6
Jun-04	-206.9	-171.9	177.2	-968.5	-28.0	-436.1	166.5
Jul-04	-100.4	-82.7	268.2	-652.7	24.2	-266.0	118.4
Aug-04	-367.5	-319.6	134.4	-1351.5	-112.3	-702.8	229.9
Sep-04	-406.3	-373.2	11.5	-1709.9	-164.5	-682.5	214.3
Oct-04	-348.2	-331.5	49.4	-1176.4	-83.4	-623.4	214.4
Nov-04	-376.7	-357.1	72.7	-2194.6	-105.1	-687.8	229.5
Dec-04	-288.8	-269.0	83.7	-883.2	-89.2	-522.9	170.5

Table B.13 Deposition velocity for ozone ( $v_{\text{do}_3}$  mm s<sup>-1</sup>) (not recalculated from flux and concentration)

	Average	Median	Max	Min	98 <sup>th</sup> %Tile	10 <sup>th</sup> %Tile	Stdev
May-01	3.58	2.68	21.37	0.02	7.86	0.61	3.12
Jun-01	3.39	2.81	15.24	0.02	6.67	0.91	2.40
Jul-01	4.43	4.20	13.38	0.01	7.42	1.72	2.26
Aug-01	4.46	3.95	14.47	0.11	8.38	1.47	2.71
Sep-01	4.03	3.56	13.58	0.03	7.70	1.10	2.59
Oct-01	4.19	3.89	14.36	0.14	7.62	0.94	2.79
Mar-02	1.82	1.46	9.57	0.03	3.38	0.42	1.38
Apr-02	2.62	2.06	14.71	0.00	5.38	0.36	2.34
May-02	6.62	5.08	29.39	0.00	14.93	1.03	5.40
Jun-02	3.68	3.03	21.14	0.01	7.67	0.67	3.01
Jul-02	5.77	4.97	22.70	0.04	11.17	1.54	3.81
Aug-02	5.22	4.35	19.87	0.00	10.77	1.18	3.74
Sep-02	5.33	4.65	22.48	0.06	9.93	1.67	3.39
Oct-02	4.49	3.92	17.91	0.03	8.69	1.23	3.05
Nov-02	4.74	4.31	27.01	0.05	8.07	1.77	2.72
Dec-02	4.75	4.32	19.28	0.14	8.20	1.92	2.56
Jan-03	2.57	2.18	19.98	0.02	5.00	0.60	1.95
Feb-03	1.76	1.31	14.88	0.01	3.89	0.25	1.64
Mar-03	1.77	1.19	13.12	0.00	4.12	0.19	1.79
Apr-03	2.37	1.41	13.63	0.00	6.24	0.18	2.61
May-03	4.05	3.38	19.20	0.00	8.43	0.69	3.13
Jun-03	4.43	3.80	23.92	0.02	8.50	1.34	3.00
Jul-03	5.94	5.33	22.16	0.15	10.92	1.73	3.72
Aug-03	4.58	3.92	24.67	0.01	8.45	1.42	3.09
Sep-03	2.78	2.38	13.48	0.00	5.52	0.40	2.11
Oct-03	3.08	2.51	15.01	0.01	6.40	0.59	2.36
Nov-03	2.63	2.23	23.88	0.01	5.12	0.54	2.19
Dec-03	2.68	2.02	17.38	0.01	5.30	0.50	2.47
Jan-04	1.91	1.51	6.54	0.08	3.97	0.51	1.45
Feb-04	2.93	2.65	12.86	0.15	5.35	1.07	1.78
Mar-04	4.24	3.73	16.78	0.06	7.65	1.69	2.40
Apr-04	6.42	6.17	18.60	0.06	10.01	3.16	2.77
May-04	7.19	6.35	29.05	0.21	12.16	2.96	4.08
Jun-04	3.74	3.32	15.01	0.03	7.25	0.89	2.52
Jul-04	2.26	1.95	13.00	0.00	4.60	0.36	1.71
Aug-04	6.02	5.32	20.95	0.08	11.01	2.15	3.55
Sep-04	7.46	7.02	22.43	0.85	11.86	3.41	3.31
Oct-04	6.44	6.20	40.07	0.26	10.57	2.45	3.32
Nov-04	5.98	5.79	28.99	0.09	9.85	2.26	3.07
Dec-04	4.50	4.32	13.25	0.15	7.73	1.80	2.31

Table B.14 Total canopy resistance for ozone ( $R_{\text{co}_3}$  s  $\text{m}^{-1}$ ) (not recalculated from flux and concentration)

	Average	Median	Max	Min	98 <sup>th</sup> %Tile	10 <sup>th</sup> %Tile	Stdev
May-01	6991	1331	326429	112	6502	349	36369
Jun-01	630	324	28733	14	1087	119	1412
Jul-01	376	201	56138	12	529	101	1966
Aug-01	358	208	8676	26	635	90	638
Sep-01	520	246	35251	36	850	98	1527
Oct-01	500	230	7032	49	1048	116	888
Mar-02	1412	591	31024	21	2303	226	3294
Apr-02	3960	413	532029	32	2727	136	26226
May-02	970	145	322381	0	902	29	10519
Jun-02	1073	276	174362	4	1410	88	7031
Jul-02	319	137	27248	0	561	35	1189
Aug-02	767	151	201809	1	741	28	7303
Sep-02	313	135	15663	0	488	33	997
Oct-02	521	191	39646	0	739	60	2133
Nov-02	339	165	21063	3	481	62	1168
Dec-02	239	155	7142	1	435	53	442
Jan-03	1081	407	45806	12	1610	164	3267
Feb-03	2514	687	105606	8	3840	177	8865
Mar-03	3592	766	520075	1	5261	186	22662
Apr-03	6129	640	922679	5	5493	99	49133
May-03	1241	237	263489	1	1378	67	9933
Jun-03	468	199	55002	5	643	67	2145
Jul-03	220	122	6624	0	476	39	360
Aug-03	484	186	91788	0	611	48	3664
Sep-03	4050	352	962152	6	2441	122	43102
Oct-03	1229	332	150803	7	1631	101	6676
Nov-03	1219	389	80938	2	1773	140	4673
Dec-03	1735	411	143752	6	1919	133	8428
Jan-04	968	542	12996	21	1702	196	1893
Feb-04	494	326	6786	1	876	145	640
Mar-04	326	211	15502	4	512	91	713
Apr-04	149	107	17516	0	230	43	537
May-04	132	96	4642	0	258	25	183
Jun-04	633	250	32256	2	1065	90	1938
Jul-04	2287	436	205045	6	2727	156	12229
Aug-04	187	118	11960	2	364	40	418
Sep-04	109	87	1114	0	212	36	88
Oct-04	145	96	3756	1	290	42	203
Nov-04	201	123	10646	3	333	60	478
Dec-04	274	187	6630	9	474	88	421

Table B.15 Bulk canopy resistance for to water-vapour ( $R_{c1w}$  s m<sup>-1</sup>)

	Average	Median	Max	Min	98 <sup>th</sup> %Tile	10 <sup>th</sup> %Tile	Stdev
May-01	61	49	130	32	95	38	25
Jun-01	151	134	1617	32	224	70	123
Jul-01	209	181	1095	36	338	95	142
Aug-01	126	102	797	41	205	58	93
Sep-01	139	115	1497	22	212	71	122
Oct-01	53	60	64	39	63	39	12
Mar-02	121	115	393	69	154	81	45
Apr-02	97	83	236	34	154	44	49
May-02	62	55	152	34	93	38	25
Jun-02	78	65	296	41	103	51	48
Jul-02	65	59	95	46	86	48	22
Aug-02	87	71	852	45	121	55	70
Sep-02	90	80	307	45	132	57	41
Oct-02	105	99	196	58	142	68	33
Nov-02	4149	3066	20232	340	6619	545	5088
Dec-02	29018	29018	57922	114	52141	5895	40876
Jan-03	3309	243	70650	47	1501	96	12907
Feb-03	2356	464	60947	117	5135	209	7086
Mar-03	710	175	102450	48	352	110	6174
Apr-03	382	155	15691	44	440	96	1232
May-03	1443	87	35253	25	2141	45	5123
Jun-03	124	99	962	41	206	61	94
Jul-03	115	98	623	35	196	59	66
Aug-03	136	122	592	47	218	69	72
Sep-03	166	149	575	45	254	92	75
Oct-03	247	207	1425	50	413	118	163
Nov-03	316	239	2105	72	514	123	305
Dec-03	223	155	641	111	439	117	160
Jan-04	305	208	1083	42	602	79	260
Feb-04	373	268	3758	84	510	138	473
Mar-04	236	191	849	73	418	110	141
Apr-04	131	109	438	22	228	63	80
May-04	131	109	625	36	230	66	76
Jun-04	135	110	643	43	236	66	86
Jul-04	143	108	754	34	266	59	104
Aug-04	107	82	525	1	193	49	78
Sep-04	140	97	1363	1	245	53	163
Oct-04	147	127	531	36	208	83	76
Nov-04	130	116	340	42	194	63	56
Dec-04	200	200	225	175	220	180	36

Table B.16 Latent Heat Flux ( $\lambda E$ ,  $W m^{-2}$ )

	Average	Median	Max	Min	98 <sup>th</sup> %Tile	10 <sup>th</sup> %Tile	Stdev
May-01	126.9	93.3	530.3	5.6	264.8	13.6	104.3
Jun-01	71.5	53.4	337.3	-34.7	155.1	12.1	61.3
Jul-01	62.7	48.5	388.2	-20.4	128.0	9.3	56.3
Aug-01	99.2	86.1	388.0	-471.1	208.8	10.9	83.2
Sep-01	62.3	38.3	525.5	-13.9	151.9	9.1	60.7
Oct-01	76.9	39.7	592.2	-6.1	181.2	15.1	101.1
Mar-02	57.1	57.5	146.6	-8.6	112.4	3.2	41.2
Apr-02	91.7	86.3	285.8	-86.3	194.4	2.8	72.7
May-02	93.8	67.9	337.0	-56.2	212.7	4.5	85.5
Jun-02	126.7	108.3	367.4	2.2	279.8	21.0	96.2
Jul-02	75.3	50.7	226.9	-5.4	169.9	7.7	64.6
Aug-02	110.4	100.4	324.2	-33.4	225.7	10.7	81.5
Sep-02	76.4	67.9	320.8	-31.4	167.9	4.3	63.1
Oct-02	47.9	30.2	214.4	-226.3	127.4	0.8	57.4
Nov-02	6.0	1.9	72.8	-104.5	27.6	-5.0	22.4
Dec-02	6.9	3.3	53.2	-19.9	23.2	-7.0	14.1
Jan-03	8.0	10.1	170.7	-282.0	48.0	-29.7	47.5
Feb-03	14.4	4.9	113.4	-73.1	51.9	-6.4	24.8
Mar-03	44.9	39.1	166.1	-66.2	100.7	0.3	39.1
Apr-03	57.9	35.6	289.7	-162.1	143.7	4.6	61.8
May-03	90.3	61.9	363.6	-74.7	220.2	0.3	88.3
Jun-03	107.5	101.0	363.5	-336.4	222.8	13.9	86.7
Jul-03	122.5	113.9	469.4	-16.3	244.4	16.6	89.9
Aug-03	81.1	69.0	342.1	-18.4	166.2	9.0	65.4
Sep-03	64.0	60.0	266.0	-8.0	126.9	6.5	46.8
Oct-03	27.6	16.2	194.6	-25.2	73.8	2.4	29.6
Nov-03	21.9	17.9	126.1	-38.3	44.4	2.2	22.6
Dec-03	15.0	11.5	73.8	-108.6	35.6	1.5	17.7
Jan-04	7.1	5.9	94.2	-114.6	24.3	-8.4	16.7
Feb-04	14.7	12.7	599.9	-755.0	45.5	0.4	86.2
Mar-04	22.7	14.8	157.0	-222.2	69.6	-7.6	36.2
Apr-04	48.8	34.4	254.6	-129.0	118.8	1.6	56.0
May-04	74.7	59.8	395.4	-205.9	186.8	2.0	73.9
Jun-04	69.3	55.6	341.8	-94.4	164.2	6.0	68.9
Jul-04	63.9	47.5	312.5	-143.8	158.7	2.5	64.3
Aug-04	59.3	35.0	423.0	-255.2	166.5	2.9	70.9
Sep-04	43.8	30.4	399.4	-319.6	126.8	-18.7	65.8
Oct-04	20.8	20.6	110.1	-264.7	69.4	-26.9	41.1
Nov-04	26.8	19.1	136.4	-29.6	54.2	6.9	25.0
Dec-04	10.3	8.6	68.7	-11.1	20.9	1.5	10.5

Table B.17 Bulk canopy CO<sub>2</sub> flux ( $F_{CO_2}$ ,  $\mu\text{mol m}^{-2} \text{s}^{-1}$ )

	Average	Median	Max	Min	98 <sup>th</sup> %Tile	10 <sup>th</sup> %Tile	Stdev
May-01	-11.62	-11.87	18.15	-63.74	9.73	-34.92	18.62
Jun-01	-3.49	-0.32	23.84	-43.02	7.48	-20.18	11.17
Jul-01	-1.38	3.62	22.60	-40.32	8.71	-17.84	11.17
Aug-01	-7.95	-9.72	18.13	-58.84	8.18	-22.63	12.77
Sep-01	-2.46	1.57	26.19	-48.13	7.22	-16.33	10.15
Oct-01	-1.65	4.51	13.40	-43.04	6.61	-15.30	11.53
Mar-02	-4.54	-5.78	6.75	-14.22	2.86	-9.18	4.54
Apr-02	-11.43	-13.73	30.62	-39.73	6.43	-27.47	13.51
May-02	-10.42	-12.36	26.29	-46.41	7.44	-27.52	14.00
Jun-02	-3.32	-1.30	13.04	-19.83	5.55	-14.52	8.31
Jul-02	-3.47	-2.99	11.75	-26.68	9.92	-19.59	11.53
Aug-02	-5.14	-6.82	33.76	-38.08	6.44	-15.63	9.48
Sep-02	-4.70	-6.69	18.67	-20.74	6.03	-13.60	7.77
Oct-02	-1.67	-3.11	24.99	-12.59	6.03	-10.17	7.19
Nov-02	-1.92	-1.58	10.71	-62.32	2.19	-5.57	8.21
Dec-02	-0.12	1.33	33.62	-35.43	2.38	-3.92	6.62
Jan-03	-0.23	0.94	24.48	-31.40	2.78	-5.46	4.73
Feb-03	-2.08	-2.72	8.22	-12.56	1.77	-5.35	2.99
Mar-03	-4.40	-5.09	10.67	-17.63	2.84	-10.90	5.14
Apr-03	-8.16	-8.39	50.15	-58.93	5.32	-23.92	12.10
May-03	-11.37	-13.03	13.26	-42.62	5.94	-27.78	13.23
Jun-03	-6.61	-5.80	15.61	-76.38	7.69	-21.17	11.88
Jul-03	-8.69	-10.43	19.40	-30.84	7.49	-20.83	10.31
Aug-03	-6.32	-7.88	20.94	-27.86	5.66	-16.81	8.49
Sep-03	-4.67	-6.11	15.00	-36.28	4.12	-11.47	6.39
Oct-03	-0.82	1.87	19.14	-16.30	4.32	-8.51	5.58
Nov-03	-0.11	1.51	13.89	-17.83	4.37	-6.35	4.52
Dec-03	2.37	2.19	45.81	-65.52	4.79	-2.35	9.08
Jan-04	-1.42	-0.59	12.03	-27.86	1.37	-4.48	3.59
Feb-04	-1.55	-1.20	11.02	-25.52	1.52	-5.28	3.75
Mar-04	-3.70	-3.59	14.09	-29.51	1.91	-10.04	5.44
Apr-04	-6.60	-6.51	30.12	-43.86	4.74	-19.07	9.45
May-04	-8.60	-8.73	23.97	-55.39	3.89	-19.99	9.86
Jun-04	-5.79	-5.87	41.57	-40.79	4.94	-17.02	9.08
Jul-04	-3.09	-3.41	71.54	-67.63	7.74	-14.40	11.19
Aug-04	-4.15	-3.85	28.61	-53.79	7.90	-17.58	10.57
Sep-04	-2.96	-2.48	22.17	-54.41	6.48	-14.16	9.07
Oct-04	-2.56	-2.77	42.51	-62.51	5.03	-9.98	8.59
Nov-04	0.61	1.66	17.54	-18.07	4.24	-4.44	3.95
Dec-04	0.61	1.17	5.11	-8.55	2.69	-2.44	2.33



## **Appendix C Relevant Publications**

All papers and other publications where I have made a contribution that has some relevance to the work presented in this thesis are listed here. Copies of those marked with a † have also been included as they contain analysis referenced in the text and of particular relevance to these results.

### **Journal Papers**

- Fowler D., Cape J.N., Coyle M., Flechard C., Kuylenstierna J., Hicks K., Derwent D., Johnson, C., Stevenson D., 1999. The global exposure of forests to air pollutants. *Water Air and Soil Pollution*, 116, 5-32.
- Smith R.I, Fowler D., Sutton M.A, Flechard C, Coyle M. Regional estimation of pollutant gas dry deposition to the UK: model description sensitivity analyses and outputs. *Atmos. Env.*, 2000, 34 (22), pp 3757-3777<sup>†</sup>
- Fowler, D., Coyle, M., Flechard, C., Hargreaves, K., Storeton-West, R., Sutton, M. & Erisman, J-W. (2001). Advances in micrometeorological methods for the measurement and interpretation of gas and particle nitrogen fluxes. *Plant and Soil*, 228, 117-129.
- Fowler D., Flechard C., Cape J.N., Storeton-West R.L. Coyle M. (2001). Measurements of ozone deposition to vegetation quantifying the flux, the stomatal and non-stomatal components. *Water, Air and Soil Pollution*, 130, 63-74<sup>†</sup>
- Fowler, D., Sutton, M.A., Flechard, C., Cape, J.N., Storeton-West, R., Coyle, M. & Smith, R.I. The control of SO<sub>2</sub> dry deposition on to natural surfaces and its effects on regional deposition. *Water Air Soil Pollution: Focus* (2001), 1, 39-48.
- Coyle M., D Fowler, R.I. Smith, K. Weston, J. R. Stedman (2002). Quantifying the spatial distribution of surface ozone concentration in the UK. *Atmos. Env.*, 2002, 36 (6), pp 1013-1024<sup>†</sup>
- Coyle M., Fowler D. and Ashmore M. New Directions: Implications of increasing tropospheric background ozone concentrations for vegetation. *Atmospheric Environment*, 37(1), pp. 153-154, Jan 2003.<sup>†</sup>
- Coyle M., R. Smith and D. Fowler. An Ozone Budget for the UK: Using measurements from the national Ozone monitoring network; measured and modelled meteorological data, and a 'big -leaf' resistance analogy model of dry deposition. *Environmental Pollution*, Vol 123 (1), pp 115 – 123, Feb 2003.<sup>†</sup>

### **Contract Reports**

- Coyle M, Fowler D, Storeton-West R, Hargreaves K, (1999). Continuous Measurements of Ozone Dry Deposition to Wheat, Sugar beat, and Potatoes, Using Micrometeorological Methods. 1999 Annual Report, DETR Project EPG 1/3/121
- Coyle M, Fowler D, Storeton-West R, (2000). Measurement and Modelling of Ozone Dry Deposition to Arable Land. 2000 Annual Report, DETR Project EPG 1/3/121
- Sutton M.A., Dragosits U., Coyle M., Smith R.I., Fowler D., Ulliyett J., Hall J. (2000). Deposition of acidifying and eutrophying air pollutants across

- Scotland - Mapping critical loads and levels exceedances. Interim report. PTI number: 070200, Scottish Natural Heritage, CEH Edinburgh.
- NEG-TAP (2001). Transboundary Air Pollution: Acidification, Eutrophication and Ground-level Ozone in the UK. Report of the National Expert Group on Transboundary Air Pollution (D Fowler Chair). UK Department of the Environment, Food and Rural Affairs
- Coyle M, Fowler D, Lewis H & Storeton-West R, 2001 Measurement of Ozone Dry Deposition to Crops and Grassland. 2001 Final Report, DETR Project EPG 1/3/121
- Ashmore, M., Coyle, M., Fowler, D. 2002. Implications of trends in background ozone concentrations for vegetation in the UK. 46pp. June 2002. Contract Report DEFRA EPG 1/3/173.
- Coyle M, Fowler D, Hargreaves K, Nemitz E and Storeton-West R, 2002. Comparison of Measurements of Ozone Dry Deposition to Crops and Grassland with the Dry Deposition Model Results. C01700 - 2001 Final Report, DEFRA Project EPG 1/3/121, CEH Edinburgh.  
<http://www.nbu.ac.uk/pollution/Publications.htm>
- Van Oijen M., Buker P., Coyle M., Fowler D., Hargreaves K., Hayes F., Levy P., Mills G., Murray M. 03 GRASSLAND: a CEH Integrating Fund Project 2001-2003, Centre for Ecology & Hydrology, 2003, Report Project No. C01756
- Fowler D., Smith R.I., Sutton M.A., Cape J.N., Nemitz E., Coyle M., Muller J., Milford C., Famulari D., Anderson-Dunn M., Tang Y.S., Storeton-West R., Crossley A., Harvey F., Twigg M., Riedo M., Loubet B., Vincent K., Hayman G., Choularton T., Beswick K. Acid deposition processes. Final report.180pp, May 2004, Contract Report, C01652 Defra

#### **Conference Proceedings**

- Fowler D., Cape J.N., Coyle M., Flechard C., Kuulenstierna J., Hicks K., Derwent D., Johnson C., Stevenson D., (1999). The global exposure of forests to air pollutants. In: Forest growth responses to the pollution climate of the 21st century, edited by L.J. Sheppard & J.N. Cape, 5-32. Dordrecht: Kluwer, 1999.
- Fowler D., Flechard C., Coyle M., Storeton-West R. (1999). Ozone fluxes to vegetation in the field: separating stomatal from non-stomatal uptake. In: Critical levels for ozone - level II, edited by J. Fuhrer and B. Aschermann. Berne: SAEFL
- Coyle M., Fowler D., Smith R. (2000) Trends in Rural Ozone Concentrations in the UK. EUROTRAC-2 Symposium 2000 Proceedings. EUROTRAC International Scientific Secretariat, Garmisch-Partenkirchen. CD ROM and WIT Press, 2001.
- Coyle M., Fowler D., Storeton-West R. Ozone deposition at a polluted site in the English Midlands. (2000) EUROTRAC-2 Symposium 2000 Proceedings. EUROTRAC International Scientific Secretariat, Garmisch-Partenkirchen. CD ROM and WIT Press, 2001
- Coyle M., Fowler D., Storeton-West R. Ozone deposition at a polluted site in the English Midlands. (2001). In: Air-surface exchange of gases and particles: poster proceedings. Poster papers from the Sixth International Conference on Air-Surface Exchange of Gases and Particles, Edinburgh 3-7 July 2000, Edited by D. Fowler et al., 58-60. Edinburgh: Centre for Ecology & Hydrology
- Fowler, D.; Coyle, M.; Flechard, C.; Hargreaves, K.; Nemitz, E.; Storeton-West, R.; Sutton, M. (2001): Advances in micrometeorological methods for the measurement and interpretation of pollutant gas and aerosol fluxes. in: EUROTRAC-2, BIATEX-2, Annual Report 1998/1999, ISS, GSF-Forschungszentrum fuer Umwelt und Gesundheit GmbH, Munich, Germany. pp 103-107.

Cape J.N., Coyle M., Fowler D. (2004): Ozone in a changing world – what do we need to know? 36th US Air Pollution Workshop, Rhinelander, Wisconsin  
Mhairi Coyle, Mike Ashmore, David Fowler, Felicity Hayes and Ron Smith. Trends in Ground-level Ozone Concentration and Their Implications for the UK. 13th WORLD CLEAN AIR AND ENVIRONMENTAL PROTECTION CONGRESS AND EXHIBITION London, UK, August 22-27, 2004



## Appendix D Simple Aqueous O<sub>3</sub>/SO<sub>2</sub>/NH<sub>3</sub> Chemistry Model

Ozone can act as an oxidising agent for SO<sub>2</sub> in water but this reaction is self limiting and quickly saturates when the pH is less than 6. However if ammonia is present at sufficient concentrations it can increase the pH and allow the SO<sub>2</sub> reaction to continue. As ozone solubility is low and the oxidation rate is very fast at high pH it can be assumed that it occurs independently of the reactions that change acidity and so a relatively simple model can be used to predict the potential ozone loss. Figure D1 illustrates the process and gives the chemical reactions (boxes A to D) that were modelled using FACSIMILE<sup>15</sup>. The model is used to predict the equilibrium pH and bisulfite concentration of the water layer and so the O<sub>3</sub> loss rate (box E):

$$F_{O_3g\_aq} = -[L k_{ox} \frac{[HSO_3^-]}{\sqrt{[H^+]}} (K_{O_3} [O_3]_g)] / M_{O_3}, \text{ g m}^{-2} \text{ s}^{-1}$$

where L = thickness of water film (m)  
 k<sub>ox</sub> = HSO<sub>3</sub><sup>-</sup> oxidation rate (M<sup>-0.5</sup>s<sup>-1</sup>)  
 K<sub>O<sub>3</sub></sub> = ozone solubility, 10<sup>-11</sup> M ppb<sup>-1</sup>  
 [O<sub>3</sub>]<sub>g</sub> = gaseous ozone concentration (ppb)  
 M<sub>O<sub>3</sub></sub> = molecular weight of ozone, 48 g mole<sup>-1</sup>

Table D1 Rate constants and parameter values used to model aqueous SO<sub>2</sub> oxidation and predict equilibrium water pH.

Parameter	Value(s)	Reference
T, water temperature	20 °C (molar volume 24 l)	
L, water film thickness	0.1 to 0.5 mm	
v <sub>dmax</sub> , air/liquid maximum transfer rate	0.2 cm s <sup>-1</sup>	
Gas and liquid concentrations		
[SO <sub>2</sub> ] <sub>g</sub>	variable	0.1 to 10 ppb
[NH <sub>3</sub> ] <sub>g</sub>	variable	1 to 10 ppb
[CO <sub>2</sub> ] <sub>g</sub>	constant	340 ppm
[CO <sub>2</sub> ] <sub>aq</sub>	initial value	1.3 x 10 <sup>-5</sup> M
Equilibrium constants (solubility) and reaction rates		
K <sub>H</sub> (SO <sub>2</sub> )	1.5 M atm <sup>-1</sup>	Maahs 1982
K <sub>H</sub> (NH <sub>3</sub> )	92.6 M atm <sup>-1</sup>	Sutton <i>et al</i> 1993
K <sub>H</sub> (CO <sub>2</sub> )	0.038 M atm <sup>-1</sup>	
K <sub>H</sub> (O <sub>3</sub> )	10 <sup>-2</sup> M atm <sup>-1</sup>	
k <sub>ox</sub>	1.3 x 10 <sup>4</sup> M <sup>-0.5</sup> s <sup>-1</sup>	Cape <i>et al</i> 1999
K <sub>D1</sub> (SO <sub>2</sub> )	0.014834 M	Cape 1984
K <sub>D2</sub> (SO <sub>2</sub> )	0.0699 x 10 <sup>-6</sup> M	
K <sub>D1</sub> (CO <sub>2</sub> )	0.417 x 10 <sup>-6</sup> M	
K <sub>D2</sub> (CO <sub>2</sub> )	4.79 x 10 <sup>-11</sup> M	
K <sub>w</sub> (H <sub>2</sub> O)	6.81 x 10 <sup>-15</sup> M	
K <sub>D</sub> (NH <sub>3</sub> )	1.71 x 10 <sup>-5</sup> M	

<sup>15</sup> The software package FACSIMILE models complex steady state and time dependent processes. It is especially suitable for solving chemical reactions with diffusion and/or advection. <http://www.esm-software.com/facsimile/>

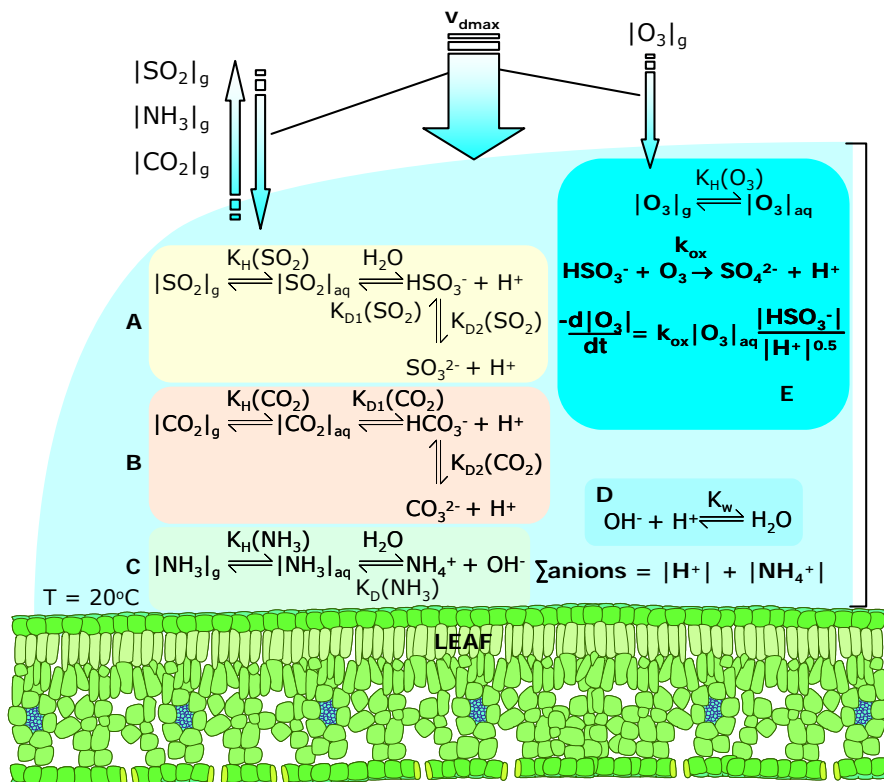


Figure D1 A simple model of aqueous  $\text{SO}_2$  oxidation used to predict the equilibrium pH of a water film. Reactions A to D are modelled until the solution reaches equilibrium and the final pH,  $[\text{HSO}_3^-]$  and  $[\text{H}^+]$  are used to predict the  $\text{O}_3$  loss rate (E).

# List of figures and tables

## Figures

- Figure 1.1 Ozone soundings by balloon sonde at Payerne, Switzerland (46.80 N, 6.95 E, 490 a.s.l.). Blue = 1976, Black = 1977, Green = 1987, Red = 1996. The annual mean tropopause height at Payerne is ~10 km, ranging from ~8 km in the winter to 12 km in the summer. Staehelin and Schmid, 1991 1-2
- Figure 1.2. Schematic representation of ozone chemistry showing the free-radical (OH) catalysed oxidation of a generic saturated hydrocarbon, RH (after PORG, 1998, Figure 2.4). 1-4
- Figure 1.3 Cartoon by Ron Cobb highlighting the issue of air pollution in California during the 1960s. 1-5
- Figure 1.4 Global distribution of total tropospheric ozone from satellite measurements of total atmospheric and stratospheric ozone (Fishman, *et al.*, 2003). 1-6
- Figure 1.5 Examples of seasonal cycles observed across the UK, from a remote rural site in the north (Strath Vaich) to a more polluted site in the south (Lullington Heath) (Figure originally presented in NEG-TAP, 2001). 1-7
- Figure 1.6 Examples of diurnal cycles in ozone concentration at (a) a rural site, (b) a city centre site and (c) at an urban and nearby rural site during a photochemical episode. Error bars show the standard deviation of hourly means. (Originally presented in NEG-TAP, 2001). 1-10
- Figure 1.7 2001 summer mean ozone concentrations in the region around London, extracted from a 1 km by 1 km map of ozone across the UK (Coyle, *et al.*, 2002) 1-10
- Figure 1.8 Examples of damage to vegetation caused by ozone: top left to right show visible injury on *potentilla*, *carex* and *dryas*; the bottom image shows early senescence (left) induced in *Lolium perenne*. All images were obtained from experiments in controlled chambers with a range of ozone concentrations (Buse, *et al.*, 2003; Van Oijen, *et al.*, 2003). 1-12
- Figure 1.9 Microscopic views of human lung tissue (epithelium, or lining) show damage resulting from exposure to relatively low levels of ozone. In the control image (left) from the lung of a person exposed only to air, the tiny cilia that clear the lungs of mucus appear along the top of the image in a neat and regular row. In the lung exposed to 20 ppb of ozone added to the air for four hours during moderate exercise, many cilia appear missing and others appear misshapen. Arrows point to tiny bodies called neutrophils in the ozone-exposed subject (right hand image). The presence of neutrophils indicates inflammation. Magnification: x400. (Aris *et al.*, 1993; NASA, 2004) 1-14
- Figure 1.10 The effects of ozone on rubber samples under mild tension, with varying degrees of anti-ozonant protection (Leith, 2005). The samples with less protection show more damage. The right-hand image shows a close-up of a samples with (left) and without (right) protection. The unprotected sample is cracked along its length. 1-15
- Figure 1.11 Monthly mean surface ozone increase (ppb) July from Y2000 to Y2100 following scenario A2x. Prather *et al.*, 2003. 1-19
- Figure 1.12 The current measured annual mean ozone concentration at Dunslair Heights, a hill-top site in the Scottish Border, and predictions of future concentrations derived from the results of Prather *et al.*, 2003 using the methodology described in Ashmore *et al.*, 2003. 1-19
- Figure 1.13 1 km x 1km maps of the current AOT40 for crops and semi-natural vegetation across the UK (Coyle *et al.*, 2004), and predictions of future levels in 2050 derived from data for the UK monitoring sites and the results

of Prather <i>et al.</i> , 2003, using the methodology described in Ashmore <i>et al.</i> , 2003 and Coyle <i>et al.</i> , 2002. The arrow indicates the colour range that exceeds the critical level of 3,000 ppbh.	1-20
Figure 2.1 Structure of the PBL and constant flux layer (its depth is ca. 15% of the PBL).	2-26
Figure 2.2 Illustration of wind speed profiles and turbulent eddy structure in different stability regimes, (a) neutral, (b) unstable and (c) stable (after Thom, 1975).	2-28
Figure 2.3. Illustration of the development of a new surface layer as air moves from one surface to another (after Monteith and Unsworth, 1990 p 233). For micrometeorological flux measurements the ratio of fetch to h should be approximately 100:1.	2-36
Figure 2.4. The rules for adding resistances in series or parallel.	2-41
Figure 2.5. The deposition resistance analogy for ozone.	2-45
Figure 2.6. Diagram showing a typical leaf's cross-section and illustration of a stoma opening and closing.	2-46
Figure 3.1. Examples of the variation of the stomatal conductance of potatoes which environmental parameters (a. photosynthetically active radiation, b. temperature, c. vapour pressure deficit and d. soil water potential), measured using leaf-level porometers in the field or controlled chambers (ICP, 2004). The scaling functions, fitted using a boundary line approach, are shown as solid lines.	3-65
Figure 3.2. Example of the phenology function, $f_{pot}$ , used to represent the variation of maximum potential stomatal conductance with leaf age.	3-66
Figure 4.1. a. The location of Easter Bush and CEH Edinburgh. b. A sketch of Easter Bush giving an indication of topography and the location of the equipment enclosure.	4-72
Figure 4.2. Photo of the "Herbomètre", the bottom of the black pole is placed on the soil and the green plate, which is attached to the yellow tube and ruler, sits on top of the vegetation. The vegetation height can then be read from the ruler.	4-75
Figure 4.3. Timelines of grazing periods (shaded blocks) and silage harvests (crosses) in each field.	4-76
Figure 4.4. Time series of measured and fitted canopy height in each field (NE top and SW bottom plot respectively). The dates indicate silage harvests; the rest of the variation is due to grazing and plant growth/senescence.	4-76
Figure 4.5. The SW field on 30/5/2003 after cutting but before lifting.	4-77
Figure 4.6. The relationship between $h$ and $LAI$ for <i>lolium perenne</i> as derived by Milford, 2004 and measurements for 2002 to 2004.	4-78
Figure 4.7. (a) A sketch of Easter Bush showing the location of major equipment and instruments (TDR = Time Domain Reflectometer, TAG = Time Averaged Gradient, TDL = Tunable Diode Laser). Photographs of all the equipment on (b) 14/6/2003 and (c) 06/08/2002.	4-80
Figure 4.8. Photograph of the Bowen ratio mast. The two top arms hold the solar radiation and $PAR$ sensors; the white "beehive" shelters the $RH/T$ probe; the two long white arms hold the thermocouples and dewpoint sensor inlets; to the left are the two net radiometers; the two thin white sticks on the right indicate the location of the soil heat flux plates and temperature probes.	4-82
Figure 4.9. A sketch of Campbell (top) and home-made (bottom) fine-wire thermocouples.	4-82
Figure 4.10. Campbell TCAV soil averaging thermocouple assembly.	4-84
Figure 4.11. Sketch of heat flux plate and soil temperature probe installation; the sensors are fully inserted into the soil then the hole back filled.	4-85
Figure 4.12. (a) The REBS Q7 net radiometer, (b) the NR-LITE and (c) both instruments in place in the field.	4-86

Figure 4.13. Photograph of the Campbell wetness sensing grid in place at Easter Bush.	4-88
Figure 4.14. Photo of the tipping bucket in place at Easter Bush with it's (a) cover on and (b) off, which shows the basin and switch.	4-89
Figure 4.15. Sketch of gradient setup.	4-90
Figure 4.16. Illustration of log spacing.	4-90
Figure 4.17. Schematic of an O <sub>3</sub> analyser.	4-92
Figure 4.20. Sketch of TDR.	4-101
Figure 4.21. Sketch of the Vaisala Present Weather Sensor.	4-102
Figure 4.22. A very soggy fieldsite, Easter Bush 24/10/2002.	4-103
Figure 4.23. The correlation between different measures of ambient air temperature at Easter Bush and Bush.	4-106
Figure 4.24. Comparison of monthly total rainfall amounts measured at Easter Bush and Bush.	4-107
Figure 4.25. 15-minute average wind direction frequency plots for each data set 2001 to 2004.	4-108
Figure 4.26. Comparison of the Q7 net radiometer with un-adjusted and wind-speed corrected data from the NR-Lite net radiometer.	4-110
Figure 4.27. Measured <i>SWP</i> and <i>SWC</i> at a site with Macmerry series soil, close to Easter Bush, and the fitted soil water release curve.	4-111
Figure 4.28. Monthly frequency pie charts for the combined wind direction dataset, showing the fraction of data from the along the fence-line and SW or NE sectors.	4-112
Figure 4.29. a) Time series of 15 minute average wind speed measured by the Gill sonic (2.15 m) and b) monthly summary statistics of the 15 minute wind speed: the box indicates the 75 <sup>th</sup> and 25 <sup>th</sup> percentiles; the black bar is the median; the red bar the average; the whiskers the 90 <sup>th</sup> and 10 <sup>th</sup> percentiles; the dots are the outliers at the 95 <sup>th</sup> and 5 <sup>th</sup> percentiles.	4-113
Figure 4.30. Annual monthly summary statistics of the 15 minute wind speeds from each sector: the box indicates the 75 <sup>th</sup> and 25 <sup>th</sup> percentiles; the black bar is the median; the red bar the average; the whiskers the 90 <sup>th</sup> and 10 <sup>th</sup> percentiles; the dots are the outliers at the 95 <sup>th</sup> and 5 <sup>th</sup> percentiles.	4-114
Figure 4.31. (a) Time series of combined 15-minute average ambient air temperatures and (b) monthly box plot of the data plotted in (a) the box indicates the 75 <sup>th</sup> and 25 <sup>th</sup> percentiles; the black bar is the median; the red bar the average; the whiskers the 90 <sup>th</sup> and 10 <sup>th</sup> percentiles; the dots are the outliers at the 95 <sup>th</sup> and 5 <sup>th</sup> percentiles.	4-115
Figure 4.32. Monthly frequency distributions of 15-minute ambient air temperature observed each year.	4-116
Figure 4.33. Overall (2001 to 2004) monthly mean ambient temperature for the two main wind sectors; the size of the symbols indicates the standard deviation.	4-117
Figure 4.34. a. Time series of <i>St</i> and <i>PAR</i> measured at Easter Bush. b. Monthly box plot of <i>St</i> measured at Easter Bush; the box indicates the 75 <sup>th</sup> and 25 <sup>th</sup> percentiles; the black bar is the median; the red bar the average; the whiskers the 90 <sup>th</sup> and 10 <sup>th</sup> percentiles; the dots are the outliers at the 95 <sup>th</sup> and 5 <sup>th</sup> percentiles.	4-117
Figure 4.35. Frequency distributions of (a) <i>St</i> and (b) <i>PAR</i> above the daylight thresholds of 50 W m <sup>-2</sup> and 104 μmol m <sup>-2</sup> s <sup>-1</sup> respectively.	4-119
Figure 4.36. a) Monthly total rainfall and (b) monthly total rainfall in the main wind sectors.	4-121
Figure 4.37. Monthly fraction of the time the wetness sensor indicates a wet surface.	4-121
Figure 4.38. Rainfall and soil water content in the SW field during 6 <sup>th</sup> September 2002 to the 9 <sup>th</sup> of September 2002.	4-122

Figure 4.39. Daily mean soil water content ( <i>SWC</i> ) of the SW and NE fields.	4-123
Figure 5.1. Examples of ogive curves for $wT$ and $wCO_2$	5-128
Figure 5.2. Example of the planar fit to $\bar{u}$ , $\bar{v}$ and $\bar{w}$ from the Gill sonic during August 2004.	5-129
Figure 5.3. Example of attenuation correction for $wCO_2$ .	5-131
Figure 5.4. Comparison of wind-speed, $u_*$ and $H$ readings from the Gill and Metek sonics.	5-134
Figure 5.5. Comparison of vapour pressure and latent heat fluxes measured by the LICOR7500 and LICOR7000 and logged on the Gill and Metek systems respectively.	5-136
Figure 5.6. Dimensions (m) of the fetch at Easter Bush.	5-139
Figure 5.7. The CNF from the Gill sonic in 2001 to 2003 and Metek in 2004, plotted by wind direction.	5-139
Figure 5.8. (a) An example of a neutral wind-speed profile (14/05/2002 18:00) and (b) the effect of different $d$ values on the log-linear profile.	5-140
Figure 5.9. Median (a) NO and (b) NO <sub>2</sub> concentrations by wind-direction at Bush. Calculated from hourly gas concentration data and wind direction measurements at Bush.	5-142
Figure 5.10. Comparison the $u_*$ and $H$ measured by the gradient and eddy-correlation systems.	5-145
Figure 5.12. Normalised frequency distributions for (a) $R_a$ and (a) $R_{bO_3}$ .	5-147
Figure 5.13. Diurnal cycles of (a) overall median and (b) seasonal median $R_a$ for Easter Bush (2001 to 2004).	5-148
Figure 5.14. Diurnal cycles of overall median $R_{bO_3}$ and $R_{bH_2O}$ at Easter Bush.	5-148
Figure 5.15. Average diurnal cycle in ozone concentrations observed at Easter Bush during October to March and April to September, 2001 to 2004; Calculated using the 30 minute average concentrations from the top height of the gradient mast.	5-151
Figure 5.16. Average ozone concentrations in 15° wind sectors during April to September and October to March 2001 to 2004; Calculated using the 30 minute average concentrations from the top height of the gradient mast..	5-151
Figure 5.17. Overall frequency distribution of 30 minute ozone concentrations measured at the top height of the gradient mast.	5-152
Figure 5.18. Annual frequency distributions of 30 minute ozone concentrations at each height on the gradient mast.	5-152
Figure 5.19.(a) Monthly average concentration measured at the top height on the gradient mast every year. (b) Time series of 30 minute average concentrations measured at the top height.	5-153
Figure 5.20. Time series of 30 minute average ozone flux calculated from (a) the gradient system (b) the Gill $u_*$ , $H$ etc and ozone gradient and (c) the Metek $u_*$ , $H$ etc and ozone gradient.	5-155
Figure 5.21..Comparison of original and revised 2002 flux measurements from each system.	5-157
Figure 5.22. Final combined time series (Gill, Metek then gradient in 2001 to 2003 and Metek, gradient then Gill in 2004).	5-158
Figure 5.23. Frequency distribution of (a) the final ozone flux data set and (b) the ozone concentration at 1m.	5-158
Figure 5.24. (a) to (d) Individual seasonal mean diurnal cycles in the total ozone flux. (e) Overall median cycles in the ozone flux, the small pale symbols show the results using all the data whereas the large symbols exclude the unusual seasons in 2001 and 2004.	5-159
Figure 5.25. The normalised frequency distributions of (a) deposition velocity $v_{dO_3}$ and (b) total canopy resistance, $R_{cO_3}$ .	5-160

- Figure 5.26. (a) Time series of 30 minute median  $v_d$ , (b) monthly box plot of  $v_d$  (the box indicates the 75<sup>th</sup> and 25<sup>th</sup> percentiles; the black bar is the median; the red bar the average; the whiskers the 90<sup>th</sup> and 10<sup>th</sup> percentiles; the dots are the outliers at the 95<sup>th</sup> and 5<sup>th</sup> percentiles) and (c) monthly median  $R_c$  with the bars indicating the 90<sup>th</sup> and 10<sup>th</sup> percentiles. 5-161
- Figure 5.27. Seasonal diurnal cycles in  $v_d$ . 5-162
- Figure 5.28. Seasonal diurnal cycles in  $R_c$ . 5-162
- Figure 5.29. The upper plot shows the complete time series of CO<sub>2</sub> concentrations, calculated at  $z_0'$  and the lower a summary box plot of the data (the box indicates the 75<sup>th</sup> and 25<sup>th</sup> percentiles; the black bar is the median; the red bar the average; the whiskers the 90<sup>th</sup> and 10<sup>th</sup> percentiles; the dots are the outliers at the 95<sup>th</sup> and 5<sup>th</sup> percentiles). 5-163
- Figure 5.30. The upper plot shows the complete time series of CO<sub>2</sub> fluxes, measured at  $\sim 2.15$  m and the lower a summary box plot of the data. 5-164
- Figure 5.31. The upper plot shows the complete time series of vapour pressure, calculated at  $z_0'$  and the lower a summary box plot of the data (the box indicates the 75<sup>th</sup> and 25<sup>th</sup> percentiles; the black bar is the median; the red bar the average; the whiskers the 90<sup>th</sup> and 10<sup>th</sup> percentiles; the dots are the outliers at the 95<sup>th</sup> and 5<sup>th</sup> percentiles). 5-164
- Figure 5.32. The upper plot shows the complete time series of water-vapour flux measured at  $\sim 2.15$ m and the time series filtered for dry-daylight condition. The lower a summary box plot of the complete time series (the box indicates the 75<sup>th</sup> and 25<sup>th</sup> percentiles; the black bar is the median; the red bar the average; the whiskers the 90<sup>th</sup> and 10<sup>th</sup> percentiles; the dots are the outliers at the 95<sup>th</sup> and 5<sup>th</sup> percentiles). 5-165
- Figure 5.33. The normalised frequency distribution of CO<sub>2</sub> flux and concentration. 5-165
- Figure 5.34. The left hand plot shows the normalised frequency distribution of water-vapour flux for the whole data set (red bars) and filtered for dry-daylight conditions (blue bars). The right hand plot is the normalised frequency distribution of vapour pressure measured at  $\sim 2.15$  m and calculated at the canopy surface ( $z_0'$ ). 5-166
- Figure 5.35. The complete time series of  $R_{c1H_2O}$  measurements with periods with  $LAI > 1.5$  highlighted. 5-167
- Figure 5.36. Summary box plot of the stomatal resistance for ozone, calculated from the dry-daylight results for water-vapour (the box indicates the 75<sup>th</sup> and 25<sup>th</sup> percentiles; the black bar is the median; the red bar the average; the whiskers the 90<sup>th</sup> and 10<sup>th</sup> percentiles; the dots are the outliers at the 95<sup>th</sup> and 5<sup>th</sup> percentiles). 5-167
- Figure 5.37. Summary of measurements pre and post the silage harvest in both fields on the 25/07/2001 (cut and lifting times are approximate). 5-170
- Figure 5.38. Summary of measurements pre and post the silage harvest in both fields on the 25/05/2003 (the time of cutting is approximate). 5-171
- Figure 5.41. Diurnal cycles in deposition velocity and canopy resistance during December, calculated from median ozone fluxes and average concentrations in 2002 and 2003. 5-173
- Figure 5.42. Overall summary of monthly deposition velocity observed during the day and night at Easter Bush. 5-177
- Figure 5.43. The canopy resistance measured during day and night periods versus surface temperature (left hand plot) and daytime value versus solar radiation (right hand plot). 5-177
- Figure 5.44. The night-time canopy resistance calculated from measurements blocked by 1°C surface temperature increases. The left hand plot shows the relationship fitted to all points including temperatures below zero and with

- standard errors ( $SE > 10\%$ ). The right hand plot shows the same data with a fit restricted to points above zero and with  $SE < 10\%$ . 5-177
- Figure 5.45. The response of night-time  $R_c$  to temperature in very dry and wet conditions. The results of curve fitting are given in Table 6.14. 5-179
- Figure 5.46. The response of night-time  $R_c$  to relative humidity (RH) in all conditions, when the surface is dry and when the surface is wet. 5-180
- Figure 6.1. Data used in the parameterisation of  $J_{mod}$ , bulk-canopy scale  $R_{c1w}$  plotted as conductance ( $g_{s_c}$ ) against (a) measured total PAR, (b) surface temperature,  $T_{z0'}$ , (b) vpd, and (c) SWC. Both the 30 minute average values and 90<sup>th</sup> percentiles are shown. The error bars show the 95% confidence level for each blocked value. The response curves are fitted to the 90<sup>th</sup> percentiles and the resulting parameter values are also shown. 6-186
- Figure 6.2. Bulk-canopy scale  $R_{c1w}$  plotted as conductance ( $g_{s_c}$ ) LAI and the fitted response curve. Both the 30 minute average values and 90<sup>th</sup> percentiles are shown. The error bars show the 95% confidence level for each blocked value. The response curve is fitted to the 90<sup>th</sup> percentiles and the resulting parameter values are also shown. 6-187
- Figure 6.3. Leaf-porometer measurements of leaf stomatal conductance ( $g_{s_l}$ ) in the field and solardomes plotted with the response curves used for  $J_{mod}$ . 6-187
- Figure 6.4. Monthly average soil respiration measured at Easter Bush. 6-189
- Figure 6.5. The Ball-Berry relationship for bulk-canopy respiration and stomatal conductance measured at Easter Bush. The error bars show the 95% confidence level for each median value. The line is fitted to the median ratio  $((-A_g - A_s - R_d)RH/C_s)$  values. 6-189
- Figure 6.6. Comparisons of leaf-level and canopy level measurements of bulk-canopy stomatal conductance with estimates from  $J_{mod}$ ,  $B_{mod}$  and  $J_{modG}$  (the error bars show the standard deviation of the leaf level measurements). 6-191
- Figure 6.7. Scatter plots of measured vs modelled estimates of bulk-canopy conductance to water-vapour. 6-193
- Figure 6.8. Monthly median estimates of bulk canopy conductance to water-vapour. NB the data sets are matched to include 30 minute periods where all 4 estimates are available and thus represent day-time dry periods only. 6-193
- Figure 6.9. Example of  $g_{s_w}$  estimated from measurement and models of a series of days in 2003. 6-194
- Figure 6.11. The variation of  $R_{ns_c}$  (dry-daylight conditions where  $LAI > 1.5$ ) with LAI, surface temperature and solar radiation. 6-197
- Figure 6.12. (a) The response of  $R_{ns_c}$  (dry-daylight conditions where  $LAI > 1.5$ ) to surface temperature and (b) the data normalised for average LAI. 6-197
- Figure 6.13. The variation of measurement and model derived estimates of  $R_{ns}$  with LAI, surface temperature ( $T_{z0'}$ ), solar radiation ( $St$ ), relative humidity (RH) and friction velocity ( $u_*$ ). 6-199
- Figure 6.14. (a) The temperature response of  $R_{ns}$  during all conditions and (b) normalised for LAI. 6-201
- Figure 6.15. (a) The temperature response of  $R_{nsN}$  in very dry and (b) very wet conditions. 6-201
- Figure 6.16. The natural logarithm of  $v_d$  for wet and dry surfaces against  $1/RT$ , which estimates the activation energy of the deposition process to the surfaces in each condition as the intercept of linear regression to each set of points. Regression lines fitted to both all the data and only those points with a standard error less than 100% are shown. 6-202
- Figure 6.17. The residuals of  $R_{nsN}$  predicted using the fitted temperature response in dry (top plots) and wet conditions (bottom plots). 6-203

- Figure 6.18. (a) The response  $R_{nsN\_dry}$  to solar radiation and (b) the fitted curve compared to the response of  $R_{nsN\_dry}$  to temperature. 6-204
- Figure 6.20. The variation of the residuals of  $R_{ns\_wet}$  with  $\log(St)$ . 6-205
- Figure 6.21. (a) The response  $R_{nsN\_wet}$  to solar radiation and (b) the fitted curve compared to the response of  $R_{nsN\_wet}$  to temperature. 6-206
- Figure 6.22. (a) The variation in all  $R_{nsN\_dry}$  data, (b)  $R_{ns\_dry}$  when  $LAI < 0.3$  and (c)  $R_{nsN\_wet}$  with friction velocity,  $u^*$ . 6-207
- Figure 6.23. The variation of surface temperature ( $T_{z0'}$ ) with friction velocity ( $u^*$ ). 6-208
- Figure 6.24. (a) The variation in  $R_{nsN\_dry}$  and (b)  $R_{nsN\_wet}$  with relative humidity, RH. 6-208
- Figure 6.25. The variation in surface temperature with humidity. 6-209
- Figure 6.26. The response curves of  $R_{nsN}$  with temperature and humidity in wet and dry conditions, plotted with  $T$  and RH increasing together. 6-209
- Figure 6.27. The response curves of  $R_{nsN}$  with temperature and humidity in (a) dry and (b) wet conditions, plotted with  $T$  increasing as RH decreases. 6-210
- Figure 6.28. Diurnal cycles during the summer and winter from the measurements and three different canopy resistance models. 6-214
- Figure a1. Scatter plot of the final (measured and modelled)  $R_{ns}$  data with  $LAI$ . 6-215
- Figure a2. 0.1 LAI block medians of  $R_{ns}$  and  $R_{nsN} (= R_{ns} \cdot LAI)$ , the error bars show one standard deviation. 6-216
- Figure a3. Revised  $R_{ns}(T_{z0'})$  relationships for wet and dry conditions using (a) and (c)  $R_{ns}$ , (b) and (d)  $R_{nsN} = R_{ns} \cdot LAI$ . The curves fitted in the original analysis with  $R_{nsN} = R_{ns}/LAI$  are shown for comparison. 6-216
- Figure a4. Residuals of measured – modelled  $R_{ns}$  values where  $R_{ns}$  has been estimated using relationships based on  $R_{ns}/LAI$  (original analysis),  $R_{ns}$  and  $R_{ns} \cdot LAI$ . 6-217
- Figure a5. The variation of  $R_{ns}$  with  $u^*$  over dry and wet surfaces at Easter Bush. 6-218
- Figure 7.1. Relative frequency distribution of the percentage uncertainties in  $u$ ,  $v$  and  $w$  measured by the Gill sonic anemometer. 7-222
- Figure 7.2. The 0.5 hourly percentage uncertainties in the ozone flux and  $25 \text{ ng m}^{-2} \text{ s}^{-1}$  block medians plotted against the flux (error bars show the standard deviation of each  $25 \text{ ng m}^{-2} \text{ s}^{-1}$  block). 7-228
- Figure 7.3. An example of measured stomatal conductance ( $g_s$ ) compared to modelled values (JMod top plot; BMod bottom plot). The error bars show the uncertainty in  $\text{mmol-H}_2\text{O m}^{-2} \text{ s}^{-1}$ . 7-231
- Figure 7.4. The uncertainty in  $1 \text{ }^\circ\text{C}$  block medians of dry  $R_{ns}$  with  $T_{z0'}$  where the error bars are calculated using either the standard error of the block values or the median total uncertainty derived from the data sets. 7-232
- Figure 8.1. The seasonal diurnal cycles of (from left to right) average ozone concentration, median ozone flux, deposition velocity and resistance. Only data for 2002 and 2004 are included due the uncertainties in the 2001 and 2004 data, which are discussed in Chapters 5 and 6. 237
- Figure 8.2. (a) The curves fitted to the response of  $R_{nsN\_dry}$  and  $R_{nsN\_wet}$  to surface temperature. (b) Arrhenius plots of the two temperature response curves. 242
- Figure D1 A simple model of aqueous  $\text{SO}_2$  oxidation used to predict the equilibrium pH of a water film. Reactions A to D are modelled until the solution reaches equilibrium and the final pH,  $[\text{HSO}_3^-]$  and  $[\text{H}^+]$  are used to predict the  $\text{O}_3$  loss rate (E). 270

## Tables

Table 1.1	Indices for assessing the effects of ozone on vegetation.....	1-13
Table 2.1	Molecular diffusivities ( $\text{cm}^2 \text{s}^{-1}$ ) for several important atmospheric trace gases.....	2-51
Table 2.2	Estimates of the non-stomatal resistance for ozone to snow, water, soil and plant surfaces. ....	2-53
Table 3.1	Summary of global models used to estimate ozone concentrations as given in Prather et al., (2003) .....	3-57
Table 3.2	Summary of some typical regional models that predict ozone concentrations.....	3-60
Table 4.3	Examples of local-scale and site-specific vegetation/atmosphere models.....	3-61
Table 4.1	Major events occurring at the Easter Bush field site .....	4-73
Table 4.2	.....	4-74
Table 4.3	Easter Bush Field Survey 18/07/02 .....	4-77
Table 4.4	Instrumentation employed at Easter Bush.....	4-81
Table 4.5	.....	4-91
Table 4.6	Summary data capture for each data set (specific data capture for some individual elements may vary slightly from these figures).....	4-104
Table 4.7	Annual %data capture for each anemometer on the wind-speed gradient. ....	4-104
Table 4.8	Percentage of the Ta time series <sup>1</sup> .....	4-105
Table 4.9	Regression statistics; overall data capture for P and % of time each data set used .....	4-105
Table 4.10	Overall data capture for rainfall and % of time each data set used. .	4-107
Table 5.1	Planar fit parameters ( $b_0, b_1, b_2$ ) and rotation angles ( $a, b$ ) .....	5-129
Table 5.2	Response times used for the LICOR flux attenuation correction low-pass filter. ....	5-132
Table 5.3	Thresholds for the RSC to exclude ~10% of the Easter Bush measurements .....	5-134
Table 5.4	Regression statistics for U, $u_*$ and H from the Metek against the Gill sonic.....	5-135
Table 5.5	Summary statistics for U, $u_*$ and H calculated from the Gill, Metek and Gradient data. All datasets area matched so they contain values for the same 0.5h. ....	5-136
Table 5.6	Regression statistics for e and $\lambda E$ from the closed-path (LICOR7000) against the open-path (LICOR75000) instrument.....	5-137
Table 5.7	Regression coefficients for the Gradient $u_*$ and H in comparison to the Gill or Metek sonics .....	5-143
Table 5.8	Linear regressions statistics for the energy balance, $(H + \lambda E)$ vs $(R_n - G)$ , from each measuring system and the combined data set, at Easter Bush. In all cases $\lambda E$ is given by the open-path LICOR7500. The slope with intercept forced through zero is given in brackets.....	5-144
Table 5.9.	Summary of publications discussing field measurements of ozone deposition to grassland.....	5-149
Table 5.10.	Regression statistics for the three ozone flux data sets.....	5-157
Table 5.11.	Data used to estimate the potential flux due to $\text{O}_3$ reacting with VOCs emitted by cut Lolium perenne. ....	5-169
Table 5.12	Monthly summary of median ozone fluxes and average concentrations measured during the day and night (standard deviation). ...	5-175
Table 5.13	Monthly deposition velocities and canopy resistance calculated from the data in Table 6.9 and the monthly median $R_a$ and $R_b$ . The standard errors given are calculated as described in Appendix A. ....	5-176

Table 5.14 Results of fitting $R_c = y_0 - a \cdot \exp(-bT)^y$ to 1°C blocked values of $R_{c\_night}$ at Easter Bush (with standard errors for the fitted parameters).....	5-178
Table 5.15 Results of fitting $R_c = y_0 - a \cdot \exp(-bRH)$ to 5% blocked values of $R_{c\_night}$ at Easter Bush (with standard errors for the fitted parameters). .....	5-180
Table 5.16 Summary of raw and final data capture (%) for the main components of the trace-gas flux measurements. ....	5-181
Table 6.1 Parameters for Jmod and JmodG.....	6-188
Table 6.2 Parameters used by the EMEP model .....	6-188
Table 6.3 Summary of measured and modelled estimates of stomatal conductance on days when leaf-level conductance was measured. ....	6-191
Table 6.4 Summary of measured and modelled estimates of canopy conductance to water-vapour ( $\text{mmol-H}_2\text{O m}^{-2} \text{s}^{-1}$ ). ....	6-194
Table 6.5 Results of fitting $R_{ns} = y_0 - a \exp(-bT)$ to 1°C blocked values of $R_{ns}$ at Easter Bush (in units of $\text{s m}^{-1}$ , with standard errors for the fitted parameters). For reference the results for $R_{c\_night}$ are also given. ....	6-199
Table 6.6 Results of fitting $R_{nsN} = y_0 - a \cdot \exp(-bx)$ to values of $R_{nsN\_dry}$ and $R_{nsN\_wet}$ blocked by solar radiation, friction velocity and relative humidity(with standard errors for the fitted parameters).....	6-210
Table 6.7 Summary statistics of each $R_{nsN}$ data set ( $\text{s m}^{-1}$ ).....	6-211
Table 6.8 Summary of preliminary model results compared to the measurements and estimates from Zhang, et al., 2002 and EMEP type models.....	6-213
Table 7.1 Summary of errors in each measurement and the main derived values. ....	7-232
Table 8.1 Summary statistics for $\text{NH}_3$ and $\text{SO}_2$ concentrations observed at Easter Bush ( $\text{NH}_3$ ) and Bush ( $\text{SO}_2$ ) during 30 <sup>th</sup> June – 30 <sup>th</sup> Sept 2002 and 1 <sup>st</sup> June to 31 <sup>st</sup> August 2003.....	241
Table B.1 Canopy height (h).....	247
Table B.2 Leaf Area Index (LAI).....	248
Table B.3 Wind-speed ( $u(1\text{m})$ ) .....	249
Table B.4 Ambient air temperature ( $T_a$ ).....	250
Table B.5 Solar Radiation ( $St$ ) .....	251
Table B.6 Relative Humidity (RH) .....	252
Table B.7 Soil Water Content at Rooting Depth (SWC) .....	253
Table B.8 Rainfall and surface wetness .....	254
Table B.9 Aerodynamic resistance at 1 m ( $R_a(1 \text{ m})$ , $\text{s m}^{-1}$ ) .....	255
Table B.10 Boundary layer resistance for ozone ( $R_{b03}$ $\text{s m}^{-1}$ ) .....	256
Table B.11 Ozone concentration at 1 m ( $\chi_{03}(1 \text{ m})$ , $\mu\text{g m}^{-3}$ ).....	257
Table B.12 Ozone flux ( $F_{03}$ $\text{ng m}^{-2} \text{s}^{-1}$ ) .....	258
Table B.13 Deposition velocity for ozone ( $v_{do3}$ $\text{mm s}^{-1}$ ) (not recalculated from flux and concentration) .....	259
Table B.14 Total canopy resistance for ozone ( $R_{c03}$ $\text{s m}^{-1}$ ) (not recalculated from flux and concentration) .....	260
Table B.15 Bulk canopy resistance for to water-vapour ( $R_{c1w}$ $\text{s m}^{-1}$ ) .....	261
Table B.16 Latent Heat Flux ( $\lambda E$ , $\text{W m}^{-2}$ ) .....	262
Table B.17 Bulk canopy $\text{CO}_2$ flux ( $F_{\text{CO}_2}$ , $\mu\text{mol m}^{-2} \text{s}^{-1}$ ).....	263
Table D1 Rate constants and parameter values used to model aqueous $\text{SO}_2$ oxidation and predict equilibrium water pH. ....	269



## References

- Allen, D. J., Dibb, J. E., Ridley, B., Pickering, K. E. and Talbot, R. W., An estimate of the stratospheric contribution to springtime tropospheric ozone maxima using TOPSE measurements and beryllium-7 simulations - art. no. 8355, *Journal of Geophysical Research-Atmospheres*, 108 (D4), 8355, 2003.
- Anfossi, D. and Sandroni, S., Ozone levels in Paris one century ago, *Atmospheric Environment*, 31 (20), 3481-3482, 1997.
- Anfossi, D., Sandroni, S. and Viarengo, S., Tropospheric Ozone in the 19th-Century - the Moncalieri Series, *Journal of Geophysical Research-Atmospheres*, 96 (D9), 17349-17352, 1991.
- Aris, R. M., Christian, D., Hearne, P. Q., Kerr, K., Finkbeiner, W. E. and Balmes, J. R., Ozone-Induced Airway Inflammation in Human-Subjects as Determined by Airway Lavage and Biopsy, *American Review of Respiratory Disease*, 148 (5), 1363-1372, 1993.
- Ashmore, M. R., Coyle, M. and Fowler, D., Implications of trends in background ozone concentrations for vegetation in the UK, pp. 46, *CEH, Edinburgh, Contract Report DEFRA EPG 1/3/173*, 2002.  
[http://www.nbu.ac.uk/pollution/docs/O3trends\\_UKveg.htm](http://www.nbu.ac.uk/pollution/docs/O3trends_UKveg.htm).
- Ashmore, M. R., Coyle, M. and Fowler, D., New directions: Implications of increasing tropospheric background ozone concentrations for vegetation, *Atmospheric Environment*, 37 (1), 153-154, 2003.
- Avissar, R., Observations of Leaf Stomatal Conductance at the Canopy Scale - an Atmospheric Modeling Perspective, *Boundary-Layer Meteorology*, 64 (1-2), 127-148, 1993.
- Baldocchi, D. D., Hicks, B. B. and Camara, P., A Canopy Stomatal-Resistance Model for Gaseous Deposition to Vegetated Surfaces, *Atmospheric Environment*, 21 (1), 91-101, 1987.
- Ball, G. R., Benton, J., Palmer-Brown, D., Fuhrer, J., Skarby, L., Gimeno, B. S. and Mills, G., Identifying factors which modify the effects of ambient ozone on white clover (*Trifolium repens*) in Europe, *Environmental Pollution*, 103 (1), 7-16, 1998.
- Ball, J. T., An Analysis of Stomatal Conductance, PhD Thesis, *Stanford University*, Stanford, California, USA, 1988.
- Ball, J. T., Woodrow, I. E. and Berry, J. A., A model predicting stomatal conductance and its contribution to the control of photosynthesis under different environmental conditions, in *Progress In Photosynthetic Research*, edited by I. Biggins, pp. 221-224, Martinus-Nijhoff, Dordrecht, 1987.
- Barford, N. C., Experimental Measurements: Precision, error and truth, 159 pp., John Wiley & Sons Ltd, 1985.
- Beadle, C. L., Ludlow, M. M. and Honeysett, J. L., Water Relations, in *Photosynthesis and production in a changing environment; A field and laboratory manual*, edited by D.O. Hall, *et al.*, pp. 113-128, Chapman & Hall, London, 1993.
- Beck, J. P. and Grennfelt, P., Estimate of Ozone Production and Destruction Over Northwestern Europe, *Atmospheric Environment*, 28 (1), 129-140, 1994.
- Beekmann, M., Ancellet, G., Blonsky, S., DeMuer, D., Ebel, A., Elbern, H., Hendricks, J., Kowol, J., Mancier, C., Sladkovic, R., Smit, H. G. J., Speth, P., Trickl, T. and VanHaver, P., Regional and global tropopause fold occurrence and related ozone flux across the tropopause, *Journal of Atmospheric Chemistry*, 28 (1-3), 29-44, 1997.

- Bell, M. and Ellis, H., Sensitivity analysis of tropospheric ozone to modified biogenic emissions for the Mid-Atlantic region, *Atmospheric Environment*, 38 (13), 1879-1889, 2004.
- Bellanger, L. and Tomassone, R., Trend in high tropospheric ozone levels. Application to Paris monitoring sites, *Statistics*, 38 (3), 217-241, 2004.
- Bentley, J. P., Principles of Measurement Systems, 503 pp., Longman Singapore Publishers, Singapore, 1988.
- Benton, J., Fuhrer, J., Gimeno, B. S., Skarby, L., Palmer-Brown, D., Ball, G., Roadknight, C. and Mills, G., An international cooperative programme indicates the widespread occurrence of ozone injury on crops, *Agriculture Ecosystems & Environment*, 78 (1), 19-30, 2000.
- Berntsen, T. K. and Isaksen, I. S. A., A global three-dimensional chemical transport model for the troposphere .1. Model description and CO and ozone results, *Journal of Geophysical Research-Atmospheres*, 102 (D17), 21239-21280, 1997.
- Berntsen, T. K., Myhre, G., Stordal, F. and Isaksen, I. S. A., Time evolution of tropospheric ozone and its radiative forcing, *Journal of Geophysical Research-Atmospheres*, 105 (D7), 8915-8930, 2000.
- Buckley, T. N., Mott, K. A. and Farquhar, G. D., A hydromechanical and biochemical model of stomatal conductance, *Plant Cell and Environment*, 26 (10), 1767-1785, 2003.
- Bungener, P., Nussbaum, S., Grub, A. and Fuhrer, J., Growth response of grassland species to ozone in relation to soil moisture condition and plant strategy, *New Phytologist*, 142 (2), 283-293, 1999.
- Burkhardt, J. and Gerchau, J., A New Device for the Study of Water-Vapor Condensation and Gaseous Deposition to Plant-Surfaces and Particle Samples, *Atmospheric Environment*, 28 (12), 2012-2017, 1994.
- Burkhardt, J., Kaiser, H., Goldbach, H. and Kappen, L., Measurements of electrical leaf surface conductance reveal recondensation of transpired water vapour on leaf surfaces, *Plant Cell and Environment*, 22 (2), 189-196, 1999.
- Buse, A., Mills, G., Harmen, H., Büker, P., Hayes, F., Williams, P., Emberson, L., Cinderby, S., Ashmore, M. R., Holland, M., De Temmerman, L. and Vegetation, I., Air Pollution and Vegetation., in *Annual Report*, edited by UNECE ICP Vegetation, CEH, 2003.  
[http://icpvegetation.ceh.ac.uk/annual\\_report\\_2003\\_pdf.htm](http://icpvegetation.ceh.ac.uk/annual_report_2003_pdf.htm)
- Businger, J. A., Wyngaard, J. C., Izumi, Y. and Bradley, E. F., Flux-profile relationships in the atmospheric surface layer, *Journal of Atmospheric Sciences*, 28, 181-189, 1971.
- Cape J.N., McFadyen G.G., Storeton-West R.L., Choularton T.W., Gallagher M.W., Bower K.N., Lee D.S., Dore C. & Berner A. Field observations of S-IV in cloud. *Atmospheric Research*, 50, 345-358. 1999.
- Chamberlain, A. C., Transport of gases to and from grass and grass-like surfaces, *Proceedings of the Royal Society of London A*, 290, 236-260, 1966.
- Chang, H. M., Chang, L. F. W. and Jeng, F. T., Interfacial transfer resistances of ozone dry deposition over agricultural soil of Tainan County, Taiwan, *Environmental Engineering Science*, 19 (3), 133-141, 2002.
- Chang, W., Heikes, B. G. and Lee, M., Ozone deposition to the sea surface: chemical enhancement and wind speed dependence, *Atmospheric Environment*, 38 (7), 1053-1059, 2004.
- Coe, H., Gallagher, M. W., Choularton, T. W. and Dore, C., Canopy scale measurements of stomatal and cuticular o<sub>3</sub> uptake by sitka spruce, *Atmospheric Environment*, 29 (12), 1413-1423, 1995.

- Colbeck, I. and Harrison, R. M., Dry deposition of ozone: some measurements of deposition velocity and of vertical profiles to 100 metres, *Atmospheric Environment* (1967), 19 (11), 1807-1818, 1985.
- Collatz, G. J., Ball, J. T., Grivet, C. and Berry, J. A., Physiological and environmental regulation of stomatal conductance, photosynthesis and transpiration: a model that includes a laminar boundary layer, *Agricultural and Forest Meteorology*, 54 (2-4), 107-136, 1991.
- Collatz, G. J., Ribascarbo, M. and Berry, J. A., Coupled Photosynthesis-Stomatal Conductance Model for Leaves of C4 Plants, *Australian Journal of Plant Physiology*, 19 (5), 519-538, 1992.
- Collins, W. J., Derwent, R. G., Garnier, B., Johnson, C. E., Sanderson, M. G. and Stevenson, D. S., Effect of stratosphere-troposphere exchange on the future tropospheric ozone trend - art. no. 8528, *Journal of Geophysical Research-Atmospheres*, 108 (D12), 8528, 2003.
- Collins, W. J., Derwent, R. G., Johnson, C. E. and Stevenson, D. S., The impact of human activities on the photochemical production and destruction of tropospheric ozone, *Quarterly Journal of the Royal Meteorological Society*, 126 (566), 1925-1951, 2000.
- Cape, J.N., The Importance of Solution Equilibria in Studying the Effects of Sulfite on Plants, *Environmental Pollution Series a-Ecological and Biological*, 34 (3), 259-274, 1984.
- Cape J.N., McFadyen G.G., Storeton-West R.L., Choularton T.W., Gallagher M.W., Bower K.N., Lee D.S., Dore C. & Berner A. Field observations of S-IV in cloud. *Atmospheric Research*, 50, 345-358. 1999.
- Corsmeier, U., Kalthoff, N., Kolle, O., Kotzian, M. and Fiedler, F., Ozone concentration jump in the stable nocturnal boundary layer during a LLJ-event, *Atmospheric Environment*, 31 (13), 1977-1989, 1997.
- Coyle, M., Ashmore, M. R., Fowler, D., Hayes, F. and Smith, R., Trends in Ground-level Ozone Concentration and Their Implications for the UK., in *13th WORLD CLEAN AIR AND ENVIRONMENTAL PROTECTION CONGRESS AND EXHIBITION*, London, UK, 2004.
- Coyle, M., Smith, R. I., Stedman, J. R., Weston, K. J. and Fowler, D., Quantifying the spatial distribution of surface ozone concentration in the UK, *Atmospheric Environment*, 36 (6), 1013-1024, 2002.
- Davison, A. W. and Barnes, J. D., Effects of ozone on wild plants, *New Phytologist*, 139 (1), 135-151, 1998.
- De Gouw, J. A., Howard, C. J., Custer, T. G. and Fall, R., Emissions of volatile organic compounds from cut grass and clover are enhanced during the drying process, *Geophysical Research Letters*, 26 (7), 811-814, 1999.
- De Gouw J.A., Howard C.J., Custer T.G., Baker B.M. & Fall R. Proton-transfer chemical-ionization mass spectrometry allows real-time analysis of volatile organic compounds released from cutting and drying of crops. *Environmental Science & Technology*, 34, 2640-2648, 2000.
- De Miguel, A. and Bilbao, J., Ozone dry deposition and resistances onto green grassland in summer in central Spain, *Journal of Atmospheric Chemistry*, 34 (3), 321-338, 1999.
- Derwent, R. G., Jenkin, M. E., Saunders, S. M., Pilling, M. J., Simmonds, P. G., Passant, N. R., Dollard, G. J., Dumitrean, P. and Kent, A., Photochemical ozone formation in north west Europe and its control, *Atmospheric Environment*, 37 (14), 1983-1991, 2003.
- Derwent, R. G., Stevenson, D. S., Collins, W. J. and Johnson, C. E., Intercontinental transport and the origins of the ozone observed at surface sites in Europe, *Atmospheric Environment*, 38 (13), 1891-1901, 2004.

- Diem, J. E., Comparisons of weekday-weekend ozone: importance of biogenic volatile organic compound emissions in the semi-arid southwest USA, *Atmospheric Environment*, 34 (20), 3445-3451, 2000.
- DoE, The United Kingdom National Air Quality Strategy, edited by Defra (formerly DoE), The Stationary Office., CM 3587, 1997.
- Droppo, J. G., Concurrent Measurements of Ozone Dry Deposition Using Eddy-Correlation and Profile Flux-Methods, *Journal of Geophysical Research-Atmospheres*, 90 (ND1), 2111-2118, 1985.
- Dyer, A. J. and Hicks, B. B., Flux-gradient relationships in the constant flux layer, *Quarterly Journal Royal Meteorological Society*, 96, 715-721, 1970.
- Emberson, L. D., 2002, Developments of the EMEP ozone deposition model - personal communication
- Emberson, L. D., Ashmore, M. R., Cambridge, H. M., Simpson, D. and Tuovinen, J. P., Modelling stomatal ozone flux across Europe, *Environmental Pollution*, 109 (3), 403-413, 2000a.
- Emberson, L. D., Simpson, D., Tuovinen, J. P., Ashmore, M. R. and Cambridge, H. M., Towards a model of ozone deposition and stomatal uptake over Europe, *EMEP*, 6/00, 2000b.  
[http://www.emep.int/reports/dnmi\\_note\\_6\\_2000.pdf](http://www.emep.int/reports/dnmi_note_6_2000.pdf)
- Entwistle, J., Weston, K., Singles, R. and Burgess, R., The magnitude and extent of elevated ozone concentrations around the coasts of the British Isles, *Atmospheric Environment*, 31 (13), 1925-1932, 1997.
- EPA, Science Algorithms of the EPA Models-3 Community Multiscale Air Quality (CMAQ) Modeling System, edited by D. W. BYUN and J. K. S. CHING, United States Environmental Protection Agency, Washington, EPA/600/R-99/030, 1999.  
<http://www.epa.gov/asmdnerl/CMAQ/CMAQscienceDoc.html>
- Erisman, J. W., Vanpul, A. and Wyers, P., Parametrization of Surface-Resistance for the Quantification of Atmospheric Deposition of Acidifying Pollutants and Ozone, *Atmospheric Environment*, 28 (16), 2595-2607, 1994.
- Erisman, J. W., Vermeulen, A., Hensen, A., Flechard, C., Dammggen, U., Fowler, D., Sutton, M., Grunhage, L. and Tuovinen, J.-P., Monitoring and modelling of biosphere/atmosphere exchange of gases and aerosols in Europe, *Environmental Pollution*, 133 (3), 403-413, 2005.
- Farquhar, G. D., Caemmerer von, S. and Berry, J. A., A Biochemical Model of Photosynthetic CO<sub>2</sub> Assimilation in Leaves of C<sub>3</sub> Species, *Planta*, 149, 78-90, 1980.
- Finkelstein, P. L., Ellestad, T. G., Clarke, J. F., Meyers, T. P., Schwede, D. B., Hebert, E. O. and Neal, J. A., Ozone and sulfur dioxide dry deposition to forests: Observations and model evaluation, *Journal of Geophysical Research-Atmospheres*, 105 (D12), 15365-15377, 2000.
- Finnan, J. M., Jones, M. B. and Burke, J. I., A time-concentration study on the effects of ozone on spring wheat (*Triticum aestivum* L) .1. Effects on yield, *Agriculture Ecosystems & Environment*, 57 (2-3), 159-167, 1996.
- Fiore, A. M., Jacob, D. J., Bey, I., Yantosca, R. M., Field, B. D., Fusco, A. C. and Wilkinson, J. G., Background ozone over the United States in summer: Origin, trend, and contribution to pollution episodes - art. no. 4275, *Journal of Geophysical Research-Atmospheres*, 107 (D15), 4275, 2002.
- Fishman, J., Wozniak, A. E. and Creilson, J. K., Global distribution of tropospheric ozone from satellite measurements using the empirically corrected tropospheric ozone residual technique: Identification of the regional aspects of air pollution, *Atmospheric Chemistry and Physics*, 3, 893-907, 2003.

- Fitzjarrald, D. R. and Lenschow, D. H., Mean concentration and flux profiles for chemically reactive species in the atmospheric surface layer, *Atmospheric Environment*, 17 (12), 2505-2512, 1983.
- Flechard, C., 1998a, Corrections to ozone fluxes for NO/NO<sub>2</sub> interactions at the Auchencorth Moss site - personal communication
- Flechard, C. R., Turbulent Exchange of Ammonia Above Vegetation, PhD thesis, University of Nottingham, 1998b.
- Foken, T., Gockede, M., Mauder, M., Mahrt, L., Amiro, B. and Munger, W., Post-field data quality control, in *Handbook of Micrometeorology*, edited by X. Lee, *et al.*, pp. 181-208, Kluwer, Dordrecht, 2004.
- Fowler, D., Cape, J. N., Coyle, M., Flechard, C., Kuylenstierna, J., Hicks, K., Derwent, D., Johnson, C. and Stevenson, D., The global exposure of forests to air pollutants, *Water, Air, and Soil Pollution*, 116 (1-2), 5-32, 1999.
- Fowler, D. and Duyzer, J. H., Micrometeorological techniques for the measurement of trace gas exchange, in *Exchange of trace gases between terrestrial ecosystems and the atmosphere*, edited by M. O. Andreae and D. S. Schimel, pp. 189-207w, John Wiley & Sons, 1989.
- Fowler, D., Flechard, C., Cape, J. N., Storeton-West, R. L. and Coyle, M., Measurements of ozone deposition to vegetation quantifying the flux, the stomatal and non-stomatal components, *Water Air and Soil Pollution*, 130 (1-4), 63-74, 2001.
- Frenzen, P. and Vogel, C. A., On the Magnitude and Apparent Range of Variation of the Von Karman Constant in the Atmospheric Surface-Layer, *Boundary-Layer Meteorology*, 72 (4), 371-392, 1995.
- Fuentes, J. D., Effect of foliage surface wetness on the deposition of ozone, Dissertation thesis, The University of Geulph, 1992.
- Fuentes, J. D., Gillespie, T. J., Denhartog, G. and Neumann, H. H., Ozone Deposition onto a Deciduous Forest During Dry and Wet Conditions, *Agricultural and Forest Meteorology*, 62 (1-2), 1-18, 1992.
- Fuhrer, J. and Achermann, B., *Critical Levels for Ozone: UNECE workshop report*, Swiss Federal Research Station for Agricultural Chemistry and Environmental Hygiene, Liebefeld-Bern, 1994.
- Fuhrer, J., Skarby, L. and Ashmore, M. R., Critical levels for ozone effects on vegetation in Europe, *Environmental Pollution*, 97 (1-2), 91-106, 1997.
- Gallagher, M. W., Beswick, K. M. and Coe, H., Ozone deposition to coastal waters, *Quarterly Journal of the Royal Meteorological Society*, 127 (572), 539-558, 2001.
- Gao, Q., Zhao, P., Zeng, X., Cai, X. and Shen, W., A model of stomatal conductance to quantify the relationship between leaf transpiration, microclimate and soil water stress, *Plant Cell and Environment*, 25 (11), 1373-1381, 2002.
- Gao, W. and Wesely, M. L., Numerical Modeling of the Turbulent Fluxes of Chemically Reactive Trace Gases in the Atmospheric Boundary-Layer, *Journal of Applied Meteorology*, 33 (7), 835-847, 1994.
- Gao, W., Wesely, M. L. and Lee, I. Y., A Numerical Study of the Effects of Air Chemistry on Fluxes of No, No<sub>2</sub>, and O<sub>3</sub> near the Surface, *Journal of Geophysical Research-Atmospheres*, 96 (D10), 18761-18769, 1991.
- Garland, J. A., The dry deposition of sulphur dioxide to land and water surfaces., *Proceedings of the Royal Society of London A*, 354, 245-268, 1977.
- Garland, J. A. and Derwent, R. G., Destruction at the ground and the diurnal cycle of concentration of ozone and other gases, *Quarterly Journal Royal Meteorological Society*, 105, 169-183, 1979.
- Garratt, J. R., *The atmospheric boundary layer*. 316 pp., Cambridge University Press, Cambridge, 1992.

- Giannakopoulos, C., Certificate of postgraduate study: Three dimensional modelling of the concentration and deposition of tropospheric trace gases., Uni of Cambridge, Cambridge, England, 1994.
- Gimeno, B. S., Bermejo, V., Sanz, J., DelaTorre, D. and Gil, J. M., Assessment of the effects of ozone exposure and plant competition on the reproductive ability of three therophytic clover species from Iberian pastures, *Atmospheric Environment*, 38 (15), 2295-2303, 2004.
- Granat, L. and Richter, A., Dry Deposition to Pine of Sulfur-Dioxide and Ozone at Low Concentration, *Atmospheric Environment*, 29 (14), 1677-1683, 1995.
- Grantz, D. A., Zhang, X. J., Massman, W. J., Delany, A. and Pederson, J. R., Ozone deposition to a cotton (*Gossypium hirsutum* L) field: stomatal and surface wetness effects during the California Ozone Deposition Experiment, *Agricultural and Forest Meteorology*, 85 (1-2), 19-31, 1997.
- Grantz, D. A., Zhang, X. J., Massman, W. J., Denhartog, G., Neumann, H. H. and Pederson, J. R., Effects of stomatal conductance and surface wetness on ozone deposition in field-grown, *Atmospheric Environment*, 29 (21), 3189-3198, 1995.
- Grontoft, T., Measurements and modelling of the ozone deposition velocity to concrete tiles, including the effect of diffusion, *Atmospheric Environment*, 38, 49-58, 2004.
- Grunhage, L., Dammgen, U., Haenel, H. D. and Jager, H. J., Response of a grassland ecosystem to air-pollutants .3. the chemical climate - vertical flux densities of gaseous species in the atmosphere near the ground, *Environmental Pollution*, 85 (1), 43-49, 1994.
- Grunhage, L. and Haenel, H. D., Platin (Plant-Atmosphere Interaction) 1: A model of plant-atmosphere interaction for estimating absorbed doses of gaseous air pollutants, *Environmental Pollution*, 98, 37-50, 1997.
- Grunhage, L. and Jager, H.-J., From critical levels to critical loads for ozone: a discussion of a new experimental and modelling approach for establishing flux-response relationships for agricultural crops and native plant species, *Environmental Pollution*, 125 (1), 99-110, 2003.
- Gusten, H., Heinrich, G., Schmidt, R. W. H. and Schurath, U., A Novel Ozone Sensor for Direct Eddy Flux Measurements, *Journal of Atmospheric Chemistry*, 14 (1-4), 73-84, 1992.
- Gutschick, V. P. and Simonneau, T., Modelling stomatal conductance of field-grown sunflower under varying soil water content and leaf environment: comparison of three models of stomatal response to leaf environment and coupling with an abscisic acid-based model of stomatal response to soil drying, *Plant Cell and Environment*, 25 (11), 1423-1434, 2002.
- Haenel, H. D. and Grunhage, L., Footprint analysis: A closed analytical solution based on height-dependent profiles of wind speed and eddy viscosity, *Boundary-Layer Meteorology*, 93 (3), 395-409, 1999.
- Han, Z. W., Ueda, H. and Matsuda, K., Model study of the impact of biogenic emission on regional ozone and the effectiveness of emission reduction scenarios over eastern China, *Tellus Series B-Chemical and Physical Meteorology*, 57 (1), 12-27, 2005.
- Hass, H., Builtjes, P. J. H., Simpson, D. and Stern, R. E. r. m., Comparison of model results obtained with several European regional air quality models, *Atmospheric Environment*, 31 (19), 3257-3277, 1997.
- Hass, H., Ebel, A., Feldmann, H., Jakobs, H. J. and Memmesheimer, M. E. r. m., Evaluation Studies with a Regional Chemical-Transport Model (Eurad) Using Air-Quality Data from the Emep Monitoring Network, *Atmospheric Environment Part a-General Topics*, 27 (6), 867-887, 1993.
- Hauglustaine, D. A. and Brasseur, G. P., Evolution of tropospheric ozone under anthropogenic activities and associated radiative forcing of climate,

- Journal of Geophysical Research-Atmospheres*, 106 (D23), 32337-32360, 2001.
- Heal, M. R., Booth, B. B. B., Cape, J. N. and Hargreaves, K. J., The influence of simplified peroxy radical chemistry on the interpretation of NO<sub>2</sub>-NO-O<sub>3</sub> surface exchange, *Atmospheric Environment*, 35 (9), 1687-1696, 2001.
- Hicks, B. B., Baldocchi, D. D., Meyers, T. P., Hosker, J. R. and Matt, D. R., A preliminary multiple resistance routine for deriving dry deposition velocities from measured quantities, *Water, Air, and Soil Pollution*, 36, 311-330, 1987.
- Hogstrom, U. and Smedman, A.-S., Accuracy of Sonic Anemometers: Laminar Wind-Tunnel Calibrations Compared to Atmospheric In Situ Calibrations Against a Reference Instrument, *Boundary-Layer Meteorology*, 111 (1), 33-54, 2004.
- Horst, T. W., A simple formula for attenuation of eddy fluxes measured with first-order-response scalar sensors, *Boundary-Layer Meteorology*, 82 (2), 219-233, 1997.
- Horst, T. W. and Weil, J. C., How Far Is Far Enough - the Fetch Requirements for Micrometeorological Measurement of Surface Fluxes, *Journal of Atmospheric and Oceanic Technology*, 11 (4), 1018-1025, 1994.
- Horvath, L., Fuhrer, E., Gyuricza, A., Lovas, K., Nagy, Z. and Weidlinger, T., Gradient Flux Measurements of Gases above Short Vegetation and Forest, in *Eurotrac Symposium '94*, edited by P. Borrel, pp. 477-478, SPB Academic Publishing, Garmisch-Partenkirchen, 1994.
- Hough, A. M., Development of a 2-Dimensional Global Tropospheric Model - Model Chemistry, *Journal of Geophysical Research-Atmospheres*, 96 (D4), 7325-7362, 1991.
- Houghton, J. T., Ding, Y., Griggs, D. J., Noguer, M., van der Linden, P. J., Dai, X., Maskell, K. and Johnson, C. A., Climate change 2001: the scientific basis: Contribution of working group I to the third assessment report of the intergovernmental panel on climate change, in *IPCC Third Assessment*, IPCC, 2001.  
[http://www.grida.no/climate/ipcc\\_tar/index.htm](http://www.grida.no/climate/ipcc_tar/index.htm)
- ICP, Mapping Manual 2004, in *Mapping Manual*, edited by UNECE Convention on Long-Range Transboundary Air Pollution, pp. 202, UNECE-LRTAP, 2004.  
<http://www.icpmapping.org>
- IIASA, The RAINS Model online, 2005: <http://www.iiasa.ac.at/rains/Rains-online.html>
- Jakobsen, H. A., Jonson, J. E. and Berge, E., Transport and deposition calculations of sulphur and nitrogen compounds in Europe for 1992 in the 50 km grid square by use of the multi-layer Eulerian model., The Norwegian Meteorological Institute, Oslo, Norway., EMEP/MSC-W Report 2/96., 1996.
- Jarvis, P. G., The interpretation of the variations in leaf water potential and stomatal conductance found in canopies in the field., *Philosophical Transactions of the Royal Society of London Series B*, 273, 593-610, 1976.
- Karenlampi, L. and Skarby, L., *Critical Levels for Ozone in Europe: Testing and Finalising the Concepts*, University of Kuopio, 1996.
- Karl T., Fall R., Jordan A. & Lindinger W. On-line analysis of reactive VOCs from urban lawn mowing. *Environmental Science & Technology*, 35, 2926-2931, 2001a.
- Karl T., Guenther A., Jordan A., Fall R. & Lindinger W. Eddy covariance measurement of biogenic oxygenated VOC emissions from hay harvesting. *Atmospheric Environment*, 35, 491-495, 2001b.

- Karl T., Harren F., Warneke C., de Gouw J., Grayless C. & Fall R. Senescing grass crops as regional sources of reactive volatile organic compounds. *Journal of Geophysical Research-Atmospheres*, 110. 2005.
- Kim, J. and Verma, S. B., Modeling Canopy Stomatal Conductance in a Temperate Grassland Ecosystem, *Agricultural and Forest Meteorology*, 55 (1-2), 149-166, 1991.
- Kirstine, W. V. and Galbally, I. E., A simple model for estimating emissions of volatile organic compounds from grass and cut grass in urban airsheds and its application to two Australian cities, *Journal of the Air & Waste Management Association*, 54 (10), 1299-1311, 2004.
- Kirstine W., Galbally I., Ye Y.R. & Hooper M. Emissions of volatile organic compounds (primarily oxygenated species) from pasture. *Journal of Geophysical Research-Atmospheres*, 103, 10605-10619, 1998.
- Klemm, O., Milford, C., Sutton, M. A., Spindler, G. and van Putten, E., A climatology of leaf surface wetness, *Theoretical and Applied Climatology*, 71 (1-2), 107-117, 2002.
- Kljun, N., Calanca, P., Rotachhi, M. W. and Schmid, H. P., A simple parameterisation for flux footprint predictions, *Boundary-Layer Meteorology*, 112 (3), 503-523, 2004.
- Kollist, H., Moldau, H., Mortensen, L., Rasmussen, S. K. and Jorgensen, L. B., Ozone flux to plasmalemma in barley and wheat is controlled by stomata rather than by direct reaction of ozone with cell wall ascorbate, *Journal of Plant Physiology*, 156 (5-6), 645-651, 2000.
- Kollner, B. and Krause, G. H. M., Changes in carbohydrates, leaf pigments and yield in potatoes induced by different ozone exposure regimes, *Agriculture Ecosystems & Environment*, 78 (2), 149-158, 2000.
- Kormann, R. and Meixner, F. X., An analytical footprint model for non-neutral stratification, *Boundary-Layer Meteorology*, 99 (2), 207-224, 2001.
- Larcher, W., *Physiological Plant Ecology*, Springer-Verlag, New York, 2001.
- Leclerc, M. Y., Shen, S. H. and Lamb, B., Observations and large-eddy simulation modeling of footprints in the lower convective boundary layer, *Journal of Geophysical Research-Atmospheres*, 102 (D8), 9323-9334, 1997.
- Lee, D. S., Lewis, P. M., Cape, J. N., Leith, I. D. and Espenhahn, S. E., The Effects of Ozone on Materials - Experimental evaluation of the susceptibility of polymeric materials to ozone, in *Air Composition and Chemistry*, edited by P. Brimblecombe, pp. 253, CUP, Cambridge, 1995.
- Lee, X., Finnigan, J. J. and Paw U, K. T., Coordinate systems and flux bias error, in *Handbook of Micrometeorology*, edited by X. Lee, et al., pp. 33-66, Kluwer, Dordrecht, 2004.
- Leith, I. D., 2005, Images of effects of ozone on rubber samples - personal communication
- Leith, I. D. and Cape, J. N., Effects of Ozone on Materials: Interim Report to AEA Technology plc, for the Department of the Environment (ITE Project Code T07058M7). CEH (formerly Institute of Terrestrial Ecology, Edinburgh), 1998.
- Lelieveld, J. and Dentener, F. J., What controls tropospheric ozone?, *Journal of Geophysical Research-Atmospheres*, 105 (D3), 3531-3551, 2000.
- Lenschow, D. H. and Delany, A. C., An Analytic Formulation for NO and NO<sub>2</sub> Flux Profiles in the Atmospheric Surface-Layer, *Journal of Atmospheric Chemistry*, 5 (3), 301-309, 1987.
- Lenschow, D. H. and Raupach, M. R., The Attenuation of Fluctuations in Scalar Concentrations through Sampling Tubes, *Journal of Geophysical Research-Atmospheres*, 96 (D8), 15259-15268, 1991.

- Leuning, R., Modeling Stomatal Behavior and Photosynthesis of Eucalyptus-Grandis, *Australian Journal of Plant Physiology*, 17 (2), 159-175, 1990.
- Leuning, R., A Critical-Appraisal of a Combined Stomatal-Photosynthesis Model for C-3 Plants, *Plant Cell and Environment*, 18 (4), 339-355, 1995.
- Levy, P., 2005, Photosynthesis parameters for *Lolium perenne* - personal communication
- Li, Q. B., Jacob, D. J., Bey, I., Palmer, P. I., Duncan, B. N., Field, B. D., Martin, R. V., Fiore, A. M., Yantosca, R. M., Parrish, D. D., Simmonds, P. G. and Oltmans, S. J., Transatlantic transport of pollution and its effects on surface ozone in Europe and North America - art. no. 4166, *Journal of Geophysical Research Atmospheres*, 107 (D13), 4166, 2002.
- Lloyd, J., Modelling stomatal responses to environment in *Macadamia intergifolia*, *Australian Journal of Plant Physiology*, 18, 649-690, 1991.
- Lohammer, T., Larsson, S., Linder, S. and Falk, S. O., FAST - Simulation models of gaseous exchange in Scots Pine, *Ecological Bulletin*, 32, 505-523, 1980.
- Lovblad, G., Erisman, J. W. and Fowler, D., Models and Methods For the Quantification of Atmospheric Input to Ecosystems, Nordic Council of Ministers, Copenhagen, Denmark, Goteborg, NORD1993:573, 1993.
- Maahs, H. G.. Sulfur-dioxide/water equilibria between 0°C and 50°C. An examination of data at low concentrations. Heterogeneous Atmospheric Chemistry. D. R. Schryer. Washington DC, American Geophysical Union: 187-195. 1982.
- Marengo, A., Gouget, H., Nedelec, P., Pages, J. P. and Karcher, F., Evidence of a Long-Term Increase in Tropospheric Ozone from Pic Du Midi Data Series - Consequences - Positive Radiative Forcing, *Journal of Geophysical Research-Atmospheres*, 99 (D8), 16617-16632, 1994.
- Massman, W. J., The Attenuation of Concentration Fluctuations in Turbulent-Flow through a Tube, *Journal of Geophysical Research-Atmospheres*, 96 (D8), 15269-15273, 1991.
- Massman, W. J., A review of the molecular diffusivities of H<sub>2</sub>O, CO<sub>2</sub>, CH<sub>4</sub>, CO, O-3, SO<sub>2</sub>, NH<sub>3</sub>, N<sub>2</sub>O, NO, AND NO<sub>2</sub> in air, O-2 AND N-2 near STP, *Atmospheric Environment*, 32 (6), 1111-1127, 1998.
- Massman, W. J., Pederson, J., Delany, A., Grantz, D., Denhartog, G., Neumann, H. H., Oncley, S. P., Pearson, R. and Shaw, R. H., An Evaluation of the Regional Acid Deposition Model Surface Module for Ozone Uptake at 3 Sites in the San-Joaquin Valley of California, *Journal of Geophysical Research-Atmospheres*, 99 (D4), 8281-8294, 1994.
- McKay, W. A., Stephens, B. A. and Dollard, G. J., Laboratory measurements of ozone deposition to sea-water and other saline solutions, *Atmospheric Environment Part A-General Topics*, 26 (17), 3105-3110, 1992.
- Mendoza-Dominguez, A., Wilkinson, J. G., Yang, Y. J. and Russell, A. G., Modeling and direct sensitivity analysis of biogenic emissions impacts on regional ozone formation in the Mexico-US border area, *Journal of the Air & Waste Management Association*, 50 (1), 21-31, 2000.
- Met, O., UK climate and weather statistics, 2004:  
<http://www.metoffice.com/climate/uk/>
- Metcalfe, S. E., Whyatt, J. D., Derwent, R. G. and O'Donoghue, M., The regional distribution of ozone across the British Isles and its response to control strategies, *Atmospheric Environment*, 36 (25), 4045-4055, 2002.
- Meyers, T. P., Finkelstein, P., Clarke, J., Ellestad, T. G. and Sims, P. F., A multilayer model for inferring dry deposition using standard meteorological measurements, *Journal of Geophysical Research-Atmospheres*, 103 (D17), 22645-22661, 1998.

- Mickley, L. J., Murti, P. P., Jacob, D. J., Logan, J. A., Koch, D. M. and Rind, D., Radiative forcing from tropospheric ozone calculated with a unified chemistry-climate model, *Journal of Geophysical Research-Atmospheres*, 104 (D23), 30153-30172, 1999.
- Milford, C., Dynamics of atmospheric ammonia exchange with intensively-managed grassland, University of Edinburgh, Edinburgh, 2004.
- Monks, P. S., A review of the observations and origins of the spring ozone maximum, *Atmospheric Environment*, 34 (21), 3545-3561, 2000.
- Monteith, J. L., Coupling of plants to the atmosphere., in *Plants and Their Atmospheric Environment*, edited by J. Grace, et al., pp. 1-29, Blackwell Scientific Publications, 1981.
- Monteith, J. L. and Unsworth, M., *Principles of Environmental Physics*, Edward Arnold, London, 1990.
- Mott, K. A. and Buckley, T. N., Stomatal heterogeneity, *Journal of Experimental Botany*, 49, 407-417, 1998.
- Mudway, I. S. and Kelly, F. J., Is There a Threshold for Ozone-Induced Pulmonary Responses in Healthy Adults?, 2003:  
<http://www.advisorybodies.doh.gov.uk/comeap/issues.htm>
- Muller, J. F., Geographical-Distribution and Seasonal-Variation of Surface Emissions and Deposition Velocities of Atmospheric Trace Gases, *Journal of Geophysical Research-Atmospheres*, 97 (D4), 3787-3804, 1992.
- Muller, J. F., Modelisation tr-dimensionnelle globale de la chimie et du transport des gaz en trace dans la troposphere, Brussels, 1993.
- Muller, J. F. and Brasseur, G., Images - a 3-Dimensional Chemical-Transport Model of the Global Troposphere, *Journal of Geophysical Research-Atmospheres*, 100 (D8), 16445-16490, 1995.
- Naja, M., Akimoto, H. and Staehelin, J., Ozone in background and photochemically aged air over central Europe: Analysis of long-term ozonesonde data from Hohenpeissenberg and Payerne - art. no. 4063, *Journal of Geophysical Research Atmospheres*, 108 (D2), 4063, 2003.
- Nakicenovic, N., Davidson, O., Davis, G., Grübler, A., Kram, T., Lebre La Rovere, E., Metz, B., Morita, T., Pepper, W., Pitcher, H., Sankovski, A., Shukla, P., Swart, R., Watson, R. and Dadi, Z., SUMMARY FOR POLICYMAKERS, EMISSIONS SCENARIOS, edited by IPCC Working Group III, pp. 27, IPCC - Intergovernmental Panel on Climate Change, 2000.  
<http://www.ipcc.ch/pub/sres-e.pdf>
- NASA, E. O., The ozone we breathe; Ozone's effects on human health, 2004:  
<http://earthobservatory.nasa.gov/Library/>
- NEG-TAP, Transboundary Air Pollution: Acidification, Eutrophication and Ground-level Ozone in the UK, pp. 314, Report of the National Expert Group on Transboundary Air Pollution (NEG-TAP) for the UK Department for Environment, Food and Rural Affairs, Scottish Executive, The National Assembly for Wales/Cynulliad Cenedlaethol Cymru and the Department of the Environment for Northern Ireland, CEH - Edinburgh, 2001.  
<http://edinburgh.ceh.ac.uk/negtap/>
- Nemitz, E., 2005, Stationarity tests for the Easter Bush field site - personal communication
- Nemitz, E., Hargreaves, K. J., McDonald, A. G., Dorsey, J. R. and Fowler, D., Meteorological measurements of the urban heat budget and CO<sub>2</sub> emissions on a city scale, *Environmental Science & Technology*, 36 (14), 3139-3146, 2002.
- Newman, P. A., Kawa, S. R. and Nash, E. R., On the size of the Antarctic ozone hole, *Geophysical Research Letters*, 31 (21), art. no.-L21104, 2004.

- Nikolov, N. and Zeller, K. F., Modeling coupled interactions of carbon, water, and ozone exchange between terrestrial ecosystems and the atmosphere. I: Model description, *Environmental Pollution*, 124 (2), 231-246, 2003.
- Norman, J. M., Simulation of microclimates, in *Biometeorology in integrated pest management*, edited by J.L. Hatfield and I.J. Thompson, pp. 65-99, Academic Press, New York., 1982.
- O'Sullivan, M., 2003, Soil water release curve for Macmerry soil series near Easter Bush, measurement data - personal communication
- Owen, S. M., MacKenzie, A. R., Stewart, H., Donovan, R. and Hewitt, C. N., Biogenic volatile organic compound (VOC) emission estimates from an urban tree canopy, *Ecological Applications*, 13 (4), 927-938, 2003.
- Padro, J., Observed Characteristics of the Dry Deposition Velocity of O<sub>3</sub> and So<sub>2</sub> above a Wet Deciduous Forest, *Science of the Total Environment*, 147, 395-400, 1994.
- Padro, J., Summary of ozone dry deposition velocity measurements and model estimates over vineyard, cotton, grass and deciduous forest in summer, *Atmospheric Environment*, 30 (13), 2363-2369, 1996.
- Padro, J., Massman, W. J., Shaw, R. H., Delany, A. and Oncley, S. P., A Comparison of Some Aerodynamic Resistance Methods Using Measurements over Cotton and Grass from the 1991 California Ozone Deposition Experiment, *Boundary-Layer Meteorology*, 71 (4), 327-339, 1994.
- Padu, E., Kollist, H., Tulva, I., Oksanen, E. and Moldau, H., Components of apoplastic ascorbate use in *Betula pendula* leaves exposed to CO<sub>2</sub> and O<sub>3</sub> enrichment, *New Phytol*, 165 (1), 131-142, 2005.
- Paulson, C. A., The Mathematical Representation of Wind Speed and Temperature Profiles in the Unstable Atmospheric Surface Layer, *Journal of Applied Meteorology*, 9, 857-861, 1970.
- Pavelin, E. G., Johnson, C. E., Rughooputh, S. and Toumi, R., Evaluation of pre-industrial surface ozone measurements made using Schonbein's method, *Atmospheric Environment*, 33 (6), 919-929, 1999.
- Pederson, J. R., Massman, W. J., Mahrt, L., Delany, A., Oncley, S., Hartog, G. D., Neumann, H. H., Mickle, R. E., Shaw, R. H., Paw U, K. T., Grantz, D. A., Macpherson, J. I., Desjardins, R., Schuepp, P. H., Pearson, R. and Arcado, T. E., California ozone deposition experiment: methods, results and opportunities, *Atmospheric Environment*, 29 (21), 3115-3132, 1995.
- Pio, C. A., Feliciano, M. S., Vermeulen, A. T. and Sousa, E. C., Seasonal variability of ozone dry deposition under southern European climate conditions, in Portugal, *Atmospheric Environment*, 34 (2), 195-205, 2000.
- Pitari, G., Mancini, E., Rizi, V. and Shindell, D. T., Impact of future climate and emission changes on stratospheric aerosols and ozone, *Journal of the Atmospheric Sciences*, 59 (3), 414-440, 2002.
- Pleijel, H., Danielsson, H., Ojanpera, K., DeTemmerman, L., Høgy, P., Badiani, M. and Karlsson, P. E., Relationships between ozone exposure and yield loss in European wheat and potato - a comparison of concentration- and flux-based exposure indices, *Atmospheric Environment*, 38 (15), 2259-2269, 2004.
- Pleijel, H., Karlsson, G. P., Danielsson, H. and Sellden, G., Surface wetness enhances ozone deposition to a pasture canopy, *Atmospheric Environment*, 29 (22), 3391-3393, 1995.
- Pochanart, P., Akimoto, H., Kajii, Y., Potemkin, V. M. and Khodzher, T. V., Regional background ozone and carbon monoxide variations in remote Siberia/East Asia - art. no. 4028, *Journal of Geophysical Research Atmospheres*, 108 (D1), 4028, 2003.

- Pochanart, P., Akimoto, H., Kinjo, Y. and Tanimoto, H., Surface ozone at four remote island sites and the preliminary assessment of the exceedances of its critical level in Japan, *Atmospheric Environment*, 36 (26), 4235-4250, 2002.
- Pochanart, P., Kato, S., Katsuno, T. and Akimoto, H., Eurasian continental background and regionally polluted levels of ozone and CO observed in northeast Asia, *Atmospheric Environment*, 38 (9), 1325-1336, 2004.
- PORG, Ozone in the United Kingdom, Third Report of the Photochemical Oxidants Review Group, The Department of the Environment Transport and the Regions, Edinburgh, 1993. <http://www.nbu.ac.uk/pollution/docs/>
- PORG, Ozone in the United Kingdom, Fourth Report of the Photochemical Oxidants Review Group, The Department of the Environment Transport and the Regions, Edinburgh, 1998. <http://www.nbu.ac.uk/pollution/docs/PORGiv.htm>
- Prather, M., Gauss, M., Berntsen, T., Isaksen, I., Sundet, J., Bey, I., Brasseur, G., Dentener, F., Derwent, R., Stevenson, D., Grenfell, L., Hauglustaine, D., Horowitz, L., Jacob, D., Mickley, L., Lawrence, M., von Kuhlmann, R., Müller, J. F., Pitari, G., Rogers, H., Johnson, M., Pyle, J., Law, K., van Weele, M. and Wild, O., Fresh air in the 21st century?, *Geophysical Research Letters*, 30 (2), art. no.-1100, 2003.
- Prather, M., Spivakowsky, C. and Logan, J., Atmospheric Methane Response to Chemistry - Results from a 3-D Chemical Tracer Model, *Abstracts of Papers of the American Chemical Society*, 193, 5-GEOC, 1987.
- Prather, M. J., Numerical Advection by Conservation of 2nd-Order Moments, *Journal of Geophysical Research-Atmospheres*, 91 (D6), 6671-6681, 1986.
- Rafarel, C. R. and Ashenden, T. W., A Facility for the Large-Scale Exposure of Plants to Gaseous Atmospheric Pollutants, *New Phytologist*, 117 (2), 345-349, 1991.
- Rafarel, C. R., Ashenden, T. W. and Roberts, T. M., An improved Solardome system for exposing plants to elevated CO<sub>2</sub> and temperature, *New Phytologist*, 131 (4), 481-490, 1995.
- Rinnan, R., Rinnan, A., Holopainen, T., Holopainen, J. K. and Pasanen, P., Emission of non-methane volatile organic compounds (VOCs) from boreal peatland microcosms - effects of ozone exposure, *Atmospheric Environment*, 39 (5), 921-930, 2005.
- Ronda, R. J., de Bruin, H. A. R. and Holtslag, A. A. M., Representation of the canopy conductance in modeling the surface energy budget for low vegetation, *Journal of Applied Meteorology*, 40 (8), 1431-1444, 2001.
- Rondon, A., Johansson, C. and Granat, L., Dry Deposition of Nitrogen-Dioxide and Ozone to Coniferous Forests, *Journal of Geophysical Research-Atmospheres*, 98 (D3), 5159-5172, 1993.
- Roy, M., 2005, Ozone measurements on Ben Nevis, email - personal communication
- Russell, G. L. and Lerner, J. A., A New Finite-Differencing Scheme for the Tracer Transport- Equation, *Journal of Applied Meteorology*, 20 (12), 1483-1498, 1981.
- Sanchez, M. L., Rodriguez, R. and Lopez, A., Ozone dry deposition in a semi-arid steppe and in a coniferous forest in southern Europe, *Journal of the Air & Waste Management Association*, 47 (7), 792-799, 1997.
- Sandroni, S. and Anfossi, D., Historical Data of Surface Ozone at Tropical Latitudes, *Science of the Total Environment*, 148 (1), 23-29, 1994.
- Savage, M. J., McInnes, K. J. and Heilman, J. L., The 'footprints' of eddy correlation sensible heat flux density, and other micrometeorological measurements, *South African Journal of Science*, 92 (3), 137-142, 1996.

- Scebba, F., Soldatini, G. and Ranieri, A., Ozone differentially affects physiological and biochemical responses of two clover species; *Trifolium repens* and *Trifolium pratense*, *Environmental Pollution*, 123 (2), 209-216, 2003.
- Schmid, H. P., Footprint modeling for vegetation atmosphere exchange studies: a review and perspective, *Agricultural and Forest Meteorology*, 113 (1-4), 159-183, 2002.
- Schuepp, P. H., Leclerc, M. Y., Macpherson, J. I. and Desjardins, R. L., Footprint Prediction of Scalar Fluxes from Analytical Solutions of the Diffusion Equation, *Boundary-Layer Meteorology*, 50 (1-4), 353-373, 1990.
- Sellden, G. and Pleijel, H., Photochemical oxidant effects on vegetation - Response in relation to plant strategy, *Water Air and Soil Pollution*, 85 (1), 111-122, 1995.
- Sillman, S., The relation between ozone, NO<sub>x</sub> and hydrocarbons in urban and polluted rural environments, *Atmospheric Environment*, 33 (12), 1821-1845, 1999.
- Simmonds, P. G., Derwent, R. G., Manning, A. L. and Spain, G., Significant growth in surface ozone at Mace Head, Ireland, 1987-2003, *Atmospheric Environment*, 38 (28), 4769-4778, 2004.
- Simpson, D., Fagerli, H., Jonson, J. E., Tsyro, S., Wind, P. and Tuovinen, J. P., PART 1: Unified EMEP Model Description., EMEP/MS-CW, EMEP Report 1/2003, 2003a. <http://www.emep.int/UniDoc/report.html>
- Simpson, D., Guenther, A., Hewitt, C. N. and Steinbrecher, R., Biogenic Emissions in Europe .1. Estimates and Uncertainties, *Journal of Geophysical Research-Atmospheres*, 100 (D11), 22875-22890, 1995.
- Simpson, D., Tuovinen, J. P., Emberson, L. and Ashmore, M. R., Characteristics of an ozone deposition module II: Sensitivity analysis, *Water Air and Soil Pollution*, 143 (1-4), 123-137, 2003b.
- Simpson, D., Winiwarter, W., Borjesson, G., Cinderby, S., Ferreiro, A., Guenther, A., Hewitt, C. N., Janson, R., Khalil, M. A. K., Owen, S., Pierce, T. E., Puxbaum, H., Shearer, M., Skiba, U., Steinbrecher, R., Tarrason, L. and Oquist, M. G., Inventorying emissions from nature in Europe, *Journal of Geophysical Research-Atmospheres*, 104 (D7), 8113-8152, 1999.
- Smith, R. I., Fowler, D., Sutton, M. A., Flechard, C. and Coyle, M., Regional estimation of pollutant gas dry deposition in the UK: model description, sensitivity analyses and outputs, *Atmospheric Environment*, 34 (22), 3757-3777, 2000.
- Smolarkiewicz, P. K. and Rasch, P. J., Monotone Advection on the Sphere - an Eulerian Versus Semi- Lagrangian Approach, *Journal of the Atmospheric Sciences*, 48 (6), 793-810, 1991.
- Soja, G. and Soja, A. M., Wheat as an ozone sensitive crop, *Acta Phytopathologica Et Entomologica Hungarica*, 30 (1-2), 59-70, 1995.
- Solberg, S., Bergstrom, R., Langner, J., Laurila, T. and Lindskog, A., Changes in Nordic surface ozone episodes due to European emission reductions in the 1990s, *Atmospheric Environment*, 39 (1), 179-192, 2005.
- Solmon, F., Sarrat, C., Serca, D., Tulet, P. and Rosset, R., Isoprene and monoterpenes biogenic emissions in France: modeling and impact during a regional pollution episode, *Atmospheric Environment*, 38 (23), 3853-3865, 2004.
- Sorimachi, A., Sakamoto, K., Ishihara, H., Fukuyama, T., Utiyama, M., Liu, H., Wang, W., Tang, D., Dong, X. and Quan, H., Measurements of sulfur dioxide and ozone dry deposition over short vegetation in northern China - a preliminary study, *Atmospheric Environment*, 37 (22), 3157-3166, 2003.
- Staehelin, J. and Schmid, W., Trend Analysis of Tropospheric Ozone Concentrations Utilizing the 20-Year Data Set of Ozone Balloon Soundings

- over Payerne (Switzerland), *Atmospheric Environment Part a-General Topics*, 25 (9), 1739-1749, 1991.
- Stedman, J. R., 2003, Current 1 km x 1 km maps of NO, NO<sub>2</sub> and NO<sub>x</sub> concentrations and emissions for the UK - personal communication
- Stedman, J. R., Vincent, K. J., Campbell, G. W., Goodwin, J. W. L. and Downing, C. E. H., New high resolution maps of estimated background ambient NO<sub>x</sub> and NO<sub>2</sub> concentrations in the UK, *Atmospheric Environment*, 31 (21), 3591-3602, 1997.
- Stevenson, D. S., Collins, W. J., Johnson, C. E. and Derwent, R. G., Intercomparison and evaluation of atmospheric transport in a Lagrangian model (STOCHEM), and an Eulerian model (UM), using Rn-222 as a short-lived tracer, *Quarterly Journal of the Royal Meteorological Society*, 124 (551), 2477-2491, 1998a.
- Stevenson, D. S., Johnson, C. E., Collins, W. J., Derwent, R. G., Shine, K. P. and Edwards, J. M., Evolution of tropospheric ozone radiative forcing, *Geophysical Research Letters*, 25 (20), 3819-3822, 1998b.
- Stohl, A., Wernli, H., James, P., Bourqui, M., Forster, C., Liniger, M. A., Seibert, P. and Sprenger, M., A new perspective of stratosphere-troposphere exchange, *Bulletin of the American Meteorological Society*, 84 (11), 1565-+, 2003.
- Stull, R. B., *An introduction to boundary layer meteorology*, Kluwer Academic Publishers, The Netherlands, 1989.
- Sutton, M. and Fowler, D., Dry deposition of ammonia to frozen land surfaces and analysis of the uncertainties in fluxes deriving from measurement errors., in *COST 611 Workshop . Development of analytical techniques for air pollution measurement.*, edited by I. Allegrini, pp. pp 9-19, CEC, Brussels., Rome (April 1992), 1992.
- Sutton M.A., Pitcairn C.E.R. & Fowler D. The Exchange of Ammonia between the Atmosphere and Plant-Communities. In: *Advances in Ecological Research*, Vol 24, pp. 301-393. 1993.
- Sutton, M. A., Fowler, D. and Moncrieff, J. B., The Exchange of Atmospheric Ammonia with Vegetated Surfaces .1. Unfertilized Vegetation, *Quarterly Journal of the Royal Meteorological Society*, 119 (513), 1023-1045, 1993.
- Sutton, M. A., Burkhardt, J. K., Guerin, D., Nemitz, E. and Fowler, D., Development of resistance models to describe measurements of bi-directional ammonia surface-atmosphere exchange, *Atmospheric Environment*, 32 (3), 473-480, 1998.
- Swap, R. J., Szuba, T. A., Garstang, M., Annegarn, H. J., Marufu, L. and Piketh, S. J., Spatial and temporal assessment of sources contributing to the annual austral spring mid-tropospheric ozone maxima over the tropical South Atlantic, *Global Change Biology*, 9 (3), 336-345, 2003.
- Tardieu, F. and Davies, W. J., Stomatal Response to Abscisic-Acid Is a Function of Current Plant Water Status, *Plant Physiology*, 98 (2), 540-545, 1992.
- Tardieu, F. and Davies, W. J., Integration of Hydraulic and Chemical Signaling in the Control of Stomatal Conductance and Water Status of Droughted Plants, *Plant Cell and Environment*, 16 (4), 341-349, 1993.
- Thom, A. S., Momentum, mass and heat exchange of plant communities, in *Vegetation and the Atmosphere*, edited by J. L. Monteith, pp. 57-109, Academic Press, London, 1975.
- Thunis, P. and Cuvelier, C., Impact of biogenic emissions on ozone formation in the Mediterranean area - a BEMA modelling study, *Atmospheric Environment*, 34 (3), 467-481, 2000.
- Trickl, T., Cooper, O. R., Eisele, H., James, P., Mucke, R. and Stohl, A., Intercontinental transport and its influence on the ozone concentrations

- over central Europe: Three case studies, *Journal of Geophysical Research-Atmospheres*, 108 (D12), art. no.-8530, 2003.
- Tuovinen, J. P., Ashmore, M. R., Emberson, L. D. and Simpson, D., Testing and improving the EMEP ozone deposition module, *Atmospheric Environment*, 38 (15), 2373-2385, 2004.
- Turner, N. C., Measurement and influence of environmental and plant factors on stomatal conductance in the field, *Agricultural and Forest Meteorology*, 54 (2-4), 137-154, 1991.
- Tuzet, A., Perrier, A. and Leuning, R., A coupled model of stomatal conductance, photosynthesis and transpiration, *Plant Cell Environ*, 26 (7), 1097-1116, 2003.
- Twine, T. E., Kustas, W. P., Norman, J. M., Cook, D. R., Houser, P. R., Meyers, T. P., Prueger, J. H., Starks, P. J. and Wesely, M. L., Correcting eddy-covariance flux underestimates over a grassland, *Agricultural and Forest Meteorology*, 103 (3), 279-300, 2000.
- UNECE, Workshop on critical levels for buildings, materials, including cultural heritage., edited by DoE, Defra (formerly DoE), London, 1993.
- Utiyama, M., Fukuyama, T., Maruo, Y. Y., Ichino, T., Izumi, K., Hara, H., Takano, K., Suzuki, H. and Aoki, M., Formation and deposition of ozone in a red pine forest, *Water Air and Soil Pollution*, 151 (1-4), 53-70, 2004.
- Valentin, K. M., Numerical modelling of the climatological and anthropogenic influences on the chemical composition of the troposphere since the last glacial maximum, Mainz, Germany, Mainz, 1990.
- van Hove, L. W. A., Bossen, M. E., San Gabino, B. G. and Sgreva, C., The ability of apoplastic ascorbate to protect poplar leaves against ambient ozone concentrations: a quantitative approach, *Environmental Pollution*, 114 (3), 371-382, 2001.
- Van Oijen, M., Buker, P., Coyle, M., Fowler, D., Hargreaves, K., Hayes, F., Levy, P., Mills, G. and Murray, M., O3 GRASSLAND: a CEH Integrating Fund Project 2001-2003, Centre for Ecology and Hydrology, C01756, 2003. <http://www.atmosci.ceh.ac.uk/docs/O3GRASSLAND.htm>
- van Oijen, M., Dreccer, M. F., Firsching, K. H. and Schnieders, B., Simple equations for dynamic models of the effects of CO<sub>2</sub> and O<sub>3</sub> on light-use efficiency and growth of crops, *Ecological Modelling*, 179 (1), 39-60, 2004.
- van Oijen, M., Firsching, K. H. and Schnieders, B. J., Modelling the effects of CO<sub>2</sub> and O<sub>3</sub> on light-use efficiency and growth of crops: theoretical paper, pp. 25, 1998.
- Vila-Guerau de Arellaano, J., Duynkerke, P. G. and Builtjes, P. J. H., The Divergence of the Turbulent-Diffusion Flux in the Surface- Layer Due to Chemical-Reactions - the No-O<sub>3</sub>-No<sub>2</sub> System, *Tellus Series B-Chemical and Physical Meteorology*, 45 (1), 23-33, 1993.
- Vingarzan, R., A review of surface ozone background levels and trends, *Atmospheric Environment*, 38 (21), 3431-3442, 2004.
- Volz, A. and Kley, D., Evaluation of the montsouris series of ozone measurements made in the 19th-century, *Nature*, 332 (6161), 240-242, 1988.
- Vuorinen, T., Nerg, A.-M. and Holopainen, J. K., Ozone exposure triggers the emission of herbivore-induced plant volatiles, but does not disturb tritrophic signalling, *Environmental Pollution*, 131 (2), 305-311, 2004.
- Walcek, C. J., Brost, R. A., Chang, J. S. and Wesely, M. L., So<sub>2</sub>, Sulfate and Hno<sub>3</sub> Deposition Velocities Computed Using Regional Land-Use and Meteorological Data, *Atmospheric Environment*, 20 (5), 949-964, 1986.

- Walton, S., Gallagher, M. W. and Duyzer, J. H., Use of a detailed model to study the exchange of NO<sub>x</sub> and O<sub>3</sub> above and below a deciduous canopy, *Atmospheric Environment*, 31 (18), 2915-2931, 1997.
- Wang, D., Hinckley, T. M., Cumming, A. B. and Braatne, J., A comparison of measured and modeled ozone uptake into plant-leaves, *Environmental Pollution*, 89 (3), 247-254, 1995.
- Wauben, W. M. F., Fortuin, J. P. F., van Velthoven, P. F. J. and Kelder, H. M., Comparison of modeled ozone distributions with sonde and satellite observations, *Journal of Geophysical Research-Atmospheres*, 103 (D3), 3511-3530, 1998.
- Webb, E. K., Profile relationships: the log-linear range, and extension to strong stability, *Quarterly Journal Royal Meteorological Society*, 96, 67-90, 1970.
- Webb, E. K., Pearman, G. I. and Leuning, R., Correction of flux measurements for density effects due to heat and water vapour transfer, *Quarterly Journal of the Royal Meteorological Society*, 106, 85-100, 1980.
- Weiss, A. and Norman, J. M., Partitioning Solar-Radiation into Direct and Diffuse, Visible and near-Infrared Components, *Agricultural and Forest Meteorology*, 34 (2-3), 205-213, 1985.
- Wesely, M. L., Parameterization of Surface Resistances to Gaseous Dry Deposition in Regional-Scale Numerical-Models, *Atmospheric Environment*, 23 (6), 1293-1304, 1989.
- Wesely, M. L., Cook, D. R. and Williams, R. M., Field Measurement of Small Ozone Fluxes to Snow, Wet Bare Soil, and Lake Water, *Boundary-Layer Meteorology*, 20 (4), 459-471, 1981.
- Weston, K., Fowler, D. and Smith, R., Rural Exposure to Ozone over the UK, in *Air Pollution II, Vol 2: Pollution Control and Monitoring*, pp. 237-244, 1994.
- Wilczak, J. M., Oncley, S. P. and Stage, S. A., Sonic Anemometer Tilt Correction Algorithms, *Boundary-Layer Meteorology*, 99 (1), 127-150, 2001.
- Wild, O., Prather, M. J., Akimoto, H., Sundet, J. K., Isaksen, I. S. A., Crawford, J. H., Davis, D. D., Avery, M. A., Kondo, Y., Sachse, G. W. and Sandholm, S. T., Chemical transport model ozone simulations for spring 2001 over the western Pacific: Regional ozone production and its global impacts - art. no. D15S02, *Journal of Geophysical Research-Atmospheres*, 109 (D15), S1502, 2004.
- Williamson, D. L. and Rasch, P. J., Two-Dimensional Semi-Lagrangian Transport with Shape-Preserving Interpolation, *Monthly Weather Review*, 117 (1), 102-129, 1989.
- Wilson, K., Goldstein, A., Falge, E., Aubinet, M., Baldocchi, D., Berbigier, P., Bernhofer, C., Ceulemans, R., Dolman, H., Field, C., Grelle, A., Ibrom, A., Law, B. E., Kowalski, A., Meyers, T., Moncrieff, J., Monson, R., Oechel, W., Tenhunen, J., Valentini, R. and Verma, S., Energy balance closure at FLUXNET sites, *Agricultural and Forest Meteorology*, 113 (1-4), 223-243, 2002.
- Wu, Y. H., Brashers, B., Finkelstein, P. L. and Pleim, J. E., A multilayer biochemical dry deposition model - 1. Model formulation - art. no. 4013, *Journal of Geophysical Research-Atmospheres*, 108 (D1), 4013, 2003.
- Yu, G. R., Nakayama, K., Matsuoka, N. and Kon, H., A combination model for estimating stomatal conductance of maize (*Zea mays* L.) leaves over a long term, *Agricultural and Forest Meteorology*, 92 (1), 9-28, 1998.
- Zeller, K., Wintertime ozone fluxes and profiles above a subalpine spruce- fir forest, *Journal of Applied Meteorology*, 39 (1), 92-101, 2000.
- Zeller, K. F. and Nikolov, N. T., Quantifying simultaneous fluxes of ozone, carbon dioxide and water vapor above a subalpine forest ecosystem, *Environmental Pollution*, 107 (1), 1-20, 2000.

- Zhang, L., Brook, J. R. and Vet, R., A revised parameterization for gaseous dry deposition in air- quality models, *Atmospheric Chemistry and Physics*, 3, 2067-2082, 2003.
- Zhang, L., Moran, M. D. and Brook, J. R., A comparison of models to estimate in-canopy photosynthetically active radiation and their influence on canopy stomatal resistance, *Atmospheric Environment*, 35 (26), 4463-4470, 2001.
- Zhang, L. M., Brook, J. R. and Vet, R., On ozone dry deposition - with emphasis on non-stomatal uptake and wet canopies, *Atmospheric Environment*, 36 (30), 4787-4799, 2002.
- Zheng, Y., Stevenson, K. J., Barrowcliffe, R., Chen, S., Wang, H. and Barnes, J. D., Ozone levels in Chongqing: a potential threat to crop plants commonly grown in the region?, *Environmental Pollution*, 99 (3), 299-308, 1998.
- Zheng, Y. B., Lyons, T., Ollerenshaw, J. H. and Barnes, J. D., Ascorbate in the leaf apoplast is a factor mediating ozone resistance in *Plantago major*, *Plant Physiology and Biochemistry*, 38 (5), 403-411, 2000.